WOFEX 2021

http://wofex.vsb.cz/2021/

19th annual workshop,
Ostrava, 1st September 2021
Proceedings of papers

Organized by

VSB – Technical University of Ostrava
Faculty of Electrical Engineering and Computer Science

VSB TECHNICAL UNIVERSITY OF OSTRAVA | FACULTY OF ELECTRICAL ENGINEERING AND COMPUTER SCIENCE

WOFEX 2021

ISBN 978-80-248-4523-4 (on-line)

DOI 10.31490/9788024845234

Page count: 467
Edition: 1st
First published: 2021

This proceedings was typeset by pdfLaTeX.

Published by Faculty of Electrical Engineering and Computer Science, VSB – Technical University of Ostrava

Preface

The workshop WOFEX 2021 (PhD workshop of Faculty of Electrical Engineering and Computer Science) was held on September 1st September 2021 at the VŠB – Technical University of Ostrava. The workshop offers an opportunity for students to meet and share their research experiences, to discover commonalities in research and studentship, and to foster a collaborative environment for joint problem solving. PhD students are encouraged to attend in order to ensure a broad, unconfined discussion. In that view, this workshop is intended for students and researchers of this faculty offering opportunities to meet new colleagues.

This book of proceedings includes 76 papers of faculty PhD students. The proceedings of WOFEX 2021 are also available at the web site http://wofex.vsb.cz/2021/. I would like to thank the authors and the Organizing Committee from Department of Computer Science, namely Jiří Dvorský and Pavel Moravec, for their arduous editing work.

September 2021

Michal Krátký
Program Committee Chair
WOFEX 2021

Organization

Program Committee

Chair:

Michal Krátký (VSB – Technical University of Ostrava)

Members:

Pavel Brandštetter (VSB – Technical University of Ostrava)
Radim Briš (VSB – Technical University of Ostrava)
Zdeněk Dostál (VSB – Technical University of Ostrava)
Petr Chlebiš (VSB – Technical University of Ostrava)
Jiří Luňáček (VSB – Technical University of Ostrava)
Stanislav Rusek (VSB – Technical University of Ostrava)
Václav Snášel (VSB – Technical University of Ostrava)
Vladimír Vašinek (VSB – Technical University of Ostrava)
Miroslav Vozňák (VSB – Technical University of Ostrava)
Ivan Zelinka (VSB – Technical University of Ostrava)

Organizing Committee

Jiří Dvorský (VSB – Technical University of Ostrava)
Pavel Moravec (VSB – Technical University of Ostrava)
Hana Dluhošová (VSB – Technical University of Ostrava)

Technical Program Committee

Marek Dvorský (VSB – Technical University of Ostrava)
Stanislav Kocman (VSB – Technical University of Ostrava)
Jan Kubíček (VSB – Technical University of Ostrava)
Pavel Moravec (VSB – Technical University of Ostrava)
Marek Nikodým (VSB – Technical University of Ostrava)
Tadeusz Sikora (VSB – Technical University of Ostrava)
Libor Štěpanec (VSB – Technical University of Ostrava)
Oldřich Vlach (VSB – Technical University of Ostrava)

Workshop Location:

Campus of VSB – Technical University of Ostrava
17. listopadu 2172/15, 708 00 Ostrava–Poruba, Czech Republic
1st September 2021
http://wofex.vsb.cz/2021/

Table of Contents

Study Programme P1807 Computer Science, Communication Technology and Applied Mathematics

Informatics (1801V001)

Computational and Applied Mathematics (1103V036)

Communication Technology (2601V018)

Study Programme P0713D060003/P0713D060004 Electrical Power Engineering

Study Programme P0714D150001/P0714D150002 Cybernetics

Study Programme P0613D140005/P0613D140006 Computer Science

Study Programme P0613D140020/P0613D140021 Computational Science

Study Programme P0714D060001/P0714D060002 Communication Technology

Study Programme P0533D110005/P0533D110006 Applied Physics

Study Programme P0588D140003/P0588D140004 Bioinformatics and Computational Biology

Study Programme P0541D170005/P0541D170006 Computational and Applied Mathematics

Study Programme P0713D060002/P0713D060001 Electrical Engineering Science

Author Index

Measurement of Outdoor Lighting System with a Focus on Obtrusive Light in the Area of the Electrical Substation TR Slavětice

Petr Běčák and Tomáš Novák

Department of Electrical Power Engineering, FEECS,
VSB – Technical University of Ostrava, 17. listopadu 15,
708 00 Ostrava – Poruba, Czech Republic
petr.becak@vsb.cz

Abstract. The article is focused on the electrical substation TR Slavětice: the lighting system for surveillance lighting, main road lighting and lighting of the entrances to the houses of secondary equipment is fitted by LED luminaires. Operational lighting including illumination of distribution fields and illumination of transformers, shunt reactors and terciars is fitted by luminaires equipped with high-pressure sodium and metal halide lamps. The surveillance lighting of the electrical substation works together with camera systems of technical system of physical protection (TSPP). The right choice of security cameras is essential at the beginning. Cameras should have a sufficient sensitivity and a resolution to detect objects properly in both day and night hours. The designing of the surveillance lighting is necessary for the camera system TSPP to work reliably and to provide expected information. The surveillance lighting is designed with respect to the position and height of the monitoring cameras and by this calculation it is set the height of the luminaires, their pitch and the appropriate type and power of the luminaire. At present, most of the lighting systems are provided by LED luminaires which compared with high-pressure sodium lamps have many benefits. Mainly wide range of luminous intensity distribution curves. Operational lighting is necessary to achieve the optimal level of illumination for inspection and possible repairs directly in the distribution fields of the electrical substation, transformers, shunt reactors and terciars. All-purpose lighting of the electrical substation causes the generation of the luminous flux into the upper hemisphere. The electrical substation TR Slavětice has all lighting systems installed without tilting the luminaires. This results only a reflected luminous flux into the upper hemisphere. This fact is also proved by the luminous analysis images.

Keywords: Measurement, Electrical Substation, Luminance Analysis, Obtrusive Light, Surveillance Lighting.

1 Introduction

The outdoor lighting of ČEPS electrical substations has undergone rapid development for the last twelve years. This development is due to several important factors. The first factor to be mentioned is the big pressure of ČEPS on the safety of its employees, which was reflected in the requirement to ensure an adequate visual task (visibility) in the hazardous areas of electrical substations not only during the day but also at night. Lighting systems operating from twilight to sunrise slightly above 4000 hours per year, which is almost half of the total number of hours per year (8760 hours) in which a fault can occur. This fault must be rectified immediately. The second important factor that led to the development of lighting systems for ČEPS outdoor electrical substations was the increased requirement to ensure the safety of the electrical substation itself. This requirement also resulted from the gradual transition to remote control of electrical substations. Originally, a microwave system with infrabarriers was used to protect the perimeter. However, it was unreliable and it generated a large number of false alarms. The optimal solution is a surveillance lighting of the perimeter and roads, which is able to provide both illumination of the area around the fence (horizontal illumination) and visibility of the electrical substation area with respect to the surroundings. Lighting systems both for surveillance purposes and for road lighting are optimized for camera system sensing requirements. The third factor was the beginning of the rapid development of new technology in lighting technology. Mainly use of the modern light sources with high efficiency in the conversion of electricity into luminous flux (LED). We must not forget the new precise and also highly efficient optical systems for directing the luminous flux which can ensure uniform illumination in illuminated areas with a minimum requirement of power consumption and with a minimum of light trespass [1], [2].

There is another factor associated with light trespass - the reduction of the obtrusive light. The significant pressure on the environment, with which the reduction of the obtrusive light is associated, was the reason for the overall change in the operation and location of lighting systems. The lighting systems were divided into those that are designed for operate all night, ie. surveillance lighting cooperating with the camera system TSPP and helping to make the perimeter and critical areas visible at the entrances to the houses of secondary equipment, and lighting systems designed to operate only in the presence of persons in the electrical substation in critical situations. It includes operational lighting including illumination of distribution fields and illumination of transformers, shunt reactors, terciars and road lighting. This relatively simple and functional division of lighting systems has reduced the total energy intensity and also significantly reduced the generation of the luminous flux outside the electrical substation and into the upper hemisphere. Another important step in reducing the emission of the luminous flux outside the electrical substation was to optimize the placement of the luminaires and ensure lighting from top to bottom, not from bottom to top. It could be achieved by installing asymmetrical luminaires with flat glass and horizontally placed optics on the portal structures of the substation itself and using the maximum heights of public lighting pillar to place other luminaires [3], [4].

2 Surveillance lighting and its requirements

Luminaires for public lighting are used for the surveillance lighting, either with high-pressure sodium lamps or with LED. The electrical substation TR Slavětice uses LED technology. The surveillance lighting serves to illuminate the perimeter of the electrical substation in order to ensure the functionality of the security camera systems (TSPP) of the security guard. The surveillance lighting is installed along the entire fence of the electric station, including the entrances to the houses and the central house, the entrances and along the fencing, which separates distribution system operator EG.D substation area from transmission system ČEPS part. Luminaires with the luminous intensity distribution curve for public lighting systems are used for illuminating the area along the fencing to provide the surveillance lighting. The lighting points are located inside the electrical substation between 2.5 to 4 meters from the fence. Luminaires are directed towards the fence. Requirements for the surveillance lighting are defined according to the technical standard TN/59/2016 of revision No. 3 as follows: the average maintained vertical illumination must be at least 10 lx. The illumination is evaluated from the point of view of the security camera at a height of 1 m above the terrain. The average maintained horizontal illumination of the reference section between the two light points must be at least 10 lx. Uniformity requirements for both cases are $U_0 = 0.4$. The limit value of the glare rating limits GRL shall not be greater than 45. The color rendering index of the lighting sources used must be at least 20. When lighting is designed it is recommended that the luminaires be placed in a higher vertical level as a security camera. Luminaires must be placed in such a way that they do not cause the camera to glare and cause the camera to pass into a saturated state.

The functionality of security cameras is that it picks up the luminance of illuminated objects. The greatest luminance is achieved when the luminous flux enters the illuminated object from the viewpoint of the camera. Standard cameras have a minimum sensitivity for color mode E = 0.4 lx and for black and white mode E = 0.05 lx. This is illumination on the chip of security camera. According to specialists, these values are however very low and their generalization may cause camera malfunctions, for example switching from the color mode to the black and white mode.

In order to ensure the optimal and correct functioning of the camera and the contrast, it is necessary that the illumination value for the color mode is at least 15 lx and for black and white 10 lx. This illumination must be at least 70 % of the area occupied by the scene. To avoid overturning, and thus reduce an image resolution, it is necessary to balance the illumination, i.e. the ratio of maximum intensity to minimum intensity, in a ratio of 6 : 1, at 4 : 1 (zoomed out) points [5].

3 Surveillance lighting and its requirements

The views of the luminance camera correspond to the possible views of the security cameras. These views are chosen as the most critical possible views of security cameras, whose task is to guard the area of the electrical substation. To evaluate the

luminance analysis, the figurines had different reflectance of the clothes, and gradually changed their positions. The luminous analysis was performed for 5 positions of the figurines for each reference section of the surveillance lighting.

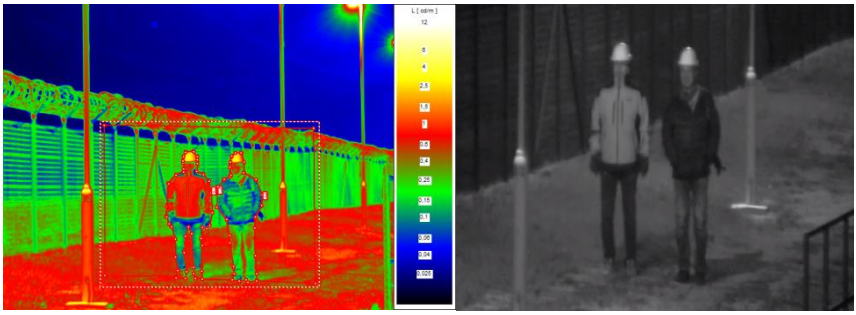

Fig. 1. Luminance analysis (left) and camera record (right).

Table 1. Calculated values from the luminance analysis of the figurines on the position 3.

	Luminance analysis of figurines				
Position 3	Average luminance of figurine		Average background luminance ($cd \cdot m^{-2}$)	Contrast of figurines and background	
	Left ($cd \cdot m^{-2}$)	Right ($cd \cdot m^{-2}$)		Left (-)	Right (-)
	0.503	0.278	0.380	0.323	0.270

Table 2. Measured horizontal and camera illuminantion on the position 3.

	Measured illuminance	
Position 3	Horizontal illumination of the referent section (lx)	Camera illumination of the referent section (lx)
	12.7	16.7

The following luminance images show the electrical substation in the surveillance lighting mode and all-purpose lighting mode – the electrical substation completely on.

The luminance analysis was evaluated for the same range of luminances in order to be able to visually compare individual cases of the generated luminous flux into the upper hemisphere.

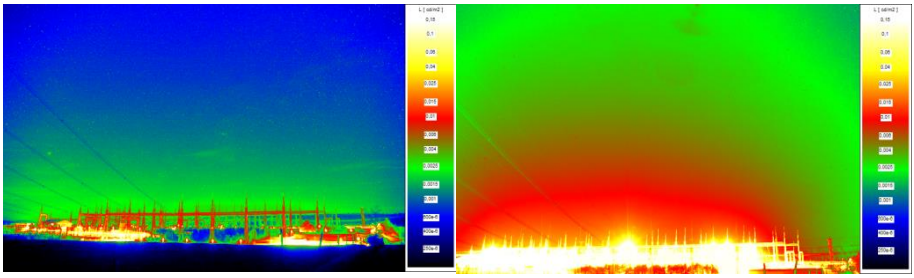

Fig. 2. Only the surveillance lighting is on (left) and all-purpose lighting is on (right).

Dark surroundings signal the minimal effect of the surveillance lighting on the lighting around the substation. Increased brightness can be observed only in the perimeter areas of the electrical substation and in the area managed by EG.D.

When the electrical substation is completely on, it is possible to identify (in the middle of the luminance map) an increased generation of luminous flux into the upper hemisphere, which is caused by improperly directed luminaire for lighting transformers. This fact does not need to be solved, because the lighting of the transformers only works in the event of a fault in the electrical substation and when testing the operation of the lighting systems.

Following luminance analysis was evaluated again for the same range of luminances in order to be able to visually compare individual cases of the generated luminous flux into the upper hemisphere.

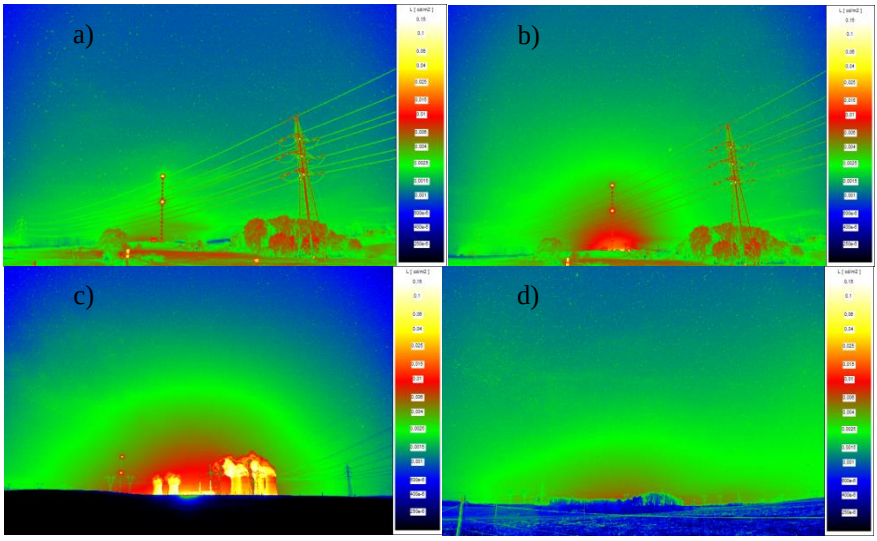

Fig. 3. Luminance maps of the surroundings of the power station generated to assess the influence of the electrical substation on the increased sky glow: a) TR Slavětice - surveillance lighting mode, b) TR Slavětice - all-purpose lighting mode, c) NPP Dukovany, d) Brno.

To compare the influence of light sources in the near and distant surroundings, the paper presents luminance maps with views of the nuclear power plant Dukovany from the TR Slavětice power station, reciprocally opposite view from the nuclear power plant Dukovany to the TR Slavětice when surveillance lighting mode and all-purpose lighting is on and also a view from the electrical substation TR Slavětice towards Brno (about 35 km as the crow flies).

The luminance maps show the minimal influence of the electrical substation TR Slavětice in the standard mode of operation (more than 99 % of the total operation of lighting systems). The electrical substation TR Slavětice in all-purpose lighting mode (in operation only a few hours per year) is still a significantly smaller light source (measured from the same distance) than the nuclear power plant Dukovany and a comparable radiation source in the given area as Brno.

4 Conclusion

Based on the above approaches to the design and implementation of large outdoor lighting systems, it can be stated that according to current standards and with a sensitive approach to the installation of lighting systems and their operation, it is possible to implement quality lighting systems. These meet not only in terms of visual requirements, but also in terms of minimizing power consumption. Furthermore, ensuring the overall safety of the illuminated space, and at the same time it is possible to minimize the influence of lighting systems on the night environment by increased brightness of the surroundings, or increased sky glow. [6]

References

1. Novák, T., Ullman, I., Sokanský, K.: Osvětlování venkovních pracovních prostor v kombinaci s kamerovými systémy. In: Kurz osvětlovací techniky XXVII, Kouty nad Desnou, 29. 9.– 1. 10. 2009. s. 316–322. ISBN 978-80-248-2087-3.
2. Habel, J., Dvořáček, K., Dvořáček, V., Žák, P.: Světlo a osvětlování. Praha: FCC Public, 2013. ISBN 978-80-86534-21-3. s. 429–431.
3. TN 59. Venkovní a vnitřní osvětlení v objektech elektrických stanic PS – Technická norma ČEPS 06/2010. Aktualizace 05/2016.
4. Sokasnký, K. a kol.: Světelná technika. Praha: České vysoké učení technické v Praze, 2011. ISBN 978-80-01-04941-9.
5. Baleja, R., Novák, T., Sokanský, K., Bos, P., Běčák, P.: Measurement of Outdoor Lighting with a Focus on Watchdog Lighting System in the Area of Electric Station TR Čechy Střed. In: 7th Lighting Conference of the Visegrad Countries, LUMEN V4 2018 – Proceedings. Article number 8521145. ISBN 978-153867923-4.
6. Ullman, I., Novák, T., Baleja, R., Běčák, P., Valíček, P., Ullman, J.: Měření venkovního osvětlení elektrických stanic ČEPS. Světlo – časopis pro světlo a osvětlování. Číslo 4-5. 2020. http://www.odbornecasopisy.cz/svetlo/casopis/tema/mereni-venkovniho-osvetleni-elektrickych-stanic-ceps--17338, last accessed 2021/13/07.

The Utilisation of Vehicle-to-Grid Technology in Power Engineering

Vojtech Blazek

Department of Electrical Power Engineering, FEECS,
VSB – Technical University of Ostrava, 17. listopadu 15,
708 00 Ostrava – Poruba, Czech Republic
vojtech.blazek@vsb.cz

Abstract. The article presents the potential use of Vehicle-to-Grid (V2G) technology and describes the developed testing platform of a Microgrid system with V2G support. V2G technologies enable battery capacity in an electric vehicle (EV) as a potential energy storage system for the distribution system. The platform, developed by the Centrum ENET research team, uses a control system based on Demand-side Response (DSR) methods, which seeks to optimise electricity consumption in the energy network effectively. Furthermore, by combining DSR and V2G technologies, the platform can utilise renewable electricity sources efficiently. Our iteration of DSR is named Active demand-side management (ADSM). The Microgrid control system with ADSM is based on artificial intelligence methods that opt to optimise the energy sources and appliances according to the priority plan of switching appliances. Finally, the article describes a simulation of an actual Microgrid model of a V2G system with a real scenario. These results will be used in the future to develop a Microgrid system located on campus VŠB – Technical University of Ostrava.

Keywords: Vehicle-to-Grid, Microgrid, Demand-side response, Renewable energy sources

1 Introduction

There is actual electric vehicle (EV) deployment in recent years, both in local and global measures [1]. With this growth are connected newly appeared ideas and technologies to utilise EV batteries in non-traditional ways [2], [3]. Vehicle-to-Grid (V2G) includes a set of technologies that allow the use of the capacity of connected EVs, hydrogen fuel cell electric vehicles (FCEV) or plug-in hybrids (PHEV), communicate with the power grid to sell demand response services by either returning electricity to the grid or by throttling their charging rate [3].

V2G technology utilises energy storage in EVs to store and discharge electricity generated from renewable energy sources (RES) such as solar and wind, with output fluctuating depending on the time of day and actual weather.[3] V2G technology can be used with vehicles that can be connected to a bidirectional V2G inverter. These are generally referred to as plug-in EVs and PHEV. Since about 95% of cars are parked at any given time, the batteries in EV could be used to let electricity flow from the car to the electric distribution network and back.

VSB – Technical University of Ostrava, 2021, ISBN 978-80-248-4523-4 (on-line).

Fig. 1. shows the potentially ideal use of EV as a possible supporting energy service in the Czech Republic. Consumption dates from 9th March 2021.

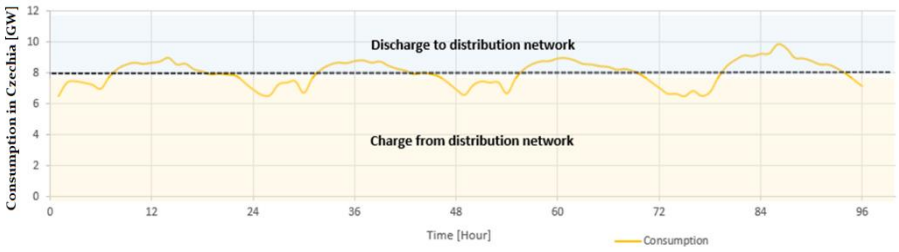

Fig. 1. Ideal use of V2G in Czechia

Today, advanced methods are used in energy to manage electricity consumption. These methods are unified under the term Demand-side response (DSR). Usually, (DSR) aims to encourage the consumer to use less energy during peak hours or move the energy use time to off-peak times such as nighttime and weekends.

Peak demand management does not necessarily decrease total energy consumption but could reduce the need for investments in networks and power plants to meet peak demands. An example is the use of energy storage units to store energy during off-peak hours and discharge them during peak hours. DSR with V2G technology represents a massive potential in the energy sector to streamline the production and consumption of electricity.

2 Testing Microgrid platform description

The centre of the Microgrid system is a hybrid inverter Schnieder Conext XW+ 8548 with 6.8 kW rated power. Accumulation is formed from 40 series-connected Ferak KPL 375 NiCd batteries with a 375 Ah, and 1.2 V rated Voltage. Two photovoltaic panels (monocrystalline and polycrystalline), each 2 kWp, are connected to the solar charge controller Xantrex XW MPPT 80 600. These controllers are DC coupled to the Microgrid. Another RES is a wind power plant with rated power 10 kW, AC-coupled through inverter Windy Boy 5000. Fig. 2 shows energy flow in our advanced Microgrid with V2H.

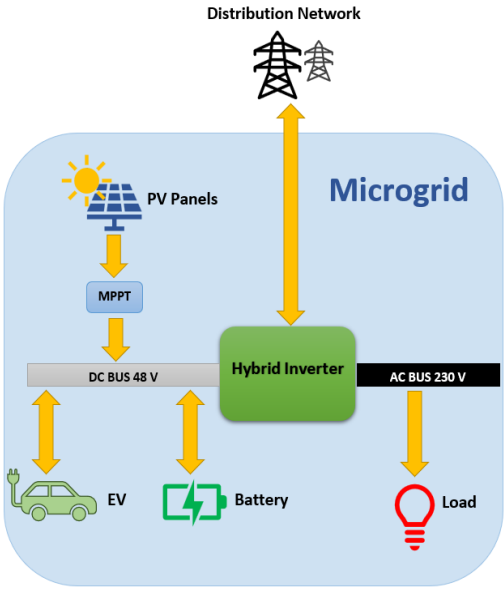

Fig. 2. Concept of energy flow in Microgrid with V2G

The Control system is driven Quido I/O module is used to control appliance switching physically. Many typical household appliances are present and connected to the system, and the programmable electronic load simulates those that are missing. The programmable electronic load has a maximum power of 4 kW with step 100 W and five options of power factor (1, 0.95 C or L and 0.5 C or L).

Active demand system management (ADSM) decides appliance switching according to the following factors – remaining energy in batteries, predicting energy consumption and generation. ADSM based on multiobjective optimisation (MOO) was applied in this experiment for hyperparameter optimisation of the random decision forest algorithm (RF). In general, the MOO problem is posed as an optimisation problem of several (mostly conflicting) objective functions [4]. According to the defined equality and inequality constraints, the input value vector X defines the search space (often called a feasible design space) for solutions. MOO is mainly based on search engine optimisation, but there is one significant difference from single-objective optimisation. In MOO, the number of solutions is defined as a feasible solution (called a Pareto front). Each of its candidates is called Pareto optimal and together, forming a so-called tradeoff curve in a chart of objective values. The Pareto optimal solutions are equally distributed on this curve toward all the optimisation functions. The solutions placed in the middle of the curve ideally hold the optimisation tradeoff toward the applied cost functions [5].

3 Experiment description

The experiment applies the ADSM system to an actual model of the Microgrid network with V2G technology. An EV with a battery capacity of 50 kWh will be connected to the system. EV was connected from 18 PM to 6 AM. The EV was connected with a 50% SoC battery, and at the end of the simulation, there was a requirement that the EV is SoC 50% again. The minimum capacity for an electric car was 5 kWh. The entire microgrid system is connected to the energy distribution network from 0 AM to 4 AM to replenish the necessary energy for its operation. Microgrid contains batteries with a total capacity of 18 kWh. The minimum capacity of a stationary battery in a microgrid system is 1.8 kWh. The microgrid system will have its own electricity consumption. This consumption represents the consumption of a real household with common electrical appliances. You can see the schedule of running appliances in Tab.1. In the simulation of the whole system, there are appliances with which the start of a start-up can be delayed.

Table 1. Appliance schedule

Appliances	ADSM	Day	Time (h:m)	Start (min)	Day	Time (h:m)	Start (min)	Day	Time (h:m)	Start (min)
Air conditioning	Yes	All days	5:00	60	All days	15:00	420			
Lights	No	All days	6:00	120	All days	18:00	240			
PC	No	All days	17:00	240	Fri	10:00	120			
Washing machine	Yes	Wed	18:00	120	Fri	18:00	120			
Fridge	All-day long									
TV	No	All days	6:00	120	Fri	16:00	360			
WiFi and standby mode in appliances	All-day long									
Boiler	Yes	All days	7:00	180	All days	20	120			
Kettle	No	All days	7:00	5	All days	15:45	5	All days	19:00	5
Microwave oven	No	All days	6:15	5	All days	16:00	5	All days	19:00	5
Vacuum cleaner	No	Wed	17:00	30	Wed					
Cooker	No	All days	10:00	180	All days					
Dishwasher	Yes	Mon	14:00	120	Wed	14:00	120	Fri	14:00	120

The schedule always shows the start time of the appliance and the time for which the appliance has been started. The missing energy that the Microgrid will be supplied from the external energy network. The simulation took place in 5 working days on weather data from 4th May to 9th May 2020.

4 Results

Fig. 3 and Fig. 4 show the consumption patterns in the V2H system. In the figures, you can see the current energy in the battery (*Battery*), car usage (*Car*), photovoltaics (*RES-PV*), Total consumption V2H (*Total LOAD*) and power supply from external network (*Grid supply*).

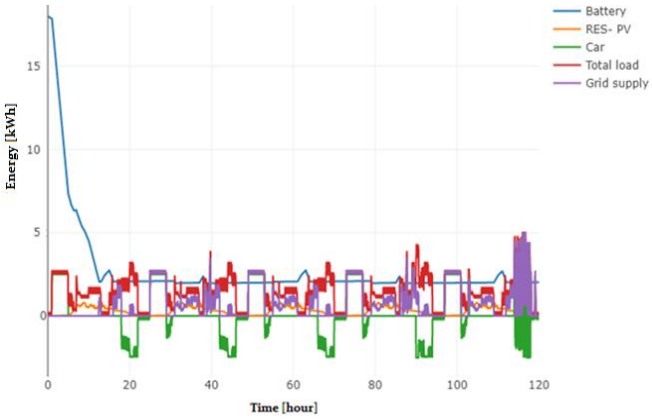

Fig. 3. Energy before optimisation

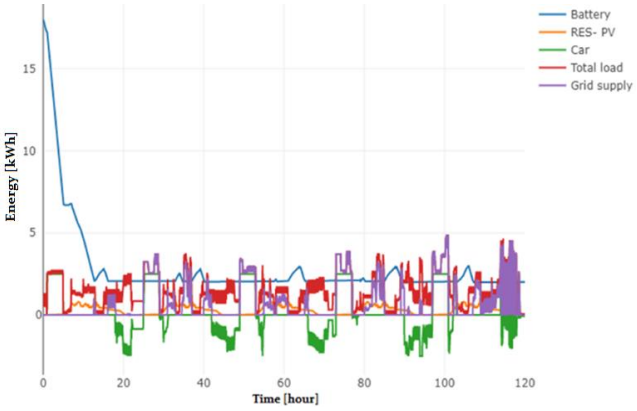

Fig. 4. Energy after optimization

Fig. 5 shows the effect of the ADSM optimisation with iteration on the energy-saving efficiency. This energy has to be supplied to the Microgrid from the external distribution network, or the regular operation of the Microgrid would be disrupted. In iteration 0, the optimisation was not started. The result of the simulation came out without optimisation came out 89.64 kWh. Results with ADSM optimisation is 67.96 kWh.

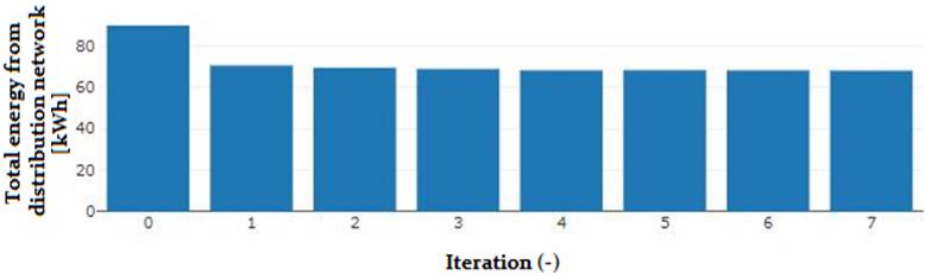

Fig. 5. Influence of optimisation iteration on optimisation efficiency

5 Conclusion

The article describes the potential use of V2G technology combined with DSR. The simulation results showed that the planned Microgrid with V2G technology could save up to 24.1% of total consumed energy over 5 days. Furthermore, according to the experiment results, the first iteration showed the highest increase in saved energy, and further iterations of optimisation no longer significantly affect the amount of saved energy.

In further work, we will continue to simulate various scenarios to create a dataset that will be used for future research purposes.

6 References

[1.] IEA (2019), "Global EV Outlook 2019", IEA, Paris, Accessed on: Jan. 23 2020, [Online], Available: https://www.iea.org/reports/global-ev-outlook-2019

[2.] Liu, C.; Chau, K. T.; Wu D. and Gao S. "Opportunities and Challenges of Vehicle-to-Home, Vehicle-to-Vehicle, and Vehicle-to-Grid Technologies," in Proceedings of the IEEE, vol. 101, no. 11, pp. 2409-2427, Nov. 2013. doi: 10.1109/JPROC.2013.2271951

[3.] Cleveland, Cutler J.; Morris, Christopher (2006). Dictionary of Energy. Amsterdam: Elsevier. p. 473. ISBN 978-0-08-044578-6.

[4.] Vantuch, T.; Mišák, S.; Ježowicz, T.; Buriánek, T.; Snášel, V. The power quality forecasting model for off-grid system supported by multiobjective optimisation. IEEE Trans. Ind. Electron. 2017, 64, 9507–9516.

[5.] Benson, Harold P. Multi-objective Optimization: Pareto Optimal Solutions, Properties. FLOUDAS, Christodoulos A. a Panos M. PARDALOS, ed. Encyclopedia of Optimization [online]. Boston, MA: Springer US, 2009, s. 2478-2481 [cit. 2021-7-21]. ISBN 978-0-387-74758-3. Dostupné z: doi:10.1007/978-0-387-74759-0_426

Design of an indoor substation

Michal Kotulla and Radomír Goňo

Department of Electrical Power Engineering, FEECS,
VSB – Technical University of Ostrava, 17. listopadu 15,
708 00 Ostrava – Poruba, Czech Republic
michal.kotulla.st@vsb.cz

Abstract. This paper is focused on design of an indoor substation, which will be used for education and testing. Paper includes description of the substation, design of a construction for all of devices, which was made. Operation of the substation is also part of this paper. Last thing are safety interlocks, which had to be made, otherwise safety of whole the whole substation was not achieved.

Keywords: Substation, Interlock system, disconnector, circuit breaker

1 Introduction

This paper describes design of an indoor substation, which will be used for laboratory metering, testing and demonstrations of substation operation. The substation will be designed to be able to handle three voltage levels 6 kV, 22 kV and 35kV. Each voltage level will have its own output, because of an individual laboratory metering and due to different rated voltages of used devices. Another unusual thing is a tight space in which the substation must fit in, that is why a construction for most of devices is needed. Safety is a number one priority and for that reason must be designed a hardwired interlock system to ensure safety of personnel and safe operation.

2 Description of substation

The substation will be powered from a three-phase circuit breaker *MCB* with rated voltage 400 V. Autotransformer *AT* is connected to the circuit breaker, which is feeding main transformer T1. Both main transformer and its disconnector *QZ1* with earthing switch *QE* and voltage measuring transformers *BVT1* are rated for 35 kV. After them are devices rated for 22 kV except of an air insulated switchgear *ZS1*, it is rated for 7,2 kV. Output from disconnector *QZ1* is connected to main circuit breaker *QB1* and current measuring transformers *BCT1*, which feeds a double busbar system through two disconnectors *QZ2*, *QZ3*. The double busbar system has a voltage measuring provided by voltage measuring transformers *BVT2, BVT3* and it has also a bus tie disconnector *QZ4*. Output for 22 kV is connected to the double busbar system and it consists of two disconnectors *QZ5, QZ6,* one main circuit breaker *QB2* and current

measuring transformers *TPU2*. Single-line diagram of a whole substation is shown in **Fig. 1**.

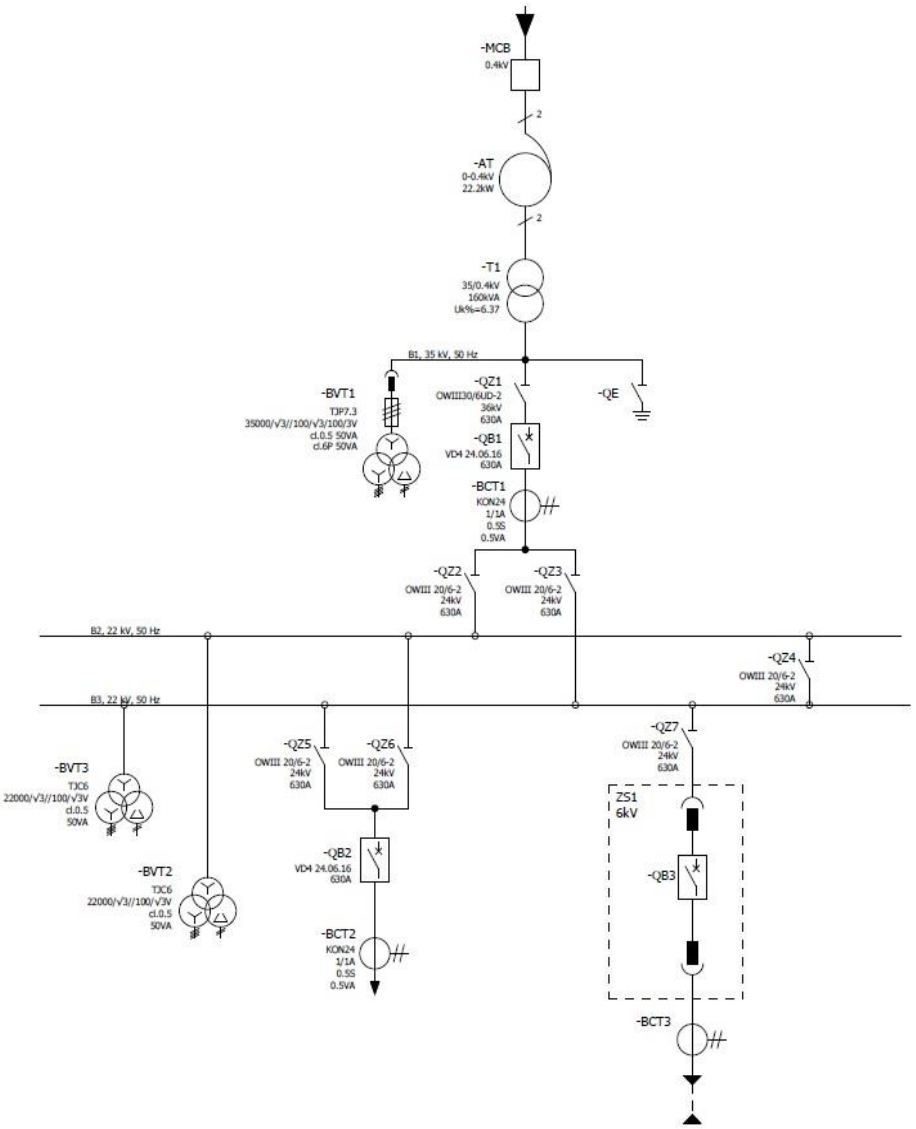

Fig. 1. Single-line diagram

3 Construction design

The space in which the substation must fit in is very small. Dimensions of the space are width 4630 mm, depth 1500 mm and height is about 6 meters. Design of the construction requires to utilize almost all space up to a ceiling. Construction will be

screwed to a floor and not to a wall because the material would not handle the weight of the substation. Outputs for 35 kV, 22 kV and 6 kV are made by isolators for each phase and they are also placed in a height, which prevents accidental touching. Whole substation will have fence around, because unqualified personnel will have access to it. The fence will contain openings for outputs and pair of doors. Hardwired interlocks will be installed to ensure a safety of personnel when entering space inside of fence. Distance between phases is 160 mm according to standard IEC61936-1. Busbars from main transformer *T1* to disconnector *QZ1* have distance between each other 360 mm, which is more than standard IEC61936-1 says.

4 Operation of substation

The substation has three separate outputs for each voltage level (which are 6 kV, 22 kV, 35 kV), but only one of them can be under voltage. Voltage selection is done by using a control cabinet, which will be installed close to the substation. Control cabinet's door contains selector switch with four positions. First of them represents an unenergized substation. Following positions represents individual voltage levels. When voltage level is selected, we may proceed with regulating the voltage to a required value. Increasing and decreasing voltage is done by two push buttons mounted on the door of control cabinet. The buttons are wired to control relay REU615, which is connected to autotransformer. Interlocks were implemented to a circuit for increasing the voltage, due to a different rated voltage of used devices. The door of control cabinet also contains a push buttons for each disconnector, earthing switch and main circuit breaker with which can be manually operated. Upper part of the door includes a voltage measuring with an emergency push button. Layout of the door is shown in **Fig. 2**.

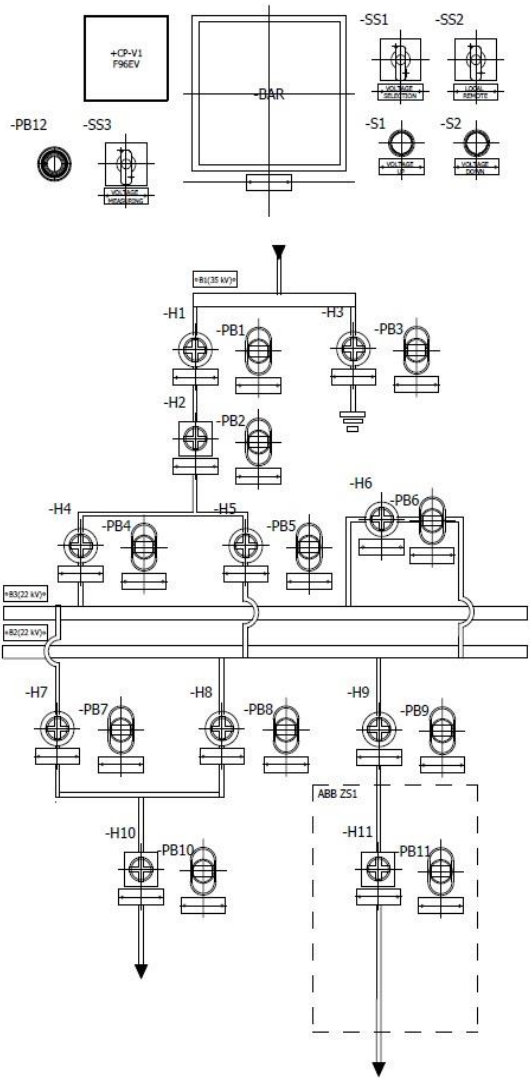

Fig. 2. Control cabinet's door layout

Startup sequence of the substation when it is unenergized (circuit breaker *MCB* opened) is following:

1. Selection of voltage level by using the selector switch.
2. Turn on or off individual disconnector and main circuit breaker according to which voltage level where selected.
3. Closing the circuit breaker *MCB.*
4. Setting a required voltage value by using push buttons on the door of control cabinet.

Startup sequence of the substation when it is energized (circuit breaker *MCB* closed) is following:

1. Decreasing voltage to zero value.
2. Selection of voltage level by using the selector switch.
3. Turn on or off individual disconnector and main circuit breaker according to which voltage level where selected.
4. Setting a required voltage value by using push buttons on the door of control cabinet.

5 Safety interlocks

The substation will serve to educational and testing purposes, that is why hardwired safety interlocks had to be made. Interlocks are also needed to ensure that devices operate correctly.
One of the interlocks is for locking disconnector *QZ1* in open position. Disconnector can be locked under following conditions:

- 35 kV is chosen with selector switch
- micro switch inbuild in autotransformer is opened by voltage exceeding 35 kV
- main circuit breaker *QB1* is closed
- earthing switch *QE* is closed
- if one of conditions above is active disconnector can be locked when it is in open position

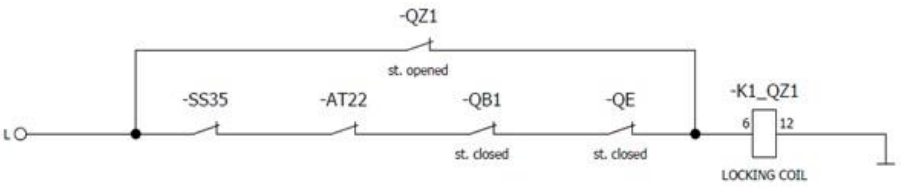

Fig. 3. Interlock for locking disconnector *QZ1*

Very important safety interlock is for increasing voltage, because only disconnector QZ1 and earthing switch QE are rated for 35 kV, which can main transformer T1 provide. The interlock is also protecting switchgear ZS1 against voltage higher than 6 kV. The interlock is shown in **Fig. 4**.

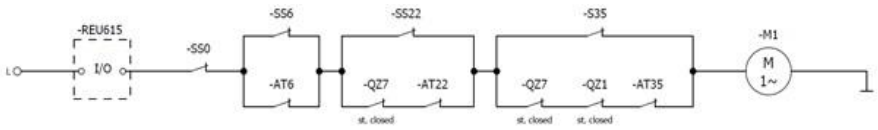

Fig. 4. Interlock for increasing voltage

Increasing voltage is not possible for following conditions below:

1. Position 0 is chosen on selector switch.
2. Position 1 is chosen on selector switch and micro switch inbuild in autotransformer is opened by voltage exceeding 6 kV.
3. Position 2 is chosen on selector switch and micro switch inbuild in autotransformer is opened by voltage exceeding 22 kV or disconnector *QZ7* is closed.
4. Position 3 is chosen on selector switch and micro switch inbuild in autotransformer is opened by voltage exceeding 22 kV or disconnector *QZ1* is closed or disconnector *QZ7* is closed.

6 Conclusion

Design of this specific indoor substation is very interesting, because there is a lot of things, which must be done differently than for a standard indoor substation. Mostly safety measures were done more thoroughly, because students and unqualified personnel can enter space where the substation will be placed. Tight space for placing the substation was another issue which complicated the design. Three different voltage levels were last thing, which rapidly influenced a design and operation plan of the substation.

7 Acknowledgment

This research was supported by the SGS grant from VSB - Technical University of Ostrava (No. SP2020/37).

References

1. Ito, H. Switching Equipment, Springer 2019
2. Krieg, T., Finn, J. Substations, Springer 2019
3. IEC 61936-1, Power installations exceeding 1 kV – Part one: Common rules

Photovoltaic power plant battery storage backup energy selected using MCA method calculation

Petr Seroiszka

Department of Electrical Power Engineering, FEECS,
VSB – Technical University of Ostrava, 17. listopadu 15,
708 00 Ostrava – Poruba, Czech Republic
petr.seroiszka.st@vsb.cz

Abstract. This article describes the use of multi-criterial analysis when selecting a backup battery to achieve reliability and continuity of data transmission between a photovoltaic power plant and an energy producer's portal. The first part defines individual accumulators and their properties. A total of six battery selection options, six characteristic evaluation criteria and an adequate choice of weightings of these criteria are described. Three MCA calculation methods were selected for evaluation and their results were compared.

Keywords: Reliability, Storage battery, Multi-criteria, Analysis, Method

1 Introduction

Multi-criteria analysis is a universal method and in this case it will serve us to evaluate six selected types of backup battery using six criteria, which will be assigned the meaning of the so-called weight. These backup batteries are used to ensure the transmission of data from the photovoltaic power plant to the electricity manufacturer's portal in the event of a failure. The output of this calculation will be the order of variants - battery according to reliability, i.e. from the most suitable battery to the least suitable battery. For this method, you must first build a basic matrix of variants of each battery, select evaluation criteria, and then assign importance to those criteria. Then, according to the chosen method of calculation of the MCA, we calculate the order and reliability of each backup battery.

2 Input data for MCA evaluation-Batteries for backing up control and communication circuits

The selected samples are batteries used for re-storage electrically and will be evaluated for simplification and presentation of this calculation method only according to selected criteria that we have borrowed from literature. The best selected battery in this case should have a high energy density (Wh/kg), as many charging cycles as possible (-), high service life (years), low self-discharge (%), fast charging capability (hours), optimally large operating temperature range (°C), low investment acquisition costs (CZK), cell voltage same as other battery types (V) and high efficiency (%). According to all

these criteria, if they are supported by numbers, it is possible to compile the calculation. We borrowed the values for MCA from literature. [5] [6]

3 Variants of backup batteries to maintain data transmission fromphotovoltaic power plant to the power manufacturer's portal in the event of a failure of the connection of the photovoltaic system to the distribution network

Variant a1 - Lead starter battery, which has the largest application in UPS and the automotive industry. This type works with a good lifespan of +5 years and 500-800 charging cycles. Self-discharge is around 20 % per month. The nominal voltage of the lead accumulator cell is 2.1 V and the real energy density is in the range of 30-50 Wh/kg. The disadvantage is the high weight due to the lead, which is there from 60 % of the battery weight and the charging time, which ranges from 2 to 16 hours.

Variant a2 - NiCd (Nickel-Cadmium) battery is an outdated type of battery, Cadmium is strongly toxic, batteries have a memory effect, are sensitive to overcharging. They have a real density of 45-80 Wh/kg, cell voltage 1.2 V, the number of charging cycles 1500, a lifespan of +5 years, a charging time of 1-2 hours. Self-discharge is around 20 % per month.

Variant a3 - NiMH (Nickel-Metal Hydride) battery with nominal cell voltage 1.2 V. The disadvantage is fast self- discharge, since on the first day it loses 5-20 % and the next days 1-4 % for each day. These batteries have a lifespan of about 3-4 years and can withstand about 500 charging cycles. Charging time is 2-4 hours.

Variant a4 - LiFePO4 battery with real energy density 90-120 Wh/kg, cell voltage 3.2 V, number of charging cycles approx. 3000, lifespan +10 years, charging time 2-4 hours and self-discharge is low 5-10 % per month. The disadvantage is the high purchase price, the advantage is light weight.

Variant a5 - Li4Ti5O12 (LTE) battery has an energy density of 60-85 Wh/kg, cell voltage 2.3 V, number of charging cycles +20000, lifespan +15 years, charging time 0.2-6 hours. The advantage is an extremely low self-discharge of 3-5 % per month, but the disadvantage is the high purchase price.

Variant a6 – Li-Pol battery has an energy density of 120-140 Wh/kg, cell voltage 3.7 V, number of charging cycles +2000, lifespan +5 years, charging time 3-5 hours. The advantage is an extremely low self-discharge of 3-5 % per month. The disadvantage is the high purchase price.

4 Criteria for survey batteries by MCA methodes

For the evaluation of batteries, we will set six criteria and further assign weight (importance) to these criteria:

f1 - energy density (Wh/kg) ……20%
f2 - number of charging cycles (-) …… 25%
f3 - lifetime (year) ……... 5%
f4 - self-discharge (%) …… 5%
f5 - fast charging capability(hour)……30%
f6 - historical cost (CZK)…….15%

5 Multi-criteria analysis – MCA

We chose three MCA methods for the calculation. The first WSA - Weighted Sum Approach method calculates maximum benefit. The IPA method - Ideal Points Analysis calculates the minimum benefit as the best option, and finally the third TOPSys method - Technique for Order Preference by Similitary to Ideal Solution - uses minimization from the ideal variant and evaluation of variants based on a preferential relationship. [1] [4] Selected battery „a" variant, evaluation criteria „f "and assigned weights (see Fig. 1).

criteria			f_1	f_2	f_3	f_4	f_5	f_6
	PbA	a_1	50	800	5	20	16	1543
	NiCd	a_2	80	1500	5	20	2	740
variants	NiMH	a_3	120	500	4	20	4	600
	LiFePO4	a_4	120	3000	10	10	8	5110
	Li4Ti5O12	a_5	85	30000	15	5	5	5600
	Li-pol	a_6	140	2000	3	5	5	4900

Fig. 1. Battery variants

6 WSA- Weighted Sum Approach

This method uses the principle of maximizing usage, but only when using a linear function.[1] [4] This method uses the principle of maximizing usage, but only when using a linear function. [1] [4] Matrix criteria after adjustment (see Fig. 2) - all criteria (max) will be maximized, and the worst values will be determined to minimize the criteria.

edit-highest values		140	30000	15	20	16	5600
criteria		$f_{1=max}$	$f_{2=max}$	$f_{3=max}$	$f_{4=min}$	$f_{5=min}$	$f_{6=min}$
	a_1	50	800	5	0	0	4057
	a_2	80	1500	5	0	14	4860
variants	a_3	120	500	4	0	12	5000
	a_4	120	3000	10	10	8	490
	a_5	85	30000	15	15	11	0
	a_6	140	2000	3	15	11	700

Fig. 2. Matrix criteria after adjustment

Maximum H and minimum D values from each column f (see Fig. 3).

H=	(	140	30000	15	15	14	5000)
D=	(	50	500	3	0	0	0)

Fig. 3. Maximum H and minimum D

Further modifications according to the literature [1], [4] will get normalized criterial matrix and Standardized criterial matrix with weight taken into account (see Fig. 4).

criteria		f_1	f_2	f_3	f_4	f_5	f_6			After sorting
weights	v	0,2	0,25	0,05	0,05	0,3	0,15			
	a_1	0,000	0,003	0,008	0,050	0,300	0,028	$u(a_1)$:	0,389	$u(a_5)$= 0,592
	a_2	0,067	0,008	0,008	0,050	0,000	0,004	$u(a_2)$:	0,138	$u(a_4)$= 0,486
variants	a_3	0,156	0,000	0,004	0,050	0,043	0,000	$u(a_3)$:	0,253	$u(a_6)$= 0,406
	a_4	0,156	0,021	0,029	0,017	0,129	0,135	$u(a_4)$:	0,486	$u(a_1)$= 0,389
	a_5	0,078	0,250	0,050	0,000	0,064	0,150	$u(a_5)$:	0,592	$u(a_3)$= 0,253
	a_6	0,200	0,013	0,000	0,000	0,064	0,129	$u(a_6)$:	0,406	$u(a_2)$= 0,138

Fig. 4. WSA-Standardized criterial matrix

Appreciation – Max. value of use is achieved according to the result in Fig. 4. for variant 5 with minimal risk of loss and maximum benefit.

7 IPA - Ideal Points Analysis

It is similar to the WSA method with the difference in mathematical solution of the value of benefit, which is a reciprocal method stated in the WSA value. [1] Again, as with the previous method, a matrix of criteria will be developed, a standardized criterial matrix, and finally a matrix of criteria taking into account weights (see Fig. 5).

criteria		f_1	f_2	f_3	f_4	f_5	f_6			After sorting
	a_1	0,200	0,247	0,042	0,000	0,000	0,122	$u(a_1)$:	0,489	$u(a_5)$= 0,408
	a_2	0,133	0,242	0,042	0,000	0,300	0,146	$u(a_2)$:	0,717	$u(a_1)$= 0,489
variants	a_3	0,044	0,250	0,046	0,000	0,257	0,150	$u(a_3)$:	0,597	$u(a_4)$= 0,499
	a_4	0,044	0,229	0,021	0,033	0,171	0,015	$u(a_4)$:	0,499	$u(a_6)$= 0,573
	a_5	0,122	0,000	0,000	0,050	0,236	0,000	$u(a_5)$:	0,408	$u(a_3)$= 0,597
	a_6	0,000	0,237	0,050	0,050	0,236	0,021	$u(a_6)$:	0,573	$u(a_2)$= 0,717

Fig. 5. IPA-Standardized criterial matrix

Appreciation – Min. value of use is achieved according to the result in Fig. 5. for variant 5 with minimal benefit.

8 TOPSIS - Technique for Order Preference by Similarity to Ideal Solution

The principle of this analysis [1] [4] is to minimize the distance from the ideal variant. The ideal option is to call it the variant for which all criteria values achieve the best values. The ideal option is usually hypothetical, the best option is chosen which is closest to the ideal option according to a certain metric. The method is based on the selection of the variant that is closest to the ideal variant represented by the vector (H1, H2, ..., Hk) and furthest from the basal variant represented by the vector (D1, D2, ..., Dk). First a standardized criterial matrix R = (rij) (see Fig. 6) and is constructed with formula (1)

$$r_{ij} = \frac{y_{ij}}{\sqrt{\sum_{i=1}^{p}(y_{ij})^2}} \tag{1}$$

criteria		f_1	f_2	f_3	f_4	f_5	f_6
	a_1	0,197	0,026	0,250	0,544	0,810	0,168
	a_2	0,315	0,050	0,250	0,544	0,101	0,080
variants	a_3	0,472	0,017	0,200	0,544	0,203	0,065
	a_4	0,472	0,099	0,500	0,272	0,405	0,555
	a_5	0,335	0,991	0,750	0,136	0,253	0,608
	a_6	0,551	0,066	0,150	0,136	0,253	0,532

Fig. 6. TOPSIS-Standardized criterial matrix

Then we calculate the weighted criterial matrix W by multiplying each j-th column of the normalized criterial matrix R by the corresponding weight. [1] (see Fig. 7).

	v	0,2	0,25	0,05	0,05	0,3	0,15
criteria		f_1	f_2	f_3	f_4	f_5	f_6
	a_1	0,039	0,007	0,013	0,027	0,243	0,025
	a_2	0,063	0,012	0,013	0,027	0,030	0,012
variants	a_3	0,094	0,004	0,010	0,027	0,061	0,010
	a_4	0,094	0,025	0,025	0,014	0,122	0,083
	a_5	0,067	0,248	0,038	0,007	0,076	0,091
	a_6	0,110	0,017	0,008	0,007	0,076	0,080

Fig. 7. TOPSIS-Weighted criterial matrix W

Maximum H and minimum D values from each column f (see Fig. 8).

H=	(	0,094	0,248	0,038	0,027	0,243	0,091)
D=	(	0,039	0,004	0,010	0,007	0,030	0,010)

Fig. 8. Maximum H and minimum D

We will now determine the ideal and basal variant in relation to the values in the weighted criterial matrix, where: $H_j=\max(w_{ij})$, i=1,2, …, k and furthermore $D_j=\min(w_{ij})$, i=1,2, …, k

In thesame step, thedistance between the variants and theideal variants according to (2) and distances of variants from the basal variant (3)

$$d_i^+ = \sqrt{\sum_{j=1}^{k}\left(w_{ij} - H_j\right)^2} \quad (2) \qquad d_i^- = \sqrt{\sum_{j=1}^{k}\left(w_{ij} - D_j\right)^2} \quad (3) \qquad c_i = \frac{d_i^+}{d_i^+ + d_i^-} \quad (4)$$

As a laststep, the calculation of the relative indicator of the distances of variant from the basal variant. Variants are sorted by the decreasing values of the indicator c_i, (4)

This we get a complete arrangement of the result of all variants TOPSIS method (see Fig. 9).

		d_i^+	d_i^-	c_i	After sorting
	a_1	0,257	0,214	0,454	$u(a_5)$= 0,607
	a_2	0,329	0,032	0,090	$u(a_1)$= 0,454
variants	a_3	0,316	0,066	0,173	$u(a_4)$= 0,342
	a_4	0,254	0,132	0,342	$u(a_6)$= 0,277
	a_5	0,171	0,264	0,607	$u(a_3)$= 0,173
	a_6	0,288	0,110	0,277	$u(a_2)$= 0,09

Evaluation: values are sorted in descending order (see Fig. 9). The highest value Ci means the best option.

9 Conclusion

In this project, we evaluated with the help of a multi-criteria analysis -MCA which of the six possible variants of the backup battery is the worst in the selected model of criterion and assigned weights and which is most favorable. At the beginning, we selected backup batteries that can ensure the continuity of the flow of data from the photovoltaic power plant to the electricity manufacturer's portal. We chose these variants- Lead starter battery, NiCd (Nickel-Cadmium) battery, NiMH (Nickel-Metal Hydride) battery, LiFePO4 battery, $Li_4Ti5O12$ (LTO) battery and Li-Pol battery. For comparison, we have chosen multi-criteria WSA, IPA and TOPSIS methods.
The result and comparison of all three methods is in Fig. 10.

WSA		IPA		TOPSIS	
u(a5)=	0,59	u(a5)=	0,408	u(a5)=	0,607
u(a4)=	0,49	u(a1)=	0,489	u(a1)=	0,454
u(a6)=	0,41	u(a4)=	0,499	u(a4)=	0,342
u(a1)=	0,39	u(a6)=	0,573	u(a6)=	0,277
u(a3)=	0,25	u(a3)=	0,597	u(a3)=	0,173
u(a2)=	0,14	u(a2)=	0,717	u(a2)=	0,09

Fig. 10. Result and comparison of all three methods

The first WSA method - the weighted Sum Approach method consisted in determining the maximum use value that was used for variant a5. According to this method, the most suitable option a5 appears to be represented by the Li4Ti5O12 (LTO) battery.

The second Ideal Points Analysis (IPA) method is similar to the WSA method. The difference is in the mathematical solution of the value of the benefit, which is a reciprocal method stated in the WSA value. The result for this method was similar to the WSA method, ie. again least risk is for variant a5.

The third TOPSIS method - the method consists in minimizing the distance from the ideal variant. Ideal variants in all criteria values achieve the best values. The result for this more complex method indicates the best variant a5 - $Li_4Ti5O12$ (LTO) battery and the worst variant a2-NiCd battery. The inclusion of investment costs in the decision-making analysis played an important role in the assessment against earlier analyses. This economic criterion is important for investors and therefore it has been included in the calculation and evaluation.

Acknowledgement

This research was supported by the SGS grant from VSB-Technical University of Ostrava No. SP 021/20.

References

1. Hradílek, Z.: Elektroenergetika distribučních a průmyslových zařízení TU Ostrava, 2008, ISBN 987-80-7225-291-6
2. Seroiszka, P., Hradílek, Z.: Problematika připojování FVE k distribuční soustavě (2018).
3. Seroiszka, P., Hradílek, Z.: Reliability of the photovoltaic system, ISBN 978-1-72811-333-3 IEEE (2019)
4. Hradílek, Z. Krejčí ,P.: The research of methods of multi – criteria analysis for increase of reliability of distribution networks by remote controled elemens" – EUROPES 2005-Banalmadena Spain 2005, ISBN 0-88986-465-9 (2005)
5. http://battery.nabizi.cz/akumulatory_c10331/
6. https://oze.tzb-info.cz/akumulace-elektriny/20319-naklady-na-akumulaci-elektricke-energie-v-komercnich-sekundarnich-clancich

A Synchronous Condenser in a Rolling Mill

Stanislav Nowak and Stanislav Kocman

Department of Electrical Engineering, FEECS,
VSB – Technical University of Ostrava, 17. listopadu 15,
708 00 Ostrava – Poruba, Czech Republic
{stanislav.nowak.st, stanislav.kocman}@vsb.cz

Abstract. In a rolling mill with a total active consumption above 10 MW the reactive consumption is compensated by two different units. A synchronous condenser and a static filter-compensation unit are connected in parallel directly at the rolling mill. The active and also the reactive consumption significantly change during the rolling mill operation.

Keywords: Active Power, Reactive Power, Rolling Mill, Synchronous Condenser, Drive.

1 Introduction

Long rolled products are among basic types of steel products. There was an opportunity to investigate the main electric supply system at a large rolling mill, producing almost 1 mil. tons of rolled products per year. It's a hot rolling mill, working on a 140 mm thick stock. The weight of the stock is about 2 tons. The process in the investigated rolling mill is continuous; it means the rolled stock goes from the first rolling stand step by step to the next rolling stands continuously [1]. The rolled metal is processed in many rolling stands at the same time; it requires a very rapid and precise control of the speed of the rolls.

The aim of the paper is to draw attention to a neglected synchronous condenser and at the same time to draw attention to its basic features. Nowadays the use of a synchronous condenser is considered archaism and most technicians do not know its possibilities and advantages compared to static compensators.

2 History

Our first measurement at the investigated rolling mill was performed in June 2020. The rolling mill is powered from the public 110 kV grid, but also a synchronous generator with the block transformer T1 is connected on the level of 22 kV. The distance between the rolling mill and the local power plant where the generator TG1 is located is about 3 km. These two power sources – the public grid and the generator TG1 [2] are connected in parallel [3]. A simplified block diagram of the supply grid is shown in Fig. 1.

VSB – Technical University of Ostrava, 2021, ISBN 978-80-248-4523-4 (on-line).

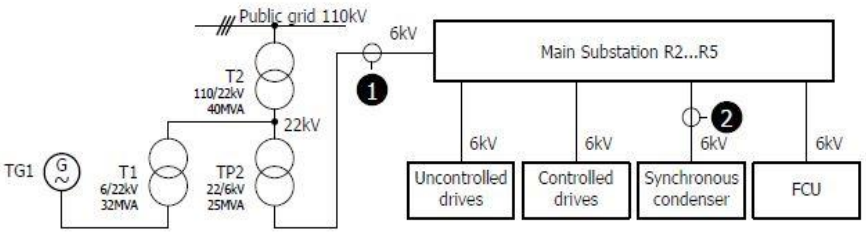

Fig. 1. Simplified block diagram of the rolling mill power system.

Another rolling mill of a similar production capacity is also powered from the point between the transformer T2 and transformer T1. The generator TG1 is controlled to produce as much power as possible. Only a small necessary amount of power is purchased from the outside.

Almost all rolling stands are driven by LV DC motors; some newly installed rolling stands are driven by LV AC asynchronous motors. All of the 36 DC motors are powered by controlled DC thyristor rectifiers. The AC motors (only four) are powered by frequency converters. The DC rectifiers are connected through the MV/LV transformers to the main supply bus, working on the level of 6 kV. All the DC controlled rectifiers are connected separately through their transformers on the levels of 500, 690, or 750 V. The mentioned rectifiers allow reversing the DC output voltage; this functionality is used only in case of emergency stop. The nameplate power of the individual motors is in the range of hundreds of kW.

The undesirable reactive power is compensated by the synchronous condenser and also by the static filter-compensation unit [5]. The filter-compensation unit – in next text FCU – is tuned to filter the third and fifth harmonics. [6]. An access to this unit was not possible, so the electrical values related to this unit were not measured. The active and reactive consumptions were measured during four rolling periods at three important points. The first and second measurement points are visible in Fig. 1.

The all time courses of the consumptions have been assessed. It can be said that the reactive consumption during the rolling cycle (measured at point 1) is considerably variable and always passes from the inductive character into capacitive character and back. It was found that the synchronous condenser, which is dedicated mainly for the controlled compensation of the reactive power, is not controlled and its reactive consumption (measured at point 2) varies little, only from 0.7 MVAr to 1.1 MVAr. The nameplate reactive consumption of the synchronous condenser is 6.5 MVAr.

The time courses of the reactive consumption of the synchronous condenser and of the whole rolling mill are shown in Fig. 2 and Fig. 3.

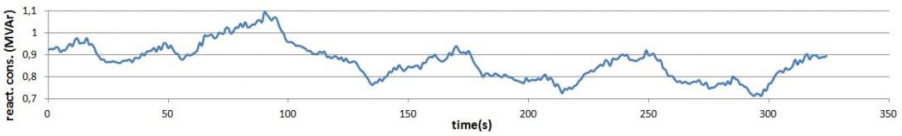

Fig. 2. The time course of the reactive consumption of the synchronous condenser.

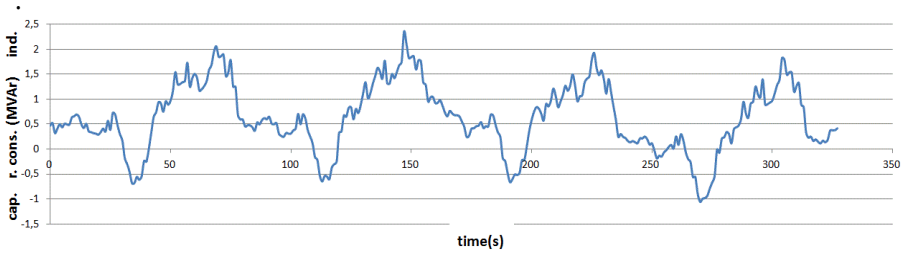

Fig. 3. The time course of the reactive consumption of the whole rolling mill.

In this case the switching off of the synchronous condenser would not mean a significant deterioration of the reactive consumption. In this way it would be possible to save almost 1.9 MWh per day. However, there are concerns that switching off the synchronous condenser may cause some problems in the reliable operation of the rolling mill. Unfortunately, it was not possible to continue with the measurement after the mentioned evaluation, as the access to the rolling mill was blocked for 10 months.

3 Subsequent evaluations of the measured values

The June 2020 recorded files contain not only data related to consumptions, but also other values. Voltage and current values are available for fundamental and higher harmonics components. It is therefore possible to compare the content of harmonic currents which flow through the synchronous condenser and the main inlet from the transformer TP2.

The standard driving set – DC motor, thyristor rectifier, and MV/LV transformer is from the 6 kV bus point of view a resistance-inductive load with nonlinear characteristic. At the connection to the harmonic voltage is the time course of the current non harmonic [7]. The level of current distortion is very variable; it depends mainly on the immediate mechanical load of the motor. The real current is composed of the current of the fundamental harmonic and superimposed components of high order harmonics. It was assumed that the harmonic components of the current, which the controlled drives generate during their work, will mainly flow through the synchronous condenser. This would mean a high risk after disconnecting the synchronous condenser.

The measurements at points 1 and 2 were not performed simultaneously. The procedure was limited by the configuration of the measuring apparatus; only 3 input channels were available for current measurement. An accurate comparison of the time courses of the individual harmonics was therefore not possible. Maxima were searched in the current values of the appropriate harmonics. These maxima were compared and it was found out that the level of harmonic current for most of harmonics is greater at point 1 than at point 2. Only for the 3rd harmonic component of the currents, the components of currents flowing through the synchronous condenser were greater than the components flowing through the inlet. This means that the filtering effect of the synchronous condenser is not very significant.

Total harmonic distortion at the point 1 is not high; the time courses of the voltage distortion *THDu* and current distortion *THDi* are shown in Fig. 4 and Fig. 5.

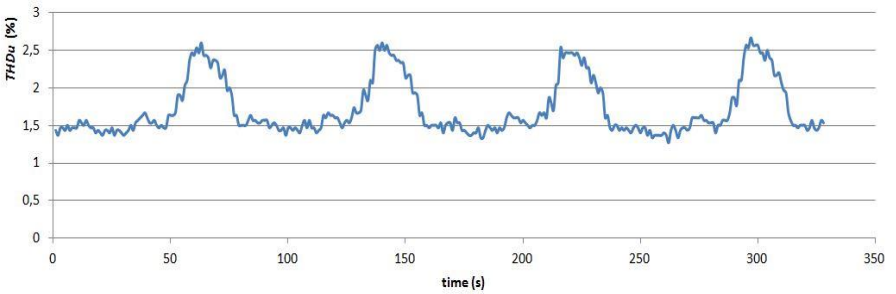

Fig. 4. The time course of *THDu* of the whole rolling mill.

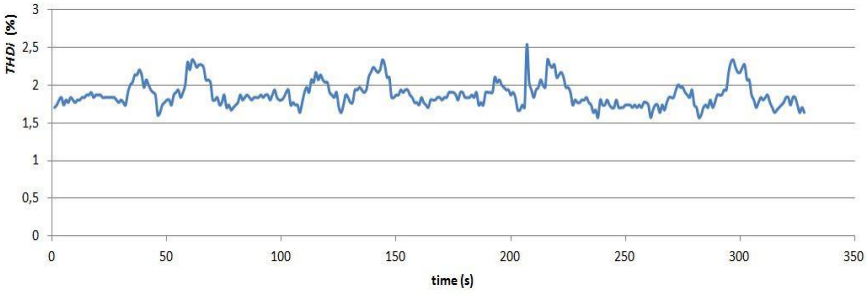

Fig. 5. The time course of *THDi* of the whole rolling mill.

4 Synchronous condenser

The synchronous condenser is almost a standard synchronous motor without a useful mechanical load. The design of the machine corresponds to this. Only air flow resistance and shear friction in rotor bearings during rotor rotation are here unwanted but necessary mechanical loads. These mechanical loads are covered by the active component of the synchronous condenser consumption. Other active energy losses occur in the stator winding (Joule losses) and in the stator steel core (eddy current losses). All these described losses cause the synchronous condenser to heat up. Joule losses in the rotor winding caused by DC excitation current also contribute to this. However, the DC excitation circuit has a separate power supply and the losses in the rotor are not related to the main supply feeder of the synchronous condenser. The reactive consumption of the synchronous condenser depends on the excitation current value. There is a value of the excitation current when the synchronous condenser operates without reactive consumption. At higher value of the excitation current, its reactive consumption has a capacitive character. When the excitation current is changes, the change in reactive consumption is relatively fast, but not immediate.

In the following text, it will be assumed that the synchronous machine is connected to the AC power supply grid. When the mechanical energy is fed to the synchronous machine, the instantaneous position of the magnetic induction vector of the rotor magnetic field precedes the instantaneous position of the magnetic induction vector of the rotating stator magnetic field. Steam or combustion turbine is used as a source of

mechanical energy in power plants. The electrical grid must be able to absorb the generated electrical energy, otherwise the synchronous operation would be disrupted and the generator would rotate uncontrollably to higher speeds. The entire device would be destroyed. To avoid this situation, the drive device (turbine) must be equipped with safety elements that do not allow excessive speeding. When mechanical energy is taken from the synchronous machine, the instantaneous position of the magnetic induction vector of the rotor magnetic field is delayed after the instantaneous position of the magnetic induction vector of the rotating stator magnetic field. The synchronous machine rotates at a synchronous speed. When the mechanical load exceeds the physical capabilities of the machine, synchronism fails and the machine stops.

In the running synchronous machine, the inertial mass of the rotor is an accumulator of mechanical energy. When the supply voltage of the machine is distorted (non-harmonic), the instantaneous voltage is higher or lower than the value corresponding to the ideal sinusoid. The synchronous machine tries to keep the instantaneous values of the voltage at its terminals at the value of the ideal sinusoid and thus adds the missing energy to the network or, conversely, draws the remaining energy from the grid. Thus, the mechanical energy of the rotational movement of the rotor is rapidly pumped or replenished. The synchronous condenser thus acts as a broadband (non-selective) filter that also stabilizes the power grid.

5 Next planned steps

From the middle of 2021 the measurement in the substations is possible again. The next measurement will be performed into two stages. The first measurement will be performed in the substation R5. Great efforts have been made to obtain permission to enter this substation. As-built diagrams were studied in detail; especially the circuit diagrams of measuring loops. The simplified diagram of the substation R5 including selected measurement points is shown in the Fig. 6.

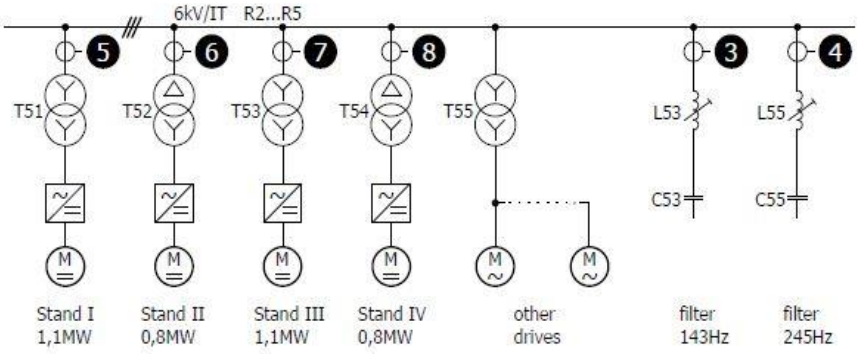

Fig. 6. A part of simplified single line diagram of the substations.

During the first measurement in the substation R5 the measuring apparatus will be step by step connected at points 3, 4, 5, 6, 7, 8. We will use the previously used C.A 8335 Qualistar+ network analyser [8] again. Records will be performed for 5 rolling cycles. During these measurements, the correctness of the as-built documentation will be verified, especially the order of voltage terminals and the directions of currents in current loops. This is very important for the next measurement.

The next measurement will be performed after evaluating the results of the first planned measurement. The currents at points 1 and 2 (see Fig. 1) and at points 3, 4, and 5 will be measured. Unfortunately, the first two measuring points are too far from the substation R5. This means the need for two time-synchronized measuring apparatuses. The result of this measurement will be a set of current values in a clear time relation. A detailed analysis of the measured data will accurately determine the role of the synchronous condenser in the absorption of undesirable harmonic components of the currents.

6 Conclusion

This paper describes a part of a complex process, the beginning of which was the finding that the synchronous condenser does not compensate for the reactive consumption of the rolling mill as expected. The operation of the synchronous condenser is not cheap, so it is necessary to consider its further operation. This assessment must be comprehensive; none of the known possible aspects can be neglected. An excessive temptation of possible savings must not cause a hasty decision.

Acknowledgment This work was supported by the Project SP2021/84 of the Student Grant System, VŠB – Technical University of Ostrava.

References

1. Ispat Guru: https://www.ispatguru.com/rolling-mill-and-its-technological-equipments/, last accessed 2020/07/16.
2. Glinka, T.: Generatory synchroniczne jako kompensatory mocy biernej i i filtry wyższych harmonicznych, Zeszyty Problemowe – Maszyny Elektryczne Nr1/2013 (98).
3. Chura, V.: Elektrotechnika pro horní a hutní inženýry, SNTL Praha 1972, DT 621.3.669.
4. Mapy.cz: https://www.mapy.cz, last accessed 2021/06/30.
5. Hradílek, Z.: Elektroenergetika průmyslových a distribučních zařízení, VŠB-TU Ostrava, 2008, ISBN 978-80-7225-291-6.
6. Firlit, A.: Pasywne i aktywne sposoby eliminacji odkształcenia napięcia, Europejski Instytut Miedzi, EIM01312-03.
7. Kůs, V.: Vliv polovodičových měničů na napájecí soustavu, BEN – Technická literatura, Praha 2002, ISBN 80-7300-062.
8. C.A 8335 Qualistar+: CHAUVIN ARNOUX User's manual, 2011.

Vehicle rolling and drag coefficient estimation

Martin Koreny

Department of Electronics, FEECS,
VSB – Technical University of Ostrava, 17. listopadu 15,
708 00 Ostrava – Poruba, Czech Republic
martin.koreny@vsb.cz

Abstract. This paper introduces estimation of rolling and aerodynamic resistance for small EV. Real data was acquired by utilizing coast-down testing and both parameters estimated by MPC (Model Predictive Control) technique.

Keywords: coast-down testing, drag resistance, MPC, rolling resistance.

1 Introduction

Aerodynamic or rolling resistance are measured by four basic techniques [1]. Testing in the aerodynamic tunnel where a vehicle or its dimensionally equivalent model is not moving. Artificial wind with regulated speed and yaw flows around the vehicle and creates aerodynamic drag which is used to determine aerodynamic resistance. This method cannot determine the rolling resistance coefficient. Analogously but purely computer-based simulation can be achieved by using CFD (Computational Fluid Dynamics) analysis, which belongs to fluid mechanics. The above two methods belong to laboratory testing. Compared to aerodynamic tunnel costs and development time can be significantly reduced thanks to no special equipment and no real model to be build.

The next two methods belong to on-road testing. Constant speed testing where the vehicle speed is maintained constant for two or more target speeds. By measuring torque aerodynamic drag can be determined. However, costs associated with an expensive torque measurement setup are considerable. Coast-down testing conditions are defined in norm ČSN 30 0554. The vehicle is accelerated up to target speed and when speed is stable traction power is disconnected by for example engaging clutch and neutral gear. The vehicle is naturally slowing down and measuring the speed profile in time is used to determine in this case both aerodynamic and rolling resistance coefficients. Testing needs to meet special conditions like limited road declination or wind speed which could be considered challenging in real road and weather conditions. Nevertheless, a low cost and simple measurement procedure decided to use this method for determining drag and rolling resistance coefficients for small EV Estrima Biro which is part of the university carsharing pool. The manufacturer does not provide drag and rolling resistance coefficients.

VSB – Technical University of Ostrava, 2021, ISBN 978-80-248-4523-4 (on-line).

2 Coast-down testing

There is a moment during cost-down testing when the tractive force [2] is zero due to the disengaged engine and the vehicle starts to decelerate. We can express the situation of the coasting vehicle as

$$0 = F_i + F_a + F_g + F_r = \dot{v}Jm + \tfrac{1}{2}\rho C_a A\left(v \pm v_p \cos(\beta)\right)^2 + g\ sin(\alpha) + g\ C_v\ cos(\alpha) \tag{1}$$

where

F_i	–	internal force (N),
F_a	–	drag resistance (N),
F_g	–	grade resistance (N),
F_r	–	rolling resistance (N),
m	–	vehicle mass (kg),
J	–	rotating parts coefficient ($-$),
v	–	vehicle speed ($m \cdot s^{-1}$),
v_p	–	wind speed ($m \cdot s^{-1}$),
g	–	gravitational acceleration ($m \cdot s^{-2}$),
α	–	road inclination angle (°),
ρ	–	air density ($kg.m^{-3}$),
A	–	vehicle front area (m^2),
α	–	road inclination angle (°),
β	–	wind yaw angle (°),
C_a	–	drag coefficient ($-$),
C_v	–	rolling resistance coefficient ($-$).

According to ČSN 30 0554 the measurement shall be made on the testing track with maximum inclination ± 1 % and wind speed up to 1,5 $m.s^{-1}$. The ambient temperature was at the measurement day 2.1 °C. Testing track altitude difference was 2 m and length 127 m as we see in Fig.1. The START point (GPS 49.8388478N, 18.1391908E) is fixed and is marked by the traffic cone and is marking the position where the vehicle shall start to decelerate by disengaging the traction power. The STOP position is only illustrative and is marking the end of the testing track. The wind speed was not measured continuously but statically before each measurement. The average wind speed was not bigger than 1.3 $m.s^{-1}$ therefore the equation (1) reduces to

$$\dot{v}Jm = -F_a - F_s - F_v = -\tfrac{1}{2}\rho C_a A v^2 - g\ sin(\alpha) - g\ C_v\ cos(\alpha) \tag{2}$$

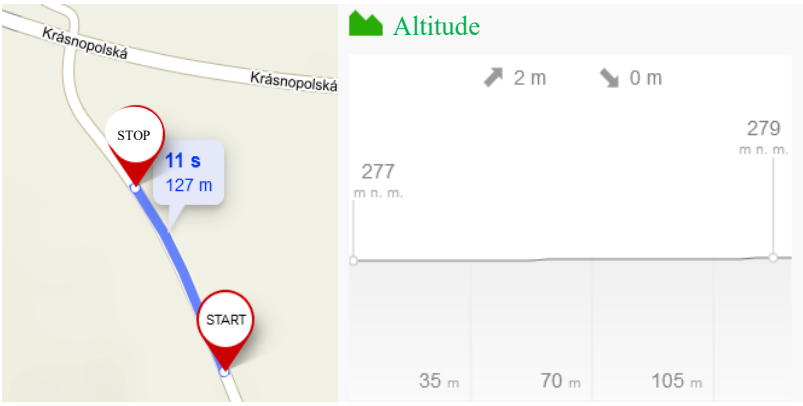

Fig.1 Testing track (www.mapy.cz)

3 Drag and rolling resistance coefficient estimation

From the equation (2) both coefficients can be determined by utilizing the dynamic estimation technique which is based on MPC (Model Predictive Control) principles. This numerical approach minimizes in our case the difference between measured vehicle speed v_m and simulated speed v see Fig.*2* of the dynamic system represented by the differential equation (2), which describes the coasting of the vehicle. Objective functions and conditions describing the task can be mathematically written as

$$\begin{aligned} &\min_{C_a, C_v} \ \|v_m - v\|_n \\ &subject\ to \quad \dot{v}Jm = -\tfrac{1}{2}\rho C_a A v^2 - g\ sin(\alpha) - g\ C_v\ cos(\alpha) \\ &0 \le C_a \le 1 \\ &0 \le C_v \le 1 \end{aligned} \tag{3}$$

The numerical solution is made in Matlab using APM library [3].

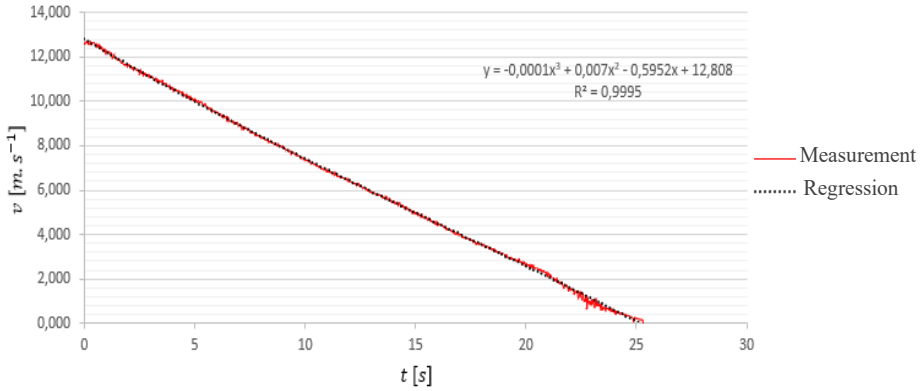

Fig.2 Deceleration during vehicle coasting

Fig.*3* shows needed files for Matlab task creation. In the csv file is on its first line header „time,v“. This header tells APM library that in the first column there are time values and in the second one vehicle speed values. Both columns are always separated by a comma.

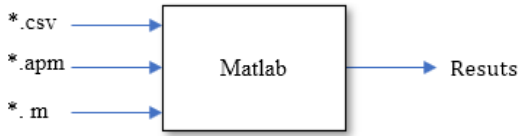

Fig.3 Interface of Matlab and APM

The listing of the APM file is shown in Fig.*4*. The file is created in Notepad++ which supports APM syntax highlighting. The file has several required sections highlighted in blue where constants, parameters or equations can be defined. A comment starts with an exclamation mark and each line of code is clearly commented. On line 9 the vehicle speed *v* has to have exactly the same name as it was described in the csv file above. The time from the csv is not necessary to be part of the APM file, because the APM library reads the value automatically. Worth noting is that care has to be taken about variable naming regarding capital and small letters. Parameters and variables names with capitals are automatically converted to small letters.

```
1   Parameters
2       m       = 529       ! Biro and driver weight (kg)
3       ro      = 1.25      ! air density (kg/m^3)
4       aa      = 1.293     ! Biro front area(m^2)
5       g       = 9.81      ! gravitational acceleration (m/s^2)
6       alfa    = 0.902333 ! road inclination angle(°)
7
8   Variables
9       v = 0               ! vehicle speed (m/s)
10      a = 0               ! vehicle acceleration (m/s^2)
11      cv = 0              ! rolling resistance coefficient(-)
12      ca = 0              ! drag coefficient(-)
13
14  Intermediates
15      !Drag resistance
16      Fa = 1/2*ro*ca*aa*v^2
17
18      !Roling resistance
19      Fv = m*g*cv*cos(3.14159265359*alfa/180.0)
20
21      !Grade resistance
22      Fs = m*g*sin(3.14159265359*alfa/180.0)
23
24  Equations
25      ! acceleration (speed derivative)
26      $v = a
27      ! force balance
28      m*a*1.04 = - Fa - Fv - Fs
```

Fig.4 APM code

```
clear all   %#ok<*CLALL>
close all

addpath('../apm'); % path to APM library
s = 'http://localhost'; % local computing server
a = 'biro_coast_estimate'; % task name

apm(s,a,'clear all');
apm_load(s,a,'biro_coast.apm'); % load apm file

csv_load(s,a,'biro_3_0bar_Precise_20ms_11.5278__3.csv');

apm_option(s,a,'nlc.imode',5);       % dynamic estimation
apm_option(s,a,'nlc.nodes',3);       % orthogonal collocation 3 nodes
apm_option(s,a,'nlc.ev_type',1);     % 1-L1 norm, 2-squared error
apm_option(s,a,'nlc.time_shift',0);  % one step
apm_option(s,a,'nlc.solver',1);      % APOPT (Advanced Process OPTimizer)
apm_option(s,a,'nlc.sensitivity',1); % sensitivity report on

apm_info(s,a,'FV','cv'); % fixed variable cv (rolling res. coefficient)
apm_info(s,a,'FV','ca'); % fixed variable ca (drag coefficient)
apm_info(s,a,'CV','v');  % controlled variable v (vehicle speed)

apm_option(s,a,'cv.status',1); % calculate cv
apm_option(s,a,'cv.dcost',0);  % penalty
apm_option(s,a,'cv.lower',0);  % lower limit
apm_option(s,a,'cv.upper',1);  % upper limit

apm_option(s,a,'ca.status',1); % calculate ca
apm_option(s,a,'ca.dcost',0);  % penalty
apm_option(s,a,'ca.lower',0);  % upper limit
apm_option(s,a,'ca.upper',1);  % lower limit

apm(s,a,'solve') % solve the optimization problem

y = apm_sol(s,a); % assign APM results to the structure y
z = y.x; % final results are in x sub-structure

disp(['cv: ' num2str(z.cv(1))]) % display cv
disp(['ca: ' num2str(z.ca(1))]) % display ca
```

Fig.5 Matlab script

Matlab script is in Fig.*5* and each line comment explains clearly the procedure. More details can be found in [3] and [4].

Tab. 1 Biro rolling and drag coefficients

Tire pressure (kPa)	Vehicle sampling (ms)	Estimation duration (s)	C_a (-)	C_v (-)
300	20	45.657	0.482	0.032
300	200	0.409	0.460	0.032
260	20	41.786	0.442	0.033
260	200	0.389	0.471	0.033
200	20	38.697	0.437	0.035
200	200	0.378	0.423	0.035

4 Conclusion

There were test rides made with three tire pressures to check the influence of the tire pressure on rolling resistance. Results are visible in Tab. 1. The rolling resistance coefficient is according to expectation rising with the lower tire pressure. The drag coefficient shows deviations caused by the wind speed influence which has an impact at low vehicle coasting speeds. As mentioned, the wind speed was not continuously measured and therefore is not compensated in the estimation. Another author's research beyond scope of the article shows that drag resistance has no significant impact on the Biro because of its maximum speed 45 km/h. This was taken into consideration for the decision of whether continuous speed measurement makes sense or not. In the results table there is also computing time available to provide reference data because the parameter estimation is planned to be part of the on-board vehicle assistant system. The computing time is valid for a 4-core processor Intel Core i7-8550U running at 1.8 GHz. As we can see ten-times difference in sampling rate results in more than a hundred times difference in the computing time.

5 Acknowledgment

In the paper, there are the results of the project reg. no. SP2021/49 funded by the Student Grant Competition of VSB-Technical University of Ostrava. This research was supervised by doc. Ing. Petr Simonik, Ph.D.

6 References

[1] ICCT, Comparison of Aerodynamic Drag Determination Procedures for HDV CO2 Certification [online], [cit.2020-04-07], last revision 14.8.2019. Available from https://theicct.org/sites/default/files/publications/ ICCT_aero_drag_briefing_20190814.pdf.

[2] VLK, F. *Dynamika motorových vozidel. 2. vyd*. Brno: Prof.Ing.František Vlk,DrSc. nakladatelství a vydavatelství, 2003. 432 s. ISBN 80-239-0024-2.

[3] *APMonitor documentation* [online], [cit.2020-12-25]. Available from http://apmonitor.com/wiki/

[4] HEDENGREN, J. D. – ASGHARZADEH SHISHAVAN, R. – POWELL, K.M. – EDGAR, T.F. *Nonlinear Modeling, Estimation and Predictive Control in APMonitor,* Computers and Chemical Engineering, Volume 70, p. 133–148, 2014, DOI: 10.1016/j.compchemeng.2014.04.013

Versatile High Current Generator & Load for Shunt Active Power Filter Method Testing

Jan Baroš[0000−0002−9377−8772]

Department of Cybernetics and Biomedical Engineering, FEECS,
VSB – Technical University of Ostrava, 17. listopadu 15,
708 00 Ostrava – Poruba, Czech Republic
jan.baros@vsb.cz

Abstract. This paper briefly introduces new experimental platform *HCGL* which is used to test Shunt Active Power Filter control methods. Experimental platform is a world–unique device and is built around National Instruments hardware and Virtual Instrumentation principle in mind. This experimental platform is designed to perform a truly objective evaluation of SAPF control methods.

Keywords: SAPF · LabVIEW · Virtual Instrumentation · CPIT TL3

1 Introduction

Due to the large expansion of nonlinear loads in modern households and industrial enterprises, it is necessary to address not only the size of the power consumed, but also its distribution into the active and reactive part. The active part of the power takes care of the operation of the device itself and the reactive part is undesirable. Although this unwanted part is necessary for the operation of the load itself (eg. rotating magnetic field of an induction motor), it unnecessarily loads the distribution network. This results in the need to dimension conductor diameters for higher powers, thus increasing production costs and prices.

One way to save money is to introduce reactive power compensation. This can be divided into passive and active. The advantages of passive compensation are low acquisition costs. The disadvantage is the inability to "prepare" the filter for the spectrum of all types of loads (inductive, capacitive, linear, nonlinear, etc.). For this reason, it is more appropriate to install an active compensator that can cover all types of loads, as it is adaptively controlled and the result of its filtering always tries to be optimal (ie. only active power flows through the network).

Active filters can be further divided into serial–voltage (VSI–Voltage Serial Inverter) and parallel–current (SAPF–Shunt Active Power Filter) ones. VSI improves voltage quality by connecting a series voltage source that compensates for the non-ideal voltage to sinusoidal voltage. However, it cannot cope with the current of higher harmonic components taken by a nonlinear load. This ailment

VSB – Technical University of Ostrava, 2021, ISBN 978-80-248-4523-4 (on-line).

is solved by SAPF, which compensates by parallel injection of a compensating current, which corresponds to the waveform of the current of higher harmonic components of the consuming load, but with the opposite sign. This corresponds to the following equations:

$$i(t) = \overline{i_L}(t) + \widetilde{i_L}(t) + i_C(t), \tag{1}$$

$$i_C(t) = (-1) \cdot \widetilde{i_L}(t), \tag{2}$$

$$i(t) = \overline{i_L}(t), \tag{3}$$

where $i(t)$ is total current that flows through connected grid; $\overline{i_L}(t)$ is the current of the fundamental harmonic component of load; $\widetilde{i_L}(t)$ is the current of the higher harmonic components of load and $i_C(t)$ is compensating current injected into grid with SAPF. Block diagram of the described system can be seen in Fig. 1.

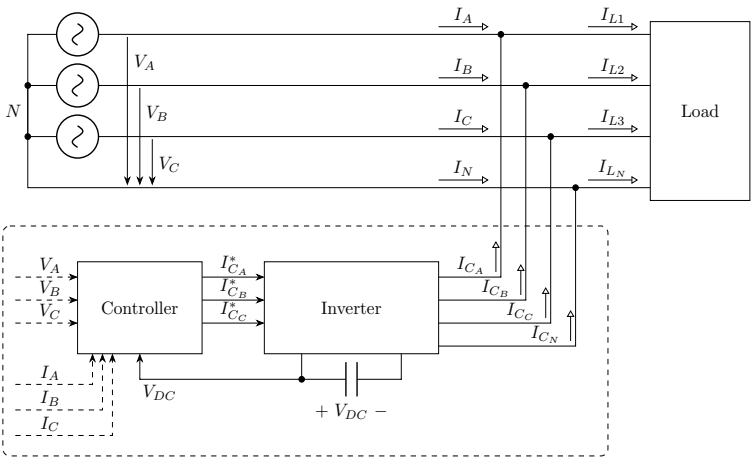

Fig. 1. Block and idea diagram of SAPF.

The following article consists totally of 4 paragraphs. Next paragraph is about SAPF control methods. Subsequent paragraph describes the experimental *HCGL* platform and its software. The article ends with a paragraph in which a total summary is made.

2 SAPF – Control Methods

Control section of SAPF can be divided into 4 basic sections: Harmonic Current Extraction, Synchronization, DC–Voltage Regulation and Current generation. There are various control methods of SAPF, which were described in many

publications through out years. Many of them were verified by real experiments on a real SAPF or in a simulation environment. However, there is no uniform test methodology for these methods and only subjective evaluation can be performed. Each or many of these methods were subjected to comparative experiments, but these experiments did not follow a uniform methodology. Therefore, it is not possible to objectively compare individual experiments of different authors[3].

The most frequently examined criterion for the methods is the ability to suppress higher harmonic components, quantified in the form of THD_I. This parameter describes in % how much current waveform differs from ideal sinusoidal shape. Another criteria examined are convergence speed, implementation difficulty, ability to work under distorted voltage conditions, parameter configuration or if the method is single/triple–phase.

Another measure that needs to be examined is objectivity towards the method itself in terms of the HW used. If an objective evaluation of the method is to be performed, it is necessary that the HW itself does not hinder the computational potential of the SAPF control method itself. Therefore it is recommended to use very–fast computational units, such as Digital Signal Processors (DSP) or Field Programmable Gate Array (FPGA). Many of authors used inappropriate HW such as Arduino or non–RTOS controller to drive SAPF. On the contrary another authors used FPGA, so again, direct comparison cannot be made.

To this day there are approximately 30 methods of Harmonic Current Extraction and 10 synchronization algorithms [2]. Other parts of SAPF control system are not signal processing related and they are not covered in this article. Subjective evaluation and comparison of these methods can be seen in Tab. 1.

3 *HCGL* Experimental Platform

In order to meet the above mentioned requirements for testing methods, it was necessary to design an experimental platform that will allow an objective comparison of SAPF control methods[4]. Schematic of the proposed experimental platform can be seen in Fig. 2.

HCGL consists of a total of six independent inventer modules (GEN 1–3 and LOAD 1–3). Three are used as controllable loads and three as current injection modules. Modules are controlled via analog input voltage, which is generated from NI 9263 analog output cDAQ modules. A total of 12 currents (grid, loads, injection, neutral), and 3 voltages (grid) are measured and connected to the cDAQ system via signal conditioning modules. The measuring system complies with following standards: IEC EN 50160 and IEC EN 61000, which are used in Power Quality area[1].

Due to the need to degrade the voltage conditions of the system, softening inductors are embedded in the network. Thanks to this, a lot of negative voltage conditions can be made.

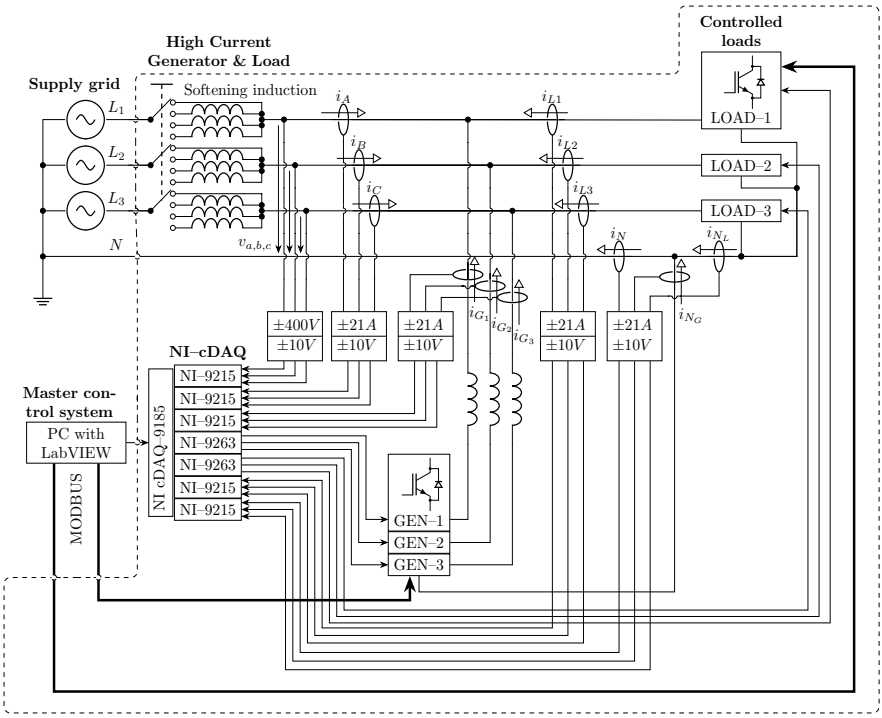

Fig. 2. High Current Generator & Load experimental platform schematic diagram.

3.1 Software

Power modules can be alternatively controlled via MODBUS communication bus, but primarily through LabVIEW application which runs on master system (PC or cRIO controller). Application is designed as modular due to future expansion of functionality. Currently the application can communicate with power modules, make measurement with respect to standards, carry out simple grid scenario and implement various SAPF control methods.

There are currently developed 6 SW modules which runs parallel and independently to each other. First module maintains the data acquisition and also generates, via a_o, the reference voltage signal for the generation of compensation current. Another module maintains the MODBUS communication with the actual generator and load modules. It is necessary to send a watchdog command through the bus every 200 ms or the timeout error occurs and the system shuts itself to error state. Third module counts the implemented method under test. The method itself and its parameters can be switched on the run. The fourth and final module maintains the grid scenario. All modules communicates between themself through FIFO queue communicating messages. The implemented SW architecture is based on the Queued–Message Handler LabVIEW design pattern.

Fig. 3. Various photos of the *HCGL* system.

Table 1. Subjective evaluation of various SAPF Harmonic Extraction control methods.

Control method	1 or 3 phase	Work under dist. voltage?	Curr. meas. only?	Auto -conf. of param.	Implemen -tation difficulty	Dynam.?	Subj. perf. of method
iPQ	3	No	No	Yes	Low	Bad	Average
CVT	3	No	No	Yes	Low	Bad	Average
PQR	3	No	No	Yes	Low	Bad	Average
UPC	3	No	No	Yes	Low	Bad	Average
PHC	3	No	No	Yes	Low	Bad	Average
SRF	3	Yes	Yes	Yes	Lower	Average	Higher
SDM	3	Yes	No	Yes	Lower	Average	Average
CCT	1,3	Yes	No	Yes	Lower	Average	Average
SMT	1,3	Yes	No	Yes	Lower	Average	Average
VF	3	Yes	No	Yes	Lower	Average	Average
CPT	1,3	Yes	No	Yes	Lower	Average	Average
FFT	1,3	Yes	Yes	No	Average	Very Bad	Average
RDFT	1,3	Yes	Yes	No	Average	Bad	Average
KF	1,3	Yes	Yes	No	Average	Average	Average
WT	1,3	Yes	Yes	No	Average	Average	Average
ADALINE	1,3	Yes	Yes	No	High	Good	High
ANFIS	1,3	Yes	Yes	No	High	Good	High
LMS	1,3	Yes	Yes	No	Average	Good	Higher
RLS	1,3	Yes	Yes	No	Higher	Good	High
Notch LMS	3	Yes	Yes	No	Higher	Good	High
Notch RLS	3	Yes	Yes	No	Higher	Good	High

4 Conclusion

Brief introduction was made in this article about experimental versatile *HCGL* platform which is currently under development at Technical University of Ostrava, Faculty of Electrotechnics and Computer Sciences in CPIT–TL3. Platform will be used in ongoing research about SAPF control methods.

Currently there are new methods, or modifications of currently existing methods, under development which will expand current portfolio of methods. There are 4 methods implemented (LMS, Notch–LMS, RLS, Notch–RLS) and objectively comparised between themselves.

The functionality of the proposed system was verified on the basis of many experiments. These experiments showed that it is necessary to replace the current control system (cDAQ+PC) with the RTOS platform NI cRIO, as the current solution is computationally insufficient.

References

1. Baros, J., Martinek R.: Wireless Power Quality Analyser Based on Virtual Instrumentation. In: IFAC-PapersOnLine 52.27, pp.465–472, IEEE, High Tatras, Slovakia, 2019.
2. Hoon, Y.: Control Algorithms of Shunt Active Power Filter for Harmonic Mitigation: A Review. Energies, pp. 2038–2051, MDPI, 2017.
3. Martinek, R. et. al: Design of a Measuring System for Electricity Quality Monitoring within the SMART Street Lighting Test Polygon: Pilot Study on Adaptive Current Control Strategy for Three-Phase Shunt Active Power Filters. Sensors, pp. 1718–1743, MDPI, 2020.
4. Martinel, R., Rzidky J: Least Mean Squares and Recursive Least Squares Algorithms for Total Harmonic Distortion Reduction Using Shunt Active Power Filter Control. Energies, pp. 1545–1565, MDPI, 2019.

Data Processing in WSN based on Compression

Monika Borova

Department of Cybernetics and Biomedical Engineering, FEECS,
VSB – Technical University of Ostrava, 17. listopadu 15,
708 00 Ostrava – Poruba, Czech Republic
monika.borova@vsb.cz

Abstract. The IoT sensor network includes a number of sensor nodes that transmit the required environmental parameters to the central cloud. In general, all IoT standards allow only a limited amount of data to be transmitted during a single period of time.
Data compression can be a solution to this problem. The article provides an overview of selected methods that can be used in WSN. It also provides a theoretical basis for further testing. Finally, a compression experiment based on neural networks is performed.

Keywords: Data compression, WSN, IoT, Wavelet transform, Neural network

1 Introduction

Environmental monitoring systems can be implemented as wireless sensor networks (WSN), which collect environmental parameters over time. Such systems are often located in remote and inaccessible places, which increases the requirements for their high reliability and energy independence. Other requirements that need to be addressed when designing the system include the number and type of input interfaces, sampling frequency, data processing capabilities, communication interface, device size, or operating temperature range.

Wireless sensor networks (WSN) belong to the category of wireless networks, which are characterized by low transmission speed, but are capable of unattended operation in the order of months to years. Such a network consists of very limited devices that cooperate with each other and ensure the processing, storage, reception or transmission of data. Most of them are networks without the need for configuration and are strictly optimized for use in specific applications. They use radio waves for communication and the range of this communication can be from centimeters to a distance of several kilometers.

Today, InternetOfThings (IoT) offers many communication technologies that can be used in the WSN environment. However, these communication interfaces are limited by the maximum amount of data transferred. This problem can be solved by processing data on the interface - edge computing. The principle of the technique is based on data processing directly in the sensor node, so that only the compressed data or the extracted information contained in them is transmitted

VSB – Technical University of Ostrava, 2021, ISBN 978-80-248-4523-4 (on-line).

to the cloud server. This approach reduces the amount of data transferred and significantly affects the overall power consumption in WSN.

The main advantage of this approach is the reduction of the amount of transmitted data, which leads to lower energy requirements for transmission. This reduction is partially offset by the energy consumed for the compression algorithms in the individual nodes. The aim is to find the optimal setting of parameters that are able to store as much information as possible in the data with reduced consumption.

Due to the growing demands for data processing and storage, it is necessary to shorten the data transfer time and move computing processes to the periphery of the network - the so-called edge computing. The goal of this method is to move high-capacity content and data management closer to the source.

This article is organized into four sections. The first section provides a brief introduction to the issue and motivation. The background section contents state of the art and general principle of selected algorithms. The experiment results are elaborated in the results section. The final section concludes achieved results.

2 Background

Many compression algorithms exist for data compression in WSNs, but it is necessary to find one that produce better compression ratios and less loss of data in the reconstructed data. Data compression techniques can be either lossy or lossless. *Lossless Compression* means that the original data stays without degradation of quality and can be reused. The original data is not changed permanently during compression, which is a great advantage. On the other hand, the compression achieved is not very high. *Lossy compression* means that parts of the original data are removed permanently to reduce file. Due to the loss of a lot of data, the data may be skewed after reconstruction and the quality degraded [1].

2.1 Related Work

Adaptive compression sampling can be used to reduce data from a smart meter, which is a method that reduces the bandwidth requirement for data transfer of individual meters [2]. In the case of compression already during data collection, it is possible to use a set of convolution neural networks, which are arranged in the tree architecture [3].

Edge computing methods use not only wireless sensor networks, but also WBSN - wireless body area network [4]. In these applications, data is collected from wearable and sensor devices (watches, pressure sensors, ...) and regularly sent to a node on the periphery. This node will then process, analyze, filter and then send the data to the cloud. A fast error-based lossy compressor is used to compress the data and uses three prediction models - preceding Neighbor Fitting, Linear-Curve Fitting and Quadratic-Curve Fitting. Subsequently, the data is encoded using Huffman coding. From the experimental result, it was

found that during a four-hour monitoring, data with a total size of 2976000 bytes were collected and after compression the size was reduced up to 103 times to 28732-41602 bytes.

The authors of the S-Health architecture based on MEC (Multi-access Edge Computing) use edge computing access for remote monitoring of patients [5]. They use neural networks, specifically Stacked Auto-Encoders, for compression. Another task in this architecture is the detection of anomalies in the source data, for example in epileptic seizures, for which Machine Learning methods are used. Thanks to this classification on the periphery, the transmitted data is significantly reduced.

The authors of [6] use Huffman coding to compress data obtained from sensor nodes. The compression of the temperature measurement data set is based on a fixed Huffman dictionary.

A compression ratio of 52.67% can be achieved using a combination of Delta and RLE (Run-Length Encoding) [7] technique. This connection was experimentally verified for data from the accelerometer, the implementation of the compression algorithm was performed on a PSoC microcontroller. The resolution of the ADC was changed to 8, 10 and 12 bits, respectively. In addition to the compression ratio, the compression factor and space saving were also determined in the calculations.

The LZW method (Lempel-Ziv-Welch 84) is very often used, which after modification is suitable for use in embedded devices. The S-LZW, or LZW for the sensor node, divides the uncompressed input bitstream into fixed-size blocks and then compresses each block separately. For each new block, a new dictionary is created using 256 codes, which represent the standard character set. Due to the limited memory capacity of individual nodes, the length of the dictionary must be limited. It may happen that a complete dictionary for the whole block will not be created. In this case, the dictionary freezes and the rest of the block is either compressed by this dictionary or is reset and formed from the beginning of [8]. This algorithm has been compared with the gzip method for compressing temperature and relative humidity data [9].

2.2 Selected Compression Algorithms

2.3 Neural network

Data compression is one of common application of neural networks. The basis is the use of a neural network that has the same number of input neurons as number of input neurons and has a smaller number of neurons in one of the hidden layers. The task of such a selected network is to learn the identity of the submitted data. After learning the network, it will be divided into two parts at the output of the mentioned hidden layer - the input half of the network now serves as a compressor and the other as a decompressor.

2.4 Methods based on dictionary coding

These are adaptive methods that create a dictionary as it passes, which is then transmitted either with the code or created by the decompression algorithm itself so that the data can be converted to its original form. This group includes various modifications of the LZ algorithm (Lempel-Ziv), which are quite often used in current formats.

Huffman coding is one of the oldest compression methods ever. The algorithm is based on the principle of building a binary tree. Characters that occur in the file with a high frequency are assigned code with a small number of bits. Conversely, characters that occur with a low frequency in the file are encoded with the longer code.

The *LZ77 algorithm* is widely used and combined with other methods. According to the principle, it is called the sliding window method. The data is presented by a string and the sliding window is divided into a part where the data is already encoded and a part with unencoded data. At the beginning, the sliding window is set to the string to be encoded so that the part for already encoded data is empty and the other part is filled with a string (or part of it). The goal is to find the longest possible match of the string in the uncoded part with the string in the coded part.

The *LZ78 algorithm* is a modification of the previous one, so it is sometimes referred to as LZ2. The algorithm creates a dictionary of phrases just like LZ77, but this word is represented by an tree. In the first step, the root of the tree with the sequence number zero is created. Then the specified string starts encoding. The first character is read. A new node with the lowest next sequence number is created, in this case one, which is connected to the node with a zero-rated edge. This edge has the value of the character that was read first. This encodes the first character, the method creates a dictionary reference in the form (0, a), where a is the first character. Next, the second character is read. If it is the same as the first one (ie it is already encoded once in the dictionary), it is not necessary to encode it, so the next character is read to it. Next, the algorithm looks for whether this pair of characters is in the dictionary. If so, the next character is read. This will proceed to the algorithm until it finds a phrase that is not in the dictionary.

3 Results

For experimental purposes we are using the dataset consist with data about temperature. A total of 14 days time-log was used, giving data at 5 minute intervals the each data series counts 288 measurement per day. Two variants of autoencoders settings were tested.

The Fig. 1 shows the setting of an autoencoder that has five neurons in the hidden layer. The original signal is plotted, and for comparison the signal that was reconstructed using a trained neural network is also plotted. The mean squared error (MSE) was determined for evaluation of distortion between these two signals. In this case, the value of MSE is 0.059.

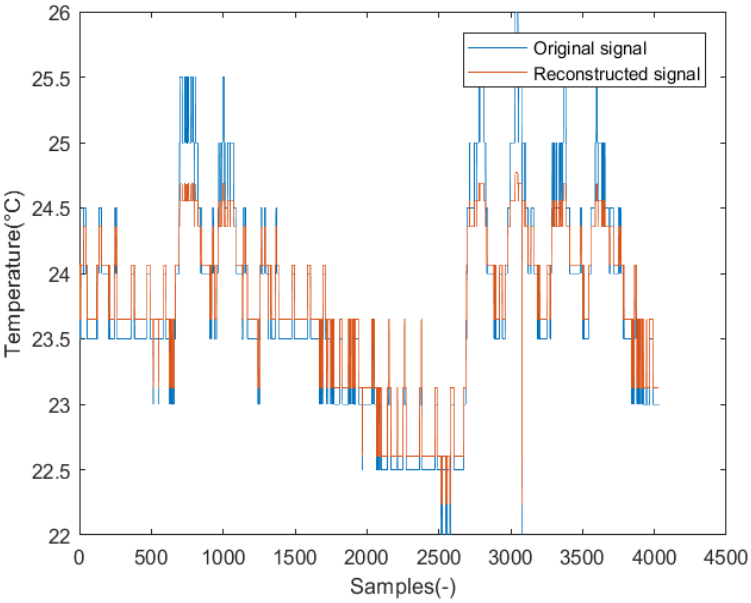

Fig. 1. Input and output of autoencoder - five neurons in hidden layer - MSE = 0.059

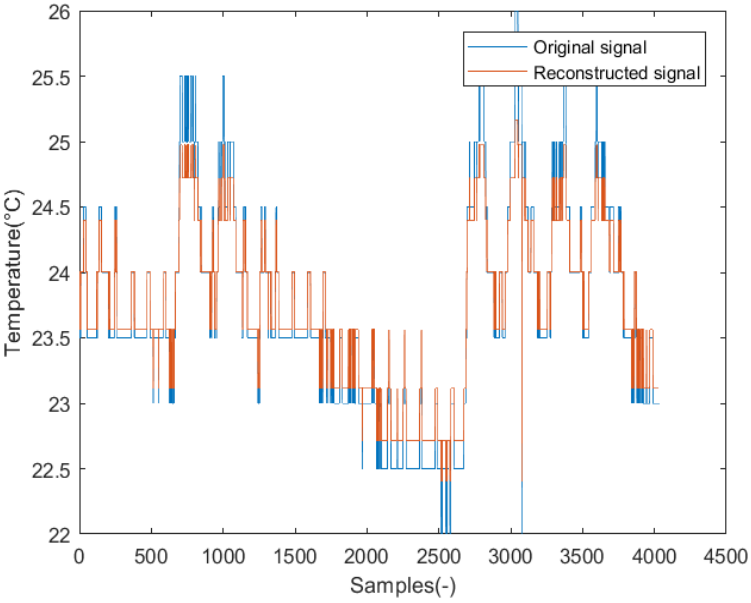

Fig. 2. Input and output of autoencoder - sixty neurons in hidden layer - MSE = 0.029

In the second case (Fig. 2), the autoenoders has sixty neurons in hidden layer and has sigmoid as an activating function. The mean squared error of this settings is 0.029.

4 Conclusion

There are many methods to reduce the amount of data in WSN. Compression algorithms can be based on one of the mathematical transformations - wavelet, cosine, or on one of the dictionary methods - Huffman, LZW, or on neural networks. In this paper, we focused mainly on methods based on dictionary creation and neural networks. This paper serves as a basis for future work.

The paper provides description and visualization of the research results describing the using of neural networks as a tool for data compression. The experiments was performed on data about temperature and the mean squared error was determined for evaluation of distortion.

References

1. Mandavi, and Prasannjit, and Mrinal, Nilotpal and Chatterjee, Kalyan and S, Dasgupta: Data Compression Using Neural Networks in Bio-Medical Signal Processing. Computer Science & Information Technology. 3. 159–167 (2013)
2. Tripathi, Sharda and De, Swades: An efficient data characterization and reduction scheme for smart metering infrastructure. IEEE Transactions on Industrial Informatics. 4300–4308.(2018)
3. Jia, Yiling and Batra, Nipun and Wang, Hongning and Whitehouse, Kamin: A tree-structured neural network model for household energy breakdown. The World Wide Web Conference. 2872–2878. (2019)
4. Azar, Joseph and Makhoul, Abdallah and Barhamgi, Mahmoud and Couturier, Raphaël: An energy efficient IoT data compression approach for edge machine learning. Future Generation Computer Systems. 168–175. (2019)
5. Abdellatif, Alaa Awad and Mohamed, Amr and Chiasserini, Carla Fabiana and Tlili, Mounira and Erbad, Aiman: Edge computing for smart health: Context-aware approaches, opportunities, and challenges. IEEE Network. 196–203. (2019)
6. Medeiros, Henry Ponti and Maciel, Marcos Costa and Demo Souza, Richard and Pellenz, Marcelo Eduardo: Lightweight data compression in wireless sensor networks using Huffman coding. International Journal of Distributed Sensor Networks. 10. (2014)
7. Hanumanthaiah, Aravind and Gopinath, Athira and Arun, Chandni and Hariharan, Balaji and Murugan, Ravisankar: Comparison of Lossless Data Compression Techniques in Low-Cost Low-Power (LCLP) IoT Systems. 2019 9th International Symposium on Embedded Computing and System Design (ISED). 1–5. (2019)
8. Sadler, Christopher M and Martonosi, Margaret: Data compression algorithms for energy-constrained devices in delay tolerant networks. Proceedings of the 4th international conference on Embedded networked sensor systems. 265–278. (2006)
9. Marcelloni, Francesco and Vecchio, Massimo: A simple algorithm for data compression in wireless sensor networks. IEEE communications letters. 411–413. (2008)

Real-time Simulator And PLC S7 1500: A Closed-loop Control

Radek Byrtus

Department of Cybernetics and Biomedical Engineering, FEECS,
VSB – Technical University of Ostrava, 17. listopadu 15,
708 00 Ostrava – Poruba, Czech Republic
radek.byrtus@vsb.cz

Abstract. This work describes a processor-in-the-loop simulation scenario based on Speedgoat real-time simulator and PLC S7 1500 1516-3 PN/DP. Nowadays, and also in the past, are real-time simulators used in many ways for testing developed control systems, mainly in hardware-in-the-loop or processor-in-the-loop testing scenarios. The main industrial sectors using this technology include the automotive and aerospace industry. The practical part of this work describes created closed-loop control scenario for speed and reliability testing of PROFINET industrial communication protocol and testing of PID_Compact block from PLC system, which is used for control of the real systems.

Keywords: Profinet · HIL · PIL · matlab · simulink · closed-loop control

1 Introduction

Since the turn of the 1970s, it has been characterized by a sharp increase in electronic systems not only in the aerospace and automotive industries[1, 2]. The size and complexity of electronic control units, production lines and all related systems is growing significantly[2–4].

However, this trend brings with it an increasing risk of errors both in the finished system and during its design. Enormous demands for testing such complex systems come from the design stage. HIL and PIL simulations are just one of the methods to perform these tests[4, 5]. Today's technologies are also increasingly based on the modeling of entire control systems or production lines, where this trend is known as digital twin[2].

It is for these reasons that from the turn of the millennium, specialized devices for performing HIL and PIL simulations are beginning to emerge. These are mainly specialized RT systems on a common x86 platform equipped with an input/output interface and also having modules for communication via industrial buses [1].

The following chapters describe PIL and HIL simulations, the closed-loop system control system used, and the results obtained. The conclusion is devoted to the evaluation of the contribution and follow-up activities.

VSB – Technical University of Ostrava, 2021, ISBN 978-80-248-4523-4 (on-line).

1.1 PIL And HIL In Comparison

Processor-in-the-loop is a test scenario, where compiled code that describes control or system model runs in external hardware called target. Target could be represented as a embedded system, single-board computer, DSP, FPGA or system with common processor/microprocessor. Controller then runs on this specific target platform. Both subsystems, controller and plant model, are linked by specific communication protocol or data exchange port. PIL simulation thus allows to test the control system already on the target platform and it is possible to verify its behavior, performance or parameters[6, 7].

Developed control system can be also tested in most closed way to the reality. The principle is based on a PIL simulation with a difference in the communication interface used. This type of simulation is used mainly for complex control tasks with a large amount of resources spent - automotive, aircraft, etc.[1–4].

In addition to the connection to the real system, special hardware is used here to simulate physical quantities. These are usually A/D and D/A converters, current loops and other sensors. The link to the interrupt system is a matter of course. By simulating the HIL type, it is possible to get as close as possible to the real control process and thus many errors can be detected before the final deployment. The differences between the individual types of simulation are described in Fig. 1 [7].

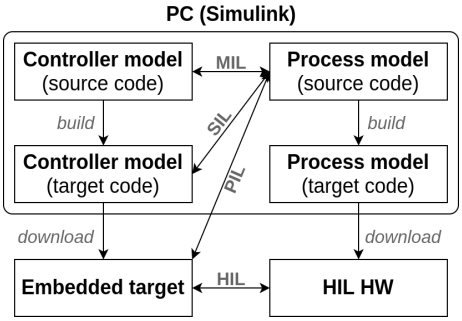

Fig. 1. Principle of MIL, PIL and HIL simulations

Hardware-in-the-loop simulators are commonly available from small portable devices to rack solutions depending on the input requirements of the simulated system. In our case there are two racks representing classic personal computer platform running Free-DOS with Simulink Real-time module and PCI bus extension used for I/O modules.

2 Closed-loop Control System

As part of the use of a simulator running in real time, a number of experiments using industrial buses were created. In most cases, these were simple communi-

cation tasks. Based on these test tasks, a more complex task was subsequently created to test the speed and reliability of the PROFINET bus. This is a task based on the regulation of the system in a closed loop. The concept of this task is based on the assumption that in a real industrial environment, PLC systems are commonly used to control various devices and systems. These systems are a common part of modern industrial production lines. It means mainly regulation of speed, temperature, angle, level, current, power, and etc. The prepared example is based on a basic analysis of real systems, thanks to which simple first and second order systems were implemented to test.

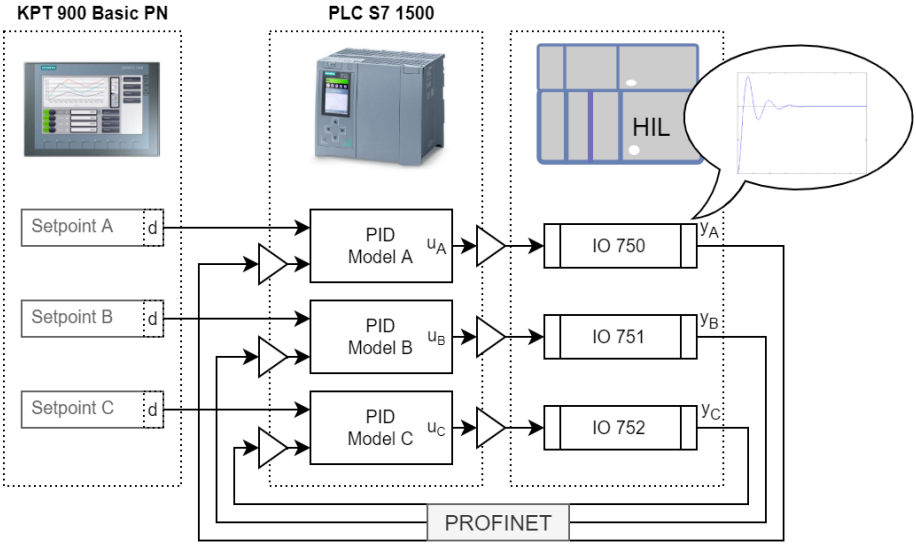

Fig. 2. Simplified idea of prepared implementation

The simplified idea of prepared testing scenario is presented on Fig. 2. Several different systems are prepared in a Simulink model - slow 1st order system, faster 2nd order system, oscillating 2nd order system and very fast 2nd order system. Each of these systems has different minimum requirements for the stability of a closed control circuit, in particular the minimum sampling frequency of the controller. It means, that it is necessary to set up PROFINET communication on lowest possible send-time period. Transfer function of prepared systems are:

$$\begin{aligned} G_A(s) &= \frac{0.375s + 1.25}{3s + 1} \quad G_B(s) = \frac{1.45}{0.3s^2 + 1.45s + 1} \\ G_C(s) &= \frac{10.64}{2s^2 + 1.6s + 8} \quad G_D(s) = \frac{1.45}{0.004687s^2 + 0.1812s + 1} \end{aligned} \tag{1}$$

2.1 Network Configuration

The basis of this project is a functional network configuration for communication between the PLC system and the real-time controller. A total of four real-time simulator modules, a PLC system, two personal computers and an analyzer for industrial communication buses were connected within the 192.168.7.x/24 subnet.

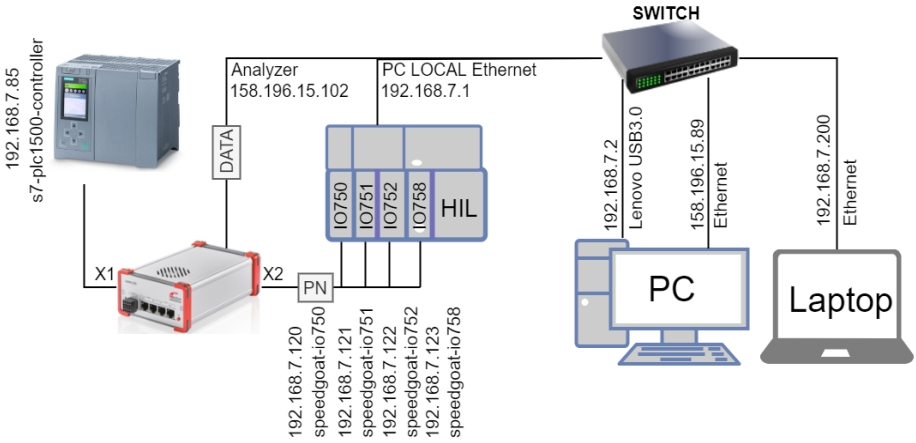

Fig. 3. Workbench network configuration

Referring to the Fig. 3 each real-time simulator module represents one designed system model. Via the PROFINET bus, these modules are connected as slave devices to the PLC system that presents the PROFINET master device. In the PLC system, their correct configuration is necessary using GSD-ML files from Hilscher and on the simulator side using configuration using own NXD files from SYCON.NET configurator application. For uploading an configuration to the real-time simulator, support code in MATLAB is created.

2.2 Testing Scenarios

PLC system program contains four cyclic interrupts with different cycle time from 200 ms to 15 ms for fastest system. In each cyclic interrupt is a PID_Compact instance and a local system model. PID controller could be connected with local model or with remote model via PROFINET. To find the correct constants of the PID controller, the built-in *pretuning* and *finetuning* functions are used, which calculate the basic and optimal control constants based on the measured system response. For comparison a MATLAB script is created, which results in the third control constants of the PID controller. PLC communication cycle is set to 2 ms and models in real-time simulator are calculated every 5 ms.

3 Results

Fig. 4 shows obtained regulation constants from different testing scenarios. Best way to obtain optimal regulation constants is to use transfer function of system and *pidtune* function in MATLAB. Also constants from *pretuning* and *finetuning* function from PLC system are working quite well, but in comparison with *pidtune* there is longer settling time and higher overshoot.

	PROFINET		LOCAL		MATLAB
	Model A				Model A
	Finetuning	Pretuning	Finetuning	Pretuning	pidtune
Kp	1,318445	15,25	1,0409	14,9617	0,827
Ti	0,801729	0,48	1,4552	0,48	0,954
Td	0,211018	0,084006	0,38535	0,084	-
	Model B				Model B
	Finetuning	Pretuning	Finetuning	Pretuning	pidtune
Kp	2,76	6,03	0,6141	3,8683	1,33
Ti	0,7411	0,472	0,4004	0,3805	0,989
Td	0,1867	0,8267	0,1057	0,0659	0,197
	Model C				Model C
	Finetuning	Pretuning	Finetuning	Pretuning	pidtune
Kp	0,7419	2,447	0,227	1,674	0,473
Ti	0,6698	0,56	0,5056	0,8045	1,02
Td	0,1805	0,9799	0,1191	0,1407	0,256

Fig. 4. Picture of table containing results

Situation with Model C (2nd order, oscillating) is shown in Fig. 5. First graph represents response of system alone without regulator. It is possible to see high overshoot and oscillation character of the system. Other graphs shows closed-loop regulation with different regulation constants. Constants obtained by *finetuning* have very similar results to *pidtune* in closed-loop.

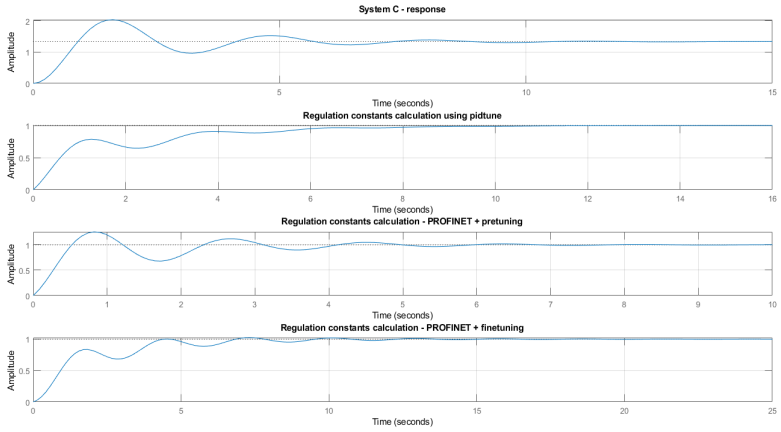

Fig. 5. Model C: Comparison of closed-loop regulation responses

4 Conclusion And Future Work

This paper describes a closed-loop regulation on PROFINET, done on real-time simulator from Speedgoat, which is located here on VSB-TU Ostrava for project purposes. As a PID controller PLC S7 1500 from Siemens is used. RT simulators are used today in every industry way, where rapid prototyping and thorough testing are used in order to tune the device or system to the highest possible level of reliability. Use of PIL and HIL simulations lower total time and final cost of development. Currently, it is possible to work with our device on simulations with the PIL and HIL approach, because a new I/O modules are installed.

Next step will be to implement hardware-in-the-loop simulation between PLC and real-time simulator using technological signals, commonly used in industry. After successful implementation, a inverted pendulum model on IRT will be tested. There is also possibility to write an publication in this topic.

Acknowledgement: The following grant si acknowledged for the financial support provided for this research by project *Centrum výzkumu pokročilých mechatronických systémů* CZ.02.1.01/0.0/0.0/16_019/0000867, VSB - Technical University of Ostrava.

References

1. M. Karpenko and N. Sepehri: Hardware-in-the-loop simulator for research on fault tolerant control of electrohydraulic flight control systems. In: American Control Conference, Jun. 2006, p. 7 pp., https://doi.org/10.1109/ACC.2006.1657454.
2. V. Mařík, Průmysl 4.0: Výzva pro Českou republiku, Vydání 1. Praha: Management Press. (2016)
3. J. Lee and M. Suh.: Hardware-in-the loop simulator for ABS/TCS, In: Proceedings of the 1999 IEEE International Conference on Control Applications (Cat. No.99CH36328), Aug. 1999, vol. 1, pp. 652–657 vol. 1, https://doi.org/10.1109/CCA.1999.806729.
4. H. K. Fathy, Z. S. Filipi, J. Hagena, and J. L. Stein: Review of hardware-in-the-loop simulation and its prospects in the automotive area. In: Modeling and Simulation for Military Applications, May 2006, vol. 6228, p. 62280E, https://doi.org/10.1117/12.667794.
5. M. Bacic: On hardware-in-the-loop simulation. In: Proceedings of the 44th IEEE Conference on Decision and Control, Dec. 2005, pp. 3194–3198. https://doi.org/10.1109/CDC.2005.1582653.
6. J. Mina, Z. Flores, E. López, A. Pérez and J. Calleja: Processor-in-the-loop and hardware-in-the-loop simulation of electric systems based in FPGA. In: 13th International Conference on Power Electronics (CIEP), 2016, pp. 172-177. https://doi.org/10.1109/CIEP.2016.7530751.
7. Z. Bubnicki and Springer Science+Business Media: Modern control theory. Berlin. Heidelberg: Springer (2010).

Enhancements of Software Defined Radio based system for V2X-VLC

Lukas Danys and Radek Martinek

Department of Cybernetics and Biomedical Engineering, FEECS,
VSB – Technical University of Ostrava, 17. listopadu 15,
708 00 Ostrava – Poruba, Czech Republic
{lukas.danys, radek.martinek}@vsb.cz

Abstract. This paper focuses on a real measurements and enhancements of a software defined radio-based system for vehicle-to everything visible light communication (SDR-V2X-VLC). The presented system is based on a novel adaptive optimization of the feed-forward software defined equalization (FFSDE) methods of the least mean squares (LMS), normalized LMS (NLMS) and QR decomposition-based recursive least squares (QR-RLS) algorithms. Individual parameters of adaptive equalizations are adjusted in real-time to reach the best possible results. Experiments were carried out on a conventional LED Octavia III taillight drafted directly from production line and universal software radio peripherals (USRP) from National Instruments. The transmitting/receiving elements used multistate quadrature amplitude modulation (M-QAM) implemented in LabVIEW programming environment. Experimental results were verified based on bit error ratio (BER), error vector magnitude (EVM) and modulation error ratio (MER). The best results were achieved using the QR-RLS algorithm. The results measured on deployed QR-RLS algorithm had significantly better Eb/N0 (improved by approx. 20 dB) and BER values (difference by up to two orders of magnitude).

Keywords: Visible Light Communication, Quadrature Amplitude Modulation, LabVIEW.

1 Introduction

VLC is an optical wireless technology which operates from 380 to 780 nm, using a visible light source as a signal transmitter, free space environment as transmission medium and the appropriate PIN photodetectors, pricier avalanche photo diodes (APDs), advanced CMOS cameras, or inexpensive solar panels as receivers.

VLC seems to be capable technology for short-range, or possibly in the future even long-range data transmissions, and accurate positioning in congested environments. Appliances vary greatly - spanning from conventional everyday lighting to vehicular solutions, deployment in hospitals (as it does not interfere

VSB – Technical University of Ostrava, 2021, ISBN 978-80-248-4523-4 (on-line).

with sensitive equipment) or simply as an alternative to typical local area networks (LAN). Rapid expansion of LED is crucial for this technology, as it offers multiple advantages such as long lifespan, low power consumption, high tolerance to humidity, high efficiency, and fast switching. However, the main advantage of VLC based on LED is the use of the visible spectrum (380–780 nm). LED can therefore perform communication functionality while maintaining the original function as illumination lighting, thus further reducing power consumption and emissions. This technology can work in a standalone mode or even as a supplementary technology to already deployed solutions, such as mobile networks. It is currently often explored as a last mile technology for some 5G scenarios.

2 Experimental Part

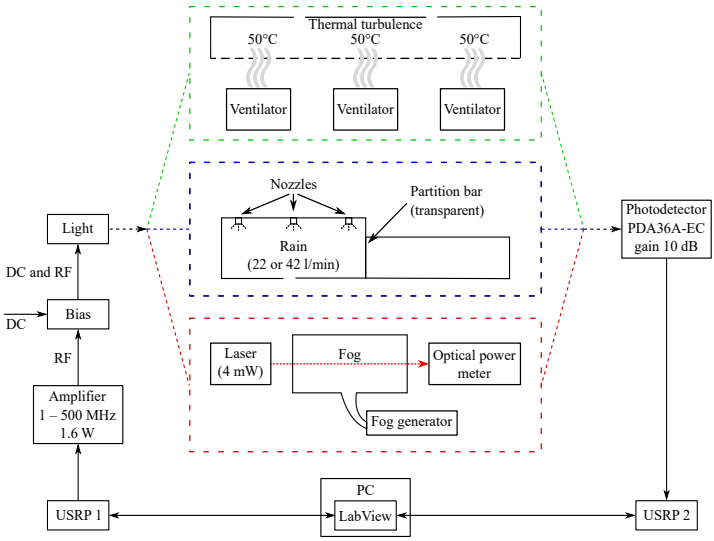

Fig. 1. Block diagram of the tested platform.

The whole testing platform is built as a virtual instrument - relying heavily on LabVIEW programming environment and software defined radios. As the scenarios with indoor light source were already tested out earlier, an "outdoor" variant was chosen for tests with adaptive equalization [1–7]. An Octavia III taillight was chosen as a transmitting element, whereas a Thorlabs PDA36A-EC photodetector was used as a receiving element. Bias-Tee XZ85-12G-S+ was used to modulate the transmitting light source. An amplifier operating at 1 MHz to 500 MHz was also incorporated on transmitting side. Two NI USRP 2921 software defined radios were used, one for each transmitting/receiving element - these radios used a set of Ettus LFTX/LFRX daughterboards instead of the

original ones. A high-end PC running LabVIEW was used for generation and evaluation of transmitted data. The block diagram of the whole platform can be seen in Figure 1.

A robust software side was developed in LabVIEW programming environment and can be divided into multiple blocks. Various parameters, such as MER, BER, SNR or RSL can be displayed. The software can also display constellation and eye diagrams.

The following configuration was used during experiments: 3 MHz carrier frequency with variable bandwidth from 1 MHz up to 4 MHz with step size of 1 MHz. Three adaptive algorithms were tested - LMS, NLMS and QR-RLS.

A first set of measurements was carried out in the empty box and was used as a reference. A frequency attenuation characteristic was measured to determine the ideal carrier frequency.

2.1 Influence of Thermal Turbulence on Visible Light Communication

A set of three electric air heaters located below the box at predefined distances was used to simulate thermal turbulence. These heaters were mounted on the bottom of the box, and vents on the top were opened to ensure proper circulation of air. In addition, windows in the laboratory were opened. The temperature in the box varied, ranging between 40 and 50 C (higher temperature was directly above the heat sources). Comparison of measured parameters and individual adaptive equalizers can be seen in Figure 2.

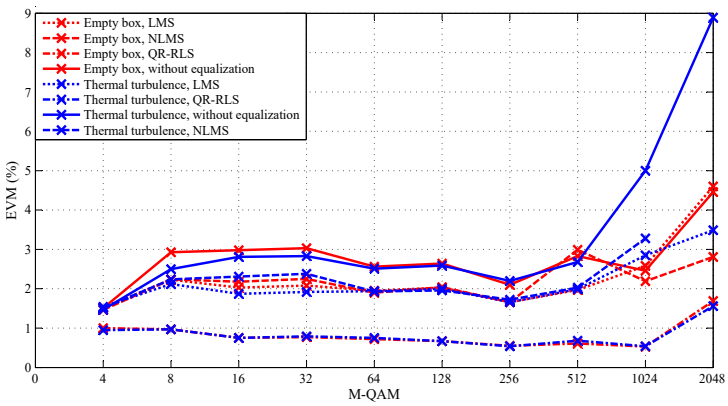

Fig. 2. Dependence of Eb/N0 on the used modulation format, 1 MHz bandwidth, comparison of the effect of temperature turbulence.

Overall, the temperature turbulence has negligible effect on the measured parameters. These parameters deteriorate only during measurements with higher state modulations (the reduction of the signal-to-noise ratio has a significantly

greater effect on higher modulations formats). QR-RLS seems to be the best adaptive algorithm for this measurement, as even at 1024-QAM, the bit error rate never exceeds 10^{-4}, while the other algorithms are approximately two orders of magnitude higher.

2.2 Influence of Rain on Visible Light Communication

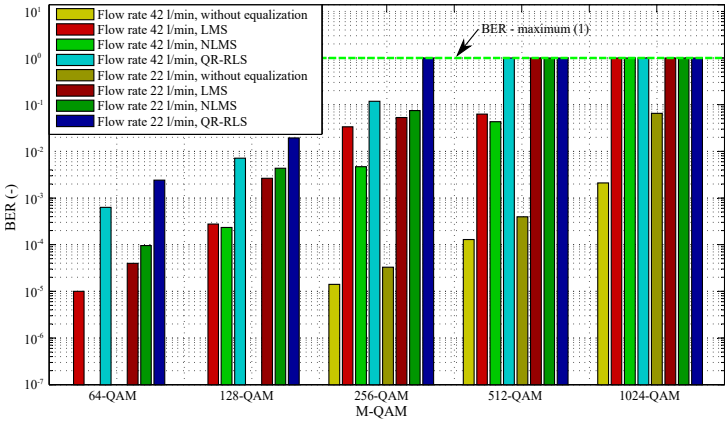

Fig. 3. Dependence of BER on the used modulation format, 1 MHz bandwidth.

Measurement of the influence of rain on communication based on VLC technology was carried out in the "modified" box environment. A 2.5 m long rain simulation construction was inserted into the box. Two flow rates (42 l/min and 22 l/min) were picked for measurements - simulating rain of various intensity. During the measurement, a partition was inserted in the middle of the box, as the water must circulate through the pump. Figure 3 cover the comparison of the BER parameter, for various multistate modulation formats and 1 MHz bandwidth.

By comparing the effect of rain intensity, it can be found out that the higher flow rates influence the measurements significantly more, as was expected. When comparing 256-QAM values from both scenarios, it can be noticed that the BER of QR-RLS algorithm is in the order of 10^{-5} for both flow rates. In comparison LMS reached only 10^{-3} for lower flow rate, whereas for higher flow rate, the values reached even 10^{-1}. In comparison, NLMS reached approx. 10^{-2} for both flow rates. When the adaptive equalization is deactivated, BER values reached 10^{-1} for lower flow rate and 1 for higher flow rate.

2.3 Influence of Fog on Visible Light Communication

The third scenario was also carried out in the box, this time with attached fog machine. The holes in the box were sealed at the beginning of the measurement

to prevent fog from escaping into the environment. Gradually, some holes were opened to support the complete dissolve of the fog. Antari Alpha F-80Z was used to generate fog.

As the fog had no constant concentration during the whole measurement and changed constantly, a way of monitoring of its density was introduced. A reference laser-photodetector combination with known power was added to the box to measure fog density. By using this laser and photodetector, the various power levels were measured as a function of time. This way it could be at least estimated how dense the fog was. This measurement can be seen in Figure 4.

Power spikes and dips are caused by fog mixing with air during the opening of previously mentioned holes. Constellation diagrams of some modulations with adaptive algorithms can be also seen in this Fig 4. The fog concentration was constantly changing; therefore, some measured values are written next to the constellation diagrams.

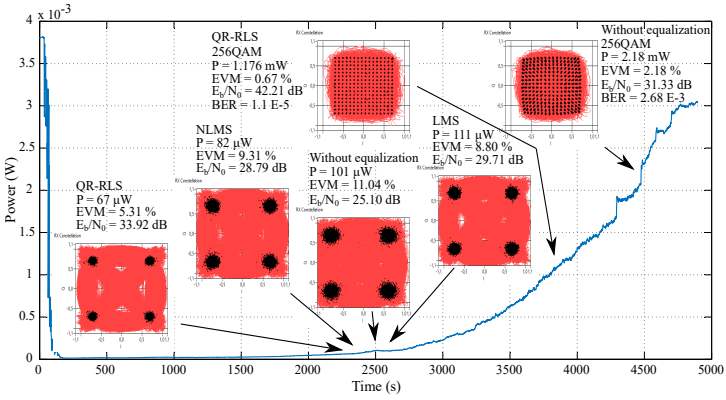

Fig. 4. Attenuation frequency characteristics of the fog simulation. The higher the power level of the reference laser, the lower the fog concentration.

3 Conclusion

This paper presents results of our ongoing research focused on VLC. The presented work deals with various aspects of FFSDE and clearly shows the positive impact of its implementation. The system itself is built as a virtual machine - leveraging advantages of virtual instrumentation, thus ensuring fast adaptivity and high degree of modularity. Throughout the experiment, various shortcomings were localized and a potential candidate for new and more suitable parts were already identified, leading to even better results

The used algorithms reached different results, depending heavily on the tested scenarios. Starting with thermal turbulence, it was clearly noticeable that it has negligible effect on the measured parameters. In the worst-case scenario,

the LMS and NLMS managed to improve the Eb/N0 parameter by approx. 3 to 4 dB, while the QR-RLS reached 9 dB. The situation is vastly different in case of rain scenarios. QR-RLS managed to improve Eb/N0 by 20 dB (in case of 22 l/min) and 22 dB (in case of 42 l/min). The most significant impact was measured during fog scenarios. Since it was hard to maintain a reliable connection a different approach was chosen. The QR-RLS again showed the best results across the board and completely outshined both the LMS and NLMS. In the most important scenarios, the QR-RLS outperformed both LMS and NLMS by more than 50%. Overall, the adaptive software equalization proved to be an important addition to any system, which can show the untapped potential of the used hardware.

4 Acknowledgement

This research was funded by the European Regional Development Fund in the Research Centre of Advanced Mechatronic Systems project, project number CZ.02.1.01/0.0/0.0/16_019/0000867 and by 543 the Ministry of Education of the Czech Republic, Project No. SP2021/32.

References

1. Danys, L., Martinek, R., Jaros, R., Baros, J., Simonik, P., Snasel, V.: Enhancements of sdr-based fpga system for v2x-vlc communications. CMC-COMPUTERS MATERIALS & CONTINUA **68**(3), 3629–3652 (2021)
2. Danys, L., Martinek, R., Slanina, Z., Kolarik, J., Jaros, R.: The impact of rain on performance of visible light communication. In: Photonics Applications in Astronomy, Communications, Industry, and High-Energy Physics Experiments 2019. vol. 11176, p. 111760Q. International Society for Optics and Photonics (2019)
3. Fajkus, M., Nedoma, J., Martinek, R., Danys, L., Fridrich, M., Mec, P., Zabka, S.: Fiber-optic bragg system for the dynamic weighing of municipal waste: A pilot study. IEEE Access (2021)
4. Martinek, R., Danys, L., Jaros, R.: Visible light communication system based on software defined radio: Performance study of intelligent transportation and indoor applications. Electronics **8**(4), 433 (2019)
5. Martinek, R., Danys, L., Jaros, R.: Adaptive software defined equalization techniques for indoor visible light communication. Sensors **20**(6), 1618 (2020)
6. Martinek, R., Danys, L., Jaros, R., Mozny, D., Siska, P., Latal, J.: Vlc channel equalization simulator based on lms algorithm and virtual instrumentation. In: 2019 International Symposium on Advanced Electrical and Communication Technologies (ISAECT). pp. 1–6. IEEE (2019)
7. Martinek, R., Jaros, R., Baros, J., Danys, L., Kawala-Sterniuk, A., Nedoma, J., Machacek, Z., Koziorek, J.: Noise reduction in industry based on virtual instrumentation. CMC-COMPUTERS MATERIALS & CONTINUA **69**(1), 1073–1096 (2021)

Double Inverted Pendulum Swing-up Solving by Direct Collocation Method

Tomas Docekal[0000−0002−9485−0924]

Department of Cybernetics and Biomedical Engineering, FEECS,
VSB – Technical University of Ostrava, 17. listopadu 15,
708 00 Ostrava – Poruba, Czech Republic
tomas.docekal@vsb.cz

Abstract. This article describes the direct collocation method used for solving optimal control problem. This method is classified as direct approach. The main idea is to transfer original optimal control problem to nonlinear programming by discretization of continuous state variable waveforms and control signal. The transferred task is solved iteratively by software for static optimization solving. Whole method is applied to case study for illustration. The state space description of double inverted pendulum is given and the swing-up maneuver is solved by Hermite-Simpson direct collocation method.

Keywords: Optimal Control Problem, Direct Method, Direct Collocation, Nonlinear Programming, Double Inverted Pendulum.

1 Introduction

The demands for increasing the control system efficiency and performance and for decreasing the production cost starts to appear in the past with industry development. Increase of computer technology performance made it possible to meet these requirements. A new branch of control theory has emerged – the modern control theory [1]. Its main task is to solve optimization problem – minimize or maximize specified cost function, which includes variety of demands.

It is possible to divide optimization problems into two types, static and dynamic. We are speaking about static optimization when the problem is connected with some steady state and we want to optimize some settings or parameters [2]. The result of optimization is not function of time. Dynamic optimization [3] is connected with time and dynamic changes. The result is control signal, which is time function.

This paper deals with optimal control problem solving by use of direct collocation. This process is described on case study, which is swing up of double inverted pendulum [4], [5].

VSB – Technical University of Ostrava, 2021, ISBN 978-80-248-4523-4 (on-line).

2 Optimal Control Problem

The main task of solving optimal control problem is to find specific control $u(t)$, which will transfer the dynamic system from initial state $\boldsymbol{x}_0 = \boldsymbol{x}(t_0)$ to final state $\boldsymbol{x}_f = \boldsymbol{x}(t_f)$. The number of different controls, which fulfill this first condition, is theoretically infinite. We call them feasible controls. By minimizing the objective function, it is possible to select one control $u^*(t)$ and corresponding state trajectories $\boldsymbol{x}^*(t)$. They are then called optimal. Generally, the optimal control problem is specified by objective function, state space description of dynamic system and initial and finite state. It is also possible to specify some constraints. For detail description, see [6].

2.1 Approaches for Optimal Control Problem Solving

There are many methods, which can be used for solving the optimal control problem. It is possible to sort them into three basic approaches [7] according to the main idea used by the method – dynamic programming [8], indirect methods [9] and direct methods [10]. This article is focused on last approach.

The direct methods approach leads to solving optimal control problem without expressing optimal condition or any other equations. The main idea is to transform the problem to nonlinear programming (static optimization) by discretization of state variable trajectories and control. This converted task is specified by decision vector $\boldsymbol{z}$, objective function J and constraints in the form of bounds or linear and nonlinear equalities and inequalities (1). The general goal of nonlinear programming is to find the decision vector (select each value that makes it up) so the objective function is minimized with respect to all constraints.

$$\begin{gathered} \boldsymbol{z} = [z_1, z_2, z_3, \dots] \\ J = f(\boldsymbol{z}) \\ \boldsymbol{l}_b \leq \boldsymbol{z} \leq \boldsymbol{u}_b \\ \boldsymbol{A} \cdot \boldsymbol{z} \leq \boldsymbol{b} \\ \boldsymbol{A}_{eq} \cdot \boldsymbol{z} = \boldsymbol{b}_{eq} \\ \boldsymbol{c}(\boldsymbol{z}) \leq 0 \\ \boldsymbol{c}_{eq}(\boldsymbol{z}) = 0 \end{gathered} \tag{1}$$

The decision vector compilation is specific for each method, it may not contain only discrete values of states and control. The great advantage is the existence of many methods for solving static optimization task. It is possible to use for example direct single shooting, direct transcription or direct collocation. Although the final methods for solving the problem can be the same as for indirect methods, the approaches are different and so the problem solved by the method. When using single shooting method for solving two-point boundary value problem (indirect approach), the result is conjugated states trajectories, which are then used together with optimal condition to derivate the control signal. When using the same method for solving nonlinear programming (direct approach), the discretized control signal is directly the result.

2.2 Direct Collocation

This is one of the advanced methods which rank among the direct approach. The first step is common for all direct methods – discretization of state trajectories and control signal. The time interval $\langle t_0, t_f \rangle$ on which the optimal control problem is solved is divided to N parts with length h. The discrete points in time are called node points [11].

The next step is specific for direct collocation methods. The state trajectory at each time interval between node points are approximated by polynomial and so the control signal. There are many different types of direct collocation method according to order of these polynomials. Generally, the coefficients of each polynomial forms the decision variables vector instead of discrete state and control values at node points.

There are three main types of constraints used by this method. The first one is used for continuity of polynomials at node points, the difference between ending point of one polynomial and starting point of second one have to be zero. The second type is used for continuity of derivation of polynomials in the same way as the first one. By these two types of constraints, the smoothness of the resulting state trajectories is ensured. Last type of constraints is used for ensuring compliance with controlled dynamic system state space description. The other points, called collocation points, are specified at the interval between node points. For example, there can be one point at the middle of interval. The state of system (each state variable value) at the collocation point is derived from the corresponding polynomial and compared with state derived from system dynamics (state space description). The differences at each collocation points have to be zero to ensure the compliance of resulting state trajectories with system dynamics.

The objective function from original optimal control problem have to be rewritten for decision vector or the state trajectories and control signal have to be determined from decision vector in each iteration firstly. It is necessary to use numerical method for objective function calculation, if there is the Lagrange term in the integral form.

2.3 Hermite-Simpson Method

One specific type of direct collocation method is called Hermite-Simpson. The cubic polynomial is used for approximation of state trajectories and linear polynomial for control signal. Basically, one collocation point at the middle of interval between node points is used.

The cubic polynomial is specified by four coefficients. This polynomial has to begin and end in the node points state values. The corresponding time derivative values at node points can be obtained from system dynamics. Based on these four values, it is possible to specific polynomial coefficients. It is also possible to derive formula to calculate collocation point value. The time derivative at this point is calculated based on polynomial and also from system dynamics. The difference of these two values has to be zero and forms the constrain for compliance with system dynamics. For detailed description and equations derivation, see [12] or [13].

The advantage of these modifications is that the discrete values of state trajectories forms decision vector directly. The state value at node point is common for two consecutive intervals (and so the slope), so constraints for trajectory smoothness are not

needed. It is also possible to limit state values by simple bounds instead of nonlinear inequalities, as these values are directly included in the decision vector.

3 Case Study: Double Inverted Pendulum Swing Up

The inverted pendulum on linear guidance system is very popular due to its properties. This system is strongly nonlinear, non-minimum phase and underactuated. That means there are more degrees of freedom (pendulum arm angle and cart position) than actuators (one actuator for moving with cart). With additional arm connected with free rotational joint to the end of previous arm, the complexity of system is significantly higher. The double inverted pendulum system consists of two pendulum arms made by some shaft, with first arm connected freely to cart at one end. The actuator is used to move with the cart along linear guidance. This system is described by six state variables, which are pendulum arms angles x_1 and x_2 (rad), pendulum arms angular velocities x_4 and x_5 (rad·s^{-1}), cart position x_3 (m) and cart velocity x_6 (m·s^{-1}). The control signal u is cart acceleration (m·s^{-2}).

The state space description of double inverted pendulum is derived from Lagrange mechanics. The total kinematic and potential energy of mechanical system have to be determined firstly together with total energy losses due to friction. Based on these, the motion equation for each pendulum arm is derived. It is possible to derive the motion equation for cart in the same way, but with selected control signal (cart acceleration) it is not needed. The equations (2), (3) and (4) show final state space description of double inverted pendulum.

$$\begin{aligned} x_1' &= x_4 \\ x_2' &= x_5 \\ x_3' &= x_6 \\ x_4' &= F_4 \\ x_5' &= F_5 \\ x_6' &= u \end{aligned} \tag{2}$$

$$\begin{aligned} F_4 = \frac{1}{\cos^2(x_1 - x_2) - p_1 p_5} [&-p_2 p_5 g \sin(x_1) - p_6 u \cos(x_1 - x_2) \cos(x_2) \\ &- p_4 x_5 \cos(x_1 - x_2) + x_4^2 \cos(x_1 - x_2) \sin(x_1 - x_2) \\ &+ p_6 g \cos(x_1 - x_2) \sin(x_2) + p_4 x_4 \cos(x_1 - x_2) + p_3 p_5 x_4 \\ &+ p_5 x_5^2 \sin(x_1 - x_2) - p_4 p_5 x_5 + p_2 p_5 u \cos(x_1) + p_4 p_5 x_4] \end{aligned} \tag{3}$$

$$\begin{aligned} F_5 = -\frac{1}{\cos^2(x_1 - x_2) - p_1 p_5} [&-p_2 g \sin(x_1) \cos(x_1 - x_2) \\ &+ p_3 x_4 \cos(x_1 - x_2) + x_5^2 \cos(x_1 - x_2) \sin(x_1 - x_2) \\ &- p_4 x_5 \cos(x_1 - x_2) + p_2 u \cos(x_1 - x_2) \cos(x_1) \\ &+ p_4 x_4 \cos(x_1 - x_2) - p_1 p_6 u * \cos(x_2) - p_1 p_4 x_5 \\ &+ p_1 x_4^2 \sin(x_1 - x_2) + p_1 p_6 g \sin(x_2) + p_1 p_4 x_4] \end{aligned} \tag{4}$$

There are parameters p_1-p_6, which are called standard dynamics parameters. They are determined by specific combinations of physical parameters, which includes pendulum arms weight, length, moment of inertia, center of gravity position and friction.

The swing-up task is solved for described system, that means transfer from lower stable equilibrium $x_0 = [\pi; \pi; 0; 0; 0; 0]'$ to upper unstable equilibrium $x_f = \mathbf{0}$. The problem is solved in Matlab with use of fmincon function. The final time t_f is specified by interval $\langle 2.3; 2.9 \rangle$, the problem can be denoted as task with free final time and fixed final state. The value of t_f is added to the decision vector to be found by optimization. The continuous signals are divided into 100 equally long intervals, that means 101 node points. The decision vector $\boldsymbol{z}$ is specified by following equation (5).

$$\boldsymbol{z} = [u_0, u_1, u_2, \dots, u_{99}, u_{100}, x_{1-0}, \dots, x_{1-100}, x_{2-0}, \dots x_{6-100}, t_f] \tag{5}$$

The objective function (6) is composed by two parts with weight coefficients. The first one is generally called as minimization of control signal energy. It is useful to obtain good results, which can be used with real system. The second part is for minimization of linear guidance length needed for swing-up maneuver. The physical limitations are specified by bounds, nevertheless the addition of this condition to objective function leads to better results with shorter used guidance length.

$$J = 10^{-4} \cdot \int_{t_0}^{t_f} u^2 \mathrm{d}t + 10^{-1} \cdot [\max(x_3) - \min(x_3)] \tag{6}$$

It is necessary to specify initial guess for solution when using fmincon function. The simple variant is used – linear interpolation between initial and final state and zero control. The obtained optimal state trajectory $x_1^*(t)$, $x_2^*(t)$, $x_3^*(t)$ and optimal control signal $u^*(t)$ are shown for illustration at fig. 1.

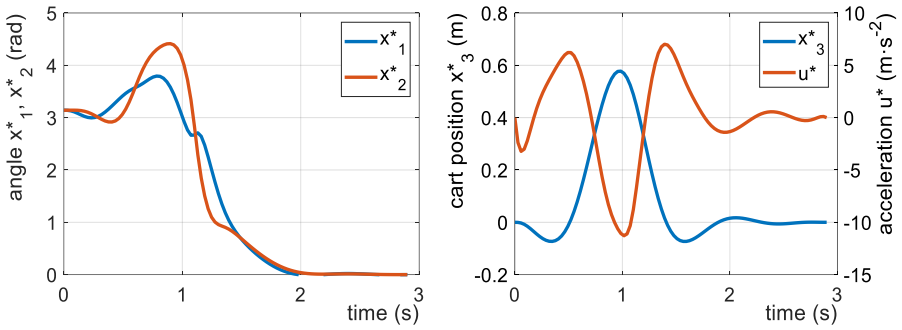

Fig. 1. Optimal state trajectory x_1*(t) and x_2*(t) (left) and optimal control signal u*(t) and state trajectory x_3*(t) (right)

4 Conclusion

This article describes one of the methods for optimal control problem solving classified as direct approach. The main idea of this approach is to transfer the optimal control

problem (dynamic optimization) to nonlinear programming (static optimization) because of many available and good quality solvers for static optimization.

The described direct collocation method is very effective way to optimal control problem solving. As shown on case study, it is usable for very complex systems also. One of next advantages is possibility to modify probably any parameter of the task and to specify the required properties. This method also allows setting of any type of constraints due to the possibility to write specific code for this purpose with different conditions. The bounds can be time varying.

The process of solving the optimal control problem by direct collocation method is more time consuming than indirect methods due to iterative execution of optimization solver. However, it is not needed to calculate condition of optimality or other equations.

References

1. Gajic, Z., Lelic, M.: Modern control systems engineering. Prentice-Hall, Inc. (1996).
2. Ozana, S., Docekal, T.: PID controller design based on global optimization technique with additional constraints. Journal of Electrical Engineering 67.3, 160-168 (2016).
3. Ozana, S., Pies, M., Docekal, T.: Dynamic optimization case studies in DYNOPT tool. AIP Conference Proceedings. Vol. 1738. No. 1. AIP Publishing LLC (2016).
4. Graichen, K., Treuer, M., Zeitz, M.: Swing-up of the double pendulum on a cart by feedforward and feedback control with experimental validation. Automatica 43.1, 63-71 (2007).
5. Salehi, M., Nikoobin, A., Shahab, E.: Optimal Swing up of Double Inverted Pendulum using Indirect Method. ADMT Journal 11.3, 101-108 (2018).
6. Betts, J., T.: Practical methods for optimal control and estimation using nonlinear programming. Society for Industrial and Applied Mathematics (2010).
7. Biral, F., Bertolazzi, E., Bosetti, P.: Notes on numerical methods for solving optimal control problems. IEEJ Journal of Industry Applications 5.2, 154-166 (2016).
8. Kirk, D., E.: Optimal control theory: an introduction. Courier Corporation (2004).
9. Naidu, D., S.: Optimal control systems. CRC press (2002).
10. Rao, A., V.: A survey of numerical methods for optimal control. Advances in the Astronautical Sciences 135.1, 497-528 (2009).
11. Yadav, V.: Direct collocation for optimal control. MEC 560's home page, Sep 30 (2016), https://mec560sbu.github.io/2016/09/30/direct_collocation.
12. Becerra, V., M.: Practical direct collocation methods for computational optimal control. Modeling and Optimization in Space Engineering. Springer, New York, NY, 33-60 (2012).
13. Kelly, M.: An introduction to trajectory optimization: How to do your own direct collocation. SIAM Review 59.4, 849-904 (2017).

Review of Three-phase Induction Motors Faults and Measurement

Jakub Dohnal

Department of Cybernetics and Biomedical Engineering, FEECS,
VSB – Technical University of Ostrava, 17. listopadu 15,
708 00 Ostrava – Poruba, Czech Republic
doh0028@vsb.cz

Abstract. Induction motors are an important part of the production processes of today's industry. Induction motors in industrial areas are influenced by electrical and mechanical effects, but also by environmental effects. It is important to ensure early detection of these faults to avoid financial losses. Motor faults can originate from electrical, mechanical, or environmental influences and their result can be fatal for the motor. To prevent this, it is necessary to correctly identify these errors and to measure the corresponding quantities that contain information about these errors. This work is a review of these motor faults and commonly measured quantities for fault detection. The quantity carrying the most information is the electric current, so it is one of the most promising quantities for fault detection.

Keywords: Induction Motor, Motor Faults, Predictive Maintenance, Rotor, Stator

1 Introduction

Appropriately selected signal processing methods can detect a malfunction or irregularity of the machine's functionality already in the initial phase of the problem. In practice, the correct and especially timely diagnosis of a rotor fault is most important, as it can have a direct effect on many secondary faults, which then can lead to serious engine damage. Today, industrial companies that use induction motors seek to minimize operating and maintenance costs. Predictive maintenance is important part of today's industry because it allows to detect motor faults in the beginning. To perform predictive maintenance, the engine characteristics must first be measured correctly, and the fault identified. This effort is directly related to the early detection of faults, which greatly depends on the measured quantities and their processing. [1, 2].

To be able to measure and identify motor errors, this review article was created, which contains an overview of these errors and the most measured quantities for the detection of these errors. The survey found that the most used measured quantities are current and vibration. The measurement of other quantities such as voltage, electro-

VSB – Technical University of Ostrava, 2021, ISBN 978-80-248-4523-4 (on-line).

magnetic field and temperature does not bring much new information, but in some cases, they can be a substitute or additional information to already measured values.

This review is related to three-phase motor testbed and will serve as a knowledge base for ongoing measurements and fault detection. The literature was selected mainly from articles dealing with the same issues of three-phase motor measurements and fault detection.

The second chapter of the article deals with induction motor faults. These faults are divided according to their place of origin and briefly described. The third chapter focuses on some measurable quantities. The chapter contains an introductory division of measurements according to categories and further the division itself according to measured quantities. The fourth chapter is a summary and conclusion of this work.

2 Induction Motor Faults

Faults on induction motors can be primarily divided into mechanical and electrical faults. Electrical faults can then be divided into rotor and stator faults.

2.1 Rotor Faults

Rotor faults make up 5% to 10% of the total list of faults that occur in induction motor [3]. It is usually associated with the occurrence of asymmetries in the rotor cage or in the rotor winding [1]. The rotor cage mainly breaks the rod or end ring but can also damage the rotor core. Rotor faults can be caused by thermal, magnetic, dynamic, environmental influences or mechanical stress [2]. High temperature and subsequent overheating of the rotor cage can cause expansion, which leads to mechanical stress. Environmental stress is mainly caused by dirt or abrasion of the rotor material [2].

Rotor rods are most often damaged by high temperatures. If the rotor bar breaks, the rotor cage cannot usually be repaired. Failure of the cage leads to the formation of shaft vibrations, bearing damage and the creation of an air gap. Thus, early detection of a broken rod not only protects the rotor, but also prevents many other possibilities of motor damage [2].

In some cases, the rotor rod breaks at the connection point, where the rod itself is connected to the end ring. Adjacent columns then carry higher currents than the values for which they are intended. This entails their faster degradation over time and, if the rod failure is not detected in time, damage to the engine core itself [6].

2.2 Stator Faults

Although the stator winding is usually well protected by more advanced insulation materials, monitoring the stator insulation is very important and necessary due to possible fatal motor damage. Between 21% and 40% of all IM faults are related to winding insulation fault [1]. Winding faults are usually associated with slow but permanent aging of the winding insulation. Older stator windings fail due to short overheating, vibrations, or short-term higher voltage [1, 3].

The importance of monitoring temperature conditions has increased in recent decades. Temperature effects have been identified as the main cause of most stator insulation failures. For this reason, many temperature relays have been developed to protect the motor from thermal overload. Temperature sensors are now part of large motors, but there are certain areas of application where it is undesirable or even impossible to use [3, 5].

An electrical short circuit is often the cause of a fault in the winding insulation. It leads to the current peak, which generates extraordinary heat and causes the insulation of the adjacent line to ignite. The insulation fault eventually spreads to the stator core. Fault propagation occurs in 20 to 60 seconds, so rapid intervention is required, otherwise the stator may be damaged fatally [5].

2.3 Mechanical Faults

One of the most common mechanical failures arise in bearing and require the deployment of special sensors to monitor their conditions. Bearing failures account for approximately 40% (high-voltage IM) to 90% (low-voltage IM) of all failures [1]. Thermal, electrical, and mechanical stresses have the greatest influence on the condition of bearings. The heat conducted from the shaft as well as shaft tension cause the bearing lubrication to dry out, which then leads to friction and bearing damage. Even vibrations of the rotor shaft can lead to bearing failure, especially on larger machines that have high output torque [5].

Eccentricity of air gaps in induction motors indicates a situation where there is an uneven air gap between the rotor and the stator. A certain level of eccentricity is common in every IM and can be encountered directly during production [1]. The resulting air gap may increase during operation due to the wear of various motor parts. The increased eccentricity leads to unbalanced magnetic traction, vibrations, loosening of the frame and windings or friction between stator and rotor, which can eventually result in damage to the stator and rotor core.

3 Induction Motor Measurement

Induction motor measurement can be split into invasive and non-invasive measurement. Methods for non-invasive acquisition of data include several easily measurable quantities, such as stator current, external magnetic field, velocity, or vibration. Other derived quantities, such as individual voltages and torque, are estimated or calculated within the control loops of the drives. In addition, quantities such as acoustic noise or temperature can rarely be considered [9]. Invasive methods of data collection are then highly dependent on the degree of induction motor modification.

Information about the healthy state is obtained and then compared with the scenario with any defect or error. Almost all methods developed so far are based on one or more techniques from the following categories [2]:

- Measurement of stator currents

- Vibration measurement
- Electromagnetic field monitoring
- Measurement of acoustic emissions
- Direct temperature measurement
- Thermal radiation sensing
- Measurement of induced voltage
- Overvoltage and load testing

Measurement techniques can be divided into online and offline. Offline techniques require the engine to be stopped or shut down completely, while online techniques allow measurements to run during operation. However, offline, unlike online methods, have the advantage of repeatability of measurements and offer a significant reduction in noise contamination [10].

3.1 Measurement of Electrical Quantities

Voltage and current variables are among the most widely used options for obtaining relevant input data for diagnostics. Stator currents are one of the most universal variables, which contain information about the state of the motor and the possible future occurrence of faults [8]. They are also the most frequently measured quantities for the purpose of monitoring engine conditions [11].

Current measurement for motor condition diagnostics has a significant advantage in the simplicity of measuring system implementation. To obtain a basic overview of the motor status, it is sufficient to use current probes and suitable hardware and software to process the signal. These measurements also do not require invasive interventions in the measured motor, which allows online condition monitoring. The term Motor Current Signature Analysis (MCSA) includes methods based on current measurement and processing, where subsequent results are used to identify or predict motor failure.

Motor voltage analysis (MVSA) includes voltage-based methods that are used for subsequent monitoring of induction motor status. MVSA methods are used in conjunction with MCSA methods to generate trends and analyze engines in real time. They focus on the early detection of stator winding problems, rotor problems, cabling, or bound loads, and even efficiency, system loads, bearing defects and much more.

3.2 Vibration Measurement

The ideal induction motor generates minimal vibration during operation. Almost all failures that occurs in the induction motor leads to vibration anomalies. Based on this assumption, it is possible to obtain information about current state of motor using the correct analytical method. Vibration measurement techniques in most cases focus on bearing failures, gearboxes, rotor eccentricities or general imbalances [2].

In practice, acceleration measurements based on accelerometers are most often used. Vibration can also be measured by measuring deflection or speed, both absolutely and relatively. Furthermore, the measurement can be divided into non-contact

(vibration sensing by laser device) or contact (vibration measurement using e.g. piezoelectric accelerometers).

3.3 Electromagnetic Field Measurement

The failure of the induction motor is also reflected in its electromagnetic field. Each type of fault introduces its own characteristic frequencies into the electromagnetic field. Based on previous knowledge of these frequencies and relevant procedures, valuable information regarding the condition of the motor can be obtained or extracted. Monitoring of the electromagnetic field can thus provide a considerable amount of information for possible identification or prediction of a fault. This is caused by electromagnetic forces, noise, and vibrations, which affect the proper functioning of the rotor, which leads to its damage [12].

3.4 Temperature Measurement

The occurrence of a motor failure leads to its sub-optimal operation and changes in operating characteristics and can cause higher consumption due to overcurrent. Problems caused by higher engine temperatures can be diagnosed by regular measurements. The temperature can be measured either directly by sensors or non-contact. The non-contact approach based on infrared thermography is most often used in real world scenarios [13]. Temperature measurement is usually performed to diagnose stator winding faults. By measuring the temperature, it is also possible to diagnose a short circuit in the winding or a fault in the shaft.

4 Conclusion

The development of a testbed for vibration measurement is currently being completed and the information contained in this work is necessary for the creation of a measuring system and the detection of induction motor faults. Knowledge of these faults, methods and possibilities of measuring quantities are the basis for their correct identification. This can further lead to the creation of a system for predictive maintenance, which is one of the goals of the project mentioned in acknowledgement. The information provided here is only part of the accumulated knowledge about the types of induction motor failures, methods of measurement and evaluation, data processing and analysis. A comprehensive overview of this information will soon be published in one of the impacted journals. Future research will be primarily focused on real measurements from the designed testbed using commercial and developed sensors.

For our testbed, current and vibration measurements look most promising. Both quantities carry a lot of useful information and can be done non-invasively. Another interesting alternative is electromagnetic field measurement. This measurement can be done with electromagnetic coil as sensor and does not need connection to electrical circuit. Voltage measurement between neutral wire of power supply and motor contains also important data about unbalanced power consumption. There are several

motors in testbed, which will reproduce mentioned faults. The task will be to identify these faults from measured data and determine the state of motor.

5 Acknowledgement

This work was supported by the European Regional Development Fund in Research Platform focused on Industry 4.0 and Robotics in Ostrava project CZ.02.1.01/0.0/0.0/17_049/0008425 within the Operational Programme Research, Development and Education, and in part by the Ministry of Education of the Czech Republic under project number SP2021/32.

References

1. Riera-Guasp M., Antonino-Daviu J. A., Capolino G.-A.: Advances in electrical machine, power electronic, and drive condition monitoring and fault detection: state of the art. IEEE Transactions on Industrial Electronics 62(3), 1746–1759 (2015).
2. Mehrjou M. R., Mariun N., Hamiruce Marhaban M.: Rotor fault condition monitoring techniques for squirrel-cage induction machine-A review. Mechanical Systems and Signal Processing 25(8), 2827–2848 (2011).
3. Bellini A., Filippetti F., Tassoni C.: Advances in diagnostic techniques for induction machines. IEEE Transactions on Industrial Electronics 55(12), 4109–4126 (2008).
4. Nandi S., Toliyat H. A., Li X.: Condition monitoring and fault diagnosis of electrical motors-a review. IEEE Transactions on Energy Conversion 20(4), 719–729 (2005).
5. Zhang P., Du Y., Habetler T. G., Lu B.: A survey of condition monitoring and protection methods for medium-voltage induction motors. IEEE Transactions on Industry Applications 47(1), 34–46 (2011).
6. Pezzani C., Donolo P., Bossio G., Donolo M.: Detecting broken rotor bars with zero-setting protection. IEEE Transactions on Industry Applications 50(2), 1373–1384 (2014).
7. Bonnett A. H., Soukup G. C.: Analysis of rotor failures in squirrel-cage induction motors. IEEE Transactions on Industry Applications 24(6), 1124–1130 (1988).
8. Sun L., Xu B.: An improvement of stator current based detection of bearing fault in induction motors. In: 2007 IEEE Industry Applications Annual Meeting, New Orleans, LA, USA, 2277–2281 (2007).
9. Filippetti F., Bellini A., Capolino G.: Condition monitoring and diagnosis of rotor faults in induction machines: State of art and future perspectives. In 2013 IEEE Workshop on Electrical Machines Design, Control and Diagnosis, Paris, France, 196–209 (2013).
10. Yousef Ben Sasi A., Gu F., Payne B., Ball A.: Instantaneous angular speed monitoring of electric motors. Journal of Quality in Maintenance Engineering 10(2), 123–135 (2004).
11. El Hachemi Benbouzid M.: A review of induction motors signature analysis as a medium for faults detection. IEEE Transactions on Industrial Electronics 47(5), 984–993 (2000).
12. Henao H., Capolino G.-A., Fernandez-Cabanas M.: Trends in fault diagnosis for electrical machines: a review of diagnostic techniques. IEEE Industrial Electronics Magazine 8(2), 31–42 (2014).
13. Singh G., Anil Kumar T. Ch., Naikan V. N. A.: Induction motor inter turn fault detection using infrared thermographic analysis. Infrared Physics & Technology 77(1), 277–282 (2016).

Electrochemical Measurement of Glucose Concentration in Simulated Body Fluid

Klára Fiedorová

Department of Cybernetics and Biomedical Engineering, FEECS,
VSB – Technical University of Ostrava, 17. listopadu 15,
708 00 Ostrava – Poruba, Czech Republic
klara.fiedorova@vsb.cz

Abstract. The work focuses on the use of electrochemical detection of glucose concentration in continuous measurement. For the measurement, Hank's balanced salt solution (HBSS) was mixed, which has a similar composition as the plasma. Detection was performed by flow analysis, where the carrier fluid is mixed with glucose from the simulated blood plasma. Glucose is captured and detected by a biosensor in the flow cell and potentiostat. The measurement was performed by analyzing HBSS with different glucose concentrations. The effects of flow and temperature on the electrochemical response were evaluated from the measured data. By optimally changing the flow and temperature of the analyzed solutions, it is possible to achieve a more sensitive measurement, but the measurement becomes more time-consuming. The results of the work serve as a basis for the own solution of continuous blood glucose measurement.

Keywords: electrochemical detection, glucose biosensor, measuring glucose concentration

1 Introduction

Today, high demands are placed on measuring the concentration of substances in solution. Electrochemical biosensors based on immobilized enzyme and physico-chemical transducer are created. They are used in the detection of glucose, viruses, bacteria, nucleic amino acids or addictive substances. Microsystem technology and nanotechnology are beginning to be applied in the construction of biosensors [1,2].

Physico-chemical converter used to read the physical quantity during the oxidation-reduction reaction. The variables are most often converted to a voltage that changes over time and is proportional to the concentration of the analyte. A change in the concentration of a analyte is expressed as a change in a voltage, electrical current, or conductivity signal. Electrochemical detection methods include voltammetry, amperometry, potentiometry, conductometry and impedimetry [1,2].

The analysis of solutions uses the methods of flow analysis in experimental cells. The cells are used to dispense the substance into the liquid stream, which carries the analyte to the sensor itself. There are three basic types of flow analysis: continuous flow analysis (CFA), injection flow analysis (FIA) and sequential injection analysis (SIA).

VSB – Technical University of Ostrava, 2021, ISBN 978-80-248-4523-4 (on-line).

Flow cells can vary in their layout and are used: thin-layer and wall-jet. For the purposes of this work, Simulated body fluids were investigated for the evaluation of biological activity of materials, apatite formation and analysis of measuring methods [3].

Microdialysis methods are used to minimize invasiveness. A fluid based on Ringer's solution is injected into the catheter placed in the tissue or solution. Molecules from around the catheter diffuse through the membrane and are led to the biosensor [4].

The article evaluates the current responses of the biosensor to glucose concentration under different measurement conditions. The measuring chain is described and the measured data are analyzed with respect to the functionality of the biosensor and use for the design and solution of own work.

2 Design and Implementation of Experimental Equipment

HBSS was used in the measurement because it has a similar concentration of substances as blood plasma. The glucose concentrations are 3, 5, 7, and 10 mmol/l with a pH 7.2 - 7.6. The exact composition of the solution is given in Table 1 [5].

Table 1. Reagents for mixing 1000 ml HBSS

Substance	Amount	Substance	Amount	Glucosa (concent.)	Amount
$NaCl$	8 g	$MgCl_2 - 6H_2O$	100 mg	0,003 mol	0.54 g
KCl	400 mg	$Na_2HPO_4 - 12H_2O$	60 mg	0,005 mol	0.90 g
$CaCl_2$	140 mg	KH_2PO_4	60 mg	0,007 mol	1,26 g
$MgSO_4 - 7H_2O$	100 mg	$NaHCO_3$	350 mg	0,010 mol	1.80 g

2.1 Experimental Measuring Chain

The measuring chain (Fig. 1) consisted of a potentiostat allowing the use of most electrochemical techniques to which a biosensor with immobilized glucose oxidase is connected (Fig. 2). It is a three-electrode biosensor with a working (Pt), reference (Ag) and auxiliary (Pt) electrode. The enzyme glucose oxidase (GOD) is immobilized on the active surface of the working electrode, ensures the capture of glucose and an oxidation reaction occurs, hydrogen peroxide is formed, which is further cleaved:

$$\begin{aligned} Glucosa + O_2 &\xrightarrow{GOD} H_2O_2 + Gluconic\ acid \\ H_2O_2 &\xrightarrow{Platinum\ working\ electrode} 2H^+ + O_2 + 2e^- \end{aligned} \quad (1)$$

During the measurement, the biosensor is stored in a flow cell, which is in a wall-jet arrangement. The entire measuring chain is driven by a linear dimmer, with adjustable flow 0.1 ml/h - 300 ml/h with an accuracy of ± 5 %. A microdialysis catheter is connected to the linear dispenser, and ensures the mixing of the carrier liquid with the measured sample. The catheter is equipped with a special membrane, for to obtain a sample without the need for blood centrifugation. Thanks to the catheter, flow analysis

can be considered as a type of FIA, where the sample is injected with a dosing tap into a continuous carrier stream and mixed with the flowing liquid. Parts of measurement chain were supplied by BVT Technologies [6].

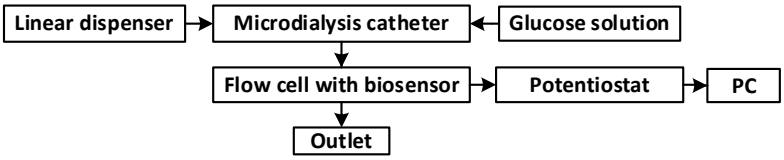

Fig. 1. Block diagram of the measuring chain connection

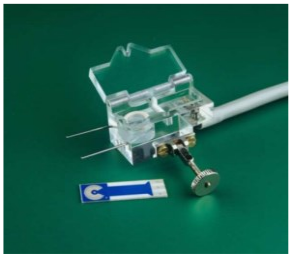

Fig. 2. Flow cell with biosensor [6]

3 Experimental Measurements

When the biosensor was first used, cyclic voltammetry (CV) was performed to determine the functionality of the sensor. Then the chronoamperometry method is selected and the measurement values are set. The value of the applied voltage is 0.65 V, which is the value used in practice for glucose sensing from a biosensor with GOD. The Oxidation and Peaks measurement mode was chosen because the ongoing reaction in the flow cell is oxidation and Peaks indicates a method based on flow analysis. The linear dispenser with NaCl solution had a flow rate of 6 ml/h, due to the response rate, the quality of the mixing of the solutions and the ability of the biosensor to capture glucose. All solutions used have a room temperature of ± 25 °C.

The first time the voltage is applied to the electrode, a high current is generated, which decreases very quickly. Waits for the current to stabilize and then it is possible to insert the catheter into the measured glucose solution. After capturing the glucose response, the catheter is transferred to NaCl solution. This step cleans the entire system of glucose molecules and does not affect the measurement of the next concentration. Furthermore, after the end of the measurement, it is necessary to rinse the whole chain with distilled water to prevent salt from settling in the catheter. After cleaning, catheter is placed in a NaCl solution to prevent drying and infestation of the microcatheter by bacteria. The biosensor must be closed in the flow cell after the measurement, as soon as it dries, the biosensor is no longer usable.

3.1 Testing the Functionality of the Biosensor

Two standard biosensors and one with an accelerated response were selected for testing, which has a thinner enzyme membrane for faster transfer of hydrogen peroxide to the working electrode. In Fig. 3 we see the results of CV. If the curve were flat and there was no increase in current, it would mean that the biosensor is inoperative.

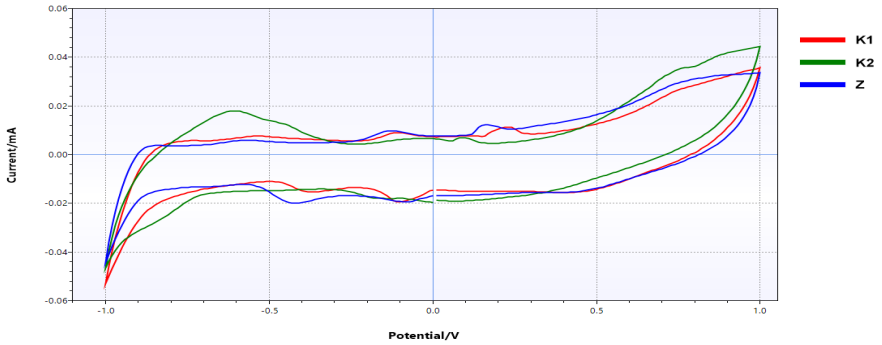

Fig. 3. Cyclic voltammetry applied to used biosensors

3.2 Measurement of the Current Response to Glucose

Measurements were performed on four HBSS with different glucose concentrations. After 500 s, the catheter is placed in a solution with a concentration of 10 mmol/l, where it is left for 50-25 s, after which time it is transferred back to the NaCl solution. Subsequently, after 175 s it is again transferred to a solution with a different concentration and the whole process is repeated.

In Fig. 4 we see the results of measuring the response of biosensors. From the measured values it is clear that respond well to the settings used and an important finding is the fact that the measured current response at repeated concentrations at the same solution concentrations does not differ.

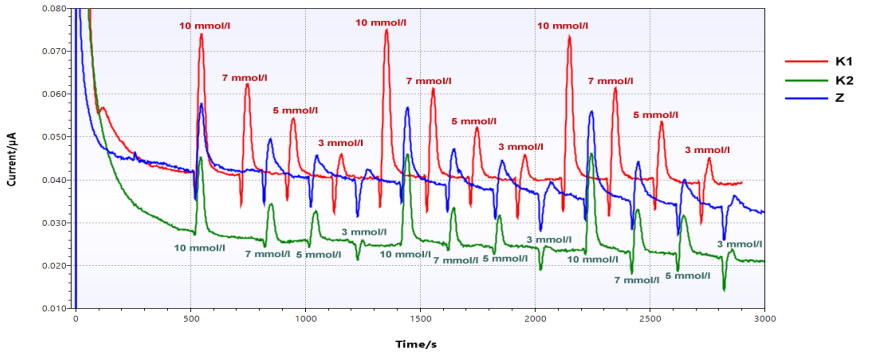

Fig. 4. Current response measurement in HBSS

A basic limit, which is a steady state, has been set for reading the peak value. Only the K1 sensor is used for further measurements, with which the most accurate results were

achieved. The average response value for a concentration of 10 mmol/l was 33.384 nA, for 7 mmol/l it averaged 21.177 nA, for 5 mmol/l the average response was measured to be 12.982 nA and for 3 mmol/l the average response was 5.744 nA.

3.3 Influence of Flow Rate and Temperature

The previous measurement was performed under standard measurement conditions used in glucose measurement. The measurements presented in this chapter are used to investigate the response of the biosensor under other conditions and to verify the possibility of using other measurement parameters. In the first measurement (Fig. 5), the flow rate was reduced to 3 ml/h and the solutions were at room temperature. In the second measurement (Fig. 6), the temperature of the solution was raised to 37 °C using a water bath at a flow rate of 6 ml/h.

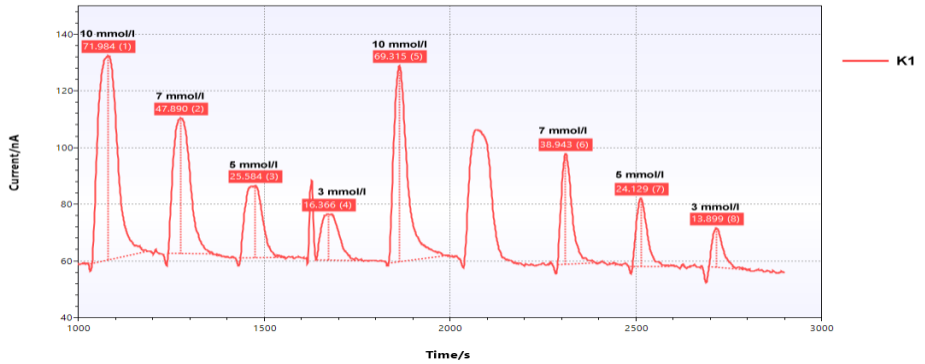

Fig. 5. Measurement of current response in HBSS at a flow rate of 3 ml/h

When testing the effect of the flow rate on the current response, it can be seen that at a flow rate of 3 ml/h, the current response is in almost all cases 2x greater than in the original measurement at 6 ml/h. For example, a concentration of 10 mmol/l have the average response value is 71,984 nA and for 3 mmol/l the average response value is 16,366 nA. This fact is attributed to better mixing of the solutions.

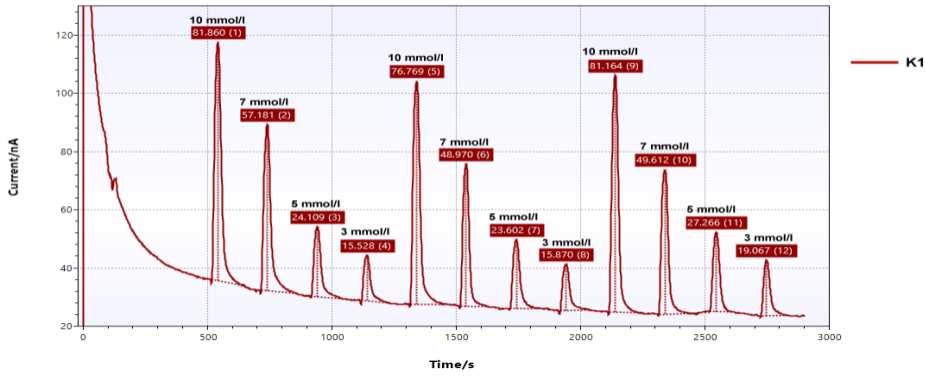

Fig. 6. Measurement of current response at a solution temperature of 37 °C

After heating the solution to 37 °C, an increase in the current response to glucose solutions can be observed again. For example, a concentration of 10 mmol/l have the average response value is 79,9314 nA and for 3 mmol/l the average response value is 16,822 nA. This phenomenon is attributed to poor diffusion in the catheter.

4 Conclusion

The measurement of glucose concentration in mixed solutions of simulated blood plasma was performed using electrochemical detection of chronoamperometry. Blood plasma was chosen because in practice it is a very often simulated body fluid.

Once the optimal setting of the carrier fluid flow rate and the applied voltage was determined, the current responses in the solutions were measured using a new biosensor. The effects on the current response were tested. The tested effects include the carrier fluid flow rate and the HBSS temperature. As the temperature increased, larger current responses were measured, but the measurement was unstable due to maintaining constant conditions and also time consuming. When testing the influence of the flow rate of the carrier liquid, a reduction of the flow by almost half proved to be effective, as the current responses were almost 2 times higher, much clearer and at the same time there is no increase in measurement time.

When measurement, a problem was sharp drop in current before the peak, which testified to the values of glucose concentration. This decrease in current was due to the use of 0.9% NaCl solution at pH 5.5 to clean the catheter. The decrease in current was caused by the reaction of the biosensor to a sudden change in pH.

The measurement results are used to consolidate knowledge about continuous glucose measurement and the information obtained will be used in the design of measurement and testing of the measurement system itself.

References

1. Kucherenko, I. S., Soldatkin, O. O., Kucherenko, D. Y., Soldatkina, O. V., & Dzyadevych, S. V. Advances in nanomaterial application in enzyme-based electrochemical biosensors: A review. Nanoscale Advances, 1(12), 4560-4577 (2019).
2. Pohanka, M., & Skládal, P. Electrochemical biosensors--principles and applications. Journal of applied biomedicine, 6(2) (2008).
3. Zagatto, E. A., & Rocha, F. R. The multiple facets of flow analysis. A tutorial. Analytica chimica acta, 1093, 75-85 (2020)
4. Hage, C., Mellbin, L., Rydén, L., & Wernerman, J. Glucose monitoring by means of an intravenous microdialysis catheter technique. Diabetes technology & therapeutics, 12(4), 291-295 (2010).
5. HBSS (Hank's Balanced Salt Solution) Preparation and Recipe. AAT Bioquest [online]. Sunnyvale, Kalifornie: AAT Bioquest, © 2019 [cit. 2021-07-19]. Dostupné z: https://www.aatbio.com/resources/buffer-preparations-and-recipes/hbss-hanks-balanced-salt-solution
6. BVT Technologies [online]. ©2021 [cit. 2021-07-19]. Available from: https://bvt.cz/

Cooperative Methods For Optimization And Control Of A Wireless Terminal Node Using Machine Learning Techniques: A Review

Karolína Gaiová

Department of Cybernetics and Biomedical Engineering, FEECS,
VSB – Technical University of Ostrava, 17. listopadu 15,
708 00 Ostrava – Poruba, Czech Republic
karolina.gaiova@vsb.cz

Abstract. Wireless sensor networks are constantly evolving and cover a wide area of everyday life extending into the industrial, commercial, and other spheres. The expansion of wireless sensor networks is caused mainly by the high progress, development, and growth of computer technologies, which, of course, entails an inherently increasing computing power. This fact is a consequence of ever-increasing requirement for all aspects of the device such as functionality, sophistication, and efficiency of applications.
Using non-traditional soft computing methods, we will achieve the development of more sophisticated and efficient model design. The goal of developing this method is to increase operation lifetime of the wireless sensor node to operate increase the required performance of the system in determining the same quality. The optimization proposal will be later supplemented by an algorithm that will be designed and applied using machine learning or soft computing techniques. The algorithm will be specified according to the following experiments.

Keywords: WSN, IoT, soft computing, machine learning, wireless node management, optimization, duty cycle.

1 Introduction

1.1 Wireless Sensor Networks

The expansion of wireless sensor networks into areas of everyday life is made possible mainly by the high growth and development of computer chips, processors, microcontrollers and other electronics and related methods. These units are becoming more and more large computing power and ever-increasing requirements for functionality and efficiency, which are caused by new trends in the application area [1].

One of the key tasks in the field of sensor system control is optimization. As development progresses in individual application areas it is necessary to solve the optimization

VSB – Technical University of Ostrava, 2021, ISBN 978-80-248-4523-4 (on-line).

not only by managing the hardware parts of the wireless terminal or network, but also by developing new algorithms [2].

The work will address the optimization and management of wireless terminals using methods for adjusting the work cycle and using planning methods. This procedure will later be supplemented by an algorithm that will be designed and applied using machine learning techniques. However, deployed models that are implemented and trained on mobile devices cannot. They can efficiently process unknown data and stimuli in new environments, which often leads to reduce accuracy and poor user experience. The trend is to retrain the model using past scanned data to improve its parameters and thus extend the ability to process of the individual terminal equipment and the whole system. It is necessary to count on huge ones computing costs and the use of a large-capacity memory unit to train the model on IoT devices, which in practice are equipped with limited hardware resources. Therefore, the only solution is to design a procedure using the computing power of the cloud and thus help mobile devices train these computationally intensive models [3].

Data purchased from the Czech Hydrometeorological Institute will be used for the experiment. The goal of developing this method is to increase the ability of the wireless sensor network to operate and its wireless terminals and increase the required endurance of the system while maintaining the same quality.

The work is divided in this way. The research survey is carried out in Part 2. It deals with the survey of already published works. Chapter 3 deals with the critique of the current situation and outlines the issues of the area. It deals with a theoretical introduction and discusses the basic concepts. The last part is the conclusion of the work and an outline of future research.

2 State Of The Art Of WSN

This chapter deals in more detail with the research of the issue of wireless terminals sensor devices. This part mention review publications of the issues. It summarizes all possible methods for practical applications and in conclusion provides the resulting list of retrieved information. Also deals with research publications on wireless control equipment using machine learning methods (e.g.: Fuzzy, Evolutionary algorithms or neural networks).

Machine learning methods are widely presented in the literature review [4] (for the period 2002-2013) and describe in particular the most common ones advantages and disadvantages of their application. In the article, which mainly concerns the specification advantages and disadvantages of each proposed or applied algorithm, are evaluated, and compared individual approaches. A comparison guide is provided here to help you design of a wireless sensor network (development of finding a suitable solution for their specific application).

Methods "Soft computing" are based on techniques, including, but not limited to fuzzy logic and expert systems, genetic algorithms, artificial neural networks, machine learning. With the arrival cheap and very powerful digital processors and the desirable reduction of costs for the individual parts of the system are clear, the technology and the application area. An overview of the current state mentioned in the method techniques soft computing are compared with traditional techniques provided by the article [5]. They describe the advantages and disadvantages individual techniques. The current state of the art and further detailed insight into the methodology in these areas and a description of the advantages and disadvantages compared to traditional computing techniques.

Detailed description of methods such as evolutionary computations, artificial neural networks, fuzzy logic, Bayesian statistics and other techniques "Soft computing" and an outline of their main advantages in this area is offered in a document [6]. The main benefit of this work is finding and verifying the fact that each specific subtype of calculation can be used separately (eg fuzzy systems, neural network ...), but the great advantage of soft computing is the complementary nature of the technology it can together create better solutions to problems that are too complex.

3 Wireless Sensor Networks Issues

Most of the works mentioned in the search use or assume the use of passive omnidirectional sensor. This means that each sensor device has a designated area that it covers (Figure 1).

For this area, it can reliably and accurately monitor specific monitored parameters. The sensors that are part of wireless terminals are divided into three categories: passive - omnidirectional, passive narrowband sensors and active sensors. Passive the sensors read the data without manipulating the environment by active probing. They have their own drive, which means that energy is only needed to amplify their analog signal. Active sensors actively sense environments, such as sonar or radar sensor, and require continuous power from the source. Narrow beam sensors are well defined an idea of the direction of measurement, like a camera. They do not have omnidirectional sensors no idea of the direction of their measurement. Sensor devices are powered by different types of devices, eg charging or non-charging battery. The operating time of the battery determines the operating time of each wireless device sensor device and thus affect the operating time of the entire wireless sensor

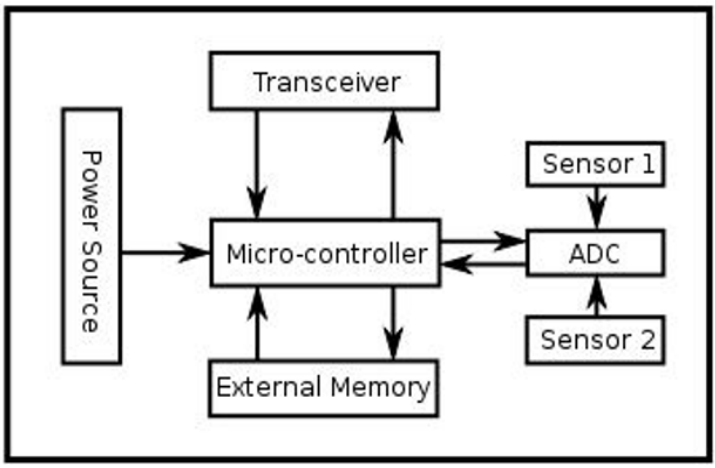

Figure 1Example of general connection of a wireless sensor device

3.1 Wireless Sensor Network Operating Time

The operating time of the wireless sensor network as a whole and of individual devices is one of key facts that we must consider when designing the model. To maximize the operating time of the sensor device after its placement within the network, we must consider all aspects, including hardware parts of the device, design of the device architecture, management algorithm and other additional protocols. One typical example is to turn off the terminal sensor device if there are no active events. This type of energy consumption management, so-called controlled events, is important for maximum battery life [7].

By defining the term network operating time (lifetime) we mean consumption system as a whole - the time of its operation (English energy consumption). There are many levels of power consumption solutions in wireless sensor networks. Only two levels of headings should be numbered. Lower-level headings remain unnumbered; they are formatted as run-in headings.

3.2 Planning And Management Strategies

The wireless sensor device or network must be set to at initialization appropriate selection of parameters that are individual for each application. To facilitate this setup, it is important to choose an appropriate system planning and management strategy. In this section is discussed how to focus on terminal equipment management scheduling, which is based on the duty cycle (from English - "duty cycle"). That is, individual wireless terminals will be turned off if needed (lack of power, existence a suitable adjacent sensor device with a larger reserve in the energy source, which is able to replace its function, etc.). This divides the task and resource of the system and also to save energy of the system as a whole. The wireless sensor device will therefore have in setting several modes to switch between. An example might be active mode, latent or standby mode and more [8].

3.3 Communication Possibilities Within The Model Design

Types of communication between terminals Basic types of communication for a wireless sensor network can be defined as follows:

- direct transmission (each end device transmits directly to the gateway),
- multihop (data is routed through individual end devices towards the gateway),
- clustering.

Within the wireless network, a central device is randomly or strategically selected - "Gateway". Furthermore, the exact number of terminal devices and their distribution in within the network.
The prerequisite is regular operation - periodic, with the same time interval - period throughout the network [9]

3.4 Methods And Algorithms For Control And Optimization Of Wireless Sensor Device

Intelligent systems designed in this way, supplemented by soft computing methods, should increase the process performance of the device and reduce costs. Intelligent systems are a must for Making complex decisions when choosing from many options is the best result to use complex algorithm. Among the basic methods of soft computing, we advise:

- Neural networks
- Fuzzy algorithms
- Evolutionary algorithms [10].

4 Conclusion

The work deals with the design of a method for wireless sensor device management using adaptive work cycle. The work considers modifications and suggestions were a suitable representation for planning and adjusting the work cycle using were selected. Data will be used for testing proposed algorithm in the form of an experiment. These considerations are intended to help reduce the computational complexity of the method, ie to optimization. The proposed method for wireless sensor networks will then be implemented using soft computing and machine learning methods. The method was designed to be robust and one of the key facts is network scalability. The proposed model consists of a network with two homogeneous terminal wireless sensors that are distributed in selected areas of the Czech Republic.

References

1. Chong, C.Y., Kumar, S.P.: Sensor networks: evolution, opportunities, and challenges. Proceedings of the IEEE (2003)
2. Kotlar, M., Boji´c, D., Punt, M., Milutinovi´c, V.: Survey of deployment locations and underlying hardware architectures for contemporary deep neural networks. International Journal of Distributed Sensor Networks (2019)
3. Dwivedi, R.K., Pandey, S., Kumar, R.: A study on machine learning approaches for outlier detection in wireless sensor network. In: 2018 8th International Conference on Cloud Computing, Data Science & Engineering (Confluence). IEEE (2018)
4. Alsheikh, M.A., Lin, S., Niyato, D., Tan, H.P.: Machine learning in wireless sensor networks: Algorithms, strategies, and applications. IEEE Communications Surveys & Tutorials (2014)
5. Ibrahim, D.: An overview of soft computing. Procedia Computer Science (2016)
6. Das, S.K., Kumar, A., Das, B., Burnwal, A.: On soft computing techniques in various areas. Computer Science & Information Technology (CS & IT) (2013)
7. Chanagala, S., Khan, Z.J.: A battery and environmental aware approach to maximize the lifetime of wireless sensor network. In: 2017 International Conference on Energy, Communication, Data Analytics and Soft Computing (ICECDS). IEEE (2017)
8. Desai, S.S., Nene, M.J.: Danes—distributed algorithm for node energy-management for self-organizing wireless sensor networks. In: 2016 IEEE International Conference on Recent Trends in Electronics, Information & Communication Technology (RTEICT). IEEE (2016)
9. Duisebekova, K.S., Sarsenova, Z.N., Pyagay, V.T., Tuyakova, Z.N., Duzbayev, N.T., Aitmagambetov, A.Z., Amanzholova, S.T.: Environmental monitoring system for analysis of climatic and ecological changes using lora technology. In: Proceedings of the 5th International Conference on Engineering and MIS (2019)
10. Liu, W.Q., Li, J.: An approach to automatic performance prediction for cloud enhanced mobile applications with sparse data. Journal of Computer Science and Technology (2017)

Automatic Generation of Programs Inside LabVIEW

Pavel Kodytek

Department of Cybernetics and Biomedical Engineering, FEECS,
VSB – Technical University of Ostrava, 17. listopadu 15,
708 00 Ostrava – Poruba, Czech Republic
pavel.kodytek@vsb.cz

Abstract. The paper deals with the problem of automatic code generation inside a graphicly oriented programing language – LabVIEW. Goal of the work is to use algorithm of artificial intelligence, namely the genetic evolution to create a program based on human specified requirements, which are stored inside and XLS document. Therefore, this enables even a person without programing skills, to be able to write a computer software (generate it). This paper deals with a basic creation of code and therefore archives the basic automated generation of programs inside LabVIEW. In the end genetic evolution-based program is able to generate basic code for a numeric variable function.

Keywords: LabVIEW, Genetic programing, Genetic Evolution, Automated code creation

1 Introduction

The technological advances associated with the current revolution in automation, collectively referred to as Industry 4.0, greatly increase the penetration of computer technology into the industry. Suppliers and developers of these technologies are producing more and more universal hardware platforms, and the only aspect that influences the behavior of these hardware platforms and their difference from other equally built hardware elements is software. Thus, the role of software as a carrier of new utility values of the final solution is growing significantly. This need implies the need for massive involvement of the profession of programmers in the development of modern production lines designed on the basis of the Industry 4.0 concept

Programming, as a process of creating instructions for a computer in order to obtain the required outputs, is a very time-consuming process that provides livelihood for many skilled workers in today's modern age/economy. Due to its complexity, this activity also offers a large number of challenges today. Efforts to meet these challenges create a demand for experts in this field, but there is a significant shortage in the labor market, which leads to the fact that the ever-expanding teams of programmers in the field of industrial automation take a long time to deliver the resulting program to the customer.

Automatic programming is a concept designed to help programmers be able to deliver the required SW products to the target customer faster. The term "automatic

VSB – Technical University of Ostrava, 2021, ISBN 978-80-248-4523-4 (on-line).

programming" itself has been perceived in different ways over time [1]. The main direction of research in this area in today's context is to support the programmer in creating a piece of code. A large part of the developed SW components is largely repeated when creating other programs, which allows the programmer to make only minor modifications to the program, instead of creating the entire program from scratch. In this paper we will deal with a sub-area where automatic programming represents a method of automatic creation of code sections.

The aim will be the development of algorithms for automatic code generation based on defined parameters in the object-oriented programming environment LabVIEW. Unlike traditional programming languages, which in some cases are used in a text nature, LabVIEW is a graphical development tool. Therefore, it is not possible to fully use the established method of the GPT-3 type of language model [2] to solve this problem, but the method of genetic programming can be used here.

This paper presents the idea of evolution algorithms and genetic programing in first chapter, explains proposed solution in second chapter and presents actual results in the last one.

2 Evolution Algorithms and Genetic Programing

In the field of artificial intelligence and computer algorithmization, the evolutionary algorithm (EA) is a subset of the optimization algorithm, and it is a general algorithm based on working with the population. The evolutionary algorithm uses mechanisms inspired by biological evolution, such as reproduction, mutation, crossing, and selection of the most suitable candidates. Candidate solutions to the optimization problem play the role of individuals in the population, and the fitness function determines the quality of the solution (sometimes also the loss function). After repeated application of the above mechanisms, the population will develop.

Evolutionary algorithms often approximate well the solution of all types of problems, because ideally, they do not make any assumption about the space being searched or investigated. Techniques from evolutionary algorithms applied to modeling biological evolution are generally limited to the study of microevolutionary processes and to make models based on cellular processes. In most real applications of evolutionary algorithms, computational complexity is a limiting factor due to the theoretically unlimited set of possible results. This computational complexity is also caused by problems associated with the evaluation of fitness functions. However, seemingly simple evolutionary algorithms can solve complex problems, and therefore there may be no direct link between the complexity of the algorithm and the complexity of the problem. [3]

The concept of genetic (GP) programming was introduced in 1992 by Koza [4]. Its original use was for the evolution of programs based on the application of evolutionary algorithms for the Lisp programming language. As with evolutionary algorithms, genetic programming is based on Darwin's theory of evolution and proceeds in accordance with the process of creating a population of sub-programs, their subsequent evaluation, selecting the most suitable parents for the next generation

and creating a new population. The overall solution procedure is conditioned by the used model of genetic programming management.

The control model, as the name suggests, determines how the process of creating new children is regulated. The two basic control models used in genetic programming are the so-called "generation control model" and the "steady state model" of control. An alternative model described by Bruce [5] is the variable population size model, however this model is used very rarely.

3 Proposed Solution in LabVIEW

LabVIEW is a programming and development environment created by National Instruments, which in today's concept also represents a graphical programming language. To date, the company has been renamed NI, but has been developing LabVIEW since 1983. It is a graphical programming language where functions (methods) are represented using graphical elements. The code in this language resembles a block diagram and the individual values and signals are displayed symbolically by wires that are connected to icons. LabVIEW is sometimes referred to as a G-type programming language.

As with human evolutionary processes, I approach the issue of coding in a similar way. Each segment (generated code) is a final representation comparable to the final representation of a cell. It therefore represents the complete characteristics of a certain descendant of a generation. As with individual cells, we are able to validate individual codes against the basic requirements for their functionality. We can perform the validation as a summ of difference betwean outputs and requirements.

Where the resulting error value is the sum of all partial differences between the setpoint for the selected combination of inputs and the actual value of the program, which is also dependent on the values of W and C (representation shown on figure 1), representing the sets Wirerer and Creator. These two sets represent complete code information and together are analogous to the complete chromosome in a normal cell. From this analogy we imply that Wirerer and Creator are sets containing a set of genes, where each gene already contains specific information about the structure or binding.

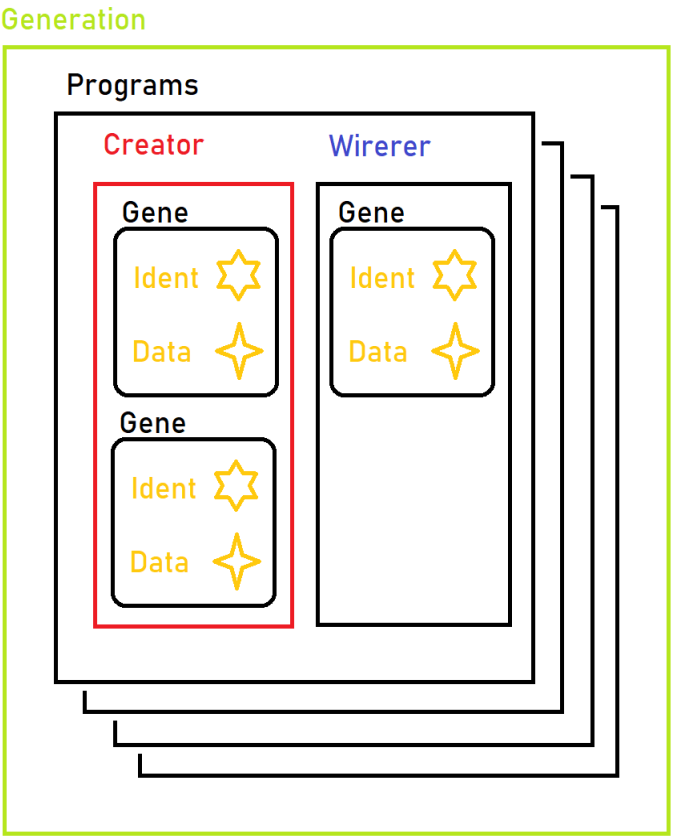

Figure 1: genetic material of population, program, and Creator / Wirerer

Just as individual genes create cell characteristics using sub-alleles, so the sub-genes contained in Creator and Wirer shape the final form and behavior of the generated code. Since it was necessary to preserve the variability of genetic information, unlike most authors, a dynamic approach to individual genes is used in the work. Each gene, therefore, contains its identifier, which is used to assign the purpose of the gene to a function in the system, and data, which contains all the necessary information about the element.

A key component for the functioning of such a system is the possibility of creation and extinction of individual genes and their functionality during the program. This property is not a common feature of the functioning of evolutionary processes in the ordinary world, but it seems necessary for the creation of computer code. To construct such a dynamic system based on working with numerical values, a textual representation of the data within the subgenes was chosen. This approach meets the theoretical level of the requirement for the possible infinity of the required genetic material within the data, and thus we are not limited by unnecessary conditions for creating programs.

4 Results

Tested problems, of a numerical nature, already represents a multi-input task, where the user requires the creation of a mathematical function between the two inputs (requirements shown in Table 1). The requirement to create an addition of these two values proved to be the most fascinating, and therefore it was included as a typical conceptual task of the system.

Table 1. Input and output values for numeric problem

Input 1	Input 2	Required output
5	10	15
6	11	17
15	42	57
17	43	60
36	44	80

A key element in examining the evolution of program evolution was to examine the behavior of a simple add function. The programs that were created in this test problem led to clear conclusions and findings that more complex mathematical functions did not reveal. The result of this process can be seen on figure 2, where on the left in the original form and on the right, the modified function using the CTRL + B method.

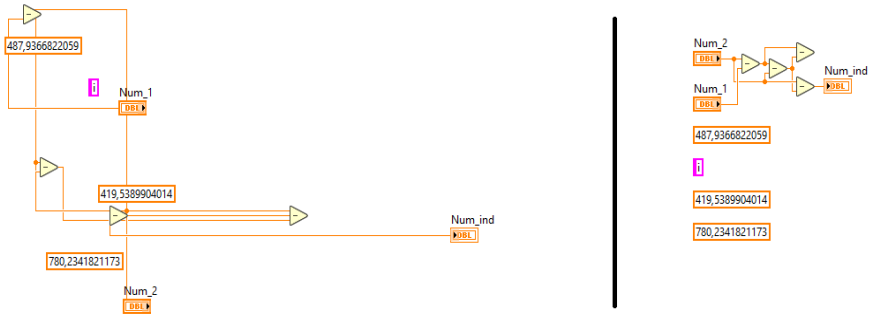

Figure 2: Created solutions for numeric problem in programing environment of LabVIEW

The first thing that is already visible in the solution itself is the occurrence of different data types. The use of strict data types was also switched off for this case of research. At the beginning (the first generation) there were many more things in the program that were related to the bool / string data type, but since the process of generating the program is terminated by randomly linking inputs and outputs, and subsequent generations, these elements began to fall out, and only the elements related to the required data type were retained. This case is not yet strictly dominant, but a positive trend has been demonstrated.

The second strange conclusion that evolution has reached is the creation of the

function Y = A + B using three subtraction functions. The resulting solution is therefore Y = A - ((A-B) -B). As a result, it is really a solution to the problem, only the solution is extremely creative. These phenomena do not occur when complexity is limited.

5 Conclusion

The work deals with the issue of automatic program creation, using artificial intelligence methods. This is currently an area with great potential for use, because the application of such algorithms and their use would simplify the daily work of the programmer, or allow the creation of the algorithm even to people unfamiliar with programming.

The results of the work provide a comprehensive insight into the issue of automatic program creation, and conduct a search of existing solutions used primarily in text-based programming languages. However, the practical part deals with the LabVIEW programming environment, which, unlike text languages, provides the ability to create programs using objects. At the same time, thanks to the difference between the objects of function and the objects of their mutual connections (connections - wires), LabVIEW provides an optimal precondition for the application of storing genetic information for an evolutionary algorithm so that this storage is very close to the genetic material of a human individual.

The achieved results confirm that in this programming environment it is possible to create codes automatically based on input and output requirements, for the investigated issues such as: bool, numeric, string and their combinations. For the tested problem of text strings, methods of various manipulation were investigated, which confirm the ability of the algorithm to iterate over a theoretically infinite number of possibilities by the method of "hill climbing" - finding the maximum. For the tested problems of the bool and numeric type, the ability of the algorithm to find the "unit value" when using the limited search space was confirmed. For testing with numerical values, the algorithm also demonstrated a degree of "fantasy" when it implemented the required addition function purely using subtraction operations.

6 References

1. RICH, C. a R.C. WATERS.: Automatic programming: myths and prospects. Computer 21(8), 40-51(1988).
2. B. BROWN, Language Models are Few-Shot Learners https://arxiv.org/abs/2005.14165
3. KOZA, John R. Genetic programming: on the programming of computers by means of natural selection. Cambridge, Mass.: MIT Press, (1992).
4. KOZA, John R. Genetic programming: on the programming of computers by means of natural selection. Cambridge, Mass.: MIT Press, (1992).
5. BRUCE, W.S. The application of genetic programming to the automatic generation of object-oriented programs. Nova Southeastern University, (1995).

Pneumatic System for Multidisciplinary Applications

Jakub Kolarik and Radek Martinek

Department of Cybernetics and Biomedical Engineering, FEECS,
VSB – Technical University of Ostrava, 17. listopadu 15,
708 00 Ostrava – Poruba, Czech Republic
{jakub.kolarik, radek.martinek}@vsb.cz

Abstract. This paper presents the inexpensive modular device for measuring of vibration and deformation applicable in healthcare as well as industry. The proposed device consists of pneumatical sensor integrated into patient bed to measure cardiorespiratory activity. This closed pneumatic system has also been used for vibration measurements in other technical fields. These experiments were performed in collaboration with undergraduate students as part of their thesis.

Keywords: Vibrations measurement, Pneumatic system, Seismocardiography, Seismograph, Traffic sensors.

1 Introduction

In this work, the problem of vibration measurement and analysis was chosen as the main topic. Vibration analysis can be used to understand the internal state of mechanical systems. The paper is a follow-up to previous work, which focused on developing all-purpose modular sensor for measuring vibrations.

The first iteration of this sensor was used as fetal phonocardiograph, to measure acoustic pressure changes caused by fetal heart cycle. The initial experiments were followed by measurement of other physiological signals, such as cardiorespiratory activity under the influence of strong magnetic field or acoustic noise. The pneumatic system was also used as the core of several student thesis to explore other possible applications, such as:

- alternative approach to measuring of seismic waves in construction industry,
- passive sensors for traffic speed estimation and vehicle type classification,
- hearth rate monitor integrated in driver seat.

The task of these modules would be to design convertor of physical quantities, precisely, to convert motion into pressure change, which were measured by pressure sensor or microphone. To modify the measuring system, it was necessary to determine the requirements for the sensor device according to the dynamics of the measured events. These requirements include the required sampling frequency, A / D converter range, or signal preprocessing and filtering to prevent aliasing. 3D printing technology was chosen for the production and design of these sensors.

VSB – Technical University of Ostrava, 2021, ISBN 978-80-248-4523-4 (on-line).

2 Pneumatic System

The presented pneumatic system has already been used in multiple projects and applications. It consists of a closed pneumatic tube connected to a pressure sensor or/and microphone. The microphone is preferred for measurement of dynamic changes and ambient vibrations. On the other hand, the pressure sensor is more suitable to capture slow phenomena and static changes in pressure corresponding to sensor deformation.

The measuring tube is terminated on one side by a microphone, and the other end contains a membrane, air cushion, or the end is sealed.

The sensor works on the principle of measuring the pressure change inside the tube. Depending on the type of embodiment, these pressure changes are caused by the movement of the membrane, deformation of the tube or by vibrations affecting tube surface.

2.1 Sensor Parameters

The sensor was used in two design embodiments. The difference in these systems lies in the hardware used. As proof of concept were used system for virtual instrumentation by NI and the low-cost device of own design as example of final product.

NI hardware parameters:

- G.R.A.S microphone Type 40 PP,
- DAQ card with NI 9234 module,
- sampling rate 51.2 kHz.

The propagation delay inside of the pneumatic tube is around 3.196 milliseconds for every meter of length. The computed speed of propagation was calculated as 308,47 ms-1, contrary to typical speed of sound around 346.13 ms-1 for temperature 25° C. This value could be interpreted as an 11 % reduction in signal propagation speed due to influence of the different acoustic impedance in the closed acoustic tube.

The closed pneumatic system also has damping properties and is resistant to ambient noise. These assumptions were confirmed in previous Article [1]. The attenuation was measured using two identical microphones inside and outside the measuring medium and usually ranged from 20 to 40 dB. Airborne interference, such as speech or sounds produced as a by-product of electrical equipment and machines (magnetic resonance, frequency converters, switched-mode power supplies, etc.), therefore has a negligible impact on this measuring system. This is caused by the transmission of sound waves, vibrations, between materials of different densities and the consequent attenuation of the energy of the sound waves as a result of passing through this interface.

3 Industrial Application Area

The industrial version of the sensor did not contain membrane, and measured signal was directly propagated through pneumatic tube surface. This system has a direct relationship between the volume and the pressure of the gas enclosed inside the tube at constant temperature. This sensor version can be used for the building industry, transport, but also security activities (occupancy sensor).

3.1 Seismography

One of the first tests in the industrial area was carried out when measuring rock blasts. Individual materials were tested in these trials. A modified sensor that consisted of a spirally twisted tube is shown in **Fig. 1**. Our measurements (see **Fig. 2**) were comparable with experimental systems based on optical fibers and reference commercial seismograph. The results of measurement were published in Sensors [2], [3]. and as student thesis [4]

Fig. 1. Reference seismograph BRS32 (left) and tested pneumatic sensor (right).

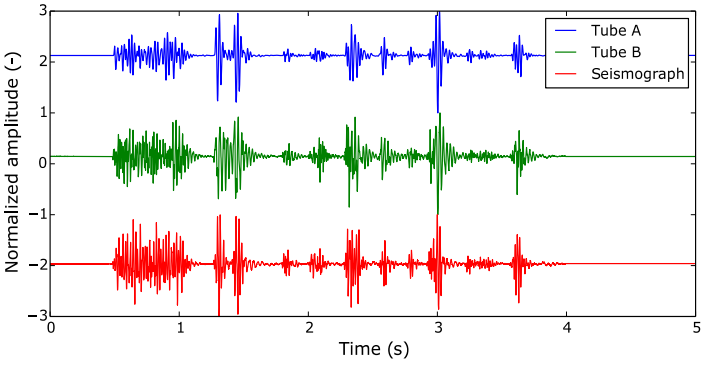

Fig. 2. The measured signals from reference seismograph BRS32 and pneumatic sensor.

3.2 Traffic Monitoring

A modified version of the sensor was used to analyze the vibrations produced by passing vehicles. As part of the experiment, trams on the route between “Hranečník” and “Karolína” were measured. Accelerometers, acoustic sensors, and pneumatic sensors were used for the measurements. The measurement is described in student Thesis [5].

Fig. 3. Track between two tram stations without interference from.

A modified version of the sensor (see **Fig. 3**) was used to analyze the vibrational manifestations of vehicles to determine their speed, number, or type of vehicles. This information can be useful in analyzing road congestion, detour planning, and optimizing approach routes for the Integrated Rescue System state departments. Another useful feature is the detection and classification of events such as car accidents or noise limits. The basic mode of vehicle detection is identical to work [7], where the difference is only with the sensor that detects the passage of the vehicle.

In case of presented student thesis [5], the device can be used as mean to monitor track condition and switches or vibrations propagated to the surroundings, which can affect the condition of the surrounding buildings in the long term.

4 Healthcare

The sensor is suitable for long-term monitoring of cardiovascular activity of a wide range of targeted users. Until now, the system has been used to monitor patients in magnetic resonance imaging, in a medical bed and as a driver monitoring system.

4.1 Monitoring Vital Functions in Cars

The student thesis [6] aim to design and implement pneumatic senor into driver seat (see **Fig. 4**). The thesis was used as proof of concept, and to test hypothesis that this system is suitable as driver vital sign monitor. By connecting similar systems, it would be possible to check the driver in the future, and in the event of a medical accident or microsleep, to stop the car at the curb.

Fig. 4. Sensors integrated in driver seat (blue arrows) and reference sensor (white arrow) to monitor vibrations of combust engines.

5 Conclusion

The system was successfully used in all the presented application areas. The sensor meets the requirements of the industrial area. Due to its dimensions, the sensor is not suitable for measuring small mechanisms (ball bearing vibrations). The first industrial example was seismographic measurement. The results were comparable to commercial devices. Measurements around the tramway also provide satisfactory results and have shown that speed and pattern detection and recognition are possible.

The prime focus of future work would be in biomedical area of cardiorespiratory measurement. The research will be mostly related to the development of variant for magnetic resonance bed as part of OPPIK project.

6 Summary of Year

The main task of my work in the academic year 20/21 was to participate in projects with multidisciplinary topic, such us:

- Development of a sensor used to improve MRI imaging. Specifically, it is a system using ballistocardiography and conventional systems for CMRI synchronization and gating at 3 Tesla [8, 9].
- Development of an ECG fetal monitoring system. The device is based on single microcontroller from nRF53 family with Bluetooth 4.0 communication interface.
- Development of an automatic parking house. The concept is based on a modular design that can be easily expanded. Car parking is handled by autonomous robots in combination with elevator system.
- Measurement and vibration analysis of heavy machinery for Industry 4.0.

References

1. Kolarik, J., Martinek, R., Slanina, Z., Kahankova, R., & Danys, L. Acoustic sensor optimization for SMART technologies. In: SPIE (Vol. 11176, p. 111765R). (2019, November).
2. Kepak, S., Stolarik, M., Nedoma, J., Martinek, R., Kolarik, J., & Pinka, M. Alternative approaches to vibration measurement due to the blasting operation: a pilot study. Sensors, 19(19), 4084. (2019).
3. Stolarik, M., Nedoma, J., Martinek, R., Kepak, S., Hrubesova, E., Pinka, M., & Kolarik, J. New Methods to Seismic Monitoring: Laboratory Comparative Study of Michelson Fiber-Optic Interferometer and Pneumatic Measurement Systems. In Photonics (Vol. 8, No. 5, p. 147). Multidisciplinary Digital Publishing Institute. (2021, May).
4. Szpyrc, M. Measurement of Blasting Operations and Vibration Monitoring by Low-Cost Pneumatic System. Bakalářská práce. Vysoká škola báňská - Technická univerzita Ostrava. In: http://hdl.handle.net/10084/140428. (2020).
5. Jícha, L. Design and Implementation of a Low-Cost System for Measurement of Selected Traffic Parameters. Bakalářská práce. Vysoká škola báňská - Technická univerzita Ostrava. In: http://hdl.handle.net/10084/140429. (2020).
6. Klaudia, J. Vital Sign Monitoring in Automotive Environments. Diplomová práce. Vysoká škola báňská - Technická univerzita Ostrava. In: http://hdl.handle.net/10084/144136. (2021).
7. Fajkus, M., Fridrich, M., Nedoma, J., Kahankova, R., Martinek, R., Bednar, E., & Kolarik, J. PDMS-FBG-Based Fiber Optic System for Traffic Monitoring in Urban Areas. IEEE Access, 8, 127648-127658. (2020).
8. Ladrova, M., Martinek, R., Nedoma, J., Hanzlikova, P., Nelson, M. D., Kahankova, R., Brablik, J. & Kolarik, J. Monitoring and Synchronization of Cardiac and Respiratory Traces in Magnetic Resonance Imaging: A Review. IEEE Reviews in Biomedical Engineering. (2021).
9. Martinek, R., Brablik, J., Kolarik, J., Ladrova, M., Nedoma, J., Kahankova, R., Jaros, R., Vojtisek, L. & Hanzlikova, P. (2019). A Comparison Between Novel FPGA-Based Pad Monitoring System Using Ballistocardiography and the Conventional Systems for Synchronization and Gating of CMRI at 3 Tesla: A Pilot Study. IEEE Access, 8, 4149-4170.

Application of Augmented Lagrange Method for Constrained Optimal Control Problem

Filip Krupa

Department of Cybernetics and Biomedical Engineering, FEECS,
VSB – Technical University of Ostrava, 17. listopadu 15,
708 00 Ostrava – Poruba, Czech Republic
filip.krupa@vsb.cz

Abstract. This work deals with the transition between limited and unlimited optimization. Only equality constraints are taken into account. The augmented Lagrange method is used to transfer constraints to an objective function and thus to create an unconstrained optimal control problem. The principle is given in a case study, which seeks the optimal control for a DC motor system. This system is simple enough to provide an analytical solution, but also complex enough to demonstrate the capabilities of the method. SFS and fminunc solvers are used and compared. Furthermore, an analytical solution, which is used to evaluate the results, is presented.

Keywords: Global optimization, Augmented Lagrangian Method, Constrained optimization

1 Introduction

These days exist many algorithms for solving global unconstrained optimization problem [1-3]. These algorithms are able to solve most classical optimization problems very quickly and efficiently. However, their limitation lies in constraints. Constraints can be further divided into equality and inequality constraints. Both types of constraints can be transferred to each other using various special adjustments [4]. In order, to use global solvers, that cannot work with constraints, for problems that contain them, several methods have been developed that convert a constrained optimization problem to a problem without constraints [5-7]. One of the most commonly used method is the Augmented Lagrangian Method (ALM).
Like penalty methods, ALM converts a constraint problem to a problem without limitation by adding a series of unconstrained problems and adding a penalty term to the objective function.

The chapter Augmented Lagrangian Method describes the basic principle of this method also the difference between this method and the penalty method. This chapter also mentions several known enhancements for ALM. In the chapter Practical demonstration on the proposed method, the ALM is applied to the problem of finding the optimal trajectory of the DC motor system. The results including three different solutions to the presented problem are shown in the Results chapter. The last chapter then contains an evaluation of the results and an outline of other possible directions of work.

© M. Krátký, J. Dvorský, P. Moravec (Eds.): WOFEX 2021, pp. 99–104.
VSB – Technical University of Ostrava, 2021, ISBN 978-80-248-4523-4 (on-line).

2 Augmented Lagrangian Method

As mentioned above, this method is used to convert a constraint optimization problem to an unconstrained problem. Let us assume we are solving constrained problem define as $\min f(x)$, subject to $c_i(x) = 0$, where $i \in \{0,1,2,\dots,m\}$ and m is number of equality constraints.

This problem can be solved by a series of problems without restrictions, where we first solve:

$$\min \Phi(x) = f(x) + \mu \sum_i c_i(x)^2 \tag{1}$$

then in each next step we solve the problem (1) again by enlarging μ. We can use the result of the previous step as an initial estimate for the next optimization step. The ALM method upgrades this general principle of penalty method by adding Lagrangian multiplier λ. Then function for minimization will be as follow:

$$\min \Phi(x) = f(x) + \sum_i \lambda_i c_i(x) + \frac{\mu}{2} \sum_i c_i(x)^2 \tag{2}$$

As you can see in (2) Lagrangian multiplier λ is vector with same length as number of constraints. In each optimization step λ is updated as follow:

$$\lambda_i \rightarrow \lambda_i + \mu \cdot c_i(x) \tag{3}$$

In equation (3) as *x* we use best solution from previous optimization step.

Earlier was mentioned that multiplier μ needs to be also updated in each step. This updation can be done by simply multiplying by 10 in each step and this approach is sufficient for most of the cases. But for better performance or in special, really difficult cases, there can be found some other, in some point of view better solutions in the literature [1,3]. These improvements consist of increasing the μ only in some cases, for example if the solution is more accurate than the selected value. In particular, a faster convergence of the method can be achieved in this way.

3 Practical Demonstration of Proposed Method

The DC motor model will be used for the case study. This model contains two states x_1 and x_2 which are defined as $\dot{x}_1 = x_2$ and $\dot{x}_2 = u$, where u is the input to the system. Furthermore, the dynamics for this model is known, which was suitably chosen (see Fig 1).

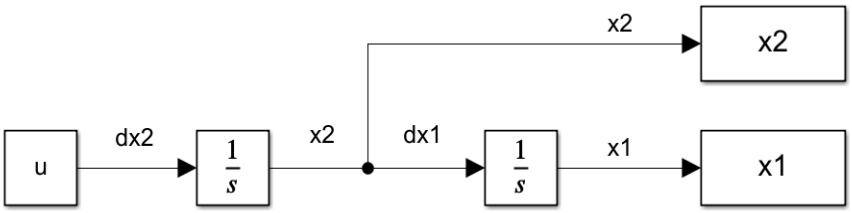

Fig. 1. DC motor model.

Equality constraints are $x_1(0) = -1, x_2(0) = 1, x_1(T) = 0,$ and $x_2(T) = 0,$ where the constant T is the final time, to change the state of the motor. In this case, T = 1s. Since the time interval was divided into 10 parts and the direct transcription method was used, the resulting number of equality constraint is 24.

The objective function was chosen as follows:

$$J = \frac{1}{2}\int_0^T u^2(t)dt \tag{4}$$

The ALM method can also be used for more complex formulations of Objective functions. In this case, we will suffice for the demonstration with the basic requirement to minimize the input energy (4).

After applying the ALM method, the following functions (5) were compiled for the unconstrained optimizer:

$$min\ \Phi(x, \lambda, \mu) = J(x) + \sum_i \lambda_i \cdot c_i(x) + \mu \cdot \sum_i c_i(x)^2 \tag{5}$$

We see that a new function will be minimized in each step, which contains not only the Objective function but also individual constraints. It is already possible to use an unconstrained optimization solver to solve this newly created problem.

A solver integrated in the Matlab environment called fminunc, a stochastic solver known as SFS [2] was used to solve the unconstraint optimization, and both results were compared not only with each other, but also with an analytical solution that can be calculated due to the simplicity of the case study.

4 Results

As mentioned above, the ALM method was implemented in Matlab. First, the problem was solved analytically. This solution can be obtained thanks to the simplicity of the system and the resulting course of control and states can be seen on Fig. 2.

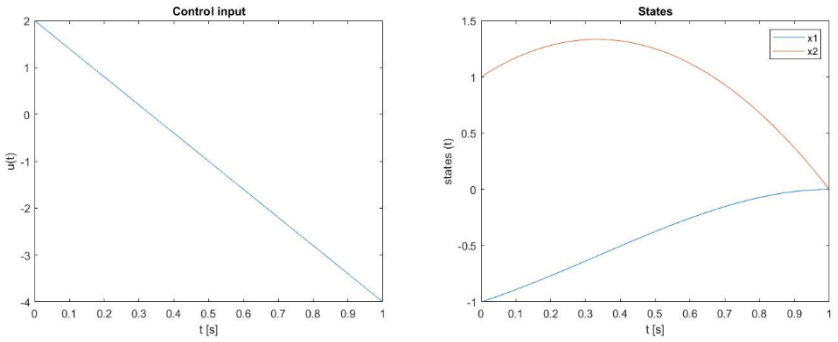

Fig. 2. Resulting input (left) and states (right) for analytical solution.

In addition to the analytical solution, two programs were created that solve an optimal control problem using the unconstrained solver SFS and fminunc. In the case of the fminunc solver, it is a solver that is part of Matlab. The SFS solver is a newly developed stochastic solution for unconstrained optimization. It is possible to get it from the authors as open blocks of code together with simple and more complex examples. Thanks to this, it is no problem to use it for your own needs with minimal effort. Another advantage of this solver is that the user does not have to set a large number of parameters, but only the basic (number of partition and maximum number of iteration).

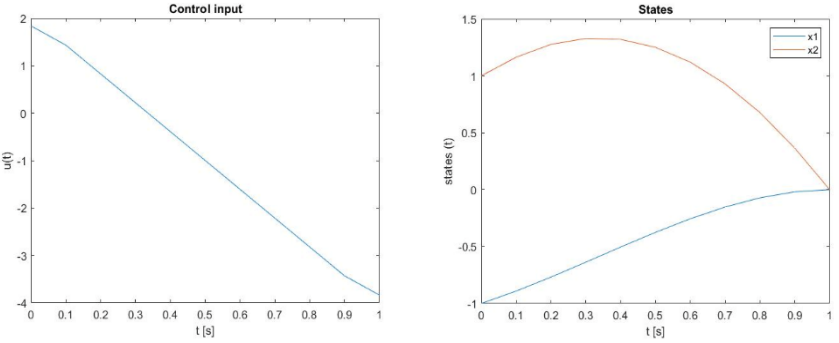

Fig. 3. Resulting input (left) and states (right) for solution with fminunc solver.

The solution with fminunc is shown in Fig. 3 and solution with SFS solver is shown in Fig. 4. Minor differences between solvers can be observed. This is due to a different approach to optimization, where the stochastic solver uses randomly generated points as the initial estimate, while the fminunc solver uses the initial estimate that must be passed to it at each step of the main loop.

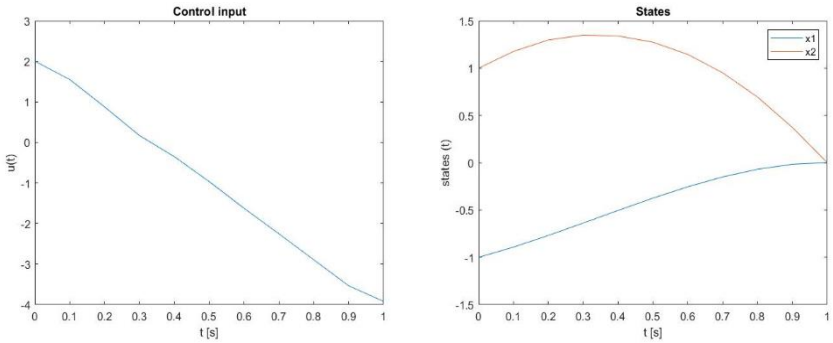

Fig. 4. Resulting input (left) and states (right) for solution with SFS solver.

From an application perspective, it is also important to consider the speed of each solution, where fminunc is approximately twice as fast as SFS for given results and settings. However, the speed of the SFS algorithm is strongly dependent on the solver settings (maximum number of iteration and tolerance) and will therefore be very different for each problem.

5 Conclusion

From the presented results we can see that ALM is a simple and functional method usable for the transition between constrained and unconstrained optimal control problem. Among the main disadvantages can be considered the need to use cyclic recalculation of the problem so the longer time is required to find the optimal solution. Despite these minor shortcomings, this method proves to be very suitable especially for use with global solvers, which often do not have the ability to enter constraints.
Further work will focus on the use of this method for more complex systems, and also verification that it is possible to successfully apply this method in industry.

References

1. Mirjalili, S., Mirjalili, S. M., & Lewis, A. Grey wolf optimizer. Advances in engineering software, 69, 46-61 (2014).
2. Salimi, H. Stochastic fractal search: a powerful metaheuristic algorithm. Knowledge-Based Systems, 75, 1-18 (2015).
3. Faris, H., Aljarah, I., & Mirjalili, S. Improved monarch butterfly optimization for unconstrained global search and neural network training. Applied Intelligence, 48(2), 445-464 (2018).
4. Mohamed, A. W., & Sabry, H. Z. Constrained optimization based on modified differential evolution algorithm. Information Sciences, 194, 171-208 (2012).
5. Mallipeddi, R., & Suganthan, P. N. Ensemble of constraint handling techniques. IEEE Transactions on Evolutionary Computation, 14(4), 561-579 (2010).
6. Michalewicz, Z. A survey of constraint handling techniques in evolutionary computation methods. Evolutionary programming, 4, 135-155 (1995).

7. Coello, C. A. C. Theoretical and numerical constraint-handling techniques used with evolutionary algorithms: a survey of the state of the art. Computer methods in applied mechanics and engineering, 191(11-12), 1245-1287 (2002).
8. Enright, P. J., & Conway, B. A. Discrete approximations to optimal trajectories using direct transcription and nonlinear programming. Journal of Guidance, Control, and Dynamics, 15(4), 994-1002 (1992).

Wood Defect Segmentation

Martin Kryl[0000−0002−5704−6507] and Petr Bilik[0000−0001−8655−778X]

Department of Cybernetics and Biomedical Engineering, FEECS,
VSB – Technical University of Ostrava, 17. listopadu 15,
708 00 Ostrava – Poruba, Czech Republic
{martin.kryl, petr.bilik}@vsb.cz

Abstract. Forestry is undoubtedly crucial part of today's industry and automation of certain visual tasks could lead to significant increase of productivity and reduction of labor cost. Fault classification caused by human-nature mistakes, present during long visual inspection routine, like eye fatigue or lack of attention, could be reduced using vision inspection system. This article focuses on testing of Convolutional Neural Network for wood type segmentation task. Particularly, state-of-the-art architecture called U-Net, which proved to be efficient not just for biomedical cases, but for wood-related tasks as well. In this case it regards to segmentation of defects on wooden slabs.

Keywords: Wood Defects Segmentation · Convolutional Neural Network · Machine Vision.

1 Introduction

There are many cases when is beneficial to locate and identify defects in wooden slabs. For instance, in constructions, the choice of the right wood quality is crucial, as it influences material used for a roof truss. Lower quality of chosen wood might lead to instability of the whole roof, which could end in disaster [1]. Similarly, various wood products, such as furniture, require certain quality of used wood material. The right wood type can also influence quality of manufactured paper [2]. Mostly trained human professionals are used for visual quality inspection. However, human inspectors tend to have high identification error rate, often caused by fatigue.

Several papers regarding the segmentation and identification of the wood defects have been published. Great effort was made by Chinesse [3–5] and Lithuanian [6] institutes. Their main motivation was based on removing defect areas of wooden slabs in order to increase quality of final product. Every team worked with their own dataset, therefore there is no objective way to compare their results and proposed solution between each other.

Consequent sections cover description of dataset acquisition followed by description of applied method. The very last chapter summarize achieved results.

VSB – Technical University of Ostrava, 2021, ISBN 978-80-248-4523-4 (on-line).

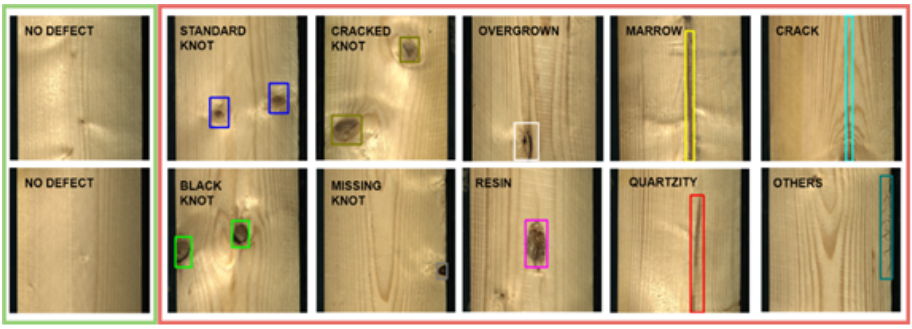

Fig. 1. Listing of wood defects.

2 Dataset

For testing was used dataset of wooden slab cross-sections which was created during standard production of Mayr-Melnhof Holz Paskov Ltd sawmill and included ten unevenly spread defect types. All of them are named in consequent table along with number of occurrences. It is natural that some of the classes are present much more often, because for instance knots are naturally included in every wooden slab. On the other hand, overgrown food defect is present just barely. For the best performance of convolutional neural networks is crucial that number of classes are evenly spread among whole training dataset. Even though, there has been great effort to split dataset to reasonable ratios, ideal balance of all classes in this particular case can not be achieved, thus some tendency, to prefer high occurred classes like live knot or dead knot, is expected. The exact decomposition of dataset is presented in table bellow (see tab. 1).

Table 1. Decomposition of dataset

	Training			Validation		
Defect type	Occur.	No. Defects	Occur. [%]	Occur.	No. Defects	Occur. [%]
Live knot	3430	2007	28,65	17794	9905	55,60
Dead Knot	2091	1514	17,47	9894	6836	30,92
Resin	1751	1330	14,63	1704	1294	5,32
Cracked knot	1076	859	8,99	1200	976	3,75
Crack	1717	1227	14,34	452	351	1,41
Marrow	778	700	6,50	403	360	1,26
Quartzity	758	595	6,33	317	252	0,99
Missing knot	295	281	2,46	208	197	0,65
Blue stain	70	55	0,58	26	22	0,08
Overgrown	6	3	0,05	4	3	0,01
Total	11972	8571		32002	20196	

3 Used Method – Convolutional Neural Network U-NET

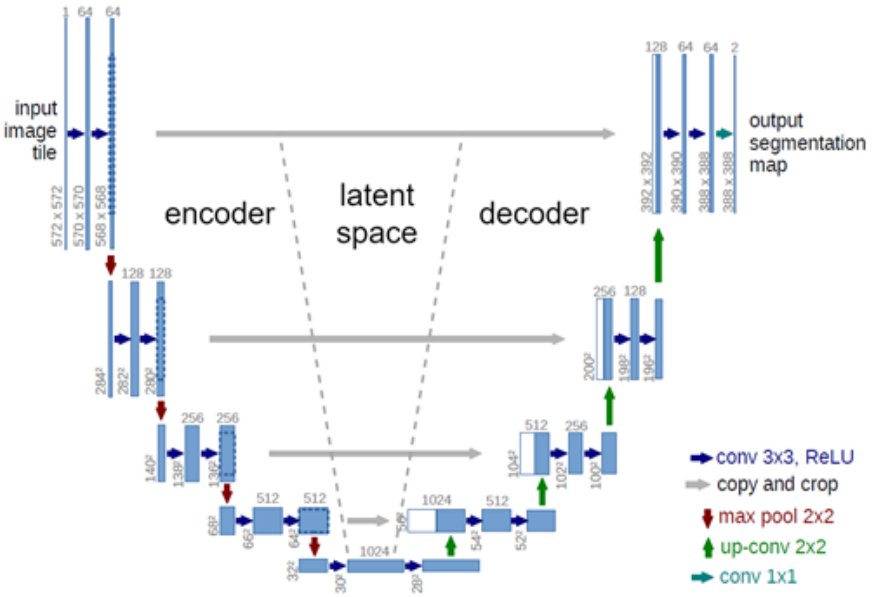

Fig. 2. U-net architecture. [7]

Is type of Convolutional Neural Network which was designed by Olaf Ronnenberg in 2015, specifically for Biomedical Image segmentation tasks [7]. The structure of it is based on autoencoder architecture consisting 2 main parts. First one is called encoder and have contracting pyramid shape resulting in compression of data to latent space, which is formed as bottleneck in the middle part. Second part is called decoder and it is shape is mirroring encoder so it has expanding function. Whole symmetric structure is shown on picture (see Fig. 2).

Encoder consist of repeated pattern of 3x3 unpadded convolution, followed by ReLU and 2x2 max pooling operation. Conversely, decoder part contains 2x2 up-convolutions followed by 3x3 convolutions and ReLU. Input of every block include upsampling operation so the final output segmentation map dimension match the dimension of input image.

Even though, U-net proved to be state-of-the-art solution by winning challenging competition in 2015 and been the most prominent so far, there has been effort to enhance it is performance since it is release. For instance, Nazanin and Lennart presented squeeze U-net [8] which managed to reduce number of parameters from original 30 M to 2,59 M, primarily aiming for portable embedded devices. In next case, Nabil and Sohel managed to increase accuracy of

original model by Inception-layers base concept of blocks structure [9]. Other mentionable promising solutions ResUNet [10], SegNet [11] and [12] presented some architecture improvements as well ,but basic concept of autoencoder has not been replaced by any significantly different approach yet.

4 Results

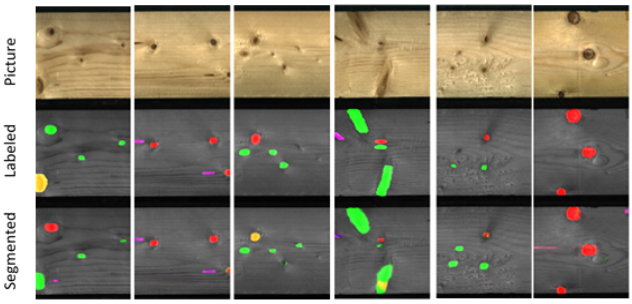

Fig. 3. Segmentation results.

Since semantic segmentation method was applied, there is no possibility to use standard metrics for object detection like Precision, Recall or mAP. Those are applicable just in case, only one class is presented for segmentation. Nevertheless the standard Mean Squared Error metric (MSE) is applied for potential comparison of new state-of-the-art models which are to come in future. Moreover, training process has to be supervised so the model does not overfit on training data. In other words, if model is trained for too many iterations, it tends to memorize all data presented in training set rather then work well on the unknown data.

$$MSE = \frac{1}{NM} \sum_{N}^{i=1} \sum_{M}^{i=1} \left(f\left(i,j\right) - \hat{f}\left(i,j\right) \right)^2 \tag{1}$$

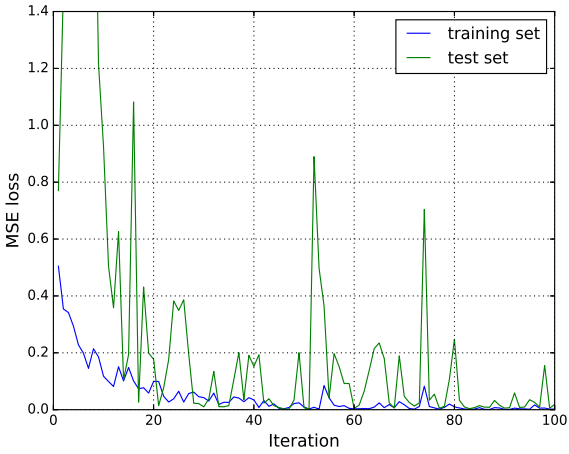

Fig. 4. MSE loss during U-net training phase.

Figure Fig. 4 represent training phase of U-net. Process was stopped when decrease in both MSE losses reached theirs bottoms. The exact MSE value is 0.0023 for the training set and 0.0183 for validation set.

According to results, it is obvious, that algorithm was able to segment defects in much more precise manner than human did (refer to ground truth data), though considering semantic segmentation does not provide information about whole object presence or location but pixel precise map, some parts of single objects were classified as different anomalies. That seems to be quite natural, because for instance there are classes knot, crack and knot with crack, so some of those could vary in comparison with ground truth data and still could be labeled as right class . Type of knots are quite hard to distinguish as well so some misclassifications could be find among final results as well.

References

1. Marzuki Khalid, Eileen Lew, Yi Lee, Rubiyah Yusof, and Miniappan Nadaraj. Design of an intelligent wood species recognition system. *Int. J. Simul. Syst., Sci. Technol.*, 9, January 2008.
2. Bin Li, Haiming Li, Quanqing Zha, Rohan Bandekar, Ahmed Alsaggaf, and Yonghao Ni. Review: Effects of wood quality and refining process on TMP pulp and paper quality. *Bioresources*, 6:3569–3584, June 2011.
3. Yi Xiang Zhang, Ya Qin Zhao, Ying Liu, Lin Quan Jiang, and Zhen Wei Chen. Identification of wood defects based on LBP features. In *2016 35th Chinese Control Conference (CCC)*, pages 4202–4205, Chengdu, July 2016. IEEE.
4. Xiaoqing Zheng, Hongcheng Wang, Jie Chen, Yaguang Kong, and Song Zheng. A Generic Semi-Supervised Deep Learning-Based Approach for Automated Surface Inspection. *IEEE Access*, 8:114088–114099, 2020.

5. Fan Yang, Yuzeng Wang, Shibing Wang, and Yunmei Cheng. Wood Veneer Defect Detection System Based on Machine Vision. In *Proceedings of the 2018 International Symposium on Communication Engineering & Computer Science (CECS 2018)*, Hohhot, China, 2018. Atlantis Press.
6. Augustas Urbonas, Vidas Raudonis, Rytis Maskeliūnas, and Robertas Damaševičius. Automated Identification of Wood Veneer Surface Defects Using Faster Region-Based Convolutional Neural Network with Data Augmentation and Transfer Learning. *Applied Sciences*, 9(22):4898, November 2019.
7. Olaf Ronneberger, Philipp Fischer, and Thomas Brox. U-Net: Convolutional Networks for Biomedical Image Segmentation. *arXiv:1505.04597 [cs]*, May 2015.
8. Nazanin Beheshti and Lennart Johnsson. Squeeze U-Net: A Memory and Energy Efficient Image Segmentation Network. In *2020 IEEE/CVF Conference on Computer Vision and Pattern Recognition Workshops (CVPRW)*, pages 1495–1504, Seattle, WA, USA, June 2020. IEEE.
9. Nabil Ibtehaz and M. Sohel Rahman. MultiResUNet : Rethinking the U-Net architecture for multimodal biomedical image segmentation. *Neural Networks*, 121:74–87, January 2020.
10. Foivos I. Diakogiannis, François Waldner, Peter Caccetta, and Chen Wu. ResUNet-a: A deep learning framework for semantic segmentation of remotely sensed data. *ISPRS Journal of Photogrammetry and Remote Sensing*, 162:94–114, April 2020.
11. Vijay Badrinarayanan, Alex Kendall, and Roberto Cipolla. SegNet: A Deep Convolutional Encoder-Decoder Architecture for Image Segmentation. *arXiv:1511.00561 [cs]*, October 2016.
12. Joseph Bullock, Carolina Cuesta-Lazaro, and Arnau Quera-Bofarull. XNet: A convolutional neural network (CNN) implementation for medical x-ray image segmentation suitable for small datasets. In Barjor Gimi and Andrzej Krol, editors, *Medical Imaging 2019: Biomedical Applications in Molecular, Structural, and Functional Imaging*, page 69, San Diego, United States, March 2019. SPIE.

Design of Optimization Algorithm for Modeling of Retinal Blood Vessels from Fundus Retinal Images

Alice Krestanova

Department of Cybernetics and Biomedical Engineering, FEECS,
VSB – Technical University of Ostrava, 17. listopadu 15,
708 00 Ostrava – Poruba, Czech Republic
alice.krestanova@vsb.cz

Abstract. This paper deals with design of optimization algorithm for segmentation retinal blood vessels. Segmentation algorithm is based on setting parameters with generator of random values in specific intervals. Parameters as length for boosting vessels, length for removing vessels, linear smoothing filter length threshold higher and lower value, clear objects smaller than (in pixels), fill holes smaller than (in pixels). These parameters are inputs for segmentation based on morphological operations. The most suitable combination of parameters is chosen by optimization procedure based on objective parameters for tracking similarity of segmentation outputs with their gold standards.

Keywords: RetCam3, DRIVE, STARE, retinopathy of prematurity, evaluation, objective parameters, segmentation, retinal blood vessels, generator random values, optimization procedure.

1 Introduction

Important area in the ophthalmology is segmentation of the retinal blood vessels [1, 2, 3]. From segmented images with extracted retinal blood vessels structure is possible to analyze and evaluate retina of patients. Ophthalmologists can observe segmented of retinal vascular structure and track objectively early diagnosis, prognosis and proposed treatment. [4] Untreated diseases can lead to retinal detachment occurs, which leads to blindness. In researches are the monitored diseases are: diabetic retinopathy, retinopathy of prematurity (ROP), atherosclerotic retinopathy, hemorrhage, age-related macular degradation (AMD), glaucoma, hypertension. [5-7]

One of observe symptom is tortuosity or curvature in the blood vessels. Tortuosity can be show in people with high blood pressure, atherosclerosis and other diseases. Retinal tortuosity is important indicator of diseases. Modern trends lead to proposing segmentation of retinal blood vessels. Almost algorithms were applied on database from fundus camera mainly DRIVE, STARE. These databases contain retinal images, which were taken in adult patients [8,9]

RetCam3 is a type of fundus camera that is used to capture the spatial image of the retina in premature and immature children. In practice, it can also be used to examine

VSB – Technical University of Ostrava, 2021, ISBN 978-80-248-4523-4 (on-line).

children under one year of age, or even older children. In older children, ophthalmoscopy is used more indirectly.

RetCam3 offers retinal visualization, the output is color images of the retina, which can be displayed in full screen for maximum visualization of details. These images can be archived in image format. In this way, the patient's medical-legal photo documentation can be created. The acquired retinal images allow the doctor to monitor the development of the disease and the effects of treatment. It is used to monitor retinopathy of prematurity and their symptoms, but it can also detect other retinal diseases such as tumors (most often retinoblastoma in young children) or various retinal anomalies. In addition to displaying the retina as an image, RetCam3 also offers a video mode, where the retina can be recorded in full resolution in up to two minutes of video.

It is primarily used to screen for retinopathy of prematurity (ROP) in preterm infants. Early screening and diagnosis are necessary as ROP can lead to retinal detachment and can cause blindness in the individual. Within the articles that used RetCam3, the research can be divided into monitoring other structures on the retina such as hemorrhage, macular pigment, another group are new / modified methods using RetCam for visualization during the use of treatment modalities and the last are segmentation and classification methods to segment / classify retinal structures in order to objectively evaluate the retina and monitor the development of the disease. [10, 11]

This article presents recent research using the RetCam3 in the next section. Section 3 describes the proposed optimization procedure for vascular bed segmentation from RetCam3 images. Section 4 presents testing of the optimization procedure on DRIVE and STARE datasets in order to objectively evaluate the quality of the algorithm against competing methods.

2 Related Works

Navarro-Blanco et al. evaluated the reliability of retinopathy screening of prematurity by RetCam 3 and evaluator variability of ROP diagnosis. Indirect ophthalmoscopy and RetCam3 imaging were used in children. The images were evaluated by 3 groups of experts: 8 ophthalmologists, 5 vision experts, 2 ophthalmologists with expertise in ROP. It was found that the diagnosis made by ROP experts is a reliable method for ROP screening using the RetCam3 camera.[12]

Murilo Ubukata Polizelli et al. studied with RetCam3 retinal haemorrhage (bleeding) in newborns in Brazil born in a high-risk pregnancy. The aim was to analyze the relationship between retinal bleeding with respect to maternal comorbidities, prenatal conditions and newborn health conditions. The prevalence of retinal hemorrhages was found to be higher in neonates in Brazil than in India and China. To determine the relationships and risk factors associated with retinal bleeding, a larger sample of retinal images of individuals than just retinal images obtained in 34 neonates should be analyzed. This is a small sample of images for analysis. [13]

Segmentation and classification algorithm for extraction of retinal blood vessels from RetCam3 images are described in this section. Aldrete et al. from the retinal

images obtained by RetCam3, they calculated the excavation / disc ratio in preterm infants.[14]

Kubicek et al. used a segmentation method using active contours based on statistical local properties in the image to extract retinal lesions.[10]

Krestanova et al. used a segmentation algorithm based on morphological operations to extract the vascular structures.[9]

In the next phase, they performed a combination of vascular bed extraction using morphological operations and a fuzzy Sobel edge detector. [10]

3 Material and Methods

A proposed optimization segmentation algorithm based on morphological operations was applied on retinal images from the private RetCam3 database. The data were obtained by the Center for Children with Visual Impairments in Ostrava. For taking the images were used RetCam3 camera with a resolution of 640x480 50 Retcam images were randomly selected from this database. These images have different image quality, contrast and next problem are observe choroidal blood vessels and movement artifact. This research builds on previous research, when gold standards were created and intervals for setting parameters of morphological operations were tested. After basic statistical testing of a segmentation algorithm based on morphological operations, it was found that this algorithm is satisfactory, but its automated modification is necessary. The automated segmentation process by optimization procedure is shown at Figure 1.

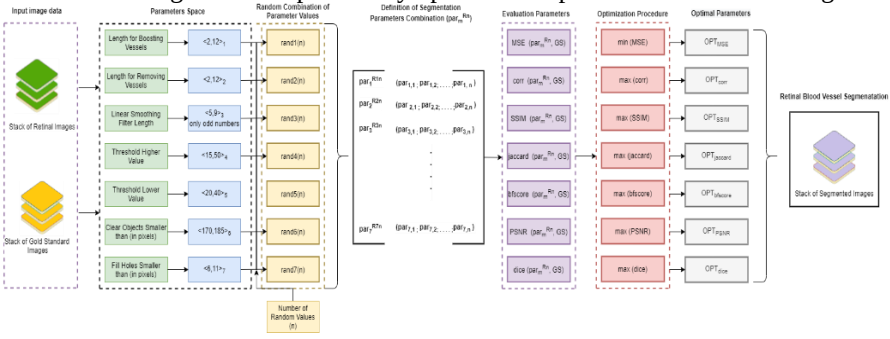

Fig.1. Block diagram of optimatization procedure for extraction retinal blood vessels

In the first step, the input image data, which represents the retinal color images and the corresponding gold standards, is read. For the DRIVE and STARE modalities, they are available from a publicly available database, and for the RetCam modality, gold standards have been created manually.

After loading the image data and their gold standards from one modality, the next step is to set the morphological and threshold parameters for the segmentation procedure. There are seven parameters: linear length of the structural element for vessel reinforcement, linear length of the structural element after vessel removal, length of the linear smoothing filter, upper threshold, lower threshold, deleting objects smaller than (in pixels), filling holes smaller than (in pixels). Based on the previous, the optimal intervals for setting these parameters were determined (see Figure 1).

In the next step, random combinations of these parameters were generated, which generated the setting of the parameter value in the set range. In this block, the number of random parameter values (n) is defined.

In the fourth step, a parameter matrix is created, which defines individual segmentation combinations of parameters. The matrix is of size 7 (number of parameters) xn (number of random parameter values).

In the fifth block, evaluation parameters are used within the automation of the segmentation algorithm. These parameters are mean square error (MSE), correlation coefficient (corr), structural similarity index (SSIM), jaccard coefficient (jaccard), BF score, PSNR (peak signal-to-noise ratio), dice coefficient. These evaluation parameters were chosen to objectively determine the degree of similarity of the segmented image to the gold standard.

The sixth block represents an optimization procedure, where the best suitable combination of parameters is selected from each evaluation parameter to determine similarity, based on the maximum or minimum value. It depends on the parameter used (see Figure 1).

The seventh block represents the selection of the most suitable combination of parameter settings, thus creating a set of output segmented images representing models of the retinal vascular system.

4 Testing of optimization procedure

In order to be able to objectively test the proposed optimization algorithm and determine its quality against other segmentation algorithms, it was applied to the dataset of DRIVE, STARE images. This is because it is the most used database in this area.

Part of the testing is to monitor the computational complexity of the algorithm when setting different combinations. It is clear from Table 1 that the higher the number of combinations, the greater the computational complexity. 25 images were used for the DRIVE database, while 50 images were used for the STARE database. It is also evident from this that the computationally complexity of a twice as large dataset was approximately twice as high.

Table 1. Computational complexity of database DRIVE with different setting number of combination

Number of combination	Computational complexity of DRIVE (25 images) [s]	Computational complexity of STARE (50 images) [s]
10	113	209
50	526	1080
100	1157	2056.9
300	3957	6870
500	5601	10751
1000	11308	24828.38

Table 2 shows the basic statistical processing of the accuracy values of the algorithm for verifying the quality of the proposed algorithm for the DRIVE and STARE

databases. The table shows that with an increasing number of combinations, there is no significant difference in accuracy values. These are differences at the level of thousands. Up to about 100 combinations of parameters, the accuracy increases, then on the contrary decreases slightly. For this reason, also due to the computational complexity, it is advisable to set the optimization process to the number of combinations of 100.

Table 2. Basic stastical analysis of accuracy with different setting number of combination

Number of combination	Median of accuracy DRIVE	Median of accuracy STARE	Average of accuracy DRIVE	Average of accuracy STARE	Variance of accuracy DRIVE	Variance of accuracy STARE
10	0.945	0.964	0.943	0.956	0.000274	0.001317
50	0.948	0.960	0.945	0.956	0.000261	0.000908
100	0.950	0.967	0.945	0.953	0.000183	0.002034
300	0.943	0.959	0.944	0.950	0.000186	0.001907
500	0.942	0.956	0.942	0.949	0.000187	0.001679
1000	0.948	0.957	0.946	0.949	0.000207	0.001842

Table 3. Basic stastical analysis of accuracy with different setting number of combination

	Proposed optimized algorithm	Frucci et al. [10]	Jiang et al. [10]	Lovely et al. [10]	Ozkava et al.]10]
Accuracy DRIVE	0.950	0.520	0.9597	0.9531	0.9561
Accuracy STARE	0.967	-	0.9579	0.9626	-

5 Conclusion

Proposed optimization algorithm based on a random value generator for setting basic parameters. These parameters are the input for setting morphological operations. The algorithm was applied to the database RetCam3, DRIVE, STARE. It was primarily designed for segmentation of retinal images taken with the RetCam3 device for extraction of the retinal vascular bed. In order to be able to objectively compare or compare the quality of the algorithm against other proposed segmentation algorithms for vascular bed extraction from the DRIVE and STARE databases. These databases are the most used in this area. It is clear from the data that the algorithm achieves the best results when setting 100 combinations of parameters. For the STARE database, the median accuracy is 0.967, and for the DRIVE database, the median accuracy is 0.950. When compared with respect to other algorithms using methods based on morphological operations, the proposed optimization algorithm does not differ much in the accuracy / quality of the algorithm (see Table 3). In contrast to, for example, the approach of Frucci et al. optimized proposed algorithm shows very good results.

References

1. Yin, Y., Adel, M., & Bourennane, S. (2012). Retinal vessel segmentation using a probabilistic tracking method. Pattern Recognition, 45 (4), 1235–1244.
2. Vega, R., Sanchez-Ante, G., Falcon-Morales, LE, Sossa, H., & Guevara, E. (2015). Retinal vessel extraction using Lattice Neural Networks with dendritic processing. Computers in Biology and Medicine, 58, 20–30.
3. Zhang, J., Cui, Y., Jiang, W., & Wang, L. (2015). Blood vessel segmentation of retinal images based on neural network. Lecture Notes in Computer Science (Including Subseries Lecture Notes in Artificial Intelligence and Lecture Notes in Bioinformatics), 9218, 11–17.
4. Onkaew, D., Turior, R., Uyyanonvara, B., Akinori, N., & Sinthanayothin, C. (2011). Automatic retinal vessel tortuosity measurement using curvature of improved chain code. InECCE 2011 - International Conference on Electrical, Control and Computer Engineering, 183–186.
5. Turior, R., Onkaew, D., Kondo, T., & Uyyanonvara, B. (2011). A novel approach for quantification of retinal vessel tortuosity based on principal component analysis. ECTI-NOC 2011 - 8th Electrical Engineering / Electronics, Computer, Telecommunications and Information Technology (ECTI) Association of Thailand - Conference 2011, 1023–1026.
6. Krestanova, A., Kubicek, J., Timkovic, J., Penhaker, M., Oczka, D., & Vanus, J. (2020). Modeling and extraction of retinal blood vessels from RetCam 3 based on morphological segmentation. In Studies in Computational Intelligence (Vol. 830, pp. 255–263). Springer Verlag.
7. Niemeijer M., "Retinopathy Online Challenge: Automatic Detection of Microaneurysms in Digital Color Fundus Photographs," in IEEE Transactions on Medical Imaging, vol. 29, no. 1, pp. 185-195, Jan. 2010
8. Chakraborti, T., Jha, DK, Chowdhury, AS, & Jiang, X. (2014). A self-adaptive matched filter for retinal blood vessel detection. Machine Vision and Applications, 26 (1), 55–68.
9. Kubicek, J., Timkovic, J., Krestanova, A., Augustynek, M., Penhaker, M., Bryjova, I.: Morphological segmentation of retinal blood vessels and consequent tortuosity extraction. J. Telecommun. Electron. Comput. Eng. 10 (1-4), 73-77 (2018)
10. Krestanova A., Kubicek J. and Penhaker M., "Recent Techniques and Trends for Retinal Blood Vessel Extraction and Tortuosity Evaluation: A Comprehensive Review," in *IEEE Access*, vol. 8, pp. 197787-197816, 2020, doi: 10.1109/ACCESS.2020.3033027.
11. Natus, Eye Imaging, (n.d.). https://newborncare.natus.com/products-services/newborn-care-products/eye-imaging (accessed April 19, 2021).
12. Navarro-Blanco C:, Peralta-Calvo J., Pastora-Salvador N., Álvarez-Rementería L., Chamorro E., Sánchez-Ramos C., Reliability of retinal imaging screening in retinopathy of prematurity, An. Pediatría (English Ed. 81 (2014). https://doi.org/10.1016/j.anpede.2013.10.011.
13. Polizelli M. U., Rodrigues de Oliveira B. M., Nakayama L., Bergamo V., Bueno de Moraes N. S., Analysis of newborn retinal haemorrhage in a tertiary hospital in Sao Paulo, Brazil with Retcam 3 fundus photos, Invest. Ophthalmol. Vis. Sci. 60 (2019).
14. Aldrete A., Paez J. H., Ingrid F., Claudia A., Retcam 3 Calculated cup/disc Ratio of Preterm Newborn Optic Nerves in a Mexican Population., Investig. Ophthalmol. Vis. Sci. J. (2015).

Magnetic Resonance Triggering Based on Ballistocardiography

Martina Ladrova and Radek Martinek

Department of Cybernetics and Biomedical Engineering, FEECS,
VSB – Technical University of Ostrava, 17. listopadu 15,
708 00 Ostrava – Poruba, Czech Republic
{martina.ladrova, radek.martinek}@vsb.cz

Abstract. Synchronization of Magnetic Resonance (MR) acquisition with the patient's cardiorespiratory activity is necessary to eliminate motion artifacts from the image, and thus, to achieve high image quality. In clinical practice, electrical measurements like ECG are standardly used to monitor cardiac activity, which suffers from the effects of magnetic field and electromagnetic interference produced by MR device. Therefore, the research started to focus on the development of new approaches based on nonelectrical principles, such as ballistocardiography (BCG) that is the main object of this paper. The last study on the proposed sensory system is described, focusing on the comparison of two BCG-based systems and standardly used ECG. The results proved a comparable image quality and moreover, improved workflow during the examination.

Keywords: Magnetic Resonance, Cardiovascular MRI, MRI Triggering, Ballistocardiography.

1 Introduction

Magnetic Resonance Imaging (MRI) is an important noninvasive tool for examining the structure of the human body and its function. Its main advantages include the absence of ionizing radiation, high contrast between different types of soft tissues, and the possibility of imaging in any spatial orientation. In addition to the high resolution of structures, MR also provides information about their basic functions (e.g., molecular water diffusion, tissue perfusion, or MR spectroscopy). These parameters help to make a more accurate diagnosis and increases the chances of proper treatment management [1].

Synchronization of MRI with cardiorespiratory activity (so-called gating or triggering) is generally used when imaging the abdominal area, where artifacts occur due to respiration, and especially the cardiovascular system, where the image is degraded by both cardiac and respiratory activity. These artifacts are characterized by blurred contours of structures, reduced resolution, or so-called ghosting artifacts. Gating of MR sequence can suppress these artifacts and helps to achieve high temporal and spatial image resolution (including high contrast and sharp contours), which are important assumptions for the overall image quality and accurate diagnostic information [2].

VSB – Technical University of Ostrava, 2021, ISBN 978-80-248-4523-4 (on-line).

Cardiac triggering of MR during myocardial imaging is essential to ensure a high-quality real-time image of the heart that is constantly in motion. By default, an electrocardiography (ECG) or vectorcardiography (VCG) are used to monitor cardiac activity. Although these methods are fast tools for cardiac function measurements from which each phase of the cardiac cycle can be read to trigger MR, many problems arise with the MR magnetic field and other MR interferences, such as artifacts arising from magnetic field inhomogeneity, radiofrequency pulses, or gradient pulses [3]. In response to these shortcomings of established methods, many studies have recently emerged, focusing on the further development of these methods in terms of software and hardware, but especially looking for new ways to measure patient vital signs that would provide an adequate alternative to ECG/VCG measurements.

The paper aims to summarize the scientific work of the author in cardiac MRI triggering. It presents the results of the literature survey (Section 2) that makes a basis for the implementation of the sensory system based on ballistocardiography (BCG), i.e., monitoring the mechanical activity of the heart. Thus, Section 3 describes the last study focusing on the comparison of the two BCG approaches proposed within the Faculty of Electrical Engineering and Computer Science, VSB-Technical University of Ostrava, with the aim to prove these methods to be suitable alternatives to standardly used ECG.

2 Recent Approaches to MRI Triggering

The comprehensive review introduced in [4] was performed to summarize the advantages and shortcomings of the individual triggering methods, currently used in clinical practice or being the subject of research. The techniques based on different principles are classified, such as electrical measurements (ECG/VCG), monitoring based on acoustic manifestations (stethoscopes, Doppler ultrasound), vibrations (accelerometers), and light transmission (pulse wave, optical fibers) or systems working directly with MR data (self-gating).

As we can see in Table 1, all discussed methods can be evaluated from the perspective of the following parameters:

- Heart rate detection *accuracy* assessed with respect to some abnormalities or technical limitations, not to the origin of MR artifacts,
- *Resistance* to MR artifacts, i.e., electromagnetic field, magnetohydrodynamic effect or acoustic disturbance, and
- *Complexity*, including computational requirements, availability, and the price of measuring system.

Computational cost is a crucial factor in the implementation of the measuring system since it determines the function in real-time. Price is also a key point of method feasibility for clinical practice. A method eligible for introduction into practice should accomplish a compromise between its complexity and performance/accuracy.

Furthermore, individual methods suffer from some specific *limitations*, such as long physiological delay, patient's physiology/pathology, or delay due to the signal

transmission, which should be eliminated or reduced as best as possible to introduce the method into practice successfully.

The alternative methods have the following common disadvantages:

- *Non-standardized sensor placement* in contrast with ECG or VCG. The sensor location highly depends on the specific patient and his body structure; some signals show very different waveforms when placed at diverse points of the chest.
- *Signal delay compared to ECG* which is given by several attributes: (1) a physiological delay between the R wave and the alternative trigger point (first heart sound, J-wave, etc.), and (2) other delays superimposed caused by the transmission medium, electronics ensuring signal state and conversion to a digital signal, or filtration used to remove undesirable components. Such a delayed trigger signal may lag behind the ECG trigger for hundreds of milliseconds, collecting data from the wrong phase of the cardiac cycle. Therefore, the image may lose its diagnostic value, and the acquisition needs to be repeated, extending the examination time.

Table 1. Classification of cardiac synchronization methods.

	Accuracy	Resistance	Complexity	Limitations
ECG	High	Low	Medium	Measures against high voltages
VCG	High	Medium	Medium	Measures against high voltages
POX	Low	High	Low	Motion artifacts, long physiological delay
STE	High	Medium	Medium	Delay due to conduction and processing
ACC	High	Medium	Medium	Delay due to conduction and processing
FOS	High	High	High	Long physiological delay
DUS	Medium	High	High	Long delay, difficult contact with the patient, heart abnormalities
S-G	Medium	High	High	Mild myocardial contractions, high heart rate, prospective triggering

* POX – pulse oximetry, STE – stethoscopes (acoustic sensors), ACC – accelerometers, FOS – fiber optic sensors, DUS – Doppler ultrasound, S-G – self-gating

3 Comparative Study on BCG Triggering

Based on the findings from the review, several prototypes of sensors involved in a pneumatic measuring system based on virtual instrumentation were designed and experimentally tested. The measuring strain consists of a sensor (a plastic funnel or a deformable airtight sensing element shaped as a tube or bellows), a pneumatic transmission line, and a measuring apparatus located outside the MR field. Preferably, materials such as polyvinyl chloride (PVC), polyurethane (PUR) or silicone are used to construct the sensing element and the pneumatic transmission line. The simplified block diagram of the signal acquisition system is shown in Figure 1.

These systems are patient-friendly and low-cost alternatives to ECG measuring in MR environment, which are completely resistant to magnetic field and electromagnetic interference due to the measuring principle based on BCG (or seismocardiography), expressing the mechanical activity of the heart.

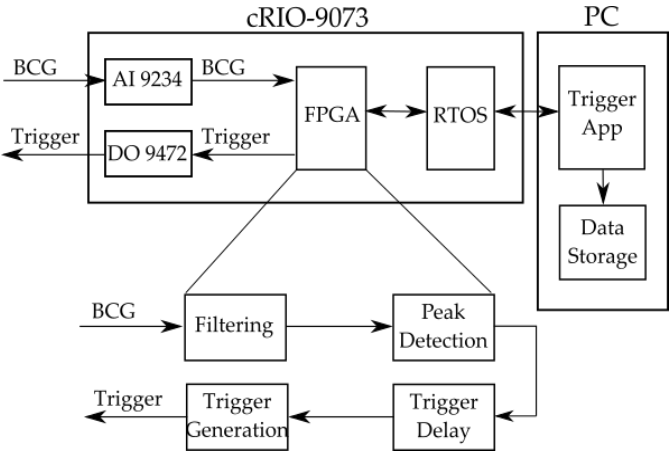

Figure 1. A block diagram of the proposed BCG-based triggering system.

The preliminary studies [5, 6] proved the compatibility of the proposed sensors with the MR environment and presented the accuracy of the heart rate detection together with the evaluation of the triggered image quality (using both objective and subjective evaluation methods). The results showed that the method could be an adequate alternative to the standardly used ECG method but also uncovered their shortcomings, such as the problematic placement of the sensor, susceptibility to vibrations of MR device or interferences caused by the size of the sensor. Therefore, these issues became the goals of further research and were considered in sensor optimization.

The last study performed presented an optimized sensor prototype in the form of the coiled tube that is placed under the patient's back. This embodiment can reduce the interference within the sensor and ensure the patient's comfort. In this study, the sensor based on optical fibers was also tested to compare two different ways of BCG measuring. This sensor based on Fiber Bragg Grating (FBG) also showed satisfactory results in the previous study [7]. The general diagram of the measuring systems employed in this comparative study is shown in Figure 2.

The study was performed on 10 subjects on 3 T Siemens Magnetom Prisma using two sequences for heart imaging:

- *True Fast Imaging with Steady State Precession* (TRUEFISP), a cinematic sequence that visualizes moving structures and the heart muscle during movement,
- *Phase Sensitive Inversion Recovery* (PSIR), a standardly used sequence for postcontrast scan that assesses contrast-induced myocardial saturation, either for early saturation of inflammatory infiltrates, or delayed saturation of intramyocardial scars).

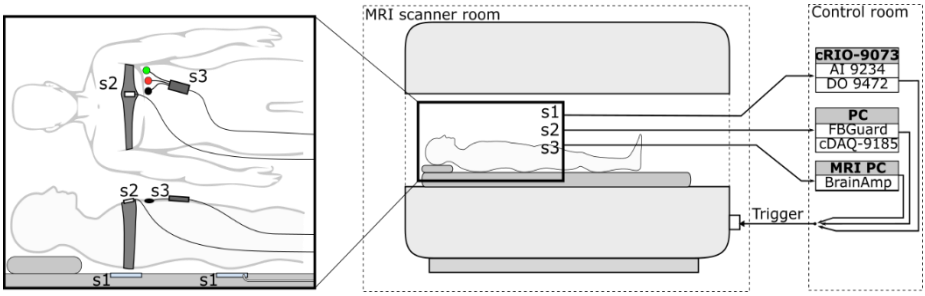

Figure 2. A simplified diagram of the triggering systems and their sensor placement (s1 - Pneumatic sensor, s2 - Optical sensor, s3 – Reference ECG).

A trigger delay was set to 200 ms after the detected BCG peak since the BCG signal is delayed compared to ECG by 200 – 250 ms. Thus, the overall delay related to R wave reaches 400 ms and the triggering pulse falls into the diastolic heart phase, which is an important criterium for examination using the above-mentioned sequences. However, according to subjective evaluation by radiology experts, the proper timing of the acquisition was not reached in many cases – probably due to the heart rate variability and sinus arrhythmia caused by the patient's breath-holding which are not compensated by the proposed system and will be the subject of further research.

The results of the study proved the comparable image quality of BCG-triggered images using both alternative methods to ECG-triggered images. The objective parameters included Signal-to-Noise Ratio, Contrast-to-Noise Ratio, Structural Similarity Index, and nonreference evaluation parameters (Blind/Referenceless Image Spatial Quality Evaluator, Naturalness Image Quality Evaluator). The subjective analysis was performed by 10 radiologists with various lengths of experience (3 – 25 years) by the blind method. They assessed the overall image quality together with recognizability of the interventricular septum and myocardium, overall recognizability of clinical symptoms in the image, stage of the heart cycle in which the scan was performed, image sharpness, the time required to recognize the structure of interest in the image, and artifact occurrence.

The ECG triggering method seems to produce the best quality images, but small differences between the methods can be observed. However, using the TRUEFISP sequence, the ECG triggering approach dominates, and the pneumatic sensor appears slightly better compared to the optical sensor. Similar findings were observed in the results of the overall recognizability of individual tissue structures and the time required to identify these structures. Based on the subjective evaluation of experts, the ECG trigger method appears to be slightly better with the PSIR sequence.

The last part of the study included the evaluation of the time required for data acquisition and patient preparation (i.e., application of sensors). Moreover, the patient's feeling during the examination was also examined. The results proved that the alternatives to ECG could accelerate the preparation of the measured subject and shorten the operator's time in the examination room. This is a noncomplicated way to increase the workflow. The patient's comfort is also significantly higher in the case of both proposed BCG systems.

4 Conclusion

The paper presented the motivation of research in alternative methods of MRI synchronization and summarized their benefits and shortcomings. Then, the proposed measuring system was briefly described and the results of the last study on alternative approaches to MRI gating based on BCG were discussed. Further work of the author will consist of the optimization of the preliminary sensor prototype, design of suitable signal processing methods, and peak detection algorithm. The proposed solution will be then experimentally validated in a real MRI environment.

References

1. GOURTSOYIANNIS, Nicholas C., ed. *Clinical MRI of the Abdomen*. Berlin, Heidelberg: Springer Berlin Heidelberg, 2011. ISBN 978-3-540-85688-7.
2. STADLER, Alfred, Wolfgang SCHIMA, Ahmed BA-SSALAMAH, Joachim KETTENBACH a Edith EISENHUBER. Artifacts in body MR imaging: their appearance and how to eliminate them. *European Radiology*. 2007, **17**(5), 1242-1255. ISSN 0938-7994.
3. OSTER, Julien a Gari D CLIFFORD. Acquisition of electrocardiogram signals during magnetic resonance imaging. *Physiological Measurement*. 2017, **38**(7), 119-142. ISSN 1361-6579.
4. LADROVA, Martina, Radek MARTINEK, Jan NEDOMA, Pavla HANZLIKOVA, Michael Douglas NELSON, Radana KAHANKOVA, Jindrich BRABLIK a Jakub KOLARIK. Monitoring and Synchronization of Cardiac and Respiratory Traces in Magnetic Resonance Imaging: A Review. *IEEE Reviews in Biomedical Engineering*. 2021. ISSN 1937-3333.
5. MARTINEK, Radek, Jindrich BRABLIK, Jakub KOLARIK et al. A Low-Cost System for Seismocardiography-Based Cardiac Triggering: A Practical Solution for Cardiovascular Magnetic Resonance Imaging at 3 Tesla. *IEEE Access*. 2019, **7**, 118608-118629. ISSN 2169-3536.
6. MARTINEK, Radek, Jindrich BRABLIK, Jakub KOLARIK et al. A Comparison Between Novel FPGA-Based Pad Monitoring System Using Ballistocardiography and the Conventional Systems for Synchronization and Gating of CMRI at 3 Tesla: A Pilot Study. *IEEE Access*. 2020, **8**, 4149-4170. ISSN 2169-3536.
7. NEDOMA, Jan, Radek MARTINEK, Marcel FAJKUS et al. A Novel FBG-Based Triggering System for Cardiac MR Imaging at 3 Tesla: A Pilot Pre-Clinical Study. *IEEE Access*. 2020, **8**, 181205-181223. ISSN 2169-3536.

Biological Wastewater Treatment Modeling: Review

Jakub Nemcik

Department of Cybernetics and Biomedical Engineering, FEECS,
VSB – Technical University of Ostrava, 17. listopadu 15,
708 00 Ostrava – Poruba, Czech Republic
jakub.nemcik@vsb.cz

Abstract. This article deals with available models describing biological wastewater treatment. Biological wastewater treatment, which is an integral part of wastewater treatment plants, reduces the concentration of undesirable substances in wastewater to an acceptable level. The levels of individual concentrations of the given substances in the wastewater are determined by the administrative authority, which monitors these concentrations of the substances contained in the water discharged from the treatment plants into the municipal waters. By modeling biological treatment, it is possible to observe and understand the internal behavior of individual processes, evaluate the behavior of the treatment itself, including its efficiency, suggest possible improvements or propose new control methods. The aim of the article is to acquaint readers with available models describing biological wastewater treatment, including their modifications, which removed or partially reduced their limitations. Furthermore, the article also provides basic information on modeling wastewater treatment.

Keywords: Activated sludge model, biological treatment model, modeling

1 Introduction

Expanding built-up areas in cities or villages, together with the increasing amount of polluted water from industrial facilities, increases the demands placed on wastewater treatment plants. These are the maximum permissible concentrations of certain types of substances contained in treated wastewater. Wastewater treatment processes can be divided into mechanical and biological processes, or primary and secondary. In the overall cleaning process, coarse impurities are first removed from the waste by mechanical treatment and then the organic impurities are removed/reduced by biological treatment [1].

Wastewater treatment consists of several parts (simple example can be seen on figure 1): a biological treatment model, a model describing the behavior of the volume in the tank and fluids flow (hydraulic model), an oxygen transfer model, and a settling reactor model. The most used method for describing biological wastewater treatment processes is Activated Sludge Processes, in which activated sludge removes impurities [2][3].

The removal of biological nitrogen, biological phosphorus and organic carbon can be achieved by a suitable design of activated sludge treatment with activated sludge [4].

VSB – Technical University of Ostrava, 2021, ISBN 978-80-248-4523-4 (on-line).

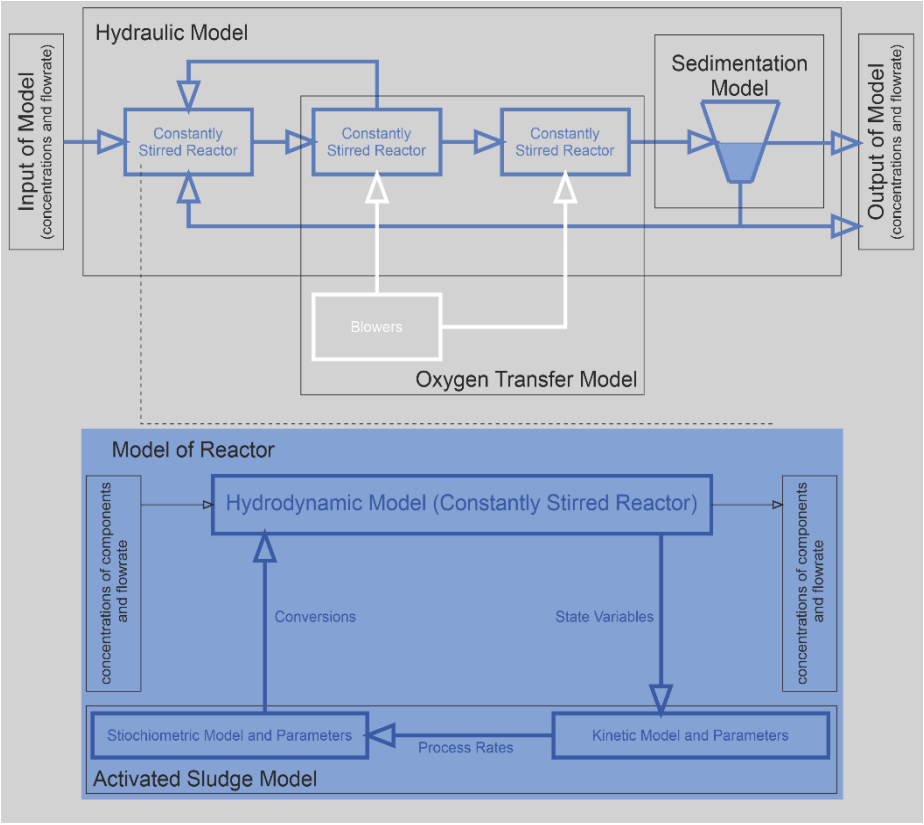

Fig. 1. Example of wastewater treatment model

The processes described by the activated sludge model depend only on the concentration in the given tank / reactor in which they take place [4].

The process of modeling biological wastewater treatment and the actual application of the model for a real system can be divided into several steps [3][4]:

- the purpose of using the model of wastewater treatment,
- model selection,
- determination of hydraulic models,
- characterization of wastewater composition,
- alignment of data with the model at steady state,
- parameter calibration,
- model verification and
- evaluation.

2 Biological Wastewater Treatment Models

The first two steps of system modeling and its application are closely related. Today, there are several models describing the biological wastewater treatment modeling problem. The models are described below.

2.1 Activated Sludge Model no. 1 (ASM1)

ASM1 was developed by a group of scientists and engineers (International Association on Water Pollution Research and Control - IAWPRC) in 1987. It is considered a reference model describing biological wastewater treatment processes using 8 processes and 13 wastewater components. It was primarily developed to describe the removal of carbon and nitrogen components at domestic wastewater with the simultaneous consumption of oxygen and nitrate as electron acceptors [2-5].

ASM1 uses matrix notation of individual processes, stoichiometric coefficients, and kinetic parameters. The original article [5] mentions typical parameters for neutral pH values and temperatures of 10°C and 20°C for municipal wastewater.

Here is the list of the selected modification of ASM1:

- modification based on temperature dependency of environment [6],
- modification to adapt the performance from SBR (sequencing batch reactor) into oxic-anoxic phases [7],
- extension of ASM1 for wastewater treatment with different chemical oxygen demand:nitrogen ratio [8],
- incorporating the inhibition effects from carbon and ammonium for two-step nitrification [9],
- modification and calibration for membrane bioreactor technology for textile wastewater treatment [10].

2.2 Activated Sludge Model no. 2 (ASM2)

During the design of the ASM1 phosphorus removal was observed, but it was not perfectly understood. After eight years, the ASM2 model was created, which was the first of the models to describe not only the removal of organic components of wastewater but also the removal of chemical phosphorus by precipitation. The model uses 19 processes and 19 wastewater components to describe the dynamics. However, over time, it has been shown to insufficiently describe the growth dynamics or decay of organisms responsible for phosphorus decomposition [2][3][11].

2.3 Activated Sludge Model no. 2d (ASM2d)

According to the above information, the ASM2 model did not sufficiently describe the growth dynamics and extinction of organisms responsible for phosphorus decomposition. Therefore, this model was extended and the ASM2d model was created, which better describes the dynamics of phosphate and nitrate. This model contains two extra

processes and the same components as ASM2 with different conversion factors in matrix notation [2][3][12].

Here is the list of the selected modification of ASM2d:

- more complex division of organic substrate [13],
- novel hydrolysis concept of ASM2d [14],
- extension of ASM2d for wastewater treatment with different chemical oxygen demand:nitrogen ratio [15],
- modification for chemical dosage [16],
- extension of phosphorus metabolic processes of the EPS into ASM2d [17].

2.4 Activated Sludge Model no. 3 (ASM3)

At the end of the 20th century, as the last of the ASM family, a model called ASM3 was developed, which, similarly to the first model, describes biological nitrogen removal using 12 processes and 13 wastewater components. During the development of this model, the shortcomings of ASM1 were eliminated [2][3][18].

Here is the list of the selected modification of ASM3:

- combination of additional processes and products with ASM3 [19],
- inclusion the two-step nitrification-denitrification [20],
- inclusion of direct heterotrophic growth on readily biodegradable substrate [21],
- extension of N_2O production [22].

2.5 Technical University Delft Phosphorus model (TUDP)

It is a metabolic structured model for biological and anoxic phosphorus removal, which uses ASM1 as a basis. This is a model that focuses in more detail on phosphorus removal. The TUDP model provides a full description of the metabolism of phosphorus accumulating organisms (PAOs), with two storage components explicitly modeled: glycogen and polyhydroxyalkanoate [2][3][23].

2.6 Bio-P Module

The ASM3 model, unlike the ASM2, ASM2d and TUDP models mentioned above, only describes the removal of carbon and nitrogen components, but not phosphorus. The concentration of phosphorus in water is one of the important parameters, the value of which is given by the appropriate administrative institution. The Swiss Federal Institute for Environmental Science and Technology (EAWAG) has developed an additional module for ASM3. This module involved biologically removed phosphorus. However, phosphorus precipitation is not considered. It is especially necessary to add phosphorus precipitation in case of high concentrations of Ca^{2+} and at high pH [2][3][24].

3 Conclusion

Modeling of biological processes extends to a wide range of scientific disciplines. The models mentioned above belong to a group of empirical models which, unlike mechanistic models, are based on the recognition of internal parameters and the description of behavior. Activated sludge models are recognized by the scientific community as standardized for the description of biological wastewater treatment processes.
The first such model was ASM1, which describes the removal of both organic carbon and nitrogen from wastewater. It should be considered that the original ASM model was created for municipal wastewater and the parameters were determined only for a narrow temperature range. However, its development continues for specific types of problems.
The ASM2 and ASM2d models were the first type to describe, among other things, biological phosphorus removal. Although ASM2d is more complex, it is further developed by the scientific community.
Although ASM3 was originally only a certain correction of the ASM1 model, thanks to the Bio-P model, it was like ASM2/ASM2d able to describe phosphorus removal.

References

1. Serdarevic, A., Dzubur, A. (2016). Wastewater process modeling. Coupled systems mechanics, 5(1), 21-39.
2. Gernaey, K. V., van Loosdrecht, M. C., Henze, M., Lind, M., Jørgensen, S. B. (2004). Activated sludge wastewater treatment plant modelling and simulation: state of the art. Environmental modelling & software, 19(9), 763-783.
3. Van Loosdrecht, M. C. M., Lopez-Vazquez, C. M., Meijer, S. C. F., Hooijmans, C. M., & Brdjanovic, D. (2015). Twenty-five years of ASM1: past, present and future of wastewater treatment modelling. Journal of Hydroinformatics, 17(5), 697-718.
4. Henze, M., van Loosdrecht, M. C., Ekama, G. A., Brdjanovic, D. (Eds.). (2008). Biological wastewater treatment. IWA publishing.
5. Henze, M., Grady, C.P.L., Jr., Gujer, W., Marais, G.V.R., Matsuo, T. (1987). Activated Sludge Model No. 1. IAWQ Scientific and Technical Report No. 1, London, UK.
6. Brikova, O. I., Grudyaeva, E. K., Dushin, S. E., & Zhukov, I. V. (2019). The Influence of Ambient Temperature on the Process of Biological Treatment in the Model ASM1. In 2019 III International Conference on Control in Technical Systems (CTS) (pp. 136-139). IEEE.
7. Freytez, E., Márquez, A., Pire, M., Guevara, E., & Perez, S. (2019). Nitrogenated substrate removal modeling in sequencing batch reactor oxic-anoxic phases. Journal of Environmental Engineering, 145(10), 04019068.
8. Gao, F., Nan, J., Li, S., & Wang, Y. (2018). Modeling and simulation of a biological process for treating different COD: N ratio wastewater using an extended ASM1 model. Chemical Engineering Journal, 332, 671-681.
9. Gao, F., Nan, J., Li, S., & Wang, Y. (2018). Modeling and simulation of a biological process for treating different COD: N ratio wastewater using an extended ASM1 model. Chemical Engineering Journal, 332, 671-681.
10. Lubello, C., Caffaz, S., Mangini, L., Santianni, D., & Caretti, C. (2007). MBR pilot plant for textile wastewater treatment and reuse. Water science and technology, 55(10), 115-124.

11. Henze, M., Gujer, W., Matsuo, T., Mino, T., Wentzel, M. C. (1995). The activated sludge model No. 2: biological phosphorus removal. Water science and technology, 31.2: 1-11.
12. Henze, M., Gujer, W., Mino, T., Matsuo, T., Wentzel, M. C., Marais, G. V. R., & Van Loosdrecht, M. C. (1999). Activated sludge model no. 2d, ASM2d. Water science and technology, 39(1), 165-182.
13. Drewnowski, J., Mąkinia, J., Szaja, A., Łagód, G., Kopeć, Ł., & Aguilar, J. A. (2019). Comparative study of balancing SRT by using modified ASM2d in control and operation strategy at full-scale WWTP. Water, 11(3), 485.
14. Drewnowski, J., Makinia, J., Kopec, L., & Fernandez-Morales, F. J. (2018). Modelization of nutrient removal processes at a large WWTP using a modified ASM2d model. International journal of environmental research and public health, 15(12), 2817.
15. Zhang, X., Nan, J., Liu, T., Xiao, Q., Liu, B., He, X., ... & Ding, A. (2021). Modeling and simulation of an extended ASM2d model for the treatment of wastewater under different COD: N ratio. Journal of Water Process Engineering, 40, 101831.
16. Ma, S., Zeng, S., Dong, X., Chen, J., & Olsson, G. (2015). Modification of the activated sludge model for chemical dosage. Frontiers of Environmental Science & Engineering, 9(4), 694-701.
17. Zu, X., Nan, J., He, L., Xiao, Q., & Liu, B. (2021). Development of a double-layer EPS-ASM2d model to illustrate the effect on mainstream biological phosphorus system in sidestream phosphorus recovery process. Science of The Total Environment, 772, 144961.
18. Gujer, W., Henze, M., Mino, T., & Van Loosdrecht, M. (1999). Activated sludge model No. 3. Water science and technology, 39(1), 183-193.
19. Gao, F., Nan, J., & Zhang, X. (2017). Simulating a cyclic activated sludge system by employing a modified ASM3 model for wastewater treatment. Bioprocess and biosystems engineering, 40(6), 877-890.
20. Iacopozzi, I., Innocenti, V., Marsili-Libelli, S., & Giusti, E. (2007). A modified Activated Sludge Model No. 3 (ASM3) with two-step nitrification–denitrification. Environmental Modelling & Software, 22(6), 847-861.
21. van Loosdrecht, M. C. M., & Orhon, D. (2003). Modification of activated sludge model no. 3 considering direct growth on primary substrate. Water Science and Technology, 47(11), 219-225.
22. Blomberg, K., Kosse, P., Mikola, A., Kuokkanen, A., Fred, T., Heinonen, M., ... & Vahala, R. (2018). Development of an extended ASM3 model for predicting the nitrous oxide emissions in a full-scale wastewater treatment plant. Environmental science & technology, 52(10), 5803-5811.
23. Van Veldhuizen, H., van Loosdrecht, M. C., & Heijnen, J. J. (1999). Modelling biological phosphorus and nitrogen removal in a full scale activated sludge process. Water Research, 33(16), 3459-3468.
24. Rieger, L., Koch, G., Kühni, M., Gujer, W., & Siegrist, H. (2001). The EAWAG Bio-P module for activated sludge model No. 3. Water research, 35(16), 3887-3903.

Tetrapolar Bioimpedance Measurement Circuit Design

Martin Schmidt and Marek Penhaker

Department of Cybernetics and Biomedical Engineering, FEECS,
VSB – Technical University of Ostrava, 17. listopadu 15,
708 00 Ostrava – Poruba, Czech Republic
{martin.schmidt, marek.penhaker}@vsb.cz

Abstract. Bioimpedance measurement offer a simple way to study the structural parameters of living tissues. It is often used for determining body composition, measuring plethysmography or pneumography. This work proposes a simple circuit using off-the-shelf components for measuring bioimpedance using tetrapolar electrode measurement. The circuit was realized, its parameters evaluated and its accuracy was tested using resistors. Whole body bioimpedance using standard hand-foot tetrapolar electrode placement with the frequency of 50 kHz was also done using the circuit in this work.

Keywords: Bioimpedance, Bioelectrical impedance, Tetrapolar measurement

1 Introduction

Bioimpedance is the electrical impedance of biological tissues to the flow of alternating current. It consists of two components: resistance and reactance. The resistance is characterized by a zero-phase shift between voltage and current, so this component is related to the active power, which manifests itself in the tissues as heat. The reactance is characterized by a phase shift of the current with respect to the voltage. The current phase shift is ± 90 °. If the phase shift is + 90 °, it is an inductive resistance (inductance), this component is related to the ability to accumulate energy in a magnetic field. A phase shift of -90 °, in turn, means capacitive resistance (capacitance), and this component is related to the ability to accumulate energy in an electric field. Biological tissues have a capacitive character due to the cell membranes [1].

The device for measuring bioimpedance parameters interacts with the object via electrodes. In the area of contact of the electrode with the tissue, there are relatively complex physical and chemical processes influencing the measurement results. The main result of these processes is a change in the charge carriers that generate the electric current. In conductors and metal electrodes, a current is generated by electrons moving in the crystal lattice of the metal, and in the tissue, it is generated by ions moving in the electrolyte solution. When the electrode touches the electrolyte, an equilibrium potential difference is created between them and a double electrical layer is formed at the interface [1, 2].

Tetrapolar measurement uses four electrodes connected to the surface of the sample, depicted in figure 1. The two electrodes used for current injection are excitation

VSB – Technical University of Ostrava, 2021, ISBN 978-80-248-4523-4 (on-line).

and the two measuring voltage drops are sensing. This connection method serves to eliminate the parasitic impedances occurring in the bipolar connection at the electrode-electrolyte interface, because in the given configuration the sensing electrodes have such a high input impedance that the current value on the sensing electrodes is negligible and therefore the voltage drop is measured only on measured section of tissue. In real circuits, however, the result is affected by the half-cell potential that arises at the interfaces between the electrode and the electrolyte and high-frequency noise resulting from parasitic capacitance [3].

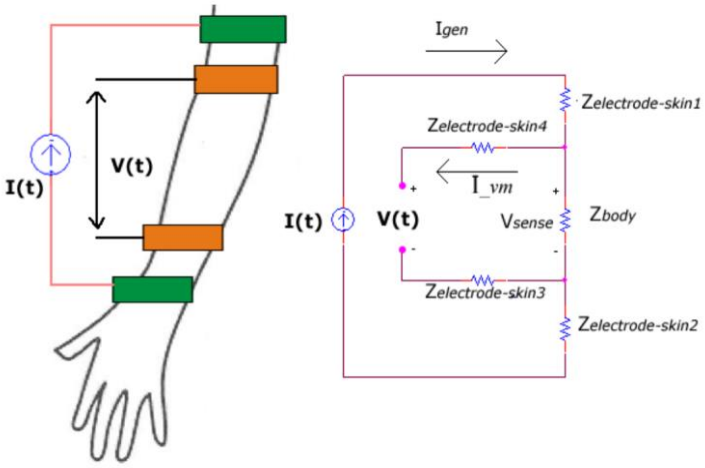

Fig. 1 Tetrapolar measurement schematic [5]

Currently, the method of measuring bioimpedance is an evolving tool for biomedical research and for clinical practice due to its simplicity and low cost of equipment. The most common application of the method is the measurement of body composition: percentage fat content in the body, total volume of body fluids or their ratio, muscle mass and bone mass. The bioimpedance method is now also used in the field of plethysmography, cardiography, pneumography and computed tomography. The purpose of these methods is to monitor and evaluate changes in volume and impedances in the blood, heart and lungs. Bioimpedance analysis of body composition helps to monitor the state of metabolism of lipids, proteins and water in the body, and therefore this method is of interest to physicians of various specializations.

The purpose of this paper is to build a circuit for tetrapolar measurement using off the shelf components. The next chapter summarizes materials and methods used, the importance of tetrapolar electrode configuration and the design of the proposed circuit. The results of testing the proposed circuit are then summarized in the last chapter [4, 5, 6].

2 Materials and Methods

The principle of operation of a tetrapolar configuration depends on the definition of an ideal current and voltage source. The ideal current source has an infinitely large

internal resistance and its VA characteristic ensures that a constant current always flows from the source at any connected load. The ideal voltage source has zero internal resistance. At any load on this internal resistance, no voltage drop occurs, and therefore the voltage at the power supply terminals is still the same. The properties of real resources can approach the ideal, but they will never reach them. In this way, after applying a current source to the excitation electrodes, the value of the current flowing through the measured area will be constant outside depending on its impedance. Thus, the sensing electrodes will measure the actual voltage drop only on the measured section of tissue. The resulting impedance can then be easily calculated according to Ohm's law [1, 4].

Bioimpedance measurement circuit needs to generate constant AC current for correct impedance measurement. For this reason, a supply circuit for creating virtual ground was created. Its schematic is shown in figure 2. The circuit is powered by 5 V from USB and creates a symmetrical ±2.5 V around virtual ground. The circuit uses a power amplifier LM386 for this purpose.

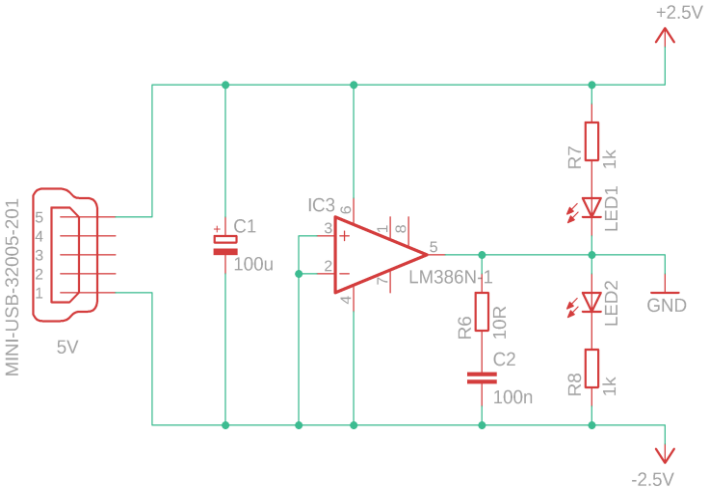

Fig. 2 Supply circuit

The measurement circuit for tetrapolar bioimpedance measurement is shown in figure 3. The noninverting input of an OPA350 operational amplifier is connected to a sine wave generator. To ensure constant current through the measured object, the current-injecting electrodes I-1 and I-2 are connected in the feedback loop of this opamp. The inverting input is connected to virtual ground through a current-setting resistor R1.

Due to safety standards, it is necessary to keep the maximum current flowing through the human body within certain limits. During the measurements the frequency of the sine wave was set to 50 kHz and the effective value of the current was set to 100 μA.

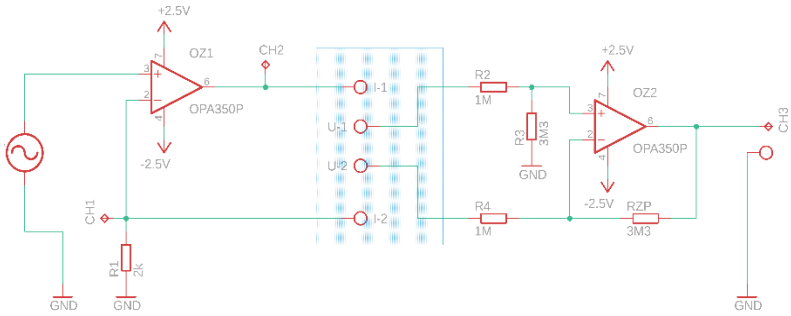

Fig. 3 Measurement circuit

The second half of the circuit is responsible for measuring the voltage drop between the voltage-sensing electrodes U-1 and U-2. It also uses OPA350 opamp, but in differential configuration. For the same signal gain from both inputs, the pair of resistors R2 and R3 must be in the same ratio as Rzp and R1. The advantage of a given type of connection is the suppression of harmonic interfering signals, the DC component of the signal or the harmonic component of noise from the distribution network. However, the disadvantage of differential opamp is the relatively low input resistance. Due to the low input resistance of the differential amplifier, the values of the resistors connected to opamp were chosen large enough so that the input resistance of the amplifier is in the order of MΩ. This solves the problem of the effect of unwanted current on the measurement result. The gain of the configuration was set to 3.3.

3 Testing and Evaluation

The accuracy of the proposed circuit was first tested by using three 1 kΩ resistors simulating the impedance of the two current injecting electrodes and the human body and the voltage was measured across the one resistor simulating the body. The input sine wave from the generator was set to 200 mV. The current setting resistor was 2 kΩ, which produced the current of 100 μA through the measured object. The results of the experiment are shown in figure 4, as measured by an oscilloscope.

The measured value of channel 1 of the oscilloscope is the voltage drop across the current-setting resistor. Channel 2 shows the value of the output voltage of OZ1, which is the sum of the voltages across the 3 resistors and the current-setting resistor. The current flowing through them is supposed to be 100 μA, so the measured value is correct, considering the sum of resistances is 5 kΩ. The value of channel 3 is the output of the differential amplifier, which should be the voltage drop on the body-simulating resistor (100 mV) with the gain of 3.3, so 330 mV. All the measured values are close to what is expected and the circuit is therefore able to measure impedance in tetrapolar measurement setup.

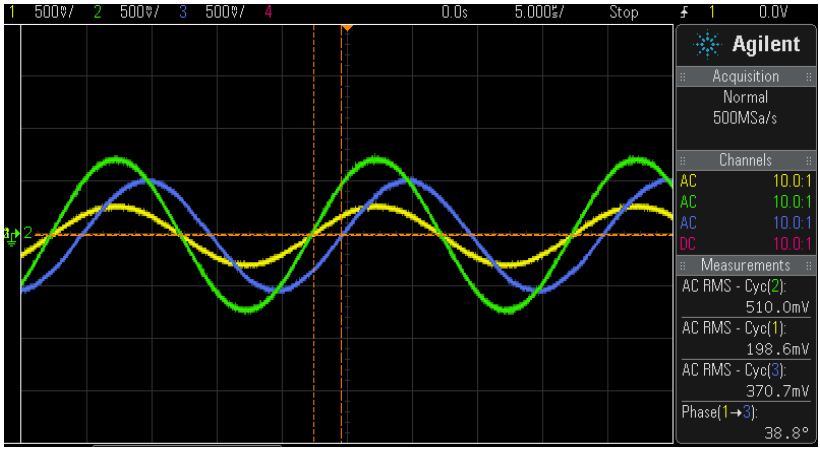

Fig. 4 Circuit testing results

It is important to note that the output shows a phase shift of 38.8° to the original signal. This shift is caused by the system itself and this value should therefore be subtracted from every measurement, because the correct value of phase angle when measuring resistors should be 0°.

The device with ECG electrodes was then used to measure bioimpedance of the human body. Using the obtained values of voltage and current on the impedance subsequently according to the relation, the active resistance of the measured area was calculated. Current electrodes were connected between the left hand and left foot with the voltage electrodes between them, 3 cm away from the current electrodes. An additional layer of conductive gel was applied to better contact at the interface between the electrodes and the measured tissue.

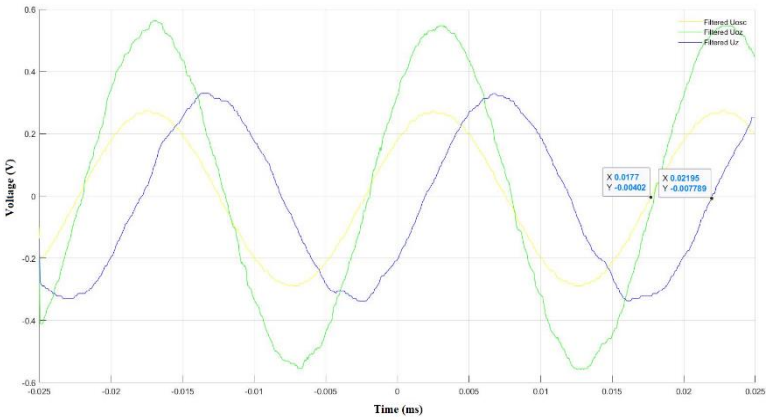

Fig. 5 Whole body bioimpedance measurement

The disadvantage of tetrapolar connection is the dependence on the distance between the excitation and sensing electrodes. In this way, due to inaccurate electrode placement, an undesirable measurement error may occur. The phenomenon was verified by further measurements with increasing distances between the sensing elec-

trodes. The measured values of voltage are shown in figure 5. The value of the measured impedance was 362.94 Ω. The measured phase angle was 26.51°, with the correction of subtracting the system phase, the value is -12.29°.

4 Conclusion

A simple circuit for tetrapolar measurement of bioimpedance was proposed in this work. The circuit uses off-the-shelf components and can be assembled quickly, for example for educational purposes. The proposed circuit was realized using a function generator as input. The accuracy of the circuit was tested on resistors and the value of system phase shift was determined to be 38.8°. The circuit was then also used for measuring whole body bioimpedance. The calculated value of bioimpedance when measuring according to standard hand-foot tetrapolar electrode placement was 362.94 Ω with phase angle of -12.29°.

References

1. Khalil, S.F.; Mohktar, M.S.; Ibrahim, F. The theory and fundamentals of bioimpedance analysis in clinical status monitoring and diagnosis of diseases. *Sensors (Basel)* 2014, *14*, 10895-10928, doi:10.3390/s140610895.
2. Rutkove, S.B. Electrical impedance myography: background, current state, and future directions. *Muscle & Nerve: Official Journal of the American Association of Electrodiagnostic Medicine* 2009, *40*, 936-946.
3. Ward, L. Is BIS Ready for Prime Time as the Gold Standard Measure? *J Lymphoedema* 2009, *4*.
4. Nescolarde, L.; Yanguas, J.; Lukaski, H.; Alomar, X.; Rosell-Ferrer, J.; Rodas, G. Localized bioimpedance to assess muscle injury. *Physiological measurement* 2013, *34*, 237.
5. Li, L.; Shin, H.; Li, X.; Li, S.; Zhou, P. Localized electrical impedance myography of the biceps brachii muscle during different levels of isometric contraction and fatigue. *Sensors* 2016, *16*, 581.
6. Bartels, E.M.; Sørensen, E.R.; Harrison, A.P. Multi-frequency bioimpedance in human muscle assessment. Physiological reports 2015, 3, e12354.

Design of a Machine Vision Control Workplace for Automated Product Inspection

Miroslav Schneider[0000−0002−6685−3044]

Department of Cybernetics and Biomedical Engineering, FEECS,
VSB – Technical University of Ostrava, 17. listopadu 15,
708 00 Ostrava – Poruba, Czech Republic
miroslav.schneider@vsb.cz

Abstract. This article discusses the description of the issue of assembling a inspection workplace using machine vision and the related choice of camera system and other components for the most suitable scanning of the inspected object. The text deals with the general design of the workplace with the widest possible use. The outputs of the realized laboratory workplaces and a description of their own constructions, justification of the use of partial components of an industrial camera, illuminators, line laser are presented here.

Keywords: Machine Vision, Camera, Camera Selection, Inspection Workplace.

1 Introduction

The solution of the design of the inspection workplace is a key step for the subsequent correct inspection of the selected product with the help of machine vision tools. Knowledge of the optical properties of individual parts of the inspected product, detailed knowledge of the parts of interest of the inspection and knowledge of the environment close to the inspection workplace is very important for the correct design. Knowledge of the environment is important to ensure the safety of human workers, especially their eyesight. Modern concepts often deal with the design of inspection workplaces for one specific product, these types are applied in large-scale industrial production what the work deals with [1] and with multispectral view [2]. Modern solutions also deal with universal multifunctional and modular systems of inspection workplaces, which have a wide range of uses. Many studies have addressed the use of robotic system as a special product holder in different poses, for example [3], [4] and with experimental using [5], [6]. The use of these universal workplaces is today the subject of research and studies, which is looking for the best and most suitable concept of optical inspection of a general product. These workplaces are designed as either fully automatic, like our example on Figure 1, or semi-automatic systems cooperating with the human worker.

VSB – Technical University of Ostrava, 2021, ISBN 978-80-248-4523-4 (on-line).

Fig. 1. Inspection workplace with robot arm holding the checked product on double upper and side camera view

If all the requirements for the inspection system are known, the capabilities of the camera system, optical components and illuminators must be taken into account in the design. The choice is standardly made expertly, or for a controlled product which is composed of several parts, experimentally. For quality control, perhaps the most important factor is the right choice of camera. As the camera is a very expensive component, its appropriate selection is very important. If we neglect the price of construction material, industrial PC and necessary SW, the price of the camera is one third of the price of workplace components. The remaining two thirds of the price usually include a set of illuminators and optical elements. However, this price distribution is not usually the rule, as each inspection camera workplace has its own specifics.

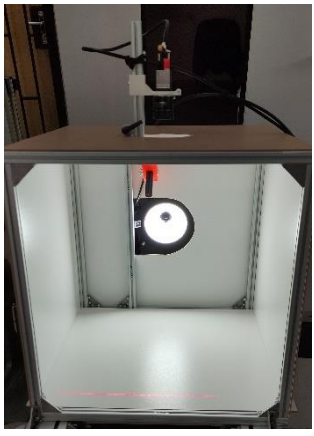

Fig. 2. Basic cube inspection workplace using two cameras, installed linear laser and domelight

This article describes the design of a workplace for a model task to inspect a product that will be stationary at the time of inspection, will be a combined structure (plastic,

metal, rubber), in the sensing space will always be placed in the same position by a robotic arm. If the product takes on a more complex shape, it is advisable to capture it with several cameras from several sides, or to manipulate it appropriately. However, because the emphasis is on the speed of inspection and its evaluation, the use of another camera is a more appropriate but more expensive solution.

The model example shows an inspection workplace in the shape of a cube with protection against external light influences. One side remained open, for easier manipulation of the robotic arm inside the cube.

Barlight, pointlight, domelight line laser, shown on Figure 2, and illuminators are installed within the cube space. The application of a line laser is conditioned by the requirement to control the specific curvature of the product as is shown on Figure 3 and Figure 4. The color of the laser beam and the power must be chosen depending on the lighting conditions so that it is easily recognizable by the camera. In the given example, due to the requirement to control the color of individual parts of the product, white LED illuminators were used.

Fig. 3. Color camera view of linear laser projection on checked product without illuminators added light

2 Camera Selection

Industrial cameras from Basler, Baumer, SVS-VISTEK, JAI, Xenics are introduced for comparison. The compared industrial cameras are divided into groups:

- Global Shutter Cameras
- Rolling Shutter Cameras
- Cameras with extended sensitivity of the scanned spectrum IR, NIR, UV

These groups include the basic division of the examined approach to machine vision depending on the method of scanning and the width of the scanned light spectrum. These approaches are different and each is suitable for the specific conditions of the scene being shot and the objects that occur in it. The models of industrial cameras below are a sample of the inexhaustible number of models of the manufacturers of these components, the indicative prices below are current in the range of 11/2020 to 2/2021 as are information shown in Tables. 1, 2 and 3.

The group of selected cameras with a global shutter includes industrial cameras capable, thanks to the principle of a global electronic shutter, capturing the captured scene in a very short time over the entire image area. Such cameras are suitable for fast-moving events or capturing moving objects in a scene.

Table 1. Example of modern Global shutter cameras for selection

Camera model	Resolution MPx / FPS	Sensor size	Sensor type	Informative Price (CZK)
acA4112-20um	12 / 23	1.1"	IMX304, monochromatic	46 990
acA4112-30um	12 / 30	1.1"	IMX253, monochromatic	74 090
EXO541MU3	20 / 18,4	1.1"	IMX541, monochromatic	129 090
VCXG-124M.I	12 / 9	1.1"	IMX304, monochromatic	49 896
a2A5328-12umBAS	24 / 12	1.2"	IMX540, monochromatic	60 690
FS-3200D-10GE	3,2 / 123	1/1,8"	IMX252, Color, multispectral	80 490

The group of selected cameras with a rolling shutter includes cameras designed for capturing static, still objects and scenes. Dynamic movement is due to the principle of the shutter, when the image is captured line by line or. columns, may manifest as blurred artifacts in the image.

Table 2. Example of modern Rolling shutter cameras for selection

Camera model	Resolution MPx / FPS	Sensor size	Sensor type	Informative Price (CZK)
a2A2590-60ucPRO	5 / 60	1/2,8"	IMX334ROI, Color	11 990
acA5472-5gm	20 / 5	1"	IMX183, monochromatic	17 090
VCXG-201M.R	20 / 6	1"	IMX183, monochromatic	21 423

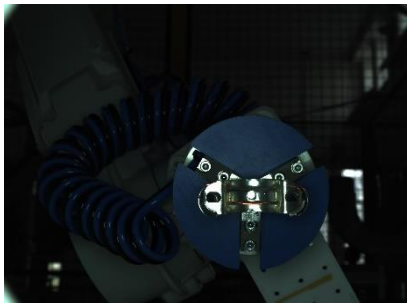

Fig. 4. Color camera view of linear laser projection on checked product with domelight illuminator added light

The group of selected cameras with extended sensitivity of the scanned spectrum includes cameras designed for specific measurements, usually for quality control, when errors of products, such as machine, electronic, food or medicines, can be detected outside the visible spectrum. There are cameras capable of sensing both visible and near NIR radiation, where a special matrix of sensor sensing cells is used for NIR sensing. There are also cameras designed to capture infrared (IR) spectra within specific scanning bandwidths. There is also an example of a special camera specialized in capturing the ultraviolet (UV) band. These special types of cameras require specific measuring conditions and the processing of their output image, as well as a special approach and methods that must be taken into account when creating a universal camera workplace.

Table 3. Example of modern Extended sensitivity cameras for selection

Camera model	Resolution MPx / FPS	Sensor size	Sensor type	Informative Price (CZK)
FS-3200D-10GE	3,2 / 123	1/1.8"	Global Shutter, Multispectral, IMX252, color +NIR	80 490
GO-5000M-USB-UV	5 / 62	1"	Global Shutter, Lince 5M, UV	82 290
Bobcat 640 CL vSWIR	0,3 / 100	16,4 mm	Global Shutter, InGaAs, vSWIR, 500-1700 nm,	606 490
acA1300-60gmNIR	1 / 60	1/1.8"	Global Shutter, Monochromatic +NIR	13 990
acA2000-165umNIR	2 / 165	2/3"	Global Shutter, Monochromatic +NIR	30 590
acA2040-90umNIR	4 / 90	1"	Global Shutter, Monochromatic +NIR	36 090

3 Conclusion

Each inspection site is specific to the needs of individual inspection, there is no single recipe for the size and shape of the site, the choice of lighting and camera components and optical elements. As part of the camera selection example, they were selected to capture a stationary product. Within the comparison of camera components suitable for the mentioned application within the project, the key parameters for examining the quality of the scanned object are the resolution parameters and the optical size of the sensor. Parameters such as frame rate and communication interface thus lose their importance for camera selection in the general level of the research environment. As part of the research testing, it is necessary to select suitable camera components from each of the above comparison tables. Of the cameras with a global shutter, shown on Table. 1, the acA4112-20um camera with a 12MPx resolution and a 1.1 "sensor is a suitable component for research purposes. Of the cameras with a shutter, shown on Table 2, it is evaluated as a suitable component for research acA5472-5gm with a 20MPx resolution and a 1" sensor. From cameras with the possibility of capturing NIR, shown on Table 3, it is evaluated as a suitable component for research purposes acA2040-90umNIR with 4MPx resolution and 1 "sensor. The following research will examine the possibility and suitability of using selected cameras for selected environments which will be elaborated by the author in future articles.

References

1. P. Tumas and A. Serackis, "Effective background subtraction algorithm for food inspection using a low-cost near infrared camera," 2017 Open Conference of Electrical, Electronic and Information Sciences (eStream), 2017, pp. 1-4, doi: 10.1109/eStream.2017.7950322.
2. R. Komura and T. Nakano, "Inspection Method of Hyper Spectral Camera with Spectrometer for Forest Observation," 2018 International Conference on Engineering, Applied Sciences, and Technology (ICEAST), 2018, pp. 1-4, doi: 10.1109/ICEAST.2018.8434487.
3. M. Priggemeyer and J. Rossmann, "Simulation-based Control of Reconfigurable Robotic Workcells: Interactive Planning and Execution of Processes in Cyber-Physical Systems," ISR 2018; 50th International Symposium on Robotics, 2018, pp. 1-8.
4. A. Wolniakowski, A. Gams, L. Kiforenko, A. Kramberger, D. Chrysostomou, O. Madsen, K. Miatliuk, H. G. Petersen, F. Hagelskjær, A. G. Buch, A. Ude, and N. Krüger (2018) Compensating pose uncertainties through appropriate gripper finger cutouts, Acta Mechanica et Automatica, vol. 12, no. 1, pp. 78-83
5. T. Ivanovska, S. Reich, R. Bevec, Z. Gosar, M. Tamosiunaite, A. Ude, F. Wörgötter (2018) Visual Inspection And Error Detection In a Reconfigurable Robot Workcell: An Automotive Light Assembly Example, Visual Computing in Engineering Applications, A special session at the International Conference on Computer Vision Theory and Applications (VISAPP), Madeira, Portugal
6. T. Jørgensen, T. Iversen, A. Lindvig, C. Schlette, D. Kraft, T. R. Savarimuthu, J. Rossmann, N. Krueger (2018) Simulation-based optimization of camera placement in the context of industrial pose estimation, International Conference on Computer Vision Theory and Applications (VISAPP), Madeira, Portugal

Monitoring of Vital Signs in a Hospital Bed: An Overview

Michaela Sidikova and Radek Martinek

Department of Cybernetics and Biomedical Engineering, FEECS,
VSB – Technical University of Ostrava, 17. listopadu 15,
708 00 Ostrava – Poruba, Czech Republic
{michaela.sidikova, radek.martinek}@vsb.cz

Abstract. This work focuses on monitoring vital signs in a hospital bed. This paper is revisional and focuses mainly on the monitoring of the following biomedical signals: capacitive electrocardiography (cECG), ballistocardiography (BCG) and electroencephalography (EEG); in combination with fiber optics and camera systems for more effective patient monitoring purposes. It also covers aspects of the occurrence of interference in the above-mentioned signals. The paper aims to summarize the results of the student's scientific work under the supervision of associate professor Radek Martinek.

Keywords: Monitoring of Vital Signs, Hospital Bed, Smart Bed, Sensors.

1 Introduction

The work deals with the monitoring of vital functions within the hospital bed, the following methods are essential for their review - cECG, BCG, EEG, optical fibers and also camera systems, which are an integral part of patient monitoring.

In hospitals we can continuously monitor critical parameters that provide valuable information about the patient's disease and allow early warning of emergencies. Measurements of vital signs include the most important parameters such as heart rate, blood pressure, arterial oxygen saturation, and respiratory rate. In clinical practice, these functions are used mainly in intensive care units, these parameters are monitored by electrocardiogram (ECG), photoplethysmogram (PPG) and arterial blood pressure sensors (invasive) or blood pressure cuffs (non-invasive). In order to allow continuous monitoring without restricting the movement and comfort of the patient, a sensor system is mounted just below the whole mattress [1,2].

The cECG [1] reflex PPG (rPPG) [3] monitoring of magnetic induction (MR), BCG, as well as camera methods (photoplethysmographic imaging, infrared thermography [4]) are among the most popular inconspicuous monitoring methods. To facilitate discreet monitoring of physiological parameters, these techniques have been integrated into everyday objects such as beds, car seats and wearable devices. Because signals from inconspicuous sensors are noisier and more sensitive to motion artifacts than commonly measured vital signs, a combination of multimodal sensors has been proposed to increase the accuracy and robustness of the measured parameters; for example, cECG and rPPG as well as cECG and BCG have been combined to reliably

VSB – Technical University of Ostrava, 2021, ISBN 978-80-248-4523-4 (on-line).

detect heart rate. Similarly, ECG and BCG as well as ECG, electromyogram, impedance plethysmogram and BCG were integrated into the home bathroom scale. **Fig. 1** shows an illustrative description and location of the systems.

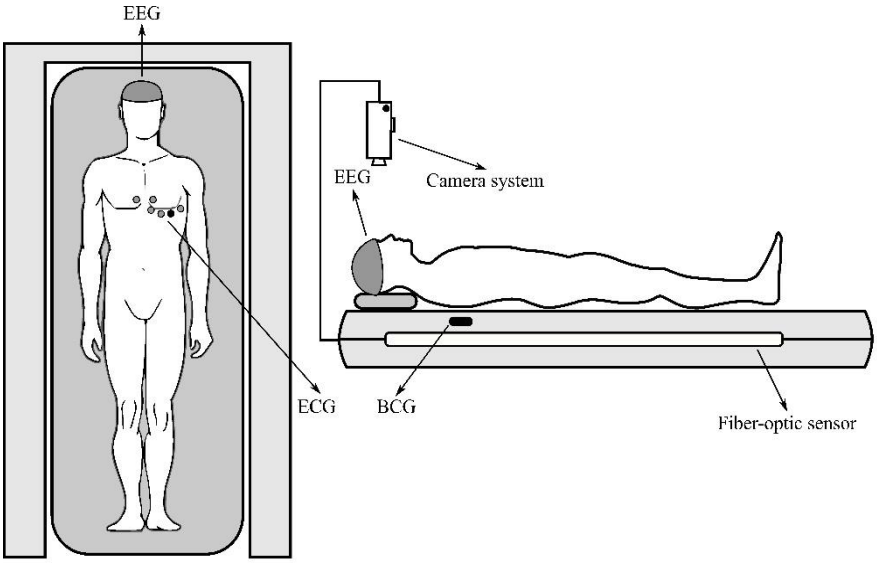

Fig. 1: Description and location of the systems.

2 Results of Literature Survey

Contactless monitoring is the future of measuring vital signs. Based on modern methods of signal and image processing, a number of technologies will be implemented in smart beds. Based on modern methods of signal and image processing, a number of technologies will be implemented in smart beds. Even if the patient is lying on the site, artifacts such as powerlines, motion artifacts, vibrations, etc. People around the world are living to an old age, so it is very important to pay attention to this industry.

For example, Mahdavi and Rosell-Ferrer [5] focused on a system based on the magnetic induction sensing method, which is designed to derive bed presence, respiration, and cardiac activity and consists of two coils for excitation and detection. The new detection coil is based on a concentric planar gradiometer to cancel the primary field. The signal acquisition system was designed using simple electronics to avoid complexity and expensive system. Waltisberg and colleagues [6] introduced a new approach to evaluating smart bed systems that continuously measure vital signs. They demonstrate that estimation accuracy (or error) and measurement coverage time are key performance metrics, describing performance trade-offs in practical smart bed systems. Based on a typical smart bed system that uses a force transducer array located between the bed mattress and the frame, it evaluates the effect of various signal filtering options to illustrate viable design options using our accuracy and coverage analysis. In a full-day recording study with six participants looking at respiratory rate estimation,

measurement coverage is a basic metric that should be analyzed along with accuracy in evaluating the performance of smart bed systems.

In 2020, authors published an article focusing on monitoring vital signs in car seats [7]. This topic is closely related to the monitoring of vital signs in hospital beds.

3 Conclusion and Future Work

One of the reasons for writing the review article was the need for continuous monitoring of key vital parameters among other hospitals, as they can provide valuable information about the patient's condition and thus enable a timely response in the event of an emergency. The following data can be considered as essential parameters: heart rate, blood pressure, arterial oxygen saturation and respiratory rate, which are used in clinical practice mainly in intensive care units. ECG, PPG) and arterial blood pressure sensors (invasive) or blood pressure cuffs (non-invasive) are used to monitor vital signs, which provide reliable data but may be inconvenient for formulas, so a sensor system mounted just below throughout the mattress (in bed), as it allows continuous monitoring without restricting movement and patient comfort.

Vital signs are an important part of monitoring a patient's condition during hospitalization because they allow immediate detection of delayed recovery or side effects. An initial search of the literature highlighted the lack of careful research on many aspects of monitoring vital signs, so we considered this review for work on a particular aspect of measuring vital signs. This work focuses on a thorough overview of monitoring functions that focus on the hospital bed. We mainly focused on signals such as cECG, BCG, EEG, but also on optical fibers and camera systems and their interference. The physical principles that are part of this issue were also explained here

Monitoring vital signs in a hospital bed is a topic of discussion. In the future, contactless monitoring of vital signs will be a very important part of any hospital. The aim of future research is to obtain satisfactory results during measurements, which would be used in practice.

At the present, the student's area of interest gets into the issue of measuring vital signs in a car seat / bed. The authors are currently finalizing a research publication on this topic.

References

1. Yu, X., Neu, W., Vetter, P., Bollheimer, L.C., Leonhardt, S., Teichmann, D., Antink, C.H.: A Multi-Modal Sensor for a Bed-Integrated Unobtrusive Vital Signs Sensing Array. IEEE Transactions on Biomedical Circuits and Systems, pp. 529-539, (2019).
2. He, D.D., Winokur, E.S., Sodini, C.G.: A continuous, wearable, and wireless heart monitor using head ballistocardiogram (BCG) and head electrocardiogram

(ECG). In: 2011 Annual International Conference of the IEEE Engineering in Medicine and Biology Society, IEEE, pp. 4729-4732, (2011).

3. Hertzman, A.B.: The blood supply of various skin areas as estimated by the photoelectric plethysmograph. American Journal of Physiology-Legacy Content, pp. 328-340, (1938).
4. Jin Fei, Pavlidis, I.: Thermistor at a Distance: Unobtrusive Measurement of Breathing. IEEE Transactions on Biomedical Engineering, pp. 988-998, (2010).
5. Mahdavi, H., Rosell-Ferrer, J.: In-bed vital signs monitoring system based on unobtrusive magnetic induction method with a concentric planar gradiometer. Physiological Measurement, pp. 1226-1241, (2017).
6. Waltisberg, D., Amft, O., Tröster, G.: Accuracy-coverage tradeoff of nocturnal vital sign estimation in smart beds. In: Proceedings of the 2014 ACM International Joint Conference on Pervasive and Ubiquitous Computing Adjunct Publication - UbiComp '14 Adjunct, pp. 1249-1256, Nex York (2014).
7. Sidikova, M., Martinek, R., Kawala-Sterniuk, K., Ladrova, M., Jaros, R., Danys, L., Simonik, P.: Vital Sign Monitoring in Car Seats Based on Electrocardiography, Ballistocardiography and Seismocardiography: A Review. Sensors, pp. 1-28, (2020).

Wireless Measurement of Environmental Quantities by use of IQRF Technology

Jan Velicka, Martin Pies, Radovan Hajovsky and Stepan Ozana

Department of Cybernetics and Biomedical Engineering, FEECS,
VSB – Technical University of Ostrava, 17. listopadu 15,
708 00 Ostrava – Poruba, Czech Republic
{jan.velicka, martin.pies, radovan.hajovsky, stepan.ozana}@vsb.cz

Abstract. The paper focuses on the design and implementation of a comprehensive monitoring system that allows long-term monitoring of selected environmental quantities especially in the interior of buildings and visualizing them using modern SW tools. The measured quantities in this case include CO_2 concentration, temperature, humidity and atmospheric pressure. The sensor part of the system uses Figaro CDM7160, Bosch BME280 and Microchip MCP9802 sensors. The IQMESH network is based on the advanced IQRF wireless technology that allows coverage of vast areas with the wireless monitoring system. Measured data from individual measurement modules is sent using Raspberry Pi or via commercial Internet gateways to native IQRF cloud storage. From there, it is forwarded through a script to a MySQL database running on the university www server, which subsequently provides for processing and visualization using the Grafana SW system.

1 INTRODUCTION

Historically speaking, the indoor carbon dioxide(CO_2) concentrations used to be lower than today. Previously, wood was burned for heating. Later, gas or oil heaters were used, which also needed a sufficient supply of oxygen from the air. With the arrival of electric heaters and central heating rooms are being gradually sealed for economic reasons. Nowadays, technologies (plastic windows, etc.) allow the creation of a sealed environment where natural ventilation has decreased about 40 times according to: [15]. Even if today rooms are no longer heated by burning, some CO_2 sources persist. The largest of all is man. Another large indoor source of CO_2 is smoking of tobacco products. The concentration of carbon dioxide affects air quality. For indoor spaces, the CO_2 concentration should be less than 1000 ppm. When this concentration is exceeded, there is a reduction in mental performance, attention deficit disorder, and with higher excess severe headaches, malaise, etc. Exceeding the concentration of 5000 ppm signifies serious health risks. The Government Decree 361/2007 Coll. states the permissible value of exposition limit (PEL) for CO_2 of 5000 ppm. The maximum value of the highest permissible concentration (HPC) with which a person can meet per shift is 25000 ppm.

VSB – Technical University of Ostrava, 2021, ISBN 978-80-248-4523-4 (on-line).

2 MEASUREMENT CHAIN DESIGN

For the monitoring of the air quality in the offices of the Department of Cybernetics and Biomedical Engineering, a measurement chain has been designed, the core element of which is the wireless measuring node, hereinafter called RMCD (Room Measurement of Carbon Dioxide).

The designed measurement chain consists of RMCD wireless measuring nodes and a central unit. The measured quantities are: CO_2 concentration, temperature, relative humidity and atmospheric pressure of the ambient air. The used sensors have digital output with IIC bus communication. Measured information from these sensors is sent via IQRF transceivers (hereinafter IQRF NODE) see [14].

- Sensor 1 - CO_2 sensor - Figaro CDM7160
- Sensor 2 - Temperature, humidity, atm. pressure sensor - Bosch BME280
- Sensor 3 - Temperature sensor - Microchip MCP9802

Where **A** indicates the SMA antenna connector, **B** is the IQRF transceiver, **C** is the charging micro USB connector, **D** is the piezo siren, which indicates CO_2 concentration above 5000 ppm. **E** is a three-colour RGB LED whose meaning is in Table 1. Module **F** is a step-up converter which increases the voltage of the backup Li-Pol battery to 5 V [12]. **G** indicates the user button that can be used to signal the CO_2 concentration when operating the RMCD on battery power. **S1** indicates the Figaro CDM7160 calibrated carbon dioxide concentration sensor. **S2** indicates the Bosch BME280 temperature, relative humidity and atmospheric pressure sensor. **S3** indicates temperature sensor Microchip MCP9802. The block diagram of RMCD design is shown in Figure 1.The indicated concentrations of carbon dioxide are summarized in Table 1.

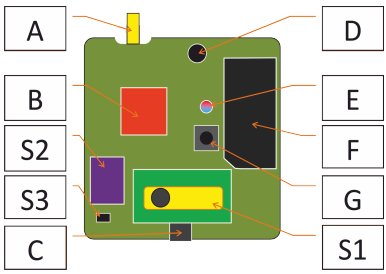

Fig. 1. Physical diagram of RMCD wireless measuring node

The number of measured quantities can be updated as necessary. In most cases, it is intended to use the full version. If necessary, it is possible to select a variant according to the current measurement requirement. The selection is made by writing a constant to the EEPROM that is part of the IQRF transceiver. The

information on the variant is stored in HWPID as part of the DPA packet, see [14] and [11]. The following variants can be selected:

- Full version (measurement of all available quantities)
- Measurement of CO_2 concentration only
- Measurement of temperature only
- Measurement of temperature, humidity and atmospheric pressure only
- Router in IQMESH (no measurement)

Table 1. Indicated concentrations of RMCD

Value of CO2 (ppm)	LED color	Comment
<600	Violet (R+B)	Outside area
600 - 799	Blue (B)	Ventilated room
800 - 999	Green (G)	Recommended concentration
1000 - 1499	Orange (R+G)	Acceptable concentration
>1499	Red (R)	Need to ventilate

The current CO2 concentration is indicated comprehensively optically (RGB LED) and acoustically (Piezo siren). This signalling is functional even without communication in the IQMESH network. If the permanent signalling is switched off, it is possible to temporarily activate it by pressing the user button (in Figure 1 marked as G). The acoustic sound signalling is independent of optical signalling. Battery life was measured for various modes. Several configurations of RMCD operation were tested. The first configuration was to change the data transmission interval to either 1 minute or 10 minutes. The second configuration was to switch the RGB LED indication to either the RGB LED permanently on or the RGB LED permanently off. In this mode, the RGB LED is turned on-demand via the user button. The battery life is summarized in Table 2.

Table 2. Comparison of battery life in various modes

	Sending 1 min	Sending 10 min
RGB LED active	16-20 hours	22-24 hours
RGB LED on-demand	32-34 hours	36-39 hours

3 PROCESSING AND VISUALIZATION

Data transfer is based on communication in the IQMESH network based on IQRF modules, see [10]. The IQRF module of the network coordinator (IQRF

COORD) is connected to Pi through the SPI bus, see [1, 2]. The communication with the network coordinator is provided by the IQRF-Daemon application. Data is transferred between IQRF-Daemon and Node-RED via MQTT. In an application created in Node-RED, the measured data is converted into a readable form and stored in a MySQL database. System Grafana is used for visualization. Block diagram of processing, archiving and visualization of measured data are draw on Figure 2.

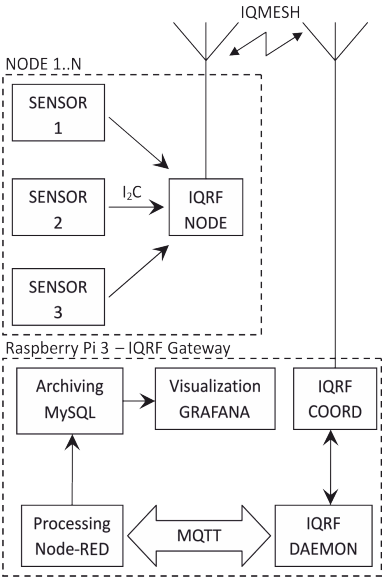

Fig. 2. Block diagram of processing, archiving and visualization of measured data

In the software system Grafana (see Figure 3) an application was created for visualization of the measured data. The courses for the selected time interval and the last measured value are displayed. The measured data can be displayed in the Grafana environment as the time course of the individual environmental variables.

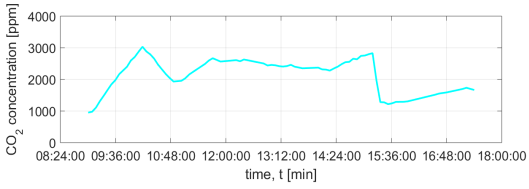

Fig. 3. Daily record of the measured environmental quantities in the laboratory EB305, FEECS, VSB-TUO

4 CONCLUSIONS

The designed and implemented comprehensive monitoring system is designed to monitor indoor air quality, mainly in the classrooms and laboratories of the Department of Cybernetics and Biomedical Engineering, VŠB - TU Ostrava. However, it is possible to deploy it in other school facilities, offices or households. Part of the monitoring system is also an application for processing and archiving of measured data. Data is processed using a Node-RED application. Processed data is stored in a MySQL database. The Grafana environment was used to visualize the measured values. Visualizations of time courses and actual values were created. Measured values are evaluated in the period in which people are expected to stay in a given room. Based on these values it was possible to determine what part of the period of occupation is spent by people in an inappropriate environment. Based on the determined facts it is possible to recommend changing or modifying the ventilation method in the rooms. Based on such changes, the work environment of students and employees could be improved. Based on experience with the pilot operation of the created monitoring system, it is possible to design its next version, which will be extended by other sensors and functionality. Other options present themselves in sensor data evaluation. Based on measured data, it would be possible to identify alarm states based on changes in individual measured quantities.

References

1. Bazydlo, P., Dabrowski, S., Szewczyk, R.: Wireless temperature measurement system based on the iqrf platform. Advances in Intelligent Systems and Computing 317, 281–288 (2015)
2. Calvo, I., Gil-García, J., Recio, I., López, A., Quesada, J.: Building iot applications with raspberry pi and low power iqrf communication modules. Electronics (Switzerland) 5(3) (2016)
3. Dedek, J., Golembiovsky, M., Slanina, Z.: Sensoric system for navigation of swarm robotics platform. In: Barbulescu, L., Roman, M., Popescu, E., Popescu, D., Sendrescu, D. (eds.) 18th International Carpathian Control Conference, ICCC 2017. pp. 429–433. Institute of Electrical and Electronics Engineers Inc. (2017)
4. Fajkus, M., Nedoma, J., Bednarek, L., Vasinek, V., Martinek, R., Bilik, P., Vanus, J.: Analysis usability of the energetically passive sensors for the load monitoring of production press machines. In: Kolcun, M., Kurimsky, J., Kolcunova, I. (eds.) Proceedings of the 9th International Scientific Symposium on Electrical Power Engineering, ELEKTROENERGETIKA 2017. pp. 692–695. Technical University of Kosice (2017)
5. Gecova, K., Vala, D., Slanina, Z., Walendziuk, W.: Air condition sensor on knx network. In: Linczuk, M., Romaniuk, R. (eds.) Proceedings of SPIE - The International Society for Optical Engineering. vol. 10445. SPIE (2017)
6. Hajovsky, R., Pies, M.: Use of iqrf technology for large monitoring systems. In: Milik, A. (ed.) IFAC-PapersOnLine. vol. 28, pp. 486–491 (2015)
7. Konecny, J., Kelnar, M., Prauzek, M.: Advanced waste rock exploring by mobile robot. In: 2nd International Conference on Machinery Electronics and Control Engineering. pp. 913–917 (2012)

8. Musilek, P., Prauzek, M., Krömer, P., Rodway, J., Barton, T.: Smart Sensors Networks: Communication Technologies and Intelligent Applications, chap. Intelligent Energy Management for Environmental Monitoring Systems, pp. 67–94. Elsevier Inc. (2017)
9. Pies, M., Hajovsky, R.: Monitoring environmental variables through intelligent lamps. In: Joukov, N., Kim, K.J. (eds.) Lecture Notes in Electrical Engineering. vol. 425, pp. 148–156 (2018)
10. Pies, M., Hajovsky, R.: Using the iqrf technology for the internet of things: Case studies. In: Joukov, N., Kim, K.J. (eds.) Lecture Notes in Electrical Engineering. vol. 425, pp. 274–283 (2018)
11. Prauzek, M., Krömer, P., Rodway, J., Musilek, P.: Differential evolution of fuzzy controller for environmentally-powered wireless sensors. Applied Soft Computing Journal 48, 193–206 (2016)
12. Slanina, Z., Dedek, J., Golembiovsky, M.: Low cost battery management system. Journal of Telecommunication, Electronic and Computer Engineering 9(2-5), 87–90 (2017)
13. Slanina, Z., Docekal, T.: Energy meter for smart home purposes. In: Tarassov, V., Abraham, A., Kovalev, S., Sukhanov, A., Snasel, V., Vasileva, M. (eds.) Advances in Intelligent Systems and Computing. vol. 680, pp. 57–66. Springer Verlag (2018)
14. s.r.o., I.T.: Iqrf - technology for wireless (2018), https://www.iqrf.org/
15. Vanus, J., Martinek, R., Bilik, P., Zidek, J., Dohnalek, P., Gajdos, P.: New method for accurate prediction of co_2 in the smart home. In: IEEE Instrumentation and Measurement Technology Conference. vol. 2016-July. Institute of Electrical and Electronics Engineers Inc. (2016)
16. Vanus, J., Sykora, J., Martinek, R., Bilik, P., Koval, L., Zidek, J., Fajkus, M., Nedoma, J.: Use of the software pi system within the concept of smart cities. In: Kolcun M., Kurimsky J., K.I. (ed.) Proceedings of the 9^{th} International Scientific Symposium on Electrical Power Engineering, ELEKTROENERGETIKA 2017. pp. 513–517. Technical University of Kosice (2017)

Statistical Analysis of Accuracy of Transformation Methods for Obtaining Derived Vectorcardiograph

Jaroslav Vondrak and Marek Penhaker

Department of Cybernetics and Biomedical Engineering, FEECS,
VSB – Technical University of Ostrava, 17. listopadu 15,
708 00 Ostrava – Poruba, Czech Republic
{jaroslav.vondrak, marek.penhaker}@vsb.cz

Abstract. Vectorcardiography (VCG), similar to a 12-lead ECG, is a method for measuring the electrical activity of the heart. Measurement of VCG in clinical practice is not common today, but information obtained from VCG may in some cases improve the accuracy of automatic detection of certain heart diseases. For this reason, there are various variants of transformation methods that transform classical 12-lead ECGs into vectorcardiographic projections. This paper deals with a statistical analysis of the accuracy of the most commonly used transformation methods. A total of three transformation methods were used, namely Kors regression, Inverse Dower and Quasi orthogonal. These transformation methods were applied to 30 patient records diagnosed with myocardial infarction from the PTB database. The transformed curves were then compared with the directly measured VCG according to Frank's lead system, which served as a reference value. In this comparison, the MSE value was calculated for each VCG lead. These values served as input parameters for the subsequent statistical analysis. A multi-sample nonparametric test of agreement of mean values - Kruskal-Wallis test - was used. After rejecting the null hypothesis of the Kruskal-Wallis test, a post-hoc analysis was performed using the Dunn method. The statistical analysis shows that, as a whole method, Kors' regression method achieves the best values.

Keywords: Vectorcardiography, VCG, Myocardial infarction, Transformation methods, Statistical evaluation.

1 Introduction

Electrocardiography (ECG) is currently the most widely used method for diagnosing heart disease. ECG is usually obtained by non-invasive recording of the potential difference between the electrodes located on the patient's chest. The most commonly used ECG system is a 12-lead ECG, which monitors basic cardiac electrical activity from 12 different measurement angles [1].

VCG is a diagnostic and lesser-known method than a standard 12-lead ECG [2]. This method can be measured by several different electrode systems, where Frank's orthogonal lead system is most often used in clinical practice. This system is measured using three orthogonal leads that measure cardiac activity with the same sensitivity. The

VSB – Technical University of Ostrava, 2021, ISBN 978-80-248-4523-4 (on-line).

advantage of this method is that it shows changes in the direction and magnitude of the electrical forces of the heart. This information is very important for the diagnosis of acute coronary syndromes. However, VCG is not commonly measured in medical practice because the interpretation of VCG is not commonly taught and requires special knowledge of the spatiotemporal degradation of cardiac vectors. Therefore, alternative VCG derivation options have been proposed [3]. Transformation methods for deriving ECG and VCG are an integral part of obtaining other useful information from measuring the electrical activity of the heart [4, 5].

The most common transformation methods are the Inverse Dower transformation (IDT), Kors regression transformation, QLSV and Quasi-orthogonal transformation which differ only by the coefficients of the respective matrix [6].

The aim of this work is to find out which of the most frequently used transformation methods achieves the highest accuracy in comparison with the VCG curve measured by the Frank lead system. Using appropriate statistical methods to analyze in which transformation methods there was no loss of clinical information. Transformation accuracy is a key factor in further analysis of VCG data and in making the correct diagnosis.

2 Material and Methods

2.1 Study Population

In this study, we used ECG signal recordings from the PTB diagnostic database, which were recorded from healthy volunteers and patients with various heart diseases. The individual records of this database consist of 15 simultaneously recorded signals: 12-lead ECGs and 3-lead Frank orthogonal systems. Signals were acquired for 2 minutes with a 16-bit resolution in the range of ± 16.384 mV and sampled at a sampling frequency of 1 kHz [7, 8]. For our purposes, 30 patient records diagnosed with myocardial infarction were selected from this database.

Raw records contain various interfering components such as power line disturbances, respiratory artifacts, or isoline fluctuations that need to be filtered. Matlab 2018b software was used for further processing.

2.2 Preprocessing

Due to the fact that these are biological data, certain interfering components are also measured. Most of the interfering signal components that could invalidate the diagnostic information have already been removed from the original database, but the data fluctuates on the isoelectric line. Before the statistical evaluation itself, it is necessary to align all data to the zero isoelectric line. The alignment was performed by applying a Savitz-Golay filter with a window length of 1200, which detected a fluctuating interfering component of the signal. The window length was based on the sampling frequency and signal length.

After aligning the data to an isoelectric line, linear transformation methods were applied to a 12-lead ECG to obtain derived VCG recordings. These derived VCG records

were then compared with directly measured orthogonal leads, which were considered here as reference values.

2.3 Statistical Analysis

When testing hypotheses, the α significance level is determined, where 95% (0.95) is considered a reliable estimate and the significance level is the remaining 5% (0.05). In statistics, the mean and median are most often determined to perform a statistical test. Statistical analysis is based on hypothesis testing, where the null hypothesis (H_0) represents equilibrium, while the alternative hypothesis (H_A) then expresses imbalance. Based on a statistical test, either the null hypothesis is rejected and the alternative hypothesis is accepted, or vice versa [9, 10].

Statistical analysis and all necessary calculations for individual methods were performed in the Matlab 2018b software environment. Statistical analysis was performed from the results of MSE (1) between the derived orthogonal system with the directly measured orthogonal system for each lead (X, Y, Z) [9].

$$MSE = \frac{1}{n}\sum_{(i)}(V_i - oV_i)^2 \tag{1}$$

Where *Vi* is the original measured value and *oVi* is the derived vectorcardiographic record of the i-th patient. With this step, we got input values for statistical analysis.

3 Results

The first step was to calculate the mean square errors according to equation (1) between the derived orthogonal system and the directly measured orthogonal system for each lead X, Y and Z. Prior to the statistical analysis itself, remote observations were detected in the data by the method of internal walls, see figure 1, which were left in the data set.

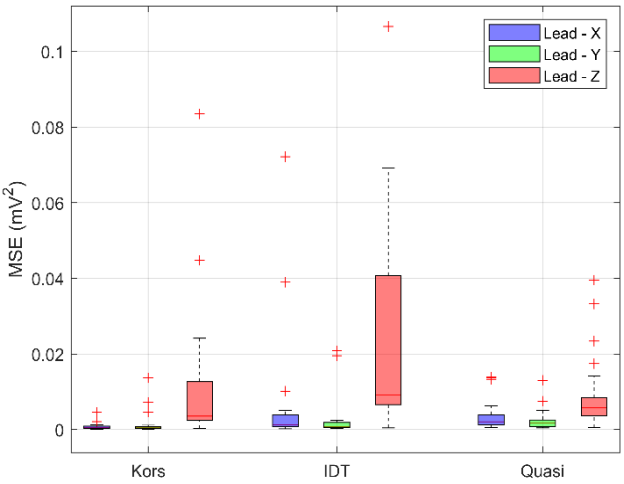

Fig. 1. *MSE for individual transformation methods in individual leads*

3.1 Normality Test

For the correct choice of the method enabling the comparison of mean square errors for individual methods and individual leads, it was necessary to verify the normality of the data using the Shapir - Willk test.

Table 1. Shapir - Willk's test, p-values of MSE for lead X, Y and Z

Lead	Kors. regress	Inv. Dower	Quasi orthogonal
X	<0,001	<0,001	<0,001
Y	<0,001	<0,001	<0,001
Z	<0,001	<0,001	<0,001

It can be seen from Table 1 that all p-values are <0.05. For this reason, the assumption of MSE normality was rejected and non-parametric tests were used in further testing.

3.2 Comparison of MSE for Compared Transformation Methods

Based on the results of the Shapir - Willk test, where all p-values are <0.001, the data were subjected to the Kruskal-Wallis test. This is a multi-sample median agreement test, generally a distribution agreement.

Table 2. Kruskal-Wallis median test of MSE for individual leads

Lead	p-value
X	<0,001
Y	<0,001
Z	<0,001

From Table 2 we can see that based on the Kruskal - Wallis test, it can be rejected for all leads that there is a statistically significant difference in the medians of MSE for all leads. In the next step, it was determined by post-hoc analysis whether there are so-called homogeneous groups of methods among the compared methods. We used Dunn's method for post hoc analysis.

Table 3. Dunn test results for lead X, Y and Z

	Lead X			
Dunn test	Tr. method	Kors	Dower	Quasi
	Kors	*	<0,001	<0,001
	Dower	*	*	0,828
	Quasi	*	*	*
	Lead Y			
Dunn test	Tr. method	Kors	Dower	Quasi
	Kors	*	0,210	<0,001
	Dower	*	*	0,136
	Quasi	*	*	*
	Lead Z			
Dunn test	Tr. method	Kors	Dower	Quasi
	Kors	*	0,002	0,990
	Dower	*	*	0,014
	Quasi	*	*	*

Based on the results of the post hoc analysis in lead X, it can be argued at the significance level of 0.05 that the mean square error of the Kors regression method is statistically significantly lower compared to the mean square errors of the quasi-orthogonal method and IDT. In the lead Y at the significance level of 0.05, the mean square error of the Kors regression method is significantly lower than for other transformation methods. At lead Z, it can be argued at the significance level of 0.05 that the mean square errors of the regression methods Quasi and Kors are significantly lower than in the IDT transformation.

4 Conclusion

In this work, a total of three transformation methods were analyzed, namely Kors' regression method, IDT and quasi-orthogonal method. These transformation methods were used for pathological records diagnosed with myocardial infarction. The results

of transformation methods were compared with directly measured VCG based on MSE calculation. The MSE values for the individual X, Y and Z leads served as input values for statistical analysis. Here it was necessary to verify that the values of the Kors regression method achieve the lowest error rate in signal transformation. After verifying that the input data do not come from a normal distribution, a nonparametric Kruskal-Wallis test was used for statistical analysis, where we rejected the null hypothesis. Due to the rejection of the null hypothesis of the Kruskal-Wallis test, a post hoc analysis - Dunn's test - was used. Based on the results of the Dunn test, it was determined which of the transformation methods can provide the most accurate derived VCG. According to the performed statistical analysis, it follows that as a whole method the Kors regression method reaches the best values and can be considered as the most accurate transformation method.

References

1. Yang, H., Bukkapatnam, S. T., & Komanduri, R. (2012). Spatiotemporal representation of cardiac vectorcardiogram (VCG) signals. Biomedical engineering online, 11(1), 1-15.
2. Rubel, P., Benhadid, I., & Fayn, J. (1991). Quantitative assessment of eight different methods for synthesizing Frank VCGs from simultaneously recorded standard ECG leads. Journal of electrocardiology, 24, 197-202.
3. Liu, G., & Yang, H. (2013). Multiscale adaptive basis function modeling of spatiotemporal vectorcardiogram signals. IEEE journal of biomedical and health informatics, 17(2), 484-492.
4. Daniel, G., Lissa, G., Redondo, D. M., Vásquez, L., & Zapata, D. (2007, November). Real-time 3D vectorcardiography: an application for didactic use. In Journal of Physics: Conference Series (Vol. 90, No. 1, p. 012013). IOP Publishing.
5. van Bemmel, J. H., Kors, J. A., & van Herpen, G. (1992). Combination of diagnostic classifications from ECG and VCG computer interpretations. Journal of electrocardiology, 25, 126-130.
6. Vozda, M., & Cerny, M. (2015). Methods for derivation of orthogonal leads from 12-lead electrocardiogram: A review. Biomedical signal processing and control, 19, 23-34.
7. Goldberger, A. L., Amaral, L. A. N., Glass, L., Hausdorff, J. M., Ivanov, P. C., Mark, R. G., ... & Stanley, H. E. (2000). Components of a new research resource for complex physiologic signals. PhysioBank, PhysioToolkit, and Physionet.
8. Bousseljot, R., Kreiseler, D., & Schnabel, A. (1995). Nutzung der EKG-Signaldatenbank CARDIODAT der PTB über das Internet.
9. Gupta, S. C., & Kapoor, V. K. (2020). Fundamentals of mathematical statistics. Sultan Chand & Sons.
10. Briš, R., Litschmannová, M.; Statistika I. Pro kombinované a distanční studium, VŠB-TU Ostrava, 2004.

Nova Star Detection using Artificial Neural Networks Time Series Classification

David Andrešič[1], Petr Šaloun[2], and Bronislava Pečíková[3]

[1]Department of Computer Science, FEECS,
VSB – Technical University of Ostrava, 17. listopadu 15,
708 00 Ostrava – Poruba, Czech Republic
david.andresic@vsb.cz
[2]Palacky University Olomouc, Krizkovskeho 511/8,
CZ-771 47 Olomouc, Czech Republic
petr.saloun@upol.cz
[3]Faculty of Informatics and Information Technologies,
Slovak university of technology in Bratislava, Ilkovičova 2, Bratislava, Slovakia
xsuchanovab@stuba.sk

Abstract. Nova stars are rare phenomena in the Universe. Knowing that some star erupted as nova as soon as possible after the eruption can therefore bring crucial information to astronomers. Giving the number of stars in the universe, monitoring of such phenomena requires automated solution which can utilize means of artificial intelligence today.
In this work, we present a case study of our star time series (a.k.a. light curves) classifier which utilizes evolutionary algorithm and artificial neural network. We used this classifier as a mean of anomaly detection when we detected a change of the predicted class in time. We describe details of our Multi-layer Perceptron classifier, its structure, training on specifically pre-processed Kepler and Kepler K2 data and its fine-tuning using Particle Swarm Optimization.

Keywords: artificial neural networks, classification, time series, big data, nova

1 Introduction

Time series are in general discrete sequences of quantity values measured in time. In astronomy, it is usually flux or magnitude on one axis and Julian date on the other axis. These time series comes from multiple observational devices and observatories designed for e.g. variable stars detection, stellar system analysis or extra-sollar planets discoveries. Finding periods in these time series is therefore crucial for further research in this area. Since we are talking about large amount of data growing exponentially during last years, we are facing a big data issues, where fast handling and analysis of these amount of data is mandatory.

In this work we utilize our previous research on this topic [1] [2] and describe its further improvement by changing the optimized structure of the artificial neural network and testing on other data set.

2 State of the Art

Most literature on time series classification makes ideal assumptions about its shape etc. [3]. Based on these assumptions, the best machine learning approach for time series classification is usually Nearest Neighbour algorithm with the relatively expensive Dynamic Time Warping as the distance measure [4]. But all these assumptions are challenging in astronomical time series since they greatly vary in lengths, periods, noisiness and are without clear borders [1].

2.1 Time Series Classification Algorithms

Today, different kinds of (deep) neural networks are used for time series analysis [5]. We can start for example with **Multi-layer Perceptron (MLP)**, **Long Short-term Memory (LSTM) [8] [9] [10]** or Recurrent Neural Network (RNN) [7] and its improvements for noisy data [11]. Another type of ANN is **Convolutional and Fully-convolutional Neural Network (CNN and FCN)**. typical for pattern recognition [12]. Last, but not least is the **LSTM Fully-convolutional Neural Network** [5] extending the FCN by LSTM module. We can also consider other ANNs, such as **Multi-scale Convolutional Neural Networks** (MCNN) which performance is (in general) heavily dependent on time series data pre-processing and optimization of huge amount of hyperparameters. Another option could be **ResNet** that does not require any either deep data pre-processing or "feature engineering" [5] [1].

2.2 Known Methods for Time Series Data Pre-processing

Time series, images or records of human speech usually consists of huge amount of data. If we attempt to classify them using a traditional backpropagation algorithm without attribute extraction, we would face overfitting [12]. In this work, we focus on **significant attributes extraction** that reduces the dimensionality of the original data by extracting only significant attributes. These can be various types of statistical attributes or even more complex types such as periodograms or generated images. According to [5], other often used methods are **Fully-convolutional Neural Network** as a method for significant attribute extraction. In [6], authors also mention **Dynamic time series wraping** and **Shapelet transformation** as a way of time series pre-processing [1].

3 Kepler K2 Data Set

As in [1] and [2] we tested our approaches on Kepler K2 data provided by NASA and containing thousands of real light curves. Data from K2 are publicly available [14] [15] and well documented [16] [17]. In this work we are interested in Kepler K2 light curves containing flux of individual objects in time. We can obtain about 40000 light curves with length up to 1300 measurements.

4 Experiments and Results

From the current state of the art and our experiments with binary classification, we know that feature extraction with deep MLP is the most promising approach, so we extracted the same statistics markers for each light curve as in [2]. All 6 variability classes and 1 non-variable class were highly imbalanced so we used oversampling (for classes with very little amount of samples) and undersampling (for classes with too high amount of samples) carefully balanced so we do not introduce any significant bias (especially with oversampling). This resulted into 400 samples for each class splitted in ratio 80:20 into train and test data set.

4.1 Multi-class Classification

In order to optimize the MLP structure and its hyperparameters, we used Particle Swarm Optimization as in [2], just with a different cost function (depicted on Fig. 1). Good optimizers are found quite quickly using our method among - the first iterations. The best one (with accuracy 73.04% over 7 classes) was found after just 11 iterations. The best fitting model contained 10 hidden layers with dropout and batch normalization layers following them. We observed that dropout was ignored while batch normalization momentum was set to 0.44. The model utilized whole 10 possible hidden layers with quite a lot of perceptrons in later layers (progression from 66 in the first layer over 847 in th 7th layer to 455 in the 10th layer). We also observed that with the PSO progression, better models utilized more and more hidden layers.

4.2 Experiments with Nova Detection

Automated sky surveys can provide light curve for basically every star in its field of view and our classifier (although trained on light curves from other instruments) should be able to perform its automated and fast classification to one of the star variability classes (if any). But it can do even more: under normal circumstances, star variability class should not change, unless something extraordinary happens. Such extraordinary phenomena could be for example the eruption of a star as a nova which might result into a change in the predicted class in compare to its older flux. *Nova Cas 2021 / CzeV3217 / V1405 Cas* is a nova that erupted in March 2021[4]. We obtained the magnitude and flux for the star from its pre-nova era from the ASAS-SN catalogue[5] which covered a period from December 19, 2020 to February 12, 2021. For the nova era of the star, we obtained the magnitude from AAVSO[6] which covers a period from March

[4] Alert Notice 735: Nova in Cassiopeia: N Cas 2021: https://www.aavso.org/aavso-alert-notice-735

[5] ASAS-SN data for *CzeV3217*: https://asas-sn.osu.edu/sky-patrol/coordinate/00745124-4307-4bd9-9d95-d59d5399975e

[6] AAVSO data for *V1405 Cas*: https://app.aavso.org/webobs/results/?star=000-BNX-642&num_results=200&page=1

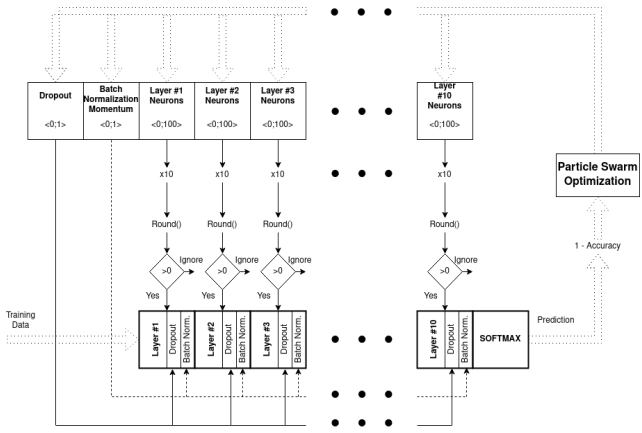

Fig. 1: Visualization of the cost function for optimizing the Kepler K2 multi-class classifier. Each PSO agent comes with a dropout, batch normalization momentum and number of neurons in MLP layer as input arguments. The MLP arguments are then multiplied by 10 and rounded. If not zeroed, then a layer with corresponding number of neurons is added, followed by dropout and batch normalization set directly. The cost function then performs learning of such MLP and calculates the accuracy, which is subtracted from 1 and serves as the output to be minimized.

17, 2021 to May 4, 2021. Based on the formula from *GNU Astronomy Utilities manual*[7] we calculated the flux value from its magnitude, taking the reference values F_r and m_r from the pre-nova data (more specifically for the timestamp 2021-01-05.2318521 which has low errors in magnitude and flux). The resulting light curves are depicted on Fig. 2. For the next steps we always applied data pre-processing steps for Kepler K2 multi-class classification (see section 4.1). First, we let our pre-trained Kepler K2 multi-class classifier to predict the class of the pre-nova light curve, which resulted into *RRab* class prediction. This is of course different from the correct one (*EW*), but as the classifier was trained on quite different data, it is not that important. Our hypothesis was that this class prediction should change when the nova erupted. To test this, we combined both the light curves into one, performed the same data pre-processing and let the pre-trained classifier to make a prediction, which resulted into *OTHPER* class that evokes some variability in the data with unknown phenomena (since our classifier was not trained for *EW+N* data, we consider this classification to be quite accurate). As the predicted class changed, our hypothesis was thus confirmed. We also discovered that 3 days after the eruption our classifier pre-trained for totally different light curves detects this change and changes the class

[7] GNU Astronomy Utilities manual: https://www.gnu.org/software/gnuastro/manual/html_node/Magnitude-to-flux-conversion.html

prediction. On Fig. 3 you can see what portion of the available post-eruption data the classifier needed to change the predicted class (the red part represents the data of the first cca 3 days). To our knowledge there is no related work that attempted to perform such experiment.

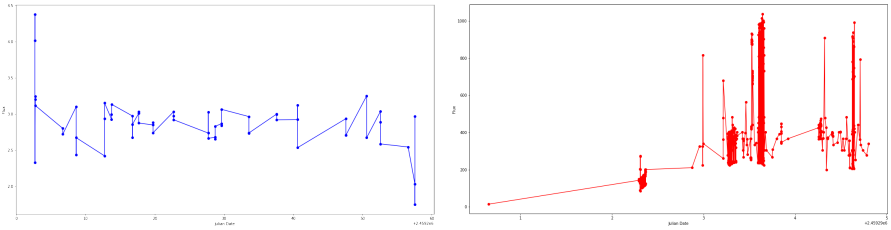

Fig. 2: Light curve of variable star *CzeV3217* before (left) and after (right) its eruption as nova.

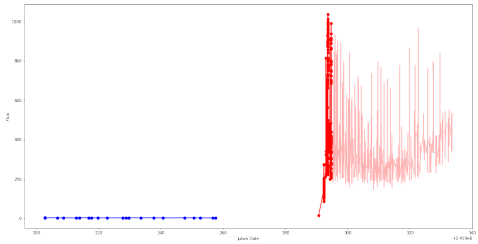

Fig. 3: Combined light curves of *CzeV3217* before and after its eruption as nova with the first 3 days after the eruption was spotted highlighted in red.

5 Conclusion

Using our approach we were able to reach a classification accuracy for light curves which is capable to challange current state-of-the-are methods even when doing a multi-class classification. Based on our experiments, we can conclude that MLP with feature extraction performs very well for this task and evolutionary engineering its structure and hyperparameters using PSO and our cost function allows to find very good classifiers among its first iterations. We also discovered that our classifier trained for Kepler K2 light curves can be used in a different way for light curves combined from other instruments. We verified that it can serve as a mean of anomaly detection such as nova eruption, which can potentially be used for automated sky surveys.

References

1. D. Andrešič, P. Šaloun, B. Pečíková, "Astronomical Time Series Classification using Artificial Neural Networks," WOFEX 2020, Ostrava, 2020.
2. D. Andrešič, P. Šaloun, B. Pečíková, "Large Astronomical Time Series Preprocessing for Classification Using Artificial Neural Networks," 2021 In: J. Paralič, P. Sinčák, P. Hartono, & V. Mařík (Eds.), Advances in Intelligent Systems and Computing. Springer International Publishing. https://doi.org/10.1007/978-3-030-63872-6
3. B. Hu, Y. Chen, and E. Keogh, "Time Series Classification under More Realistic Assumptions," in Proceedings of the 2013 SIAM International Conference on Data Mining. Philadelphia, PA: Society for Industrial and Applied Mathematics, may 2013, pp 578–586.
4. Petitjean, F., Forestier, G., Webb, G. I., Nicholson, A. E., Chen, Y., & Keogh, E. (2014). Dynamic Time Warping Averaging of Time Series Allows Faster and More Accurate Classification. In 2014 IEEE International Conference on Data Mining. IEEE. https://doi.org/10.1109/icdm.2014.27
5. KARIM, F., MAJUMDAR, S., et al.: LSTM Fully Convolutional Networks for Time Series Classification, In: IEEE Access,vol. 6, 2017, pp. 1662 - 1669
6. CUI, Z., CHEN, W., CHEN, Y.: Multi-Scale Convolutional Neural Networks for Time Series Classification, In: arXiv:1603.06995v4, 2016
7. Jeffrey L. Elman. 1990. Finding Structure in Time. Cognitive Science 14, 2 (1990), 179–211. https://doi.org/10.1207/s15516709cog1402_1
8. Sepp Hochreiter and Jürgen Schmidhuber. 1997. Long Short-Term Memory. Neural Comput. 9, 8 (Nov. 1997), 1735–1780. https://doi.org/10.1162/neco.1997.9.8.1735
9. Hochreiter S. 1991. Untersuchungen zu dynamischen neuronalen Netzen. Master's thesis. TU Munich.
10. Sepp Hochreiter, Yoshua Bengio, Paolo Frasconi, and JÃijrgen Schmidhuber. 2001. Gradient Flow in Recurrent Nets: the Difficulty of Learning Long-Term Dependencies. (2001).
11. C. Lee Giles, Steve Lawrence, and Ah Chung Tsoi. 2001. Noisy Time Series Prediction using Recurrent Neural Networks and Grammatical Inference. Machine Learning 44, 1 (01 Jul 2001), 161–183. https://doi.org/10.1023/A:1010884214864
12. LeCun, Y., BENGIO, Y.: Convolutional Networks for Images, Speech, and Time-Series
13. SAMUS, N., et al.: General Catalogue of Variable Stars: Version GCVS 5.1, In: Astronomy Reports, vol. 61, 2017, No. 1, pp. 80-88
14. ARMSTRONG, D., et al.: K2 Variable Catalogue I: A Catalogue of Variable Stars from K2, In. eprint arXiv:1411.6830, 2014
15. ARMSTRONG, D., et al.: K2 Variable Catalogue: Variable Stars and Eclipsing Binaries in K2 Campaigns 1 and 0. In: Astronomy and Astrophysics, 2015
16. THOMPSON, S., et al.: Kepler: A Search for Terrestrial Planets, 2016
17. JENKINS, M.: Kepler data preprocessing handbook, 2017
18. Sammon, J. W. (1969). A Nonlinear Mapping for Data Structure Analysis. IEEE Transactions on Computers, C-18(5), 401–409. https://doi.org/10.1109/t-c.1969.222678
19. Wu, Y.-L., Agrawal, D., & El Abbadi, A. (2000). A comparison of DFT and DWT based similarity search in time-series databases. In Proceedings of the ninth international conference on Information and knowledge management - CIKM '00. ACM Press. https://doi.org/10.1145/354756.354857

Intelligent Question Answering in TIL

Michal Fait

Department of Computer Science, FEECS,
VSB – Technical University of Ostrava, 17. listopadu 15,
708 00 Ostrava – Poruba, Czech Republic
michal.fait@vsb.cz

Abstract. The paper deals with natural language processing and question answering over large corpora of formalized natural language texts. Our background theory is the system of Transparent Intensional Logic (TIL) which is a partial, hyperintensional, typed λ-calculus. Having a fine-grained analysis of natural language sentences in the form of TIL constructions, we apply Gentzen's system of natural deduction adjusted for TIL to answer questions in an 'intelligent' way. It means that our system derives logical consequences entailed by the input sentences rather than merely searching by keywords. This system is suitable to answering Yes/No questions. The main novelty of this paper is the analysis and answering of Wh-questions that transform into λ-terms referring to α-objects where α is not the type of a truth-value.

Keywords: Natural Language Processing; Question Answering; Transparent Intensional Logic; TIL; Natural Deduction

1 Introduction

In the era of information overload, the systems that can answer questions raised over the large corpora of text data in an 'intelligent' way gain more and more interest in the research community. We have a lot of textual data that we need to formalize in a proper way so we can effectively obtain information explicitly stated in them or, more importantly, we can apply rules of the proof calculus to check whether we can possibly infer an answer that is implicit ("hidden") in the labyrinth of input text data. To achieve such a goal, logic and computational linguistics are the disciplines that should work hand in hand in natural language processing and question answering.

We use the system of *Transparent Intensional Logic* (TIL) that is a *hyperintensional*, *typed* λ-calculus with *procedural semantics* (see [6], [7]). Abstract procedures are assigned to the expressions of the natural language as their *meanings*, and they produce lower-order objects as their product, or, in some well-defined cases, they *may fail* to produce an object. In the case of *empirical sentences* (like "Tom is a professor.") the produced entity is a *possible world intension* (*PWS*). In the case of *mathematical sentences* (like "2 + 2 = 4") the denoted object is an *extension*. TIL makes it possible to properly formalize all semantically rich features of natural language like referring to a

© M. Krátký, J. Dvorský, P. Moravec (Eds.): WOFEX 2021, pp. 163–168.
VSB – Technical University of Ostrava, 2021, ISBN 978-80-248-4523-4 (on-line).

non-existent object, or hyperintensional contexts where the object of predication is the meaning of another expression.

In TIL, we use adjusted proof calculi to derive consequences of the input text data, and we can also prove validity of an argument in the natural language. These calculi had to be modified with respect to the *technical properties of TIL* and *semantic features of natural language*. These properties and features are reflected in the system by presenting *special rules*. The first proof system that we have exploited and adjusted for TIL is the system of Natural Deduction [2], and the second is the General Resolution Method [4]. We demonstrated that these systems can be used for answering so called *Yes/No questions*.

However, there is a very important class of questions, that we cannot simply answer Yes or No. To answer them properly, we should provide the reference to some specific object. For example, we may ask "Who is the brother of John?", or "When did Michael visit Prague?" This kind of questions are called *Wh-questions*. The answer is then, for instance, 'Peter' or 'on April 1st 2000'. Hence, the answer can be a reference to an individual, a number, a set of individuals, and so on. The main goal of this paper is to present a method for answering Wh-questions within the natural deduction system.

The rest of the paper is organized as follows. Section 2 presents basic analysis of questions and answers. In Section 3 we demonstrate the method of answering Wh-questions using the system of natural deduction. Concluding remarks are in Section 4.

2 Analysis of Questions and Answers Using TIL

In this chapter, I present TIL analysis of questions and their adequate answers. I am not going to introduce the foundations of TIL, as these can be found in numerous papers and books, see, for example, [6] or [7].

In TIL, we distinguish between *empirical expressions* like "Is Tom in the theatre?" "The richest man in the world", and *analytical expressions.* The latter are typically expressions of mathematical/logical language like "*Sin*(π) = 0", "prime number", etc. The same distinction also applies to questions as a special case of sentences; thus, we distinguish between *empirical questions* and *mathematical questions*.

In the *mathematical case*, we obtain a construction that produces an extension of type $\alpha \neq (\beta\omega)$ for any type β. *Adequate answer* provides an arbitrary α-object. If the provided object is the same as the object constructed by question, then the answer is right. For example, we may ask for the solution of the equation *Sin*(x) = 0. This question encodes the following construction ($x \rightarrow \tau$, *Sin*/($\tau\tau$), =/($o\tau\tau$)):

$$\lambda x\, [{}^0{=}\, [{}^0\mathit{Sin}\ x]\ {}^00] \rightarrow_v (o\tau).$$

The right answer of type ($o\tau$) conveys multiples of the number π, i.e. {…, -2π, -π, 0, π, 2π, …}.

Next, I am going to focus on empirical questions. In the *empiric case*, TIL analysis of a question results in a construction that produces an α-intension, i.e. an object of type $\alpha_{\tau\omega}$. *Adequate answer* provides the value of this intension in the world w and time t of evaluation, i.e. an α-object. If the provided value is the same as the value of the

intension encoded by the question, the answer is right, otherwise the answer is not right. In TIL, we analyze questions in the same way as their declarative counterparts. For example, consider the following sentences: "Tom is a student.", "Is Tom a student?" These two sentences denote the same object of type $o_{\tau\omega}$, namely the proposition that Tom is a student (*Tom*/ι; *Student*/$(o\iota)_{\tau\omega}$):

$$\lambda w \lambda t\, [{}^0\mathit{Student}_{wt}\, {}^0\mathit{Tom}] \rightarrow_v o_{\tau\omega}.$$

This specific kind of questions, where α is equal to o, are *Yes-No questions*. To answer such a question, we should provide value of type o, i.e. True (Yes) or False (No).

The second case, when α is not equal to o, are *Wh-questions*. The type α can be, for example, type ι of individuals; in such a case an adequate answer is a name of an individual like *Tom* or *Eve*. If α is equal to (οι), we should provide as an answer a set of individuals like {*Tom*, *Mary*, *Frank*, …}. If α is equal to τ, then an answer should be a number or time; and so like. As an example of a Wh-question, we analyse the sentence "Who are the members of the European Union?"

$$\lambda w \lambda t\, \lambda x\, [{}^0\mathit{Member\text{-}of}_{wt}\, x\, {}^0\mathit{EU}] \rightarrow (o\iota)_{\tau\omega}$$

Types: *Member-of*/$(o\iota\iota)_{\tau\omega}$; *EU*/ι; $x \rightarrow \iota$;

The adequate and right answer is the set {Germany, France, Greece, Italy, Czech Republic, Poland, …}/(οι).

3 Question Answering Within Natural Deduction

At this point, we can demonstrate the method that we use in the natural deduction system to answer Wh-questions over the knowledge base of formalized natural language texts. Here we partly draw on material from [3, §5] where this method has been specified. When applying natural deduction to answer a Wh-question, we seek the base of constructions to look for a construction with which the construction encoded by the question can be *unified*.

For instance, possible direct answer to the question

(1) "Who are the first three players in WTA ranking singles?"

is a set of individuals, currently[1] {Ashleigh Barty, Naomi Osaka, Aryna Sabalenka}, which is an object of type (οι). Thus, the analysis of this question comes down to the construction of the property of individuals, an object of type $(o\iota)_{\tau\omega}$:

(1∗) $\lambda w \lambda t\, \lambda x\, [[{}^0\mathit{WTA\text{-}Ranking}_{wt}\, x] \leq {}^0 3] \rightarrow (o\iota)_{\tau\omega}$

Types: $x \rightarrow_v \iota$; *WTA-Ranking*/$(\tau\iota)_{\tau\omega}$: attribute of an individual that is a function assigning to individuals their current position (if any) in WTA ranking singles; 3/τ; ≤/(οττ).

[1] written on July 15, 2021

On the other hand, the direct answer to the question

(2) "Who is the No. 1 player in WTA ranking singles?"

should be a single individual; currently, she is 'Ashleigh Barty'. Hence, the analysis of the question must produce an individual office (or role), an object of type $\iota_{\tau\omega}$.

Here is how:

(2*) $\lambda w \lambda t\, [{}^0\mathrm{I}\ \lambda x\, [[{}^0\mathit{WTA\text{-}Ranking}_{wt}\ x] = {}^0 1]] \rightarrow (o\iota)_{\tau\omega}$

Additional type: I/(ι(οι)): the singularizer, i.e. a function that associates a set S of individuals with the only member of S provided S is a singleton; otherwise, if S is an empty or multi-valued set, the value of I is undefined.

Note that the question presupposes that the set of individuals to whom the WTA ranking is assigned is non-empty. If it were empty, then there is no direct answer, and our method provides a complete answer informing that the presupposition is not true. In our case, the answer would be that there is nobody to whom the WTA ranking is assigned.[2] The problem to solve is now this. Having derived a knowledge base of sentences formalized in the form of TIL constructions of propositions, we need a method on how to answer also Wh-questions. Assume, for instance, that we have extracted and formalized the sentence:

(3) "Ashleigh Barty is No.1 in WTA ranking singles."

(3*) $\lambda w \lambda t\, [[{}^0\mathit{WTA\text{-}Ranking}_{wt}\ {}^0\mathit{Barty}] = {}^0 1]$

To answer the question (2), we aim at finding a suitable substitution for the variable *x* occurring in (2*). In other words, we look for a proper construction with which (2*) can be unified. Obviously, in this simple example (3*) can serve the goal. Here is the derivation of the desired answer "Barty":

1)	$\lambda w \lambda t\, [{}^0\mathrm{I}\ \lambda x\, [[{}^0\mathit{WTA\text{-}Ranking}_{wt}\ x] = {}^0 1]]$	Question
2)	$[{}^0\mathrm{I}\ \lambda x\, [[{}^0\mathit{WTA\text{-}Ranking}_{wt}\ x] = {}^0 1]]$	λ-E, 1)
3)	$[[{}^0\mathit{WTA\text{-}Ranking}_{wt}\ x] = {}^0 1]$	I-E, λ-E, 2)
4)	$\lambda w \lambda t\, [[{}^0\mathit{WTA\text{-}Ranking}_{wt}\ {}^0\mathit{Barty}] = {}^0 1]$	assumption
5)	$[[{}^0\mathit{WTA\text{-}Ranking}_{wt}\ {}^0\mathit{Barty}] = {}^0 1]$	λ-E, 4)
6)	$\boldsymbol{x = {}^0\mathit{Barty}}$	Unification, 3) & 5)

When deriving the answer to a Wh-Question, we apply an adjusted algorithm of unification as known from the general resolution method. We look for a construction with the same constituents as a given question up to the variable the value of which we want to obtain.

Here is another example, taken from [3, §6.2]. In a base, we have the following two sentences:

[2] The general analytic schema for questions with presuppositions applies a rigorously defined, strict function "If-then-else". Where *P* is a presupposition of a question *Q*, in plain English, the schema is "If *P* then *Q* else non-*P*". For details, see [1], [5].

A. The Mayor of Ostrava regrets that the President of TUO does not know (yet) that he (the President of TUO) will go to Brussels.
B. The President of TUO is prof. Snášel.

Now we can raise, for instance, this question

Q. Where does prof. Snášel go?

To deduce an answer from our mini knowledge base, we first formalise the sentences (A), (B) and the question (Q):

Types: Snasel, *Brussels*/ι; *Go*/$(o\iota\iota)_{\tau\omega}$; *Regret, Know*/$(o\iota{*_n})_{\tau\omega}$; *Mayor* (-of Ostrava), *President* (-of TUO)/$\iota_{\tau\omega}$; *he* $\rightarrow_v$ ι.

A. $\lambda w\lambda t\,[{}^0Regret_{wt}\ {}^0Mayor_{wt}\ {}^0[\lambda w\lambda t\,\neg[{}^0Know_{wt}\ {}^0President_{wt}\ [{}^0Sub\ [{}^0Tr\ {}^0President_{wt}]\ {}^0he\ {}^0[\lambda w\lambda t\,[{}^0Go_{wt}\ he\ {}^0Brussels]]]]]]]$
B. $\lambda w\lambda t\,[{}^0President_{wt} = {}^0Snasel]$

Q. $\lambda w\lambda t\,\lambda x\,[{}^0Go_{wt}\ {}^0Snasel\ x]$

Having applied λ-E and I-E rules to the construction of the question, we get the construction $[{}^0Go_{wt}\ {}^0Snasel\ x]$. Our task is applying deduction rules until we derive construction $[{}^0Go_{wt}\ {}^0Snasel\ x]({}^0O/x)$. Then the object *O* is the answer:

1.	$[{}^0Regret_{wt}\ {}^0Mayor_{wt}\ {}^0[\lambda w\lambda t\,\neg[{}^0Know_{wt}\ {}^0President_{wt}\ [{}^0Sub\ [{}^0Tr\ {}^0President_{wt}]\ {}^0he\ {}^0[\lambda w\lambda t\,[{}^0Go_{wt}\ he\ {}^0Brussels]]]]]]]$	∅
2.	$[{}^0President_{wt} = {}^0Snasel]$	∅
3.	$[{}^0True_{wt}\ {}^{20}[\lambda w\lambda t\,\neg[{}^0Know_{wt}\ {}^0President_{wt}\ [{}^0Sub\ [{}^0Tr\ {}^0President_{wt}]\ {}^0he\ {}^0[\lambda w\lambda t\,[{}^0Go_{wt}\ he\ {}^0Brussels]]]]]]$	1, F1
4.	${}^{20}[\lambda w\lambda t\,\neg[{}^0Know_{wt}\ {}^0President_{wt}\ [{}^0Sub\ [{}^0Tr\ {}^0President_{wt}]\ {}^0he\ {}^0[\lambda w\lambda t\,[{}^0Go_{wt}\ he\ {}^0Brussels]]]]]_{wt}$	3, *True* – E
5.	$[\lambda w\lambda t\,\neg[{}^0Know_{wt}\ {}^0President_{wt}\ [{}^0Sub\ [{}^0Tr\ {}^0President_{wt}]\ {}^0he\ {}^0[\lambda w\lambda t\,[{}^0Go_{wt}\ he\ {}^0Brussels]]]]]_{wt}$	4, ^{20}-E
6.	$\neg[{}^0Know_{wt}\ {}^0President_{wt}\ [{}^0Sub\ [{}^0Tr\ {}^0President_{wt}]\ {}^0he\ {}^0[\lambda w\lambda t\,[{}^0Go_{wt}\ he\ {}^0Brussels]]]]$	5, β-r
7.	$[{}^0True_{wt}\ {}^2[{}^0Sub\ [{}^0Tr\ {}^0President_{wt}]\ {}^0he\ {}^0[\lambda w\lambda t\,[{}^0Go_{wt}\ he\ {}^0Brussels]]]]$	6, F2
8.	${}^2[{}^0Sub\ [{}^0Tr\ {}^0President_{wt}]\ {}^0he\ {}^0[\lambda w\lambda t\,[{}^0Go_{wt}\ he\ {}^0Brussels]]]_{wt}$	7, *True* – E
9.	${}^2[{}^0Sub\ [{}^0Tr\ {}^0Snasel]\ {}^0he\ {}^0[\lambda w\lambda t\,[{}^0Go_{wt}\ he\ {}^0Brussels]]]_{wt}$	8,2, SI
10.	${}^2[{}^0Sub\ {}^{00}Snasel\ {}^0he\ {}^0[\lambda w\lambda t\,[{}^0Go_{wt}\ he\ {}^0Brussels]]]_{wt}$	9, *Tr*
11.	${}^{20}[\lambda w\lambda t\,[{}^0Go_{wt}\ {}^0Snasel\ {}^0Brussels]]_{wt}$	10, *Sub*
12.	$[\lambda w\lambda t\,[{}^0Go_{wt}\ {}^0Snasel\ {}^0Brussels]]_{wt}$	11, ^{20}-E
13.	$[{}^0Go_{wt}\ {}^0Snasel\ {}^0Brussels]$	12, β-r

The resulting construction $[{}^0Go_{wt}\ {}^0Snasel\ {}^0Brussels]$ can be unified with the question $[{}^0Go_{wt}\ {}^0Snasel\ x]$ by substitution $({}^0Brussels/x)$. So, the desired answer is *Brussels*.

4 Conclusion

In this paper, we introduced the method for answering Wh-questions that extends the system of natural deduction. The analysis of such questions yields constructions of the form λ*x* [...]. A direct answer provides the value of the variable *x* by the substitution that unifies a given query with an appropriate sentence from an input knowledge base. Future research will concentrate on the comparison of this approach with the system of deriving answers utilizing the backwards-chaining strategy of general resolution method.

Acknowledgements. This research was supported by the Grant Agency of the Czech Republic, project no. GA18-23891S, "Hyperintensional Reasoning over Natural Language Texts", and by the internal grant agency of VSB-Technical University of Ostrava, project SGS No. SP2021/87, "Application of Formal Methods in Knowledge Modelling and Software Engineering IV".

References

1. Duží, M. (2010): Tenses and truth-conditions: a plea for if-then-else. In the *Logica Yearbook 2009*, Peliš, M. (ed.), pp. 63-80, London: College Publications.
2. Duží, M., Fait, M. (2020): Integrating special rules rooted in natural language semantics into the system of natural deduction**.** In the proceedings of *ICAART 2020*, the *12th International Conference on Agents and Artificial Intelligence*, Ana Rocha, Luc Steels, Jaap van der Herik (eds.), vol.1, pp. 410-421, Malta, Valletta.
3. Duží, M., Fait, M. (2021): A Hyperintensional Theory of Intelligent Question Answering in TIL. In *Natural Language Processing in Artificial Intelligence - NLPinAI 2020*, Loukanova, R. (ed.), Studies in Computational Intelligence (SCI). Cham: Springer.
4. Duží, M., Fait, M., Menšík, M. (2019): Adjustment of Goal-driven Resolution for Natural Language Processing in TIL. In proceedings of the *Thirteenth Workshop on Recent Advances in Slavonic Natural Languages Processing*, *RASLAN 2019*, Horák, Aleš and Rychlý, Pavel and Rambousek, Adam (eds), pp. 71-81, Brno: Tribun EU.
5. Duží, M., Jespersen, B. (2020): An intelligent question-answer system over natural language texts. In *Lecture Notes in Electrical Engineering* 554, I. Zelinka, P. Brandstetter, T.T. Dao, Vo.H. Duy, S.B. Kim eds., AETA 2018 – Recent Advances in Electrical Engineering and Related Sciences: Theory and Applications, pp. 162-174, Springer.
6. Duží, M., Jespersen B., Materna, P. (2010): *Procedural Semantics for Hyperintensional Logic; Foundations and Applications of Transparent Intensional Logic*. Logic, Epistemology and the Unity of Science, vol. 17. Berlin: Springer.
7. Tichý, P. (1988): *The Foundations of Frege's Logic*. Berlin, New York: De Gruyter.

ICO Prediction Using Ridge Regression Model

Tran Kim Toai[1, 3], Roman Senkerik[2], Vo Thi Xuan Hanh[3], and Vo Minh Huan[3]

[1]Department of Computer Science, FEECS,
VSB – Technical University of Ostrava, 17. listopadu 15,
708 00 Ostrava – Poruba, Czech Republic
[2]Faculty of Applied Informatics, Tomas Bata University in Zlin,
T. G. Masaryka 5555, 760 01, Zlin Czech Republic
[3]Ho Chi Minh University of Technology Education, Vietnam;
No 1 Vo Van Ngan Street, HCMC
huanvm@hcmute.edu.vn

Abstract. The paper aims to predict ICO (Initial Coin Offering) price after six months using the ridge regression model. The linear regression model has problems with overfitting and multicollinearity that make the ICO prediction inaccurate. A dataset includes 109 ICOs obtained from the cryptocurrency websites after data pre-processing. The dataset consists of 12 fields, covering the main factors that affect the price of an ICO. One-hot encoding technique is applied to convert the alphanumeric form into a binary form to perform better predictions; thus, the dataset has been expanded to 128 columns and 109 rows. The ridge regression algorithm overcomes the correlation problems that independent variables are highly correlated in the case of dealing with the ICO data. It would otherwise be difficult to achieve high precision prediction. After the training process with the cross-validation technique and the parameter fitting process, the three best models were obtained based on metrics of RMSE (Root Mean Square Error), R2 (R-Squared), and MAE (Mean Absolute Error). The test results show that the presented ridge regression approach gives the most accurate prediction results of 92% actual value.

Keywords: ICO, Prediction, Ridge regression, Linear regression, One-hot encoding.

1 Introduction

ICO (Initial Coin Offering) price prediction is a significant issue in business, especially for investors and consultants. Price prediction by machine learning is becoming a new trend because of its accuracy and efficiency in various applications [1-4]. Many algorithms are used for prediction, such as multivariate linear regression, ridge regression, neural networks, support vector machine, and others [1-2]. Which, of course, leads to the question of why ICO price forecasting is necessary? It is crucial to predict the upcoming ICO price in the near future time horizon. When companies, investors, or consultants have a specific number of predictions with high accuracy, they will base on that result, from which they will take appropriate steps.

The presented ICO price forecasting system is divided into two main parts: the algorithm part and the dataset. The dataset contains the maximum amount of available

© M. Krátký, J. Dvorský, P. Moravec (Eds.): WOFEX 2021, pp. 169–175.
VSB – Technical University of Ostrava, 2021, ISBN 978-80-248-4523-4 (on-line).

and relevant information related to ICOs. The data has been carefully selected and filtered (removing invalid data). The forecast algorithm uses ridge regression to execute ICO prediction returning the expected price of an ICO after six months.

The sequence of the following steps determines the originality of the presented research. This paper describes in detail the process of collecting data from cryptocurrency websites. The dataset in the machine learning model encounters some problems such as multicollinearity and overfitting that are also analyzed here. We have applied a machine learning algorithm called ridge regression to predict expected cryptocurrency prices after six months while solving the problems mentioned above with collected data.

2 Process of data collection

We have created a dedicated API written in C# language that retrieves raw ICO data from reputable cryptocurrency sites like tokendata.io, icostats.com, icodrops.com, prediction.com, coinmartketcap.com. This raw dataset that has not been processed for use includes more than 2500 ICOs that require data preprocessing steps. The data preparation stage is the process of cleaning invalid ICO data and formatting raw ICO data for further processing. This step enables ICO data to become accessible for training and analysis. Moreover, ICOs that are older than six months are also filtered. The final complete dataset has 109 ICOs, with 109 rows and 12 columns.

The dataset consists of 12 fields, covering the main factors that affect the price of an ICO. The 12 specific factors (believed to affect the price of an ICO) include Price USD; Price BTC; Total supply; Market Cap; Available Supply; USD raised; Ethereum price at launch; Bitcoin price at lunch; Month ICO was launched; Date ICO was lunched; Country of ICO launch; ICO Durations day.

Overall, 106 ICOs are used to train the model, and 3 ICOs are used to test the algorithm's accuracy. We separate 106 ICOs into two parts, including cross set (X_cross, y_cross) and test holdout set (X_test_holdout, y_test_holdout) with the rate of 80% for cross set and 20% for the holdout test set. This cross set is used to train the ridge regression model. The cross set is separated into two subsets: Training set (X_train, y_train) and validation set (X_val, y_val) at the rate of 80% for the training set and 20% for the cross-validation. The goal of cross-validation is to estimate the expected level of fit to a dataset that was used to train a model. Details regarding the dataset splitting are given in Table 1.

Table 1: The dataset structure

Cross data	Test holdout data	Test data
85 ICO	21 ICO	3 ICO

One-hot encoding is used to perform better predictions because categorical variables need to be converted to a binary form that can be fed to the machine learning model. However, this will increase the number of inputs. In this dataset, the one-hot encoding technique is applied to the last four fields including ICO duration, date, month and

county. The data have to be converted from alphanumeric form. So, the dataset will no longer be 12 columns but up to 128 columns, the number of rows is still 109 rows.

3 Data Analysis

Fig. 1 shows an overview of the correlation between inputs and outputs as well as directly between inputs. Large font size numbers highlight strong correlations with significant correlation coefficients. The main diagonal of the figure represents the names of the inputs and outputs that are variable names along with the corresponding histogram. The elements above the diagonal show the correlation coefficients and the significance level as stars for each input pair and between input and output. Each significance level is associated with a symbol. One star, two stars, and three stars correspond to low significance, medium significance, and high significance.

The elements below the diagonal display the bivariate scatter plots with a fitted line for each input pair and between input and output. If input pairs or input and output pairs have a high correlation coefficient, then the scatter plot corresponding to these pairs has the distributed data in a linear line shown by the red line. The red line on the figure shows a perfect linear relationship between two variables in that all points fall directly on a straight line. Large amounts of points are far around a linear line that indicates a week relationship between two variables.

After analyzing the correlation between the inputs and the output, there are two inputs, Price USD and Price BTC, which have a strong correlation with the output. In contrast, the remaining inputs have a weak correlation or are almost no correlation.

A simple linear model can be built to predict and get good results if the correlation coefficient is high between input and output. As given by the preliminary analysis of the dataset, many inputs are related to the output. Although the correlation is weak, there are still correlations with each other. It means that even though there are two highly correlated inputs, Price_USD and Price_BTC, it is not possible to predict the output only through these two inputs and consider the remaining inputs meaningless. Thus, the model has to consider all inputs.

Based on data analysis presented in Fig. 1, market_cap_usd and availabe_supply variables have a correlation close to 0. That is, the two variables are independent of each other. Table 2 shows that the regression coefficients, the standard error, and the Sum. Sq. are almost unchanged in the case of combining two variables of market_cap_usd and Availabe_supply, compared to the case of considering each individual variable. The standard error is used to measure the accuracy of an estimated regression system. The smaller the standard error is, the more accurate is the estimated regression system. We conclude that two variables are independent inputs.

From Fig. 1 depicting the correlation between variables of usd_raised and ico_duration, it follows that these two variables have correlation coefficients close to 0.77. Table 3 shows that regression coefficients change significantly when using a model including variables that are strongly correlated with each other.

Unlike two almost independent variables of market_cap_usd and availabe_supply in Table 2, two variables of usd_raised and ico_duration have a high correlation in Table 3. The regression coefficient of the two combined variables is much different from that

of each independent variable. Specifically, the regression coefficients of usd_raised and ico_duration were reduced when two variables are included in the model.

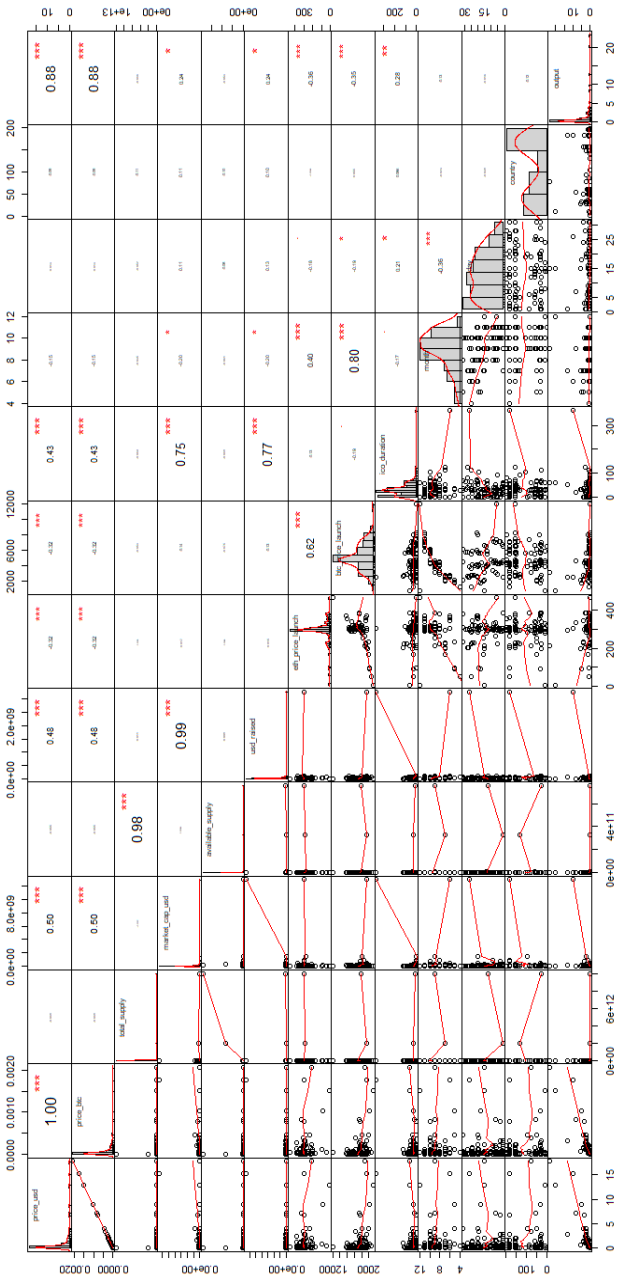

Fig. 1. Correlation graph between inputs and between input

Fig.1 determines that inputs are related to each other, namely pairs of (price_usd & price_btc), (total_supply & available_supply), (market_cap_usd & usd_raised),

(btc_price_launch & month), (usd_raised & ico_duration), (market_cap_usd & ico_duration).

Table 2: Regression coefficient and standard error of market_cap_usd and availa-ble_supply variables

Model	X1	Se(X1)	X2	Se(X2)	Sum Sq
market_cap_usd	6.652e-10	2.576e-10	--	--	73.87
available_supply	--	--	-2.258e-12	4.198e-12	3.39
both variables	6.653e-10	2.584e-10	-2.265e-12	4.092e-12	73.87/3.41

Table 3: Comparison of regression coefficients and standard error of usd_raised and ico_duration after combination.

Model	X1	Se(X1)	X2	Se(X2)	Sum Sq
usd_raised	2.580e-09	1.028e-09	--	--	70.06
ico_duration	--	--	0.024117	0.007755	104.36
both variables	3.794e-10	1.595e-09	2.188e-02	1.222e-02	70.06/34.92

Table 4: Overfiting analysis in multivariable regression model with test_holdout dataset

	Training Error	Test Error
Model	0.002627	11.545914

As can be seen in Table 4, the training error is 0.002627 after fitting a linear model with coefficients to minimize the residual sum of squares between the observed target in the dataset and targets predicted by the linear combination. This error can be considered as a perfect prediction on the train set. However, the prediction value and the actual value do not match with high precision, as mentioned above. The prediction value has deviated a lot from the actual value. Based on two training error and test error parameters, it is possible to conclude that overfitting exists, causing the prediction linear regression model to become misleading.

4 Ridge Regression Model

Ridge regression is a variant of linear regression to overcome the phenomenon of multicollinearity and overfitting [4]. Like linear regression, ridge regression also tries to fit the data using the residual sum of squares minimization function. The equation of ridge regression has the form (1).

$$J(\theta) = \frac{1}{2N}\left(\sum_{i=1}^{N}(h_\theta(x^{(i)}) - y^{(i)})^2 + \lambda\sum_{i=1}^{N}\theta_i^2\right) \quad (1)$$

In the equation (1), $\mathbf{x}^i$ is the symbol for the inputs of i^{th} training sample. N is the sample size. $\mathbf{y}^i$ is the actual value corresponding to i. The θ values are model coefficients. The

parameter λ (called lambda parameter) is used to adjust the model complexity. This parameter λ is also called the regularization parameter. The λ parameter is changed slightly to avoid the overfitting problems but still keep the generality of the model. The parameter λ is often used to evaluate the model complexity with large parameter values representing a complex model. By adding an amount of $\lambda \sum_{i=1}^{N} \theta_i^2$ into the equation (1), which is large when θ is large, the ridge regression favors models with small θ values. Therefore, non-significant variables with lower coefficient θ will decrease to zero.
The parameter λ is the parameter to correct the model complexity. When λ is large, most of the model parameters will decrease to zero leading to the underfitting phenomenon. When λ is small, returning to normal linear regression leads to overfitting. Choosing the right parameter λ is extremely important and may be difficult task. We have executed numerous experiments with λ parameter value during training. The best training model achieved also represents the optimum lambda parameter value.

5 Experiment with Ridge Regression Algorithm

The accuracy result of the algorithm has been calculated by the formula RMSE (Root Mean Square Error), R2 (R-Squared), and MAE (Mean Absolute Error) [3]. To analyze and evaluate the presented approach with ridge regression algorithm, the training process has been executed on 10000 iterations with cross-validation technique to generate the three training models according to each evaluation metric of RMSE, R2, MAE.

After training is complete, the test phase has been performed by evaluating the X_test_holdout dataset with each trained model. The returned results are the predicted values, along with the given data in y_test_holdout for performance calculations. Fig.2 (a), (b), (c) correspond to the evaluation results with the three prediction models. In terms of accuracy, the model achieved rMSE=0.748, Rsquared=0.709, MAE=0.562, respectively.

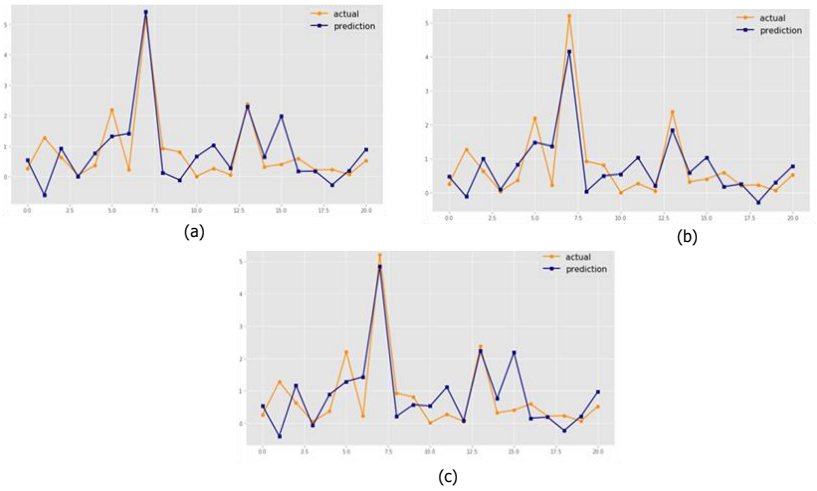

Fig.2. Comparison of results between y_test_holdout and y_pred_holdout in ridge regression model (a) rMSE=0.748 (b) Rsquared=0.709 (c) MAE=0.562.

Table 5 shows the predicted results according to three test ICOs which is selected from 109 ICOs. The test set of three ICOs is an observation set used to evaluate the performance of the three best models using three performance metrics such as RMSE, R^2, and MAE. All three models have quite accurate results. The model with the R^2 metric gives the most accurate ICO prediction results up to 92% actual price in the case of 0x ICO.

Table 5: Predicted results of 3 ICOs using Ridge. regression model.

ICO name	Best RMSE	Best R2	Best MAE
0x	0.94 (86%)	1.178859 (92%)	1.17286 (92%)
Modum	4.377(63%)	2.263788 (76%)	2.19421 (73%)
Crypto20	1.267 (75%)	1.092449 (87%)	1.1756 (81%)

6 Conclusion

The price of an ICO cryptocurrency depends on many factors. The 12 factors affecting the price of ICO are considered in this paper for building the dataset and further analyses. This paper focuses on the phenomenon of multicollinearity, overfitting, variable correlations, and aims to find a suitable algorithm model. Ridge regression algorithm using a dedicated lambda coefficient is a nonlinear regression method that can overcome the challenges of data problems encountered that multivariate regression cannot solve. A processed dataset consists of 85 ICOs for training and 21 ICOs for test holdout, and 3 ICOs for testing to create the three best models based on three metrics of RMSE, R-square, and MAE. The ICO price forecast accuracy after six months is up to 92% actual value using the ridge regression model.

References

1. Hartmann, F., Wang, X., & Lunesu, M. I. A hierarchical structure model of success factors for (blockchain-based) crowdfunding (2018).
2. Anchaya C., et al.: Can Tweets predict ICO success? Sentiment Analysis for Success of ICO Whitepaper: evidence from Australia and Singapore Markets. 15th International Joint Symposium on Artificial Intelligence and Natural Language Processing (iSAI-NLP) (2020).
3. Yaohao P., et al.; The best of two worlds: Forecasting high frequency volatility for cryptocurrencies and traditional currencies with Support Vector Regression. Expert Systems With Applications 97 p.p.177–192 (2018).
4. Deanna N. G.: Ridge Regression and Multicollinearity: An In-Depth Review. SAS Global Forum (2018).

Preprocessing optimization using GPU parallelism on natural gas dataset

Vojtěch Kotík and Jan Platoš

Department of Computer Science, FEECS,
VSB – Technical University of Ostrava, 17. listopadu 15,
708 00 Ostrava – Poruba, Czech Republic
{vojtech.kotik, jan.platos}@vsb.cz

Abstract. This paper presents current state of our research related to solving natural gas consumption forecasting tasks. We created state of the art dataset. We have proved high usability by experiments and proposed methodology. These results were published and dataset was made publicly available. Following experiments are focused on improving model performance. Part relevant to preprocessing optimization is covered in this work.

Keywords: gas consumption prediction, big data, machine learning, cuda

1 Introduction

Natural gas consumption forecasting tools gained significant importance in recent decades. There were multiple reasons for this. Natural gas is considered to be the cleanest of all fossil fuels. Air pollution and CO2 emissions produced during the utilization of any fuel are important factors influencing the decision–making process.

Our recent research in this scope consisted of creation of state of the art dataset, forecasting methodology proposal and performed experiments [8].

Some of the researchers, like Soldo [6] and Tamba et al. [10], created literature review studies. These offer an overview of available methods at a given date, which we can consider as a form of research baseline. These reviews include an algorithms performance and precision overview useful to the new researchers trying to get into this field. Evaluated methods included approximation principles [2]. The main works that used this approach were [1, 5, 3] and many others. Another large group of applied algorithms is the application of Artificial neural networks. Suykens et al. [7] have developed a non–linear model of the Belgian gas consumption with utilization of the weather and market data about oil prices. Khotanzad et al. [4] prepared a two–stage model that combines regular feedforward neural networks and functional link neural networks on the first level and nine different mixing strategies on the second level. A combination of classical

VSB – Technical University of Ostrava, 2021, ISBN 978-80-248-4523-4 (on-line).

and fuzzy neural networks was developed by Viet and Mańdziuk [11]. This approach was tested on weekly data with short, middle and long term forecasting horizons. Another application of the hourly based data was performed by Szoplik [9], who efficiently used Multilayer perceptron on the gas consumption enriched with the weather data. During cross–method comparisons, researchers often encounter hurdles created by different metrics, forecasting horizons and input data used in the individual works. That means that a simple evaluation of outcomes against each other is not a trivial task and sometimes can be even impossible, as stated by Tamba et al. [10]. This is the issue we have attempted to cover by our research efforts. Therefore we made our dataset publicly available after paper submission.

Our subsequent experiments conducted also computational difficulty optimization using parallel computing methods. This paper covers experiments related with parallel processing of preprocessing phase.

2 Dataset

Our created dataset covers six whole years from January 1, 2013 to December 31, 2018. All data features are available at an hourly frequency. The whole dataset is composed of 52,584 data points. These data points were assembled from three main components.

The first component was created from consumption data. Prague is the capital city of the Czech Republic and its distribution network consisted of 422,926 customers in 2018. Total consumption was 3.82 billion m^3. Residential sector included 381,914 households (33.3% of consumption). Industrial sector consisted from 177 big (24.8% of consumption), 39,175 medium (18.9% of consumption) and 1,652 small customers (21.9% of consumption). Missing remainder to 100% were operational losses that occurred during distribution, e.g., pipeline leak. The heating season in the Czech Republic is from September 1 to May 31. Usually, it is required for the heating season to begin that the temperature drops below +13°C for two consecutive days, and no warming is forecasted for the next days. The heating season usually represents about 70% – 75% of the whole year's consumption.

The second component includes weather variables. We have used data from the Prague LKPR airport weather station. Airports are required to periodically issue METAR (aerodrome routine meteorological report) information. Those reports are archived and preserved for a long time.

The third component representing economic features are natural gas price data. We have obtained price data from the Czech energy regulation office and included them in the dataset.

3 Methods

First of evaluated frameworks was CuPy – a NumPy compatible array library accelerated by CUDA. CUDA is parallel computing platform and API created by

NVIDIA. It enables use of NVIDIA GPU resources by software layer that gives access to the GPU virtual instruction set and parallel computational elements. It was initially released by NVIDIA at 2007 and is maintained since then. In the first step data are copied from main memory to GPU memory. CPU then initiates the GPU compute kernel. GPU CUDA cores execute the kernel in parallel mode. In the end resulting data from GPU memory are copied to main memory.

CuPy is an open source array library that is accelerated with NVIDIA CUDA. CuPy can be used with Python and uses CUDA related libraries like cuBLAS, cuDNN, cuRand, cuSolver, cuSPARSE, cuFFT and NCCL to use most of the GPU architecture. Most operations perform well on GPU using CuPy out of the box. CuPy interface is compatible with NumPy and in most cases can be used as direct replacement.

4 Experiment

The first step in the preprocessing pipeline was reducing the gas consumption time dependency and extraction of it as additional features. The current value is heavily dependant on the prior values as we can judge from the strong autocorrelation of the consumption time series. Daily and half–daily seasonal patterns with peaks at lag numbers, which are multiplies of the number 24, respectively 12, corresponding to the hours in a day are apparent from the autocorrelation plot. We did a first–order seasonal differencing of the time series with a lag of 24 to reduce part of the time dependency with respect to the forecast horizon and autocorrelation values. The second step was the decomposition of the differenced time series into additive components. STL (Seasonal and Trend decomposition using Loess) was used for this purpose, which decomposed the time series into trend, periodic and residual component. Consumption did not follow any deterministic trend, so finally, the trend component was merged with the residual one. The Augmented Dickey–Fuller test for the unit root of the merged time series was done to check if the stationarity expectations were met. We rejected the null hypothesis at the significance level of 5% with the $p - value \ll 0.05$ and took the stationarity expectation as fulfilled. The final step was the transformation of the time series to the form suitable for the single model forecasting. Time series transformed in this way served as the forecasted variable for the algorithms. Predicted values were finally obtained by reversing the whole process and used for computation of all evaluation metrics.

This pipeline was basic setting for our experiment. First stage included CPU computing. Whole pipeline was run fifteen times. We have measured separately times for each pipeline step and included summary result of whole pipeline. CPU results can be found at Table 1. Experiment with same settings was then run on the NVIDIA GPU. Result can be found at Table 2. Speedup on GPU was significant, completing pipeline in under half of time needed by CPU. The most significant speedup was gained by using GPU in the preprocessing phase and Random forest model training in the end of the pipeline. Speedup of full pipeline is depicted in figure 1. Speedup of STL phase can be seen in figure 2.

Table 1. CPU – seconds

Iter.	pre–STL	STL	post–STL	ML phase	Full
1	19.78	261.98	20.27	106.75	408.78
2	17.85	254.51	20.32	104.63	397.31
3	18.10	259.61	20.98	111.36	410.04
4	18.32	262.03	20.38	105.85	406.58
5	18.50	271.73	20.65	105.76	416.65
6	19.44	276.77	21.16	114.48	431.87
7	18.91	274.47	21.03	114.93	429.34
8	18.88	264.45	20.14	102.15	405.62
9	18.12	247.68	20.18	101.57	387.56
10	18.16	245.10	20.22	103.00	386.47
11	18.98	248.29	20.48	105.50	393.24
12	18.37	245.88	20.42	104.80	389.48
13	18.37	245.81	20.42	116.45	401.06
14	18.41	245.30	20.44	105.22	389.37
15	18.40	244.92	20.46	104.20	387.98

Table 2. GPU – seconds

Iter.	pre–STL	STL	post–STL	ML phase	Full
1	0.85	174.87	8.73	5.78	190.22
2	0.81	190.41	9.01	5.76	205.98
3	0.79	191.06	9.25	5.80	206.90
4	0.83	183.50	8.15	5.68	198.16
5	0.79	168.58	1.41	5.82	176.60
6	0.78	171.44	1.47	5.82	179.51
7	0.81	171.16	1.45	5.72	179.15
8	0.77	170.20	1.57	5.81	178.35
9	0.79	171.34	1.45	5.84	179.43
10	0.84	171.91	1.49	5.83	180.06
11	0.80	170.19	1.44	5.75	178.18
12	0.81	163.42	1.59	5.64	171.45
13	0.81	172.78	1.55	5.79	180.93
14	0.78	173.62	1.45	5.81	181.66
15	0.81	171.91	1.50	5.76	179.98

5 Conclusion and further research

We have prepared state of the art dataset, proposed methodology and performed experimental evaluation of consumption prediction. After paper publication we focused on model optimization. We have performed basic evaluation of possibilities to compute preprocessing phase in paralell environment using GPU. These will serve as baseline for our future development of forecasting model.

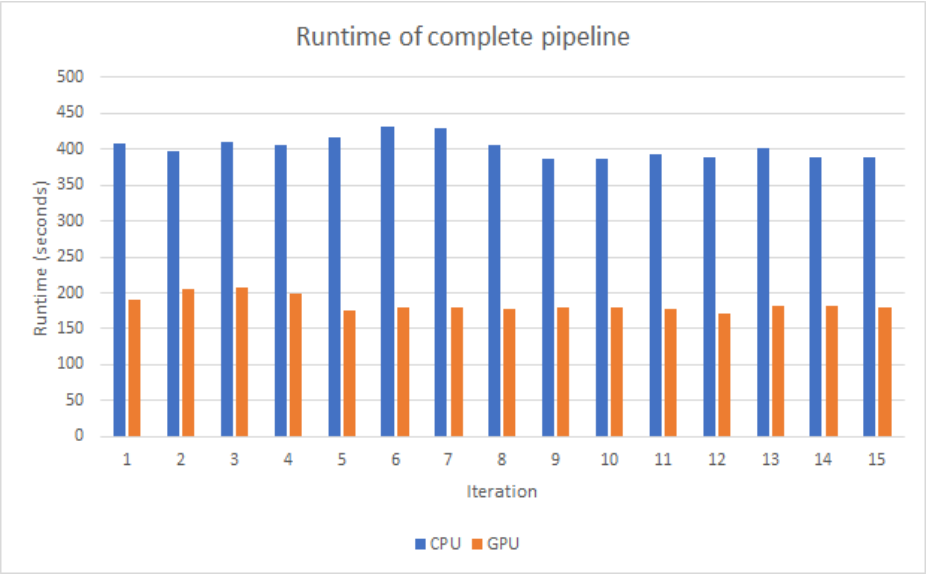

Fig. 1. Full pipeline – CPU vs GPU

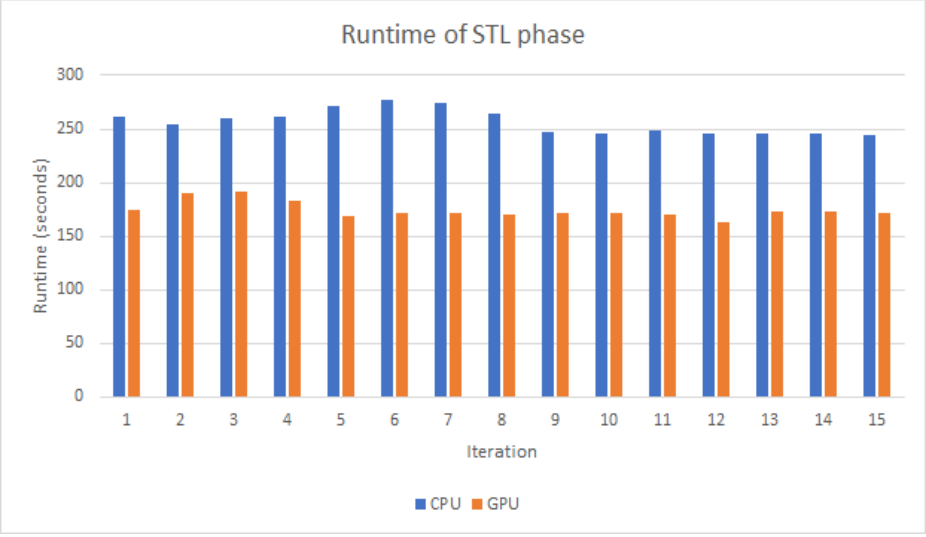

Fig. 2. STL phase – CPU vs GPU

References

1. Hubbert, M.K.: Energy from fossil fuels. Science **109**(2823), 103–109 (1949). https://doi.org/10.1126/science.109.2823.103
2. Hubbert, M.K.: Nuclear energy and the fossil fuel. Drilling and Production Practice **1** (January 1956)
3. Imam, A., Startzman, R.A., Barrufet, M.A.: Multicyclic hubbert model shows global conventional gas output peaking in 2019. Oil and Gas Journal **102**(31) (August 2004)
4. Khotanzad, A., Elragal, H., Lu, T..: Combination of artificial neural-network forecasters for prediction of natural gas consumption. IEEE Transactions on Neural Networks **11**(2), 464–473 (2000)
5. Siemek, J., Nagy, S., Rychlicki, S.: Estimation of natural-gas consumption in poland based on the logistic-curve interpretation. Applied Energy **75**(1), 1 – 7 (2003), energex 2002 - Oil and Gas - Topic III and Nuclear Energy - Topic IV
6. Soldo, B.: Forecasting natural gas consumption. Applied Energy **92**, 26 – 37 (2012)
7. Suykens, J., Lemmerling, P., Favoreel, W., De Moor, B., Crepel, M., Briol, P.: Modelling the belgian gas consumption using neural networks. Neural processing letters **4**(3), 157–166 (1996)
8. Svoboda, R., Kotik, V., Platos, J.: Short-term natural gas consumption forecasting from long-term data collection. Energy **218**, 119430 (2021). https://doi.org/https://doi.org/10.1016/j.energy.2020.119430, http://www.sciencedirect.com/science/article/pii/S0360544220325378
9. Szoplik, J.: Forecasting of natural gas consumption with artificial neural networks. Energy **85**, 208 – 220 (2015)
10. Tamba, J.G., Essiane, S.N., Sapnken, E.F., Koffi, F.D., Nsouandélé, J.L., Soldo, B., Njomo, D.: Forecasting Natural Gas: A Literature Survey. International Journal of Energy Economics and Policy **8**(3), 216–249 (2018), https://ideas.repec.org/a/eco/journ2/2018-03-28.html
11. Viet, N.H., Mańdziuk, J.: Neural and fuzzy neural networks in prediction of natural gas consumption. Neural Parallel & Scientific Comp. **13**, 265–286 (2005)

Twitter mentions network of Czech politicians

Jakub Plesnik, Miloš Kudělka, and Eliska Ochodkova

Department of Computer Science, FEECS,
VSB – Technical University of Ostrava, 17. listopadu 15,
708 00 Ostrava – Poruba, Czech Republic
jakub.plesnik@vsb.cz

Abstract. This paper presents new datasets based on the interaction of Czech politicians on the social network Twitter. Paper describes how the dataset has been obtained and describes its properties. The analytic part of the paper uses non-symmetric dependency to detect ego zones to reveal more information about data structure.

Keywords: mention network, politics, twitter, dependency, ego-zones

1 Introduction

Analysis of political networks is an important task, which allows us to study and build an understanding of political subjects, their interactions, and the structures they form. Multiple approaches exist for constructing a Twitter-based network (retweets, mentions, reactions, comments). For political networks, it has been proven that mentions better reflect cross-party and cross-ideological connections [1]. Furthermore, previous research has shown that politicians actively use mentions to converse with each other publicly [2]. The average percentages show that EU leaders slightly prefer mentions (46% over 42% retweets), while Italian MPs prefer retweets (43% over 36% mentions); this may vary for other countries [3].

In this paper, we introduce and analyze the mentions network between Czech politicians on the social network Twitter. Main focus of our analysis is identifying groups of nodes defined by the ego to reveal new information about the relationship between egos. The main focus of our analysis is identifying groups of nodes defined by the ego to reveal new information about the relationship between egos. Many publications work with Twitter as a source for political networks, e.g., the paper where authors analyze social media and political communication in the election to the European Parliament [4]. Studies of party polarization based on Twitter mention network between Members of Parliament refutes polarization in MPs Twitter network [2].

As mentioned, our analysis focuses on the detection of groups of nodes around the ego. Thus we need an algorithm that can detect groups of nodes with overlaps. Various methods are described and compared in a detailed overview of overlapping community detection algorithms in social networks. The best performing methods based on modularity score are presented in Chen et al. and

VSB – Technical University of Ostrava, 2021, ISBN 978-80-248-4523-4 (on-line).

Newman et al. [5]. Our paper uses an algorithm based on non-symmetric structural dependency, which can detect so-called ego zones - groups of nodes defining the sphere of influence or dependency [6].

2 Obtaining data

We have obtained a new dataset for analysis of the political scene in the Czech Republic that contains interactions of politics on the social network Twitter. Network has been constructed through a Python script that downloads all tweets for accounts listed in the input file and then constructs a mention network. Downloading itself is implemented through Twitter API using the Tweepy library. [1]

Fig. 1: Process of obtaining data

The first part of the scripts uses HTTP GET *list/members* which returns the members of the specified list. Lists are a feature that helps organize tweets by a group of members of the list. We used a list from the account of a non-profit organization, "Hlidac statu", which focuses on transparency and control of the state contracts. This list contains both current and former politicians with active Twitter accounts. The list contains all leading politicians from the Chamber of Deputies of the Parliament or the Senate.

The second part of the script fetches tweets for each user retrieved from the list. Tweets are available through API endpoints GET *statuses/user_timeline* and GET *statuses/mentions_timeline*. We used the *user_timeline* endpoint which returns a collection of the most recent Tweets of a given user. Stored tweets can be used for further analysis.

After downloading, scripts iterates over tweets and looks for mentions to other politicians. The output of this step is a directed network where nodes are individual Twitter accounts. A directed edge between nodes A and B exists if tweets of account A contain mentions of account B. Network is directed, and edge A, B weight is equal to the total number of mentions of B by A.

3 Dataset

The result of our data crawling is a directed network in form of edge list $Source; Target; Weight$ and second file for linking node id to users twitter handle $id; label$. Table 1 contains the basic properties of the complete dataset and the same for the largest connected component of the graph.

[1] https://www.tweepy.org/

Table 1: Properties of obtained dataset

Name	N	E	Avg. Degree	Avg. Weighted degree	Avg. CC	Modularity
Full	229	3108	13.572	69.205	0.298	0.218
LCC	190	3105	16.342	83.368	0.359	0.211

3.1 Dependency network

Our first goal of the analysis is to obtain information about the structure of the network. For this purpose, we used an algorithm for non-symmetric dependency [6]. This algorithm provides information about dependency between individuals in the network, and it is base for the definition of ego zones.

Definition 1. *Structural dependency $D(x, y)$ between nodes x and y is defined as*

$$D(x,y) = \frac{w(x,y) + \sum_{v_i \in CN(x,y)} w(x,v_i) \cdot r(x,v_i,y)}{\sum_{v_j \in N(x)} w(x,v_j)} \tag{1}$$

$$r(x,v_i,y) = \frac{w(v_i,y)}{w(x,v_i) + w(v_i,y)} \tag{2}$$

where $CN(x, y)$ is set of all common neighbors of x,y. $N(x)$ is set of all neighbors of x, $w(x, y)$ is weight of edge between x, y, and $r(x, v_i, y)$ is the coefficient of dependency of node x on node y via the common neighbor v_i [6].

When we project the definition of dependency into our domain, we can say that politician B is dependent on politician A, if B mentions A in their tweets multiple times, or many times mentions politician C_i that also mentions politician A. We assume a close relationship exists between all subjects inside the network, so the direction of the edges in the original network may be neglected. Therefore, the input for the dependency algorithm is an undirected network.

Resulted dependency network is directed, and the direction of the edge means who is dependent on whom. The network is displayed in Figure 2. Nodes in such a network can be divided into three groups, marked by color, based on a property called a prominence.

1. Strongly-prominent - Red nodes represent politicians who are not dependent on any other political, but there are politicians dependent on them. (yellow, green)
2. Weakly-prominent - Yellow nodes represent politicians who are dependent on at least one red or yellow node, but there is also at least one node that depends on them (yellow, green).
3. Non-prominent - Green color represents nodes of politicians that are one way dependent on another politician, and there is no node dependent on them.

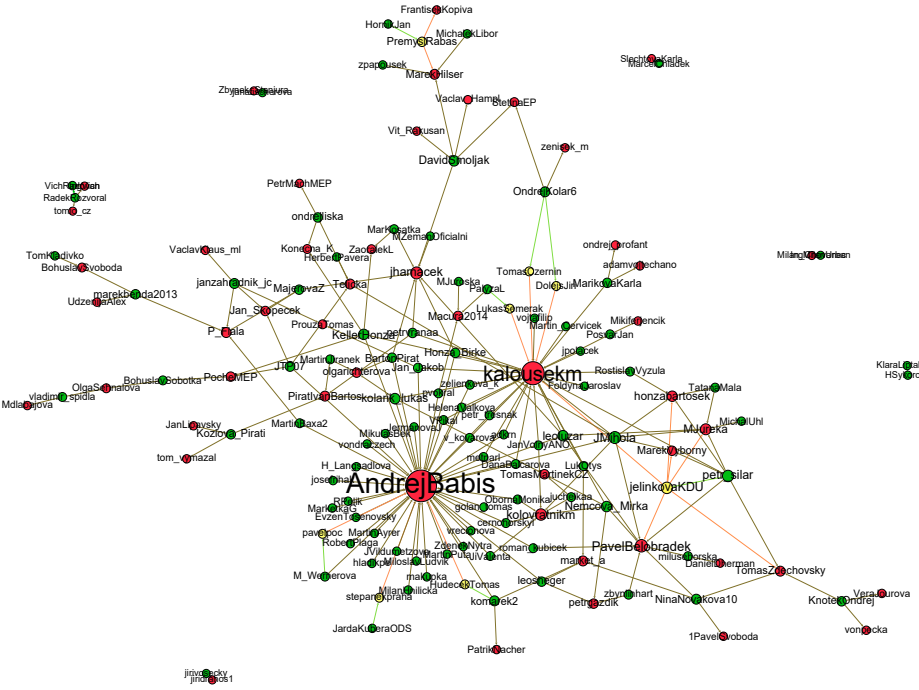

Fig. 2: Dependency network

3.2 Detection of egozones

With the application of structural dependency we can identify ego zones, also called dependency zones. Ego zones are groups of nodes defined by a central node called ego and its surroundings. In Figure 3, we can see ego zones and their hierarchical structure. Zones in this network have been detected with a minimal size of 3 nodes. Each ego zone is named by a politician, who is the ego of the given zone. It is important to note that zones can overlap.

The color of the zone describes the zone placed in the hierarchical structure. Red zones are top-level zones, called super zones. Super zones are not nested in any other zone but contain nested zones. Green zones exist on the lowest level, and they do not have any nested zones, but they are nested in others. Yellow marks zones that are super zones to at least one other zone but themselves are nested by another larger zone.

We identified six important ego zones, where the two largest exist around A. Babis and M. Kalousek. In the context of the Czech political scene: at the time of network construction, A.Babis was a Czech Prime Minister, and M. Kalousek was one of the front faces of opposition parties. M. Kalousek is also a former member of the parliament, retired shortly after the data were obtained. These

two are key players on the political scene, staying on opposing sites. Their zones do not have any super zones, but they share a significant number of smaller zones. That can be seen as overlapping spheres of influence or, in our case, spheres of dependency. Members of these zones are directly or indirectly dependent on both egos of top-level zones. The largest zones are created around egos that are not dependent on each other.

There are other significant ego zones in the network around J. Hamacek, P. Belobradek, and I. Bartos. All these politicians are leaders of other parties from the Czech parliament.

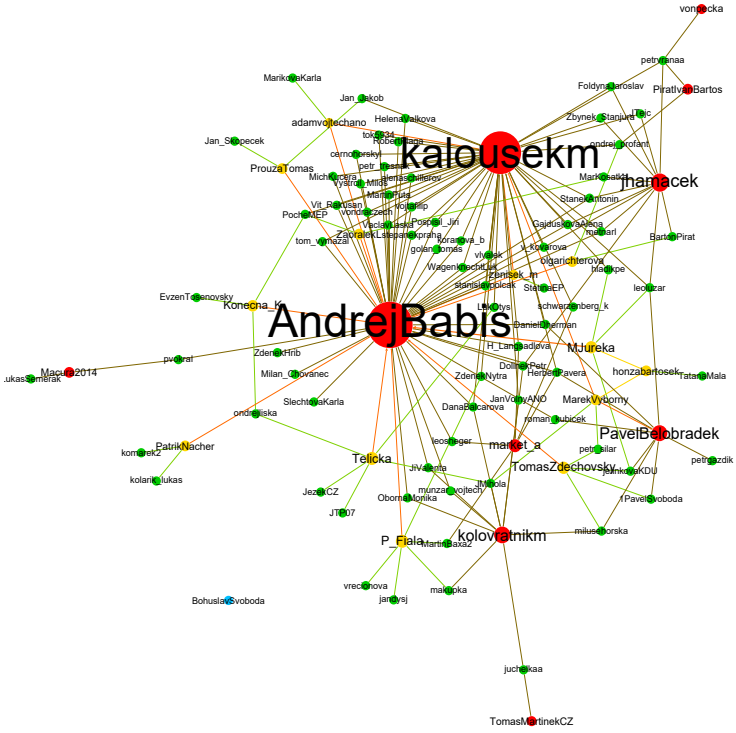

Fig. 3: Egozones network

3.3 Closer look on prominent nodes

After a closer look into the data, we discovered interesting differences in the behavior of individual politicians. We can see that MK has the highest in and out-degree, which means he is very active in mentioning others, but he is also often the target of a mention. His political rival AB is also mentioned many times, but he uses different strategies in mentioning others. There are very few

mentions from AB to others, and when there are, they are exclusively targeted to members of his party, Karel Havlicek(25), Adam Vojtech(17), Robert Plaga(11), and Alena Schillerova(10). Comparison is visible in Table 2. The column ratio is computed as the ratio between weighted in and out degrees.

Table 2: Comparison of in/out degrees of prominent nodes

Name	In-Degree	Out-Degree	Weighted In-Degree	Weighted Out-Degree	W. Ratio
AB	131	18	2787	105	26.5
MK	93	91	878	1183	0.74

For comparison MK most often mentions Andrej Babis (294), Jan Hamacek (91), Alena Schillerova (78), and only in fourth place is his party member from TOP09 Tomas Czernin(45). As much as we found this behavior interesting, the detailed explanation is out of the scope of this paper.

4 Conclusion

The network presented in this work reveals interaction between politicians on social network Twitter through mentions in their tweets. For analysis, we used non-symmetric dependency to identify crucial roles and structures in the network. With non-symmetric dependency, we have identified roles of the nodes; from that, we detected ego zones (dependency zones) and found that party leaders are often in the role of egos, and zones are formed around them. Zones have a hierarchical structure and can overlap.

We have identified interesting differences in the strategy of mentions between politicians that have shown to be the most important for the whole network. The result of this work may be used as a ground for future research from the politology or sociology fields or as an exemplary application of non-symmetric dependency in network analysis.

References

1. Rosa Borge Bravo & Marc Esteve Del Valle (2017) Opinion leadership in parliamentary Twitter networks: A matter of layers of interaction?, Journal of Information Technology & Politics, 14:3, 263-276, DOI: 10.1080/19331681.2017.1337602
2. Esteve Del Valle, Marc & Broersma, Marcel & Ponsioen, Arnout. (2021). Political Interaction Beyond Party Lines: Communication Ties and Party Polarization in Parliamentary Twitter Networks. Social Science Computer Review. 10.1177/0894439320987569.
3. Arnaboldi, V., Passarella, A., Conti, M. and Dunbar, R. (2017), Structure of Ego-Alter Relationships of Politicians in Twitter. J Comput-Mediat Comm, 22: 231-247. https://doi.org/10.1111/jcc4.12193

4. Nulty, Paul & Theocharis, Yannis & Popa, Sebastian & Parnet, Olivier & Benoit, Kenneth. (2016). Social media and political communication in the 2014 elections to the European Parliament. Electoral Studies. 44. 10.1016/j.electstud.2016.04.014.
5. Devi, J. & Eswaran, Poovammal. (2016). An Analysis of Overlapping Community Detection Algorithms in Social Networks. Procedia Computer Science. 89. 349-358. 10.1016/j.procs.2016.06.082.
6. Kudelka, M., Ochodkova, E., Zehnalova, S. et al. Ego-zones: non-symmetric dependencies reveal network groups with large and dense overlaps. Appl Netw Sci 4, 81 (2019). https://doi.org/10.1007/s41109-019-0192-6
7. Devi, J. & Eswaran, Poovammal. (2016). An Analysis of Overlapping Community Detection Algorithms in Social Networks. Procedia Computer Science. 89. 349-358. 10.1016/j.procs.2016.06.082.

Overlapping community detection based on closed trail components percolation

Petr Prokop and Jan Platoš

Department of Computer Science, FEECS,
VSB – Technical University of Ostrava, 17. listopadu 15,
708 00 Ostrava – Poruba, Czech Republic
{petr.prokop, jan.platos}@vsb.cz

Abstract. Detection and analysis of communities in networks are common tasks of network data analysis. From a global perspective, communities allow us to provide a structural description of a complex system. Individual communities also identify groups of interacting nodes and give us insight into nodes properties. Nodes often belong to multiple clusters and communities form overlap.
Closed trail distance can be used for formulating closed trail components, which are subgraphs composed of nodes with low mutual cyclic distance. Due to the structural property of closed trail components, the components can be used in the community detection task. In this paper, we proposed a method to process the detected closed trail components and form communities.
The quality of the detected communities were compared with known methods for overlapping clustering using artificial networks generated by the LFR framework.

Keywords: Overlapping community detection · Higher order graph structures · Closed trail distance

1 Introduction

Using graph representation and utilizing network analysis tools can be beneficial for studying relationships between objects. Usually, these objects form community structure with different levels of overlapping between different communities [2]. A general description of community is set different objects connected more frequently among themselves in comparison to the rest of the network. In case of possible belonging of object to multiple communities, we are talking about overlapping communities.

There are many algorithms in the literature dedicated to the detection of overlapping communities based on different principles. Some of them use the structural form of the network for community detection, while other algorithms use the principle of label propagation to find communities in terms of dynamic properties of networks.

VSB – Technical University of Ostrava, 2021, ISBN 978-80-248-4523-4 (on-line).

In previous work Closed Trail (CT) distance and Closed Trail components ($k-CT$) were defined and used to express clustering and closure coefficients [5], allowing to distinguish types of real networks and express their relationship to known random network models. This cyclic distance has also been used for disjoint community detection, where the advantage of cyclic distance over shortest path in community detection has been verified.

2 Description of proposed methods

In graph $G = (V, E)$ we are able to use Closed Trail distance $d_{CT}(u, v) = \min_{CT(u,v) \in G} |CT(u, v)|$, where $CT(u, v)$ is a closed trail that contains the vertices $u,\ v$. This cyclic distance describes the structural relation between a pair of nodes in a better way in comparison with well-known shortest path [7].

We can use CT distance to identify structural components of the graph. Specifically we are able to detect maximal $k-CT$ components, which are maximal subgraphs of nodes where every two vertices lie on closed trail with a length $\leq k$.

The proposed methods for overlapping community detection uses $k-CT$ components with various parameter k. Usually, many $k-CT$ components are detected in the networks and they are highly similar and overlapping. Therefore postprocessing step for forming communities has to be done. Distance between components need to be defined to merge similar components using agglomerative clustering and form clusters of $k-CT$ components representing the detected overlapping communities. Multiple strategies for measuring distance between components are described in the following subsection.

2.1 Strategies for building a community structure from structural components

After identifying the $k-CT$ components, it is important to use defined distance between components to determine the components to merge into communities. All maximal $k-CT$ components are denoted by $K_1, \ldots, K_n$. These components represent the sets of nodes in the original graph, in following definitions the set of nodes of the component K is denoted as $V(K)$. Before defining distances, we need to define the part of the components that are without overlap of the other component $K^e_{i,j \in \{1,\ldots,n\}} = V(K_i) \setminus V(K_j)$.

Inspired by the well-known CPM algorithm and its sequential percolation of cliques, first methods rally on intersection between the two communities, therefore $V(K_i) \cap V(K_j) \neq \emptyset$ must be satisfied for determining distance between component K_i and K_j. Distances between components without intersection are not defined in this case. Distance used between $k-CT$ components in hierarchical agglomerative clustering (HAC) is given by formula 1.

$$d_I(K_i, K_j) = \begin{cases} \min_{u_i \in K^e_{i,j}, u_j \in K^e_{j,i}} d_{CT}(u_i, u_j) & V(K_i) \cap V(K_j) \neq \emptyset \\ \infty & V(K_i) \cap V(K_j) = \emptyset \end{cases} \quad (1)$$

Ignoring the requirement for direct intersection between two components, we can define the distance between all pairs of components K_i and K_j in the same way as in first case regardless of the intersection. Moreover, the aggregation of the distance expression from nodes to components can be extended according to the linkage type of hierarchical agglomerative clustering. These distances between $k - CT$ components are defined by formulas 2, 3 and 4.

$$d_S(K_i, K_j) = \min_{u_i \in K^e_{i,j}, u_j \in K^e_{j,i}} d_{CT}(u_i, u_j) \tag{2}$$

$$d_C(K_i, K_j) = \max_{u_i \in K^e_{i,j}, u_j \in K^e_{j,i}} d_{CT}(u_i, u_j) \tag{3}$$

$$d_A(K_i, K_j) = \operatorname*{average}_{u_i \in K^e_{i,j}, u_j \in K^e_{j,i}} d_{CT}(u_i, u_j) \tag{4}$$

3 Empirical results

The quality of the detected communities was evaluated by comparing qualitative measures over a set of artificial networks generated using Lancichinetti-Fortunato- Radicchi (LFR) framework described in following section.

The Clique Percolation Method (CPM)[4], Speaker-listener Label Propagation Algorithm (SLPA)[8] and Democratic Estimate of the Modular Organization of a Network (DEMON)[1] algorithms were selected to compare the quality of overlapping community detection. CPM is a well-known technique for community detection, communities are formed by merging adjacent cliques of size k if they share $k - 1$ nodes. The SLPA algorithm is based on the label propagation algorithm, extended by adding memory for labels to the nodes during label propagation step. DEMON exploits the ego-network structure to detect overlapping communities.

3.1 Networks for benchmarking

The availability of real data with annotated overlapping communities is not sufficient. Artificially generated networks were used to evaluate the detected communities using the LFR framework. The framework allows to generate graphs with a power-law distribution of node degree and community size according to other specified parameters such as the number of overlapping nodes in the network or the mixing parameter.

Sixty networks were generated for experiment according to different input parameters for graph generation. Networks of 300 nodes were generated with power law coefficients 2 for degree distribution and 1 for community size distribution. Different parameter configurations were used by combining additional parameters namely the average and maximum degree of nodes corresponding to $(\langle k \rangle, k_{max}) \in \{(10, 30), (7, 50)\}$. Minimum and maximum size of communities were set to $(c_{min}, c_{max}) \in \{(7, 50), (10, 100)\}$. Values for mixing parameter used were $\mu \in \{0.1, 0.3, 0.5\}$. And the number of overlapping nodes and the number of communities to which the overlapping node belongs were set to $(on, om) \in \{(0, 0), (30, 3), (30, 5), (90, 3), (90, 5)\}$.

3.2 Proposed methods parameterization

Due to the large number of distinct $k-CT$ components for $k >= 5$, we used only values for parameter $k \in \{3, 4\}$. Since HAC was used, need to specify a maximum distance parameter allowing the components to merge and form communities has to be given.

The proposed experimental methods worked with the levels of termination of the merging of components into communities according to the linkage strategy during component formation. This level is the only parameter except for parameter k, so it was kept as a parameter in our methods and the experimental results are compared according to the specific parameters setting on set of benchmarking networks.

3.3 Experiment evaluation

Because of generated networks with known community structure were used in experiment, it was possible to use external evaluation criteria to assess the quality of various algorithms. For disjoint communities evaluation Normalized Mutual Information(NMI) can be used, expressing the correctness of the inclusion of community nodes in comparison with ground truth communities. However, multiple definition of NMI based measures for evaluating overlapping community structures are known in literature, for this work were selected Overlapping Normalized Mutual Information (ONMI) [3]. Other measure used in this work is traditional data classification measure F1-score [6].

The evaluation metrics achieved high variance for single algorithm evaluation due to the very various networks generated by the rich configurations of input parameters for network generation using LFR framework. For this reason, ranking methods were performed for each of the 60 distinct networks according to certain external evaluation criteria.

Due to the possibility of parameterizing each community detection method, algorithms with multiple different settings were run. All settings of community detection algorithm were evaluated according to the average score by an external criterion and only the best parameters of community detection algorithms were selected for intercomparison with other community detection algorithms.

Figure 1 shows a comparison of the best method settings by ranking according to an external criterion for each network out of 60 benchmark networks. When comparing the detected communities using ONMI, the SLPA algorithm performed the best, while the d_A method with parameter $k = 3$ performed the best among the proposed methods, achieving comparable quality of detected communities in comparison to CPM and DEMON algorithms. When comparing the results of the detected communities by F1 score, the d_C method with parameter $k = 3$ came out the best. The d_S method produced the worst quality of detected communities according to both criteria.

Visualizations interpreting the results of the overlapping community structure detected by the selected algorithms for one of the 60 generated graphs is shown on figure 2.

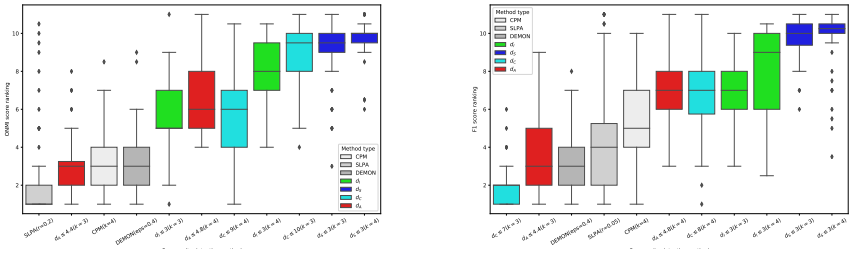

(a) Ranking by ONMI score (b) Ranking by F1 score

Fig. 1: Ranking of community detection algorithms over benchmark of 60 artificially generated networks. Only best configuration of parameters was used for every algorithm selected by external criterion.

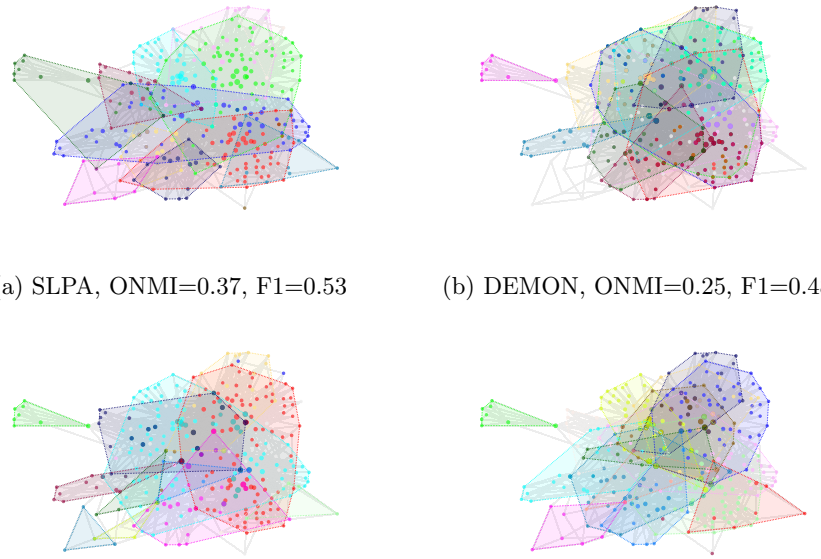

(a) SLPA, ONMI=0.37, F1=0.53 (b) DEMON, ONMI=0.25, F1=0.48

(c) $d_A \leq 4.4$, ONMI=0.31, F1=0.46 (d) $d_C \leq 7$, ONMI=0.34, F1=0.62

Fig. 2: Detected overlapping community structure by the best ranking algorithms for the graph generated using parameters $k = 7, k_{max} = 50, c_{min} = 10, c_{max} = 100, \mu = 0.1, on = 30, om = 5$. In the first row, the community structure is detected by methods from literature and result of proposed methods is visualized in the second row

4 Conclusion and further research

Novel approaches for detecting overlapping communities using $k - CT$ components were defined. The comparable quality of community structure found by the proposed methods using the d_A or d_C strategy in comparison to known algorithms from literature were shown experimentally.

Further research should focus on verifying the feasibility of applying the proposed approach using a case study to real networks. The next part should investigate the strength and quality of the detected overlapping communities also by internal evaluation using conductance or modularity.

References

1. Coscia, M., Rossetti, G., Giannotti, F., Pedreschi, D.: Demon: a local-first discovery method for overlapping communities. In: Proceedings of the 18th ACM SIGKDD international conference on Knowledge discovery and data mining. pp. 615–623 (2012)
2. Fortunato, S., Hric, D.: Community detection in networks: A user guide. Physics Reports **659** (07 2016). https://doi.org/10.1016/j.physrep.2016.09.002
3. McDaid, A.F., Greene, D., Hurley, N.: Normalized mutual information to evaluate overlapping community finding algorithms. arXiv preprint arXiv:1110.2515 (2011)
4. Palla, G., Derényi, I., Farkas, I., Vicsek, T.: Uncovering the overlapping community structure of complex networks in nature and society. nature **435**(7043), 814–818 (2005)
5. Prokop, P., Snasel, V., Dráždilová, P., Platos, J.: Clustering and closure coefficient based on k – ct components. IEEE Access **PP**, 1–1 (05 2020). https://doi.org/10.1109/ACCESS.2020.2998744
6. Rossetti, G., Pappalardo, L., Rinzivillo, S.: A novel approach to evaluate community detection algorithms on ground truth. In: Complex networks VII, pp. 133–144. Springer (2016)
7. Snasel, V., Dráždilová, P., Platos, J.: Closed trail distance in a biconnected graph. PLOS ONE **13**, e0202181 (08 2018). https://doi.org/10.1371/journal.pone.0202181
8. Xie, J., Szymanski, B.K., Liu, X.: Slpa: Uncovering overlapping communities in social networks via a speaker-listener interaction dynamic process. In: 2011 ieee 11th international conference on data mining workshops. pp. 344–349. IEEE (2011)

Comparison of on-the-fly and neural network molecular dynamics

Stanislav Paláček

Department of Applied Mathematics, FEECS,
VSB – Technical University of Ostrava, 17. listopadu 15,
708 00 Ostrava – Poruba, Czech Republic
stanislav.palacek@vsb.cz

Abstract. A full quantum description of the most chemical processes is computationally demanding, therefore many simplifications have to be made in investigation of chemical reactions. In molecular dynamics nuclei are treated as classical objects while electrons are treated quantum mechanically. Within my work I have developed a package of programs called MULTIDYN3.0, which have been implemented using FORTRAN language. In the core of MULTIDYN3.0 multistep and Runge-Kutta methods for integration of ordinary differential equations (i.e. equations of motion) are implemented. Quantum behavior of electrons are modeled with help of external quantum chemistry program for ab-initio calculations, for example MOLPRO [2]. Ab-initio calculations represent the most computational effort. Therefore if the ab initio calculations are performed on the fly during the integration of equation of motions it still takes a large amount of computing time. On the other hand ab initio data can be fitted using neural networks. For this purpose I have also implemented a package for creating and training of neural networks called NEURON4DYN. In the section results I will provide comparison of calculated cross sections of interacting system $N_2 + He^+$ calculated on-the-fly and using neural network potential energy surface.

Keywords: molecular dynamics, ab initio calculations, potential energy surfaces

1 Equations of motion

For more detailed description see for example [1]. In the following text coordinates of electrons will be denoted by $\mathbf{r}$ and coordinates of atomic nucleus by $\mathbf{R}$. M_α denotes mass of atomic nucleus α. $\mathcal{H}_e(\mathbf{r}, \mathbf{R})$ is electronic Hamiltonian, i.e. Hamiltonian that governs the motion of electrons when nuclei are at fixed positions $\mathbf{R}$.

VSB – Technical University of Ostrava, 2021, ISBN 978-80-248-4523-4 (on-line).

In the semiclassical approximation atomic nuclei are treated classically and are described by a classical Hamilton equations of motion

$$\begin{aligned} \frac{d\mathbf{P}_\alpha}{dt} &= -\frac{\partial H_R}{\partial \mathbf{R}_\alpha} = \mathbf{F}_\alpha, \\ \frac{d\mathbf{R}_\alpha}{dt} &= \frac{\partial H_R}{\partial \mathbf{P}_\alpha} = \frac{\mathbf{P}_\alpha}{M_\alpha}. \end{aligned} \tag{1}$$

$\mathbf{P}_\alpha$ denotes momentum of nucleus α, H_R is Hamilton function for classical system of atoms, F_α is force acting on atom α. Electrons are described by time dependent Schrödinger equation

$$\mathcal{H}_r(\mathbf{r}, \mathbf{R}(\mathbf{t}))\phi(\mathbf{r}, t) = i\hbar\frac{\partial}{\partial t}\phi(\mathbf{r}, t). \tag{2}$$

Where $\phi(\mathbf{r}, t)$ is electronic wave function. This wave function can be expanded using a complete orthonormal set (Schauder basis) on the Hilbert state space of electrons $\phi_j(\mathbf{r}, \mathbf{R})$:

$$\phi(\mathbf{r}, t) = \sum_j c_j(t)\phi_j(\mathbf{r}, \mathbf{R}). \tag{3}$$

In general, functions $\phi_j(\mathbf{r}, \mathbf{R})$ are orthonormal with respect to integration over coordinate space of electrons

$$\int \phi_i(\mathbf{r}, \mathbf{R})\phi_j(\mathbf{r}, \mathbf{R})d\mathbf{r} = \delta_{ij}, \tag{4}$$

where δ_{ij} is the Kronecker delta function. There are also defined the following matrix elements:

$$\mathbf{d}_{ij}^{\alpha}(\mathbf{R}) = \int \{\phi_i(\mathbf{r}, \mathbf{R})[\nabla_{R_\alpha}\phi_j(\mathbf{r}, \mathbf{R})]\}d\mathbf{r}, \tag{5}$$

Each of these matrix elements depends on the coordinates of atomic nuclei $\mathbf{R}$. $\mathbf{d}_{ij}(\mathbf{R})$ are called nonadiabatic coupling vector.

In this paper $\phi_j(\mathbf{r}, \mathbf{R})$ will denote adiabatic, in literature also known as Born-Oppenheimer, basis functions. Electronic wave function can be then written as

$$\phi(\mathbf{r}, t) = \sum_j c_j(t)\phi_j(\mathbf{r}, \mathbf{R}). \tag{6}$$

Where c_j denotes adiabatic amplitude of state j and $|c_j|^2$ gives probability of finding system in adiabatic state j. The adiabatic wave functions are defined as eigenfunctions of $\mathcal{H}_e(\mathbf{r}, \mathbf{R})$ for given positions $\mathbf{R}$ of nuclei

$$\mathcal{H}_e(\mathbf{r}, \mathbf{R})\phi_j(\mathbf{r}, \mathbf{R}) = \varepsilon_j(\mathbf{R})\phi_j(\mathbf{r}, \mathbf{R}), \tag{7}$$

where $\varepsilon_j(\mathbf{R})$ is a potential energy surface of adiabatic state j.

If expansion (6) of electronic wave function is inserted into Schrödinger equation of motion for electrons (2), multiplied from left by $\phi_i(\mathbf{r}, \mathbf{R})$ and integrated over the space of electrons coordinates $\mathbf{r}$, the folowing equations is obtained

$$\dot{c}_j = -\frac{i}{\hbar}\varepsilon_j c_j - \sum_{i\alpha} c_i \dot{\mathbf{R}}_\alpha \mathbf{d}^\alpha_{ji}(\mathbf{R}). \tag{8}$$

Forces which act on atoms can be obtained using Hellmann-Feynman [3] theorem

$$\mathbf{F}_\alpha = -\sum_i |c_i|^2 \nabla_\alpha \varepsilon_i + \sum_{i \neq j} c_i^* c_j (\varepsilon_j - \varepsilon_i) \mathbf{d}^\alpha_{ji}. \tag{9}$$

The first term in equation (9) is weighted average of forces of all adiabatic states and the second term takes into account quantum forces sesulting from nonadiabatic transitions in the electronic subsystem.

2 Artificial neural networks

Artificial neural networks (ANN) are computing systems inspired by the biological neural networks that form brains. Such systems are learned on examples without a need of programming any task specific rules. ANNs have found many applications. Typically they are widely used in an image recognition.

Basic units of such ANNs are nodes commonly called neurons. An artificial neuron has several inputs and only one output. Mathematically it can be described by equation:

$$y = \phi(\sum_{j=1}^{n} w_j x_j + b), \tag{10}$$

where $x_1, ..., x_n$ are the input signals, $w_1, ..., w_n$ are the synaptic weights of the neuron, b is the bias, ϕ is the activation function, y is the output signal of the neuron. Activation function $\phi : \mathbb{R} \to \mathbb{R}$, also referred to as transition function define the output of a neuron. There exist several types of activation functions. Most widely in output neurons are used identity function:

$$\phi(x) = x \tag{11}$$

and in internal neurons are used sigmoid function:

$$\phi(x) = \frac{1}{1 + e^{-x}}. \tag{12}$$

There exist a lot of ways how to interconnect neurons in ANNs, however feedforward neural networks (FFNN) are very typical. Neurons are grouped into layers and signals travel from the first layer (the input layer) to the last layer (the output layer). Each neuron from the current layer is connected with each neuron of the next forward layer. Shortly ANN can be defined as high dimensional function.

3 Learning algorithms

A scalar cost function E is very important in learning of any neural network, it gives us measure how good or bad the prediction of neural network is in comparison with the expected value. Ideally, we want the cost function to be zero. In learning process weights and biases of a neural network are gradually adjusted until good predictions are obtained.

Backpropagation followed by a gradient descent method, [9] chapter 7, is basic and most widely used learning algorithm of neural networks. In my application I have decided to use algorithm call global extended Kalman filter (GEKF). More detailed description of this algorithm can be found in [10] and more general informations about Kalman filters can be found in [11]. GEKF training algorithm as is given in [10] is based on the following recursion formulas:

$$\mathbf{K}_k = \lambda^{-1}\mathbf{P}_{k-1}\mathbf{H}_k[\mathbf{I} + \lambda^{-1}\mathbf{H}_k^T\mathbf{P}_{k-1}\mathbf{H}_k]^{-1} \tag{13}$$

$$\mathbf{P}_k = \lambda^{-1}\mathbf{P}_{k-1} - \lambda^{-1}\mathbf{K}_k\mathbf{H}_k^T\mathbf{P}_{k-1} + \mathbf{Q}_k \tag{14}$$

$$\mathbf{w}_k = \mathbf{w}_{k-1} + \mathbf{K}_k\boldsymbol{\xi}_k \tag{15}$$

Vector $\mathbf{w}_k$ represents the estimate of the parameters of a neural network at step k. Symbol $\mathbf{K}_k$ is the Kalman gain matrix, and $\boldsymbol{\xi}_k = \mathbf{y}_k - \hat{\mathbf{y}}_k$ is an error vector. Here $\mathbf{y}_k$ is the target output vector and $\hat{\mathbf{y}}_k$ is the output of the network. Symbol $\mathbf{P}_k$ represents an approximate error covariance matrix, $\mathbf{H}_k$ is a matrix of derivatives of the network outputs with respect to all trainable parameters. $\mathbf{Q}_k$ is the process noise covariance matrix. This algorithm attempts to find parameters of NN which minimize a cost function written in the form of $\sum_{p=1}^{k} \boldsymbol{\xi_k}^T \boldsymbol{\xi_k} \lambda^{k-p}$.

4 Representation of PES by NN

In a representation of potential energy surface (PES) by neural networks symmetries of a system must be properly taken into account. There exist many approaches to do so. Translation and rotation symmetry can be simply incorporated by a proper choice of some internal coordinates. Another problem is the incorporation of permutation symmetries, i.e. the invariance of the potential energy surface with respect to the permutation of identical particles. To do so it is convenient to use method called Fundamental Invariants (FI) [14] which were inspired by Permutation Invariant Polynomials (PIP) [12],[13]. In the FI neural network fitting approach a subset of invariant polynomials (known as fundamental invariants) is used as the input vector to the network. FI contain the least number of invariants which can generate all the invariant polynomials [15],[16]. Mathematical background of fundamental invariants was developed decades ago. The fundamental invariants can be calculated with Kings's algorithm [17] using computer program called Singular [18].

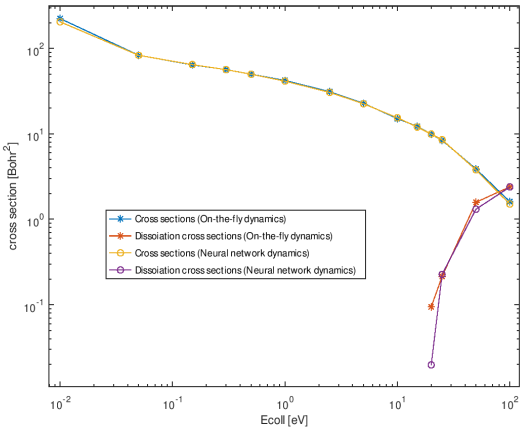

Fig. 1. Comparison of cross sections calculated using on-the-fly dynamics and neural network dynamics.

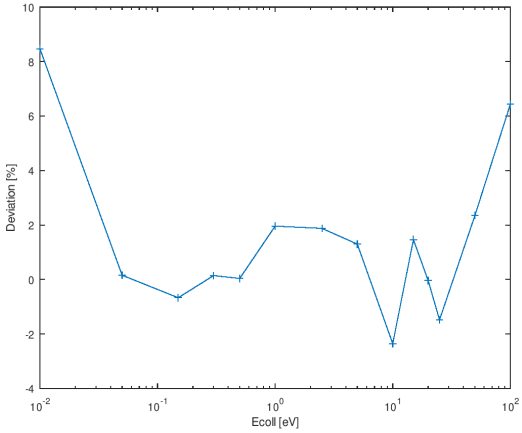

Fig. 2. Deviation in percentage between cross sections obtained on-the-fly and by neural network dynamics.

5 Results

On the figure 1 and 2 we can see comparison between cross sections obtained by direct on the fly dynamics with neural network dynamics. Results from both approaches are consistent, deviations between both approaches expressed in percentages are mostly below two percent except for the lowest and highest collision energies were it goes up to eight and six percent respectively.

References

1. *Moddern Methods for multidimensional Dynamics Computations in Chemistry*, J.C. Tully, *Nonadiabatic Dynamics*, 1998, World Scientific
2. MOLPRO, version 2019.2, a package of ab initio programs, H.-J. Werner, P. J. Knowles, G. Knizia, F. R. Manby, M. Schütz, and others , see https://www.molpro.net.
3. *Quantum Simulations of Complex Many-Body Systems: From Theory to Algorithms*, N.L. Doltsinis, *Nonadiabatic Dynamics: Mean-Field and Surface Hopping*, 2002, 1st ed. Jülich: NIC-Secretariat
4. Cramer, Christopher J. Essentials of computational chemistry: theories and models. West Sussex, England, New York: J. Wiley, 2002.
5. Glover, W.J., 2014. Communication: Smoothing out excited-state dynamics: Analytical gradients for dynamically weighted complete active space self-consistent field. The Journal of Chemical Physics 141, 171102. https://doi.org/10.1063/1.4901328
6. Balázs Csanád Csáji: Approximation with Artificial Neural Networks (2001)
7. Cybenko, G.: Approximations by superpositions of sigmoidal functions (1989)
8. Kurt Hornik: Approximation Capabilities of Multilayer Feedforward Networks (1991)
9. Raul Rojas: Neural Networks - A Systematic Introduction, Springer-Verlag, Berlin, New-York, (1996), http://page.mi.fu-berlin.de/rojas/neural/index.html.html
10. T. B. Blank and S. D. Brown: Adaptive, global, extended Kalman filters for training feedforward neural networks, Journal of Chemometrics, vol. 8, no. 6, pp. 391–407, (1994)
11. Haykin, Simon S., ed. 2001: Kalman Filtering and Neural Networks. Adaptive and Learning Systems for Signal Processing, Communications, and Control. New York: Wiley.
12. Jiang, Bin, and Hua Guo: Permutation Invariant Polynomial Neural Network Approach to Fitting Potential Energy Surfaces. III. Molecule-Surface Interactions. The Journal of Chemical Physics 141 (3): 034109. (2014) https://doi.org/10.1063/1.4887363.
13. Z. Xie and J. M. Bowman: Permutationally Invariant Polynomial Basis for Molecular Energy Surface Fitting via Monomial Symmetrization, Journal of Chemical Theory and Computation, vol. 6, no. 1, pp. 26–34, Jan. (2010).
14. K. Shao, J. Chen, Z. Zhao, and D. H. Zhang: Communication: Fitting potential energy surfaces with fundamental invariant neural network, J. Chem. Phys., vol. 145, no. 7, p. 071101, Aug. 2016.
15. H. Derksen a G. Kemper: Computational Invariant Theory. Berlin, Heidelberg: Springer Berlin Heidelberg, (2015)
16. R. P. Stanley, Invariants of finite groups and their applications to combinatorics, Bulletin of the American Mathematical Society, vol. 1, no. 3, pp. 475–512, May 1979.
17. King, Simon A.: Minimal Generating Sets of Non-Modular Invariant Rings of Finite Groups. Journal of Symbolic Computation 48 (January): 101–9. (2013) https://doi.org/10.1016/j.jsc.2012.05.002.
18. Decker, W.; Greuel, G.-M.; Pfister, G.; Schönemann, H.: SINGULAR 4-1-2 — A computer algebra system for polynomial computations. http://www.singular.uni-kl.de (2019).

Comments on Techniques Related to Estimating Number of Groups for Spectral Clustering

Marek Pecha and David Horák

Department of Applied Mathematics, FEECS,
VSB – Technical University of Ostrava, 17. listopadu 15,
708 00 Ostrava – Poruba, Czech Republic
marek.pecha@vsb.cz

Abstract. Determining the number of groups or dimension of a feature space related to an initial dataset projected to null-space of the Laplace type operators is a fundamental problem of applications exploiting a spectral clustering techniques. This contribution provides theoretical extensions and comments to estimating it using the Bartlett's test.

Keywords: spectral clustering; Bartlett test; nullity; Laplace-type operators

1 Introduction

We introduce a part of an ongoing research focused on cluster analysis with application of 2-phase image segmentation in this contribution. Presented results arised during international cooperation with Bulgarian Academy of Sciences, in particular with Stanislav Harizanov and Svetozar Margenov, and are summarized in [3]. The software module called speclus4py that implements published techniques related to spectral clustering is distributed as a conda package[1] under the 3-Clause BSD License.

A bottom line of the spectral clustering methods is geometrically based on assuming that the initial set X is sampled from a (Riemannian) manifold Ω containing multiple connected components forming non-overlapping parts of the domain. In a traditional approach related to spectral clustering, vectors belonging to the initial set X are projected onto the null space $\mathrm{Null}(\boldsymbol{L})$ of the Laplace-Beltrami-type operator $\boldsymbol{L} \in \mathbb{R}^{n \times n}$. A dimension of the appropriate $\mathrm{Null}(\boldsymbol{L})$ is equal to:

$$\dim \mathrm{Null}(\boldsymbol{L}) = \alpha(\Omega)\,, \tag{1}$$

where $\alpha(\Omega)$ denotes an algebraic connectivity associated with the underlying graph G_Ω capturing geometry of the discretized manifold Ω. Then, such transformed samples are clustered, e.g. by applying vector quantification techniques namely k-means or k-means+. In many practical applications employing the spectral clustering, one assumes that an actual number of clusters k^* follows:

$$k^* = \dim \mathrm{Null}(\boldsymbol{L}). \tag{2}$$

[1] https://anaconda.org/ml4py/speclus4py

The last step of spectral clustering is commonly based on the vector quantification using the k-means-type algorithms. Related underlying model is a form of the Gaussian mixture model constrained to hard assignments, equal mixture weights, spherical covariance matrices associated with the clusters. Therefore, k^* could be estimated such that it minimizes the Bayesian or Akaike information criterion. While features of the projected samples are basically relaxed indicator vectors of clusters, this works well, when we consider the equality (2). However, this minimization could be unclear, when a priori known $k^* < \dim \mathrm{Null}(\boldsymbol{L})$. This is a case of 2-phase image segmentation, for example. Thus, it is reasonable to determine $\dim \mathrm{Null}(\boldsymbol{L})$ for general purposes.

A numerical approach to determine the nullity of any operator can be done by exploiting the transformation to the row canonical form. Unfortunately, the complexity $O(n^3)$ associated with this approach induces a computational overhead. Another type of numerical-based approach was proposed by Zelnik and Perona [4], which reconstructs indicator vectors of clusters $\boldsymbol{Z}$ from features of projected samples by their rotations. Since we do not consider the equality (2) in general, we do not need this original reconstruction.

Equivalently, determining a dimension of an operator null-space corresponds to estimating multiplicity of its zero eigenvalues. It can be done empirically or monitoring eigengap between the smallest and rest of eigenvalues by analyzing a variation rate using the scree test. It seeks an inflexion point of the eigenvalue profile. However, this profile can have multiple inflexions in case of real-world data, which makes the test unreliable in practice. Thus, it is better to focus on homoscedasticity (equality of variances) of the k smallest eigenvalues instead of analyzing the second derivative of the scree plot.

2 Estimator of $k^* = \dim \mathrm{Null}(\boldsymbol{L})$

Testing equality of variances among eigenvalues was firstly proposed by Bartlett [1] in the context of estimating the number of factors associated with the q largest eigenvalues of the covariance matrix $\boldsymbol{\Sigma} \in \mathbb{R}^{n \times n}$, which are suitable to retain in the sense of PCA. The standard Bartlett test formulates the null-hypothesis H_0 that k eigenvalues associated with unselected eigenvectors of $\boldsymbol{\Sigma}$ have a small magnitude and small variance. Assuming this, taking the likelihood ratio statistic $V_k = \prod_{i=q+1}^{d} \lambda_i / \bar{\lambda}_k$, $d = k + q$, $\bar{\lambda}_k = \frac{1}{k} \sum_{i=q+1}^{d} \lambda_i$, and linkage factors into account, the statistic T defined as

$$
\begin{aligned}
F &= \left(n - q - \frac{k^2 + 1}{3k} - \frac{1}{6} + \sum_{i=1}^{q} \frac{\bar{\lambda}_k^2}{\left(\lambda_i - \bar{\lambda}_k\right)^2} \right), \\
T &= -F \ln V_k,
\end{aligned}
\tag{3}
$$

follows χ^2 distribution with $\frac{1}{2}(k-1)(k+2)$ degrees of freedom. Principle of the test is to find the smallest acceptable a value of q so that $P(X < T) \leq 1 - \alpha_{crit}$, where α_{crit} is a significance level.

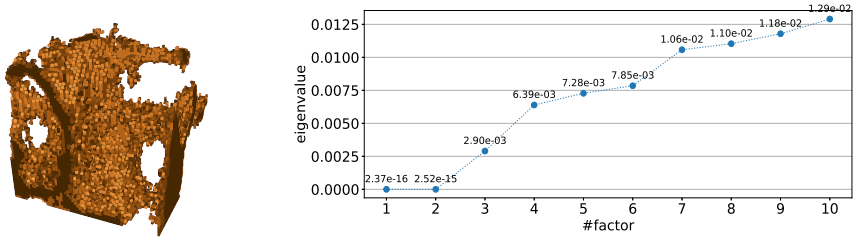

Fig. 1: From left: a visualization of a trabecular bone 3D model depicted on the left side, an example of a horizontal slice associated with an underlying volumetric image, dimensions are $65 \times 65 \times 65$, a profile of the first 10 eigenvalues associated with the 3D unnormalized Laplacian.

From a concept point of view, we can straightforwardly see similarities between the spectral clustering and PCA. Both involve eigen decomposition of the square commonly symmetric matrix, however locations of relevant information are associated with opposite parts of spectra. This arises from the fact that the Laplacian matrix is considered as the scaled precision matrix $\boldsymbol{Q}$, which is pseudoinverse of covariance matrix:

$$\boldsymbol{L} = \delta \boldsymbol{Q} = \boldsymbol{\Sigma}^{\dagger}, \tag{4}$$

when an underlying model is a form of the Gaussian Markov Random Field model. By $\boldsymbol{L}$ and related underlying graph G, we basically model a reversed Karhunen-Loeve stochastic process.

Since, $\boldsymbol{\Sigma}$ measures dispersion data around mean, $\boldsymbol{L}$ is considered as precision measurement and displays how data are well-clustered. Hence, Laplace-Beltrami-type operators are suitable for problems containing data clustering. Consequently, the eigenvalues of $\boldsymbol{L}$ are reciprocal eigenvalues of $\boldsymbol{\Sigma}$ in the sense of pseudoinverse. Further, inverting variables change only a distribution shape, not its type. Thus, we can exploit $T \sim \chi^2$ for testing homoscedasticity of the smallest eigenvalues of $\boldsymbol{L}$, ergo estimating $\dim \mathrm{Null}(\boldsymbol{L})$. Such idea was firstly proposed by Bruneau et al. in [2].

Table 1: Comparison of Bartlett's et al. test statistic (tstat. type 1) and test statistic proposed by Bruneau et al. (tstat. type 2) on benchmark illustrated in Figure 1.

Dataset	tstat. type	df	tstat. value	p-value	H_0
Bone	1	2	0.00	0.00	accepted
	2		0.19	0.09	rejected

Indifference of the original works by Bartlett [1], they use slightly modified a test statistic T, where the addend $-\frac{1}{6}$ in F (3) is avoided. We can observe that

a such modified test statistic is more sensitive to numerical errors going from eigensolvers than the original one (3).

We demonstrate this on trabecular bone dataset, see Figure 1. For computing eigensystem, we employed ARPACK implementation of the Lanczos method called from the SLEPc framework. We set relative tolerance $rtol = 0.1$ to obtain low-precision results, which are typical in case of machine learning. Since related underlying volumetric image consists of two values, specifically 0 (*air*) and 255 (*bone*), we try to model an elemental 2-phase volumetric segmentation so that $k^* = 2$. For constructing the unnormalized $\boldsymbol{L}$, 26 nearest local neighbours (*knn*) were used to capture better a mesh-geometry. For statistical estimation of the null-space dimension, we exploit the original test statistic (tstat. type 1) and the modified one proposed by Bruneau et al. (tstat. type 2) such that we formulate H_0 that the first 2 of 10 computed eigenvalues (in ascending order) have equal variance.

Analysing results in Table 1, we can see, p-value associated with the original test statistic (3) is exactly 0. Thus, we accept H_0 at all significance levels. While the hypothesis test using the modified one provided p-value 0.09, we reject H_0 at all standard significance levels.

Algorithm 1: EigenvalsPostprocess

Input : $\boldsymbol{\Lambda}$, $\boldsymbol{err}$

for $i = 1 \rightarrow d$ **do**
  if $err_i \geq 1.$ **then**
    break;
  $exp \leftarrow \text{Floor}\left(\log_{10}\left(err_i\right)\right)$;
  $\widehat{\lambda}_i \leftarrow \text{Round}\left(\lambda_i, -1 * exp\right)$;
  if $\widehat{\lambda}_i = 0$ **then**
    $\widehat{\lambda}_i \leftarrow \text{Pow}\left(10, exp\right)$;
    if $\lambda_i < 0$ **then**
      $\widehat{\lambda}_i \leftarrow -\widehat{\lambda}_i$;

Output: $\widehat{\boldsymbol{\Lambda}} = \text{diag}\left(\widehat{\lambda}_1, \widehat{\lambda}_2, \ldots, \widehat{\lambda}_d\right)$

Programmers of speccalt[2] try to overcome this issue by considering values lower than 1e−12 as value exactly equals to 1e−12. From the perturbation theory, we know that eigengap is inversely proportional to perturbation related to $\boldsymbol{L}$. Thus, value 1e−12 could be some extremely small value and could not be associated with an exact 0 for some real-world application. A more proper way to solve this numerical issue could be rounding decimal places affected by numerical errors that their locations are determined by means of absolute errors of solution. This post-processing approach is outlined in Algorithm 1.

[2] `https://cran.r-project.org/web/packages/speccalt/index.html`

Another common issue goes from rounding-off errors caused by limits of floating-point arithmetic. Eigensolver could return some small negative eigenvalues very close to 0 even if $\boldsymbol{L}$ is a symmetric positive definite matrix. By similar comments as in the previous case, we cannot implicitly consider these eigenvalues as 0. On the other side, comparing negative eigenvalues causes non-defined value related to (3), specifically in the term $\ln V_k$. Since the test is based on analysing variances among eigenvalues, we can shift them to be positive without loss of generality so that

$$\hat{\lambda}_i = \lambda_i + 2|\lambda_0|. \tag{5}$$

Considering presented remarks and observations, we can finally introduce a technique for estimating a number of clusters k^* summarized in Algorithm 2; the algorithm returns a basis of related null-space $\boldsymbol{BV}$ as well.

Algorithm 2: ESTIMATOR OF $k^* = \dim \mathrm{Null}(\boldsymbol{L})$

Input : $X = \{\boldsymbol{x}_1, \boldsymbol{x}_2, \ldots, \boldsymbol{x}_n\}$, $\sigma \in \mathbb{R}^+$, type = {un, sym, rw}, knn, α_{crit}

$\boldsymbol{L} \leftarrow$ CONSTRUCTGRAPHLAPLACIAN (X, knn, σ);
if *type = sym* **then**
  $\boldsymbol{L} \leftarrow \boldsymbol{D}^{-\frac{1}{2}} \boldsymbol{L} \boldsymbol{D}^{-\frac{1}{2}}$;
else if *type = rw* **then**
  $\boldsymbol{L} \leftarrow \boldsymbol{D}^{-1} \boldsymbol{L}$
/* Find the first d eigenpairs */
$\boldsymbol{L} = \boldsymbol{E} \boldsymbol{\Lambda} \boldsymbol{E}^{-1}$;
Determine absolute errors of eigenpairs $\boldsymbol{err}$;
$\boldsymbol{\Lambda} \leftarrow$ EIGENVALSPOSTPROCESS $(\boldsymbol{\Lambda}, \boldsymbol{err})$;
if $\boldsymbol{\Lambda}$ *contains negative values* **then**
  /* Shift eigenvalues */
  $\boldsymbol{\Lambda} \leftarrow (5)$;
for $k = 2 \rightarrow d$ **do**
  $\bar{\lambda}_k \leftarrow \frac{1}{k} \sum_{i=1}^{k} \lambda_i$;
  $F \leftarrow k - 1 - \frac{2*k^2+k+2}{6k} + \sum_{i=k+1}^{d} \frac{\bar{\lambda}_k}{\lambda_i - \bar{\lambda}_k}$;
  $V_k \leftarrow \prod_{i=1}^{k} \lambda_i / \bar{\lambda}_k$;
  $df = \frac{1}{2}(k-1)(k+2)$;
  if $P_{\chi^2_{df}}(X < -F \ln(V_k)) > 1 - \alpha_{crit}$ **then**
    $k^* \leftarrow k - 1$;
    $\boldsymbol{BV} \leftarrow \{e_1, \ldots, e_{k^*}\}$;
    break;

Output: k^*, $\boldsymbol{BV}$

3 Concluding comments

The original Barlett test [1] requires sorted eigenvalues. Conventional eigensolvers typically return sorted eigenvalues in ascending order. Nevertheless, the

smallest ones could oscillate around 0, when we set a target eigenvalue around which the spectrum is being computed. In our case, it can be suitable to choose an exact 0 value as this target. Since Algorithm 2 tests homoscedasticity of the smallest eigenvalues, it works for unsorted sufficiently small non-negative eigenvalues such that the last ones are significantly different. However, an issue could occur when positive and negative values alternate. Then, the proposed transformation (5) could not shift all eigenvalues to be positive and evaluating natural logarithm could fail. In this case, we propose to sort eigenvalues in ascending order before their postprocessing to avoid this issue related to evaluating a test statistic (3).

Occasionally, an eigensolver could attain some eigenvalues equal to exact 0, which causes an issue related to evaluating a test statistic (3) due to V_k term again. There could be two approaches on how to overcome this issue. A convenient way can be substituting the zero by a similar approach as this outlined in the Algorithm 1. Using an absolute numerical error related to a particular eigenpair, we can estimate the possible exact zero value as follows:

$$0 \approx \textsc{Pow}\left(10, \textsc{Floor}\left(\log_{10}\left(err_i\right)\right)\right). \tag{6}$$

The last issue, which could arise, is connected with computing a product of fractions $\lambda_i/\bar{\lambda}_k$ related to the term V_k. Suppose a variance among the first k eigenvalues is sufficiently small. In that case, we divide small numbers of a relatively similar order, then the product of this sequence typically goes to a number $\gg 0$. An actual value depends on the tolerance of an eigensolver, a numerical error related to result, etc. However, the issue could arise when a gap between k and $k+1$ eigenvalue is significantly large. Then, the first k fractions are $\ll 1$ and their product goes to 0, or more precisely, it goes the smallest normal floating point number, i.e. the smallest usable number. When, we multiply this small number by another sufficiently small number, the result underflows and we obtain numerically exact 0 that, again, causes an issue with evaluating natural logarithm in the test statistics. Thus, we can additionally check if a current multiplication does not result in 0 during computation of the product. If it does, we can substitute the result by the smallest normal floating point number. An application that exploits proposed approach is demostrated in a preprint [3].

References

1. Bartlett, M.S.: Properties of sufficiency and statistical tests. Proceedings of the Royal Society of London. Series A - Mathematical and Physical Sciences **160**(901), 268–282 (may 1937). https://doi.org/10.1098/rspa.1937.0109
2. Bruneau, P., Parisot, O., Otjacques, B.: A heuristic for the automatic parametrization of the spectral clustering algorithm. In: 2014 22nd International Conference on Pattern Recognition. pp. 1313–1318 (2014). https://doi.org/10.1109/ICPR.2014.235
3. Pecha, M.: General Technique for Estimating Number of Groups for Spectral Clustering (2021). https://doi.org/10.36227/techrxiv.13553705.v1, Preprint
4. Zelnik-manor, L., Perona, P.: Self-tuning spectral clustering. In: Saul, L.K., Weiss, Y., Bottou, L. (eds.) Advances in Neural Information Processing Systems 17, pp. 1601–1608. MIT Press (2005)

Coding Systems for Ordinal Variables – Problems and Possibilities

Adéla Vrtková

Department of Applied Mathematics, FEECS,
VSB – Technical University of Ostrava, 17. listopadu 15,
708 00 Ostrava – Poruba, Czech Republic
adela.vrtkova@vsb.cz

Abstract. Ordinal variables are a special type of categorical variables whose categories are naturally ordered. Its nature which is on the border of nominal variables and numerical variables requires a suitable coding system or, preferably, a suitable adaptation of an applied algorithm. In this paper, several lesser-known coding systems for ordinal variables are discussed and a brief summary of adaptations of well-known classification algorithms towards utilization of ordinal variables is provided.

Keywords: ordinal variable, coding system, rank-hot encoding, Helmert coding, forward difference coding, backward difference coding

1 Motivation

Our previous research has been focused on various aspects of solving classification problems - exploring different classification algorithms, methods for variable selection and also possibility of application of the classification algorithms on a very special type of data - compositional data. However, adaptations of the algorithms towards utilization of ordinal variables as both independent and dependent variables have not been explored enough yet.

A possible adaptation can start with a proper choice of a coding system. Ordinal variables are a special type of categorical variables whose categories are naturally ordered. Unlike nominal variables (categorical variable with unordered categories), encoding ordinal variables is a bigger challenge. Treating ordinal variables as nominal variables results in information loss - the information about the order of the categories is ignored. On the other hand, treating ordinal variables as numerical (continuous) variables assumes the variable to be measured on a metric scale.

Some traditional methods, such as the logistic regression or the ordinal logistic regression, are well established, directly adapted for the nominal or ordinal response variable, so technically, the main subject of discussion lies in application of different coding systems only for independent variables. On the other hand, in the field of neural networks research, different studies aiming for their

VSB – Technical University of Ostrava, 2021, ISBN 978-80-248-4523-4 (on-line).

adaptation towards the utilization of ordinal variables have been published with significantly different approaches and strategies, these studies will be discussed later in the paper.

Therefore, the paper summarizes several lesser-known coding systems for ordinal variables. Simultaneously, it discusses related problems, advantages and further possibilities. A short overview of adaptations of well-known classification algorithms towards utilization of ordinal variables is also given.

2 Coding Systems

One of the most popular coding systems for categorical variables in general is *One-Hot encoding* which transforms one categorical variable with K classes to K binary variables. Each new variable (also called dummy variable) indicates belonging to one of the original classes. Technically, only $K - 1$ variables are sufficient because belonging to one chosen class could be represented with zeros in all $K - 1$ dummy variables. The latter is preferable because using K dummy variables as representation of a categorical variable with K classes leads to *the dummy variable trap* - presence of redundancies and severe multicollinearity.

Described system is extremely useful for nominal variables. It is highly inappropriate for ordinal variables, unfortunately, there are still tutorials and publications ignoring this fact. Let's summarize several coding systems which are more appropriate for ordinal variables.

2.1 Rank-Hot Encoding

A coding system Rank-Hot encoding can be perceived as a modification of above-described One-Hot encoding [9]. This method is commonly suggested in questions and answers websites for programmers. However, it doesn't have a fixed name. The encoding is slightly different to One-Hot encoding but both create $K - 1$ new binary variables (for an ordinal variable with K levels). A category which is ranked as the "lowest" is expressed with zeros in all new variables. Then the number one is assigned to each level up to and including the level which is actually assigned to a particular unit.

The difference between One-Hot and Rank-Hot encoding is shown in Table 1 using a typical example of an ordinal variable from a field of biomedicine which is a rating system of patient's clinical status - no symptoms, minor, moderate, severe. In the example, three new binary variables are created as replacement for the original ordinal variable with four levels.

The advantage of the system is its simplicity and the fact that it actually somehow integrates the ordinal nature of the variable. Also, it does not assume anything about the "distance" between levels. However, the system might be rather problematic with regression models (a reader might think about the interpretation of corresponding regression coefficients) and may be more suitable for machine learning algorithms.

Table 1: Demonstration of One-Hot and Rank-Hot encoding

Rating	**One-Hot**	**Rank-Hot**
no symptoms	[0, 0, 0]	[0, 0, 0]
mild	[1, 0, 0]	[1, 0, 0]
moderate	[0, 1, 0]	[1, 1, 0]
severe	[0, 0, 1]	[1, 1, 1]

2.2 Helmert Coding

Helmert coding also creates $K-1$ new variables as replacement for an ordinal variable with K levels. However, the new variables are not binary. Consider an ordinal variable with K levels which is replaced with $K-1$ variables, z_{ji} stands for the value of the j-th observation in the i-th new variable, $i = 1, ..., K-1$. Helmert coding is given as follows [1, 13, 15]:

$$z_{ji} = \begin{cases} -\frac{1}{K-i+1}, & \text{if } j\text{-th observation belongs to the } l\text{-th level,} \\ & \text{where } i < l,\ l = 2, ..., K-1, \\ 1 - \frac{1}{K-i+1}, & \text{if } j\text{-th observation belongs to the } i\text{-th level,} \\ 0, & \text{if } j\text{-th observation belongs to the } s\text{-th level,} \\ & \text{where } s < i,\ s = 1, ..., K-1. \end{cases}$$

When applied on the independent variables in regression models, the obtained corresponding regression coefficients can be interpreted within the meaning of the comparison of the mean of dependent variable of each level to the mean of dependent variable for all subsequent levels, eventually, for logistic regression, within the meaning of the comparison of the odds for a modelled event for each level to the geometric mean of odds for a modelled event of all subsequent levels. The system can be also used with other machine learning methods. However, from our available literature, application outside of regression models seems to be rather marginal.

2.3 Forward and Backward Difference Coding

Analogously to the previous system, the forward and backward difference coding lead to creation of $K-1$ new variables which generally are not binary as replacement for an ordinal variable with K levels. The forward difference coding is given as follows:

$$z_{ji} = \begin{cases} -\frac{i}{K}, & \text{if } j\text{-th observation belongs to the } l\text{-th level,} \\ & \text{where } i < l,\ l = 2, ..., K-1, \\ 1 - \frac{i}{K}, & \text{if } j\text{-th observation belongs to the } i\text{-th level,} \\ 1 - \frac{i}{K}, & \text{if } j\text{-th observation belongs to the } s\text{-th level,} \\ & \text{where } s < i,\ s = 1, ..., K-1, \end{cases}$$

and the backward difference coding is given as follows:

$$z_{ji} = \begin{cases} \frac{i}{K}, & \text{if } j\text{-th observation belongs to the } l\text{-th level,} \\ & \text{where } i < l,\ l = 2, ..., K-1, \\ -(1-\frac{i}{K}), & \text{if } j\text{-th observation belongs to the } i\text{-th level,} \\ -(1-\frac{i}{K}), & \text{if } j\text{-th observation belongs to the } s\text{-th level,} \\ & \text{where } s < i,\ s = 1, ..., K-1, \end{cases}$$

where z_{ji} was defined in the previous subsection [1, 13, 15].

When applied on the independent variables in regression models, the obtained corresponding regression coefficients can be interpreted within the meaning of the comparison of the mean of dependent variable of each level to the mean of dependent variable of the next (forward) or prior (backward) level, eventually, for logistic regression, within the meaning of the comparison of the odds for a modelled event for each level to the odds for a modelled event of the next (forward) or prior (backward) level. Its application with regression models and other machine learning methods is analogous to the Helmert coding.

3 Discussion and future work

Various coding systems (for both nominal and ordinal variables) are commonly associated with encoding independent variables for regression models where the choice of the coding system directly affects the interpretation of the obtained regression coefficients and their amount. Therefore, it is important to consider the final interpretation of the coefficients before the selection of a coding system. The advantage of the regression models (namely logistic regression and ordinal logistic regression [2]) is that it is not necessary to encode the dependent nominal or ordinal variable because they don't model the variable directly but they work rather through related probability and odds. With a proper choice of coding systems for independent variables, the nature of all included variables is fully respected. Although there are many variations of regression models (non-linear, robust, etc.), real-life problems could require application of more complex models.

As mentioned before, from our available literature, there are many different approaches and strategies for adaptation of neural networks towards utilization of ordinal variables. Some of them deal with ordinal variables in a role of input variables, some of them focus on an ordinal variable only in a role of the output variable. For example, authors in [3] focused only on the ordinal target variable in neural networks and suggested application of suitable encoding (Rank-Hot encoding) of the variable with a proper choice of link functions. Authors in [10] published a comparative study of using different coding systems (including Helmert and Backward difference coding) for input and outputs variables in neural networks. However, the authors didn't distinguish nominal and ordinal variables in the discussion and they treated them equally. Due to the variety of strategies whose performance usually depends on the analysed dataset,

a researcher might consider application of different classification methods whose adaptations towards utilization of ordinal variables are more straightforward and generally are more transparent and interpretable.

The last discussed widely-used classification algorithm is the random forests algorithm. Recently, there have been a significant development in adaptation of the random forests. For example, authors in [14] suggested implementation of fuzzification to convert ordinal variables into numbers by the means of user-informed approach and demonstrated its application with the random forests, the LASSO regression or the support vector machines. The paper directly addressed the problem with the representation of the ordinal variables in machine learning algorithms. A concept of ordinal forests was published in [5] which is a method based on random forests for an ordinal dependent variable, the method has already been implemented in R package [6].

For future work, we would like to continue in the research related to classification algorithms and the medical data analysis which is the crucial supporting part of the prepared dissertation, so far, several articles have been published related to this topic [11,12,16,17]. Other scientific cooperation also continues with the University Hospital Ostrava which resulted in several publications [4,7,8].

Acknowledgement

The author acknowledges the support of VSB - Technical University of Ostrava (Project No. SP2021/103).

References

1. R library contrast coding systems for categorical variables, https://stats.idre.ucla.edu/r/library/r-library-contrast-coding-systems-for-categorical-variables/
2. Agresti, A.: Categorical data analysis. 3rd edn, 752 (2019)
3. Cheng, J., Wang, Z., Pollastri, G.: A neural network approach to ordinal regression. In: 2008 IEEE international joint conference on neural networks (IEEE world congress on computational intelligence). pp. 1279–1284. IEEE (2008)
4. Formánek, M., Formánková, D., Hurník, P., Vrtková, A., Komínek, P.: Epstein-barr virus may contribute to the pathogenesis of adult-onset recurrent respiratory papillomatosis: A preliminary study. Clinical Otolaryngology 46(2), 373–379 (2021)
5. Hornung, R.: Ordinal forests. Journal of Classification 37(1), 4–17 (2020)
6. Hornung, R.: ordinalForest: Ordinal Forests: Prediction and Variable Ranking with Ordinal Target Variables (2021), https://CRAN.R-project.org/package=ordinalForest, r package version 2.4-2
7. Jaluvka, F., Ihnat, P., Madaric, J., Vrtkova, A., Janosek, J., Prochazka, V.: Current status of cell-based therapy in patients with critical limb ischemia. International journal of molecular sciences 21(23), 8999 (2020)
8. Khismatullin, R.R., Nagaswami, C., Shakirova, A.Z., Vrtková, A., Procházka, V., Gumulec, J., Mačák, J., Litvinov, R.I., Weisel, J.W.: Quantitative morphology of cerebral thrombi related to intravital contraction and clinical features of ischemic stroke. Stroke 51(12), 3640–3650 (2020)

9. Lowe, S.C.: Rank-hot encoder for ordinal features, https://scottclowe.com/2016-03-05-rank-hot-encoder/
10. Potdar, K., Pardawala, T.S., Pai, C.D.: A comparative study of categorical variable encoding techniques for neural network classifiers. International journal of computer applications 175(4), 7–9 (2017)
11. Procházka, V., Jonszta, T., Czerny, D., Krajca, J., Roubec, M., Hurtikova, E., Urbanec, R., Streitová, D., Pavliska, L., Vrtkova, A.: Comparison of mechanical thrombectomy with contact aspiration, stent retriever, and combined procedures in patients with large-vessel occlusion in acute ischemic stroke. Medical science monitor: international medical journal of experimental and clinical research 24, 9342 (2018)
12. Prochazka, V., Jonszta, T., Czerny, D., Krajca, J., Roubec, M., Macak, J., Kovar, P., Kovarova, P., Pulcer, M., Zoubkova, R., et al.: The role of von willebrand factor, adamts13, and cerebral artery thrombus composition in patient outcome following mechanical thrombectomy for acute ischemic stroke. Medical science monitor: international medical journal of experimental and clinical research 24, 3929 (2018)
13. Řeháková, B., et al.: Kontrasty v logistické regresi. Sociologický časopis/Czech Sociological Review 44(04), 745–765 (2008)
14. Seveso, A., Campagner, A., Ciucci, D., Cabitza, F.: Ordinal labels in machine learning: a user-centered approach to improve data validity in medical settings. BMC Medical Informatics and Decision Making 20(5), 1–14 (2020)
15. Skákalová, L.: Lineární modely s kategoriálními vysvětlujícími proměnnými. Diplomová práce, Univerzita Palackého v Olomouci, Přírodovědecká fakulta Olomouc (2016)
16. Vrtková, A.: Predicting clinical status of patients after an acute ischemic stroke using random forests. In: 2017 International Conference on Information and Digital Technologies (IDT). pp. 417–422. IEEE (2017)
17. Vrtková, A., Procházka, V.: Comparing the performance of regression models, random forests and neural networks for stroke patients' outcome prediction. In: 2019 International Conference on Information and Digital Technologies (IDT). pp. 543–550. IEEE (2019)

Incomplete Tournaments Scheduling

Jakub Závada

Department of Applied Mathematics, FEECS,
VSB – Technical University of Ostrava, 17. listopadu 15,
708 00 Ostrava – Poruba, Czech Republic
jakub.zavada@vsb.cz

Abstract. This work is a summary of my results achieved during the academic year 2020/2021. My research during this academic year was focused on the scheduling of incomplete tournaments, and builds on my previous research on this topic. The main goal is to provide methods of fair scheduling of incomplete tournaments. Incomplete tournaments are such tournaments that the number of rounds played in the tournament is not large enough to ensure that participants play each other. Natural condition in this type of tournaments is that the strength of opponents of each participant of the tournament should be similar to the strength of opponents of other participants. Every participant is represented by a vertex and every match between two participants is represented by an edge between corresponding vertices. Edge coloring is used to divide matches into rounds, vertex labeling is used to describe the strength of each participant, and edge orientation is used to determine which participant has an advantage in a match (e.g. first-move advantage in chess tournament).

Keywords: edge coloring, edge orientation, labeling, incomplete tournament

1 Introduction

Incomplete tournaments are common in some sports and games. Chess tournaments are one of the most typical examples of incomplete tournaments. Chess tournaments are often organized in such way that a large number of players participate and only small number of rounds is played. Another example are football competitions. As of the 2024/2025 season, the main stage of the Champions League and other international European competitions will follow a new format [1] which is an incomplete tournament with 36 teams.

For the rest of this text let n denote the number of participants and r the number of rounds. Each participant plays exactly one match in each round. This is obviously impossible if the number of participants is odd. A standard solution of this problem in chess tournaments is a "bye" [2]. It can be described in a simplified way so that a dummy player who loses all his games is added to the tournament if the number of participants is odd. So, we can assume that the number of participants is always even.

VSB – Technical University of Ostrava, 2021, ISBN 978-80-248-4523-4 (on-line).

Since each participant usually meets only a minority of his possible opponents during the incomplete tournament, we should ensure comparable conditions for all participants. Swiss system [3] is usually used in chess tournaments. This system uses the results of previous rounds to decide how to schedule the following round. In football competitions it is better to schedule all rounds ahead (for instance because fans then have more time to plan the traveling to away matches). The Swiss system cannot be used in such case, therefore it is useful to use graph theory to find different systems of scheduling.

If we want to use graph theory to schedule an incomplete tournament ahead, we should keep in mind that we have to ensure comparable conditions for all participants. It means at least that the total strength of opponents of any participant is the same or similar to the total strength of opponents of any other participant, and also that each participant should play the same number of matches with and without an advantage (of first move in chess, home stadium in football etc.). If the number of rounds is odd, the difference between the number of matches with advantage and without advantage should be exactly 1 for each participant. Furthermore, the matches with advantage should alternate with the matches without disadvantage for each participant as much as possible. It is not always possible (and also it is not desirable) to ensure regular alternation for all participants, but we will show that we can ensure that no participant has a series of more than two consecutive with advantages nor without advantages in r-round tournament with n participants in which each participant plays in each round.

2 Obtained Results

My work on handicap cubic graphs presented during the last WOFEX workshop [4] was summarized (and defended during the state doctoral exam) in thesis during the academic year 2020/2021. Recently it was extended by a research related to the use of edge orientation for describing which participant has the advantage in a match, and also by a small research related to creating tournaments with more rounds. Creating tournaments with more rounds is very important, because 3-round tournaments are not common in practice, and their use is primarily theoretical.

2.1 Adding More Rounds into the Tournament

Generally it is difficult to find an r-regular connected handicap graph on n vertices with a proper r-edge-coloring. A graph should be connected if we want it to represent a fair scheduling of incomplete tournament. In most cases such graph even does not exist. But if we have a handicap (or for instance distance magic) r-regular graph G, we can often use it to create a new graph G', which still holds all required properties, in such way that we just add appropriate edges to G.

Example of such process is given in the Fig. 1, where red, green and blue edges are edges of connected handicap cubic graph on 36 vertices. When we add appropriate gray and black edges, we get a connected handicap 5-regular graph on 36 vertices. After adding yellow and purple edges to that 5-regular graph, we have a connected handicap 7-regular graph on 36 vertices. Vertices are labeled with numbers $1, \ldots, 36$, the weight (the sum of labels of all neighbors) of vertex with label i is $w(i) = 111 + i$.

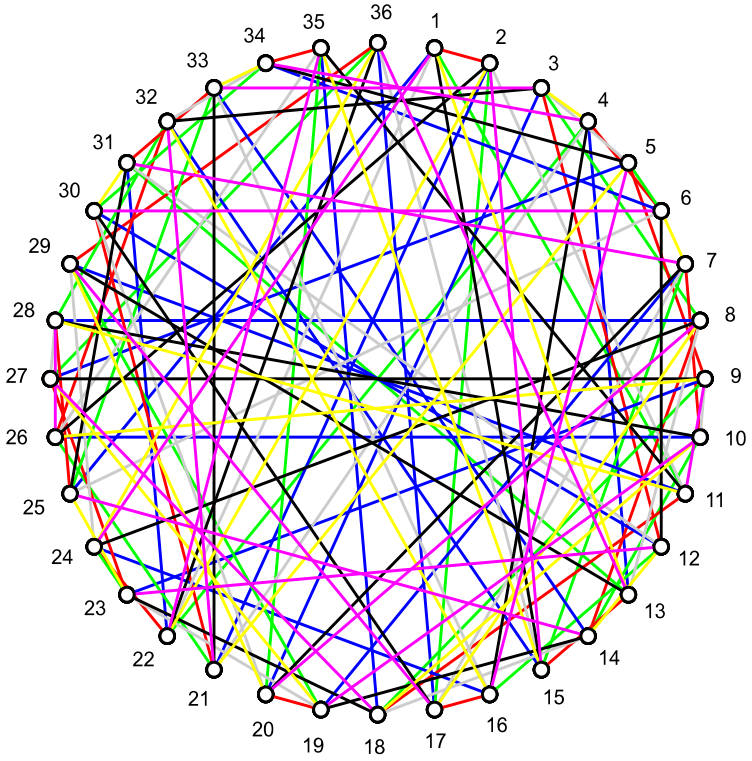

Fig. 1. 7-regular handicap graph on 36 vertices.

The main idea is to add edges of cycles C_4 such that the sum of the opposite labels is $n+1$. For instance in Fig. 1 we can see a cycle 1–22–36–15 colored by gray and black color. If we can divide all vertices into such cycles, we get a 5-regular handicap graph G' from the starting 3-regular graph G. If G is a connected r-regular handicap graph edge-colored by r colors, G' is again handicap and obviously also connected, $(r+2)$-regular and edge-colored by $r+2$ colors.

2.2 Edge Orientation

We recall here once again that the edge orientation can be used to describe an advantage (of first move, of home stadium etc.) in a given match. If the edge

uv is oriented from u to v, then the advantage is on the side of the participant represented by vertex u.

Our aim is to schedule the tournament so that the difference between the number of matches with the advantage and the number of matches without the advantage is minimized for each participant. The algorithm presented in my master thesis on the optimal orientation of (almost) regular graphs [5] can be used to solve the problem. This algorithm does not ensure regular alternation of advantages and disadvantages for each participant, but is good enough to show that each r-regular graph G on n vertices can be oriented so that the maximum outdegree in G is $\lceil \frac{r}{2} \rceil$ and the minimum outdegree in G is $\lfloor \frac{r}{2} \rfloor$ if we use that algorithm. This is exactly what we need to show that we minimize the difference between the number of matches with advantage and the number of matches without advantage for each participant at the same time. If r is even, each participant plays exactly half of matches with advantage and the other half of matches without advantage, since $\lceil \frac{r}{2} \rceil = \lfloor \frac{r}{2} \rfloor$ for even r. And if r is odd, half of participants plays $\lceil \frac{r}{2} \rceil$ matches with advantage and $\lfloor \frac{r}{2} \rfloor = \lceil \frac{r}{2} \rceil - 1$ without advantage. The other half of participants plays $\lceil \frac{r}{2} \rceil$ matches without advantage and $\lfloor \frac{r}{2} \rfloor = \lceil \frac{r}{2} \rceil - 1$ with advantage. So, for each participant it holds that the difference between the number of his matches with and without advantage is exactly 1 if r is odd and exactly 0 if r is even.

The algorithm from [5] is not designed to ensure the regular alternation of matches with and without the advantage for each participant. But actually, in most cases it is not even possible to ensure it, as is shown in the following Theorem 1.

Theorem 1. *Let graph G represent a tournament, in which each of n participants plays r matches in r rounds. It is possible to ensure that no participant has a series of two or more consecutive matches with advantages nor a series of two or more consecutive matches without advantages if and only if G is bipartite.*

Proof. It is assumed that each of n participants plays r matches in r rounds. It means that the graph has a proper edge coloring with r colors, since r rounds are represented by r colors.

If graph G is bipartite, let's call the partities A and B. For odd i each edge of color i can be oriented from A to B, for even i the orientation of each edge can be from B to A. It means that each participant represented by a vertex in partite set A has advantages exactly in odd rounds, whilst each participant represented by a vertex in partite set B has advantages exactly in even rounds.

To show that the condition of biparticity is necessary, let's assume that the matches with and without advantages alternate regularly for each participant. We start with an obvious observation that exactly half of participants has an advantage in the first round. Then none of these participant has an advantage in the second round, all of them have an advantage in third round etc. It means that there is no match between these participants, and hence no edge between corresponding vertices in G. Similar situation is between the other half of participants. So, there is no edge between vertices representing the participants starting

with an advantage, and also there is no edge between vertices representing the participants starting without the advantage. Hence, each of these halves always forms one partite set of a bipartite graph. □

So, if we want all participants to play with alternating matches with and without advantages, we have to divide them into two groups A and B with no head to head matches inside a group. This is probably not very good solution to ensure fair conditions, so it would be better to allow two, but no more, consecutive matches with (or without) an advantage.

But let's stay for a while with bipartite graphs just to mention that during our follow-up research we found out that handicap and distance magic bipartite graphs exist only for numbers of vertices n divisible by 4. Currently, we try to find out whether n needs to be divisible by 8 for handicap graphs. Current examples show only that bipartite distance magic graphs exist also for $n \equiv 4 \pmod 8$. For handicap graphs we found out that bipartite handicap cubic graphs exist for every n divisible by 8, whilst for $n \equiv 4 \pmod 8$ we do not have a single example of bipartite handicap graphs on n vertices, even after we used a computer to check the biparticity of all connected handicap cubic graphs with $n \equiv 4 \pmod 8$ up to $n = 44$. For $n = 52$ and $n = 60$ we have already checked only selected graphs, but still none of them is bipartite. On the other hand, our calculations which eliminated all other possibilities of n, did not eliminate $n \equiv 4 \pmod 8$, so this remains as the only open case.

Now we can move on to the algorithm which ensures that no participant plays more than two consecutive rounds with the advantage nor more than two consecutive rounds without the advantage. The algorithm is described in the proof of the following Theorem 2.

Theorem 2. *In a tournament, in which each of n participants plays r matches in r rounds, we can always ensure that no participant has a series of three or more consecutive matches with advantages nor a series of three or more consecutive matches without advantages.*

Proof. We provide an algorithm which returns the requested orientation of edges. Suppose that all edges are properly colored by r colors such that all matches of round i are represented by edges of color i. Graph G, which represents the tournament, is r-regular and properly edge-colored by r colors. So, if we take any vertex u, each color appears on exactly once edge incident with u. Now let's take colors 1 and 2 and start orienting the edges in any vertex v_1. We find the edge of color 1 incident to v_1, the other endvertex of this edge we denote v_2. Then the edge v_1v_2 is oriented from v_1 to v_2. Now let's find an edge of color 2 incident with v_2. This edge v_2v_3 we orient from v_2 to v_3. Then we orient the edge v_3v_4 of color 1 from v_3 to v_4. Now we know that the participant represented by vertex v_2 plays without the advantage in round 1 and with the advantage in round 2, whilst the participant represented by vertex v_3 plays with the advantage in round 1 and without the advantage in round 2. We continue with alternating orientation of edges of colors 1 and 2 until we get back to the vertex v_1. Now we check whether all edges of colors 1 and 2 are oriented. If not, we find a vertex with unoriented

incident edge of color 1 and repeat the process. When all edges of colors 1 and 2 are oriented, we start the same process with colors 3 and 4 etc. Such orientation ensures that each participant plays one game with the advantage and one game without the advantage in rounds 1 and 2, as well as in rounds 3 and 4 etc. So, in any even round each participant, who had the advantage in the previous round, do not have an advantage. And similarly, each participant who had not an advantage in the previous odd round, has an advantage. This ensures that no participant plays more than two consecutive rounds with the advantage nor without the advantage. If r is odd, we can orient all edges of color r arbitrarily. □

3 Conclusion

During academic year 2020/2021 I focused on the topics related to scheduling of incomplete tournaments. Previous results were defended during my state doctoral exam and extended by new results regarding the alternation of matches with and without an advantage of first move, home stadium etc. The results are going to be presented also during the CSGT21 – The 56th Czech and Slovak Conference on Graph Theory 2021 in Rajecké Teplice.

Acknowledgments

This work is supported by SGS grant no. SP2021/103, VŠB – Technical University of Ostrava.

References

1. New format for Champions League post-2024: everything you need to know. *UEFA.com* [online]. 2021 [cit. 2021-7-10]. Available at: https://www.uefa.com/uefachampionsleague/news/0268-12157d69ce2d-9f011c70f6fa-1000–new-format-for-champions-league-post2024-everything-you-need-to-know.
2. What is a 'bye' in a tournament? *Chess.com [online]*. 2021 [cit. 2021-7-10]. Available at: `https://support.chess.com/article/1310-what-is-a-bye-in-a-tournament`.
3. Swiss-system tournament. *Wikipedia: the free encyclopedia* [online]. San Francisco (CA): Wikimedia Foundation, 2001- [cit. 2021-7-10]. Available at: Available at: `https://en.wikipedia.org/wiki/Swiss-system_tournament`.
4. Závada, J.: Graph Theory in Sport Tournaments Scheduling. In: *WOFEX 2020 : 18th annual workshop, Ostrava, 8th September 2020 : proceedings of papers*. Ostrava: VŠB – Technical University of Ostrava, 2020, pp. 338–342. ISBN 978-80-248-4422-0. DOI: 10.31490/9788024844220.
5. Závada, J.: Minimalizace odchozího stupně vrcholu v téměř pravidelném grafu. Ostrava, 2017. Master thesis. VŠB – Technical University of Ostrava. Supervisor: M. Kubesa.

Simulation of the Efficiency of Fog Computing

Jakub Jalowiczor

Department of Telecommunications, FEECS,
VSB – Technical University of Ostrava, 17. listopadu 15,
708 00 Ostrava – Poruba, Czech Republic
jakub.jalowiczor@vsb.cz

Abstract. This paper summarizes part of my recent research, which aims to study the effectiveness of fog computing applied to a network based on LoRa technology. The efficiency is studied in a simulation. The result of the simulation is the average execution time of the received message. First, the standard LoRaWAN architecture is briefly discussed, followed by a description of the proposed architecture and the simulation itself. At the end of the paper, sections devoted to my participation in research projects and publishing activities are presented.

Keywords: LoRaWAN · Fog computing · Simulation.

1 Introduction

As the name suggests, my recent research focuses on the efficiency of fog computing. As part of the research, fog computing was applied to the network based on LoRa technology. The regular LoRaWAN network function corresponds to the cloud computing paradigm, which is not always an effective solution. The main limitation of the cloud computing paradigm is the large distance between the cloud and end nodes, which influences latency, jitter, and location awareness. The increasing curve of connected IoT end nodes leads to higher demands for speed and data volume. This can lead to the point when cloud computing is not sufficient for specific IoT use cases.

The fog computing paradigm provides data processing closer to end nodes, and thus the network may be able to respond faster and according to current conditions [1]. The term fog represents an analogy to the lower proximity to end nodes, which can be defined as a cloud closer to the ground. The fog node typically cooperates with the cloud, which can be used for more complex tasks or as a storage for historical data.

2 Description of the Research

The standard LoRaWAN network architecture includes end nodes, LoRa gateways, a network server, and an application server. From the point of view of end nodes, the LoRa gateway is the closest part of the network, and its main function is the transformation of RF packets into IP packets, which are subsequently

VSB – Technical University of Ostrava, 2021, ISBN 978-80-248-4523-4 (on-line).

forwarded to the associated network server [2, 3]. Therefore, the LoRa gateway does not make any decisions based on the actual data received from end nodes. This operation corresponds to the cloud computing paradigm [4]. The standard LoRaWAN architecture can be seen in Figure 1

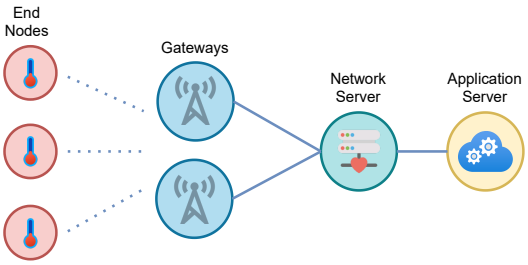

Fig. 1. Standard LoRaWAN architecture.

The simulated architecture, which supports fog computing, integrates the network and application servers into the gateway while maintaining its standard functionality. This change allows the gateway to process the received messages accordingly. A cloud server is presented in the architecture to store historical data. The proposed architecture can be seen in Figure 2.

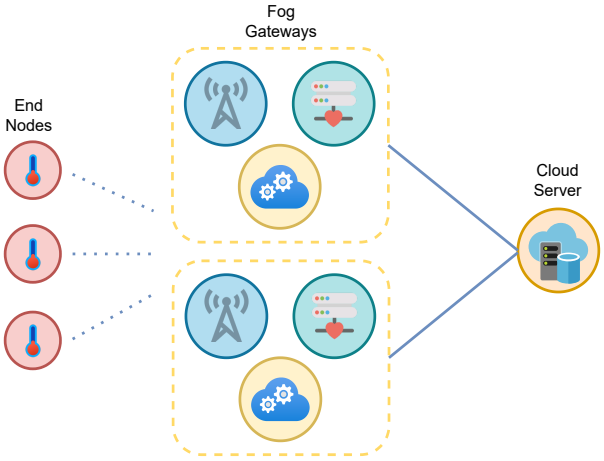

Fig. 2. The proposed architecture.

As the simulated architecture adopts fog computing, it contains three layers. The architecture model can be seen in Figure 3. Individual IoT end nodes are

located in the bottom layer. The fog layer is presented in the middle of the model and includes fog nodes intended for partly autonomous decision-making. The fog nodes operation is mainly affected by the received traffic and collaboration with the cloud layer. The cloud layer is the upper layer in the model and includes a cloud server [5].

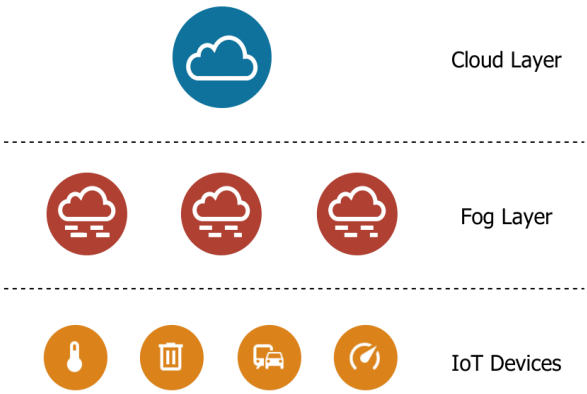

Fig. 3. Three-layer fog computing architecture model.

Because an IoT communication network can be seen as a queuing system, the idea of the research is to apply queuing theory and compare the proposed architectures in terms of service time. Messages from end nodes are requests to be served. The LoRa gateway, network server and application server are queuing nodes. If we assume that the packet forwarder in the gateway can receive up to eight messages at the same time with different spreading factors on different channels [6], the queuing node representing the gateway consists of eight servers serving the requests concurrently. To secure identical conditions throughout the whole process of simulation, we presume that all end nodes fall into the class A, use the ABP activation method, and send messages without the need for acknowledgement.

The graphical programming environment Simulink that is an extension of the software tool Matlab was used for the simulation. The term private and public message was used to decide between fog or cloud computing (private - fog computing, public - cloud computing). The simulation was performed for 10,000 messages and subsequently, the average execution time was calculated. The execution time was measured from the time when the message is received by the fog gateway to the time when the decrypted payload of the message was stored in a database. A diagram of the simulation model can be seen in Figure 4.

The average service time in the case of private-only messages was 209.81 ms for the proposed architecture. This is the shortest time for any possible combination of inputs. If all messages were public, the fog computing operations

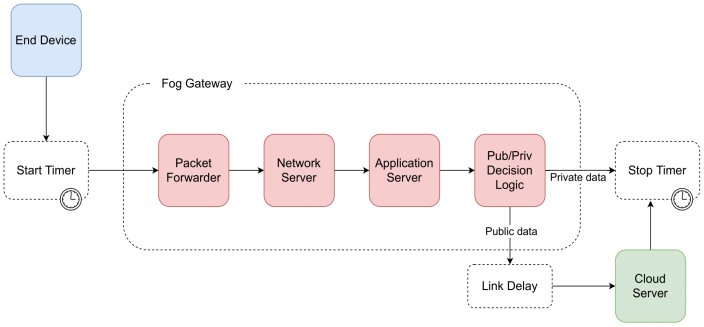

Fig. 4. Diagram of the simulation

remained inactive and the average service time was 217.78 ms. The results can be seen in Table 1.

Table 1. Comparison of simulation results.

Time	Result
Average execution time	209.96 ms
Best case execution time	209.81 ms
Worst case execution time	217.78 ms

3 Conclusion

The proposed architecture is only one of the solutions that have been investigated in the research. The results of the research are used as a basis for my dissertation thesis. The complete results of the simulations were published in a special issue of the journal Sensors – Cloud and Edge Computing in Wireless Sensor Networks and Internet of Things.

4 Participation in Research Projects

Reg. No. EG19_262/0020122 – Development of external modules TAMAS II, Ministry of Industry and Trade programme OP PIK, 2020 – 2022, PI at VSB-TUO: Dr. Tovarek, my position: junior researcher (3/2021 – still active).

5 Publishing Activities

Jalowiczor, J., Rozhon, J., Voznak, M.: Study of the Efficiency of Fog Computing in an Optimized LoRaWAN Cloud Architecture. Sensors. 21, (2021).

Rozhon, J., Rezac, F., Jalowiczor, J., Behan, L.: Augmenting Speech Quality Estimation in Software-Defined Networking Using Machine Learning Algorithms. Sensors. 21, (2021).

References

1. Puliafito, C., Mingozzi, E., Longo, F., Puliafito, A., Rana, O.: Fog Computing for the Internet of Things. ACM Transactions on Internet Technology. 19, 1-41 (2019).
2. LoRaWAN 1.0.4 Specification, `https://lora-alliance.org/resource_hub/lorawan-104-specification-package`. Last accessed: 12 Jul 2021
3. Jalowiczor, J., Gresak, E., Rezac, F., Rozhon, J., Safarik, J.: Development and deployment of the main parts of LoRaWAN private network. Autonomous Systems: Sensors, Processing, and Security for Vehicles and Infrastructure 2019. 2- (2019).
4. Dillon, T., Wu, C., Chang, E.: Cloud Computing: Issues and Challenges. In: 2010 24th IEEE International Conference on Advanced Information Networking and Applications. pp. 27-33. IEEE (2010).
5. Yi, S., Hao, Z., Qin, Z., Li, Q.: Fog Computing: Platform and Applications. In: 2015 Third IEEE Workshop on Hot Topics in Web Systems and Technologies (HotWeb). pp. 73-78. IEEE (2015).
6. iC880A-SPI LoRa™ Concentrator. `https://wireless-solutions.de`. Last accessed: 13 Jul 2021

Fiber-optic sensors in geo-science engineering

Stanislav Zabka

Department of Telecommunications, FEECS,
VSB – Technical University of Ostrava, 17. listopadu 15,
708 00 Ostrava – Poruba, Czech Republic
stanislav.zabka@vsb.cz

Abstract. This article deals with the theme of using the fiber-optic interferometric sensor based on Michelson interferometer for monitoring parameters of dynamic and acoustic effects due to the blasting operations. The main scientific objective of this paper suggested is the examination of the alternate approach to measuring dynamic and acoustic effects caused by blasting operations using optical fibers. The presented article also summarizes the author's activities during his study, his research and development activities related to the studies and research projects.

Keywords: optical fiber, interferometric sensor, civil engineering

1 Introduction

Allow me to introduce myself. My name is MSc. Stanislav Zabka. I am a doctoral student at the Faculty of Electrical Engineering and Computer Science at the Technical University of Ostrava. My education program is called Computer Science, Communication Technology and Applied Mathematics and field of study called Communication Technology. I am also working (part-time job) as a Java developer in big software corporation and I am using these skills to achieve the best results when it comes to creating software that handles and computes big data from sensors. In my five years of study, I am extended my knowledge especially in the field of using fiber-optic sensors in human and technical science. I am also a participle of six research projects. To date 7/2021, I have a total of 21 accepted publications (h-index 5) and 7 utility models.

2 About my work

Blasting operations have played a great role in human lives for a long time. They are an integral part of the extraction of mineral resources, both on the ground and underground, and they are also part of technological procedures in the execution of underground works. Seismic and acoustic effects are essential adverse effects in the execution of blasting operations.

© M. Krátký, J. Dvorský, P. Moravec (Eds.): WOFEX 2021, pp. 224–229.
VSB – Technical University of Ostrava, 2021, ISBN 978-80-248-4523-4 (on-line).

Sensor technologies based on fiber optics can form novel alternative method of implementing the monitoring the effects of blasting operations. Proposed sensor is based on the Mach-Zehnder interferometer. According to relation (1), a total of three parameters can be defined (refractive index n, wavelength λ and geometric length L representing the optical path), which can cause a phase change marked $\Delta\phi$ occurring in the measuring arm of the interferometer due to impact of the measured value. [1-2]

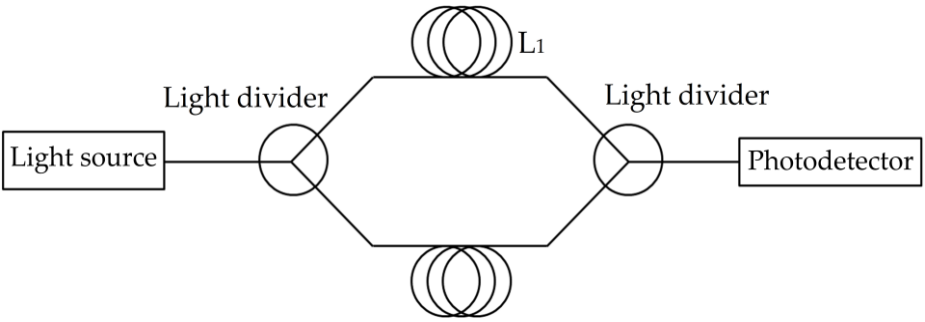

Fig. 1. Schematic diagram of the proposed interferometric sensor.

Seismic manifestations consisting of frequencies (ω) that affect the measuring part of the sensors marked L_1. The result is a change in the optical length of the interferometric sensor arm (can be defined as the product of the geometric length L and the refractive index n). [2-4]
According to relation (2), the resulting phase change marked $\Delta\phi$ can be defined as:

$$\begin{aligned} \Delta\phi &= 2\pi L\, n/\lambda \\ \Delta\phi &= kLn, \\ k &= 2\pi/\lambda. \end{aligned} \tag{1}$$

$$\Delta\phi = 2\pi\frac{n}{\lambda}\,\delta L + 2\pi\frac{L}{\lambda}\,\delta n - 2\pi nL\left(\frac{1}{\lambda^2}\right)\delta\lambda. \tag{2}$$

The technical precondition of the solution is measuring vibrations and sound due to the blasting operations by experimentally developed interferometer and comparative measuring using standard instruments for seismic and acoustic monitoring. Both, sectional and station measuring were realized. Mainly the type of blasting operations (small extent or large extent), timing methods, localization of blasting operation (underground or surface) was taken into account, and also the variable geological environment in case of vibrations, all within the context of the fiber-optic interferometer structure, settling method at the station, orientation towards the source or distance from the blasting operation executed. The ideal configuration of optical fibers in the interferometer for the real recording of the acoustic effect and dynamic response of the rock environment or dynamic response of the foundation structure of the building was searched for. For vibrations, also with respect to the space motion of the mass point divided into three

components – vertical, horizontal radial, and horizontal transversal, since current fiber-optic interferometers do not deal with this at all. For vibration measuring, stress also is put on experiments in the so-called near zone (i.e. at small distances from the source of vibrations) and applicability of the fiber-optic interferometer in the first tens of meters from the blasting operation executed in connection with the execution of underground works shallowly under the surface of municipal lands. Real photo from real measurement is shown in Figure 2. [5]

Fig. 2. Real photo from real measurement.

Presented results of realized pilot experimental measuring of blasting operation effects in an open pit. The result of recorded vibration indications, air blast wave, and acoustic effect in the area of time and frequency obtained from Mach–Zehnder's interferometer is shown in figure 3. In both, the amplitude and frequency area, it is possible to monitor significant compliance as in the case of data acquired from the seismic station, while the device based on the Mach–Zehnder's interferometer is capable to record frequencies corresponding with both, vibrations and acoustic indications.

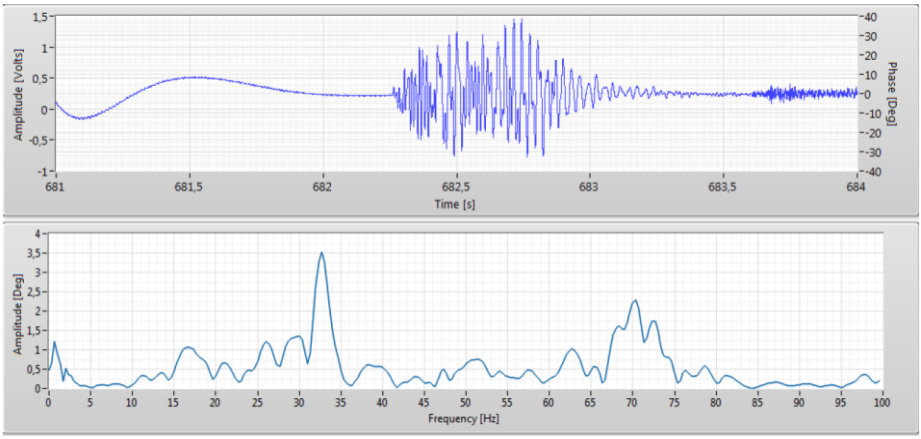

(a)

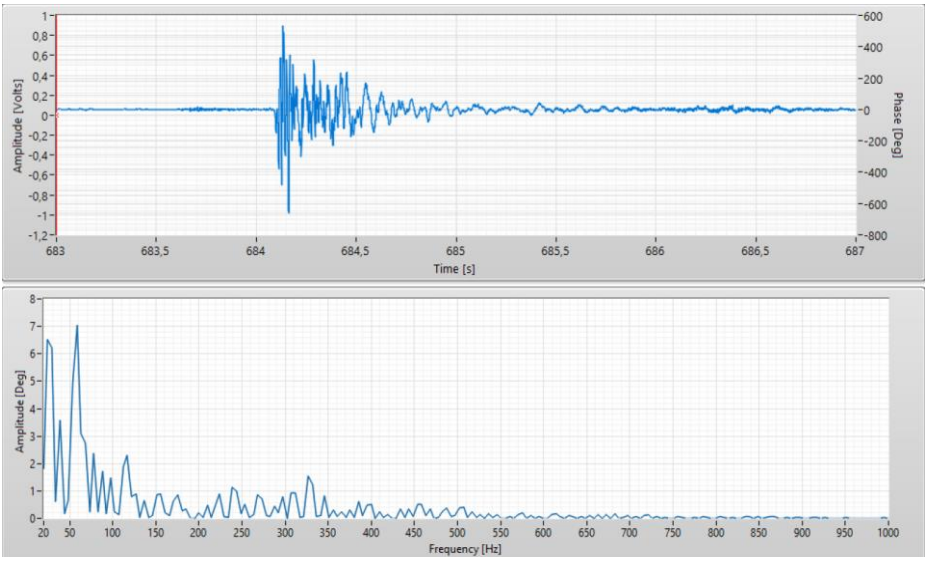

(b)

Fig. 3. (a) Record demonstrating vibrations made by using Mach–Zehnder interferometer – blasting operations of large extent, bench blast in the Kotouc Stramberk quarry; (b) A record demonstrating an air blast wave and sound effect by using Mach–Zehnder interferometer – blasting operations of large extent, bench blast in the Kotouc Stramberk quarry.

3 Projects

As part of my studies, I was actively involved in solving 8 projects, namely:

1. Measuring the weight of trash bins, while being lifted by the truck.
2. SGS SP2017/79 - New types of photonic systems for IoT.

3. SGS SP2018/184 - Optical communication technologies and sensors.
4. SGS SP2019/80 - New Fiber Optic Technologies for Comm. and Sensors.
5. SGS SP2019/85 - Advanced Signal Processing Methods.
6. SP2020/38 - Fiber-optic technologies for industrial applications.
7. SP2020/156 - Advanced Signal Processing Methods II.
8. SP2021/45 - Fiber-optic Sensory Systems

Now we prepared the project (TREND) to the Technology Agency of the Czech Republic. This preparing project focuses on applied research of new type of monitoring techniques based on optical fibers during the excavation of underground constructions (road and train tunnels). The project uses optical fibers in primary part of tunnels for monitoring stress and temperature.

4 Publication activities

During the dates 9/2016 and 7/2021, I have a total of 21 accepted papers and 7 utility models, please see my Scopus Author ID 57191343671. My author *h*-index = 5.

5 Pedagogic part and other activities at the Department of Telecommunications

In the winter and summer semester, I was part of courses UDKT (Introduction to communication technologies) and OAK (Optical Atmospheric communications) as help for academic teachers.

6 Future work

Now I am focusing on the individual subjects of my Ph.D. study and my dissertation thesis. Also, I will be actively involved in the above-mentioned project entitled “Monitoring of the primary lining of tunnels with optical fibers”, where my role will focus on implementation of optical fibers.

References

1. Stolarik, M., Pinka, M., Zabka, S., Novak, M. "Dynamic effect of harmonic vibrations: Various approaches to monitor, " In: Proceedings of SPIE - The International Society for Optical Engineering. SPIE: Berlin. 2018. DOI: 10.1117/12.2325740.
2. Wang, L., Fang, N. "Applications of Fiber-Optic Interferometry Technology in Sensor Fields," Optical Interferometry (2017), ISBN 978-953-51-2955-4.
3. Xu, Y., Lu, P., Qin, Z., Harris, J., Baset, F., Lu, P., Bhardwaj, V.R., Bao, X. "Vibration sensing using a tapered bend-insensitive fiber based Mach-Zehnder interferometer," (2013) Optical Express, 21, pp. 3031.

4. Chen, J., Chang, T., Fu, Q., Lang, J., Gao, W., Wang, Z., Yu, M., Zhang, Y., Cui, H.L. "A Fiber-Optic Interferometric Tri-Component Geophone for Ocean Floor Seismic Monitoring," (2017) Sensors, 17, pp. 47.
5. Broz, M., Strunc, J., Malek, J., Linda, M. "New generation seismological datalogger BRS32-USB and its application in induced seismicity monitoring," (2014), EGRSE Journal, pp.35–47.

Methods for Partial Discharge Data Analysis

Ondřej Kabot

Department of Electrical Power Engineering, FEECS,
VSB – Technical University of Ostrava, 17. listopadu 15,
708 00 Ostrava – Poruba, Czech Republic
ondrej.kabot@vsb.cz

Abstract. This article describes basic knowledge about partial discharges activity detection on medium voltage overhead powerlines. There are also described methods used for partial discharge data analysis that are required for testing and development of new methods for detection of partial discharge activity. Various methods used for analysis are described. Information obtainable by performing detailed analysis of acquired data is described. In the end the usefulness of partial discharge activity detection is summarized, and measurement conducted in paper is evaluated.

Keywords: Partial Discharge, Electrical Field, Detection, Analysis, Covered Conductor, Insulation, Matlab.

1 Introduction

1.1 Partial discharges

To increase reliability of 22 kV distribution network overhead powerlines, there is effort to replace bare AlFe conductors with CCs (Covered Conductors) in forested areas. These conductors consist of aluminum core made from multiple braids and from XLPE (cross-linked polyethylene) isolation, that does not prevent electrical injury, but protects the powerline from contact with vegetation. Some of them also have semiconductive layer to improve geometry of electrical field. Because of XLPE isolation, contact with vegetation does not cause ground fault, but partial discharges start to appear around the point of contact. Partial discharge activity causes degradation of isolation and if it was undetected and fault wasn't removed, it could result into isolation failure and contact would change into ground fault. [1]

At VSB-TUO a novel method for detection was developed and is now commercially used by two distribution system operators in Czech Republic. In effort to improve the detector and to develop new ones, various measurements are being conducted on many types of CCs with different detection methods. Data are acquired by oscilloscope and exported, so further analysis can be conducted by using various programs. As there is need for detailed analysis, visualization of acquired data is not sufficient method. Matlab scripts were created to analyze signals acquired from detectors and

VSB – Technical University of Ostrava, 2021, ISBN 978-80-248-4523-4 (on-line).

AnsysMaxwell software was used to create models for visualization of electrical field distribution.[5]

1.2 Measurement description

For all measurements described in this paper, same measurement setup was used, only thing that varied, were sensors. One of the sensors was also considered as referential as it is already tested and is commercially used. Measurement of this sensor is depicted on the Fig. 1. HIF stands for high impedance fault, simulating contact with vegetation. In this case the contact was simulated by copper tape with conductive adhesive, wrapped around the conductor. It does not replicate real contact with vegetation but provides us with ability to replicate the measurement with same severity of the fault and same contact area. The sensor itself is described as SLI (Single Line Inductor). And CD is capacitive divider, that is used to lower the voltage of acquired signal. The second sensor was ground sensor, that allows contactless detection of partial discharge activity and is installed in the axis of the powerline. There were two major goals of these measurements. Comparison of various covered conductors including quantification of partial discharge activity on each of them and comparison of two different types of detection. By the principle the contactless detection will not be as sensitive as contact one. Goal of this part of the measurement was to determine the difference between the two sensors. In this measurement ground sensor was not placed under ground but on it with grounding rods on each end that were inserted into the ground. The measurement setup is shown on Fig. 2. [2]

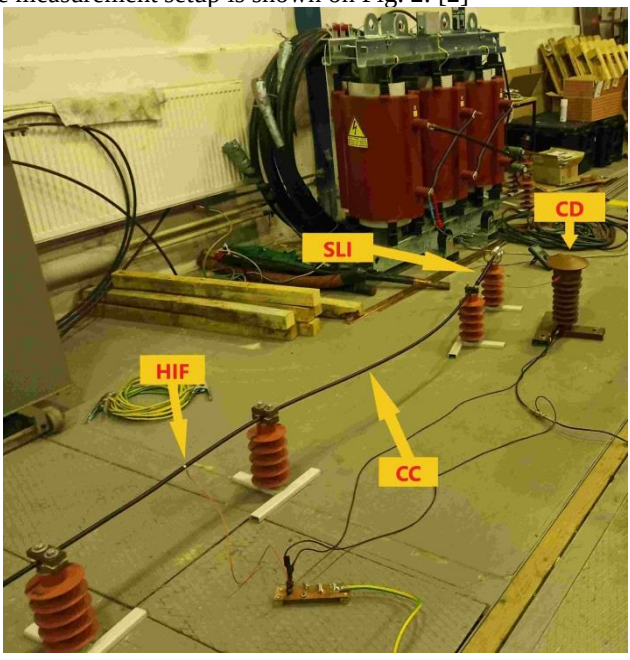

Fig. 1. Measurement of various types of CCs

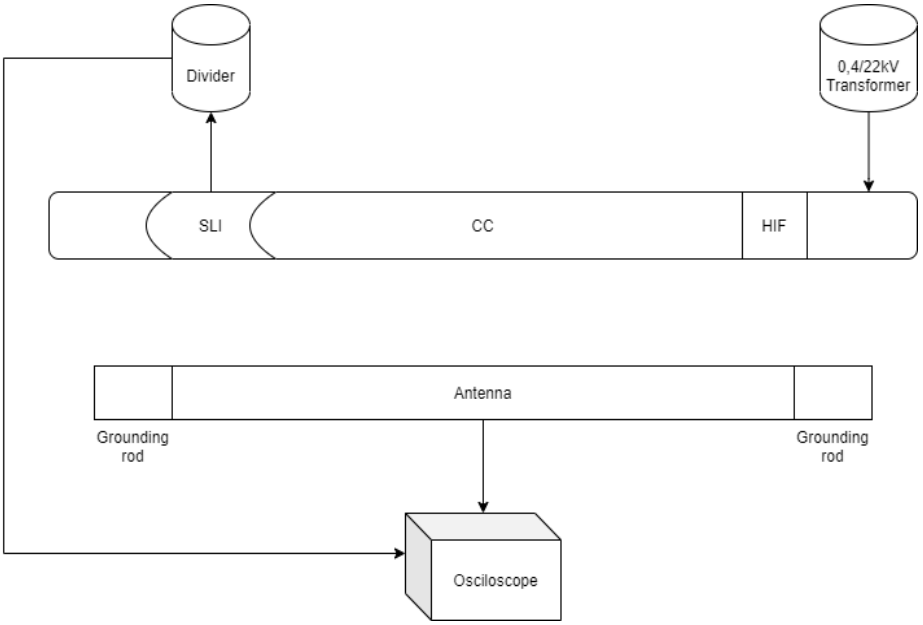

Fig. 2. Measurement setup for comparison of two sensors

2 Data analysis

For the purpose of acquired data analysis was created Matlab script, that was able to analyze all the measurements conducted for one CC. Since the first measurement involved only SLI detector, there was quite significant difference between signal and interferences. Because of this, there was no need for implementation of filters, only function used was threshold for removal of the interferences. Script used is shown on Fig. 3. The main loop of the script is set to end after 10 repetitions since there were always 10 measurements for each sample. As a first step, threshold is applied to the signal to remove the interference as shown on Fig. 4. After this script counts and stores peak amounts for each measurement and when loop ends, calculates average value and standard deviation. The loop also stores data for histogram creation. All resulting values are shown in Tab. 1. [4]

Table 1. Pulse count and standard variation s

Sample	Average pulse count	Standard variation s
1	937	76
2	568	49
3	1890	40
4	571	61
5	1009	40

Table 2. Table with values for each sample of CC

```
n_i = 1;
d = [0:1000:10000]
e = [0:0.5:5]
ba=0
ga=0

va = {0, 0, 0, 0, 0}
npeaksa = {0, 0, 0, 0, 0}
allnpeaksa = 0
ahpeaks = 0
hap = {0, 0, 0, 0, 0, 0, 0, 0, 0, 0}
AA = {A1, A2, A3, A4, A5, B1, B2, B3, B4, B5}

while n_i <=10

    xpeaksa = (AA{n_i});                % duplication
    thresholda = 4800;                  % Threshold value
    meanxa = mean(AA{n_i});
    % application of threshold
    xpeaksa(abs((AA{n_i})) <= thresholda) = meanxa;
    chapeaksa{n_i} = xpeaksa
    npeaksa{n_i} = (findpeaks(xpeaksa)) % peak search
    % counting of peaks
    va{n_i} = numel(npeaksa{n_i})
    allnpeaksa = allnpeaksa + numel(npeaksa{n_i})

    aa=hist(npeaksa{n_i}, d)
    ba=ba+aa

    n_i=n_i+1;
end
%calculation of average peak count and variance
totalnpeaksa = allnpeaksa/10
ba=ba/10
ga = cell2mat(va)
sqrt(var(ga))
```

Fig. 3. Script for analysis of various CCs

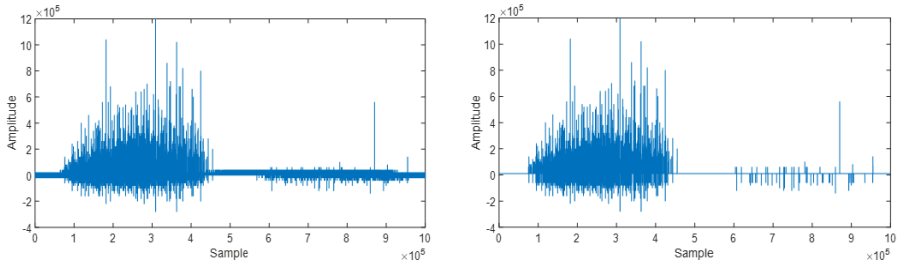

Fig. 4. Signal before and after removal of interference [5]

The analysis of second measurement was more difficult because the signal from ground sensor had small difference between useful signal and interference. Because of this, there could not be used threshold like in the previous case. For this purpose a

filter was created, that filtered data based on steepness of the edge of the pulse. This method increased the difference between signal and interference as shown on Fig. 5..

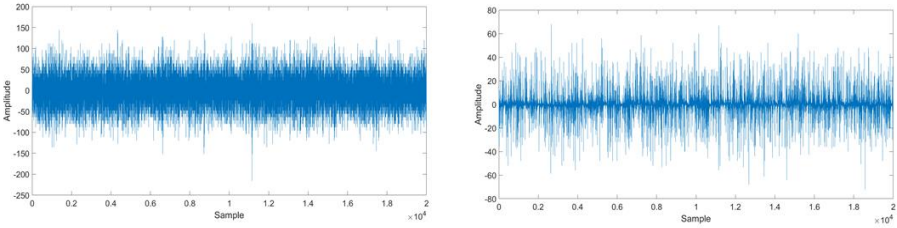

Fig. 5. Signal from ground detector before and after filter application

3 Visualization

For purpose of visualization of electric field distribution in various CCs, 3D models were created using SolidWorks software. The models of CCs were then imported into AnsysMaxwell, where they were converted into 2D models for purpose of electric field simulation. The core of the CCs was set as aluminum with voltage 12,7 kV since the voltage is between line and ground. The outer edge of the isolation was set to a ground potential, since the HIF created in our measurements was around whole diameter and connected to ground. The results can be seen on Fig. 6.

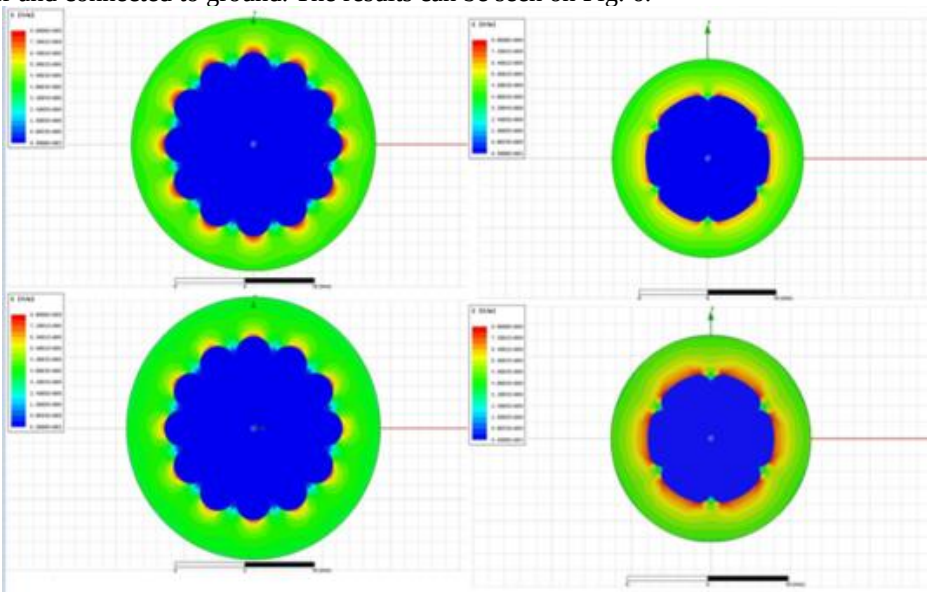

Fig. 6. Simulation of electric field distribution in the CCs [5]

The fifth sample was not simulated as it contained semiconductive layer with unknown properties and the simulation would not be correct.

4 Conclusion

Detection of partial discharge activity on CCs in forested areas is very important as it can prolong lifetime of the powerline and increase reliability of the network. The research of new more accurate and cost-effective solutions is needed to make the detectors more common.

From first measurement it is apparent that count of partial discharges is directly related to number of points of origin, which is demonstrated on Fig. 6. Which corresponds with Tab. 1.

The second measurement shows that interferences are a big issue in partial discharge detection. By using contactless method, the distributor can install the detector without shut down of the powerline. That usually means easier installation and removal of high voltage part of the detector, there can be significant reduction in installation price.

Various methods used for acquired data analysis and for visualization provide better ability to understand the issues various CCs and detectors. That allows more focused research of this field.

References

1. M. Lehtonen: Fault rates of different types of medium voltage power lines in different environments. Proceedings of the 2010 Electric Power Quality and Supply Reliability Conference, Kuressaare, 2010, pp. 197-202.
2. S. Mišák and V. Pokorný: Testing of a Covered Conductor's Fault Detectors. IEEE Transactions on Power Delivery, vol. 30, no. 3, pp. 1096-1103, June 2015.
3. H. Illias, G. Chen and P. L. Lewin: Partial discharge behavior within a spherical cavity in a solid dielectric material as a function of frequency and amplitude of the applied voltage. IEEE Transactions on Dielectrics and Electrical Insulation, vol. 18, no. 2, pp. 432-443, April 2011.
4. X. Han, N. A. Heckert, J. J. Filliben and Y. Wang: Statistical analysis of partial discharge phenomena. Time of occurrence distributions. 1998 Annual Report Conference on Electrical Insulation and Dielectric Phenomena, Atlanta, GA, USA, 1998, pp. 407-411 vol. 2.
5. O. Kabot, J. Fulneček, S. Mišák, L. Prokop and J. Vaculík, "Partial Discharges Pattern Analysis of Various Covered Conductors," 2020 21st International Scientific Conference on Electric Power Engineering (EPE), 2020, pp. 1-5, doi: 10.1109/EPE51172.2020.9269171.

Control system for V2H/V2G technology meeting requirements of the CHAdeMO standard

Martin Kosinka[1][0000−0002−9677−7177] and Lukáš Prokop[2][0000−0003−0495−5499]

[1]Department of Electrical Power Engineering, FEECS,
VSB – Technical University of Ostrava, 17. listopadu 15,
708 00 Ostrava – Poruba, Czech Republic
[2]ENET Centre, VSB – Technical University of Ostrava,
17. listopadu 15, 708 00 Ostrava – Poruba, Czech Republic
{martin.kosinka, lukas.prokop}@vsb.cz

Abstract. There is a trend of transition from centralized to the distributed generation of electricity in order to increase the involvement of electricity generation from renewable resources. This will lead to a reduction in pollution and greenhouse gas emissions. The electricity generation from renewable sources requires installing the appropriate battery storage as a means to power supply microgrid / power grid when renewable sources of electricity do not generate electricity. At the same time, there is an increasing demand for electric vehicles, whose battery capacity is gradually increasing. The Vehicle To Home / Vehicle To Grid systems utilize energy from electric vehicle battery to power microgrid or power grid. These systems need a charging/discharging station also called electric vehicle supply equipment, which main parts are the bidirectional inverter and the control unit ensuring communication with an electric vehicle using an appropriate standard. The aim of this paper is to introduce a developed energy flow control unit enabling charging/discharging electric vehicle in accordance with the CHAdeMO standard.

Keywords: Energy Flow Control Unit, Vehicle To Home, Vehicle To Grid, CHAdeMO standard, Energy management, Electric Vehicle, Renewable energy, Control System

1 Introduction

It is assumed that electric vehicle (EV) is the most time parked. Therefore it will be an opportunity to share the electric energy of the EV´s battery with a microgrid (from the size of a flat/house to the size of a municipal building) or a power grid. In general, there are applications in which the electric vehicle can be used not only as an appliance but also as an auxiliary or temporary source of electricity. Technologies utilizing energy from EV battery to power microgrid / power grid are called Vehicle To Home (V2H) / Vehicle To Grid (V2G). Batteries are the most expensive element in the microgrid's electrical infrastructure. Using an electric vehicle battery as a secondary accumulator in microgrid will decrease the total price of the microgrid battery storage and justifies the high price of the EV. V2H/V2G technologies will also serve as a backup source of

electricity during distribution grid power outages, while meeting power quality parameters. Use of EV battery would increase the nominal capacity of the microgrid's battery storage, thus prolonging the running time in off-grid mode during a blackout. Design and implementation of a proposed control system for V2H/V2G systems is described in this paper. Developed control system is called the Energy Flow Control Unit (EFCU).

2 Topology of the V2H/V2G systems

The EFCU manages the flow of electricity from the battery of an EV to power the microgrid in case of a V2H system or supply power grid in case of a V2G system and control the storage of excess energy back into the battery of the EV. The aim of the EFCU is to act as an interface between the superior Microgrid management system, the EV battery management system (BMS) and the bidirectional inverter. The EFCU forms together with a bidirectional inverter an Electric Vehicle Supply Equipment (EVSE) see Fig. 1. In this topology, the EFCU gets an energy flow plan from a superior Microgrid management system and manages charging/discharging of an EV battery according to this plan, which could be computed using neural networks and sent to the EFCU via Ethernet or WiFi technology. Microgrid management system gets from the EFCU important dataset for generating an energy flow plan. This dataset includes user and vehicle identification, EV connection state (connected/disconnected), mode of operation (appliance/generator), current battery capacity, maximum capacity, user defined schedule of EV arrival/departure, desired percentage of battery state of charge (SoC) at the time of departure and physical safe minimum SoC of the EV battery.

The off-board topology of the V2H/V2G system, which places the EVSE outside of the EV, was chosen in this development as it is not restricted to space requirements like on-board topology where the EVSE must be placed inside the EV. Also, strict automotive requirements must meet on-board topology.

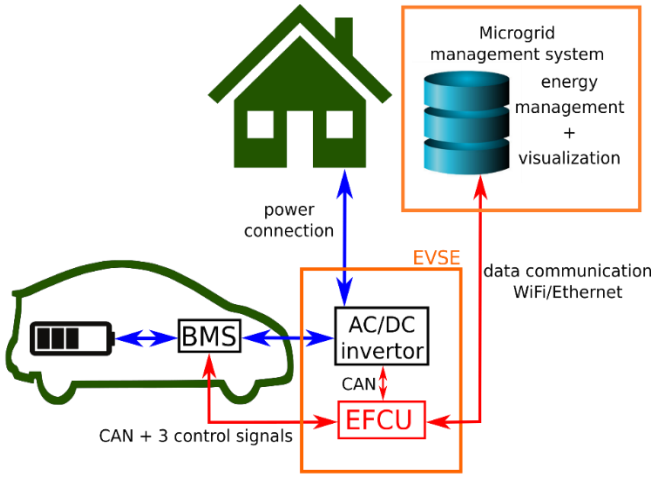

Fig. 1. Off-board V2H topology

3 Design and implementation of the EFCU electronics

The CHAdeMO DC fast charging standard was chosen to be implemented in the EFCU as it supports V2H/V2G technology and furthermore, Nissan Leaf EV (which has CHAdeMO interface) was available for testing with the developed EFCU. CCS standard, the most widely used standard for fast charging of electric vehicles in Europe, does not yet support bidirectional energy flow in V2H/V2G technology. It will be supported when ISO 15118-20 standard will be published [5].

There was needed to design a printed circuit board (PCB) for the EFCU in accordance to communicate with all peripherals including BMS of the EV battery, bidirectional inverter (in this case AC/DC variant, DC/DC variant is also applicable according to the topology used in microgrid), wattmeter (which measures DC current and voltage on the interface between EVSE and EV, these values are needed in the communication with EV through CHAdeMO standard) and Microgrid management system. Development of the bidirectional inverter and Microgrid management system was part of another research project [6][7]. Hardware design (selection of appropriate peripherals and communication interfaces) of the EFCU followed the requirements of the CHAdeMO standard published in the specification: *IEEE Standard Technical Specifications of a DC Quick Charger for Use with Electric Vehicles* and specification in draft state: *IEEE Draft Standard Technical Specifications of a DC Quick and Bi-directional Charger for Use with Electric Vehicles* [3][4].

Raspberry Pi single board computer in version 3B+ was chosen as a computing unit for the EFCU. All hardware communication interfaces except Ethernet interface were designed on PCB including two CAN bus interfaces, RS485 serial communication interface for communication with wattmeter through Modbus RTU standard, two digital outputs for implementation charge sequence signals defined in the CHAdeMO standard and digital input implementing vehicle permission signal also defined in the CHAdeMO standard. The block diagram of the EFCU is shown in the Fig. 2.

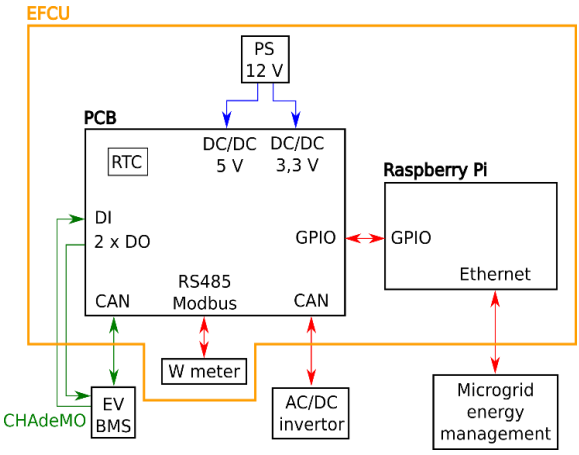

Fig. 2. Block diagram of the EFCU

Hardware realization of the EFCU is shown in the photo in the Fig. 3. Designed PCB (in the centre of the photo) has LED indication of the DC power supply voltage level 3.3 V and 5 V generated by DC/DC converters for supplying electronics placed on the designed PCB. Indication of the charging sequence signals (defined by the CHAdeMO standard) and LED signals of the running communication through field buses are also present. Raspberry Pi single board computer is connected with the designed PCB via a flexible bus. Whole EFCU hardware is supplied by the Elko DC power supply with a power 54 W, which covers the power required by the CHAdeMO standard, required to power the Raspberry Pi single board computer and other electronics.

Fig. 3. Hardware realization of the EFCU

4 Software of the EFCU

The software for EFCU is written in the object-oriented language Python, which is suitable for prototype development due to the available libraries and simplicity. When designing the software architecture, emphasis was placed on a modular approach for future extensibility and versatility. Communication with the EV BMS was programmed as a finite state machine, see Fig. 4. The algorithms were designed according to the requirements of the CHAdeMO standard.

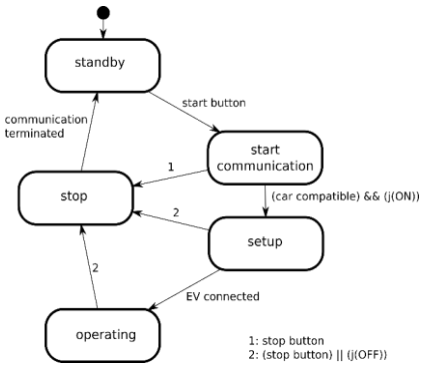

Fig. 4. State diagram of the EFCU

The program of the EFCU was divided into threads and processes, because there are strict time requirements in the CHAdeMO standard and threads in Python language do not support real parallelism on multi-core CPU. That is why more processes with interprocess communication means were used. The program of the EFCU from data flow point of view, is shown in Fig. 5.

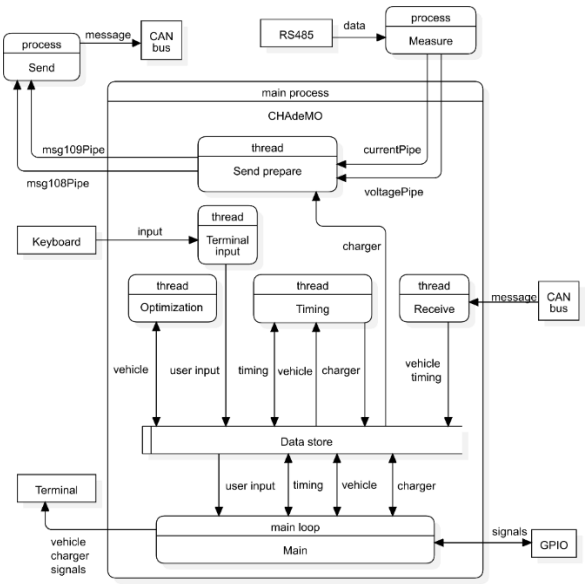

Fig. 5. Data flow diagram of the EFCU

5 Testing the EFCU

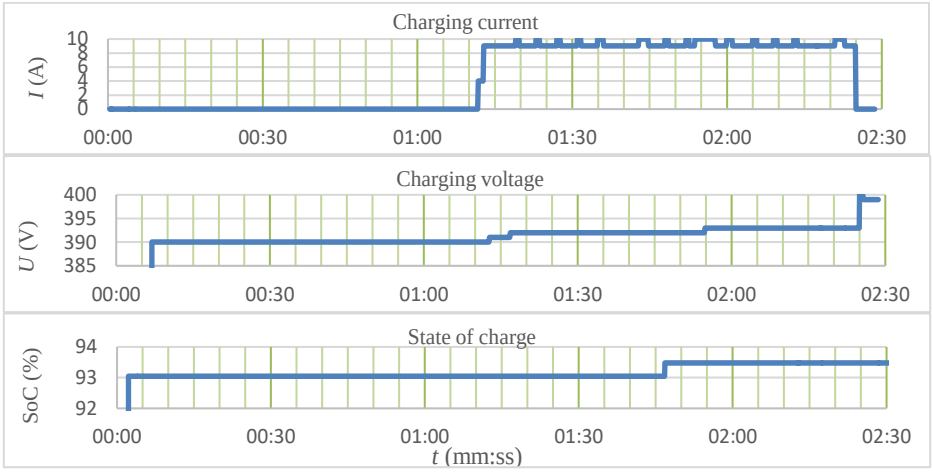

Fig. 6. Testing EFCU communication with the EV during charging

Communication according to the CHAdeMO standard between the developed EFCU and EV was tested during charging and discharging the EV. Chart from charging the EV is shown in Fig. 6. The time sequence of digital signals and digital communication signals via the CAN bus was also tested. All CHAdeMO sequence signals and signals in digital communication via CAN bus met the requirements and came in the right order.

6 Conclusion

The developed EFCU control unit has been tested to meet the CHAdeMO time requirements in communication with the EV. The EFCU is modularly programmed, it could be with slight effort used with another bidirectional inverter or Microgrid management system.

Work on this control unit was published in 2 articles on the 20th International Conference on Control, Automation and Systems (ICCAS 2020), held on the 13th to 16th of October 2020 in Busan, Korea [1][2].

Affiliation

Development of this control unit was carried out in the premises of the ENET Centre and supported by ENET Centre.

This work was supported by the Doctoral grant competition VSB - Technical University of Ostrava, reg. no. CZ.02.2.69/0.0/0.0/19_073/0016945 within the Operational Programme Research, Development and Education, under project DGS/TEAM/2020-017 "Smart Control System for Energy Flow Optimization and Management in a Microgrid with V2H/V2G Technology".

References

1. Kosinka, M., Slanina, Z., Petruzela, M., Blazek, V.: Control system for V2H applications. In: *2020 20th International Conference on Control, Automation and Systems (ICCAS)*, 2020, pp. 916-921, doi: 10.23919/ICCAS50221.2020.9268383.
2. Kosinka, M., Slanina, Z., Petruzela, M., Blazek, V.: "V2H control system software analysis and design," *2020 20th International Conference on Control, Automation and Systems (ICCAS)*, 2020, pp. 972-977, doi: 10.23919/ICCAS50221.2020.9268432.
3. "IEEE Standard Technical Specifications of a DC Quick Charger for Use with Electric Vehicles," in IEEE Std 2030.1.1-2015, vol., no., pp.1-97, 5 Feb. 2016, doi: 10.1109/IEEESTD.2016.7400449.
4. "IEEE Draft Standard Technical Specifications of a DC Quick and Bi-directional Charger for Use with Electric Vehicles," in IEEE P2030.1.1/D1, February 2021, vol., no., pp.1-159, 9 Feb. 2021.
5. ISO/DIS 15118-20: Road vehicles — Vehicle to grid communication interface — Part 20: 2nd generation network layer and application layer requirements. *International Organization for Standardization* [online], https://www.iso.org/standard/77845.html.
6. Hrbac, R., Kolar, V., Hrdina, L.: Bi-directional charger with a high power density for smart grids. In: *20th International Scientific Conference on Electric Power Engineering, EPE 2019*. ISBN 978- 172811333-3.
7. Blazek, V., Petruzela, M., Vantuch, T., Slanina, Z., Misak, S., Walendziuk, W.: The Estimation of the Influence of Household Appliances on the Power Quality in a Microgrid System. In: *Energies*. BASEL: MDPI Open Access Publishing, 2020, 13(17), ISSN 1996-1073.

Low-potential waste heat use in localized vertical farming

Lukas Vavra and Radomír Goňo

Department of Electrical Power Engineering, FEECS,
VSB – Technical University of Ostrava, 17. listopadu 15,
708 00 Ostrava – Poruba, Czech Republic
lukas.vavra1@vsb.cz

Abstract. As our world is challenged with massive population growth, one of the main problems humans face is the lack of arable land and freshwater. This leads us to the necessity to find more energy, space, and water-efficient ways to grow food. One of those potential ways of achieving this is vertical farming (VF), which is characterized by multiple shelves stacked vertically and side-by-side where the produce grows horizontally, or by so-called growing towers, where the produce grows to the sides. These shelves are filling the volume of warehouse or container-type space which consequently allows for 5 to 10 times the number of lettuce greens and herbs to be produced for given footprint of land, compared to the traditional farming. These systems offer significant benefits for water and space efficiency, yet they also suffer from high energy demands. Those demands are primarily on lights, temperature and humidity management, and air circulation. As such, there is significant potential for improvement in those areas in the form of new technology or in the form of integration of those vertical farms into the existing systems in mutually beneficial applications.

Keywords: Low-potential waste heat, Vertical farming, Localization, Urban farming, Efficiency

1 Introduction

Growing crops, then transporting them from farm to the distribution network to customers, requires significant amounts of energy. Most of the energy use in the food system occurs beyond the farm gate; the United Nations Food and Agriculture Organization (FAO) estimates that over 75% of energy use in the food system of high-income nations occurs after cultivation [9]. Regarding this, cuts on energy use can be achieved by usage of localized energy waste products of local business and industries. Such localization of food production would consequently lead to cutting energy loses on mentioned transportation, packaging, etc.

The first challenge that vertical farmers must overcome is figuring out how much cooling, dehumidification and heating is required to manage the temperature and humidity of the grow space. This must be considered during the whole year regarding change in outside temperatures as seasons change. And then finding local institutions and businesses with waste energy required for its use.

2 Low-potential waste heat

Many institutions, businesses and industrial complexes produce large amounts of waste heat and carbon dioxide through burning fossil fuels or natural gases. This waste heat and carbon dioxide is then wasted as unwanted byproduct.

These waste products can be used as energy stream for localized vertical farm in urban setting, which would be situated near this source of waste heat.

2.1 Heating

Heating is one of the most important processes to consider when building vertical farm, especially if the implementation of the VF is in the form of greenhouse or large warehouse-type growing complexes.

For example, heating of greenhouses is achieved with the use of natural gas, the consumed energy can reach the 31.6 MJ with 2.02 kg of CO_2 to produce 1 kg of tomatoes. Since the majority of greenhouses use fossil fuels to meet their heating demand such as natural gas, diesel, fossil fuel and liquid petroleum gas, it is of vital importance to strongly limit the greenhouses heat losses and to upgrade the heating systems [3].

The energy related to the heating and the cooling requirements in a lettuce production greenhouse is estimated by using the following equation:

$$Q = U \cdot A \cdot (T_{in} - T_{out}) \tag{1}$$

where

Q = Heat that is lost or gained due to the outdoor temperature ($kJ \cdot h^{-1}$)

U = Total heat transfer coefficient ($kJ \cdot h^{-1} \cdot m^{-2} \cdot °C^{-1}$)

A = Surface area of greenhouse (m^2)

T_{in} = Temperature inside the greenhouse

T_{out} = Temperature outside the greenhouse

In a small VF, lighting contributes the greatest source of heat, followed by motors used to operate fans, pumps and automation. This is not the case in large commercial greenhouses which often lose heat due to its size and air circulation requirements. The following loss of heat depends on the external climatic conditions and it is a decisive factor of the air technique modification to be used.

Furthermore, the heat transfer coefficient depends on the coverage material of each greenhouse, while the efficiency of cooling and heating systems depends on the height of the greenhouse ceiling [2]. Considering the potential size of these objects as the most efficient systems space wise are the tallest ones, they would require external sources of heat.

2.2 Humidity

Most food crops thrive in an environment with 40% to 50% humidity. Water vapor, a byproduct of plant transpiration, can build up in indoor farming structures, even those equipped with passive ventilation systems. Aside from causing issues such as the corrosion of metal equipment, trapped water vapor increases humidity in the growing environment. Dehumidifiers, however, can help maintain ideal humidity levels [8].

Dehumidification systems can also be made to recapture that water vapor and circulate it into the growing system itself. In California, one of the nation's most agriculturally rich states, anywhere from 1800 to 3500 cubic meters of water may be required to grow an acre of lettuce. In a vertical, indoor farm with a water capturing and recirculating dehumidification system, requirements for new water can drop to as low as 14 cubic meters, allowing for drastically reduced resource use and costs [8].

2.3 Dehumidification

Dehumidification is required to remove the moisture added to the air through evapotranspiration from plants and the irrigation system. This depends on variables such as air temperature, humidity, light temperature and intensity, irrigation system and air movement in the growing space.

Closed systems refer to absolute mechanical support of the cooling and dehumidification system by air treatment units. The air treatment unit consists of a heat exchanger that is connected to a ventilator. The purpose of the ventilator is to withdraw air from the interior of the greenhouse, cool it, dehumidify it, and then distribute it back into the greenhouse. Furthermore, in closed-systems water usually follows a close loop that allows the collection, recycle and re-distribution of the irrigation water both for irrigation purposes but also for cooling and heating purposes from inside the distribution pipes between the plant lines [1].

Heating systems in very small regulated vertical farms are rarely required due to the heat naturally generated by the lights in the growing space. However, such systems then require constant cooling which means that used air-conditioning system would take out the hot air and replace it with very cold air instead. This massive drop in temperature in one part of the vertical farm would cause harm to the plants, which is why we need to reheat it first, before sending it back into the growing space.

The stored energy is therefore used for reheating of this cold air.

3 Vertical farms linked with District Heating

District heating (DH) and vertical farms can develop side by side. Increases in the energy efficiency of modern buildings is reducing the heat consumption from District heating. Future development of VFs can help to compensate for the heat consumption reduction in the housing building stock and create possibilities to develop DH into new areas where normal heat demand is too low [4].

VF can potentially be integrated into every district heating network. The system needs low temperatures and can therefore be used to reduce the return temperature in the DH network, thereby increasing the efficiency of the network. In some cases, VF can, in a very intense production system, have a heat surplus that could be used to increase temperatures in the DH network when located in places far away from heat production. As all vertical farms are individual systems, as with DH, the local framework must be investigated how the systems can be linked to provide benefits for both sides. This includes deciding which types of VFs should be placed at various points along the DH network depending on the types of crops grown, their heat and energy requirements, and the in tensity of the production. VFs with lower heat requirements for example should be placed towards the end of the DH line to help lower the return temperature [4].

3.1 Waste heat in vertical farms

Because of the reduced space requirement, vertical stacks can be made more compact, fitting in a greater amount of effective growing space in each area. This also increases the light usage however, and in a working indoor farming growing basil plants this can create a LED energy usage of approximately 16 kWh/m^2 [7].

At this rate, even given the low heat waste resulting from LED lighting systems, such grow rooms can produce heat more than the required 21 °C for basil [8] or any other farm using LED lights. This provides an opportunity for sharing heat back into the district system or to neighboring buildings. This becomes even more so with higher temperature crops such as tomatoes that can be grown at temperatures of up to 30 °C.

3.2 Lowering return temperature

District heating efficiency relies partly on the difference between supply and return temperature. Lower return temperatures can lead to lower pumping costs and network heat loss. A key feature of the 4th Generation District Heating (4GDH) developments is to move towards low temperature systems, lowering the supply temperature to 50 °C and the return temperature to 20 °C – 25 °C [5].

VFs provide a useful low temperature building type to achieve this low return temperature. Usual grow room temperatures in urban farming vary greatly depending on the crop type being grown. This can range from 15 °C for certain lettuce types, to highs of 30 °C for tomato crops, usually with lower temperatures during the night. Average temperatures for lettuce, for example, are typically 21 °C during the day and 19 °C at

night. This provides a stable requirement for low temperature heating and provides a low temperature network part that can be added to the DH network [6].

While cooling may be required in summer months, during the winter period VFs may serve as ultra-low temperature demand buildings, particularly at nighttime. Positioning of VFs close to combined heat and power systems (CHPs) can help to get the reduction in return temperature required for the transformation from high to low temperature DH systems to achieve the long term vision of reducing the annual average return temperature to 20 °C [6].

References

1. Qian T. Wageningen University. Crop Growth and Development in Closed and Semi-Closed Greenhouses. pp. 1–112 (2017)
2. Avgoustaki D.D., Xydis G.: Advances in Food Security and Sustainability Volume 5, pp 1-51 (2020)
3. Xydis G., Liaros S., Avgoustaki D.D. Small scale plant factories with artificial lighting and wind energy microgeneration: a multiple revenue stream approach. (2020)
4. Matthew Gentry., Local heat, local food: Integrating vertical hydroponic farming with district heating in Sweden (2019)
5. Lund, et al. 4th Generation District Heating (4GDH) Integrating smart thermal grid into future sustainable energy system. Energy. 68:1 – 11 (2014)
6. Averfalk, et al. Annex XI final report: transformation roadmap from high to low temperature district heating systems. (2017)
7. Luuk G., Esteban B., Andy V.D.D., Ilias T., Cecilia S. Plant factories versus greenhouses: comparison of resource use efficiency. Agric Syst; 160:31 – 43 (2017)
8. DCA homepage, https://www.dehumidifiercorp.com/vertical-farming-dehumidifiers/, last accessed 2021/07/21
9. Eugene M.: Considerations for reducing food system energy demand while scaling up urban agriculture, Environmental Research Letters, volume 12 (2017)

Use of a distributed control system for substation control

Matouš Vrzala and Radomír Goňo

Department of Electrical Power Engineering, FEECS,
VSB – Technical University of Ostrava, 17. listopadu 15,
708 00 Ostrava – Poruba, Czech Republic
matous.vrzala@vsb.cz

Abstract. This article is focused on the possibilities of substation control using the 800xA control system from company ABB. This control system is one of the distributed control systems (DCS), which are the opposite of a centralized control systems. It is therefore not necessary to connect all signals and measured quantities to the central unit, but it is enough to connect them, for example, to the controller in the place of technology. The controllers are then connected by a communication bus. This control system will be used for controlling of many technological processes and at least two substations at the Technical University of Ostrava. Thanks to this control system, it is no longer necessary to control each element of substation manually at the place of a device, but the entire substation can be controlled from one control room. It is even possible to control the control of all substation elements from one graphical display. The first prerequisite for the full use of this system is the use of multifunctional IEDs (intelligent electronic devices). By default, one IED controls one substation feeder. IEDs communicates together and with DCS according to the standard IEC 61850. First of all, it is important to create a software or "Application Configuration" for every IED in ABB software PCM600. When it is done communication is set between PCM600 and 800xA, so all measured and calculated variables and control signals are then available in 800xA. The last activity is the creation of a graphic display for controlling the substation. It is suitable for this display to looks like single line diagram and after double-clicking on each element, the so-called faceplate of the element is displayed. Substation elements can be controlled from faceplates which means a big improvement for fast, clear and reliable substation control.

Keywords: substation control, 800xA, intelligent electronic device, distributed control systems

1 Introduction

The development of information technologies has meant a great development of automation in almost all technical fields in recent decades, and the electrical power engineering is no exception. Thanks to the smaller dimensions of components and the

increasing performance of electronics, it is now possible to control many more devices from one place. This can be used very well to control substation elements. It is no longer necessary to control each element manually at the place of a device, but the entire substation can be controlled from one control room. Thanks to the most advanced control systems, we can even control all substation elements from a single graphic display. [1]

Automation has probably the largest application in the industry. In addition to electronic devices, industrial automation is today often applied also to power devices, various generators and motors, for which the simplest and most reliable control and management is desired. [2] Large industrial companies sometimes have their own substation or more substations, and therefore there are requirements for the control of production processes (e.g. motors) and at the same time the control of the substations. Today, this can be implemented using state-of-the-art distributed control systems within a single software from a single PC. [3] One of these systems is the 800xA from the company ABB, which is very complex system and can be used to create applications to control many various processes. It is therefore suitable both for controlling substations and for controlling technological devices (motors etc.). This system is already installed at VŠB-TUO and is to be used in the future for the control and management of two substations and many technologies in the planned building CEETe. CEETe will be a research center that will use modern methods to convert waste and other alternative fuels into useful forms of energy. These modern technologies will also be used in education, so that students will be able to learn about them.

2 Settings of IEDs in software PCM600

Software PCM600 consists of few tools for IED setting and management. First necessary tool is "Project Explorer". Each project begins by inserting individual IEDs into it. In this way, it is possible to create either a set of IEDs or a substation with different voltage levels with substation feeders, where is usually one IED for each feeder. The Fig. 1 shows the structures.

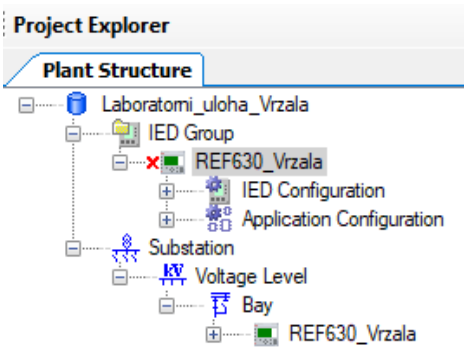

Fig. 1. Plant structure in PCM600

Configuration of an application is prepared by tool which is called just "Application Configuration" which provides programming using function blocks. Every protection, measuring or other function has its own function block with inputs and outputs for variables. Scheme of Application Configuration is shown in Fig. 2. [6]

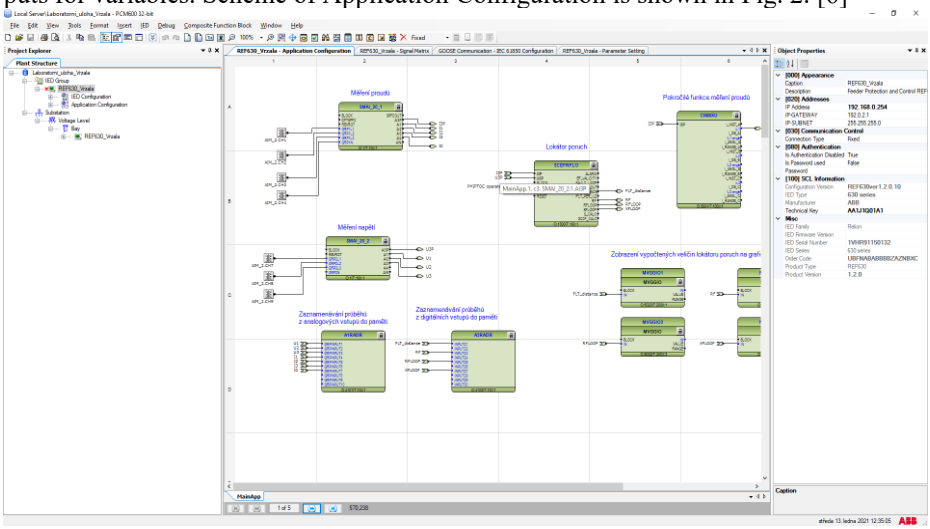

Fig. 2. Application Configuration tool in PCM600 software

All measured values as well as any analog or digital signals can be sent to and received from other IEDs. This communication is called GOOSE and follows standard IEC 61850. [8] Similarly, all this data can be sent and received from the superior system, which is called MMS communication and in PCM600 it is referred to as Client-Server Communication. In this way, the set values of the individual function blocks can also be sent. As part of this communication, so-called datasets are sent. These can be created in the tool "IEC 61850 Configuration". Individual signals can be inserted into datasets as shown in Fig. 3, the name of which follows a exactly defined structure: [5], [8]

1. LD - Logical Device - this corresponds to the designation of any logical component of the IED to which the signal relates.
2. LN - Logical Node - this corresponds to any specific element (device or device function) to which the signal relates (e.g., switch, disconnector, fault recorder or one of their functions)
3. DO - Data Object - indicates a set of attributes that are somehow bound together. For example, the data attributes of object "A" are all related to the value of the electrical current. These data objects can be divided into other sections such as in this case: A.phsA, A.phsB, A.phsC
4. FC - Functional Constraints - indicates a narrower set of attributes than DO, for example MX indicates attributes that provide information about the measured or calculated value - so they are typically analog signals. In contrast, ST indicates a set of attributes that provide information about the status of a function - typically

digital signals - 0 means off, 1 on; or 0 function (eg alarm) is not active, 1 function is active. These Functional Constraints can be added as an item to the dataset, so there is no need to add each attribute separately.

5. DA - Data Attribute - indicates a very specific signal. For example, cVal.mag.f specifically indicates the instantaneous current value. In this way, one signal can be added to the dataset one by one.

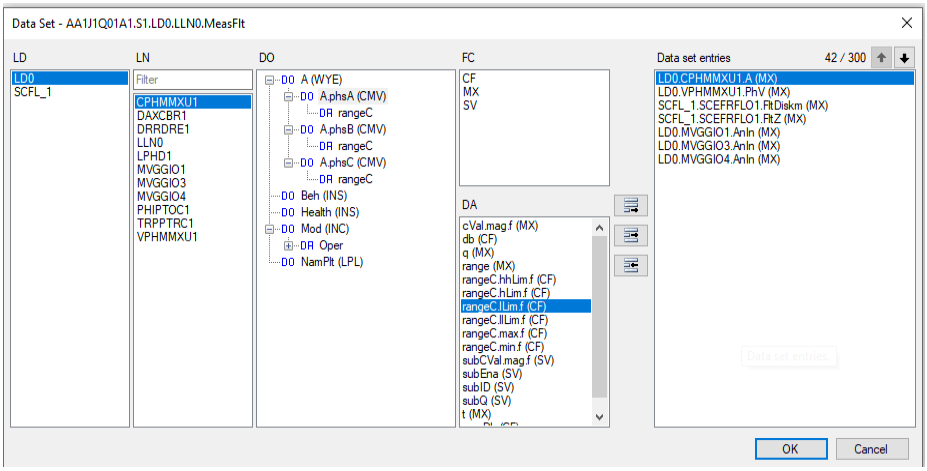

Fig. 3. Creating datasets

3 Settings of substation control in software 800xA

There are two possibilities how to control IEDs in 800xA software. First option is to use signal mapping in special library for IEC 61850 and set everything in the "Object type structure" of 800xA, second option is to use controller (e.g. AC800M) and set everything in the "Control builder" tool. For both options, the graphic display is created in the "Functional structure". When using Object type structure there is needed for every element (switching device etc.) to create a list of required signals which are already in datasets and define from which IED the signal should be received. The main part of the AC800M controller is a processor (e.g. PM860) and the second key component is the CI868 communication card, which the controller communicates with IEDs via Ethernet by protocol IEC 61850. In the 800xA tool "Control builder" it is then necessary to assign the IED to the communication card and define names of logical devices and logical nodes. [4], [7]

Then it is possible to create graphical display for easy and clear control of substation. To display the status of individual substation elements, measurements and diagnostics in the 800xA system, a graphical display is created, which may have a look similar to an SLD drawing. Fig. 4 below shows a substation with several voltage levels and a branched busbar system. There it is possible to easily monitor the status of the switching elements.

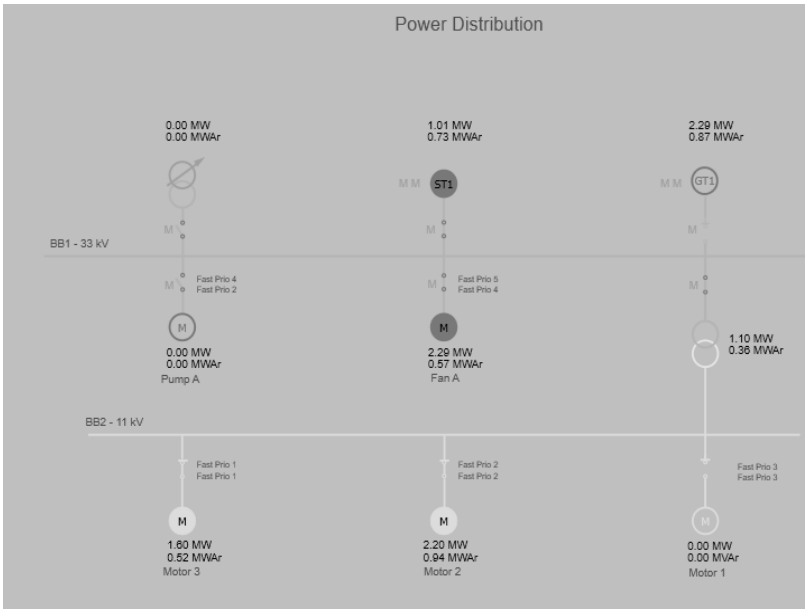

Fig. 4. Graphical display for substation control

The individual elements can be double-clicked, which, for example, displays an element window (so-called faceplate) to the operator in the control room, where he can see information about the status of the element, measured values and alarms (warnings). An example of a faceplate for a switch can be seen in Fig. 5. The faceplate itself has three tabs there. The Main tab provides a graphical display of the status and the measured value (analog signals). The Status tab provides information about the status of the circuit breaker (binary signals). The Monitor tab displays a warning that the entered values have been exceeded (again, these are binary signals). All these signals are sent by IED of the substation feeder (eg ABB REF630) within the above-mentioned communication according to the IEC61850 protocol.

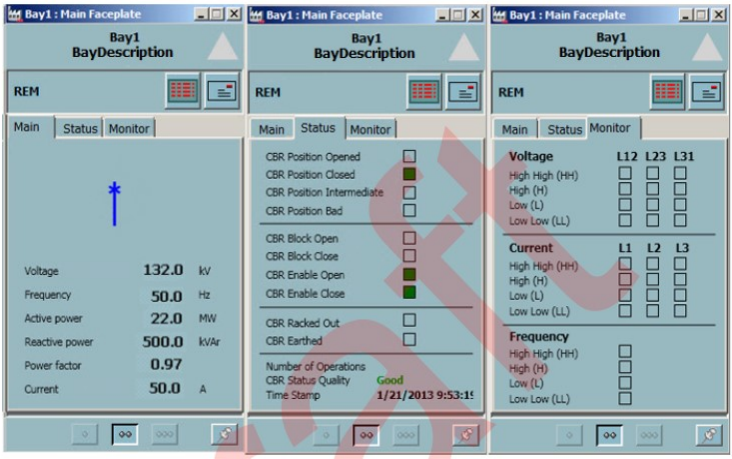

Fig. 5. Faceplates

4 Conclusion

Nowadays we have a new modern solution for control of substations – substation automation. Distributed control systems as 800xA from ABB provide possibility to control all elements of substation from one screen. Important requirement is use of modern multifunctional protection relays called also IEDs. When there are installed IEDs at substation feeders supporting standard IEC 61850 then communication via datasets with control system can be established. Therefore, control of substation can be more clear, reliable and faster than ever before.

Acknowledgement: This research was supported by the SGS grant from VSB - Technical University of Ostrava (No. SP2021/20).

5 References

1. J. D. McDonald, *Substation automation. IED integration and availability of information*, in IEEE Power and Energy Magazine, vol. 1, no. 2, pp. 22-31, March-April 2003, doi: 10.1109/MPAE.2003.1192023.
2. Y. Oualmakran, J. Meléndez and S. Herraiz, *Opportunities and challenges for smart power restoration and reconfiguration smart decisions with smart grids*, 11th International Conference on Electrical Power Quality and Utilisation, 2011, pp. 1-6, doi: 10.1109/EPQU.2011.6128807.
3. M. Otčenášek. *Distributed control systems and its utilization in practice.* Brno: Brno University of technology, Faculty of Electrical Engineering and Communication, 2007.
4. L. Andersson, C. Brunner and F. Engler, *Substation automation based on IEC 61850 with new process-close technologies,* 2003 IEEE Bologna Power Tech Conference Proceedings, 2003, pp. 6 pp. Vol.2-, doi: 10.1109/PTC.2003.1304321.
5. *System 800xA + ABB REF Protections IEC61850 Expert workshop*, ABB University, 2019
6. *RELION® protection and control 630 series Technical Manual*. VAASA, Finland: ABB Distribution Solutions Distribution Automation, 2014
7. *Course T315C System 800xA - AC 800M Engineering*, Part-1 Control Builder, ABB University, 2019
8. International Electrotechnical Commission. *IEC 61850: Communication networks and systems in substations*. vol. IEC 61850.2 (2013).

Non-Invasive Fetal Electrocardiogram Extraction for Heart Rate Monitoring and ST Analysis

Kateřina Barnová and Radek Martinek

Department of Cybernetics and Biomedical Engineering, FEECS,
VSB – Technical University of Ostrava, 17. listopadu 15,
708 00 Ostrava – Poruba, Czech Republic
{katerina.barnova, radek.martinek}@vsb.cz

Abstract. This paper focuses on a non-invasive fetal electrocardiogram extraction based on a combination of non-adaptive and adaptive algorithms. The experiments were performed on real recordings from the Abdominal and Direct Fetal Electrocardiogram Database and evaluated according to the accuracy of detection of fetal QRS complexes, determination of fetal heart rate and ST analysis. In terms of fetal QRS complexes detection and fetal heart rate estimation, the accuracy was high for all tested recordings. For seven out of eight recordings, it was possible to perform ST analysis with high accuracy compared to the reference fetal scalp electrode. The results of the experiments demonstrated that non-invasive ST analysis is feasible and that it provides access to equivalent diagnostic information obtained by invasive fECG monitoring.

Keywords: Non-invasive fetal electrocardiography (NI-fECG), independent component analysis (ICA), recursive least squares (RLS), fetal heart rate (fHR), ST analysis (STAN), fetal hypoxia.

1 Introduction

Electronic fetal monitoring is an integral part of modern obstetrics, serving mainly to diagnose fetal hypoxia. Fetal hypoxia is one of the most common causes of perinatal morbidity and mortality, thus an accurate diagnosis of hypoxia is a primary goal in fetal monitoring. Cardiotocography (CTG) is currently used in clinical practice, allowing simultaneous monitoring of fetal heart rate (fHR) and uterine contractions. However, some studies [1], [2] show that CTG is not a sufficiently accurate technique, as it is burdened with high false positivity in detecting hypoxia leading to a high number of unnecessarily performed cesarean sections. Cesarean section is a surgical procedure that can cause health complications for both mother and newborn [3]. Therefore, there are demands from physicians to find new solutions for non-invasive fetal monitoring.

Fetal electrocardiography (fECG) appears to be a promising method for determining fetal hypoxia more accurately, as it carries information about changes in waveform morphology. Changes in waveform morphology, such as the T/QRS ratio or the length of the QT interval, are associated with fetal hypoxia. In clinical practice,

© M. Krátký, J. Dvorský, P. Moravec (Eds.): WOFEX 2021, pp. 253–258.
VSB – Technical University of Ostrava, 2021, ISBN 978-80-248-4523-4 (on-line).

T/QRS ratio analysis (ST analysis or STAN) is performed by an invasive recording of fECG from the fetal head or hip. However, this procedure can be performed only during labor, and in addition, is associated with a risk of developing infection [4]. For these reasons, the aim of this paper was to determine whether it is possible to determine fHR and ST analysis from non-invasively recorded fECG signals from the abdominal area of the mother as accurately as using invasive fECG.

The paper structure includes the following sections: section 2 deals with a description of the database, extraction algorithms and the principle of monitoring fHR and determining ST analysis. Section 3 presents the achieved results and publications where these results have been published. Section 4 summarizes the benefits and limitations of the proposed approach and outlines future challenges.

2 Material and Methods

This section describes independent component analysis (ICA) and recursive least squares (RLS) algorithms that have been used to extract fECG recorded from the mother's abdomen. The database used and the methods for determining fHR and ST analysis are also described.

2.1 Dataset

The experiments were performed on 8 real recordings from the Abdominal and Direct Fetal ECG Database [5]. The recordings were obtained from women between the 38th and 42nd weeks of gestation using the KOMPOREL system. Each recording contains 4 abdominal signals (aECG), an annotation with R-peaks reference positions, and an ideal fECG signal from the scalp electrode. The abdominal signals were recorded using the Ag-AgCl electrodes, while the direct signals were recorded by means of spiral fetal scalp electrode. The signals of 5 minutes length each were digitized with a 16-bit resolution at 500 Hz sampling frequency for aECG signals and 1000 Hz for a direct reference fECG. Although the database includes a total of 12 recordings, we only used 8 of them (r01, r02, r03, r05, r06, r08, r09, and r10), as the remaining 4 records (r04, r07, r11, and r12) were not of sufficient quality to perform morphological analysis.

2.2 Fetal Electrocardiogram Extraction

In non-invasive abdominal aECG signals, the fECG is accompanied by maternal electrocardiogram (mECG) and noise. The mECG and fECG signals overlap in both the time and frequency domains, and therefore conventional filtering methods are not effective enough. Thus, the use of advanced signal processing methods is required for fECG extraction.

For this multichannel method, at least two aECG signals were used for each recording. First, these signals were filtered using a bandpass finite impulse response filter with cut-off frequencies of 3 and 150 Hz and a filter order of 500 to eliminate

the variations in isolines. The preprocessed aECG signals were decomposed by the ICA method into three components corresponding to the mECG, the aECG with an enhanced fetal component (denoted as aECG*) and the noise. The first two estimated signals (mECG and aECG*) by the ICA method were used as inputs for the adaptive RLS algorithm. The mECG signal was adjusted by the filter into a shape of the mECG component in the aECG* signal. This modified mECG signal was subtracted from the aECG*, thus generating the resulting fECG signal.

2.3 Fetal Heart Rate Monitoring

The detection of R-peaks was done using an R-peaks detector, which was based on the continuous wavelet transform (the first-order Gaussian wavelet base and five levels of decomposition). The detection accuracy of estimated fetal R-peaks was determined by comparison with annotations indicating the positions of fetal R-peaks (true positive, false negative and false positive values were determined and the accuracy – ACC, the sensitivity – SE, the positive predictive value – PPV and F1 indices were calculated). Based on the detected positions of the R-peaks, fHR was determined and evaluated by comparing fHR traces and Bland-Altman plots (mean values μ and values of $\pm 1.96\sigma$ were calculated).

2.4 ST Analysis

The ST analysis was inspired by the principle of STAN devices used in clinical practice. The STAN device analyses every 30 ECG complexes and compares them with the baseline value [6]. Similarly, we performed ST analysis on 30 averaged consecutive fECG complexes. In order to perform the analysis of T/QRS ratios, in addition to R-peaks, it was necessary to detect S-peaks and T-waves. Fetal S-peaks were detected as the lowest value in the interval between the R-peak and the following 40 ms. The T-wave detection was performed based on the approach proposed in [7]. The fECG signal was duplicated, filtered by a Butterworth bandpass filter with cut-off frequencies of 0.5 and 10 Hz. The fQRS complex was suppressed and the T-wave was detected by thresholding. The ST analysis was performed by calculating T/QRS ratios for each averaged fECG complex and compared to the reference ratios determined from the reference fECG signal using Bland-Altman plots (mean values μ and values of $\pm 1.96\sigma$ were calculated).

3 Results and Publications

Using the ICA-RLS method, statistical results showed high accuracy in the detection of fQRS complexes, as F1 > 90% was achieved for all recordings. Similarly, an accurate determination of fHR for all eight recordings was achieved as low mean values μ and values of $\pm 1.96\sigma$ were obtained. In addition, ST analysis was highly accurate for all recordings except r06, where a high value of $\pm 1.96\sigma$ was achieved. The results of the statistical indices were supported by means of a graphical illustration. Fig. 1. dis-

plays fHR traces and ST analysis marked with a star '*' (similarly to conventional STAN monitors used in clinical practice). The top arrows indicate the names of the recordings related to the given section of the graph. The upper waveform represents fHR traces obtained by the ICA-RLS method compared to the reference fHR traces created using the annotations. The lower part shows the results of the ST analysis. The T/QRS ratios obtained by the method were compared with the T/QRS ratios determined using the reference signal. More detailed results achieved using the ICA-RLS method in the determination of fHR and ST analysis were presented in [8].

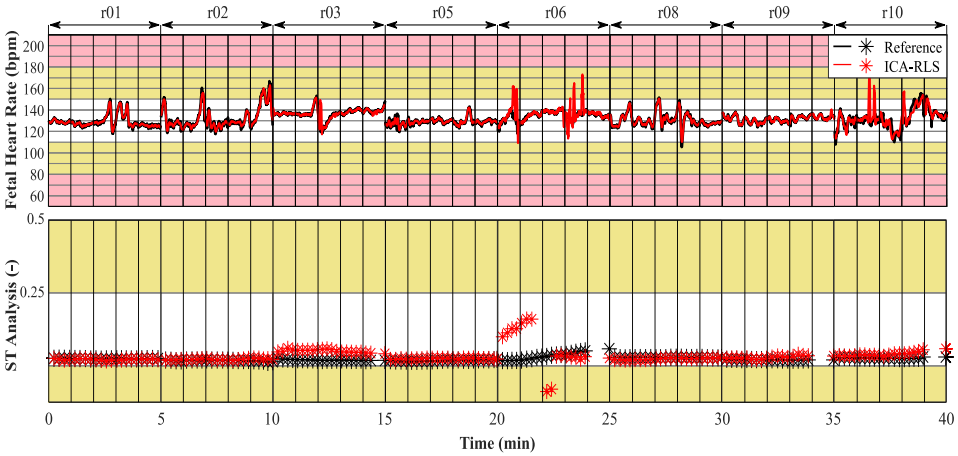

Fig. 1. Visual comparison of the fHR traces and ST analysis.

This paper builds on previously presented experiments where the ICA [9] or a combination of ICA and principal component analysis (PCA) [10] was used for fECG extraction. However, fECG extraction was not accurate enough and therefore an adaptive RLS algorithm was incorporated. The results using the ICA-RLS method proved to be very promising in the determination of fHR. Further improvement of the results was achieved by adding a postprocessing method. In [11] a wavelet transform (WT) and in [12] an empirical mode decomposition (EMD) was used, therefore ICA-RLS-WT and ICA-RLS-EMD were created. In both cases, a slightly more accurate extraction was achieved when determining fHR, however, the morphology of the signal was altered, and the results of the ST analysis were less accurate compared to ICA-RLS. Comparison of performance of ICA-RLS, ICA-RLS-WT and ICA-RLS-EMD methods in evaluating the accuracy of detection of fQRS complexes, determination of fHR and ST analysis is summarized in Table 1.

Table 1. Comparison of performance of ICA-RLS, ICA-RLS-WT and ICA-RLS-EMD methods in evaluating the accuracy of detection of fQRS complexes, determination of fHR and ST analysis. All values in the table indicate the average value determined for the eight records used for the experiments.

Methods	fQRS complexes detection				Determination of fHR		ST analysis	
	ACC (%)	SE (%)	PPV (%)	F1 (%)	μ (bpm)	±1.96σ (bpm)	μ (-)	±1.96σ (-)
ICA-RLS	95.13	98.07	96.82	97.43	0.20	5.80	0.008	0.031
ICA-RLS-WT	95.44	96.86	98.36	97.58	0.06	4.53	0.173	0.478
ICA-RLS-EMD	97.29	98.44	98.76	98.59	0.18	5.24	0.446	0.689

Fig. 2 shows the waveforms of the ideal reference fECG signal, the aECG signal containing a mixture of mECG, fECG and noise, and the examples of fECG signal extraction using the ICA-RLS method, and the effect of postprocessing when applying the WT or EMD algorithm. For the signal extracted by ICA-RLS, residues of the maternal component can be seen, leading to lower accuracy in the detection of fQRS complexes and the determination of fHR. Using postprocessing methods WT or EMD, these residues were reliably eliminated, but the signal morphology was altered in both cases, leading to worse results in ST analysis. Thus, it can be stated that in the case of the need for accurate detection of fQRS complexes and accurate determination of fHR, it is suitable to use WT or EMD method for signal postprocessing. However, if a deeper morphological analysis is required, the use of these methods is not recommended as they have a negative effect on the signal morphology (on all elements of the PQRST complex), which may lead to an unnecessary loss of valuable clinical information.

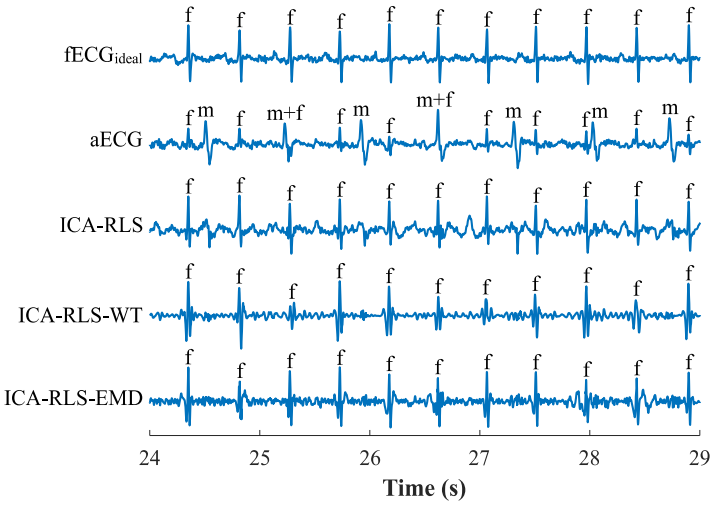

Fig. 2. An example of an ideal reference fECG, aECG (mixture of mECG, fECG and noise) and extracted fECG signals using ICA-RLS, ICA-RLS-WT and ICA-RLS-EMD methods.

4 Conclusion and Future Work

The results of our experiments have shown that the combination of ICA and the adaptive RLS algorithm was able to extract high-quality fECG and accurately determine fHR for all tested recordings. In addition, an accurate non-invasive ST analysis was performed for seven out of eight recordings. This demonstrates that morphological analysis can be performed on non-invasive fECG signals while achieving similar results as when direct invasive fECG signal is used. However, to perform an accurate morphological analysis, attention must be paid to the selection of suitable filtration methods and high-quality recorded input aECG signals must be used. Future research will focus on the analysis of other morphological elements (such as QT interval analysis) that may help to refine the determination of fetal hypoxia. In addition, the functionality of the proposed method will be verified for a larger number of recordings.

References

1. J. Spilka et al., “Analysis of obstetricians’ decision making on CTG recordings”, Journal of Biomedical Informatics, vol. 51, pp. 72-79, 2014.
2. T. P. Sartwelle, “Electronic Fetal Monitoring: A Bridge Too Far”, Journal of Legal Medicine, vol. 33, no. 3, pp. 313-379, 2012.
3. J. Sandall et al., “Short-term and long-term effects of caesarean section on the health of women and children”, The Lancet, vol. 392, no. 10155, pp. 1349-1357, 2018.
4. L. Cordero and E. H. Hon, “Scalp abscess: A rare complication of fetal monitoring”, The Journal of Pediatrics, vol. 78, no. 3, pp. 533-537, 1971.
5. J. Jezewski et al. “Determination of fe-tal heart rate from abdominal signals: evaluation of beat-to-beat accuracy in re-lation to the direct fetal electrocardiogram”, Biomedizinische Technik/Biomedical Engineering, vol. 57, no. 5, Jan. 2012.
6. E. Chandraharan, Ed., Handbook CTG Interpretation: From Patterns to Physiology. Cambridge, U.K.: Cambridge Univ. Press, 2017.
7. M. Elgendi et al., “Fast T Wave Detection Calibrated by Clinical Knowledge with Annotation of P and T Waves”, Sensors, vol. 15, no. 7, pp. 17693-17714, 2015.
8. R. Martinek et al., “Non-Invasive Fetal Electrocardiogram Extraction Based on Novel Hybrid Method for Intrapartum ST Segment Analysis”, IEEE Access, vol. 9, pp. 28608-28631, 2021.
9. R. Jaros, R. Martinek, K. Barnova, and M. Ladrova, "Extraction of Fetal Electrocardiogram by Independent Component Analysis", in 2019 International Symposium on Advanced Electrical and Communication Technologies (ISAECT), 2019, pp. 1-5.
10. R. Jaros, R. Martinek, K. Barnova, and M. Ladrova, “Use of a Hybrid Method ICA-PCA-ICA for Fetal Electrocardiography Extraction”, in 2019 International Symposium on Advanced Electrical and Communication Technologies (ISAECT), 2019, pp. 1-6.
11. R. Jaros, R. Martinek, R. Kahankova, and J. Koziorek, “Novel Hybrid Extraction Systems for Fetal Heart Rate Variability Monitoring Based on Non-Invasive Fetal Electrocardiogram”, IEEE Access, vol. 7, pp. 131758-131784, 2019.
12. K. Barnova, R. Martinek, R. Jaros, and R. Kahankova, “Hybrid Methods Based on Empirical Mode Decomposition for Non-Invasive Fetal Heart Rate Monitoring”, IEEE Access, vol. 8, pp. 51200-51218, 2020.

Continuous Noninvasive Blood Pressure Estimation from Pulse Transit Time

Daniel Barvik[0000−0001−7699−8792] and Martin Cerny[0000−0002−8893−2587]

Department of Cybernetics and Biomedical Engineering, FEECS,
VSB – Technical University of Ostrava, 17. listopadu 15,
708 00 Ostrava – Poruba, Czech Republic
{daniel.barvik, martin.cerny}@vsb.cz

Abstract. Noninvasive continuous blood pressure estimation is a promising alternative to minimally invasive blood pressure measurement using cuff and invasive catheter measurement, because it opens the way to both long-term and continuous blood pressure monitoring in ecological situation. The most current estimation algorithm is based on pulse transit time measurement where at least two measured signals need to be acquired. From the pulse transit time values, it is possible to estimate the continuous blood pressure for each cardiac cycle. This measurement highly depends on arterial properties which are not easily accessible with common measurement techniques; but these properties are needed as input for the estimation algorithm. With every change of input arterial properties, the error in the blood pressure estimation rises, thus a periodic calibration procedure is needed for error minimization. Recent research is focused on simplified constant arterial properties which are not constant over time and uses only linear model based on initial measurement.

Keywords: Noninvasive continuous blood pressure · cuffless blood pressure · pulse transit time · pulse wave analysis.

1 Introduction

Blood pressure (BP) is an important parameter of human health, since hypertension is a major risk factor of the cardiovascular system [18, 3]. Continuous measurement of blood pressure helps with the hypertension treatment and it shows the dependence of blood pressure on the whole vascular system and indicates the vascular properties [18, 3]. Nowadays, the continuous measurement of blood pressure is only possible with an invasive measurement method using catheter as the gold standard. This method measures BP at any arterial site using a strain gauge. Other blood pressure measurements are only in discrete time with long intervals between measurements [19]. These noninvasive methods primarily require an inflatable cuff [15]. Pulse transit time (PTT), the time delay of pulse wave travel between two arterial places, or pulse wave velocity (PWV) promising methods for noninvasive and continuous estimation of blood pressure using nonobstructive sensors instead of inflated cuff for conventional blood

pressure measurements. These methods estimate the BP without applying an external pressure [19, 17].

The blood pressure values vary periodically from the maximal systolic blood pressure to minimal diastolic blood pressure. Typical blood pressure value of healthy person is 120 over 80 millimeters of mercury. The BP could be much higher or lower to maintain homeostasis and accommodation to external conditions or due to vascular pathologies. In the long-term measurement the vascular properties vary as the blood pressure. These variations cause an increasing error in continuous BP measurement based on pulse transit time [18].

2 Methods of PTT Measurement

The pulse delay between two known places on artery is the pulse transit time [18, 21, 19, 20]. Most conventional method to calculate PTT is using at least two signal generated by cardiovascular system, the R peak of electrocardiogram (ECG) signal as reference and the arrival of pulse wave detected by photoplethysmography (PPG) sensor [18, 23, 21, 11]. For PTT calculation specific points on PPG wave must be detected. In the literature, most papers report the use of the steepest point of the pulse wave, or the maximum of the first derivative and alternatively the annulation of the second derivative [9, 24, 18]. The key for better accuracy of PTT calculation is the synchronous acquisition of multiple biosignals, for example ECG and PPG. The PPG sensor is located on the finger, for a where good light absorbance conditions, but with the narrowing of blood vessel, the pulse wave changes the shape [24]. With the rising blood pressure the pulse wave velocity is increasing and the pulse transit time is decreasing.

PTT is mostly calculated as time interval between ECG, PPG and tonoarteriography (TAG), which is an unobtrusive continuous arterial BP signal recorded by a pressure sensor placed mostly on radial artery of the same arm as the PPG sensor [7, 24]. This method cannot eliminate the pre-ejection period. But this pre-ejection period can be easily eliminated using other signals than the ECG as a reference. The pre-ejection period is not correlated with the blood pressure value and it causes the error in the BP estimation algorithm [7, 24]. One of the methods for PEP elimination is impedance cardiography (ICG) [22, 10], in this method electrodes are placed on the chest to detect the aortic valve opening. After aortic valve opening, the blood is expelled and that provokes a measurable decrease in chest impedance. Together, the ECG, ICG, and PPG on the chest can be synchronized and used to eliminate the PEP to obtain a clear PTT value [8].

Additionally other biosignals illustrated in Figure 1 can be used for detecting PTT. The rapid acceleration of ejected blood from heart can be detected using the ballistocardiography (BCG) method due to mass movement in great vessels and PTT can be estimated as a delay between BCG and PPG [8].

The micro vibrations detection of seismocardiography (SCG) is one of the options for PTT measurement. These vibrations are produced by heart contraction and ejection of the blood. With seismography method the mechanical events

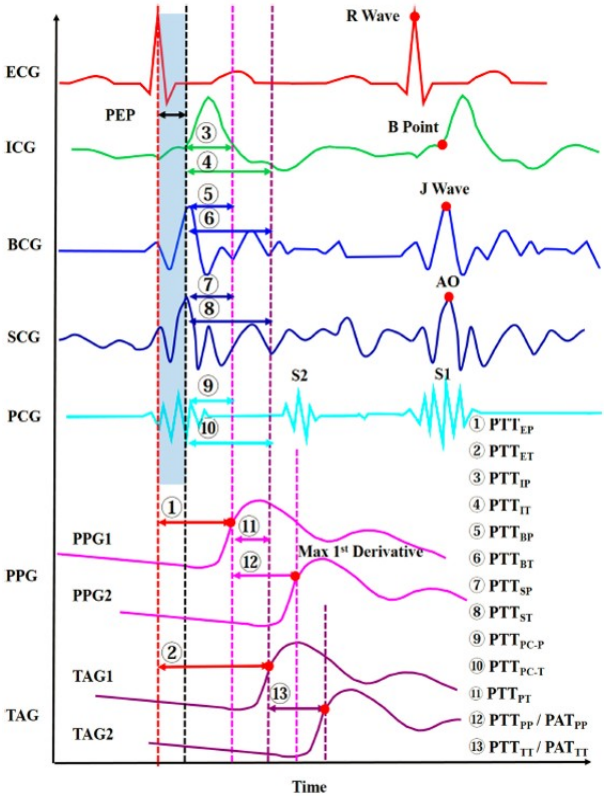

Fig. 1. Comparison of methods for PTT calculation [8].

are detected such opening and closure of mitral and aortic valves. This events can be used for PTT calculation excluding pre-ejection period [2, 6].

The sound of the mechanical activity of the heart can be recorded by using phonocardiography (PCG) method. As in the previously mentioned methods, this recorded sound can be the start point of pulse transit time measurement with the eliminated pre-ejection period [5, 1].

3 Discussion

All mentioned methods calculates pulse transit time with respect to heart activity but one of the efficient method of the pre-ejection period elimination uses measurement of PPG or TAG in close sensor placement, ideally on one arterial segment [8, 13, 16].

The most comfortable method for PTT measurement should avoid to use the electrode on patient chest, but only measurement sites should be located on one or maximally two sites on the hand like a wrist and finger [13, 16] or two places on the forearm [16]. Unfortunately, the approach of seismocardiogram and

ballistocardiogram is not applicable whilst they are sensitive to micro-vibrations of human heart and it is not reachable for normal conventional measurement. In addition, the phonocardiography and impedance cardiography use sensors on the chest, which are not comfortable for the patient. From this methods, the best solution is only the use of hand-placed sensor system. This sensor would be more precise, because of almost constant vessel properties on small sensor distance. This measurement could be done by measuring impedance plethysmogram IPG [4, 14] or PPG.

The best approach to measure PTT seems to be the measurement on single vessel, because the vessel exhibits constant parameters such as his diameter, compliance, stiffness. This measurement method uses the two ICG or PPG close each other on one vessel or their combination. Also the use of tonometry in addition with PPG sensor on the wrist and fingertip can be useful for PTT detection [16, 12, 24]. In central arteries the blood pressure strongly depends on vascular elasticity, whereas in peripheral arteries the correlation between PTT and BP is lower due to smooth muscle contractions. The peripheral arteries have many curvatures, branches, and terminals where the reflection occurs. The pulse wave is therefore composed from original forward wave and many backward reflected waves [16]. The artery stiffness highly depends on age of the test subject and it also affects the shape of the pulse wave [24].

4 Conclusion

Based on the literature review the estimation method of CNIBP is significantly dependent on lag between electrical activity of heart and valve closure. Thus for our measurement we will use the promising IPG method directly on arteries with conventional PPG biosignal measurement. These measurement would be done ideally on one artery to eliminate change of arterial properties e.g. diameter, wall thickness and stiffness.

References

1. Babu, K.A., Ramkumar, B., Manikandan, M.S.: Automatic Identification of S1 and S2 Heart Sounds Using Simultaneous PCG and PPG Recordings. IEEE Sensors Journal **18**(22), 9430–9440 (Nov 2018). https://doi.org/10.1109/JSEN.2018.2869416
2. Cai, X., Roscoe, B.J., Alamgir, Z.M., Sani, S.N., Wang, R., Schuckers, S.C., Stoian, A., Robinson, C.J.: Latencies of Cardiac-Linked Seismic Pulses in Head Accelerometer Measurements. In: 2013 39th Annual Northeast Bioengineering Conference. pp. 201–202 (Apr 2013). https://doi.org/10.1109/NEBEC.2013.107
3. Chung, W.Y.: High Blood Pressure — NHLBI, NIH. https://www.nhlbi.nih.gov/health-topics/high-blood-pressure
4. Corciova, C., Ciorap, R., Zaharia, D., Matei, D.: Hemodynamic monitoring using peripheral impedance plethysmography. In: 2011 7TH INTERNATIONAL SYMPOSIUM ON ADVANCED TOPICS IN ELECTRICAL ENGINEERING (ATEE). pp. 1–4 (May 2011)

5. Dastjerdi, A.E., Kachuee, M., Shabany, M.: Non-invasive blood pressure estimation using phonocardiogram. In: 2017 IEEE International Symposium on Circuits and Systems (ISCAS). pp. 1–4 (May 2017). https://doi.org/10.1109/ISCAS.2017.8050240
6. Di Rienzo, M., Lombardi, P., Scurati, D., Vaini, E.: A new technological platform for the multisite assessment of 3D seismocardiogram and pulse transit time in cardiac patients. In: 2016 Computing in Cardiology Conference (CinC). pp. 781–784 (Sep 2016)
7. Ding, X., Dai, W., Luo, N., Liu, J., Zhao, N., Zhang, Y.: A flexible tonoarteriography-based body sensor network for cuffless measurement of arterial blood pressure. In: 2015 IEEE 12th International Conference on Wearable and Implantable Body Sensor Networks (BSN). pp. 1–4 (Jun 2015). https://doi.org/10.1109/BSN.2015.7299405
8. Ding, X.R., Zhao, N., Yang, G.Z., Pettigrew, R.I., Lo, B., Miao, F., Li, Y., Liu, J., Zhang, Y.T.: Continuous Blood Pressure Measurement From Invasive to Unobtrusive: Celebration of 200th Birth Anniversary of Carl Ludwig. IEEE Journal of Biomedical and Health Informatics **20**(6), 1455–1465 (Nov 2016). https://doi.org/10.1109/JBHI.2016.2620995
9. Ding, X., Yan, B.P., Zhang, Y.T., Liu, J., Zhao, N., Tsang, H.K.: Pulse Transit Time Based Continuous Cuffless Blood Pressure Estimation: A New Extension and A Comprehensive Evaluation. Scientific Reports **7**(1), 11554 (Sep 2017). https://doi.org/10.1038/s41598-017-11507-3
10. Forouzanfar, M., Baker, F.C., Colrain, I.M., de Zambotti, M.: Automatic Artifact Detection in Impedance Cardiogram Using Pulse Similarity Index. In: 2019 41st Annual International Conference of the IEEE Engineering in Medicine and Biology Society (EMBC). pp. 2629–2632 (Jul 2019). https://doi.org/10.1109/EMBC.2019.8856542
11. Gan, L., Wang, C., Liu, H., Zhang, L.: Cuff-Less Methods for Blood Pressure Measurement. In: 2019 Chinese Automation Congress (CAC). pp. 4926–4930 (Nov 2019). https://doi.org/10.1109/CAC48633.2019.8997340
12. Gao, M., Cheng, H.M., Sung, S.H., Chen, C.H., Olivier, N.B., Mukkamala, R.: Estimation of Pulse Transit Time as a Function of Blood Pressure Using a Nonlinear Arterial Tube-Load Model. IEEE Transactions on Biomedical Engineering **64**(7), 1524–1534 (Jul 2017). https://doi.org/10.1109/TBME.2016.2612639
13. Huynh, T.H., Jafari, R., Chung, W.Y.: Noninvasive Cuffless Blood Pressure Estimation Using Pulse Transit Time and Impedance Plethysmography. IEEE Transactions on Biomedical Engineering **66**(4), 967–976 (Apr 2019). https://doi.org/10.1109/TBME.2018.2865751
14. Kumar, R., Kumar, S., Bin Queyam, A., Sengupta, A.: An Experimental Validation of Bio-Impedance Technique for Medical Non-Medical Application. In: 2018 8th International Conference on Cloud Computing, Data Science Engineering (Confluence). pp. 14–15 (Jan 2018). https://doi.org/10.1109/CONFLUENCE.2018.8442494
15. Lass, J., Meigas, I.C., Karai, D., Kattai, R., Kaik, J., Rossmann, M.: Continuous blood pressure monitoring during exercise using pulse wave transit time measurement. In: The 26th Annual International Conference of the IEEE Engineering in Medicine and Biology Society. vol. 1, pp. 2239–2242 (Sep 2004). https://doi.org/10.1109/IEMBS.2004.1403652
16. Li, Y., Chen, X., Zhang, Y., Deng, N.: Noninvasive continuous blood pressure estimation with peripheral pulse transit time. In: 2016 IEEE Biomed-

ical Circuits and Systems Conference (BioCAS). pp. 66–69 (Oct 2016). https://doi.org/10.1109/BioCAS.2016.7833726
17. Muehlsteff, J., Aubert, X., Schuett, M.: Cuffless Estimation of Systolic Blood Pressure for Short Effort Bicycle Tests: The Prominent Role of the Pre-Ejection Period. In: 2006 International Conference of the IEEE Engineering in Medicine and Biology Society. pp. 5088–5092 (Aug 2006). https://doi.org/10.1109/IEMBS.2006.260275
18. Mukkamala, R., Hahn, J.O., Inan, O.T., Mestha, L.K., Kim, C.S., Töreyin, H., Kyal, S.: Toward Ubiquitous Blood Pressure Monitoring via Pulse Transit Time: Theory and Practice. IEEE Transactions on Biomedical Engineering **62**(8), 1879–1901 (Aug 2015). https://doi.org/10.1109/TBME.2015.2441951
19. Peter, L., Noury, N., Cerny, M.: A review of methods for non-invasive and continuous blood pressure monitoring: Pulse transit time method is promising? IRBM **35**(5), 271–282 (Oct 2014). https://doi.org/10.1016/j.irbm.2014.07.002
20. Peter, L., Kracik, J., Cerny, M., Noury, N., Polzer, S.: Mathematical Model Based on the Shape of Pulse Waves Measured at a Single Spot for the Non-Invasive Prediction of Blood Pressure. Processes **8**(4), 442 (Apr 2020). https://doi.org/10.3390/pr8040442
21. Poon, C., Zhang, Y.: Cuff-less and Noninvasive Measurements of Arterial Blood Pressure by Pulse Transit Time. In: 2005 IEEE Engineering in Medicine and Biology 27th Annual Conference. pp. 5877–5880 (Jan 2005). https://doi.org/10.1109/IEMBS.2005.1615827
22. Rachim, V.P., Huynh, T.H., Chung, W.Y.: Wrist Photo-Plethysmography and Bio-Impedance Sensor for Cuff-Less Blood Pressure Monitoring. In: 2018 IEEE SENSORS. pp. 1–4 (Oct 2018). https://doi.org/10.1109/ICSENS.2018.8589559
23. Teng, X., Zhang, Y.: Continuous and noninvasive estimation of arterial blood pressure using a photoplethysmographic approach. In: Proceedings of the 25th Annual International Conference of the IEEE Engineering in Medicine and Biology Society (IEEE Cat. No.03CH37439). vol. 4, pp. 3153–3156 Vol.4 (Sep 2003). https://doi.org/10.1109/IEMBS.2003.1280811
24. von Wowern, E., Östling, G., Nilsson, P.M., Olofsson, P.: Digital Photoplethysmography for Assessment of Arterial Stiffness: Repeatability and Comparison with Applanation Tonometry. PLoS ONE **10**(8) (Aug 2015). https://doi.org/10.1371/journal.pone.0135659

A Large-scale High-resolution Wood Surface Defects Dataset

Alexandra Bodzas

Department of Cybernetics and Biomedical Engineering, FEECS,
VSB – Technical University of Ostrava, 17. listopadu 15,
708 00 Ostrava – Poruba, Czech Republic
alexandra.bodzas@vsb.cz

Abstract. The complexity of wood manufacturing processes and heterogeneity of wood material result in numerous visible structural defects. In many market leader companies, these defects are still controlled manually by trained specialists, which is not only biased but also less effective. Several automated vision-based systems have been proposed to overcome the disadvantages of manual inspection. Although some researchers achieved a high recognition rate, most of these studies lacked extensive databases and authentic data. To address the lack of such datasets, we proposed a complex technical solution, with which we were able to acquire an extensive set of data from a sawmill production line during harsh manufacturing conditions. The acquired dataset contains more than 43 000 labeled high-resolution images and covers overall ten types of the most frequent wood surface defects

Keywords: Wood defects, Wood surface defects, Quality control

1 Introduction

In the wood industry and forestry, each step of the manufacturing process affects material utilization and cost efficiency [1]. The diversity of wood material and the complexity of manufacturing processes may lead to various defects, which not only degrade the wood's mechanical properties but also reduce its aesthetic value. Furthermore, that has a significant impact on its commercial value and material utilization [2]. Despite the growing automation in these industry sectors, some market leader companies still utilize trained experts to perform quality control [3]. Besides the fact that the manual examination is biased and tedious, it was found by Urbonas *et al.* [4] that due to the distraction and eye fatigue, manual inspection rarely reaches 70 % reliability. [5]

To address the disadvantages of manual quality control processes, several automated systems have been proposed. Even though these developed systems were able to achieve satisfying results, most researchers in the field worked with limited datasets acquired in laboratory conditions. Such datasets are usually characterized by a limited

VSB – Technical University of Ostrava, 2021, ISBN 978-80-248-4523-4 (on-line).

number of materials and cannot capture sufficiently the variability of the observed defects, especially in such cases, where the defect's variability might be limitless. To deal with the lack of large-scale datasets in this field, we proposed an experiment with a goal to create an extensive database of wood surface defects. Unlike other conducted studies, we set our experiment in the industry during the production, which allowed us to capture a large number of authentic data from the sawmill production line. [5] The following chapters give an overview of the used materials and methods in all experiment stages, from acquisition to data labeling, and describe the technical validation of the dataset.

2 Materials and methods

To face the challenges arising from the manufacturing process, such as the high speed of the conveyor belt reaching the speed of 9.6 m s-1 and heavy vibrations with centimeters long peaks, we designed and implemented a hardware and software solution. The aim of this study, therefore, was to create a sufficiently robust, and at the same time portable solution, which can be easily implemented and can acquire high-resolution images at the sawmill production line. [5]

2.1 Acquisition Equipment

The designed construction carrying the camera and the light was assembled from ITEM aluminum profiles. To avoid acquiring blurry images and synchronize the conveyor's heavy vibrations with the mounted camera, we fixed the whole mechanical construction to the production line and the floor. [5]

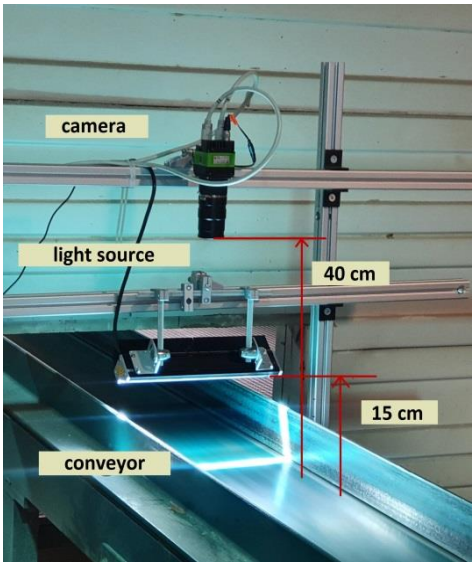

Fig. 1: The mechanical construction with the mounted camera SW-4000TL-PMCL and the ligh source Corona II [5]

Since the speed of the conveyor reached the speed of 9.6 m s^{-1}, we selected a trilinear line scan camera SW-4000TL-PMCL manufactured by JAI, which is able to acquire high-resolution images at the speed of 66 kHz. The required speed of the image acquisition was achieved by connecting the camera interface to a high-performance Camera Link frame grabber with the maximum high data throughput up to 1800 MB s^{-1}. To achieve the required field of view, the Kowa LM50LF line scan camera lens was used. Due to the low shutter setting of the camera, we had to use a powerful light source, which would sufficiently illuminate the desired field of view during the high-speed acquisition. For this purpose, we used a linear LED light Corona II by Chromasens, which can provide a light intensity of 3.5 million lux. [5]

2.2 Data Acquisition

Setting the sampling frequency to 66 kHz allowed us to capture approximately 66.4 images per second, which resulted in a data transfer speed of 773 MB s^{-1}. To overcome these challenges arising from the high data transfer rate, we separated the acquisition and saving processes. In a simple term, the acquisition process was responsible for capturing a set of 84 images and saving the images into the PC's RAM, and the saving process managed the transfer of the images from the computer's RAM to the local hard disk. Since transferring such a large amount of data between different software has a negative impact on the CPU utilization and would decrease the camera's frame rate, we utilized an optimized frame grabber software microDisplay X from

Silicon Software. During the acquisition, the whole software ran in an automated way through a developed automatic clicker with a feedback loop based on the captured computer screen. Basically, the software reads the information from the screen and on the basis of the received information decides, whether the acquisition or the saving process is already completed. [5]

2.3 Post-processing and Data Labeling

Overall 60 480 images were acquired during four hours of continuous acquisition. Since the selected third-party software had limited functionality, the acquisition had to be performed in a continuous mode, without any camera trigger option. Due to this fact, we captured a large number of images of an empty conveyor or small wood parts. To filter these data, we employed an offline histogram-based algorithm based on a sum calculation of the image green color space histogram with a simple threshold technique. Since the proposed filtration proved 100 % reliability on 1500 randomly chosen samples, we applied the algorithm on the whole dataset, which resulted in a final number of 20 275 images. Additionally, to remove the undesirable background from the remaining images, we performed image cropping that not only reduced the size of the file but also decreased the potential computation time. To perform this operation without any significant data loss, a simple straight-line edge detection technique in a vertical direction was used. This changed the image resolution to the size of 2800×1024 and reduced the overall size of the dataset by almost 80 GB. [5]

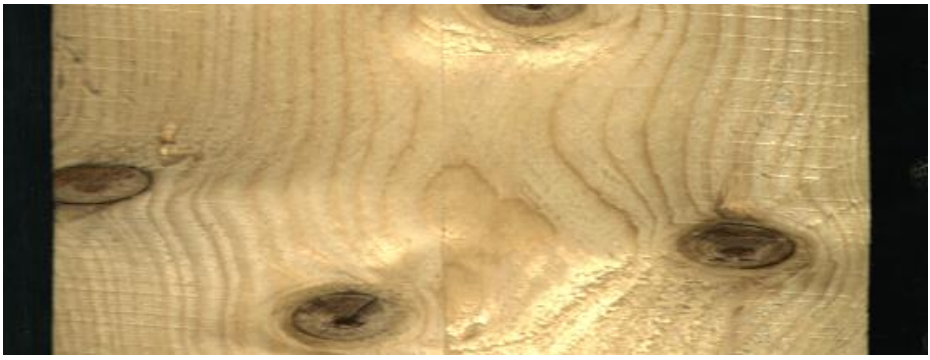

Fig. 2: Wood surface defect dataset sample

The dataset annotation was in this experiment performed manually by a trained person. Using a customized annotation tool allowed us to create for each image in the dataset a semantic segmentation map and a bounding box label comprising left, top, right, bottom defect coordinates in the form of percent divided by 100. [5]

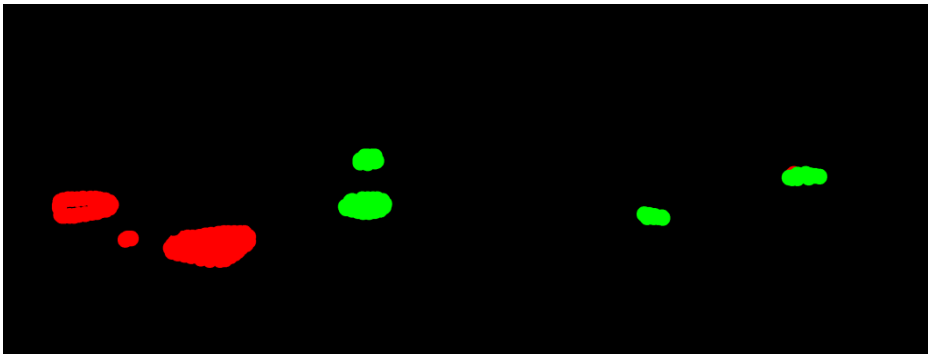

Fig 3: Sample of a semantic segmentation label map: Red stands for dead knots, green represents live knots

3 Dataset Validation

To validate the dataset and assess the quality of the assigned labels, a deep learning-based classification was employed. The classification was performed by a convolution neural network detector based on the ResNet-50 model [6] with added Batch Normalization and ReLu layers after each convolution layer. The input layer and, therefore, all images were down-sampled to the size of 1024×357. To train the selected neural network architecture, a transfer learning paradigm with pre-trained weights from the COCO dataset [7] was used. During the training process, we implemented data augmentation and divided the dataset into training and testing set in a conventional ratio of 40/60. Moreover, several parameters were additionally modified to increase the detection accuracy. These included especially sizes, strides, ratios, and scales. The implemented values for all modified parameters are demonstrated in Table 3. [5]

Table 1: Performance of the particular classification algorithms

Parameters	Values
Size	32, 64, 128, 256, 512
Stride	8, 16, 32, 64, 12
Ratio	0.3, 0.55, 1, 2, 3.5
Scale	0.6, 0.8, 1

At the beginning of the training, the first four layers of the network were frozen. After freezing the layers, we tuned the neural network by unfreezing the layers in reverse order except for the Batch Normalization. The whole neural network model was afterward fine-tuned at a low training speed. The trained model yielded an accuracy of 81 % with a higher amount of false positives. To reduce the number of false or inaccurate classifications, the dataset was re-evaluated by a second trained person, who didn´t participate in the initial labeling process. [5]

4 Conclusion

In this paper, we addressed the lack of extensive wood defect databases by proposing a data acquisition experiment in an industrial environment. To deal with all challenges arising from the sawmill production line, we designed and implemented a HW and SW solution, which was able to run in an automated mode. The annotated dataset is publically available on a public repository and contains 1 992 high-resolution images of sawn timbers without any defects and 18 283 images with one or more wood surface defects. The dataset captures overall 10 types of the most common wood surface defects, including knots, dead knots, knots with cracks, cracks, resins, marrow, quartzity, missing knots, blue stains, and overgrown. Moreover, to provide researchers with more valuable information, all dataset samples are complemented with two types of labels: a bounding box label and a semantic label map.

References

1. Broman O, Fredriksson M.: Wood material features and technical defects that affect yield in a finger joint production process. Wood Mater. Sci. Eng (2012)
2. Ding F, Zhuang Z, Liu Y, Jiang D, Yan X, Wang Z.: Detecting defects on solid wood panels based on an improved SSD algorithm. Sensors (2020)
3. Gu IYH, Andersson H, Vicen R.: Automatic classification of wood defects using support vector machines. In: Bolc L, Kulikowski JL, Wojciechowski K, (eds). Lecture Notes in Computer Science. Berlin: Springer Science+Business Media, p. 356-367 (2009)
4. Urbonas A, Raudonis V, Maskeliūnas R, Damaševičius R.: Automated identification of wood veneer surface defects using faster region-based convolutional neural network with data augmentation and transfer learning. Appl. Sci (2019)
5. Kodytek P, Bodzas A and Bilik P. A large-scale image dataset of wood surface defects for automated vision-based quality control processes [version 1; peer review: awaiting peer review]. F1000Research (2021).
6. He K, Zhang X, Ren S, Sun J.: Deep Residual Learning for Image Recognition. 2016 IEEE Conference on Computer Vision and Pattern Recognition (2016)
7. Lin T, Maire M, Belongie S, Hays J, Perona P, Ramanan, et al.: Microsoft COCO: Common objects in context. ECCV. (2014)

Estimation of a Next Day Solar Energy Availability Based on Values of Atmospheric Pressure Using Deep Learning

Tereza Paterová and Michal Prauzek

Department of Cybernetics and Biomedical Engineering, FEECS,
VSB – Technical University of Ostrava, 17. listopadu 15,
708 00 Ostrava – Poruba, Czech Republic
{tereza.paterova, michal.prauzek}@vsb.cz

Abstract. This article is focused on predicting a daily total solar energy for the next day by a deep feedforward neural network in combination with deep learning approach features. Forecasting future solar irradiance is used as a support parameter to control the operation duty-cycle, data collection or communication activities at energy-independent energy-harvesting embedded devices. The prediction is based on previous hourly-measured atmospheric pressure values. For prediction, a back-propagation algorithm in combination with deep learning methods is used for multilayer network training. It is concluded that the presented neural network approach gave satisfying predictions in early spring, autumn, and winter. In a particular setting, the proposed solution provides better results than a model using the support vector regression method (e.g., the MAPE value of proposed algorithm is 0.032 less than support vector regression method MAPE value).

Keywords: Energy management, Neural networks, Prediction algorithms.

1 Introduction

Energy-independent embedded systems are specially designed for deployment sites, where it is not possible to connect such devices to a power grid. A common solution for supplying energy to these devices is using batteries to satisfy energy demands [1, 2]. This paper focuses on the application of deep learning and NN approaches, especially on deep feedforward networks, to forecast the next-day solar energy availability from atmospheric pressure in an energy-harvesting embedded system. A back-propagation method is used to train multilayer NN in combination with deep learning methods such as optimalization, batch-normalization and initialization of weights. The algorithm implementation was executed in the C programming language. The results of each combination are compared to previous published approaches and an overall evaluation is provided.

© M. Krátký, J. Dvorský, P. Moravec (Eds.): WOFEX 2021, pp. 271–276.
VSB – Technical University of Ostrava, 2021, ISBN 978-80-248-4523-4 (on-line).

Article is divided into five sections which are organized as follows: the recent work section represents the state of the art. The theoretical background section provides overall description of Deep feedforward networks. The deep learning experiment section describes an experiment design, reference algorithm and evaluation criteria. The results section provides experiment results along with a discussion. The final section summarizes the overall contribution of the paper and possible challenges in future work.

2 Recent Work

In general, predicting future solar irradiance is an important topic in the renewable energy generation field. It is used to improve the planning and operation of photovoltaic systems [3]. The accuracy of the prediction improves the performance and stability of the systems [4]. The solar availability can be predicted using many methods such as statistical methods, artificial neural networks (NN), support vector machines and autoregressive moving averages [3]. Besides these methods, other methods can also be used (regression tree, random forest, gradient boosting, and many others) in the context of the estimation of future solar energy [5].

Machine learning (ML) methods such as deep NN are suitable for estimating future solar energy because they add complexity to a model without specifying what form the variation should take and allow the extraction of high-level features [7]. Deep learning enables the computational model (e.g., a multilayer NN) to create and remember a new representation of the input data. Deep learning provides tools for solving complex problems using multilayer NN. A fusion of NN and deep learning approaches leads to Deep NN, which can be defined as NN with several (at least three or more) hidden layers [6].

3 Deep Feedforward Networks

The deep feedforward NN are formed by the hidden layers. The input and output layer are defined by the structure of input and output data. The properties of a NN are determined by a topology, number, and width of the hidden layers [8].

One of the deep learning methods is the gradient descent algorithm, which is used for NN learning. In general, there are three basics configurations of the gradient descent – a batch gradient descent (an ordinary gradient descent), a stochastic gradient descent and a mini-batch gradient descent – which differ according to the volume of data from the total dataset that is used to calculate the gradient of the objective function [9]. The most-used gradient algorithm for descent optimization is back-propagation (BP). BP is a commonly used algorithm for training the multilayer feed forward NN [10]. There are various learning parameters such as the learning rate, momentum or activation function which can improve the BP learning algorithm [11]. The training of deep NN is complicated by the fact that the inputs of all neurons in the hidden layers and output layer are affected by the parameters of the previous layer's neurons. During training, the parameters of neurons and thus the activation variables and inputs of neurons are changing. Changes in neuron inputs in the previous layer are transmitted to the current and subsequent layer. This propagation causes instability leading to reduced convergence or

even divergence in the deeper layers. Such a problem is described as a change in the distribution of layer inputs. The change in layer distribution is referred to as an internal covariance shift. The aim of the batch normalization is to reduce the internal covariance shift by adding a normalization layer [12, 13].

4 Deep Learning Experiment

The aim of the presented experiment was forecasting a solar energy availability for the following day by using a deep learning algorithm with a multilayer perceptron. A back-propagation algorithm was used to train multilayer NN in combination with deep learning methods such as optimalization, batch-normalization or the initialization of weights. The structure of the network was designed by an experimentally chosen number of layers and various types of activation functions (sigmoid, hyperbolic tangent, softsign and ReLU (R), identity (I)). BP in three variants of gradient mode (mini-batch gradient descent (M), stochastic gradient descent (S) and batch gradient descent) was selected for the network training. The optimization was chosen among three optimization modes (ADAM, RMSProp with Nesterov Momentum (RMSProp) and Nesterov Momentum (NEST), none of them). There were three options to select from the initialization of the weights (Xavier, Sigmoid and Glorot). Each of these deep learning methods has several configurations which will be compared. Two datasets (2012, 2013) which contain hourly measured values of atmospheric pressure were used in this experiment. The dataset from the entire year of 2012 was used for training the deep NN and the dataset from the entire year of 2013 was used for the algorithm testing. The values of the atmospheric pressure in one day (24 values) and value of available daily solar energy represented one input vector of the NN. The output vector consisted of an estimate of the value of the available solar energy for the following day. The range of input and output data values was normalized to a range from 0 to 1. Equation 1 was used to calculate an estimate of the available daily solar energy $\hat{E}_A$, which is dependent on the day of the year, solar elevation, and solar altitude. These parameters are represented by: θ is the site latitude, τ is the transmissivity estimate and G is the extra-terrestrial solar radiation. This calculation was taken from [14] and $\hat{E}_A$ values were used for designing the output vector of the training dataset for NN learning.

$$\hat{E}_A = 3600\tau G \int_{-\phi}^{\phi} \sin(\theta)\, d\theta \tag{1}$$

The deep learning experiment algorithm for one configuration of deep learning methods is composed of a following steps. First, a test configuration of deep learning methods is set. Then the NN training is performed using the dataset 2012. Subsequently, the trained network is tested using the dataset 2013, which results are the prediction of available solar energy. Then, the evaluation parameters of the resulting dataset are calculated. Outputs of the forecast algorithm were validated by a Mean absolute percentage error (MAPE) that is calculated by following equation,

$$MAPE = \frac{1}{n}\sum_{i=1}^{n} \frac{|x_i - y_i|}{y_i} \tag{2}$$

where is *n* the number of the predictions, y_i is the real value of the pressure and x_i is the predicted value of the pressure. All the experimentally chosen combinations of the learning algorithm settings and other forecasting approaches were compared using a Root mean square error (RMSE) calculation,

$$RMSE = \sqrt{\frac{1}{n}\sum_{i=1}^{n}(x_i - y_i)^2} \tag{3}$$

where *n* is the number of the predictions, y_i is the real value of the pressure and x_i is the predicted value of the pressure. The evaluation parameters were compared among all chosen combinations of the learning algorithm settings. The ability of the deep learning system to estimate daily solar energy was compared to the evolutionary-fuzzy prediction scheme (FR) and support regression model (SV). The reference results, which stated FR demonstrates better results than SV, were obtained from [14].

5 Results and Discussion

The NN was tested with experimentally chosen settings of training parameters. Table 1. shows the MAPE and RMSE values of the individual configuration settings in the deep learning experiment, which performed best in experimental testing. The N2 configuration has the lowest value of MAPE (0.235) of all the proposed setting combinations. A comparison of MAPE values of the N1 (0.244) and N2 (0.235) configurations, which had the same settings except for the number of layers, shows that it is better to choose a larger number of layers for a more accurate forecast. A1 (MAPE = 0.249) and A2 (MAPE = 0.240) also had the same configuration apart from initialization method and their comparison showed that the mode with Sigmoid is better than with Xavier. Once the optimization methods were compared, it was shown that the best results are characterized by NEST (N1 – MAPE = 0.244), followed by ADAM (A1 – MAPE = 0.249, A4 – MAPE = 0.310) and RMSProp (R1 – MAPE = 0.330).

Table 1. Results of the experiment individual configuration settings.

Label	Algorithm	Mode	Optimalization	Initiation	Act. function	MAPE (%)	RMSE (MJ/m^2)
A1	BP	M	ADAM	Xavier	R, R, I	0.249	2.958
A2	BP	M	ADAM	Sigmoid	R, R, I	0.240	2.945
A3	BP	S	ADAM	Xavier	R, R, R, I	0.240	3.009
A4	BN	M	ADAM	Xavier	R, R, R, I	0.310	3.248
N1	BN	M	NEST	Xavier	R, R, I	0.244	3.020
N2	BN	M	NEST	Xavier	R, R, R, R, R, I	0.235	2.935
R1	BP	M	RMSProp	Xavier	R, R, I	0.330	3.402
R2	BP	M	ADAM	Sigmoid	R, R, R, R, R, I	0.249	2.975

Regarding the gradient mode, it was empirically established that the batch gradient was not suitable for network training with the dataset (2012) because of unsatisfactory results. Therefore, no configuration with the batch gradient mode appeared in the top results of Table I and the gradient descent mode was just chosen from among the mini-batch mode and stochastic batch mode. A comparison of the results of A3 (MAPE =

0.240) with A1 (MAPE = 0.249) and A4 (MAPE = 0.310) shows that the stochastic gradient descent is significantly better than the mini-batch.

A comparison of the results from the previous study to the deep learning experiment is shown in Table 2. The table shows that the best result was achieved using the evolutionary fuzzy rules model (FR), which exceeds all the predictions obtained. However, the best forecasts from trained NN surpassed all the above support vector regression models (SV). It could also be said that the forecasts in spring, autumn and winter were more accurate in the case of the deep learning experiment because there were no significant fluctuations in daily solar energy availability. In terms of summer months and late spring, the forecast did not correspond to sudden fluctuations, which are typical for these months.

Table 2. Comparison of the Deep learning experiment result (N2) to reference approaches (FR, SV R_L, SV_RP, SV_RR).

Model	MAPE (%)	RMSE (MJ/m^2)
N2	0.235	2.935
FR	0.224	2.960
SV R_L	0.267	3.160
SV RP	0.362	3.444
SV RR	0.387	3.472

6 Conclusions

This paper introduces the application of deep learning methods with the aim of training a multilayer NN, which can use a prediction tool to estimate future incoming solar energy. The BP algorithm in combination with deep learning methods, such as optimalization, batch-normalization and the initialization of weights, was used for network training. It could be said that the results of the experiment are comparable, and settings of the proposed solution is better than models using the support vector regression method. The results also showed that the forecast of the deep learning model did not perform with as satisfactory results in comparison to the evolutionary fuzzy rules method. Also, it could be clearly concluded that the NN gave satisfying predictions in early spring, autumn, and winter because there were no significant fluctuations in daily solar energy availability. In terms of the summer months and late spring, the forecast did not correspond to sudden fluctuations, which are typical for these months. It is important to emphasize that the outcome of the learning process was greatly affected by the initialization of the parameters that used pseudo-random number generators. Therefore, different NN training results could be achieved with the same settings. A possible improvement could be the use of more datasets measured over several years to train the NN. Another possible aspect could be using the Dropout or L2 control method.

7 References

1. Kromer, P., Prauzek, M., Musilek, P.: *Harvesting-aware control of wireless sensor nodes using fuzzy logic and differential evolution.* In 2014 11th Annual IEEE International Conference on Sensing, Communication, and Networking Workshops, SECON Workshops (2014). DOI: 10.1109/SECONW.2014.6979705
2. Ramesh, U., Sentilles, S., Crnkovic, I.: *Energy management in embedded systems: Towards a taxonomy* (2012). DOI: 10.1109/GREENS.2012.6224254
3. Alzahrani, A., Shamsi, P., Dagli, C., Ferdowsi, M.: *Solar irradiance forecasting using deep neural networks.* Computer Science (2017). Available: https://doi.org/10.1016/j.procs.2017.09.045
4. Alzahrani, A., Kimball, J. W., Dagli, C.: *Predicting solar irradiance using time series neural networks.* 2014. DOI: 10.1016/j.procs.2014.09.065
5. Voyant, C., Notton, G., Kalogirou, S., Nivet, M., Paoli, C., Motte, F., Fouilloy, A.: *Machine learning methods for solar radiation forecasting: A review.* Renewable Energy, 105, 569-582 (2017). DOI: 10.1016/j.renene.2016.12.095
6. Díaz–Vico, D., Torres–Barrán, A. Omari, A., Dorronsoro, J. R.: *Deep neural networks for wind and solar energy prediction.* Neural Processing Letters, 46(3), 829-844 (2017). DOI: 10.1007/s11063-017-9613-7
7. Martens, J., Sutskever, I.: *Training deep and recurrent networks with hessian-free optimization*. Neural Networks: Tricks of the Trade, pp. 479–535 (2012). Available: https://doi.org/10.1007/978-3-642-35289-8_27
8. Hinton, G., Deng, L., Yu, D., Dahl, G., Mohamed, A., Jaitly, N., Senior, N., Vanhoucke, V., Nguyen, P., Sainath, T.: *Deep neural networks for acoustic modeling in speech recognition.* IEEE Signal Processing Magazine (2012). DOI: 10.1109/MSP.2012.2205597
9. Bengio. Y.: Practical recommendations for gradient-based training of deep architectures. (2012). DOI: 10.1007/978-3-642-35289-8-26
10. Nawi, N. M., Hamzah, F., Hamid, N. A., Rehman, M. Z., Aamir M., Ramli, A. A.: *An optimized back propagation learning algorithm with adaptive learning rate.* International Journal on Advanced Science, Engineering and Information Technology, 7(5), 1693-1700 (2017). DOI: 10.18517/ijaseit.7.5.2972
11. Zhao, Z. Yang, Z., Lin, H., Wang, J., Gao, S.: *A protein-protein interaction extraction approach based on deep neural network.* International Journal of Data Mining (2016). Available: https://doi.org/10.1504/IJDMB.2016.076534
12. Ioffe, S., Szegedy, Ch.: *Batch normalization: Accelerating deep network training by reducing internal covariate shift*. Proceedings of the 32nd International Conference on Machine Learning, PMLR 37:448-456 (2015).
13. Arpit, D., Zhou, Y., Kota, B., Govindaraju, V.: *Normalization propagation: a parametric technique for removing internal covariate shift in deep networks.* In: Proceedings of the 33rd international conference on machine learning, ICML 2016, New York City, NY, USA, June 19–24, pp 1168–1176 (2016).
14. Kromer, P., Musilek, P., Rodway, J., Reformat, M., Prauzek, M.: *Estimating Harvestable Solar Energy from Atmospheric Pressure Using Support Vector Regression*. 2015 International Conference on Intelligent Networking and Collaborative Systems. IEEE, 192-199 (2015). DOI: 10.1109/INCoS.2015.58. ISBN 978-1-4673-7695-2.

A publication where the results have been published: Paterová, T., Prauzek, M.: Estimating Harvestable Solar Energy from Atmospheric Pressure using Deep Learning. Electronics (2021).

Nonlinear optimization of Tractor-Trailer using SOLNP*

Akshaya Raj[0000−0003−1601−7010] and Stepan Ozana[0000−0003−1102−8204]

Department of Cybernetics and Biomedical Engineering, FEECS,
VSB – Technical University of Ostrava, 17. listopadu 15,
708 00 Ostrava – Poruba, Czech Republic
{raj0048, stepan.ozana}@vsb.cz

Abstract. This paper presents SOLNP, a module used to solve the non-linear problem of a system along with direct collocation. It uses a tractor-trailer system as an example to showcase how the solver works and performs as a tractor-trailer system is highly nonlinear, and as the number of links increases the stability decreases. The paper covers both forward and reverse motion of the tractor-trailer system.

Keywords: Nonlinear · SOLNP · Tractor-trailer · Optimal control problem · Sequential Quadratic Programming · optimization

1 Introduction

Tractor-Trailer systems have a large application field like farming, transportation, geological surveys. A wealth of research is found in the area of path tracking problems for vehicles with and without tractors. It is a nonlinear problem which has non-holonomic constraints[1].

The problem of path tracking for a vehicle/tractor-trailer is of great interest to both application and theoretical purposes [2]-[3]. On the applications front, it provides guidance for industrial vehicles, such as mining trucks, road paving vehicles, travelling etc. On the theoretical front, it turns out to be a challenging problem for researchers to solve and apply various nonlinear control techniques [4]-[5].

The aim of this paper is to solve the nonlinear problem of tractor-trailer system using SOLNP,a sequential Quadratic Programming(SQP) solver [6]. SQP is a highly effective optimization method that can solve nonlinear constraints. It models an approximate solution x^k using quadratic programming, and uses that to generate the next approximation, $x^k + 1$. This iteration occurs until the solution converges to x^*. The main advantage of this method is that it is not a feasible-point method, which means that the initial point and the future iterations need not be feasible. This solves the problem of finding a feasible starting point which can be as complex as finding a solution.

* Supported by VŠB - Technical University of Ostrava.Faculty of Electrical Engineering and Computer Science. Department of Cybernetics and Biomedical Engineering.

The rest of the paper is organized as follows. In Section 2, a kinematic model for the tractor-trailer system is derived. Results are shown in section 3. Conclusion is given in Section 4.

2 Kinematics of the car model

The kinematic model to given to better understand the model of the vehicle being dealt with. The derivation of the kinematic model is performed with the assumption that the vehicle doesn't skid. Fig.1 represents the car model being discussed in the paper.

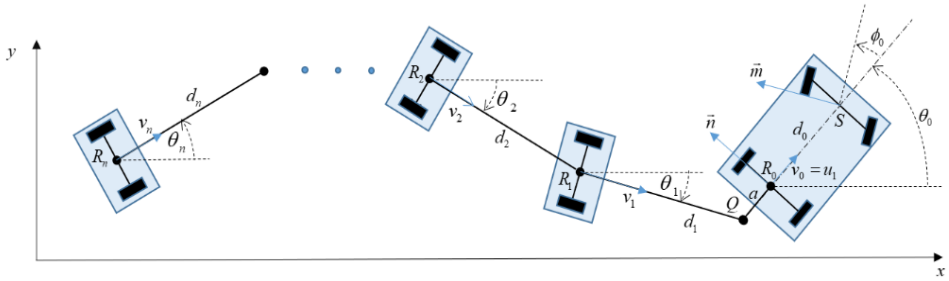

Fig. 1: Geometrical model of the car

The geometry of the tractor-trailer system is shown in Fig.1,where ϕ is the angle of the front wheels with respect to the longitudinal axis of the vehicle,θ_1 is the heading of the vehicle; (x,y) is the position of the vehicle ,$\theta_2 - \theta_n$is the heading of trailer.

The position of the vehicle in the fixed coordinate system is determined by the coordinates, the x y point R_0 and its orientation by an angle θ_0. The first trailer behind the car is connected by a hinge located at the point Q lying on the axle of the car at a distance from the center R_0 of the rear axle. Driving a vehicle is more complicated. Other trailers are always connected by means of a joint in the center of the axle of the previous trailer. Eq.1 gives the mathematical model of the fixed coordinate system.

$$\begin{aligned}
&\vec{R}_0 = [x_0, y_0] \\
&\vec{Q} = [x_0 - a\cos(\theta_0), y_0 - a\sin(\theta_0)] \\
&\vec{R}_i = [x_i, y_i] = \left[x_0 - a\cos\theta_0 - \textstyle\sum_{j=1}^{i} d_j \cos(\theta_j), y_0 - a\sin\theta_0 - \sum_{j=1}^{i} d_j \sin(\theta_j 0\right], \\
&\quad i = 1, \ldots, n
\end{aligned} \tag{1}$$

$$
\begin{aligned}
\dot{\phi}_1 &= \frac{u_1}{d_0}\tan(\phi_0) - \frac{u_1}{d_1}\left[\sin(\phi_1) - \frac{a}{d_0}\cos(\phi_1)\tan(\phi_0)\right] \\
\dot{\phi}_2 &= \frac{u_1}{d_1}\left[\sin(\phi_1) - \frac{a}{d_0}\cos(\phi_1)\tan(\phi_0)\right] \\
&- \frac{u_1}{d_2}\sin(\phi_2)\left[\cos(\phi_1) + \frac{a}{d_0}\sin(\phi_1)\tan(\phi_0)\right] \\
\dot{\phi}_3 &= u_1\left[\frac{1}{d_2}\sin(\phi_2) - \frac{1}{d_3}\sin(\phi_3)\cos(\phi_2)\right]\left[\cos(\phi_1) + \frac{a}{d_0}\sin(\phi_1)\tan(\phi_0)\right] \\
\dot{\phi}_4 &= u_1\left[\frac{1}{d_3}\sin(\phi_3)\cos(\phi_2) - \frac{1}{d_4}\sin(\phi_4)\cos(\phi_2)\cos(\phi_3)\right] \\
&\left[\cos(\phi_1) + \frac{a}{d_0}\sin(\phi_1)\tan(\phi_0)\right] \\
\dot{\phi}_n &= u_1\left[\frac{1}{d_{n-1}}\sin(\phi_{n-1})\cos(\phi_2)\cos(\phi_3)\ldots\cos(\phi_{n-2})\right. \\
&- \frac{1}{d_n}\sin(\phi_n)\cos(\phi_2)\cos(\phi_3)\ldots\cos(\phi_{n-1}) \\
&\left[\cos(\phi_1) + \frac{a}{d_0}\sin(\phi_1)\tan(\phi_0)\right] \\
\phi &= \phi_1 + \phi_2 + \ldots + \phi_n
\end{aligned}
\tag{2}
$$

The first four equations in Eq.2 correspond to the previously derived car model, the remaining n equations represent the dynamic behavior of the n-trailers.

3 Results

This section presents results obtained from finding a feasible path for the main vehicle alone moving forward.

The following set of results are of the main vehicle moving forward from $[-2, 3]$.

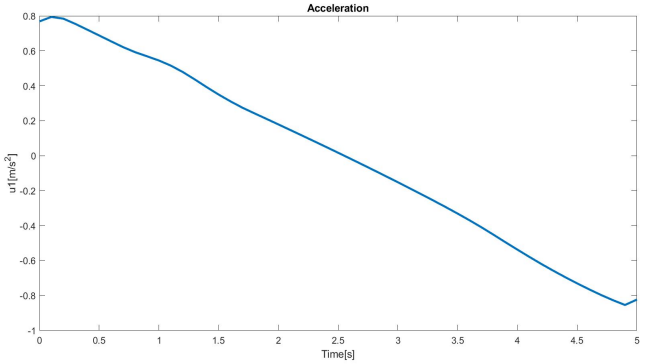

(a) Acceleration

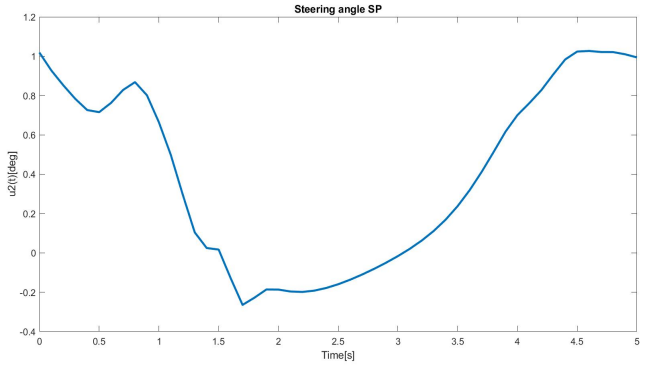

(b) Control input-Steering angle

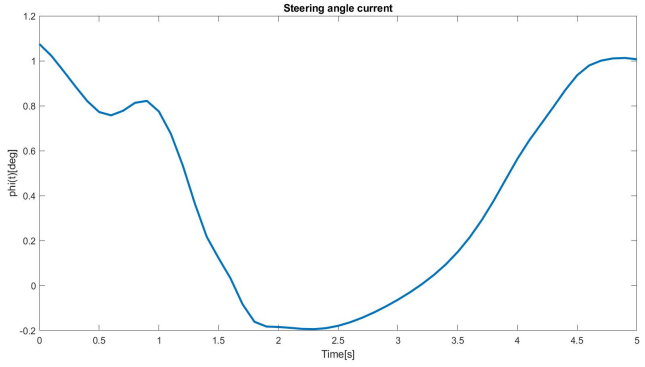

(c) Steering Angle

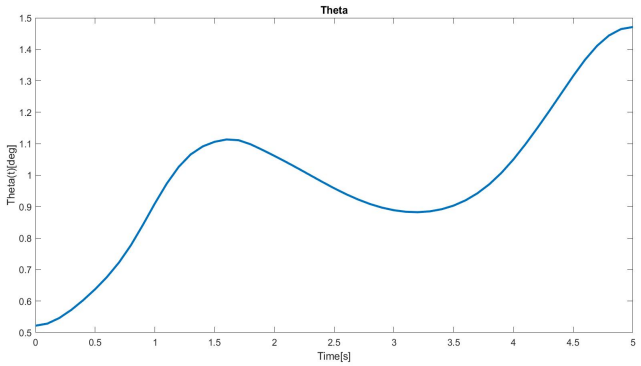

(d) Theta

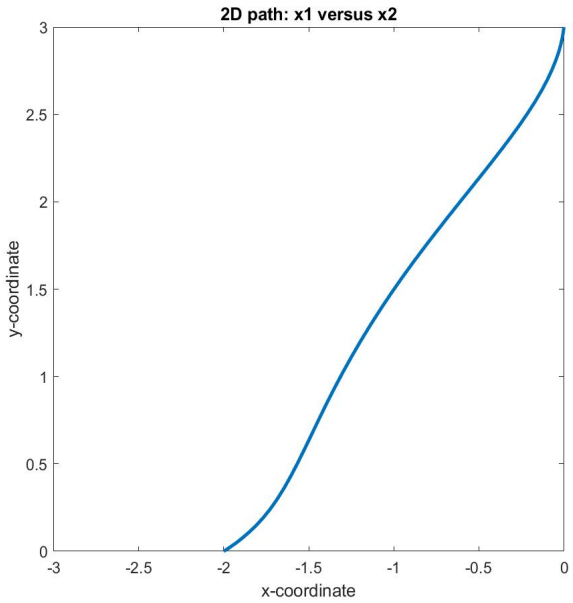

(e) Feasible path

Fig. 2: Forward movement of the vehicle

4 Conclusion

In this paper, we presented the solution of a nonlinear linear system using SOLNP, a solver used to manage the non-linearity of a system. The desired result of moving the vehicle forward is achieved and a feasible path is given by the solver given the initial and the final coordinates.

For future work, the task will be extended to adding links to the main vehicle which makes it highly non-linear which makes the solution complex and makes

convergence challenging. Another future goal is to work with a global solver that provides a better solution.

References

1. Tong Wu and John Y Hung. Path following for a tractor-trailer system using model predictive control. In *SoutheastCon 2017*, pages 1–5. IEEE, 2017.
2. Cédric Pradalier and Kane Usher. A simple and efficient control scheme to reverse a tractor-trailer system on a trajectory. In *Proceedings 2007 IEEE International Conference on Robotics and Automation*, pages 2208–2214. IEEE, 2007.
3. Cedric Pradalier and Kane Usher. Robust trajectory tracking for a reversing tractor trailer. *Journal of Field Robotics*, 25(6-7):378–399, 2008.
4. P Bolzern, RM DeSantis, and Arturo Locatelli. An input-output linearization approach to the control of an n-body articulated vehicle. *J. Dyn. Sys., Meas., Control*, 123(3):309–316, 2001.
5. Dean F Hougen, Maria Gini, and James Slagle. Rapid unsupervised connectionist learning for backing a robot with two trailers. In *Proceedings of International Conference on Robotics and Automation*, volume 4, pages 2950–2955. IEEE, 1997.
6. Yinyu Ye. Solnp users'guide. *University of Iowa*, 1989.

Patient Localization Technologies Overview for Home Care and Assisted Living

Michal Strýček and Martin Černý

Department of Cybernetics and Biomedical Engineering, FEECS,
VSB – Technical University of Ostrava, 17. listopadu 15,
708 00 Ostrava – Poruba, Czech Republic
{michal.strycek, martin.cerny}@vsb.cz

Abstract. The paper presents a short overview of current indoor localization technologies and techniques. The technologies are divided based on the need to carry a tag or a wearable on person for the localization to work. The overview mentions radio-frequency methonds (WiFi, Bluetooth, RFID, ultra-wide band) and specialized mmWave and UWB radars, sensoric floors or PIR sensors. The availability of the systems in private homes and specialized Home Care centers is discussed. The usefulness to develop a testbed for comparison and testing of devices is presented.

Keywords: indoor localization, home care, overview, telehealth

1 Introduction

As today world's population is getting older, the need for assisted living technologies rises. The demographic ageing trends in Europe show the tendency of increased life expectancy and with older age the quality of life changes negatively. To try to maintain the living quality, assisted living systems are used. In Home Care the location aware solution can have a benefit for telemedicine [14], the uses include: monitoring of daily activities, location-aware physiological data for telemedical purposes, possibility of fall detection or in case of institutionalized patients with Alzheimer's disease or dementia the prevention of wandering. To solve these problems multiple localization approaches are available. This paper presents an overview of such technologies and discusses the accuracy, usecases and the availability.

2 Current State

With the number of current localization technologies a sorting into specific groups is needed to better distinct between them. This paper takes inspiration in [3, 22] and presents a classification based on whether or not a need to carry a wearable device is present in the solution or not. The first category of

VSB – Technical University of Ostrava, 2021, ISBN 978-80-248-4523-4 (on-line).

"wearables" includes devices which need to be carried on person for the localization solution to work. The need to carry additional device of any form can be of offsetting. The second category includes solutions that can track patients, however the distinction between different subjects is problematic. Furthermore the classified solutions often use similar algorithms or principles to obtain the patient's position, differing in technology used to determine distance to specific nodes or in the signal acquisition.

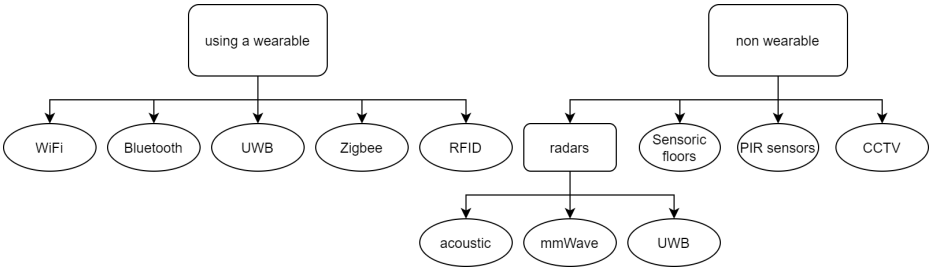

Fig. 1. Classification of localization technologies

2.1 Wearables

Methods and technologies discussed in this subsection require a person to carry a device used for localization. The techniques are most commonly based on Received Signal Strength Indicator (RSSI) [2, 8] or Channel State Information (CSI) [20]. The value can be converted to the estimated distance using path-loss algorithms [10] or can be used to build RSSI indoor maps to use with various machine learning algorithms [21]. To increase the precision of some solutions, the Angle of Arrival (AoA) method has been used [22, 18], this approach uses arrays of antennae to determine the angle of the incoming signal. Different approaches use signal propagation time to estimate the distance between nodes. Some methods use hybrid approaches in which different technologies or methods are used simultaneously [4].

As most of the current smart phones and personal electronics are Wi-Fi enabled, it is one of the most common technologies used for indoor localization. Already deployed access points can be used for localization purposes, however, to achieve good accuracy of the system, optimization of access point placement is required [22, 23] or efficient algorithms are needed to improve accuracy. The aforementioned approaches of RSSI, AoA, signal travel time or combination of them can be used.

Bluetooth methods mostly take advantage of the low cost and high availability of Bluetooth Low Energy (BLE) devices. The most popular applications use BLE beacons (a device sending messages periodically) as anchors to build a localization network [4]. The RSSI, AoA, signal travel time methods can be used

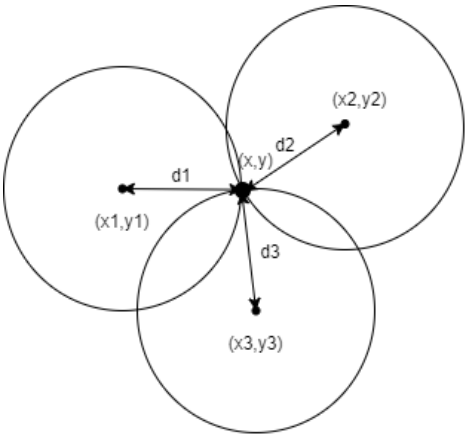

Fig. 2. Basic trilateration problem.

to derive the user's location. However, because most of the solutions depend on the RSSI the accuracy is mostly around 2 meters [25, 13].

Using UWB for indoor localization purposes has multiple advantages. The relatively high accuracy of the applications and the ability of UWB to penetrate objects or walls are among the main [22]. The layout of the solutions consists of anchor nodes and a UWB tag. The primary localization method used in UWB solution is Time of Flight, the short duration of the UWB pulses make the method more resilient to multipath noise. Approaches using deep learning has been also presented in the literature [11].

A classic layout of the RFID localization system consists of passive RFID tags, which are placed in the area [14]. A RFID reader uses the placed tags to determine its location. However, due to the short range of the passive tags, the solely RFID based systems are more appropriate for object localization [23]. For more robust applications, hybrid systems present a more suitable solution [7, 17].

2.2 Non Wearables

The technologies and methods discussed in this subsection can be used to track patients without the need to have them carry additional hardware. The methods can be divided into radars, acoustic methods, positioning floors, passive infra-red sensory fields and LIDARS. The upside of not using the tag devices establishes a new problem to identify different objects.

Millimetric Waves (a band of spectrum between 30 GHz and 300 GHz) has been used in tracking and localization of persons [24, 9]. UWB technology has also been utilized, but new algorithms for handling of the UWB signal scattering had to bee introduced [9].

Positioning floors are matrices of sensors build into the the floor. The main difference is between the sensors used to create the sensory matrix, two of the

most used are capacitive sensors [15] and pressure sensors [12]. The accuracy is determined by the resolution of the inlayed matrix in the floor.

Using a matrix of PIR sensors and object aware map, the rough position of a person can be estimated [19]. But due to the low accuracy of the method and the requirement of prior knowledge about subject daily habits make it difficult to implement.

LIDAR is widely used to perform robot localization or even simultaneous localization and mapping (SLAM) for robot indoor navigation. Approaches for tracking people and objects have also been explored in the literature [1, 16].

3 Discussion

The indoor localization field is a wide area that includes many different techniques and technologies. The most common are wearable radio-frequency solutions. However from patients point of view these solution require a wireless tag or device to be carried at all times, this device can be a wearable such as smart watches or bands, but the requirement is binding. The accuracy of solutions are dependent not only on deployed technology but even the area. For the radio-frequency technology the dispositions of the building, wall thickness or even materials play a big role in signal propagation.

On the other hand solutions without any on-person devices bring new problems such as patient identification, unreliable detection. Most of the solutions present themselves as mere presence and fall detectors. New solutions using UWB to develop 3D radars start to emerge, even for detection of biological rhythms as breathing and heart rate. These present new trends in Home Care as they can be used as passive sensors and only require attention from the personnel or responsible person.

These systems are not only useful in specialized Home Care facilities, but can also be applied into private housing. As many of them specialize in fall detection which is a primary use case and point of interest in such devices for the elderly. This mainly because the fear of falling in this demographic and recurring incidents can diminish the quality of life [5, 6].

4 Future Work

In the future the possibility to develop a testbed to validate, compare and develop existing and new solutions will be explored. This "localization testbed" should include high precision reliable localization technologies to act as reference. Tools to synchronise time base for each solution should be developed and the need to invent standardised process for testing of the solutions should be explored.

References

1. Benedek, C.: 3d people surveillance on range data sequences of a rotating lidar. Pattern Recognition Letters **50**, 149–158

(2014). https://doi.org/https://doi.org/10.1016/j.patrec.2014.04.010, https://www.sciencedirect.com/science/article/pii/S0167865514001287, depth Image Analysis
2. Benkic, K., Malajner, M., Planinsic, P., Cucej, Z.: Using rssi value for distance estimation in wireless sensor networks based on zigbee. In: 2008 15th International Conference on Systems, Signals and Image Processing. pp. 303–306. IEEE (2008)
3. Byrne, C.A., Collier, R., O'Hare, G.M.: A review and classification of assisted living systems. Information **9**(7), 182 (2018)
4. Davidson, P., Piché, R.: A survey of selected indoor positioning methods for smartphones. IEEE Communications Surveys & Tutorials **19**(2), 1347–1370 (2016)
5. Gálvez-Barrón, C., Formiga, F., Miñarro, A., Macho, O., Narvaiza, L., Dapena, M.D., Pujol, R., Rodríguez-Molinero, A.: Pain and recurrent falls in the older and oldest-old non-institutionalized population. BMC geriatrics **20**(1), 1–9 (2020)
6. Gazibara, T., Kurtagic, I., Kisic-Tepavcevic, D., Nurkovic, S., Kovacevic, N., Gazibara, T., Pekmezovic, T.: Falls, risk factors and fear of falling among persons older than 65 years of age. Psychogeriatrics **17**(4), 215–223 (2017)
7. Hasani, M., Talvitie, J., Sydänheimo, L., Lohan, E.S., Ukkonen, L.: Hybrid wlan-rfid indoor localization solution utilizing textile tag. IEEE Antennas and Wireless Propagation Letters **14**, 1358–1361 (2015)
8. Heurtefeux, K., Valois, F.: Is rssi a good choice for localization in wireless sensor network? In: 2012 IEEE 26th international conference on advanced information networking and applications. pp. 732–739. IEEE (2012)
9. Huang, X., Cheena, H., Thomas, A., Tsoi, J.K.: Indoor detection and tracking of people using mmwave sensor. Journal of Sensors **2021** (2021)
10. Miranda, J., Abrishambaf, R., Gomes, T., Gonçalves, P., Cabral, J., Tavares, A., Monteiro, J.: Path loss exponent analysis in wireless sensor networks: Experimental evaluation. In: 2013 11th IEEE international conference on industrial informatics (INDIN). pp. 54–58. IEEE (2013)
11. Poulose, A., Han, D.S.: Uwb indoor localization using deep learning lstm networks. Applied Sciences **10**(18), 6290 (2020)
12. Qian, G., Zhang, J., Kidane, A.: People identification using floor pressure sensing and analysis. IEEE Sensors Journal **10**(9), 1447–1460 (2010)
13. Röbesaat, J., Zhang, P., Abdelaal, M., Theel, O.: An improved ble indoor localization with kalman-based fusion: An experimental study. Sensors **17**(5), 951 (2017)
14. Santoso, F., Redmond, S.J.: Indoor location-aware medical systems for smart homecare and telehealth monitoring: state-of-the-art. Physiological measurement **36**(10), R53 (2015)
15. Sousa, M., Techmer, A., Steinhage, A., Lauterbach, C., Lukowicz, P.: Human tracking and identification using a sensitive floor and wearable accelerometers. In: 2013 IEEE International Conference on Pervasive Computing and Communications (PerCom). pp. 166–171. IEEE (2013)
16. Taipalus, T., Ahtiainen, J.: Human detection and tracking with knee-high mobile 2d lidar. In: 2011 IEEE International Conference on Robotics and Biomimetics. pp. 1672–1677. IEEE (2011)
17. Tejaswini, K.D., Balasubramanian, V.: A scalable and hybrid location estimation algorithm for long-range rfid systems. International Journal of Wireless Information Networks **25**(2), 186–199 (2018)
18. Xiao, J., Zhou, Z., Yi, Y., Ni, L.M.: A survey on wireless indoor localization from the device perspective. ACM Computing Surveys (CSUR) **49**(2), 1–31 (2016)

19. Yang, D., Sheng, W., Zeng, R.: Indoor human localization using pir sensors and accessibility map. In: 2015 IEEE International Conference on Cyber Technology in Automation, Control, and Intelligent Systems (CYBER). pp. 577–581. IEEE (2015)
20. Yang, Z., Zhou, Z., Liu, Y.: From rssi to csi: Indoor localization via channel response. ACM Computing Surveys (CSUR) **46**(2), 1–32 (2013)
21. Yiu, S., Dashti, M., Claussen, H., Perez-Cruz, F.: Wireless rssi fingerprinting localization. Signal Processing **131**, 235–244 (2017)
22. Zafari, F., Gkelias, A., Leung, K.K.: A survey of indoor localization systems and technologies. IEEE Communications Surveys & Tutorials **21**(3), 2568–2599 (2019)
23. Zafari, F., Papapanagiotou, I., Christidis, K.: Microlocation for internet-of-things-equipped smart buildings. IEEE Internet of Things Journal **3**(1), 96–112 (2015)
24. Zeng, Y., Pathak, P.H., Yang, Z., Mohapatra, P.: Human tracking and activity monitoring using 60 ghz mmwave. In: 2016 15th ACM/IEEE International Conference on Information Processing in Sensor Networks (IPSN). pp. 1–2. IEEE (2016)
25. Zhuang, Y., Yang, J., Li, Y., Qi, L., El-Sheimy, N.: Smartphone-based indoor localization with bluetooth low energy beacons. Sensors **16**(5), 596 (2016)

Nerve Stimulation based on Dental Pressure Detection

Marta Ševčáková and Vladimír Kašík

Department of Cybernetics and Biomedical Engineering, FEECS,
VSB – Technical University of Ostrava, 17. listopadu 15,
708 00 Ostrava – Poruba, Czech Republic
{marta.sevcakova, vladimir.kasik}@vsb.cz

Abstract. This paper discusses the development of a bionic device able to capture different force levels applied during grinding and/or clenching teeth, detecting, and translating this mechanical information into different levels of electrical stimuli. The designed prototype sends the detected force levels via RF communication to the stimulation circuit, which stimulates trigeminal nerve branches in three preset modes based on their magnitude and duration. Frequencies of stimulation around 100 Hz have a strong analgesic effect and frequencies 150 - 200 Hz have a muscle relaxant effect. Above threshold motor intensity is used to induce a muscle relaxant effect. The stimulation current value depends on the force applied while bruxism episode occurs.

Keywords: Nerve stimulation, Dental pressure, Bite force, Bruxism

1 Introduction

Biomechanical factors, like excessive loads on the tooth during clenching and grinding, are the cause of most complications in the teeth structure in case the patient has prostheses, it may result in serious damage, the same situation with healthy teeth. [1] Often occur headaches, neck pain, reside in the lack of sensitivity to the forces exerted by the clenched jaw muscles. With the focus on dental medicine and orthodontics, the purpose of the developed system is to prevent the consequences of tooth wear, rupture on the teeth, headaches, or temporomandibular joint displacement because of excessive forces exerted on them due to the bruxism or/and temporomandibular disease. Bruxism is a very common disease and has been defined by the American Academy of Sleep Medicine as the “repetitive jaw muscle activity characterized by the clenching or grinding of teeth and/or bracing or thrusting of the mandible.”. [1] Stimulation around 100 Hz have a strong analgesic effect and frequencies 150–200 Hz have a muscle relaxant effect. Above threshold sensitive intensity is used for analgesia, threshold motor intensity is used to induce a muscle relaxant effect. [2] The electrical stimuli will then be sent to the brain through the nerve system allowing restoring the healthy neural activity of the facial muscles during sleep to lower the occurrence of excessive clenching and involuntary parafunctional grinding of the teeth. As result, the organism acts in defence and decreases mandibular muscle contraction. [2] The following pages describe the stimulation process andaddress the issue of the development of the smart mouthguard.

VSB – Technical University of Ostrava, 2021, ISBN 978-80-248-4523-4 (on-line).

2 Materials and Methods

For the stimulation was chosen a biphasic rectangular waveform was, thus it is possible to minimize adaption to the stimulation pulses described in Fig.1. According to the literature, to achieve the most effective permissible stimulation results, the stimulation pulse times t1 and t3 should be lasting 100 or 200 µs, based on the stimulation regime. [4,5] If the stimuli pulse time is short, the intensity must increase for contraction or inhibition to even occur. On the other hand, if the duration of the stimuli was applied for unnecessarily long to the muscle, it might cause pain, damage of the muscle fibers, or even burn the patient, which is not desirable, so the goal is to put as little strain on the patient as possible. Time t4 determines pacing rate (frequency) therefore it is different in each stimulation mode, lasts 5140–9580 µs. The frequency range of the stimulator is between 100–180 Hz, based on the needs of each mode. [2,6,8] The minimal time of stimulation is 1s. The duration of the time t2, between the positive and negative pulse, is 20 µs, thanks to this delay the stimulation is going to be more comfortable for the patient. The pulse amplitude is in a range of 0–3,3V and it is regulated by the force of the bite.

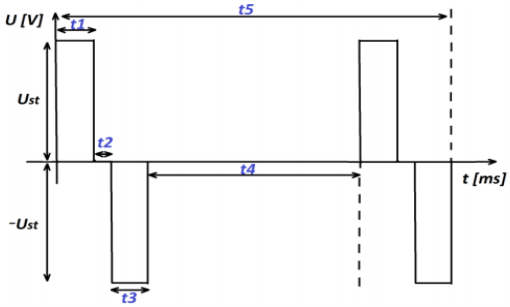

Fig. 1. Design of the biphasic stimulation pulse

The mouthguard system comprises the part shown below (Fig.2). The concept was divided into two modules communicating through RF transmitters, namely, a sensing module (SENSE) connected to pressure sensors and a stimulation module (STIM) connected to stimulating electrodes, placed on the skin above the node of the trigeminal nerve.

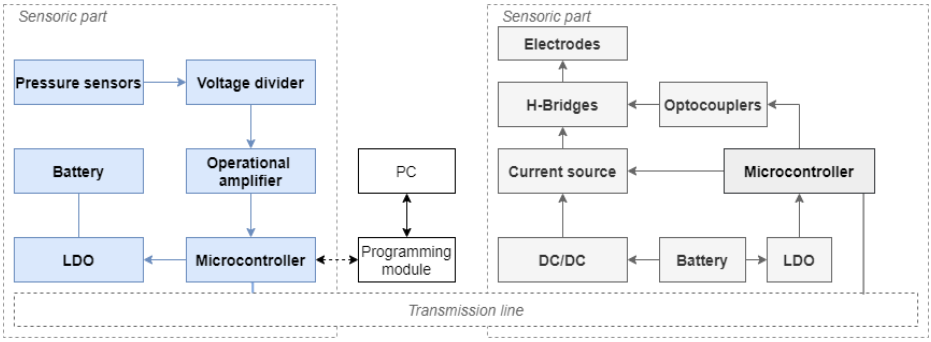

Fig. 2. Block diagram of the mouthguard system design

SENSE module

The sensing module represents the generation, processing, and transmission of information about the applied bite force. Ergo, the piezoresistive sensor detects the occurrence of grinding or clenching teeth, due to an increase of the exerted pressure and converts it into electrical information. The preamplifier is used as a signal conditioning circuit between the force sensor and the data acquisition system. The microcontroller collects this information, formats it to be transmitted to the stimulation module. The principle of operation of the piezoresistive sensor depends on a variable resistor, where the more force is applied, the lower the electrical resistance is. To achieve accurate pressure sensing, both in the vertical axis of the bite and the excursive movements, the sensors should be placed at an angle of 30° above the premolars of the lower jaw. Because in this area the anatomical structure of the teeth fits directly into the premolars in the upper jaw. The mouthguard is made of clear silicon

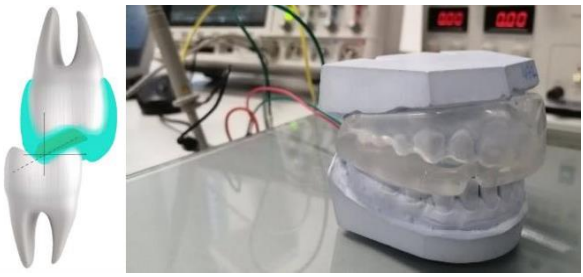

adjusted for medical purposes.

Fig. 3. The model of a prototype. On the left is shown the placement of the sensor in the mouthguard**.** On the right **is** the prototype of the sense module during the measurement

STIM module

The stimulation module performs the reception and processing of the transmitted information and provides nerve stimulation. It is composed of a microcontroller that includes the receiver of data communication with the first module and a DAC outputs that regulates the output of the current source, which will convert the information from SENSE into the analogue current values, that will then be applied to the nerve stimulation electrodes. In order to achieve current regulation, high precision, low power, low-cost integrated difference amplifiers, such as the AD8277, was used. Using the H- Bridge, to switch the polarity and to create the desired biphasic pulse. The design of the H-Bridge allows the direction of the load current to change polarity. The H-bridge transistors are the P-MOSFET and N-MOSFET types due to their low voltage drop across this switching element. The supply voltage is applied to the pull-up resistors, which serve to maintain the control level on the gate of the transistor. The transistors contained in the H-Bridge are separated by optocouplers. The electrodes of the stimulation module will be placed close to the trigeminal ganglion. The communication between the two modules is wireless through RF communication. The LDO and DC/DC converter serve as a voltage stabilizer even when the battery is discharged. For patients comfort and safety the device is for battery use only.

Data in Fig. 4 below shows achieved output data of the Sense module. Clearly shows all 3 case scenarios: Clenching, Grinding and Combination of movements.

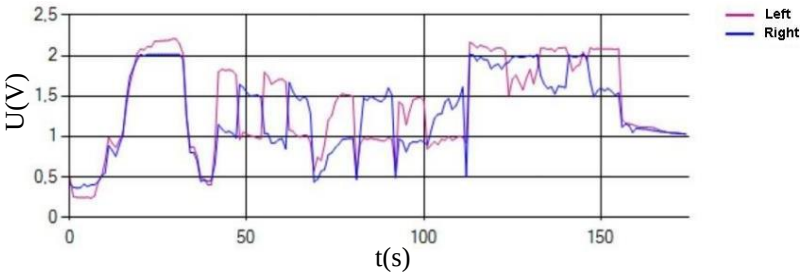

Fig. 4. Real-time sense module output data. (0–40 s) force is applied perpendicular to the jaw – clenching, (45–110 s) parallel movement – grinding, (110–160 s) combinationof these movements).

The stimulation mode selection

The bottom graph (Fig. 5) shows measured data described in Fig. 4. in combination with simulated Grinding mode stimulation. The amplitude of the stimulation signal depends on the average output data of right (sP) and left (sL) sensors. Stimulation will not proceed if the pressure applied to the sensors is less than 90 N and higher than 250 N. The division into modes is done as follows. If the absolute value of the difference of sL and sP is lower than 30 N, it is a movement in the z-axis, perpendicular to the plane of the jaws – Clenching mode. If the value is higher, it is either Combo or Grinding mode. These are divided further according to the force level. If the force on both sensors is higher than 250 N, Combo mode would be selected. And since it is physiologically almost impossible to exert such a high force while only moving the jaws to the sides, the Grinding mode would be selected. Parameters were selected based on the literature research. [3–6]

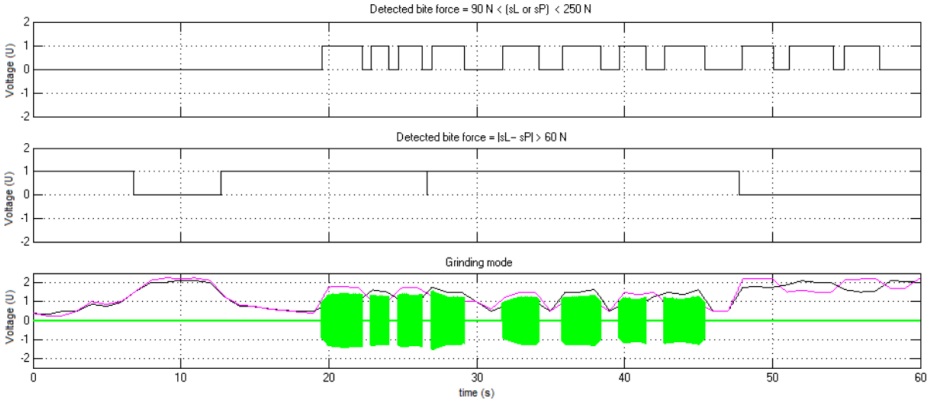

Fig. 5. The example of simulation of mode selection. The top graph represents logic values (0,1) if the detected force is higher than 90 N and at the same time both sensors detect force lower than 250 N. The middle graph shows logic 1 if the difference in force is applied on the left side or right side is higher than 60 N. The bottom graph then showsthe area of stimulation in Grinding mode.

3 Results

The ČSN EN 60601-2-10 standard specifies a maximum effective permissible stimulation current value of 50 mA for stimulation up to 400 Hz.[7] Based on the obtained data, it is possible to say that the requirements were met. MCU generates the signal that is exerted to the H-Bridge, which leads to the biphasic pulse needed for effective stimulation. The H-bridge was tested over time to see if it would be possible to switch the phase of the signal. During testing was found that the designed H-bridge fulfils the conditions. Testing of stimulation pulses was performed with a load resistance of 500 Ω and 1k Ω (Fig. 6).

During the test was applied mechanical force of approximately 400 N in the vertical axis, indicating clenching, however, while performing excursive movement of the jaw, meaning that the Combo mode should be selected. The functionality was tested in laboratory conditions using a load resistor representing tissue resistance. According to the presented Fig. 7., the voltage value Pk-Pk is 8 V, meaning that the amplitude of the stimulation signal would be 8 mA. The stimulation delay between pulses in Fig 7. is 6,25 ms, which corresponds to the programmed value. This value determines the frequency for the stimulation 150 Hz, meaning the Combo mode was correctly selected.

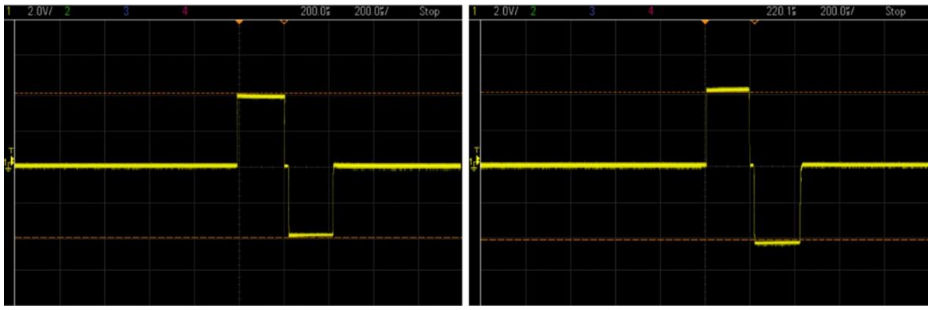

Fig. 6. On the left side is the output from the H-bridge to Rz = 500 Ω at the output Pk - Pk 4 V and on the right side is the output from the H-bridge to Rz = 1 kΩ at the output Pk - Pk 4 V

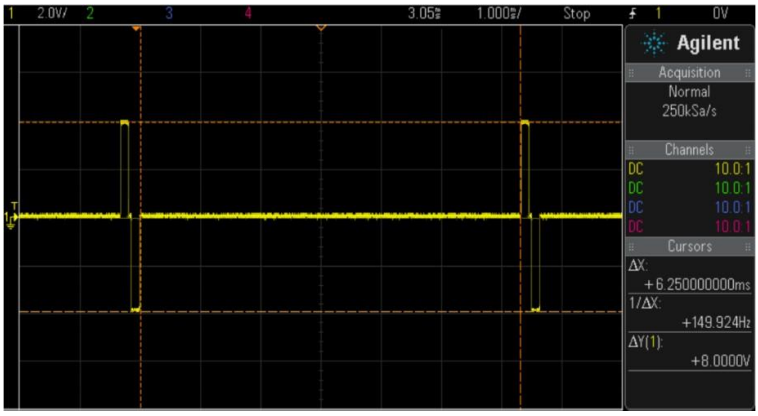

Fig. 7. Stimulation output program - Combo mode

4 Conclusion

The software design of a feedback system for stimulation of the trigeminal nerve operating in three stimulation modes was implemented. The hardware design included the comparison and subsequent selection of a suitable piezoresistive pressure sensor, design of a circuit capable of safe nerve stimulation, the implementation of RF communication used for data transfer between the sensing and stimulation module, and the design of the jaw model. The sensing circuit was tested to determine the characteristics of the piezoresistive sensor. The mouthguard holds teeth apart (2 – 5 mm), thus not only it provides mechanical protection, but also the angle the jaws make provides the free airways indirectly helping with sleep apnea (and snoring). The stimulating circuit was tested to verify the functionality of each stimulation mode. The functionality test was successfully performed in laboratory conditions using a load resistor representing tissue resistance. Sufficient pulse amplitude was achieved with both a 500 Ω and 1k Ωload.

5 References

[1] Sateia, M.J.: *International Classification of Sleep Disorders-Third Edition*. Chest 146(5), 1387–1394 (Nov 2014). https://doi.org/10.1378/chest.14-0970

[2] Vyskotová, J.: Přístrojová technika v rehabilitaci pro biomedicínské techniky. VŠB - Technická univerzita Ostrava, Ostrava (2006)

[3] *Design of Efficient and Safe Neural Stimulators.* Springer Science+Business Media, New York, NY (2016)

[4] van Dongen, M., Serdijn, W.: *Design of Efficient and Safe Neural Stimulators: A Multidisciplinary Approach*. Analog Circuits and Signal Processing, Springer International Publishing: Imprint: Springer, Cham, 1st ed. 2016 edn. (2016). https://doi.org/10.1007/978-3-319-28131-5 PENHAKER, Marek a Martin AUGUSTYNEK. Zdravotnické elektrické přístroje 1. 1. vyd. Ostrava: Vysoká škola báňská – Technická univerzita Ostrava, 2013, ISBN 978-80-248- 3107-7.

[5] Penhaker, M., Augustynek, M.: *Zdravotnické elektrické přístroje 1*. VŠB - Technická univerzita Ostrava, Ostrava (2013)

[6] Takaki, P., Vieira, M., Bommarito, S.: *Maximum Bite Force Analysis in Different Age Groups*. International Archives of Otorhinolaryngology 18(03), 272–276 (Apr 2014). https://doi.org/10.1055/s-0034-1374647

[7] ČSN EN 60601-2-10. *Zdravotnické elektrické přístroje: Část 2-10: Zvláštní požadavky na bezpečnost nervových a svalových stimulátorů*. 2001

Pancreatic MRI: 3D Reconstruction and 3D Printing of Pancreas from MRI Images

Dominik Vilimek[0000−0003−3781−12800] and Marek Penhaker[0000−0001−9527−4642]

Department of Cybernetics and Biomedical Engineering, FEECS,
VSB – Technical University of Ostrava, 17. listopadu 15,
708 00 Ostrava – Poruba, Czech Republic
{dominik.vilimek, marek.penhaker}@vsb.cz

Abstract. The magnetic resonance imaging (MRI) becoming more sophisticated diagnostics tool. Especially, in acquiring high quality images which could be used to extraction of clinically significant features such as volume of pancreas and assessment of fat fraction. Moreover, the non-invasive quantification pancreas is very important, especially in association with civilian diseases. In this study a segmentation and 3D reconstruction of pancreas was performed. T1 VIBE DIXON images acquired from 1.5 T Siemens Magnetom Sempra were used to create a 3D model. With a 3D printing technology reconstruted model was created. Such model could find a application in many clinical relevant task. Moreover, used algorithms could be the basis of further artificial inteligence approaches.

Keywords: Magnetic resonance imaging, Pancreas, 3D reconstruction, 3D Medical image processing

1 Introduction

The global prevalence of overweight and obesity is growing rapidly [7, 10], with many metabolic consequences that increase the risk of metabolic syndrome (MetS), type 2 diabetes (T2D) and cardiovascular disease (CVD) [6]. The association between pancreatic fat, obesity and MetS is well documented in recent literature [17, 4, 13, 27]. Moreover, it has been shown that exposure of pancreatic islets to increased fatty acids causes beta cell dedifferentiation, which is likely underlaying mechanism for T2D, further emphasizes the importance of precise quantification of pancreas fat content [24, 26].

Pancreatic magnetic resonance imaging (MRI) become a valuable clinical tool for diagnostic of several pancreatic diseases. The ability to accurately and non-invasively quantify organs fat infiltration such as the liver and pancreas remains a critical part of understanding the link between obesity and related diseases such as T2D.

Actually, MRI represents one of the most evolved method of fat quantification [20]. One of possibilities is single voxel proton magnetic resonance spectroscopy (MRS), which is expected to be the gold-standard non-invasive technique for such measurements [9, 19, 1]. However, it is a relatively complicated

VSB – Technical University of Ostrava, 2021, ISBN 978-80-248-4523-4 (on-line).

procedure that carries a lot of challenges such as: good shimming quality and suppression of respiratory and cardiac movement artifacts. Due to these technically demanding challenges, the reported reproducibility of fat infiltration measurements by MRI is relatively poor, and it also differs significantly between MR vendors and field strength [3, 8, 2, 12].

Another technique is to measure proton density fat fraction (PDFF) [18], with the use of a chemical shift-based gradient-echo (GRE) MRI technique (DIXON method) for the quantification of pancreatic fat. Recent findings show that pancreatic fat fraction calculated from MRI is positively correlated with liver histology and the degree of steatosis [22, 1, 21]. Moreveover, further observations indicate that the Dixon MRI technique is also significantly correlated (0.76 %) with the volume of fat fraction measured by dual energy CT [11]. Another technique is use of 3D Gradient echo Volumetric interpolated Breath-Hold Examination (VIBE) [14]. However, there is a problem of unequal accumulation of fat in the pancreas, especially focal accumulation in the tail and front of the head of the pancreas.

2 Material and Methods

This paper deals with medical image segmentation of pancreas acquired by 1.5 T Siemens Magnetom Sempra scanner (Siemens, Erlanger, Germany) using the GRE 3D VIBE sequence within 2-point DIXON method. The parameters were set as follow: TR 6.85 ms, TE_1 2.39 ms, TE_2 4.77 ms, average 2, FoV 380 mm, acq. matrix $195x320$ mm, Slice thickness 3.0 mm and with CAIPIRINHA parallel imaging technique. Pancreas was manually segmented using the 3D Slicer (version 4.11.20210226) by image analysis with more than 2 years of experience and validated by a radiologist with more than 5 years of experience. Then the 3D model of pancreas was created and exported to .stl format. Post-processing of 3D model was performed in Autodesk Meshmixer (version 3.5.474) and 3D printed using the Ender 3 PRO.

3 Results

Firstly, a manual segmentation of the pancreas was performed using a segment editor in a 3D slicer. Due to the complicated localization of the pancreas in the abdominal cavity, it was necessary to excrete all surrounding tissues and vessels. Figure 1 shows the resulting 3D reconstruction of the pancreas.

To achieve an accurate 3D model, it was necessary to perform smoothing and removal of unwanted structures as shown in Figure 2.

Finally, a 3D model of the pancreas was printed using an Ender 3 PRO printer using polylactide fibers (PLA), see Figure 3.

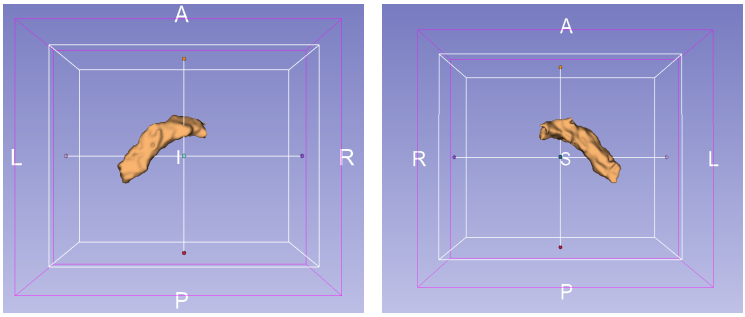

Fig. 1: 3D reconstruction of pancreas.

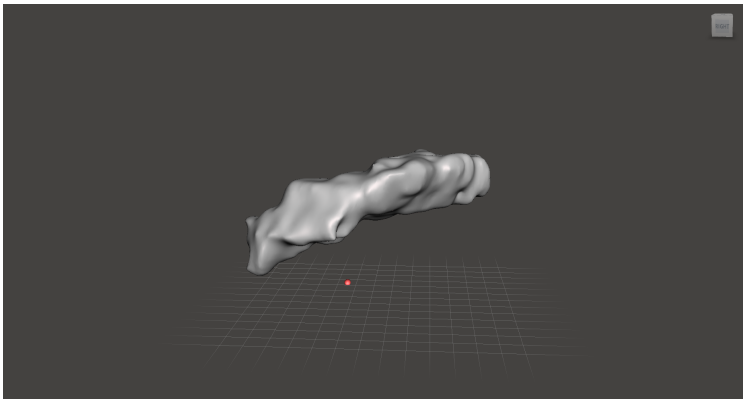

Fig. 2: Smoothed model ready for 3D printing.

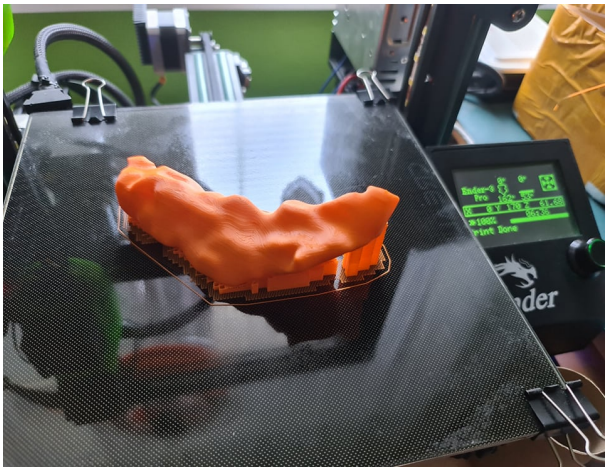

Fig. 3: Resulting 3D model of pancreas created from pancreatic MR images.

4 Conclusion and Discussion

Recently, magnetic resonance imaging have become a more sophisticated. Within used of fast sequences with excellent diagnostics quality can be achieved many diagnostically important features such as volumetry of pancreas, quantification of fat fraction and so diagnosis of a acute pancreatitis or pancreatic cancer. However, the processing of these data are still limited and complicated.

In this paper, we implemented a 3D reconstruction of pancreas from MRI images and with use of a 3D printing technology create a 3D model. Such model, could be use for presurgical planning, clinical practice or as a decision support. Moreover, 3D reconstruction could be used for calculation of fat fraction and therefore lead to creation of automated methods for non-invasive quantification of pancreas.

This work clearly has some limitations. However, based on ours previous recent research [25, 16, 23, 5, 15] we believe that work could be the basis for a greater analyses. This could hypothetically lead to creation of automated methods based on machine and deep learning algorithms. Another future work could be also a verification of 3D reconstructed model and feature extraction such as volumetry, energy, entropy, fat fraction and others. Research into solving this problem is already ongoing.

References

1. Aliyari Ghasabeh, M., Shaghaghi, M., Khoshpouri, P., pan, L., Pandy, A., Pandy, P., Zhong, X., Kannengiesser, S., Kamel, I.R.: Correlation between incidental fat deposition in the liver and pancreas in asymptomatic individuals. Abdominal Radiology **45**(1), 203–210 (Jan 2020). https://doi.org/10.1007/s00261-019-02206-w
2. Artz, N.S., Haufe, W.M., Hooker, C.A., Hamilton, G., Wolfson, T., Campos, G.M., Gamst, A.C., Schwimmer, J.B., Sirlin, C.B., Reeder, S.B.: Reproducibility of MR-Based liver fat quantification across field strength: Same-Day comparison between 1.5T and 3T in obese subjects: 1.5T vs. 3T Liver Fat Quantification. Journal of Magnetic Resonance Imaging **42**(3), 811–817 (Sep 2015). https://doi.org/10.1002/jmri.24842
3. Coe, P.O., Williams, S.R., Morris, D.M., Parkin, E., Harvie, M., Renehan, A.G., O'Reilly, D.A.: Development of MR quantified pancreatic fat deposition as a cancer risk biomarker. Pancreatology **18**(4), 429–437 (Jun 2018). https://doi.org/10.1016/j.pan.2018.04.001
4. de Boer, T.P., Nalos, L., Stary, A., Kok, B., Houtman, M.J.C., Antoons, G., van Veen, T.a.B., Beekman, J.D.M., de Groot, B.L., Opthof, T., Rook, M.B., Vos, M.A., van der Heyden, M.a.G.: The anti-protozoal drug pentamidine blocks KIR2.x-Mediated inward rectifier current by entering the cytoplasmic pore region of the channel. British Journal of Pharmacology **159**(7), 1532–1541 (Apr 2010). https://doi.org/10.1111/j.1476-5381.2010.00658.x
5. Elavsky, S., Jandačková, V., Knapová, L., Vašendová, V., Sebera, M., Kaštovská, B., Blaschová, D., Kühnová, J., Cimler, R., Vilímek, D., Bosek, T., Koenig, J., Jandačka, D.: Physical activity in an air-polluted environment: Behavioral, psychological and neuroimaging protocol for a prospective cohort study (Healthy Aging

in Industrial Environment study – Program 4). BMC Public Health **21**(1), 126 (Dec 2021). https://doi.org/10.1186/s12889-021-10166-4

6. Filippatos, T.D., Alexakis, K., Mavrikaki, V., Mikhailidis, D.P.: Nonalcoholic Fatty Pancreas Disease: Role in Metabolic Syndrome, "Prediabetes," Diabetes and Atherosclerosis. Digestive Diseases and Sciences (Jan 2021). https://doi.org/10.1007/s10620-021-06824-7
7. Hales, C., Caroll, M., Fryar, C., Ogden, C.: Prevalence of obesity and severe obesity among adults: United States, 2017–2018 (Jun 2020)
8. Hernando, D., Sharma, S.D., Aliyari Ghasabeh, M., Alvis, B.D., Arora, S.S., Hamilton, G., Pan, L., Shaffer, J.M., Sofue, K., Szeverenyi, N.M., Welch, E.B., Yuan, Q., Bashir, M.R., Kamel, I.R., Rice, M.J., Sirlin, C.B., Yokoo, T., Reeder, S.B.: Multisite, multivendor validation of the accuracy and reproducibility of proton-density fat-fraction quantification at 1.5T and 3T using a fat-water phantom: Proton-Density Fat-Fraction Quantification at 1.5T and 3T. Magnetic Resonance in Medicine **77**(4), 1516–1524 (Apr 2017). https://doi.org/10.1002/mrm.26228
9. Hu, H.H., Kim, H.W., Nayak, K.S., Goran, M.I.: Comparison of Fat-Water MRI and Single-Voxel MRS in the Assessment of Hepatic and Pancreatic Fat Fractions in Humans. Obesity **18**(4), 841–847 (Apr 2010). https://doi.org/10.1038/oby.2009.352
10. Janssen, F., Bardoutsos, A., Vidra, N.: Obesity Prevalence in the Long-Term Future in 18 European Countries and in the USA. Obesity Facts **13**(5), 514–527 (2020). https://doi.org/10.1159/000511023
11. Kameda, F., Tanabe, M., Onoda, H., Higashi, M., Ariyoshi, S., Ihara, K., Iida, E., Furukawa, M., Okada, M., Ito, K.: Quantification of pancreas fat on dual-energy computed tomography: Comparison with six-point Dixon magnetic resonance imaging. Abdominal Radiology (May 2020). https://doi.org/10.1007/s00261-020-02583-7
12. Kang, G.H., Cruite, I., Shiehmorteza, M., Wolfson, T., Gamst, A.C., Hamilton, G., Bydder, M., Middleton, M.S., Sirlin, C.B.: Reproducibility of MRI-Determined proton density fat fraction across two different MR scanner platforms. Journal of Magnetic Resonance Imaging **34**(4), 928–934 (Oct 2011). https://doi.org/10.1002/jmri.22701
13. Khoury, T., Asombang, A.W., Berzin, T.M., Cohen, J., Pleskow, D.K., Mizrahi, M.: The Clinical Implications of Fatty Pancreas: A Concise Review. Digestive Diseases and Sciences **62**(10), 2658–2667 (Oct 2017). https://doi.org/10.1007/s10620-017-4700-1
14. Koc, U., OCAKOĞLU, G., Algin, O.: The efficacy of the 3-dimensional vibe-caipirinha-dixon technique in the evaluation of pancreatic steatosis. Turkish Journal of Medical Sciences **50**(1), 184–194 (2020). https://doi.org/10.3906/sag-1909-83
15. Kubicek, J., Strycek, M., Cerny, M., Penhaker, M., Prokop, O., Vilimek, D.: Quantitative and Comparative Analysis of Effectivity and Robustness for Enhanced and Optimized Non-Local Mean Filter Combining Pixel and Patch Information on MR Images of Musculoskeletal System. Sensors **21**(12), 4161 (Jun 2021). https://doi.org/10.3390/s21124161
16. Kubicek, J., Tomanec, F., Cerny, M., Vilimek, D., Kalova, M., Oczka, D.: Recent Trends, Technical Concepts and Components of Computer-Assisted Orthopedic Surgery Systems: A Comprehensive Review. Sensors **19**(23), 5199 (Nov 2019). https://doi.org/10.3390/s19235199

17. Ogata, Y., Sakurai, N., Suzuki, H., Aoki, K., Saito, K., Shibata, D.: The prediction of local modular structures in a co-expression network based on gene expression datasets. Genome Informatics. International Conference on Genome Informatics **23**(1), 117–127 (Oct 2009)
18. Patel, N.S., Peterson, M.R., Brenner, D.A., Heba, E., Sirlin, C., Loomba, R.: Association between novel MRI-estimated pancreatic fat and liver histology-determined steatosis and fibrosis in non-alcoholic fatty liver disease. Alimentary Pharmacology & Therapeutics **37**(6), 630–639 (Mar 2013). https://doi.org/10.1111/apt.12237
19. Perman, W.H., Cem Balci, N., Akduman, I.: Review of Magnetic Resonance Spectroscopy in the Liver and the Pancreas. Topics in Magnetic Resonance Imaging **20**(2), 89–97 (Apr 2009). https://doi.org/10.1097/RMR.0b013e3181c422f1
20. Sakai, N.S., Taylor, S.A., Chouhan, M.D.: Obesity, metabolic disease and the pancreas—Quantitative imaging of pancreatic fat. The British Journal of Radiology p. 20180267 (Jun 2018). https://doi.org/10.1259/bjr.20180267
21. Sarma, M.K., Saucedo, A., Darwin, C.H., Felker, E.R., Umachandran, K., Kohanghadosh, D., Xu, E., Raman, S., Thomas, M.A.: Noninvasive assessment of abdominal adipose tissues and quantification of hepatic and pancreatic fat fractions in type 2 diabetes mellitus. Magnetic Resonance Imaging **72**, 95–102 (Oct 2020). https://doi.org/10.1016/j.mri.2020.07.001
22. Sijens, P.E.: MRI-determined fat content of human liver, pancreas and kidney. World Journal of Gastroenterology **16**(16), 1993 (2010). https://doi.org/10.3748/wjg.v16.i16.1993
23. Stanke, L., Kubicek, J., Vilimek, D., Penhaker, M., Cerny, M., Augustynek, M., Slaninova, N., Akram, M.U.: Towards to Optimal Wavelet Denoising Scheme—A Novel Spatial and Volumetric Mapping of Wavelet-Based Biomedical Data Smoothing. Sensors **20**(18), 5301 (Sep 2020). https://doi.org/10.3390/s20185301
24. Talchai, C., Xuan, S., Lin, H.V., Sussel, L., Accili, D.: Pancreatic β Cell Dedifferentiation as a Mechanism of Diabetic β Cell Failure. Cell **150**(6), 1223–1234 (Sep 2012). https://doi.org/10.1016/j.cell.2012.07.029
25. Vilimek, D., Kubikova, K., Kubíček, J., Barvik, D., Penhaker, M., Cerny, M., Augustynek, M., Oczka, D., Vondrak, J.: A Quantitative and Comparative Analysis of Edge Detectors for Biomedical Image Identification Within Dynamical Noise Effect. In: Nguyen, N.T., Jearanaitanakij, K., Selamat, A., Trawiński, B., Chittayasothorn, S. (eds.) Intelligent Information and Database Systems, vol. 12034, pp. 90–101. Springer International Publishing, Cham (2020)
26. White, M.G., Shaw, J.A., Taylor, R.: Type 2 Diabetes: The Pathologic Basis of Reversible β-Cell Dysfunction. Diabetes Care **39**(11), 2080–2088 (Nov 2016). https://doi.org/10.2337/dc16-0619
27. Yao, W., Guo, Z., Wang, L., Li, K., Saba, L., Guglielmi, G., Cheng, X., Brown, J., Blake, G., Liu, B.: Pancreas fat quantification with quantitative CT: An MRI correlation analysis. Clinical Radiology **75**(5), 397.e1–397.e6 (May 2020). https://doi.org/10.1016/j.crad.2019.12.017

Simulating Manufacturing Processes With A Digital Twin

Adam Vujtek

Department of Cybernetics and Biomedical Engineering, FEECS,
VSB – Technical University of Ostrava, 17. listopadu 15,
708 00 Ostrava – Poruba, Czech Republic
adam.vujtek@vsb.cz

Abstract. In current production, resource optimisation is used as much as possible to make production more efficient. The production process tries to maximize output with the fewest inputs and to predict problems that can arise from both wear and human error.
In our research, we simulate the wear of machine components over time. To do this, I use a digital twin of the manufacturing process. In my work, I use Siemens Plant Simulation Software to simulate the production line and monitor individual production parameters. We use API applications to work with the data. We have measured real wear data and then we apply optimization methods on top of that and try to estimate the wear time (machine cycles). We then send these simulated digital twin values back to the application. I then compare the actual and simulated values and try to achieve as little difference as possible. In my work, it can be seen that the estimated data and the real data can have a large difference, and this is because some components can have non-linear wear that is very difficult to estimate.

Keywords: Digital Twin · Optimalization Methods · Siemens Plant Simulation Software · Machine Wears · Efficiency Production.

1 Introduction

There are many ways to streamline the production of a product. However, we will look at how to optimally monitor the production in progress, analyze the production data,and then create a digital twin that simulates the exact production use case, and then use the api to transfer the measured data to our program, which will use optimization methods to try to estimate the future attributes of each part over time. We then send this simulated data back to the created digital twin via the api and explore these simulated values in a visual environment.
The virtual digital twin is now commonly used to simulate the final product and especially to predict the product properties. These properties are often understood as throughput, torque, power consumption. Energy or other performance characteristics. It is necessary that the virtual twin always matches the real data, i.e. that the configuration of the digital twin matches its real twin. [5]

In the following chapters I will discuss the digital twin and its creation depending on the production process of each production line. I will then display this digital twin in Siemens simulation software. After that, I will deal with the streamlining of data collection using IoT technology. In the next chapter, I discuss the prediction and analysis of the error rate of the digital twin, and in the following chapter I show my results, which I simulated using optimization methods, and compare them with the actual measured values.

2 Digital Twin Of The Production Plant

It often happens that the production of a certain product needs to be transferred to another plant or expanded and deployed in a new production plant. The digital twin should describe the real system with all its attributes. The digital twin can also include models of the final products and simulations of the operators who operate the plant. [7]
Individual sub-models can be used to individually simulate and optimize production processes. The digital twin can be can be used to detect physical and material collisions, eliminate bottlenecks in production and analyse system throughput. [7]

3 Creating A Digital Twin For Production

The digital twin should always match the real data. Real data collection is all the more valuable and more real when the virtual and physical twins are connected through the Internet of Things. By combining the virtual and digital twin, it allows to compare actual and expected results in different spheres. The digital twin ensures that so-called smart data can be extracted from the raw data. However, it is realistic that in this model we can often encounter a mismatch between the expected data and the measured performance or data collection from the physical twin.
Deviations and outliers from simulated values can classify problems in production, which can then be analysed and corrected to return production to positive results.With this data collection, we try to extract as many attributes as possible from the production process as a function of time to get an idea of the behaviour of the process over time.[4].
Figure 1 shows the different states that a digital twin object can be in. In each iteration, the digital twin is refined with respect to the real system.

4 Single Points For Effective Data Collection

4.1 Improving The Performance Of The Physical Twin

There is a need to get the most out of the available productive assets. Therefore, it is necessary to monitor equipment and products using IoT. Therefore, there

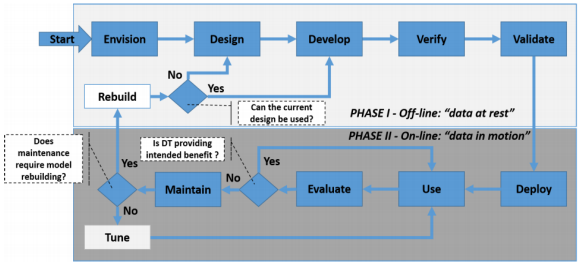

Fig. 1: High-level view of DT lifecycle [4]

is a need to aggregate, filter and analyse sensor data and simulate maximum possible load on the physical twin. The results of the data collection can be displayed on production dashboards and thus prevent problems. [3]

4.2 Predicting And Analysing The Future Error Rate Of The Physical Twin

One of the optimal ways to streamline production is through predictive analytics. Until the advent of digital twin, machine service intervals were estimated using manufacturer's tables. Using the digital twin and sensors, we are able to collect data over a period of time that can indicate machine wear and tear or periodic failures on a particular process. Hidden faults, anomalies can also be found on this data.[6] If we have enough of this data, we can accelerate the time course on the digital twin and simulate machine behaviour in the future and thus find the most optimal time when the machine needs to be repaired/adjusted to keep costs as low as possible. In this way, we defacto avoid the situation where the machine would need to be put into offline and investigate errors that have occurred. In fact, we simulate these errors before they start. [7]

5 Using Siemens Plant Simulation Software For Simulation Digital Twin

Plant simulation is a computer application developed by Siemens PLM Software for modeling, analysis, process simulation and optimization of production systems and processes, material flow and logistics operations. Using a digital twin, the software is able to optimize material flow, resource utilization and optimize company logistics. The software handles all levels of production planning, from global planning to specific production lines. The software belongs to the PLM (product lifecycle management) software family together with the digital factory. Together, these applications allow the digital twins to simulate and compare production alternatives, including logical production processes. [2].
In the image 2 you can see the newly created project in Siemens plant software

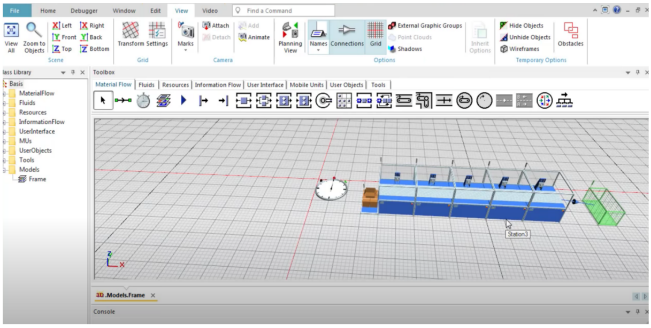

Fig. 2: Digital twin processing in the application [1]

for creating and simulating a digital twin. When creating a new project, you can directly use one of the several templates offered by the application.

6 Components Wear Simulations Via API

Each working cycle of the machine and its parts was recorded in a database. The output in this thesis is a simplified table of results, as the original file has over 1200 rows.

6.1 Real Wear Of Components

Using gyroscopes and laser sensors, the wear and tear of the individual components of the production machine is sensed on a real model. The machine consists of three components. Where the first two components are rotary and the third component performs linear motion. The data was taken from a sample production machine. the data is shared through api web interface. Our aim was to estimate the wear behaviour of the machine in future.
In the table 1 you can see the real wear of the machine components. The measured data was collected over 800 cycles. In this table only part of the collected data is shown for a better overview.

Table 1: Real wear of components

number of cycles	1st worn part (%)	2nd worn part (%)	3rd worn part (%)
1	0	0	0
20	0	0	0
50	5	2	1
100	7	4	1
200	10	9	2
400	14	14	3
800	17	19	5

6.2 Virtual Wear Of Components

The following evolution of the values for the individual parts was estimated by simulating the mathematical model. Where the input was data from real operation and the output was the estimated data for each component, how the wear of each component could continue. We used a combination of optimization methods to process the virtual data and attempted to implement a custom algorithm for wear detection. In the table 2 you can see the simulated values that came out with our proposed algorithm 1.

Listing 1: Optimalization alghoritm

```
List<DigitalTwinData> GetSimulatingDigitalTwinData(DigitalTwinData originalData,
    int numberOfFutureEstimatedData)
{
    DigitalTwinData result=null;
    if(originalData==null)
        return null;
    if(originalData.MeasuredDataCount>=numberOfFutureEstimatedData)
    {
        return null;
    }

    for(int i=originalData.MeasuredDataCount;i<numberOfFutureEstimatedData;i++)
    {
        if(result==null)
            result=new DigitalTwinData();

        result.measuredData.Add(
            OptimalizationMethod(originalData,i); //my private method
        );
    }
    return result;
}
```

Table 2: Virtual wear of components

number of cycles	1st worn part (%)	2nd worn part (%)	3rd worn part (%)
1	0	0	0
20	0	0	0
50	5	2	1
100	7	4	1
200	10	9	2
400	14	14	3
800	17	19	5

Table 3: Table difference between measured and estimated values

	the difference between the measured and estimated value		
number of cycles	1st components (%)	2nd components (%)	3rd components (%)
1000	4,55	17,39	16,67
1200	8,33	15,38	0,00
1600	3,57	16,67	10,00

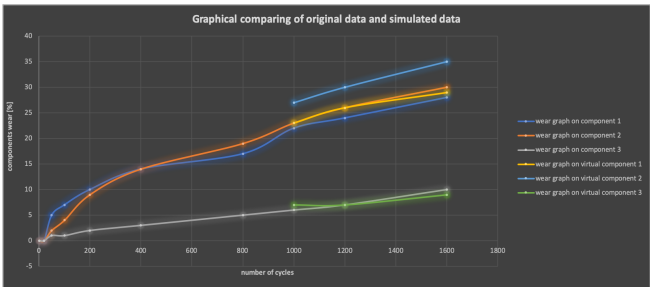

Fig. 3: Visualisation of measured and estimated data

7 Conclusions

Based on the measurements made in the 6 section, it is clear that the difference between the simulated values of the digital twin and the real data can reach an error of up to 20 %, as can be seen in the 3 table. The graph 3 visualizes these data and shows the deviations to the measured and simulated data.This is due to the fact that the wear is not linear, but some random variables enter into it, such as component oscillations and temperature fluctuations. Our goal is to achieve an error rate of no more than 5 %. In order to achieve this, we also need to monitor the sub-attributes of the individual parts. Then we will be able to generate a better simulation algorithm.

References

1. Plant simulation, `https://www.plm.automation.siemens.com/global/en/products/manufacturing-planning/plantsimulation-throughput-optimization.html`
2. Manufacturing planning with a digital twin (2021), `https://blogs.sw.siemens.com/tecnomatix/manufacturing-planning-with-a-digital-twin`
3. Kadera, P., Jirkovský, V.: Industrial information systems introduction (2017)
4. Qamsane, Y., Moyne, J., Toothman, M., et al.: A methodology to develop and implement digital twin solutions for manufacturing systems. IEEE Access **9**, 44247–44265 (2021). https://doi.org/10.1109/ACCESS.2021.3065971, `https://ieeexplore.ieee.org/document/9378543/`
5. Qi, Q., Tao, F.: Digital twin and big data towards smart manufacturing and industry 4.0. IEEE Access **6**, 3585–3593 (2018). https://doi.org/10.1109/ACCESS.2018.2793265, `http://ieeexplore.ieee.org/document/8258937/`
6. Schroeder, G.N., Steinmetz, C., Rodrigues, R.N., et al.: A methodology for digital twin modeling and deployment for industry 4.0. Proceedings of the IEEE **109**(4), 556–567 (2021). https://doi.org/10.1109/JPROC.2020.3032444, `https://ieeexplore.ieee.org/document/9247401/`
7. Siderska, J.: Application of tecnomatix plant simulation for modeling production and logistics processes. Business, Management and Education **14**, 64–73 (06 2016). https://doi.org/10.3846/bme.2016.316

Seeking Appropriate Textual Sources

Adam Albert

Department of Computer Science, FEECS,
VSB – Technical University of Ostrava, 17. listopadu 15,
708 00 Ostrava – Poruba, Czech Republic
adam.albert@vsb.cz

Abstract. When seeking relevant text sources based on user's preferences, important sources may be overlooked. This study summarizes recommendation of additional appropriate text sources based on data mining methods. We have proposed two methods using Association rules extraction and Formal Conceptual Analysis that deal with an explication of an atomic concept provided by the user. Methods provide plausible results that may help the user to choose relevant textual sources.

1 Introduction

This paper is a summary of current research of my colleagues and myself. In previous research, we have proposed an algorithm that automatically builds explications of atomic concepts from natural-language sentences mentioning the respective atomic concept. These are formalized into the language of TIL constructions and used as an input for a supervised machine learning algorithm that creates the explications. After observation of explications, the user can choose an explication that might be interesting for him. We present the theory of recommending relevant text sources which might seem not relevant to the user at first sight. Methods of recommendation are processing explications that are organised into the form of an incidence matrix. Rows of the matrix represent explications and columns represent constructions of properties contained in explications.

A text source recommendation based on the data mining method of Association rules has been presented in [1]. This method extracts rules in a form $A \Rightarrow B$ where A is an antecedent and B the consequent of the rule. The rule states that if an explication contains all concepts of properties from A then to a certain degree it probably also contains concepts of properties from B. The certain degree of probability is represented by a *minimal support* of the rule. Based on the *recommendation rule* described in the following chapter, other appropriate text sources are presented to the user.

In [2], we proposed yet another method of recommendation of appropriate text sources. This method exploits the theory of Formal Conceptual Analysis (FCA). The FCA method extracts so called *formal concepts* that consist of two sets; the set of objects and the set of attributes that are shared by all objects

VSB – Technical University of Ostrava, 2021, ISBN 978-80-248-4523-4 (on-line).

of the formal concept. Using obtained formal concepts, the *Relevant ordering* presents appropriate text sources to the user.[1]

The paper is structured as follows. Chapter 2 presents a brief summary of the explication process. The method based on Association rules is presented in chapter 3. Chapter 4 presents the method based on FCA. Chapter 5 concludes the paper.

2 Explications

An input for recommendation methods are explications of atomic concepts. In short, explication is the process of refinement of a vague or inaccurate expression into an adequately accurate one. For simplicity, we refer to the refinement defining a particular concept as the explication of that concept.

These explications are obtained by a symbolic method of supervised machine learning. The method was adjusted to the natural-language processing. The algorithm deals with positive and negative examples in the form of natural language sentences formalized into the language of TIL constructions. The algorithm consists of three methods; Generalization, Refinement and Specialization. Generalization utilizes heuristic functions to generalize the explication by processing positive examples. The Refinement method inserts new concepts of properties from positive examples into the hypothetical explication. The Specialization refines the explication with new concepts of properties from negative examples in a negated way.[2]

Using the above mentioned algorithm, we obtain different explications of an atomic concepts from different text sources. For example, we can obtain the following explication of the wild cat:

$e_1 = [{}'Typ\text{-}p\ \lambda w \lambda t\ \lambda x[[{}'\leq\ [{}'Weight_{wt}\ x]\ {}'11]\ \wedge\ [{}'\geq\ [{}'Weight_{wt}\ x]\ {}'1.2]][{}'Wild\ {}'Cat]]\ \wedge$
$[{}'Req\ {}'Mammal\ [{}'Wild\ {}'Cat]]\ \wedge\ [{}'Req\ {}'Has\text{-}fur\ [{}'Wild\ {}'Cat]] \wedge [{}'Typ\text{-}p\ \lambda w \lambda t\ \lambda x[[{}'\leq$
$[[{}'Average\ {}'Body\text{-}Length]\ x]\ {}'80]\ \wedge\ [{}'\geq\ [[{}'Average\ {}'Body\text{-}Length]\ x]\ {}'47]][{}'Wild\ {}'Cat]] \wedge$
$[{}'Typ\text{-}p\ \lambda w \lambda t\ \lambda x[[{}'=\ [[{}'Average\ {}'Skull\text{-}Size]\ x]\ {}'41.25]][{}'Wild\ {}'Cat]] \wedge [{}'Typ\text{-}p\ \lambda w \lambda t\ \lambda x[[{}'=$
$[[{}'Average\ {}'Height]\ x]\ {}'37,6]][{}'Wild\ {}'Cat]]$

This example of explication of the wild cat has been obtained from the following sentences: The weight of a wild cat is between 1.2 and 11 kilograms. The wild cat is a mammal. The wild cat has a fur. The body length of the wild cat is from 47 to 80 cm. The average skull capacity of the wild cat is 41.25 cm^3. The average height of the wild cat at the withers is 37.6 cm.

Both methods of recommendation of appropriate text sources were demonstrated on the same data set containing eight different explications of the wild cat from eight different text sources. Due to the lack of space, only the incidence matrix created from these explications is presented in Table 1.

Rows of this table represent the obtained explications, columns represent particular concepts of attributes. Column numbers denote the following concepts:

[1] More in the following chapter.

[2] More about the algorithm can be found in [3].

Table 1. Incident matrix

O/A	1	2	3	4	5	6	7	8	9	10	11	12	13	14	15	16	17
$\mathbf{e_1}$	1	1	1	1	1	1	1	1	0	0	0	0	0	0	0	0	0
$\mathbf{e_2}$	0	0	0	0	0	0	0	0	1	1	1	0	0	0	0	0	0
$\mathbf{e_3}$	0	0	0	0	0	0	0	0	0	0	0	1	1	1	1	1	1
$\mathbf{e_4}$	1	1	0	0	0	0	1	0	0	0	1	0	0	0	1	1	0
$\mathbf{e_5}$	0	0	0	0	1	0	0	0	0	0	1	0	0	0	1	1	0
$\mathbf{e_6}$	0	0	0	0	1	0	0	0	0	0	1	0	0	1	0	1	0
$\mathbf{e_7}$	1	1	1	0	0	0	0	0	1	0	1	0	0	1	1	0	0
$\mathbf{e_8}$	0	0	0	0	1	0	0	0	0	1	0	0	0	0	0	1	0

1. $'Mammal$
2. $'Has\text{-}fur$
3. $\lambda w \lambda t \lambda x['\leq ['Weight_{wt}\ x]\ '11]$
4. $\lambda w \lambda t \lambda x['\geq ['Weight_{wt}\ x]\ '1.2]$
5. $\lambda w \lambda t \lambda x['\geq [['Average\ 'Body\text{-}Length]\ x]\ '47]$
6. $\lambda w \lambda t \lambda x['\leq [['Average\ 'Body\text{-}Length]\ x]\ '80]$
7. $\lambda w \lambda t \lambda x['= [['Average\ 'Skull\text{-}Size]\ x]\ '41.25]$
8. $\lambda w \lambda t \lambda x['= [['Average\ 'Skull\text{-}Height]\ x]\ '37.6]$
9. $\lambda w \lambda t \lambda x['Live\text{-}in_{wt}\ [\lambda w \lambda t \lambda y[[['Mixed\ 'Forrest]_{wt}\ y] \vee [['Deciduous\ 'Forrest]_{wt}\ y]]]]$
10. $\lambda w \lambda t \lambda x['\geq ['Territory\text{-}Size_{wt}\ x]\ '50]$
11. $\lambda w \lambda t \lambda x[['Ter\text{-}Marking_{wt}\ x\ 'Clawing] \vee ['Ter\text{-}Marking_{wt}\ x\ 'Urinating] \vee ['Ter\text{-}Marking_{wt}\ x\ 'Leaves\text{-}Droppings]]$
12. $\lambda w \lambda t \lambda x['\leq ['In\text{-}Heat\text{-}Periodwt\ x]\ '8]$
13. $\lambda w \lambda t \lambda x['\geq ['In\text{-}Heat\text{-}Periodwt\ x]\ '2]$
14. $\lambda w \lambda t \lambda x['Seek_{wt}\ x\ 'Mate\ ['Loud\ 'Meow]]$
15. $\lambda w \lambda t \lambda x['= ['Pregnancy\text{-}Periodwt\ x]\ '65]$
16. $\lambda w \lambda t \lambda x['\leq ['Litter\text{-}Size_{wt}\ x]\ '4]$
17. $\lambda w \lambda t \lambda x['\geq ['Litter\text{-}Size_{wt}\ x]\ '3]$

3 Seeking Appropriate Textual Sources Using Association rules

The method of extraction of Association rules is used for example in market survey or risk management. A typical application of this method is the market basket analysis. The goal is to obtain hidden associations among the items in a data set that meet the predefined threshold of minimal support. The recommendation algorithm exploits hidden associations presented as association rules among the properties contained in explications.[3]

Definition 1. *(**support**) Let $I = i_1, \ldots, i_n$ be a set of items and $D = T_1, \ldots, T_n$ a data set records such that each $T_i \subseteq I$. Then **support** of a set of items (itemset) $A \subseteq I$ in D is*

$$supp(A) = \frac{|\{t \in D : A \subseteq t\}|}{|D|} \tag{1}$$

[3] More about Association rules extraction can be found in [4].

Definition 2. *(**association rule**, **confidence**) Let $I = i_1, \ldots, i_n$ be a set of items and $D = T_1, \ldots, T_n$ be a data set records such that each $T_i \subseteq I$. Furthermore, let $A, B \subseteq I$ such that $supp(A \cup B) \geq k$, where k is a predefined treshold. Then $A \Rightarrow B$ is an **association rule** iff $A \cap B = \emptyset$ and $A, B \neq \emptyset$. **Confidence** of the rule $A \Rightarrow B$ is*

$$conf(A \Rightarrow B) = \frac{supp((A \cup B))}{supp(A)} \tag{2}$$

First, the algorithm extracts item-sets that meet the minimal support k. Then the confidence of rules is computed. Rules that do not meet the minimal confidence are discarded. Then recommended sources are computed. Finally, the appropriate textual sources are presented to the user.

Definition 3. *(**recommendation rule**) Let $A \Rightarrow B$ be an association rule, $E = \{e_1, \ldots, e_n\}$ the set of all explications, $e \in E$ the user-selected explication, and let $Prop(x)$ be the set of all constituents occurring in an explication x. Then the rule $A \Rightarrow_e B$ is a rule of recommendation generated by the selected explication e iff:*

$$\begin{gathered} A \subseteq Prop(e) \\ B \subseteq \left(\bigcup_{i=1}^{n} Prop(e_i) \right) \backslash Prop(e) \\ supp(A \cup B) \geq min\text{-}supp \\ conf(A \Rightarrow B) \geq min\text{-}conf \end{gathered} \tag{3}$$

Definition 4. *(**recomended sources**) Let $A \Rightarrow_e B$ be a recommendation rule for an explication e. Let exp(d,c) be an explication of an input atomic concept c extracted from a textual document d. Then the set of recommended sources dealing with the concept c according to the rule $A \Rightarrow_e B$ is a set of text-sources RS such that*

$$RS = \{d : (A \cup B) \subseteq Prop(exp(d, c))\} \tag{4}$$

An example of the process is presented in [1].

4 Seeking Appropriate Textual Sources Using Formal Conceptual Analysis

Formal Conceptual Analysis (FCA) is the method of studying how objects are hierarchically grouped by common attributes. FCA is used in the fields such as information retrieval, software engineering, machine learning, knowledge discovery etc. FCA deals with the formal context that consists of the set of objects, the set of attributes and the relation between these two sets. The result of the

analysis is the set of formal concepts. The formal concept is a tuple of objects and attributes that are shared among all objects of the formal concept.[4] In our case, explications represent objects and the concepts of properties are attributes. User chooses the explication and the method will present other appropriate text sources based on the obtained formal concepts and the relevant ordering described below.

Definition 5. *(**formal context**) Let B be a non empty finite set of objects, let M be non empty finite set of attributes and let I be a binary relation $I \subseteq G \times M$ called incidence that expresses which objects have which attributes. Then (G, M, I) is called formal context.*

Definition 6. *(**formal concept, extent, intent**) Let (G, M, I) be a formal context, then $\beta(G, M, I) = \{(O, A) | O \subseteq G, A \subseteq M, A^{\downarrow} = O, O^{\uparrow} = A\}$ is a set of all formal concepts of context (G, M, I) where $I \subseteq G \times M, O^{\uparrow} = \{a | \forall o \in O, (o, a) \in I\}, A^{\downarrow} = \{o | \forall a \in A, (o, a) \in I\}$. $A^{\downarrow}$ is called **extent** of formal concept (O,A) and $O^{\uparrow}$ is called **intent** of formal concept (O, A)*

Definition 7. *(**significant objects**) **Significant objects** of object **e** in $\beta(G, M, I)$ is set $SO(e) = \bigcup_{i=1}^{n} O_i^e$, where O^e is extent of a concept $(O, A) \neq (G, B), e \in O, B \subseteq M$. Namely, significant objects of object **e** is union of all extents where the object **e** is as an element.*

Definition 8. *(**relevant ordering**) Let $SO(e)$ is a set of significant objects of an object **e**, let $\gamma(e)$ is a set of concepts (O, A) where $e \in O$,i.e.: $\gamma(e) = \{(O^e, (O^e)^{\uparrow}) | (O^e, (O^e)^{\uparrow}) \neq (G, B), B \subseteq M, (O^e, (O^e)^{\uparrow}) \in \beta(G, M, I)\}$, then $\boldsymbol{a} \sqsubseteq \boldsymbol{b}$ is in **relevant ordering**[5] iff*

$$max(|(O^a)^{\uparrow}|) \leq max(|(O^b)^{\uparrow}|), a, b, \in SO(e), (O^a, (O^a)^{\uparrow}), (O^b, (O^b)^{\uparrow}) \in \gamma(e).$$

Applications of the FCA method and the relevant ordering can be found in [2].

5 Conclusion

In conclusion, the user can find relevant text sources based on observation of sought atomic concept explications. However, he may miss other appropriate textual sources due to a sheer number of obtained explications or due to the lack of knowledge about the concepts etc. Thus, there is a need for an automated method of recommendation of other appropriate text sources. We have proposed two methods based on data mining algorithms that address this issue [1], [2]. Both methods produce similar results on the same data set. In [6], the optimization of recommendation was proposed. In future research, we would like to focus on pre-processing of natural language before the explication process. I have obtained a support for my research from "Podpora vědy a výzkumu v Moravskoslezském kraji 2020, (RRC/02/2020) program".

[4] More on FCA can be found in [5].

[5] Classical concept ordering is defined as: $(O, A) \sqsubseteq (O_1, A_1)$ iff $A \subseteq A_1$

References

1. Albert, A., Duží, M., Menšík, M., Pajr, M., Patschka, V. (2020): Search for Appropriate Textual Information Sources. In the *Proceedings of EJC 2020, 30th International Conference on Informational Modelling and Knowledge Bases*, Bernhard Thalheim, Marina Tropmann-Frick, Hannu Jaakkola & Yasushi Kiyoki (eds.), June 8-9, 2020, Hamburg, Germany, pp. 228-247.
2. Menšík, M., Albert, A., Patschka, V. (2020): Using FCA for Seeking Relevant Information Source. In *RASLAN 2020*, Brno: Tribun EU, 2020, 144 p. ISBN 978-80-263-1600-8, ISSN 2336-4289.
3. Menšík, M., Duží, M., Albert, A., Patschka, V., Pajr, M. (2019): Seeking relevant information sources. In Informatics'2019, *IEEE 15th International Scientific Conference on In-formatics*, Poprad, Slovakia, pp. 271-276.
4. Agrawal, R., Imielinski, T., and Swami, A. N. (1993): Mining association rules between sets of items in large databases. In Proceedings of the 1993 ACM SIGMOD *International Conference on Management of Data*, pp. 207-216.
5. Ganter, B., Wille, R. (1999): *Formal Concept Analysis: Mathematical Foundations.* 1st ed., Berlin: Springer. ISBN 978-3-540-62771-5.
6. Menšík, M., Albert, A., Patschka, V., Pajr, M. (2021). Improvement of Searching for Appropriate Textual Information Sources Using Association Rules and FCA. To appear in *Proceedings of the 31st International Conference on Information Modelling and Knowledge Bases, EJC 2021.*

Optimized data structure for k-mer indexing*

Rostislav Hřivňák[0000−0002−5229−3891]

Department of Computer Science, FEECS,
VSB – Technical University of Ostrava, 17. listopadu 15,
708 00 Ostrava – Poruba, Czech Republic
rostislav.hrivnak.st@vsb.cz

Abstract. This paper presents novel design of fast index data structure for k-mer indexing whose performance does not depend on size of the input alphabet σ. The need for such data structure comes from two facts - first is that common data structures used for indexing of data in the area of genome alignment are based on suffix data structures, such as the Suffix Trees, FM-indexes, and Suffix Arrays, whose search performance depends on the size of the input alphabet size σ. Second is that the input data for our newly developed genome aligner have integer alphabet, i.e. its size is theoretically infinite. These two facts together means that the standard approach is not suitable for our application. Functional implementation of the ternary tree and index was developed, tested, and compared to a standard implementation of the Suffix Tree based index. Implementation of the presented data structure was optimized using Single Instruction Multiple Data (SIMD) instruction set which further sped up construction and search performance on technical level by enabling high single core parallelism.

Keywords: Data structures · K-mer · Index · Genome alignment.

1 Introduction

1.1 Motivation

Whole genome alignment (WGA), which is sometimes called mapping, is a process when two genomes, or their parts, are compared and the differences are found and annotated (1)(5)(4). Retrieved information is then used by medical professionals to identify causes of illness or to precisely target treatment. Thanks to new long-read DNA scanning tools and methods, scientist can scan a patient's whole genome very quickly. One of the tools available for such long-read genome scanning is a product from Bionano Genomics called Saphyr (2), which allows up to six human samples to be processed per day with 100 times coverage. The Saphyr device labels DNA with fluorescent markers markers, which are then scanned by the camera under the microscope. The positions of the labels are measured in base pairs from the start of the scanned DNA fragment so that the

* This work is supported by the SGS project, VSB-Technical University of Ostrava, under the grant no. SP2021/94, grant of Ministry of Health of the Czech Republic no. NU20-06-00269 and Celgene Research Grant-CZ-102.

distances between these label sites can be calculated. This sequence[1] of label site distances represents scanned DNA fragment.

In contrast, standard genome aligners (12) works with a size-4 alphabet, where each letter represents one nucleotide. Most commonly used indexes are based on suffix data structures. MUMmer (11) aligner up to version 3 uses suffix tree (ST) (13), and MUMmer version 4 uses a suffix array (10). STAR (6) aligner improves the speed of the suffix array as it does not compress it. The next data structures used by the aligners are variations of FM-indexes (3), which are compressed variations of the suffix array. This data structure is used by the BOWTIE2 (9) or HISAT (7) aligners. The HISAT2 (8) aligner uses graph-based FM-indexes.

1.2 Data structure design

In this article, an alternative approach is presented using a ternary search tree (TST) which is a data structure for indexing multiple strings and then searching for their prefixes. If the functionality of the ST is replicated with the TST data structure, then all the m suffix strings of the indexed string S of length m must be indexed in the TST. Values in the TST index can be the starting positions of the suffixes relative to the source string S. Values can also reference multiple source strings.

Another approach to replicating the functionality of the ST with the TST is to use the concept of k-mers. String S of length m can be split into $m - k + 1$ k-mers of length k. The resulting k-mers are then used as keys in the TST index, and the values are k-mer starting offsets relative to source string S. When searching for any string of length k, the TST index now has the same functionality as the ST on string S because TST contains all of the sub-sequences of length k from input string S.

The TST data structure has several advantages. Most important is that TST search performance does not depend on the size of the input alphabet σ. TSTs search performance is given by the $O(\log n)$ average time complexity (in the worst case, $O(n)$, which can be considered impossible to achieve on the vast majority of real-life data), where n is the total number of nodes stored in the TST. Second is that TST is an "auto-compressing trie," i.e., sequences of keys that share a common prefix or are equal and are never stored more than once in the TST. Disadvantage of the TST is that it has a higher memory consumption compared to the ST. This is given by the fact that it is prefix-based data structure where each string must be indexed separately.

The TST index can be used as a base data structure for the so-called ternary search trees forest (TSTF). TST is used as a value in the hash table, and the key (hash) is calculated from the first n characters (numbers) of the indexed string (k-mer). This operation splits one TST into many smaller trees and leads to considerably quicker search times, as the number of comparisons at the top

[1] In this article, the terms *sequence*, *string*, and *word* denote the sequence of positive integer numbers, and the term *letter* will denote the element of such a sequence.

of the TST is substituted by a constant time access to the hash table. The introduction of hash table leads to increased memory demands on the whole TSTF index. Another disadvantage of the TSTF is that the data for searching must be prepared by calculating the hash of the first n key values using the same hash function that is used in the TSTF. Then, each search key must be placed into the collection of keys with the same hash. This enables a parallel search in the TST inside the TSTF. Search data preprocessing can be performed during the data loading or search data generation step of the genome mapping process so it is not part of the search operation itself. A challenge, which must yet be solved, is to implement an approximate search algorithm for the TSTF because of the hash table usage. The algorithm must return a set of TSTs from hash table that are close enough to a given key with given tolerance parameters.

2 Results

2.1 Test methodology

Performance of the new TST and TSTF data structures were compared to standard (i.e. not optimized) C++ implementation of Suffix Tree (ST) and Generalized Suffix Tree (GST). Human genome hg38 data in FASTA format were labeled with "*cttaag*" sequence and the k-mers were produced and indexed. Only first chromosome, then first 3 chromosomes and first 5 chromosomes were used for testing. Suffix Tree was filled with whole string of label distances as it allows direct search for k-mers. Then all k-mers which were indexed in the index were looked up. Different sized alphabets were obtained by label distances coding by logarithmic function. This results in much smaller alphabet, see table 1. K-mer sizes were chosen to be 5 and 20 for testing purposes. All tests were conducted on a desktop class computer with AMD Ryzen 7 3700X 4.2 GHz, 32GB RAM 3200 MHz, and a NVMe SSD hard drive. Implementation was done in C++ 17 and built using a mingw-64 GCC 9.3.0 compiler with no special optimization. Tests were executed on Linux Ubuntu running on a Windows Subsystem for Linux 2 (WSL2) in Windows 10.

2.2 Test results

Tables 2 and 3 demonstrates how the search performance of the studied data structures depends on the alphabet size. For 5-mer with no alphabet coding the results show that the presented TST and TSTF data structures are up to **31-times** faster than the ST data structure. When alphabet size is reduced by logarithmic coding (which leads to lower precision, but ST is faster), the TST and TSTF data structures are still **2.5-times** faster than the ST. The search speed of TST and TSTF is roughly the same in both experiments, yet the search speed of ST (and also GST) gets much faster as the σ decreases. This fully agrees with the theory that the search performance of the ST strongly depends on the alphabet size, and the performance of the TST does not. Please note that presented times

are times to search for all k-mers which were indexed in the index. Table 4 shows how the search performance of the studied data structures depends on the size of the input set. K-mers of length 20 were chosen because from previous results we can expect longer search times due to the their length. Similar results to the previous case can be observed. When the count of k-mers increases, the search for values takes progressively longer, yet the TST and TSTF data structures demonstrate a much better performance than the ST-based data structures - up to **15-times** for five chromosomes with no coding, which are split into 5-mers. Because of the chosen test methodology, the count of k-mers that are looked up in the index grows along with the count of chromosomes in the input. To show the difference in net search performance, the total search time must be divided by the total count of k-mers. Table 6 shows the net search times per one value for 5-mers with no alphabet coding (the observed largest performance difference between the data structures) and 20-mers with logarithmic alphabet coding (the smallest observed performance difference between the data structures).

Table 5 demonstrate the relationship of the data structure sizes on k-mers counts and that all of the data structures grows linearly larger when the count of k-mers grows. Please note the total size of the data structures, which are in order of tens of megabytes for the first five human chromosomes. This value can be extrapolated to hundreds of megabytes for the whole human genome when labeled with the "*cttaag*" label sequence.

Table 1. Alphabet sizes σ for different alphabet coding

Chromosomes count	None	Logarithmic
1	13,111	2,471
3	16,802	2,934
5	18,539	3,129

Table 2. Performance of data structures for different alphabet sizes σ and no alphabet coding: all measured times are in ms; TSTF and ST results are highlighted

σ	5-mers				20-mers			
	TSTF	TST	GST	**ST**	**TSTF**	TST	GST	**ST**
13,111	**14**	16	307	**282**	**30**	26	1,458	**285**
16,801	**25**	41	776	**695**	**50**	62	3,411	**699**
18,539	**33**	60	1,183	**1,047**	**70**	106	4,880	**1,077**

3 Conclusion

Novel approach was presented how a TST data structure can be used to implement a k-mer index on large alphabets. Its theoretical average search time

Table 3. Performance of data structures for different alphabet sizes σ and logarithmic alphabet coding: all measured times are in ms; TSTF and ST results are highlighted

σ	5-mers				20-mers			
	TSTF	TST	GST	**ST**	**TSTF**	TST	GST	**ST**
774	**9**	16	42	**24**	**17**	24	85	**25**
894	**23**	37	118	**57**	**42**	57	220	**62**
950	**35**	55	170	**90**	**63**	95	371	**106**

Table 4. Performance of data structures for different counts of 20-mers: all measured times are in ms; TSTF and ST results are highlighted

K-mer count	No coding				Logarithmic coding			
	TSTF	TST	GST	**ST**	**TSTF**	TST	GST	**ST**
44,652	**30**	26	1,458	**285**	**17**	24	85	**25**
96,137	**50**	62	3,411	**699**	**42**	57	220	**62**
142,587	**70**	106	4,880	**1,077**	**63**	95	371	**106**

Table 5. Data structure sizes for different alphabet sizes σ, for 5 chromosomes (142,587 k-mers): TSTF uses SUM hash function; all measured values are in kB, TSTF and ST results are highlighted

σ	5-mer			20-mer			**ST**
	TSTF	TST	GST	**TSTF**	TST	GST	
950	**19,145**	15,929	23,170	**46,689**	43,491	123,413	**8,172**
3,129	**25,881**	18,088	26,311	**53,328**	45,656	126,563	**7,306**
18,539	**46,266**	18,972	27,596	**72,959**	46,540	127,849	**7,331**

Table 6. Data structure net search performance: all measured values are in nanoseconds; TSTF and ST results are highlighted

K-mer count	No coding, 5-mer				Logarithmic coding, 20-mer			
	TSTF	TST	GST	**ST**	**TSTF**	TST	GST	**ST**
44,652	**314**	358	6,875	**6,316**	**381**	537	1,904	**560**
96,137	**260**	426	8,072	**7,229**	**437**	593	2,288	**645**
142,587	**231**	421	8,297	**7,343**	**442**	666	2,602	**743**

complexity is $O(\log n)$, where n is a total count of nodes in the TST; therefore, it is independent of alphabet size σ. Combining TST with the hash table further improves the search speed by utilizing $O(1)$ access time with the underlying TST. Subsequently, data structure indexing and search performance was further improved using single core parallelism with an SIMD AVX2 instruction set.

Work presented in this article is a high level overview of the data structure which is being developed for k-mer indexing. Many implementation details were omitted from the article because of space constraints. Full version of the article is now undergoing review process in IEEE Access journal, but the result is not currently known yet and the final form of the original paper is subject to change.

References

[1] Anisimova, M.: Evolutionary Genomics. Springer Nature (2019)
[2] Bionano: Bionano saphyr. https://bionanogenomics.com/products/saphyr/ (2021), accessed: 2021-03-13
[3] Burrows, M., Wheeler, D.: A block-sorting lossless data compression algorithm. In: Digital SRC Research Report. Citeseer (1994)
[4] Delcher, A.L., Kasif, S., Fleischmann, R.D., Peterson, J., White, O., Salzberg, S.L.: Alignment of whole genomes. Nucleic acids research **27**(11), 2369–2376 (1999)
[5] Dewey, C.N.: Whole-genome alignment. Evolutionary Genomics pp. 237–257 (2012)
[6] Dobin, A., Davis, C.A., Schlesinger, F., Drenkow, J., Zaleski, C., Jha, S., Batut, P., Chaisson, M., Gingeras, T.R.: Star: ultrafast universal rna-seq aligner. Bioinformatics **29**(1), 15–21 (2013)
[7] Kim, D., Langmead, B., Salzberg, S.L.: Hisat: a fast spliced aligner with low memory requirements. Nature methods **12**(4), 357–360 (2015)
[8] Kim, D., Paggi, J.M., Park, C., Bennett, C., Salzberg, S.L.: Graph-based genome alignment and genotyping with hisat2 and hisat-genotype. Nature biotechnology **37**(8), 907–915 (2019)
[9] Langmead, B., Salzberg, S.L.: Fast gapped-read alignment with bowtie 2. Nature methods **9**(4), 357 (2012)
[10] Manber, U., Myers, G.: Suffix arrays: a new method for on-line string searches. siam Journal on Computing **22**(5), 935–948 (1993)
[11] Marçais, G., Delcher, A.L., Phillippy, A.M., Coston, R., Salzberg, S.L., Zimin, A.: Mummer4: A fast and versatile genome alignment system. PLoS computational biology **14**(1), e1005944 (2018)
[12] Pang, A., Lee, J., Anantharaman, T., Lam, E., Hastie, A., Borodkin, M.: Comprehensive detection of germline and somatic structural mutation in cancer genomes by bionano genomics optical mapping. J. Biomol. Technol **30**, S9 (2019)
[13] Weiner, P.: Linear pattern matching algorithms. In: 14th Annual Symposium on Switching and Automata Theory (swat 1973). pp. 1–11. IEEE (1973)

Leveraging social networks for structural outlier detection in time-series data

Radek Svoboda and Jan Platoš

Department of Computer Science, FEECS,
VSB – Technical University of Ostrava, 17. listopadu 15,
708 00 Ostrava – Poruba, Czech Republic
{radek.svoboda, jan.platos}@vsb.cz

Abstract. Many research efforts have already been made in this area of natural gas consumption forecasting. However, the datasets used in these works could often not be published and used by other researchers. This complicates further research and the comparison of forecasting methods. We have addressed this issue in out recent work by the creation of a new dataset. We have taken into account state-of-the-art research works and included many data features that were previously proven to have a significant impact on the precision of the model. We made this dataset available for everyone to use for their research purposes. In this paper we further extend our work with detecting abrupt changes in the time-series endogenous variable using ordinal partitioning method for the time series data embedding into the form of social network. The social network enables us to detect structural outliers in the data which have a significant impact on the accuracy of the forecasting models.

Keywords: Natural gas consumption · Social network embedding · Pattern mining · Time-series outliers

1 Introduction

This article covers part of our experiments related to natural gas consumption forecasting research. In our previous work [3] we have studied related articles [5] about the natural gas consumption topic and gained key insights about the relevant dataset features from them [2, 4]. The gained insight enabled us to create and publicly release our own state of the art dataset together with our published forecasting methodology. The dataset is composed of the time series data and covers the time period from January 1, 2013 to December 31, 2018. Based on the operation of the gas trading market, we have decided to use the next 24 hours as a forecast horizon because the gas trade is usually realized for the next day, so the last known value is for the midnight of the previous day. Various types of outliers happen to be present in the data, although structural ones are the most significant given the forecast model accuracy. We are interested in possible transformations of the time series data to other representations which

make analysis of the proposed models possible. In this paper we have decided to evaluate transformation of the time series data using social network embedding and detection of structural outlier patterns in the transformed data.

2 Method description

We have decided to adapt Ordinal Partitioning method for the social network embedding purposes which enables us to filter structurally different curves in the gas consumption variable. The method was introduced by McCullough et al. [1] and this sections provides general description of the mentioned method.

Purpose of the method is to embed the time series data in a form of a discrete data points into the fixed dimensional space of dimension D with chosen embedding lag τ. In the first step is the original time series data $x = (x_1, x_2, x_3, ..., x_n)$ embedded into the D-dimensional vector $v = \left(x_i, x_{i+\tau}, x_{i+2\tau}, ..., x_{i+(D-1)\tau}\right)$. Subsequently this sub-sampled vector is encoded using the ordinal ranks in a descending order, output of this phase is an ordinal partitioned embedding permutation $s = \{\pi_1, \pi_2, ..., \pi_D\}; \pi \in \{1, 2, ..., D\}; \pi_i \neq \pi_j \Leftrightarrow i \neq j$.

Rank for elements of vector v, that are equal, is assigned by order of appearance in the vector. Proposed partitioning of the time series is possible with both overlapping and non-overlapping window. Each embedding permutation is mapped to a node in the social network. The edge between nodes exists if the transition between permutations exists, e.g. if the permutation s_4 is followed by the permutation s_7, there is an edge from node n_4 to node n_7. Edges are directed and weighted, weight of an edge is based on the number of mentioned transitions between embedding permutations.

3 Experiment setup overview

The series of experiments that were conducted in our previous work [3] demonstrated the usability of the proposed dataset for the task of forecasting natural gas consumption. The results in Table 1 clearly show that every machine learning model was able to outperform both traditional approaches. Moreover, we can see that the direct single-model approach, which was the simplest one of the proposed models, was able to provide forecasts with MAPE lower by 7.52 % than the Multiple linear regression approach, which used 24 partial models in total, and 3.19 % lower than ARIMA, which is an approach using only a single model as well.

The accuracy of all the proposed models is negatively affected by abrupt structural distortions of the forecast variables. These distortions may lead to a decrease in accuracy, not solely in the forecast horizon in which the phenomenon occurred but in the next forecast horizon as well as a result of the interdependence of the consecutive values of the forecast variable. We can see example of this phenomenon in Figure 1(b) in which abrupt change on 09-10-2018 caused high forecast inaccuracy not only in that day but in the next day forecast as well.

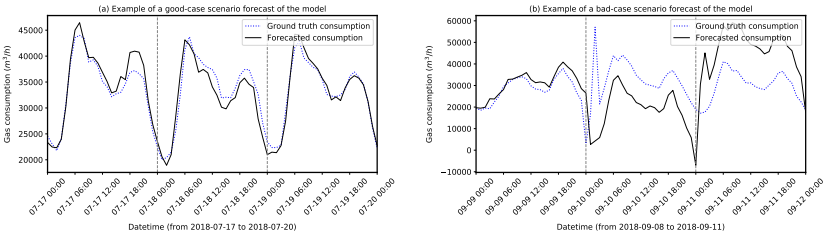

Fig. 1: Examples of a good (a) and bad (b) case forecasting scenario for the model.

To be able to detect these abrupt changes in the endogenous variable the Ordinal partitioning method was adopted. The forecasting approach in the conducted experiment dealt with hourly forecasts with 24 hour long forecast horizon starting at midnight each day. Due to this fact we have used non-overlaping window with 24 hours width starting at midnight for the network embedding as well. Our experiment conducted of embedding the time-series data into the D-dimensional space with different embedding lag (denoted as π) values. The lag values were in range of 3 to 8 hours which led to creation of 5 different embedding networks. Higher embedding lag values lead to lower number of nodes in the network and vice versa.

Table 1: Machine learning approach results from the hourly perspective compared with statistical approaches. RF indicates the Random forest algorithm, LGB the Light gradient boosting algorithm. SM stands for single model and MM for multiple models. MLR stands for multiple linear regression and ARIMA for autoregressive integrated moving average.

Approach/Metric	Algorithm	MAE	MSE	MAPE	SMAPE	R2
Statistical	MLR	10.34e+03	21.66e+07	14.80	14.69	0.961
	ARIMA	8.87e+03	18.68e+07	10.47	10.51	0.967
Direct SM	RF	6.65e+03	10.92e+07	7.52	7.36	0.981
	LGB	6.31e+03	9.72e+07	7.28	7.13	0.983
Direct MM	RF	5.70e+03	8.57e+07	6.12	6.01	0.985
	LGB	5.80e+03	8.60e+07	6.61	6.50	0.985

4 Experiment results

Examples of chosen embedding networks created using the Ordinal partitioning method visualizations are depicted on Figures 2a and 2b. Size of each node corresponds to its weighted degree, color denotes median absolute percentage error

of forecasts obtained by Direct single model solution created upon the methodology we proposed in our previous work [3]. There is a re-occurring phenomenon in all the different embedding networks which is that the nodes representing less frequent motifs have lower weighted degrees. We can see that this phenomenon is apparent in all the embedding networks although in the denser networks there is also small portion of nodes that has relatively low Median APE but their weighted degree is low as well. This effect is the most noticeable in network created with lower τ values, most noticeably in network created with $\tau = 4$ and it becomes less prevalent with higher τ values.

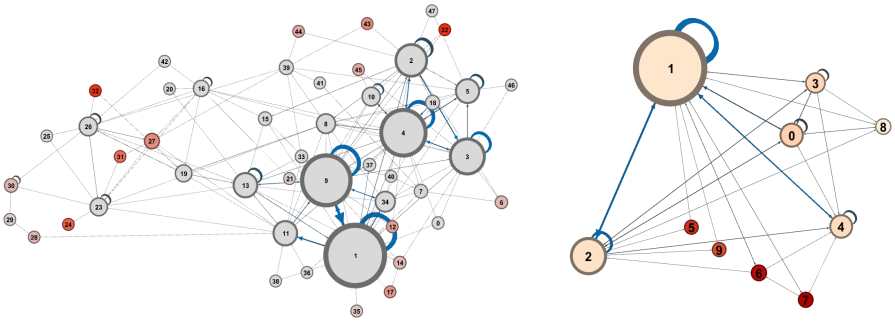

(a) Network created using permutation of length 6 ($\tau = 4$)

(b) Network created using permutation of length 4 ($\tau = 6$)

Fig. 2: Chosen embedding networks

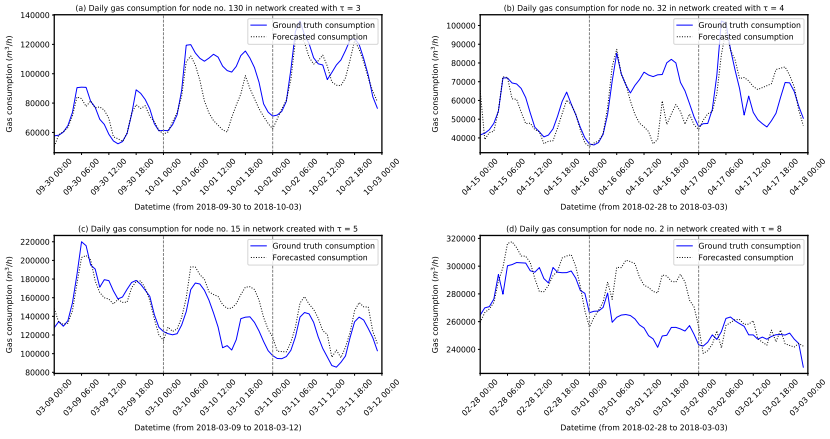

Fig. 3: Example daily consumption patterns for nodes with low weighted degree values in chosen networks.

5 Conclusions

Goal of our work was to analyze the performance of our proposed natural gas consumption forecasting methodology according to the structural outliers occurrences in the data. We have successfully adapted social network embedding for time-series data using Ordinal partitioning algorithm on our dataset dealing with natural gas consumption. The used approach enabled us to detect structural outliers in the data which can have a significant impact on the accuracy of forecasting models as we could see in Figure 1.

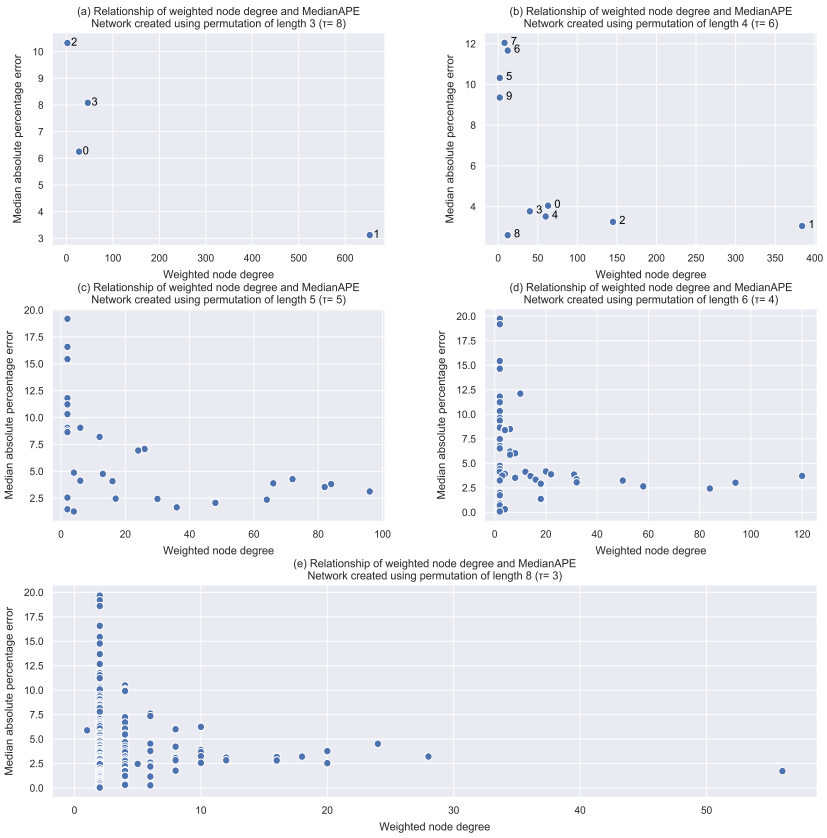

Fig. 4: Scatter plots showing the relationship between weighted node degree and median absolute percentage error for networks created with different τ parameter values.

Embedding lag value is the most important hyper-parameter in the phase of embedding network construction thus the embedding suitability varies depending on the τ value. Value of τ in not the only parameter which could be tuned, sliding window width is very important as well but due to the fact that our forecasts are

computed on the daily basis for the next 24 hour long forecast horizon, the sliding window width was fixed in our case as well as the requirement of usage of non-overlapping windows because of the forecast horizon. Every created embedding network could be used for identifying the time-series data portions suspicious of abrupt change occurrence as we can see in Figure 3. However our experiments showed that the embeddings are not equal in sense of suitability for the outlier detection task and results for the analyzed dataset show that higher τ values are more convenient for this task due to their ability to capture more general motif in the data thus it reduces variance of the obtained embedding and has better noise filtering capabilities. This insight is apparent on the scatter plots depicted in Figure 4 in which we can clearly see that for embedding networks with higher τ values the division of the nodes into two groups (see Figure 4 (a) and (b)) is possible. The first group represent very common pattern in data with high re-occurrence rate thus the nodes have very high weighted degree and low median absolute percentage error compared to the second group of nodes with much lower weighted degree and commonly higher median absolute percentage error due to the infrequency of the captured pattern. We can see this property in embedding networks created with lower τ values as well but it is apparent that the nodes with lower weighted degree are more common thus there are nodes with low values of both weighted degree and median absolute percentage error which makes outlier detection more difficult. Nodes with this properties can not be marked as an outliers straight away but it would be better to take them as nodes suspicious of representing abrupt data changes with some level of certainty based for example on their weighted degree.

Our future work will focus on implementing the insight gained from the outlier detection using embedding featured in this work into our forecasting methodology for ability to identify uncommon motifs with a goal to reduce the subsequent forecast inaccuracy in case of abrupt changes in the endogenous variable.

References

1. McCullough, M., Small, M., Stemler, T., Iu, H.H.C.: Time lagged ordinal partition networks for capturing dynamics of continuous dynamical systems. Chaos: An Interdisciplinary Journal of Nonlinear Science **25**(5), 053101 (2015). https://doi.org/10.1063/1.4919075, https://doi.org/10.1063/1.4919075
2. Soldo, B.: Forecasting natural gas consumption. Applied Energy **92**, 26 – 37 (2012)
3. Svoboda, R., Kotik, V., Platos, J.: Short-term natural gas consumption forecasting from long-term data collection. Energy **218**, 119430 (2021). https://doi.org/https://doi.org/10.1016/j.energy.2020.119430, http://www.sciencedirect.com/science/article/pii/S0360544220325378
4. Tamba, J.G., Essiane, S.N., Sapnken, E.F., Koffi, F.D., Nsouandélé, J.L., Soldo, B., Njomo, D.: Forecasting Natural Gas: A Literature Survey. International Journal of Energy Economics and Policy **8**(3), 216–249 (2018), https://ideas.repec.org/a/eco/journ2/2018-03-28.html
5. Tonković, Z., Zekić-Sušac, M., Somolanji, M.: Predicting natural gas consumption by neural networks. Tehnički vjesnik **16**(3), 51–61 (2009)

Security of Heterogeneous Multi-Core SoCs

Daniel Trnka

Department of Computer Science, FEECS,
VSB – Technical University of Ostrava, 17. listopadu 15,
708 00 Ostrava – Poruba, Czech Republic
daniel.trnka.st1@vsb.cz

Abstract. Some real-time applications can't be controlled from general-purpose operating systems like Linux, because of non-predictable response time or from the security point of view. Mission-critical applications can be split into a minimal real-time part running on a microcontroller and a non-real-time part running on an operating system. Heterogeneous SoC architectures offer a combination of microcontroller and application cores in a single package which reduces PCB footprint and allows to dynamically use of peripherals or memories on demand. Unlike two separated cores on PCB, memories and other SoC blocks are accessible by both cores and can extend the size of vector attacks. This paper shows the easy way of Linux process privilege escalation from the microcontroller core and also the other way of modifying microcontroller instructions from the Linux application.

Keywords: heterogeneous multi-core SoC, TrustZone, embedded

1 Introduction

Real-time applications, which are typically found in industry and mission-critical applications have special requirements regarding the predictability and guaranteed response time to events. General-purpose operating systems like Linux don't fulfil these requirements and can't be therefore used in such demanding installations. To address these strict real-time requirements, several modified Linux kernels were proposed[1], nevertheless, the real-time code of their drivers still runs with the same privilege and within the same address space as other kernel codes. This often means that such drivers may not be applicable from the security point of view in mission-critical systems.

Having a general-purpose operating system is not always required. Less complex applications running directly on microcontrollers without the operating system can be more easily optimised for lower latencies and suit better for hard real-time tasks. A large number of embedded applications are programmed as a single purpose application running directly on a specific controller. However, today's requirements are not only limited to read the inputs and control the peripherals, but also report the state over the network or perform computationally intensive calculations. This leads to an increasing amount of code that may influence the latency and introduce new vectors of attacks.

VSB – Technical University of Ostrava, 2021, ISBN 978-80-248-4523-4 (on-line).

Fortunately, most large and complex applications can be easily split into critical and non-critical parts and executed separately on isolated processors. The critical part may be run on a microcontroller with the minimum code complying with the real-time requirements. Meanwhile, the non-critical part may be executed on a more powerful processor with the general-purpose operating system, making the development easier. These processors are normally interconnected via a communication channel. The disadvantage of this and similar solutions may be the requirement of larger areas on the printed circuit board and the inability to reassign the peripheral from the non-critical processor to the critical processor during the development.

With the increasing number of real-time applications, some vendors started to combine different cores into a single System on a Chip (SoC) package. These heterogeneous multicore SoCs provide many advantages compared to the individual cores and are the subjects of many studies[2]. The use of heterogeneous SoCs brings also a new type of security concerns and problems like the responsibility of clock control or peripheral sharing, like external buses and interfaces[3].

2 Default Core Isolation Mechanisms

The standard configuration of both examined SoCs (i.MX8MQ and STM32MP1) does not have any core memory isolation enabled by default. All cores have their resources mapped to their address spaces and these are fully accessible without any restrictions. This practically means that the operating system can stop the Cortex-M4 core anytime, modify its instructions and memory, alter the peripherals states, and change the peripherals clocking or gating. Such modifications can be made by an attacker or by an error in the kernel code. Since the Linux kernel is monolithic, the kernel code and all third party drivers are running with the same access privileges to all resources of the SoC. Any single vulnerability in any module has the potential to compromise the security of the whole system.

By default, userspace applications use their own virtual address space and do not have raw access to other SoC resources. To overcome this, the kernel provides an interface to access the resources.

Intentionally written malicious code is not the only concern. Unintentional corruption may happen relatively easy as most Cortex-M4 firmwares are mainly developed in C language that is error-prone, especially to memory errors, which can be even more disastrous in the case of heterogeneous SoCs. For example, an invalid assignment to a pointer may overwrite Linux kernel memory or memory of Linux processes and cause fatal system errors. It is quite hard to debug accidentally overwritten process memory as no one expects that the private memory of the process may be modified from the outside of the system[4]. As an example, a firmware compromised by an attacker may intentionally modify some vital structures and lead to privilege escalation or modifying network packets.

Nevertheless, the situation is not so futile as it seems at first glance. We can adopt several software and hardware means to prevent most of these incidents. The choice of the programming language is one of the significant factors

that can influence the number of unintentional memory errors. As an example, the Rust language is being primarily designed with security in mind and is recommended for embedded designs[5]. The compiler performs compile-time and run-time memory safety checks that lead to more reliable and safe code[6]. Nevertheless, the proper selection of the programming language is not enough to make the system secure. The security features implemented in hardware are required to check if access to the memory region or a resource will be permitted.

The Cortex-M specification has an optional feature to enable the Memory Protection Unit (MPU) that can be configured to protect up to 8 or 16 memory regions. This configuration can be enforced in user mode or privileged mode, so even interrupt routines can not access the protected regions. Unfortunately, the MPU is seldomly used in real-time products[7] and must be explicitly configured by the firmware. Moreover, the instruction for MPU activation can be easily removed from the firmware and it is also possible to completely disable the MPU in runtime.

3 Privilege Escalation from M4 Core

Malicious firmware can tamper with any interesting kernel structure and the operating system may not even be able to detect it. This paper demonstrates process permission escalation that would be hardly detectable by the kernel or other user application. In our scenario, the processor's application cores are executing an unprivileged userspace process that checks the process's user id (`uid`) in a loop, waiting until the `uid` is set to zero and then starts a privileged shell. Such a situation would normally never happen unless the kernel memory is corrupted.

The process info is stored in the process control block, located in the kernel memory, residing in DDR memory. For simplicity, our malicious Cortex-M4 firmware scans the whole DDR memory for a substring of the process name, which is also a part of process control block called as `task_struct` in Linux kernel terminology. The substring will be found in memory multiple times. The following heuristics are used to locate `task_struct`. The starting address of the process name (`comm`) must be aligned since all fields of the struct are aligned. Two pointers to the credentials must proceed with the process name (these pointers must be as well aligned and belong to the kernel virtual address mapped to the DDR memory range). The kernel virtual address can be then transformed to the physical address range by masking the highest bits and adding the starting offset of the DDR memory. When the pointers correspond to these requirements, the physical address is dereferenced on the Cortex-M4 core and checked if the current `uid` matches the expected unprivileged value. If so, the `uid` value is changed to zero. The userspace process detects the `uid` change and starts a privileged shell.

The effect of the `uid` change does not have to be immediately detected by the userspace process since this is not a standard `uid` modification by the kernel and data can be cached. The process credentials are composed of multiple fields

that should be modified atomically. These credentials are not frequently changed so the synchronisation is optimized for zero-overhead reading with a mechanism called read-copy update (RCU)[8]. The new credentials are updated by making a local copy of the current credentials. This copy is modified and the pointer to the credentials is replaced with the new one. The memory barrier ensures this change is visible on all other cores and the old credentials are deallocated when there is no reader.

This demonstration shows how easy is to tamper the internal kernel structure and make security incident. Such modifications are not easily detectable by the kernel. The kernel address space layout randomization (KASLR) will not protect us from this threat and not even make this attack harder, because this technique just moves the data to a different location. This technique is vulnerable to brute-force attack that is able to scan and search for the concrete structure.

The randomization of structure layout makes this attack harder because all fields of the structs are shuffled randomly at compile time by the GCC extension. Unfortunately, the shuffle seed must be publicly available so out-of-tree kernel modules can be compiled[9]. This feature is not enabled in most distributions and won't guard against previously described brute force attacks.

4 Firmware modification from application cores

ARM Cortex-M4 core can be as well decommissioned by modifying its control registers from the application cores or by modifying its instructions. Instructions of ARM Cortex-M4 (located in static or dynamic memories) may be accessible to the privileged user through `/dev/mem` mapping device or from the kernel space even by a third-party driver.

This paper demonstrates simple instructions modification of possibly critical firmware running on Cortex-M core from the application cores. The listing 1 shows a simple disassembled firmware with an infinite loop that checks the value of a local variable `allowed` with `cmp` instruction which sets status flags. The following instruction `bne.n` then jumps to the address `0x1000001c` containing the `else` branch if the condition is not fulfilled. This instruction is encoded in 16bit thumb encoding in two bytes `0xd1 0x03`. The first nibble encodes the branch instruction with the condition encoded in the second nibble. The following byte encodes the relative jump address in the range from -256 to 254 with even increments due to instruction alignment. For the demonstration purposes, the condition can be easily replaced from equality (`0000`) to non-equality (`0001`). As explained earlier, the memory segment with instructions can be available for the system kernel or userspace process by mapping the memory through `/dev/mem` device. The condition can be easily replaced by changing the first instruction byte from `0xd1` to `0xd0`. The core will then immediately start executing the branch that was only executable under the full filled condition.

Listing 1. Disassembled code for modification

```
1000000e:       78fb            ldrb    r3, [r7, #3]
10000010:       2b2a            cmp     r3, #42 ; 0x2a
10000012:       d103            bne.n   1000001c <main+0x1c>
10000014:       4805            ldr     r0, [pc, #20]
10000016:       f000 f8d7       bl      100001c8 <iprintf>
1000001a:       e7f8            b.n     1000000e <main+0xe>
1000001c:       687b            ldr     r3, [r7, #4]
1000001e:       1c5a            adds    r2, r3, #1
10000020:       607a            str     r2, [r7, #4]
10000022:       4619            mov     r1, r3
10000024:       4802            ldr     r0, [pc, #8]
10000026:       f000 f8cf       bl      100001c8 <iprintf>
1000002a:       e7f0            b.n     1000000e <main+0xe>
```

5 TrustZone

ARM has introduced an embedded security technology called ARM TrustZone that provides system-wide security extensions that are different for Cortex-A and Cortex-M series optimized for low latencies. It was studied in detail in many publications and unfortunately, the documentation is sometimes missing or requires signing a non-disclosure agreement with a vendor[10].

One of the TrustZone mechanisms is the logical split of the processor to secure the world and the normal world. The secure world's optionally authenticated code can manage the security configuration of the whole SoC and provide services like secure storage or encryption to Linux in a normal world.

Application cores, Cortex-M4 core and other masters like USB, ethernet, etc are connected to peripherals, memories and other slaves via buses. AMBA 3 bus architecture defines three protection signals `AxPROT` - the last one defines the normal or secure world access. But it may not be sufficient for multi-master buses for better isolation so the AMBA 5 adds additional non-secure access identifier (NSAID) 4 bit signals to restrict access up to 16 masters.

Both protection signals are defined in the specification without any requirements. The protection can be checked by bus address decoders or directly by the addressed slave. A slave can provide isolated peripheral in multiple non-secure domains, provide additional functionality for the secure world, or partition the memory for each domain. IP blocks are often reused across SoCs which complicates the support for additional protection signals and increases the complexity and the size of SoC. The security is based on the trust of these signals. Untrusted IP on the bus can set the `AxPROT` signal and access secure resources.

The ARM provides TrustZone bus controllers adding the security layer between the bus and target slave peripherals so no further IP modifications are needed. The TZC-380 has at least two configurable regions that are limiting the access according to `AxPROT` signals, that can isolate the secure region from non-secure but is not able to isolate regions from multiple non-secure bus masters.

6 Conclusion

Today real-time applications are getting more complex than ever before because they need to communicate over a network. Networking frameworks are often large and may break the determinism or add the delay to real-time applications which is not desired. These mixed critical applications are often split into multiple processors, but it requires more space on the PCB and more complicated development. Heterogeneous SoCs with different cores can fill the requirements with a single package but opens new security issues and new problems that were not possible in separated processors. This paper demonstrates an easy way how to escalate the Linux process from the microcontroller core and how to modify instructions of real-time Cortex-M4 application from the Linux side. These issues are possible on systems with disabled or misconfigured TrustZone configuration, because security extensions are left to vendors and are not always publicly documented. Both examples are available on Github[1].

References

1. F. Reghenzani, G. Massari, and W. Fornaciari, "The real-time linux kernel: A survey on preempt_rt," *ACM Computing Surveys (CSUR)*, vol. 52, no. 1, pp. 1–36, 2019.
2. D. Shin, J. Lee, J. Lee, J. Lee, and H.-J. Yoo, "Dnpu: An energy-efficient deep-learning processor with heterogeneous multi-core architecture," *IEEE Micro*, vol. 38, no. 5, pp. 85–93, 2018.
3. E. Benhani, L. Bossuet, and A. Aubert, "The security of arm trustzone in a fpga-based soc," *IEEE Transactions on Computers*, vol. 68, no. 8, pp. 1238–1248, 2019.
4. W. Chen, J. Bhadra, and L.-C. Wang, "Soc security and debug," in *Fundamentals of IP and SoC Security*, pp. 29–48, Springer, 2017.
5. T. Uzlu and E. Şaykol, "On utilizing rust programming language for internet of things," in *2017 9th International Conference on Computational Intelligence and Communication Networks (CICN)*, pp. 93–96, IEEE, 2017.
6. A. Balasubramanian, M. S. Baranowski, A. Burtsev, A. Panda, Z. Rakamarić, and L. Ryzhyk, "System programming in rust: Beyond safety," in *Proceedings of the 16th Workshop on Hot Topics in Operating Systems*, pp. 156–161, 2017.
7. W. Zhou, L. Guan, P. Liu, and Y. Zhang, "Good motive but bad design: Why arm mpu has become an outcast in embedded systems," *arXiv preprint arXiv:1908.03638*, 2019.
8. P. E. McKenney and J. D. Slingwine, "Read-copy update: Using execution history to solve concurrency problems," in *Parallel and Distributed Computing and Systems*, vol. 509518, 1998.
9. N. Hussein, "Randomizing structure layout," *LWN.net*, 2017.
10. J. Winter, "Experimenting with arm trustzone–or: How i met friendly piece of trusted hardware," in *2012 IEEE 11th International Conference on Trust, Security and Privacy in Computing and Communications*, pp. 1161–1166, IEEE, 2012.

[1] `https://github.com/trnila/heterogeneous_soc_escalation`

Movement characteristics of two models with closed curve equilibrium*

Judita Buchlovská Nagyová[1,2] [0000−0001−7782−4268]

[1]IT4Innovation, VSB – Technical University of Ostrava,
17. listopadu 15, 708 00 Ostrava – Poruba, Czech Republic
[2]Department of Applied Mathematics, FEECS,
VSB – Technical University of Ostrava, 17. listopadu 15,
708 00 Ostrava – Poruba, Czech Republic
judita.buchlovska.nagyova@vsb.cz

Abstract. The aim of this article is to analyze the dynamical properties of two models with closed curve equilibrium. The first model, introduced by Gotthans and Petržela [1], is motivated by an electronic circuit. The second model [2] is a generalisation of the previous model with a right hand side that is not a C^1 function. The corresponding three-variable models are given as a set of nonlinear ordinary differential equations. The dynamics of the models are studied depending on several parameters (see [3, 4]). For this purpose, mainly new methods, as the approximate entropy and the 0-1 test for chaos, are applied. Using these tools, the dynamics are quantified and qualified. It is shown that depending on the system's parameters, the system exhibits both irregular (chaotic) and regular (periodic) character.

Keywords: Gotthans-Petržela model · Zhu-Du model · The 0-1 test for chaos · Approximate entropy.

1 Introduction

Chaotic systems, apart from naturally arising from many problems in fields such as biology, chemistry, economy, and engineering, can also be utilized for security applications, as their behaviour greatly depends on initial conditions and values of parameters. Therefore, new chaotic systems are discovered. As chaos is often associated with singular saddle-type fixed points, the research on systems with equilibrium with specific properties has drawn interest. In [1, 2], a new family of chaotic systems has been introduced with infinite equilibrium points.

* This work was supported by The Ministry of Education, Youth and Sports from the Large Infrastructures for Research, Experimental Development, and Innovations project "e-INFRA CZ – LM2018140" and by Grant of SGS No. SP2021/103, VSB - Technical University of Ostrava, Czech Republic.

2 The models

The first model (1), introduced by Gotthans and Petržela in [1], is motivated by a lumped electronic circuit, and it is introduced as a system of three differential equations in its dimensionless form:

$$\begin{aligned} \frac{dx}{dt} &= az, \\ \frac{dy}{dt} &= bxz + cz^3, \\ \frac{dz}{dt} &= x^2 + y^2 - r^2 + dxz, \end{aligned} \tag{1}$$

where r is the radius of circular equilibrium and a, b, c, and d are free parameters. It is easy to see that the set of equilibria forms a circle on the plane $z = 0$.

The second model (2), introduced by Zhu and Du in [2], is the generalisation of the first model (1), and the set of equilibria forms a closed curve. Its shape depends on the value of parameter k.

$$\begin{aligned} \frac{dx}{dt} &= z, \\ \frac{dy}{dt} &= -z(ay + by^2 + xz), \\ \frac{dz}{dt} &= |x|^k + |y|^k - 1, \end{aligned} \tag{2}$$

where a, b, and k are free parameters.

3 Simulations and main results

For the first model (1), the major outcomes of this paper were reached by simulations for free parameters a and d in a range of $a \in [-0.5, -0.1]$ and $d \in [-0.5, -0.1]$ with 0.01 step. More precisely, simulations were performed using the Runge–Kutta fifth order integration method in MATLAB with final time 10^6 and time step 0.1.

The simulations of the second model (2) were done for free parameters a, b and k, in a range $a \in [3.2, 6.5]$ and $b \in [4, 6]$ for $k = 3$, and $a \in [4, 7.5]$ and $b \in [2.65, 4.5]$ for $k = 5$, with 0.05 step. This range of parameters shows the transition between periodic and chaotic dynamics. The non-smooth nature of the system prevents finding the solutions for certain combinations of parameters, which makes the simulations problematic. The computations were performed using the *ode*45 solver in MATLAB with final time 20000 and time step 0.001.

In both cases, the system is assumed to be in the rest position in the beginning. That is, initial conditions equal

$$(x_0, y_0, z_0) = (0, 0, 0).$$

The behaviour of the systems was investigated using phase diagrams, amplitude frequency spectrum (FFT), and Poincaré sections for a relevant choice of free parameters. To underline the dynamics of the system, bifurcation diagrams were plotted. Consequently, the 0-1 test for chaos and the approximate entropy were computed for a given range of parameters. The approximate entropy shows the complexity of the system and detects an increase of unpredictability as the values of approximate entropy get higher. On the other hand, the 0-1 test for chaos splits the intervals of the parameters for which regular and chaotic character appears.

3.1 Phase diagrams, Poincaré sections, Fourier spectra and bifurcation diagrams

The movement character of the models (1) and (2) can be periodic as well as chaotic. Phase diagrams, Poincaré sections, and Fourier spectra illustrating different dynamics are shown in Figs. 1 and 2 for the Gotthans-Petržela models, and Figs. 3 and 4 for the Zhu-Du models.

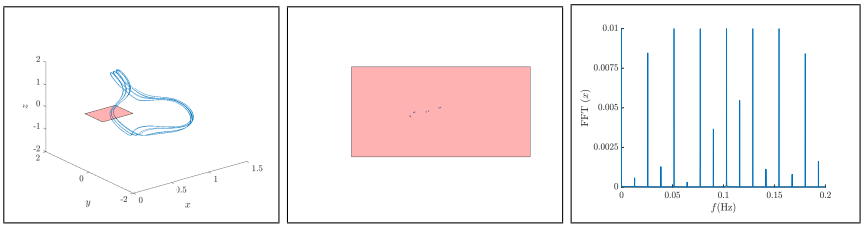

Fig. 1. Gotthans-Petržela model: phase diagram with Poincaré section and Fast Fourier transform of variable x for $a = -0.2$ and $d = -0.5$ showing regular dynamics.

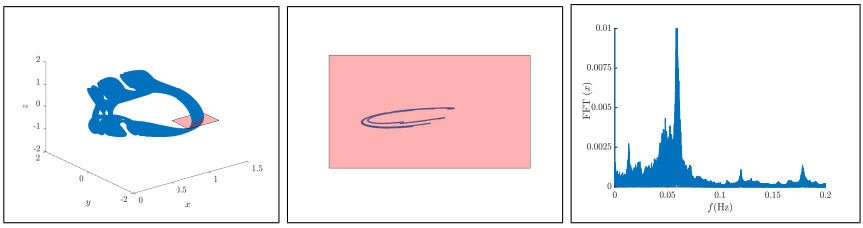

Fig. 2. Gotthans-Petržela model: phase diagram with Poincaré section and Fast Fourier transform of variable x for $a = -0.1$ and $d = -0.1$ showing chaotic dynamics.

Next, bifurcation diagram of the model (1) were done with respect to the free parameter a for variable x in Fig. 5. The bifurcation diagram is shown on the left, and it corresponds to the range $a \in (-0.5, -0.1)$. On the right, a magnification is

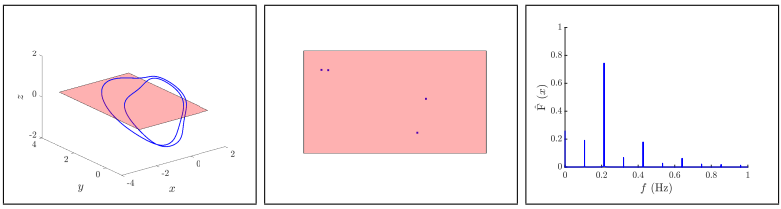

Fig. 3. Zhu-Du model: phase diagram with Poincaré section and Fast Fourier transform of variable x for $a = 3.5$, $b = 4$ and $k = 3$.

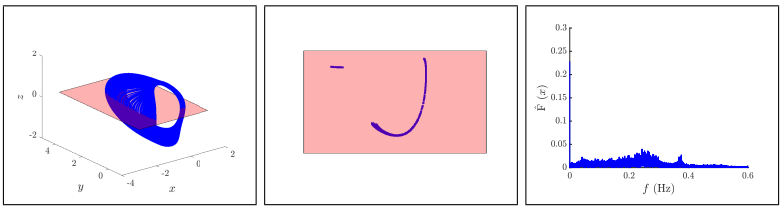

Fig. 4. Zhu-Du model: phase diagram with Poincaré section and Fast Fourier transform of variable x for $a = 5$, $b = 5.2$ and $k = 3$.

shown for $a \in (-0.15, -0.1)$, where the "period doubling" effect with "windows" is visible.

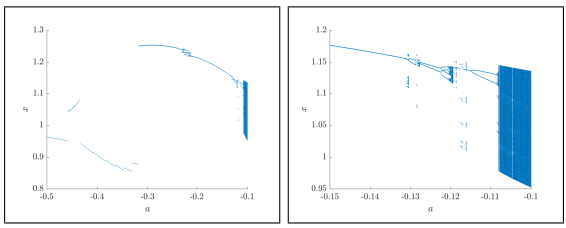

Fig. 5. Gotthans-Petržela model: Bifurcation diagram of x with respect to a: left $a \in (-0.5, -0.1)$, right $a \in (-0.15, -0.1)$.

To investigate the range of regular and chaotic dynamics of the system (2), the bifurcation diagrams were done with respect to the free parameter a for variable x. The outputs are shown in Fig. 6. Regular dynamics is shown in the beginning of the interval, followed by chaotic behaviour of the system.

3.2 The approximate entropy

The approximate entropy, introduced by Pincus [5], is a method for quantifying the amount of regularity or unpredictability in a time-series. The higher the value of approximate entropy, the more the system fluctuates and becomes unpredictable. Fast approximate entropy, proposed by J. Tomčala in [9], is a

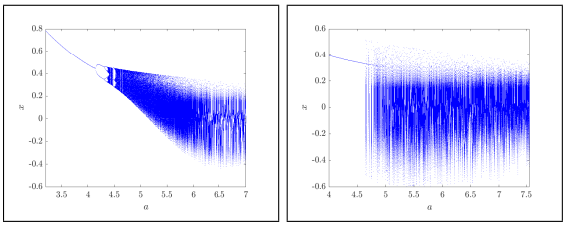

Fig. 6. Zhu-Du model: Bifurcation diagram of x with respect to a, for $b = 4.95$ and $k = 3$ (left) and for $b = 3.45$ and $k = 5$ (right).

modification of the approximate entropy algorithm, introduced in [5], leading to its acceleration.

The computations were done using the free software environment R along with the *TSEntropies* package [8]. The output of fast approximate entropy depending on a and d is visible in Fig. 7. The output of approximate entropy for the system (2) depending on a and b and for $k = 3$ and $k = 5$ are shown in Fig. 7. The correlation between results of neighboring parameters detects increase (or decrease) of the system's complexity.

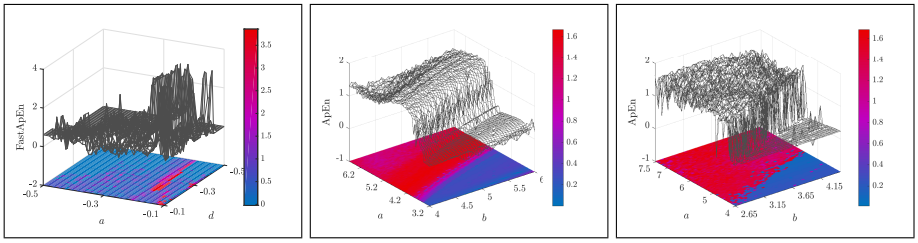

Fig. 7. Results of approximate entropy: Gotthans-Petržela model (left), Zhu-Du model for $k = 3$ (middle) and Zhu-Du model for $k = 5$ (right).

3.3 The 0-1 test for chaos

The 0-1 test for chaos, compared to the approximate entropy, is a method for strictly distinguishing regular and chaotic dynamics of a deterministic system. Introduced by Gottwald and Melbourne [6], it became a popular tool for chaos detection. The evaluation of the test results in values close to either 0 or 1, with 0 corresponding to regular dynamics and 1 to chaotic behaviour.

The computations of the 0-1 test for chaos were done using the free software environment R along with the *Chaos01* package [7]. The output of the 0-1 test for chaos for the Gotthans-Petržela model depending on a and d is in Fig. 8. The results of the 0-1 test for chaos for the Zhu-Du model (2) depending on parameters a and b for $k = 3$ and $k = 5$ are shown in Fig. 8. The test splits the region of parameters into parts of regular and chaotic dynamics.

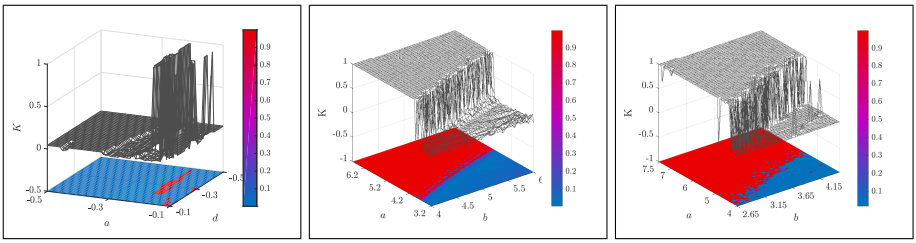

Fig. 8. Output of the 0-1 test for chaos: Gotthans-Petržela model (left), Zhu-Du model for $k = 3$ (middle) and Zhu-Du model for $k = 5$ (right).

4 Conclusions

In this paper, the Gotthans-Petržela model (1) and the Zhu-Du model (2), were constructed and their dynamics depending on various free parameters deeply researched. The equations of motion were simulated in MATLAB using the Runge–Kutta integration method for each free parameter setting. The dynamics of the models are showing regular as well as irregular patterns. This characteristics were observed using phase portraits, the Fourier spectra and bifurcation diagrams. The fast approximate entropy and the 0-1 test for chaos were utilized for qualification and quantification of movement character.

References

1. Gotthans, T., Petržela, J.: New class of chaotic systems with circular equilibrium. Nonlinear Dynamics **81**, 1143–1149 (2015)
2. Zhu X., Du W-S.: A New Family of Chaotic Systems with Different Closed Curve Equilibrium. Mathematics **7**(1), 94 (2019)
3. Lampart M., Nagyová J.: Movement Characteristics of a Model with Circular Equilibrium. In: Chaos and Complex Systems, pp. 45–55 Springer, Cham (2020)
4. Buchlovská Nagyová J.: Movement characteristics of a non-smooth model with a closed curve equilibrium. Journal of Physics: Conference Series **1730**, 012097 (2021)
5. Pincus S.M.: Approximate entropy as a measure of system complexity. Proceedings of the National Academy of Sciences **88**(6), 2297–2301 (1991)
6. Gottwald G.A., Melbourne I.: A new test for chaos in deterministic systems. Proceedings of the Royal Society A **460**(2042), 603–611 (2004)
7. Martinovič T.: Chaos01: 0-1 Test for Chaos, https://CRAN.R-project.org/package=Chaos01 (2019)
8. Tomčala J.: TSEntropies: Time Series Entropies, https://CRAN.R-project.org/package=TSEntropies (2018)
9. Tomčala J.: Acceleration of time series entropy algorithms. The Journal of Supercomputing **75**, 1443–1454 (2019)

Diagnosing Diabetic Retinopathy using Artificial Intelligence

David Číž[1], Vojtěch Cima[2], and Jakub Beránek[2]

[1]Department of Applied Mathematics, FEECS,
VSB – Technical University of Ostrava, 17. listopadu 15,
708 00 Ostrava – Poruba, Czech Republic
david.ciz@vsb.cz
[2]IT4Innovation, VSB – Technical University of Ostrava,
17. listopadu 15, 708 00 Ostrava – Poruba, Czech Republic
{vojtech.cima, jakub.beranek}@vsb.cz

Abstract. Diabetic retinopathy (DR) affects 80-100% of insulin-treated diabetics and more than 60% of non-insulin-treated diabetics with more than 20 years of diabetes. It is the main cause of blindness in the adult population aged 20-65 in the developed countries and the most common complication of diabetes. Early and accurate diagnosis is key to a successful treatment. Currently, it takes 15 minutes for a specialized retinal ophthalmologist to subjectively evaluate patient's images. This process could be automated using recent advancements in computer vision. Our approach uses state-of-the-art deep convolutional neural networks to categorize and segment defects in retinal scan images, with promising results. Our aim is to decrease the evaluation time to mere seconds, with performance comparable to a thorough doctor's analysis.

Keywords: Deep learning · Artificial intelligence · Diabetic retinopathy.

1 Introduction

Artificial intelligence (AI) is quickly improving thanks to algorithmic and technological advances. In recent years, it has particularly succeeded in advancing the field of computer vision. It has been also leveraged in the context of medical image processing, for example to detect abnormal cell growth [1] or detecting breast cancer [2].

The aim of this work is to examine the viability of using deep learning approaches for detecting diabetic retinopathy (DR). This could automate the preventive examination of ocular background (retina) images in order to detect the disease or its progression as soon as possible and thus reduce the subsequent costs of further treatment of patients.

We have designed a solution that leverages two approaches – classification and segmentation. Section 2 describes the classification approach, which predicts the severity of the disease, and Section 3 focuses on the segmentation approach, which precisely locates individual DR-related defects in input retina images.

For all of our experiments, we have used a dataset containing thousands of retina image samples that were labeled by medical experts.

2 Classification

This approach aims to create a model (classifier) that takes an image of a retina as an input and predicts the severity of the DR disease based on the image. There are five recognized severity categories, ranging from no DR to severe DR (see Table 1).

Severity	Description
1	no DR
2	mild non-proliferative DR
3	moderate non-proliferative DR
4	severe non-proliferative DR
5	proliferative DR

Table 1: DR classification classes.

We have designed, implemented and evaluated several architectures that classify the severity of diabetic retinopathy. All architectures are based on deep learning methods, more precisely convolutional neural networks (CNN). Our initial experiments were focused on evaluating whether existing well-functioning architectures, such as ResNet [3] and VGGNet [4], are viable for solving this problem.

Based on our experiments, we have chosen the ResNet-50 architecture. We have used the following techniques in our training workflow, which can be seen in Figure 1.

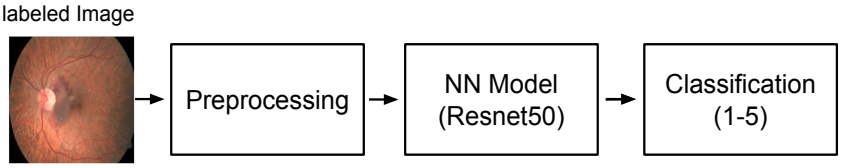

Fig. 1: Classification training workflow

Transfer learning We use ResNet parameters pretrained on the ImageNet dataset [5] to bootstrap the learning process. This technique significantly

reduces the time required to train the model and it also reduces potential overfitting, which could arise due to the relatively small number of samples in the used dataset.

Data preprocessing and augmentation All images are resized to 224×224 pixels, which corresponds to the size of the ResNet-50 input layer. During the training process, train samples are modified by augmentations such as rotation and translation. The augmentations are very mild and non-destructive because of the sensitive nature of the dataset.

Model output Due to the nature of the problem, we have experimented with discrete and continuous variants of model output, where the latter proved to be a better fit for this domain. The continuous scale allows better granularity of the network output with a possibility to discretize the output if necessary.

Model evaluation For an objective evaluation of predictive performance, a division of data into mutually exclusive training and validation sets is used. The split ratio is 80% for training and 20% for validation images.

The classification performance of our model evaluated on both portions of the dataset can be seen in the form of a confusion matrix in Figure 2. On the training set, the model has very high accuracy. On the validation set, the model is still fairly accurate, however it sometimes misclassifies the image into a severity category that is one level below or above the actual category.

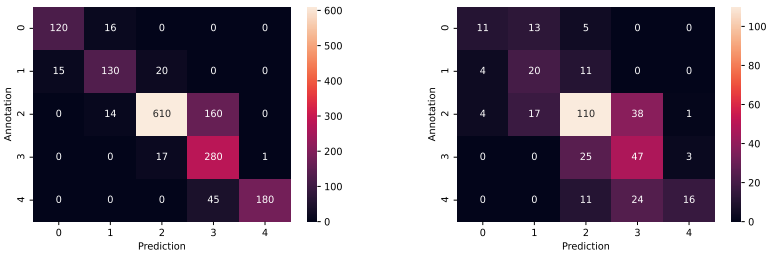

(a) Training set (b) Validation set

Fig. 2: Classification confusion matrices.

3 Segmentation

The goal of this approach is to create a model that takes an image of a retina as an input and predicts the locations of selected distinct defects that may indicate the presence of the retinopathy disease. There are 13 distinct recognized categories of defects.

As with classification, we have evaluated several architectures that are commonly used for semantic segmentation, such as U-Net [6] and DeepLab [7]. U-net

proved to be a better fit for this task. U-net is an instance of an autoencoder that takes an image as an input and produces an image with the same dimension as its output.

We have used a similar training workflow as in the classification approach, with several modifications related to the use of segmentation. The entire segmentation training workflow can be seen in Figure 4.

Data preprocessing The dataset contains polygon annotations that describe defects in the input images. During preprocessing, we convert these polygons to bitmaps so that they can be used as training labels for U-Net. The model thus receives RGB images as input and output a bitmap with the predicted locations of a single defect category in the input image.

Data augmentation Some of the annotated defects are very small. Resizing the retina images to a small resolution could thus make the annotated defect disappear completely, which is undesirable. For that reason, we employ patching. We divide every image and its corresponding bitmap label into multiple patches (sub-images) of the same size, and use these patches as inputs to the model. This causes the defects to take up a much larger part of the image, which is beneficial for the model.

Model evaluation We evaluate the model performance using the well-known Jaccard Index [8] and DICE [9] metrics.

We limited the scope of our experiments on the combination of two defects (microaneurysm and hemorrhage). We have prioritized these defects because they had the largest amount of available annotations. Our model has achieved Jaccard index of 0.3 and DICE coefficient of 0.42.

A selection of retina images and their corresponding labels and predicted defects can be seen in Figure 5.

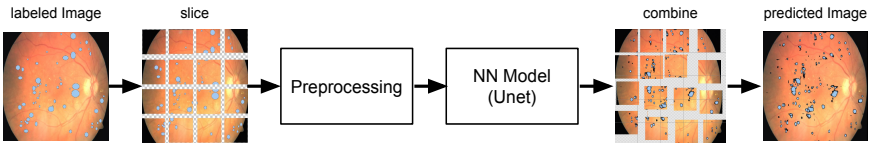

Fig. 4: Segmentation training workflow

4 Conclusion

We have demonstrated that modern deep learning methods can be used to analyze images of retinas, using both classification and segmentation approaches. Our experiments with both approaches show promising results. We plan to further fine-tune the models and employ more augmentation techniques to improve the performance of the generated predictions.

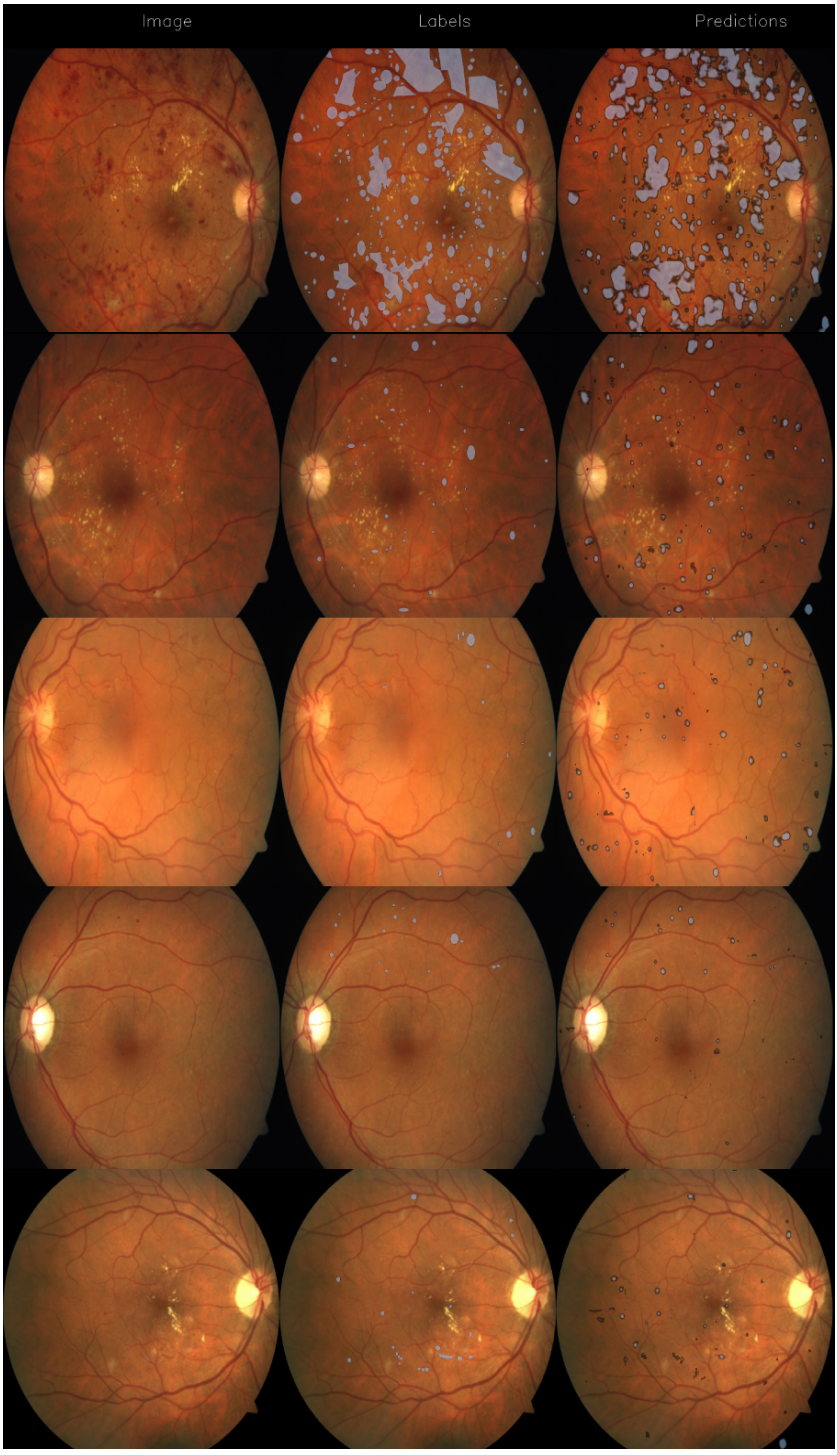

Fig. 5: Selection of images with labels (middle) and predicted defect locations

References

1. J. G. Nam, S. Park, E. J. Hwang, J. H. Lee, K.-N. Jin, K. Y. Lim, T. H. Vu, J. H. Sohn, S. Hwang, J. M. Goo, *et al.*, "Development and validation of deep learning–based automatic detection algorithm for malignant pulmonary nodules on chest radiographs," *Radiology*, vol. 290, no. 1, pp. 218–228, 2019.
2. Y. Liu, T. Kohlberger, M. Norouzi, G. E. Dahl, J. L. Smith, A. Mohtashamian, N. Olson, L. H. Peng, J. D. Hipp, and M. C. Stumpe, "Artificial intelligence–based breast cancer nodal metastasis detection: insights into the black box for pathologists," *Archives of pathology & laboratory medicine*, vol. 143, no. 7, pp. 859–868, 2019.
3. K. He, X. Zhang, S. Ren, and J. Sun, "Deep residual learning for image recognition," in *Proceedings of the IEEE conference on computer vision and pattern recognition*, pp. 770–778, 2016.
4. K. Simonyan and A. Zisserman, "Very deep convolutional networks for large-scale image recognition," *arXiv preprint arXiv:1409.1556*, 2014.
5. J. Deng, W. Dong, R. Socher, L.-J. Li, K. Li, and L. Fei-Fei, "Imagenet: A large-scale hierarchical image database," in *2009 IEEE conference on computer vision and pattern recognition*, pp. 248–255, Ieee, 2009.
6. O. Ronneberger, P. Fischer, and T. Brox, "U-net: Convolutional networks for biomedical image segmentation," in *International Conference on Medical image computing and computer-assisted intervention*, pp. 234–241, Springer, 2015.
7. L.-C. Chen, G. Papandreou, I. Kokkinos, K. Murphy, and A. L. Yuille, "Deeplab: Semantic image segmentation with deep convolutional nets, atrous convolution, and fully connected crfs," *IEEE transactions on pattern analysis and machine intelligence*, vol. 40, no. 4, pp. 834–848, 2017.
8. P. Jaccard, "The distribution of the flora in the alpine zone. 1," *New phytologist*, vol. 11, no. 2, pp. 37–50, 1912.
9. L. R. Dice, "Measures of the amount of ecologic association between species," *Ecology*, vol. 26, no. 3, pp. 297–302, 1945.

Scientific data visualizations in Blender

Marketa Hrabankova[1, 2][0000−0002−4554−0428]

[1]IT4Innovation, VSB – Technical University of Ostrava,
17. listopadu 15, 708 00 Ostrava – Poruba, Czech Republic
[2]Department of Applied Mathematics, FEECS,
VSB – Technical University of Ostrava, 17. listopadu 15,
708 00 Ostrava – Poruba, Czech Republic
marketa.hrabankova@vsb.cz

Abstract. This paper describes a software, which is being developed to provide high-quality visualization of scientific data together with fast pre-processing, which is utilizing HPC cluster resources. Aesthetically pleasing and entertaining visualization is very important to attract broader audience to the area of research being generally hard to comprehend. Developed software integrates Blender and Vistle tool. Both applications are open-source, Blender is a 3D graphics software and Vistle is a tool for scientific data reading and processing. Interconnection of these two tools is realized via tcp socket interface and the design allows to run Vistle on HPC cluster for fast data pre-processing. Vistle runs in the background and Blender serves as user interface and all setting of a pipeline is performed in Blender node editor. The pipeline setting is sent to Vistle using python interface and computed data are sent back to Blender through tcp connection. Received data are transformed into Blender objects and whole scene can be rendered or visualized in VR environment.

Keywords: scientific data visualization · rendering · HPC · Blender.

1 Introduction

Visualization of data from large computations on High-Performance Computing (HPC) systems in a high-quality is of great importance. There are multiple tools for scientific data visualization already available, such as ParaView, VisIt, Vistle, VMD or Vapor [8, 9, 2, 10, 4]. Purpose of these tools is data analysis and visualization is not an important part of the software. The main aim is at experts in the area of interest and the tools do not provide features to create an aesthetically pleasing visualization, which is understandable to a broader audience. Furthermore, showcasing and control of the scene in Virtual Reality (VR) is limited or not supported. In order to gain a full control over a general 3D scene and to improve a quality of the visualization, visual effect software is used, such as 3DS Max, Maya, Houdini or Blender [1, 6, 5, 3]. These tools provide a possibility to achieve a realistic look via full control over camera, lights, materials and animations with the support of photo-realistic renderers being an important part of

the software. On the contrary, the possibility to read and process scientific data in these tools is highly limited or not supported. Considering all the options and limitations of these two types of software, interconnection of these tools can be highly beneficial. It can be educational, aesthetic and entertaining as reported in [12]. Such visualization can speak not only to scientists, but to more people [13, 11], and can bring newcomers to areas that are otherwise difficult.

In this paper, a software, which is being developed in a form of a Blender add-on, is described. Purpose of the software is to provide a high-quality and aesthetically pleasing visualizations of scientific data and to allow effective exploration of the data in a VR environment. The software combines tool capable of scientific data processing called Vistle and Blender tool, which is a 3D graphics software.

2 Software description

In order to achieve scientific data visualizations and processing in a high quality, an open-source based software integrating Vistle [2] and Blender [3] tool is being developed.

Vistle is an open-source tool, which is able to utilize HPC cluster resources for scientific data reading and processing. Domain decomposition used during simulation of a physical problem can be reused and whole pre-processing computation can be distributed among multiple compute nodes. Vistle is designed as several separate processing modules, each module is an MPI program that uses OpenMP within compute nodes. Different file formats are supported for reading including VTK, OpenFOAM or Dyna3D.

Blender tool is an open-source 3D graphics creation suite, which provides full control over 3D content. With photo-realistic renderers and other features (such as control over camera, light etc.), it is possible to create high-quality animations with realistic look. Visualization of a whole 3D scene in VR environment is also supported in Blender.

2.1 Vistle and Blender interconnection

The software for scientific data reading, processing and visualization is developed in a form of an add-on for Blender tool. With this approach, all original features of Blender can be used and new features can be added. Vistle runs as a separate application and interconnection of Blender and Vistle is designed in a way, that Vistle can run remotely on HPC cluster and Blender can run on local computer. Applications are connected via tcp sockets and proper SSH port forwarding has to be set to interconnect a local computer and a cluster. Vistle provides python interface to control whole execution of a pipeline and this interface is used in the add-on to set up the pipeline and all parameters of the computation in Vistle. For computed data sending from Vistle to Blender for visualization, new module in Vistle was created. This module sends all collected data from Vistle computation via tcp socket to Blender.

2.2 User interface in Blender

All interaction of a user with the application happens via Blender and Vistle runs only in a background. Blender nodes editor functionality was chosen to be used as it is similar to Vistle modules editor. New nodes in Blender were created according to elementary modules in Vistle. The nodes can be connected to create a pipeline as it can be done in Vistle and parameters of each node correspond to Vistle modules parameters. With this approach, everything needed for the pipeline execution is set within Blender and all setting is passed to Vistle via python interface. Example of a pipeline, which can be created and set in Blender user interface, is in Figure 1.

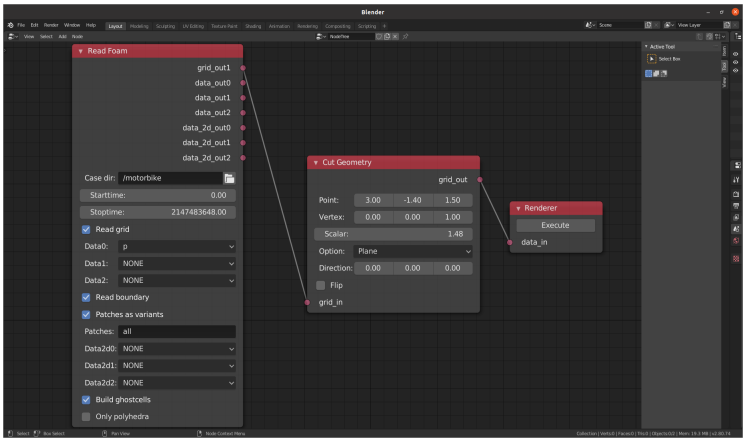

Fig. 1. Example of a pipeline in Blender user interface.

2.3 General workflow

Visualization of scientific data via Blender add-on consists of several steps. Firstly, Vistle runs separately on cluster (or local computer) and waits for connection on particular port. Blender runs on local computer and connects to the particular port, which allows to use Vistle python interface for Vistle control from Blender. As a next step, separate thread is started within Blender and the thread waits for connection from Vistle module and after connection it waits or receives and processes computed data from Vistle.

After all required initial steps, Blender nodes can be added and connected according to user preferences. Every time a node is added in the editor, appropriate command is sent via python interface and particular module is spawned in Vistle. When the newly created Vistle module for data sending to Blender is spawned, it connects to Blender separate thread, which is waiting for the connection, and later computed data are sent through this connection. Node parameters in Blender can be set according to actual user requirements (including

path to data folder) and when everything regarding pipeline is set properly in Blender node editor, user can choose to execute the pipeline, which sends proper commands to Vistle to set up the pipeline according to Blender settings and to execute the whole pipeline in Vistle. After the computation in Vistle (consisting of data reading and processing, which can be divided among several nodes), Vistle module for data sending to Blender sends raw data in a form of arrays for processing in Blender together with basic headers for correct data decoding.

Data is received in Blender in the separate thread and it is firstly decoded and converted to particular data format according to received headers. Blender objects cannot be created and added to a scene in the separate thread created in the add-on, thus the Blender timer functionality is used to do the objects creation by Blender main threads. With the Blender timer, it is possible to receive data and create objects in an asynchronous manner. Created objects are added to the scene and can be visualized and rendered.

3 Results

Implemented add-on was tested with Blender 2.80 and the interconnection with Vistle works properly even in the case that Vistle runs on a cluster and Blender runs on a local computer. Elementary nodes for data processing were created in Blender node editor and polygonal geometry and streamlines computed in Vistle can be visualized within the Blender environment. The workflow was demonstrated on dataset from OpenFOAM CFD tool [7] and the result is shown in Figure 2.

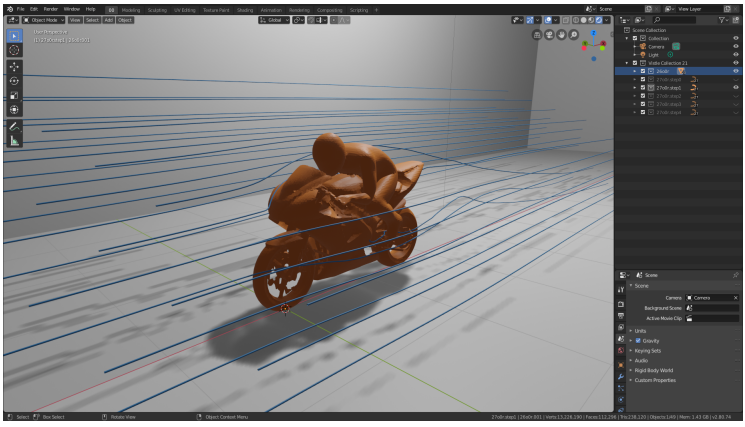

Fig. 2. Result of scientific data visualization workflow in Blender.

4 Conclusion

Proposed solution provides possibility to create high-quality visualizations of scientific data. Blender is very powerful tool supporting many visual effect features and together with Vistle it is possible to utilize HPC cluster resources for fast data pre-processing. Future development will include implementation of more modules in Blender UI and support for convenient color ramp setting as it is an important part of visualization. Another research will be focused on computed data reduction for faster data sending and rendering.

5 Acknowledgments

This work was supported by the Doctoral grant competition VSB - Technical University of Ostrava, reg. no. CZ.02.2.69/0.0/0.0/19_073/0016945 within the Operational Programme Research, Development and Education, under project DGS/TEAM/2020-008 "Development of a tool for scientific data processing and visualization in VR with multi-user support".

The work has been performed under the Project HPC-EUROPA3 (INFRAIA-2016-1-730897), with the support of the EC Research Innovation Action under the H2020 Programme; in particular, the author gratefully acknowledges the support of Uwe Wössner and Martin Aumüller from the visualization department and the computer resources and technical support provided by HLRS.

References

1. 3ds Max | 3D Modeling, Animation & Rendering Software | Autodesk. https://www.autodesk.com/products/3ds-max/, Last accessed 13 Jul 2021
2. HLRS High Performance Computing Center Stuttgart - Vistle. https://www.hlrs.de/vistle/, Last accessed 13 Jul 2021
3. Home of the Blender project - Free and Open 3D Creation Software. https://www.blender.org, Last accessed 13 Jul 2021
4. Home | VAPOR. https://www.vapor.ucar.edu, Last accessed 13 Jul 2021
5. Houdini - 3D modeling, animation, VFX, look development, lighting and rendering | SideFX. https://www.sidefx.com/, Last accessed 13 Jul 2021
6. Maya Software | Computer Animation & Modeling Software | Autodesk. https://www.autodesk.com/products/maya/, Last accessed 13 Jul 2021
7. OpenFOAM® - Official home of The Open Source Computational Fluid Dynamics (CFD) Toolbox. https://openfoam.com, Last accessed 13 Jul 2021
8. ParaView. https://www.paraview.org/, Last accessed 13 Jul 2021
9. VisIt. https://visit.llnl.gov/, Last accessed 13 Jul 2021
10. What is VMD? https://www.ks.uiuc.edu/Research/vmd/allversions/what_is_vmd.html, Last accessed 13 Jul 2021
11. Arroio, A.: Context based learning: A role for cinema in science education. Science Education International **21** (2010)
12. Cawthon, N. and Moere, A. V.: The Effect of Aesthetic on the Usability of Data Visualization. In: 2007 11th International Conference Information Visualization (IV '07). pp. 637–648 (2007). https://doi.org/10.1109/IV.2007.147

13. Dubeck, L. and Moshier, S. and Boss, J.: Fantastic Voyages: Learning Science through Science Fiction Films. Springer, New York (2003)

Comparing implemented Runge-Kutta methods for solving ODE's in four different programming languages

Andrii Patrikei[1,2][0000−0003−2015−4843]

[1]IT4Innovation, VSB – Technical University of Ostrava,
17. listopadu 15, 708 00 Ostrava – Poruba, Czech Republic
[2]Department of Applied Mathematics, FEECS,
VSB – Technical University of Ostrava, 17. listopadu 15,
708 00 Ostrava – Poruba, Czech Republic
andrii.patrikei.st@vsb.cz

Abstract. This paper deals with basic concepts of solutions of ODEs. It is described the fundamental theoretical background and benchmark results of Runge-Kutta methods implemented in different programming languages. The performance benchmarks comparison for four programming languages is given, and as a conclusion, MATLAB and Julia have the best performance for solving ordinary differential equations as shown on Lorentz system example.

Keywords: Ordinary differential equation · Open-source packages · Performance.

1 Introduction

Differential equations have great practical importance in modern life. They are used to model the behavior of complex systems from biology, economics, physics, chemistry, engineering, and many other sciences. For example, the movement of a harmonic oscillator, the population growth of species, or the change in investment return over time. There are many types of differential equations and tools for working with them. In this paper, a comparison of time elapsing to solving ordinary differential equations using implementations of *ode*45 [1] function in MATLAB [2], *deSolve* [3] R package, *SciPy* [4] Python package and *Differential Equations* [5] Julia package is described. This approach is focused to introduce the possibility of using other programming languages as an alternative to MATLAB for solving ordinary differential equations. It is composed of three sections: brief introduction to Runge-Kutta [7] method for solving ordinary differential equations, application of Runge–Kutta methods for solving ODE's in four languages, and working-time benchmarks for different ordinary differential equations solvers.

2 Brief introduction to Runge-Kutta methods for solving ordinary differential equations

We begin by considering one of the most popular algorithm for the numerical solution of ordinary differential equations - Runge-Kutta methods. It is a family of iterative methods, used to approximate solutions of Ordinary Differential Equations (ODEs). Such methods use discretization to calculate the solutions in small steps. The approximation of the "next step" is calculated from the previous one, by adding s terms (1).

$$y_{n+1} = y_n + h \sum_{i=1}^{s} b_i k_i, \tag{1}$$

In this article we are interested in *ode*45 function for solving ODE's. This function implements a Runge-Kutta method with a variable time step for efficient computation. *ode*45 is designed to handle the following general problem (2):

$$\frac{dx}{dt} = \boldsymbol{f}(t, \boldsymbol{x}),\ \boldsymbol{x}(t_0) = \boldsymbol{x}_0, \tag{2}$$

where t is the independent variable, $\boldsymbol{x}$ is a vector of dependent variables to be found and $\boldsymbol{f}(t, \boldsymbol{x})$ is a function of t and $\boldsymbol{x}$. The mathematical problem is specified when the vector of functions on the right-hand side of Eq. (2), $\boldsymbol{f}(t, \boldsymbol{x})$, is set and the initial conditions, $\boldsymbol{x} = \boldsymbol{x}_0$ at time t_0 are given.

3 Application of Runge–Kutta methods for solving ODE's in MatLab, *deSolve* R package, *SciPy* Python package and *Differential Equations* Julia package by example of solving Lorenz system

We apply *ode*45 function implemented in four programming languages for solution to the well-known system introduced by Edward Lorenz [8]. *SciPy* has implemented a *RK*45 [9] function as an alternative to a MATLAB ode45 function. The Lorenz system (3) has three-degree of freedom with x, y, and z variables:

$$\begin{cases} \frac{dx}{dt} = ax + yz \\ \frac{dy}{dt} = b(y - z) \\ \frac{dz}{dt} = xy + cy - z \end{cases} \tag{3}$$

and parameters a, b, c, where parameters are set as $a = -8/4, b = -10, c = 30$, initial conditions are $(x_0, y_0, z_0) = (1, 1, 1)$. Simulations were performed with initial time $t_0 = 0$ to the final time $t_{max} = 100$ with integration step of 0.01 in corresponding integral curve which is given in Fig. 1.

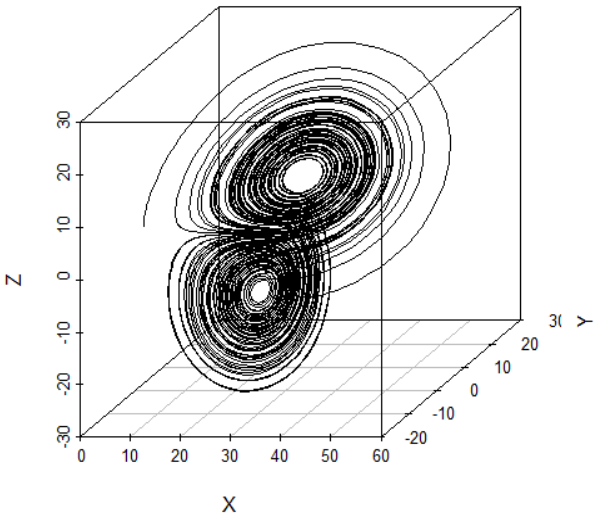

Fig. 1. Trajectory of the system (3).

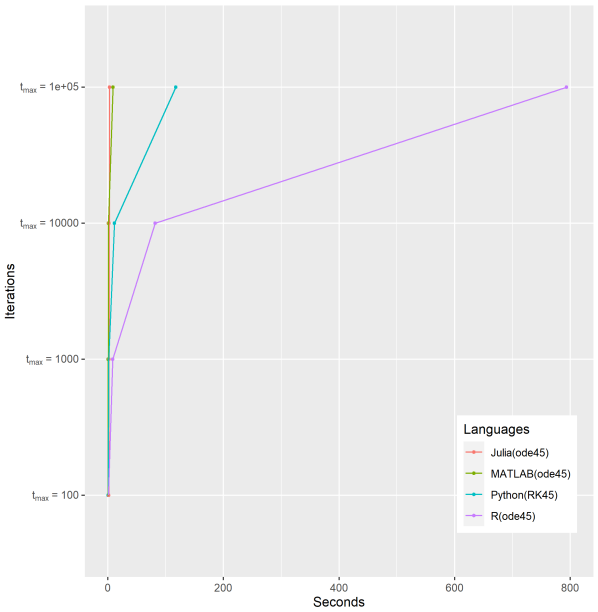

Fig. 2. Elapsed time measurements with different t_{max} for the solution of Lorenz system by various programming languages.

4 Working-time benchmarks in ODE solvers from different languages (MATLAB, Python(SciPy), Julia, R(deSolve))

The following benchmarks in Fig. 2. demonstrate the performance differences due to using similar algorithms from packages in the main scripting languages for solution of Lorenz system. It takes into account solver elapsing time of *ode*45 function. These were run with MATLAB (2021a), *deSolve* (1.2.8) R package, *SciPy* (1.6.2.) Python Package, *DifferentialEquations* (6.18.0) Julia package on Intel Core i5-8259U Processor.

5 Conclusions

In this short paper, it was been shown that *Differential Equations* Julia package can be an alternative for solving ODE's. A given benchmark is shown a good perfomance for simple autonomous ODE. Hence it remains, as an open problem is Julia a good alternative programming language for solving non-autonomous ODE's.

References

1. Auburn University Page, `https://www.eng.auburn.edu/~tplacek/courses/3600/ode45berkley.pdf`. Last accessed 11 June 2021
2. MATLAB Homepage, `https://www.mathworks.com/products/matlab.html`. Last accessed 11June 2021
3. The R Project for Statistical Computing Homepage, `https://www.r-project.org/`. Last accessed 11 June 2021
4. DeSolve Homepage, `https://cran.r-project.org/web/packages/deSolve/deSolve.pdf`. Last accessed 11 June 2021
5. SciPy Homepage, `https://www.scipy.org/`. Last accessed 28 June 2021
6. Julia Homepage, `https://diffeq.sciml.ai/release-1.8/index.html`. Last accessed 11 June 2021
7. Wikipedia Page, `https://en.wikipedia.org/wiki/Runge-Kutta_methods`. Last accessed 11 June 2021
8. The University of Oxford Department of Physics Page, `https://www2.physics.ox.ac.uk/sites/default/files/profiles/read/lect6-43147.pdf`. Last accessed 11 June 2021
9. SciPy Page, `https://docs.scipy.org/doc/scipy/reference/generated/scipy.integrate.RK45.html`. Last accessed 11 June 2021

Benchmarking DGX-A100 vs. DGX-2

Matej Spetko[1, 2][0000−0002−5486−0503]

[1]IT4Innovation, VSB – Technical University of Ostrava,
17. listopadu 15, 708 00 Ostrava – Poruba, Czech Republic
[2]Department of Applied Mathematics, FEECS,
VSB – Technical University of Ostrava, 17. listopadu 15,
708 00 Ostrava – Poruba, Czech Republic
matej.spetko@vsb.cz

Abstract. This paper presents the performance, power consumption, and thermal behavior analysis of the new Nvidia DGX-A100 server containing eight A100 Ampere architecture GPUs. The results are compared against the previous generation of the server, Nvidia DGX-2, equipped with Volta architecture V100 GPUs. The performance of floating-point computing units was measured using a custom synthetic benchmark. Furthermore, thermal stability was investigated. To determine the best energy-efficient configuration of the GPUs a Dynamic Frequency and Voltage Scaling (DVFS) analysis was performed. In this configuration, the A100 GPU achieves an efficiency of 51 GFLOPS/W for double-precision workload and 91 GFLOPS/W for the double-precision workload on tensor cores, which makes it the most energy-efficient accelerator for high-performance computing.

Keywords: DGX-A100 · DGX-2 · tensor cores · performance analysis · energy efficiency · dynamic voltage and frequency scaling (DVFS)

1 Introduction

In this paper, I provide a comparison in terms of performance and power consumption of two flagship GPU servers from Nvidia – DGX-2 based on Volta GPU architecture and its successor DGX-A100 based on Ampere architecture. The performance of these two systems was evaluated using a synthetic benchmark, designed to measure and achieve the peak performance of both CPUs as well as Nvidia GPUs. This benchmark was modified to support data types introduced in Ampere architecture as well as Tensor Core units and it was able to match and verify the peak performance of both A100 and V100 GPUs. The throughput of memory and NVLink interconnect was also measured. Furthermore, I evaluated thermal stability and GPU power consumption. In addition, a Dynamic Voltage and Frequency Scaling (DVFS) was performed for compute-bound, memory-bound, and communication workloads and stated the most efficient configuration for each of these workloads.

The parameters of both GPU servers are shown in table 1. These servers are designed for machine learning tasks but can also be used in high-performance computing. DGX-2 contains 16 V100 GPUs interconnected with NVLink. These GPUs can do the computation in half-precision – 16-bit floating-point numbers. This reduced precision can be used on regular compute units as a vector of 2 – half2. They can be also used on Tensor Cores – special compute units performing matrix operations. DGX-A100 contains only 8 A100 GPUs. The throughput of its NVLink interconnect has doubled and Tensor Cores can compute in double-precision. Further hardware description, as well as more detailed experiment analysis and results evaluation, is published in MDPI Energies [8].

2 Measurement methodology description

The Mandelbrot benchmark is designed to measure the pure floating point performance of the processor at a very high arithmetic intensity. It executes the Mandelbrot iterations $z_{k+1,i} = z_{ki}^2 + c_i$ where $z_{0i} = 0$, and the constants c_i are from the Mandelbrot set of complex numbers. For simplicity and efficiency are these constants selected from the numbers on the real axis. The Mandelbrot iterations may be repeated indefinitely and remain bounded. To measure Tensor Core performance the Mandelbrot benchmark may be naturally extended to the matrix domain. In matrix form, the square matrix Z is updated as $Z_{k+1} = Z_k * Z_k + C$, where the $*$ refers to matrix-matrix multiplication, the matrix $Z_0 = \mathbf{0}$, and the square matrix C has eigenvalues from the Mandelbrot set. Such matrix iterations may be repeated indefinitely and matrix Z will remain bounded. [1]

The memory subsystem throughput was measured by STREAM [2] benchmark modified for GPUs with all it's functions: copy, scale, add, triadd. The

Table 1. Parameters of both DGX servers.[4, 3, 5–7]

	DGX-2	DGX-A100
CPU model	Intel Xeon 8168	AMD EPYC 7742
PCI Express Version Support	3.0	4.0
FP64 Performance (double)	125 TFLOPS	77 TFLOPS
FP32 Performance (float)	250 TFLOPS	156 TFLOPS
BF16 Performance (Bfloat16)	–	312 TFLOPS
FP16 Tensor Core Perf. (half)	2 PFLOPS	2.5 PFLOPS
TF32 Tensor Core Perf. (tensor float TC)	–	1248 TFLOPS
FP64 Tensor Core Perf. (double TC)	–	156 TFLOPS
Number of GPUs	16	8
GPU model	V100-SXM3	A100-SXM4
GPU SM / Memory Maximum Frequency	1597 / 958 MHz	1410 / 1215 MHz
GPU Power consumption (single GPU)	350 W	400 W
GPU Memory Size (single GPU)	32 GB	40 / 80 GB
GPU Memory Bandwidth (single GPU)	980 GBps	1555 / 2039 GBps
NVLink Bandwidth (bidirectional)	300 GBps	600 GBps

throughput of the NVLink interconnect was measured by performing unidirectional as well as bidirectional P2P data transfer between two GPUs. I measured energy consumption with frequency scaling of three types of workload: compute bound represented by Mandelbrot benchmark, STREAM benchmark as a memory bound workload, and P2P data transfer between 2 GPUs over NVLink. GPU energy consumption was measured with Nvidia Management Library – `NVML` which provides an interface for monitoring Nvidia GPUs as well as access to a counter with GPU's total energy consumption. To analyze power and thermal properties the Nvidia System Management Interface – `nvidia-smi` was used. The frequency of V100 GPU was scaled from a maximum of 1597 MHz to 675 MHz with 7 MHz predefined steps. The frequency of A100 GPU was scaled from 1410 MHz to 690 MHz with 15 MHz predefined steps. The frequency of HBM2 memory of both GPUs can not be tuned.

3 Performance Results

The results of Mandelbrot Benchmark, STREAM benchmark, and NVLink P2P transfer are shown in Table 2. It also compares the measurements with the performance specification from Ampere and Volta architecture whitepapers provided by Nvidia. [3, 7] The measured performance is within Nvidia's specification except for half2 datatype on A100 GPU, when the GPU reached its power limit and scaled-down its frequency to 1380 MHz causing 3 % performance loss.

Table 2. Table with the performance specification of V100 and A100 GPUs provided by Nvidia compared to the results measured by Mandelbrot Benchmark, STREAM benchmark and NVLink P2P data transfer measurement. [3, 7]

Mandelbrot Benchmark [TFLOPS]

	V100		A100	
	Specification	**Measurement**	**Specification**	**Measurement**
double	8.177	8.1765	9.7	9.715
float	16.353	16.3530	19.5	19.375
half2	32.707	32.7038	78	75.654
tensor	130.484	130.7928	312	310.3
Bfloat16	–	–	39	38.752
double TC	–	–	19.5	19.435

STREAM [GBps]

GPU	V100	A100
specification	980.99	1555.00
copy	825.47	1329.58
scale	826.52	1327.59
add	873.63	1376.84
triadd	872.37	1377.21

NVLink P2P transfer

GPU	V100	A100
specification unidir.	150.00 GBps	300.00 GBps
specification bidir.	300.00 GBps	600.00 GBps
measured latency	2.45 us	3.65 us
measured unidir.	145.16 GBps	281.00 GBps
measured bidir.	266.46 GBps	531.17 GBps

3.1 Power and Thermal Properties

On both GPU servers the cold air is not distributed equally among all the GPUs due to their physical layout. The GPUs are placed on the GPU boards in two rows with each board containing 8 GPUs. GPUs in the first row are directly facing the cold air intake, whereas GPUs in the second row receive air heated from the first row GPUs. This causes that the second row GPUs run at higher temperatures, reach their power limit more easily, and due to this, they throttle down their frequencies.

On DGX-2 the peak temperature difference between the first row and second row GPUs is 15 °C during full Tensor Core load, and some second row GPUs throttle down their frequencies to as low as 1575 MHz with 1 % performance loss. On DGX-A100 this temperature difference is 10 °C during half2 workload with some second row GPUs reaching 1350 MHz from the maximum frequency of 1410 MHz. During single-precision workload on DGX-2, a 100 W power consumption variation was observed. On DGX-A100 this variation is within 50 W.

3.2 Frequency Scaling

The dynamic voltage and frequency scaling test was performed to achieve higher energy efficiency. The first frequency scaling test was done for all data types of Mandelbrot benchmark, each performing 81920×10^9 floating-point operations. The top two plots in figure 1 display the results on a logarithmic scale. In general, the most energy-efficient frequency for the compute-bound workload on V100 GPU is 1057 MHz. In this configuration, 39 % of the energy can be saved while the run-time increases by 51 %. Running double-precision workload at the base frequency the energy efficiency of V100 reaches 24.8 GFLOPS/W whereas at 1050 MHz it can reach 40.67 GFLOPS/W. The A100 GPU has its most energy-efficient frequency between 1035 – 1020 MHz. With a 36 % time increase, the achievable energy savings are in the range of 25 – 35 % depending on the data type. The energy efficiency for double-precision workload increases from 35 GFLOPS/W at the maximum frequency to 51 GFLOPS/W for the most energy-efficient frequency. This number can be increased even more by using Tensor Cores for double-precision workload with 92 GFLOPS/W.

The second frequency scaling test was done using the STREAM benchmark by transferring 7.924 TB of data. Two plots in the middle of figure 1 show the results. During this memory-bound workload, the V100 GPU can save up to 31 % of the energy by scaling down to 1005 MHz while the transfer time increased by 2 %. For A100 the optimal frequency for energy consumption was not found as it was still decreasing at the minimal measured frequency of 690 MHz. The frequency 945 MHz was selected as optimal for this case because it has the best ratio between the transfer time and energy consumed.

The last frequency scaling experiment was done for unidirectional P2P transfer of 859 GB of data over NVLink. The results are shown in two bottom plots in figure 1. The V100 GPU can save up to 26 % of energy by running this experiment at 1140 MHz without any throughput penalty. On the other hand, for

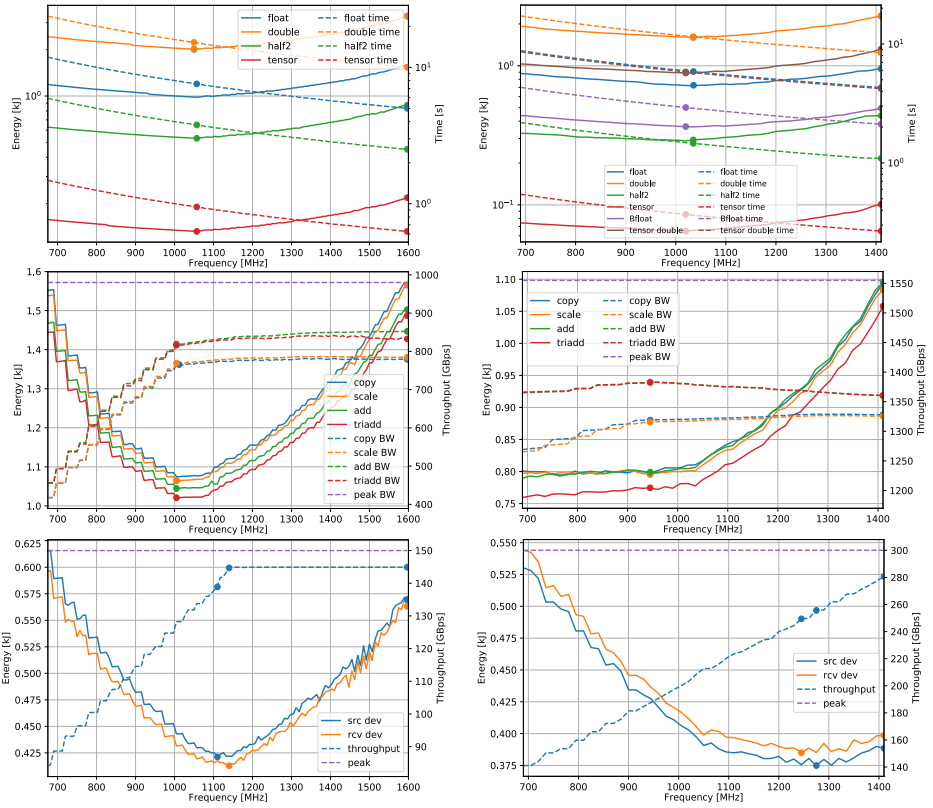

Fig. 1. The result of frequency scaling experiment: plots for V100 GPU are on the left and for A100 on the right. The top two plots show Mandelbrot benchmark. The two plots in the middle show STREAM benchmark and bottom two plot shows P2P transfer over NVLink.

A100 the optimal frequency is 1275 – 1245 MHz, and the energy savings are only 3.4 % with a 10 % throughput penalty.

4 Conclusion

The performance of floating-point units, as well as Tensor Cores, was measured on A100 and V100 GPUs with the synthetic benchmark. The results confirm their performance specification. Moreover, the highest power consumption on A100 GPU was measured while performing half-precision workload on regular compute units. During this workload type, the streaming multiprocessor reached its power limit and lowered its frequency resulting in a 3 % performance reduction. Due to the physical layout and cooling solution design on DGX-2 and DGX-A100 servers power-throttling occurred for some GPUs in the second row.

Examined GPUs can improve their energy efficiency by scaling down their frequency. V100 GPU can save up to 39 % of energy with a 51 % time increase

for the compute-bound workload. The same workload on A100 can save 25 – 35 % energy depending on the data type with a 36 % time increase. Running double-precision compute-bound workload at the energy-optimal frequency the V100 achieved an energy efficiency of 40 GFLOPS/W. For the same workload in the most energy-efficient configuration, the A100 reached 51 GFLOPS/W in double-precision and 91 GFLOPS/W in double-precision on Tensor Cores. For memory-bound workload on V100, it is possible to save 31 % of energy and on A100 27 % without a significant throughput loss. During the NVLink communication, the V100 can save 25 % energy without any throughput penalty. Major improvement in the default energy efficiency of both V100 and A100 may be achieved by scaling down the SM frequency to approximately 1100 MHz via DVFS.

5 Acknowledgments

This work was supported by The Ministry of Education, Youth and Sports from the Large Infrastructures for Research, Experimental Development, and Innovations project "e-Infrastructure CZ – LM2018140".

This work was also partially supported by the SGC grant No. SP2020/21 "Infrastructure research and development of HPC libraries and tools II", VŠB – Technical University of Ostrava, Czech Republic.

References

1. IT4Innovations: Mandelbrot CPU benchmark. https://code.it4i.cz/jansik/mandelbrot, "[Online; accessed 2019-07-12]"
2. McCalpin, J.D.: Memory bandwidth and machine balance in current high performance computers. IEEE Computer Society Technical Committee on Computer Architecture (TCCA) Newsletter pp. 19–25 (Dec 1995)
3. NVIDIA Corp.: NVIDIA TESLA V100 GPU ARCHITECTURE. http://images.nvidia.com/content/volta-architecture/pdf/volta-architecture-whitepaper.pdf (August 2017), "[Online; accessed 2019-07-12]"
4. NVIDIA Corp.: DGX-2/2H SYSTEM User Guide. https://docs.nvidia.com/dgx/pdf/dgx2-user-guide.pdf (May 2019), "[Online; accessed 2019-07-15]"
5. NVIDIA Corp.: DGX A100 SYSTEM User Guide. https://docs.nvidia.com/dgx/pdf/dgxa100-user-guide.pdf (November 2020), "[Online; accessed 2020-12-01]"
6. NVIDIA Corp.: NVIDIA A100 TENSOR CORE GPU. https://www.nvidia.com/content/dam/en-zz/Solutions/Data-Center/a100/pdf/a100-80gb-datasheet-update-a4-nvidia-1485612-r12-web.pdf (November 2020), "[Online; accessed 2020-12-01]"
7. NVIDIA Corp.: NVIDIA A100 Tensor Core GPU Architecture. https://www.nvidia.com/content/dam/en-zz/Solutions/Data-Center/nvidia-ampere-architecture-whitepaper.pdf (August 2020), "[Online; accessed 2020-12-03]"
8. Spetko, M., Vysocky, O., Jansik, B., Riha, L.: DGX-A100 face to face DGX-2 – performance, power and thermal behavior evaluation. Energies **14**(2) (2021). https://doi.org/10.3390/en14020376, https://www.mdpi.com/1996-1073/14/2/376

System of five PDMS sensors with optical FBG for traffic density monitoring

Michael Fridrich[0000−0002−7047−7272]

Department of Telecommunications, FEECS,
VSB – Technical University of Ostrava, 17. listopadu 15,
708 00 Ostrava – Poruba, Czech Republic
michael.fridrich@vsb.cz

Abstract. This article deals with the development of a sensor used to measure selected parameters of car traffic in urban traffic. The sensor is made of five fiber Bragg gratings (FBG) encapsulated in Polydimethylsiloxane polymer (PDMS). The advantage of this sensor is inexpensive and easy implementation in the milled upper part of the road, covered with an asphalt mixture. The functionality of the sensor was verified in real traffic. The presented article summarizes author's activities during the first two years of studies, his research and development activities related to the study.

Keywords: FBG sensor · Fiber Bragg Grating · PDMS · car speed · car detection · traffic monitoring.

1 Introduction

Allow me to introduce myself. My name is Michael Fridrich. I am a Ph.D. student at the Faculty of Electrical Engineering and Computer Science at the Technical University of Ostrava. My educational program is called Communication Technology. In my first two years of my studies, I have been extending my knowledge especially in the field of optical fiber Bragg Grating sensors. To date 07/2021, I have a total of 8 accepted or published publications and 3 utility models.

2 About my dissertation work

During the first two years of my study I have proposed different types of FBG sensors [1–3] that can be used in the actual traffic to monitor the density and speed of traffic.

2.1 Fiber Bragg Grating

Fiber Bragg grating is formed in the optical fiber core by a periodic change of the refractive index. The structure of a uniform Bragg grating in which there are periodically changing layers of the refractive index of core n_1 with a higher refractive index index n_3 is shown in Figure 1. The uniform Bragg grating is

VSB – Technical University of Ostrava, 2021, ISBN 978-80-248-4523-4 (on-line).

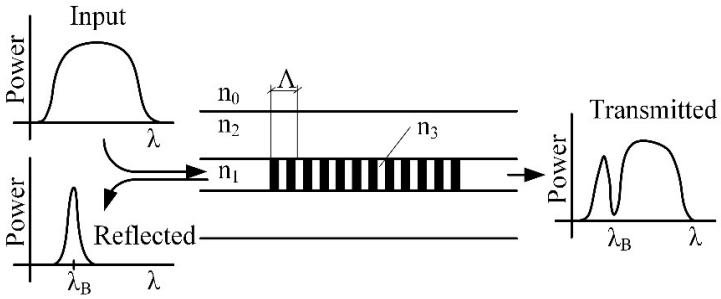

Fig. 1. Structure of uniform Bragg grating.

characterized by a constant size of the induced refractive index $\delta n = n_3 - n_1$ and a constant period of changes of refractive index.

The structure of the Bragg grating reflects a narrow frequency band of the broadband light and transmits the others. The central part of the reflected spectrum is called the Bragg wavelength λ_B and is given by:

$$\lambda_B = 2n_{eff}\Lambda, \tag{1}$$

where n_{eff} is the effective refractive index defined by the structure of the Bragg grating and Λ is the distance between the periodical changes to the refractive index in the core of the optical fiber [4]. The Bragg wavelength is the geometric and optical properties that change under the influence of mechanical and thermal stresses. The relation of the Bragg wavelength change, the relative deformation and temperature is expressed by Equation 2.

$$\frac{\Delta\lambda_B}{\lambda_B} = k\epsilon + (\alpha_\Delta + \alpha_n)\,\Delta T \tag{2}$$

where $\Delta\lambda_B$ is Bragg wavelength shift, k is deformation coefficient, ϵ is deformation, α_Δ is the coefficient of thermal expansion, α_n is the thermo–optic coefficient and Δ T is change of temperature [2].

The relation in Equation 2 suggests that thermal and deformation sensitivity changes with the absolute value of the Bragg wavelength. With regard to the values of coefficients stated in the above relations, the standardized deformation coefficient at a constant temperature is expressed by Equation 3

$$\frac{1}{\lambda_B}\frac{\Delta\lambda_B}{\Delta\epsilon} = 0.78 \cdot 10^{-6} \quad \mu strain^{-1}. \tag{3}$$

2.2 Design of PDMS-FBG sensor

In the first phase of the experiment, we created a prototype of PDMS-FBG sensor sized 60 x 30 x 7 mm. In this sensor we used single-mode fiber G.657.A with acrylate primary protection and FBG with a wavelength of 1548.388 nm.

The FBG fiber was attached to a mold made from 3D printing and then cast into a PDMS Sylgard 184 which is a silicone elastomer. Curing was performed for 90 minutes at 80 °C. Figure 2 shows the sensor schematically.

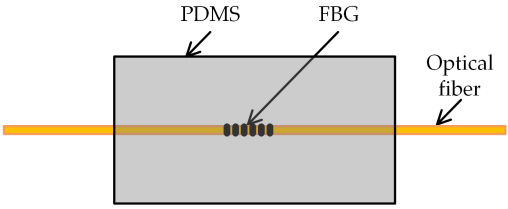

Fig. 2. Illustration of PDMS-FBG sensor.

Subsequently, a 2 m long groove was milled into the roadway, which was 10 mm wide and 15 mm deep. The tested sensor was placed in this groove. In the second step, the groove with the sensor was filled with Biolast 2K asphalt (Nadler Strasentechnik, Barleben, Germany). The cold asphalt curing took place outdoors (temperature of 23 ± 1 °C) and took 90 min. Figure 3(a) shows the mounting of the sensor before pouring asphalt and Figure 3(b) shows the sensor covered with cold asphalt in the roadway.

(a) (b)

Fig. 3. PDMS-FBG sensor placement in widened milled in groove (a); PDMS-FBG sensor covered with cold asphalt (b).

In the next step, the analysis of the sensor properties (sensitivity, wavelength shift during curing,...) was performed. This information was further used to design a complete measuring system.

2.3 Design and implementation of PDMS-FBG sensor-chain for single-line traffic monitoring

Based on the performed analysis, we determined the spatial sensitivity at ± 30 cm. To cover the entire width of the 3.2 m lane, a sensor chain with five PDMS-FBG sensors was designed, see Figure 4.

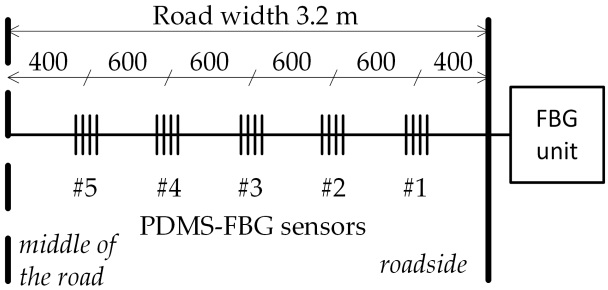

Fig. 4. Single-line PDMS-FBG sensor deployment in the road with connection to the FBG evaluation unit.

In the next phase, it was also necessary to determine the spectral spacings of individual PDMS-FBG sensors. These spacings had to be defined by the maximum possible sensor deflection caused by the car passage. Spacings must prevent overlapping of adjacent spectra, i.e. signal crosstalk. From this analysis, we decided to use fibers with the following wavelengths:

ID	λ_B (nm)			
	Design	Used FBG	PDMS-FBG sensor	PDMS-FBG sensor in the road
1	1531	1531.243	1531.605	1531.912
2	1535	1535.031	1535.343	1535.585
3	1539	1539.113	1538.894	1539.201
4	1543	1542.989	1543.580	1543.963
5	1547	1547.203	1547.828	1547.188

Table 1. Used FBG.

2.4 LONG-TERM MEASUREMENT AND EXPERIMENTAL VERIFICATION IN REAL OPERATION

Measurements in real traffic took place in the city of Ostrava (Part Vresina, GPS: 49°50'03.3"N 18°07'25.5"E). The measurement lasted 18 days. Subsequently, the analysis of data from which we detected 3978 was performed with an overall detection success rate of 99.62%. A reference camera record was used to analyze the data. The number of individual passes on each day is shown in Figure 5.

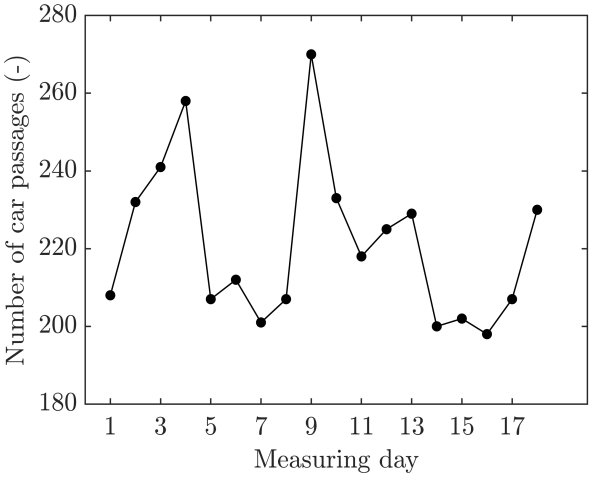

Fig. 5. Results of traffic density monitoring.

3 Projects

During my second year of study, I participated in 4 projects.

- MP6379121 - Development of new implants for growth regulation of lower limb in sterile finish - faculty FMT
- SP2021/45 - Fiber optic sensor systems - faculty FEI
- CK01000098 - Unique fiber optic sensor for detecting rail vehicles - faculty FEI
- TP01010036 - The complex system of automatic detection and classification of flat wheels for rail transportation. PRE SEED fond II VSB – TUO - faculty FEI

4 Publications and pedagogic activities

I have a total of 8 accepted or published papers and 3 utility models.

- Fridrich, M.; Fajkus, M.; Mec, P.; Nedoma, J.; Kostelansky, M.; Bednar, E. Portable Optical Fiber Bragg Grating Sensor for Monitoring Traffic Density. Appl. Sci. 2019, 9, 4796.
- Nedoma, J.; Stolarik, M.; Kepak, S.; Pinka, M.; Martinek, R.; Frnda, J.; Fridrich, M. Alternative Approaches to Measurement of Ground Vibrations Due to the Vibratory Roller: A Pilot Study. Sensors 2019, 19, 5420.
- Jan Nedoma, Michal Kostelansky, Michael Fridrich, Jaroslav Frnda, Miroslav Pinka, Radek Martinek, Martin Novak, Stanislav Zabka. Fiber Optic Phase-Based Sensor for Detection of Axles and Wheels of Tram Vehicles. Communications [Internet]. 2020Jul.8 [cited 2020Jul.16];22(3):119-27. Available from: http://komunikacie.uniza.sk/index.php/communications/article/view/1576

- M. Fajkus et al., "PDMS-FBG Based Fiber Optic System for Traffic Monitoring in Urban Areas," in IEEE Access, doi: 10.1109/ACCESS.2020.3006985.
- Frnda, J.; Nedoma, J.; Martinek, R.; Fridrich, M. Predicting Perceptual Quality in Internet Television Based on Unsupervised Learning. Symmetry 2020, 12, 1535.
- J. Nedoma et al., "A Novel FBG-based Triggering System for Cardiac MR Imaging at 3 Tesla: A Pilot Pre-Clinical Study," in IEEE Access, doi: 10.1109/ACCESS.2020.3028224.
- Martinek, R.; Vanus, J.; Nedoma, J.; Fridrich, M.; Frnda, J.; Kawala-Sterniuk, A. Voice Communication in Noisy Environments in a Smart House Using Hybrid LMS+ICA Algorithm. Sensors 2020, 20, 6022.
- Stolarik, M.; Pinka, M.; Nedoma, J.; Fridrich, M. Variability of Seismic Loading over the Surface of a Concrete Slab in Interaction with the Subsoil. Sustainability 2020, 12, 9530.
- Portable grid sensor for detecting vehicles. Registration number 33827
- Chain sensor for monitoring road traffic. Registration number 34137
- EMI-compatible fiber optic grid pressure sensor. Registration number 34467

In the winter semester, I was part of courses Introduction to Communication Technologies as a substitute for academic teachers and Physics I as a help for academic teacher.

5 Future work

Now, I focus on the Ph.D. study and individual subjects. I also work with colleagues on the preparation of new and current projects and other impacted publications.

References

1. Kersey, A.D.; Davis, M.A.; Patrick, H.J.; LeBlanc, M.; Koo, K.P.; Askins, C.G.; Putnam, M.A.; Friebele, E.J. Fiber grating sensors. J. Lightwave Technol. 1997, 15, 1442–1462, doi:10.1109/50.618377.
2. Fridrich, M.; Fajkus, M.; Mec, P.; Nedoma, J.; Kostelansky, M.; Bednar, E. Portable Optical Fiber Bragg Grating Sensor for Monitoring Traffic Density. Appl. Sci. 2019, 9, 4796.
3. Fajkus, M. et al., "PDMS-FBG Based Fiber Optic System for Traffic Monitoring in Urban Areas," in IEEE Access, doi: 10.1109/ACCESS.2020.3006985.
4. A. Othonos, "Fiber bragg gratings," Review of Scientific Instruments, vol. 68, no. 12, pp. 4309–4341, dec 1997.

Gamma Radiation Effects in Standard Optical Fibers

Lukáš Hájek

Department of Telecommunications, FEECS,
VSB – Technical University of Ostrava, 17. listopadu 15,
708 00 Ostrava – Poruba, Czech Republic
lukas.hajek@vsb.cz

Abstract. The proposed article describes the irradiation process in standard telecommunication optical fiber. Four samples of a different optical fiber according to ITU-T G.652, G.655, and G.657 standards were used and tested in special laboratories at UJV–Řež. All samples were exposed to 50 kGy gamma irradiation dose and optical attenuation was monitored before, during, and after the test. Two well-known methods of optical insertion loss measurement were used for optical attenuation measurement. Insertion loss measurement method and OTDR (Optical Time Domain Reflectometry). Analysis of all results proofed the different behavior of RIA (Radiation-Induced Attenuation) for different types of fibers and measured wavelength. Finally, a mathematical model of the irradiation process was obtained for each optical fiber and measured wavelength.

Keywords: Gamma radiation, optical fiber, optical attenuation, insertion loss, RIA, OTDR.

1 Introduction

Optical fibers have a lot of advantages throw them they have become the most usable and promising technology in high-data-rate telecommunication networks nowadays. Long-range and almost limitless data throughput are not all advantages in optical fiber technology. The future of this technology is hidden in optical fiber sensors. Sensors based on optical fibers have plenty of applications. Optical fiber sensors are widely used in many kinds of industries. For example, we could find them in the building industry for monitoring of buildings constructions, bridges movements, tunnel monitoring, etc. Sensors are also used in safety applications as distributed optical sensors for temperature or strain monitoring so we can detect fires in buildings or ground movements etc.

And therefore, optical fiber sensors are so important in the future for safety applications in new generation nuclear plants [1], [2], [3]. Not only just for data communications purposes but more for sensors applications will be optical fibers more and more often used in Nuclear Industry [2]. But there is also a negative effect in optical fibers in connection with irradiation. Optical fibers exposed to the irradiation process change the atomic structures of silica glass (SiO_2) material. Those changes make an insertion loss

of optical fiber higher and higher over the acceptable limit. This fact complicates the usage of optical fibers in this kind of industry in foreseeable future.

2 Experiment

2.1 Sample description

Four samples and one reference fiber path were prepared for irradiation test. All samples have approximate length around 200 m and the reference fiber was 3 m long. We used the reference fiber for minimizing of temperature drift of optical source and photodetector in measurement device. Summary of used samples and their parameters:

- S1 – ITU-T G.655, this fiber has special refraction index profile and is called as Dispersion-shifted fiber (DSF) – 208,65 m.
- S2 – ITU-T G.652.D, a standard optical fiber is used for standard communication purposes – 211,28 m.
- S3 – ITU-T G.657.A, a bending-loss insensitive single-mode optical fiber – 203,02 m.
- S4 – ITU-T G.652.D, a standard optical fiber in secondary protection – 200,67 m.
- S5 – reference patch cord ITU-T G.652.D. (3 m)

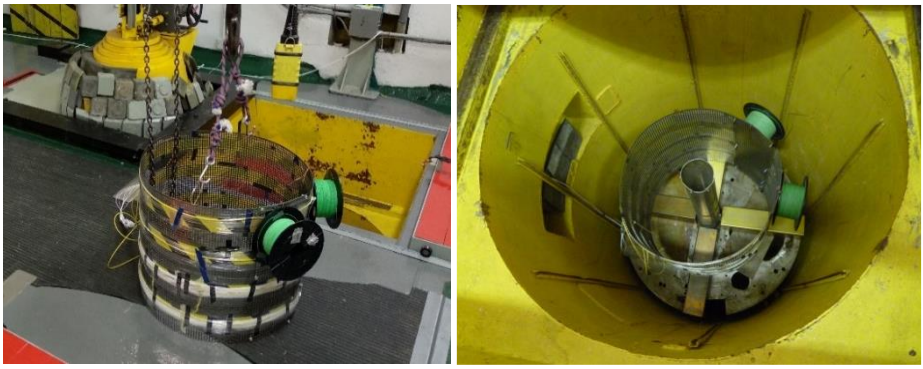

Fig. 1. Optical fiber samples were prepared on stainless steel performed drum, which was placed inside irradiation chamber.

3 Results and discussion

Radiation test is possible to divide into two parts. The first part is called RIA (Radiation Induced Attenuation) and shows increasing of optical loss in time effected by gamma irradiation. Second part is called relaxation and shows decreasing of optical loss over time (approximately 14 days) after irradiation. In this phase, optical attenuation is recovered nearby its basic state.

3.1 RIA (Radiation Induced Attenuation)

Figures 1 and 1 is show the development of attenuation in time (the radiation process took 90 hours). Radiation-Induced Attenuation has similar trends for all samples. We can see that a higher wavelength means higher optical attenuation. The most significant impact is in the case of sample 1. The sample has more than twice higher optical attenuation if we compare 1310 and 1550 nm.

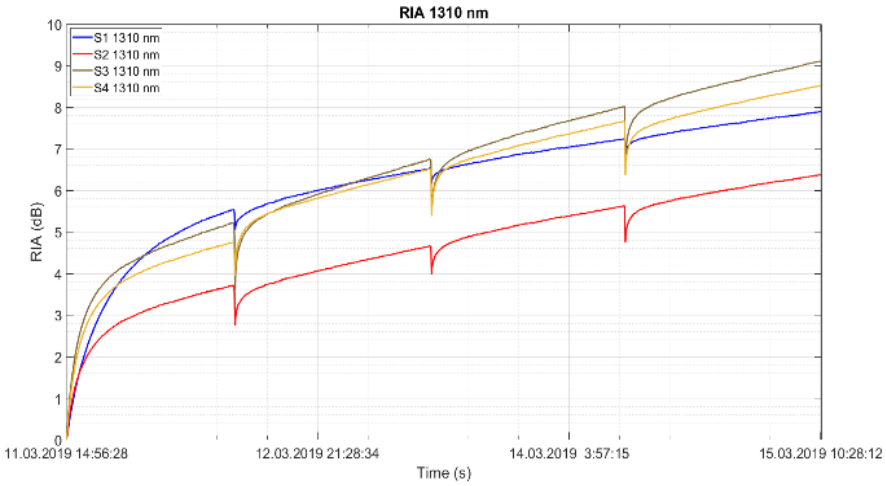

Fig. 2. Graph of Radiation Induced Attenuation of fiber samples during irradiation process for 1310 nm.

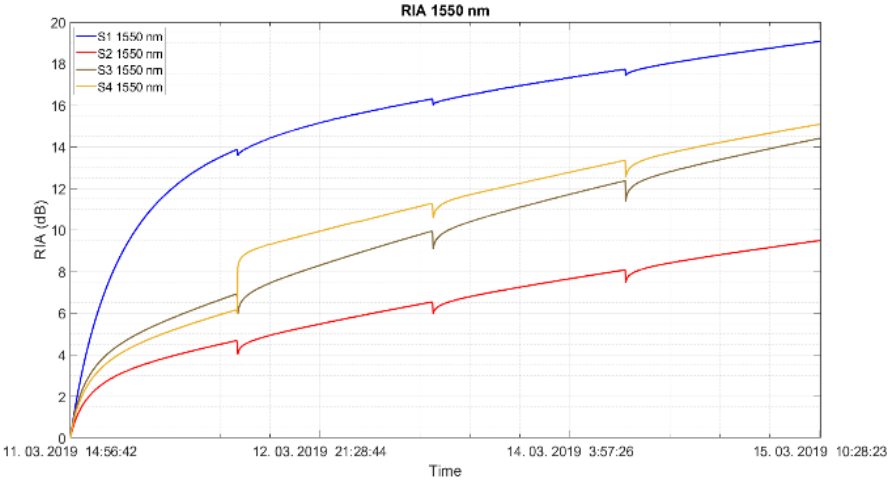

Fig. 3. Graph of Radiation Induced Attenuation of fiber samples during irradiation process for 1550 nm.

The difference between wavelength and optical fiber types is also shown in table 1. This measurement was made in regular time breaks by the OTDR method. 4 breaks during the test wear were made in total. In table 1 is the "0" row. This is the basic point before the radiation test started. Breaks could be seen also in Figures 1 and 1. In those pictures are small, inverted peaks. It is the point when OTDR measurement was made and attenuation in the optical fibers started to recover.

Table 1. Results of optical attenuation for OTDR measurement**.**

Insertion Loss (dB)								
Sample	**S1**		**S2**		**S3**		**S4**	
λ (nm)	1310	1550	1310	1550	1310	1550	1310	1550
0	0,017	0,044	0,121	0,177	3,633	2,287	0,104	0,174
1	6,13	15,33	4,712	5,546	9,717	9,465	6,325	6,976
2	6,932	16,599	5,844	7,371	11,288	13,802	7,521	8,642
3	8,153	19,529	6,206	8,476	11,918	13,75	7,961	11,626
4	8,148	19,553	6,931	9,642	13,985	18,785	8,918	12,967

3.2 Relaxation of optical attenuation

After the radiation test, the recovery process was observed. At the end of radiation optical attenuation is recovered back to lover values. But suddenly it will not be recovered completely. Also, in this case, we can see that sample 1 changes a slope of recovery with wavelength and kind of fiber.

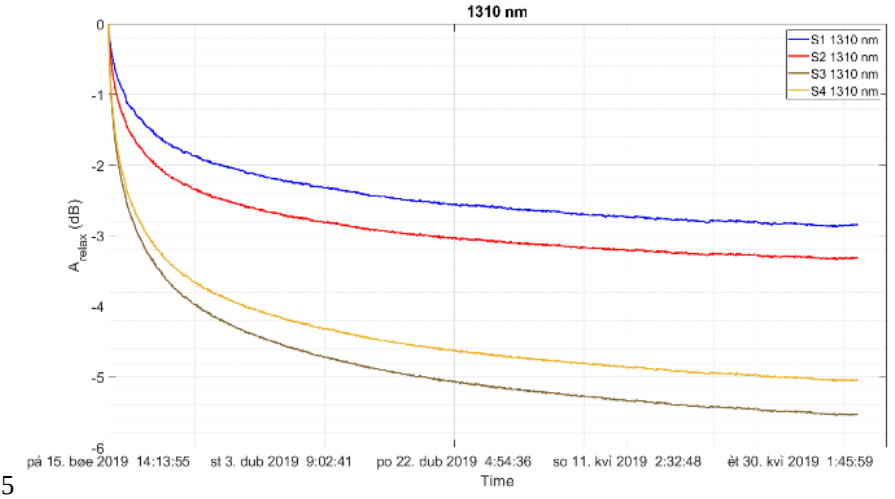

Fig. 4. Graph of Relaxation process of optical fiber samples after irradiation process for 1310 nm.

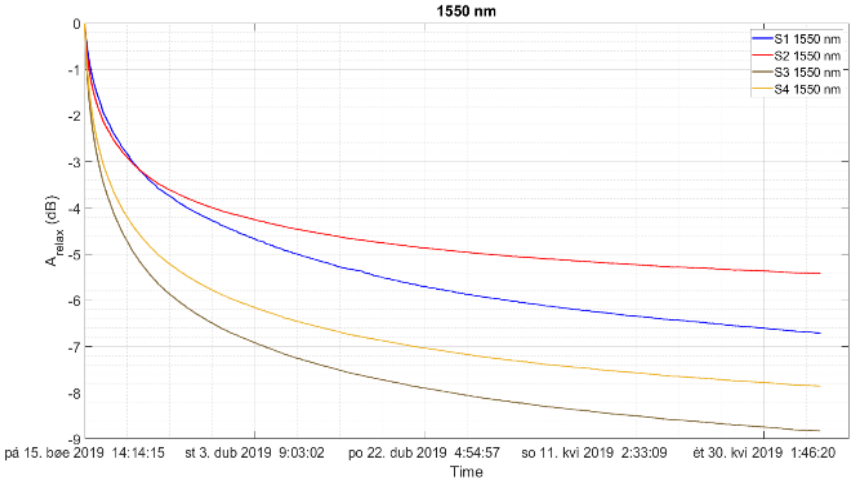

Fig. 5. Graph of Relaxation process of optical fiber samples after irradiation process for 1550 nm.

Table 1. Results of optical attenuation for OTDR measurement in different phases of the test.

Insertion Loss (dB)								
Sample	**S1**		**S2**		**S3**		**S4**	
λ (nm)	1310	1550	1310	1550	1310	1550	1310	1550
0	1,508	1,558	1,709	1,352	6,541	4,422	2,174	2,243
1	9,386	20,634	8,069	10,845	15,636	18,831	11,623	17,171
2	7,747	19,282	5,877	9,267	12,225	16,305	8,238	12,748
3	5,690	15,015	3,335	5,275	7,922	9,818	4,288	6,976

4 Conclusion

Optical fibers definitely will be used in foreseeable future in every aspect of ordinary life. But it will take a longer time than optical fibers replace standard metallic data cables in places with the occurrence of radiation. The study above showed how radiation affects standard telecommunications optical fibers. The results show that using those kinds of fibers in the primary circuit of nuclear plants is impossible due to the extremely high optical attenuation. In these areas, a special kind of optical fiber must be used. For example, fluoride doped optical fiber is one variant of this special optical fiber [4].

Acknowledgement

This work was supported by Technology Agency of the Czech Republic (TA CR) project "Development of the method for accelerated ageing of passive photonic components with orientation to plants with higher degree of ionizing radiation occurrence." (TK01020162).

5 Projects

The content mentioned above is based on my research at a project supported by the Technology Agency of the Czech Republic (TA CR) named "Development of the method for accelerated aging of passive photonic components with orientation to nuclear plants with a higher degree of ionizing radiation occurrence.". I participate in other projects such as "Development and testing of hybrid cables, hermetic cable bushings and modulus for nuclear energetics." and "The unique fiber-optic sensor for detecting rail vehicles". My interest is focused on applications of fiber optics sensors in the industry.

6 Publication activities

I am author of 42 articles registered on the Scopus database, 3 utility models, and 1 patent.

References

1. Berghmans, F., Deparis, O., Coenen, S., Decreton, M. and Jucker P. Optical fibres in nuclear radiation environments. (1995).
2. Ferdinand, P., Magne, S. and Laffont, G. Optical Fiber Sensors to improve the safety of Nuclear Power Plants. (2013).
3. Rizzolo, S., Perisse, J., Boukenter, A., Ouerdane, Y., Marin, E., Macé, J., Cannas, M. and Girard, S. Real time monitoring of water level and temperature in storage fuel pools through optical fibre sensors. Scientific Reports. (2017).
4. Youngwoong, K., Seongmin, J., Seongmook, J., Seung, H., L. and Won-Taek H. Gamma-ray radiation response at 1550 nm of fluorine-doped radiation hard single-mode optical fiber. (2016).

3D printed sensor for monitoring vital functions of the human body

Michal Kostelanský

Department of Telecommunications, FEECS,
VSB – Technical University of Ostrava, 17. listopadu 15,
708 00 Ostrava – Poruba, Czech Republic
michal.kostelansky.st@vsb.cz

Abstract. This article describes the biomedical fiber-optic sensor as a sensor for monitoring vital functions of the human body. The sensor is based on Fiber Bragg Grating (FBG), and it is encapsulated by using 3D print technique with PLA material. This article also presented summary of the author's activities during the second year of his study.

Keywords: fiber bragg grating, vital functions, fiber optic sensor

1 Introduction

Allow me to introduce myself. My name is Michal Kostelanský. I am studying for Ph.D. at the Faculty of Electrical Engineering and Computer Science at the Technical University of Ostrava. During my doctoral studies I focus on Fiber Bragg Grating sensors in biomedical applications. To the date 7/2021, I have a total of 4 accepted or published publications.

2 About my project and dissertation work

During my second year of study, I designed the measuring sensor for monitoring respiratory rate of the human body which is based on Fiber Bragg Grating, and it is encapsulated by using 3D print technique with PLA material. The sensor designed in this way can be used in magnetic resonance imaging. The great advantage of this sensor is that it does not have to be attached to the patient's body with a flexible chest strap, but it is sufficient to be fastened with medical adhesive tape. This means that the patient is not difficult to handle.

Fiber-optical Bragg gratings are most commonly used fiber-optical sensors for their spectral characteristics [1]. Repeated changes in refractive index of the core of an optical fiber creates the grating. Spectral reflection of a selected wavelength, known as Bragg wavelength, occurs on periodic interfaces. All the other wavelengths pass through the Bragg grating without damping. Figure 1 shows the structure of the FBG.

VSB – Technical University of Ostrava, 2021, ISBN 978-80-248-4523-4 (on-line).

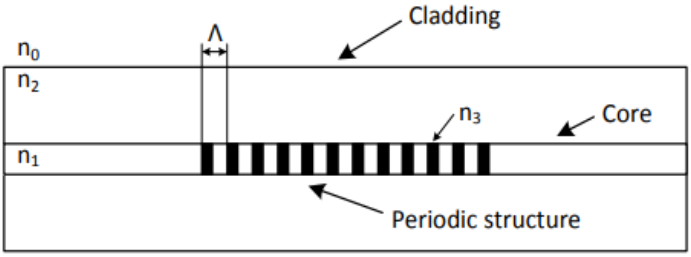

Fig.1. Example of structure of Fiber Bragg Grating.

The Bragg wavelength λ_B is given by following equation:

$$\lambda_B=2n_{eff}\Lambda, \tag{1}$$

where n_{eff} is the effective refractive index of the optical fiber with Bragg grating and Λ is the period of changes in the refractive index pitch for the fiber‘s core.

The primary use of FBG is based on the deformational and temperature sensitivities. Based on the temperature evolution of mechanical stress, the Bragg wavelength shift can be defined as:

$$\frac{\Delta\lambda}{\lambda_0} = k\varepsilon + (\alpha_n + \alpha_\Lambda)\Delta T, \tag{2}$$

where *k* is the deformational coefficient, α_n is the optical temperature coefficient, α_Δ is the coefficient of thermal expansion, ΔT is the temperature change and ε is the applied deformation. Deformational dependence and temperature dependence are determined both by the parameter values and the central Bragg wavelength. Normalized deformational and temperature coefficients [2] are introduced for determination of the individual sensitivities. Normalized deformational coefficient is given by:

$$\frac{1}{\lambda_B}\frac{\Delta\lambda_B}{\Delta\varepsilon} = 0{,}78 * 10^{-6}\mu\text{strain}^{-1}, \tag{3}$$

and normalized temperature coefficient by:

$$\frac{1}{\lambda_B}\frac{\Delta\lambda_B}{\Delta T} = 6{,}678 * 10^{-6}{}^{\circ}\text{C}^{-1}, \tag{3}$$

I have created a prototype of a measuring sensor which was tested in magnetic resonance imaging (MRI) scanner (3T MRI scanner, CEITEC MU, Brno). Real photo from the measurement in MRI is shown on Figure 2. The sensor was created by the

encapsulation of the Bragg grating structure into Polylactic acid (PLA), which is a typical material for 3D printing and there is a possibility to use it in MRI.

Fig.2. Real photo from the measurement in MRI.

Sensor dimensions are 40 mm diameter and 0,4 mm width. 3D model of the sensor is shown on Figure 3.

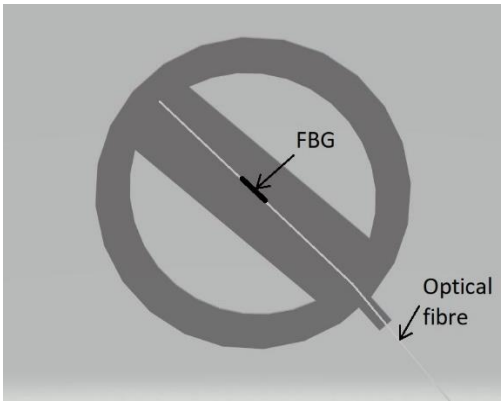

Fig.3. 3D model of the sensor.

The key experimental results of respiratory rate measurements in the laboratory environment (three volunteers) are summarized in Table 1. The data from designed sensor and the data from manual notes (breaths counting), which was as a reference were compared by the objective madicine used the Bland-Altman method [3]. The reproducibility is considered to be good if 95% of the results lie within a ± 1.96 SD (Standard Deviation) range.

Tab.1. Table of results from measurement in the laboratory environment.

Subject	Rec. time (s)	RR	
		Number of breaths	Samples in ± 1.96 SD (%)
Male1	600	118	**> 95**
Male2	600	112	**> 95**
Female1	600	128	**> 95**

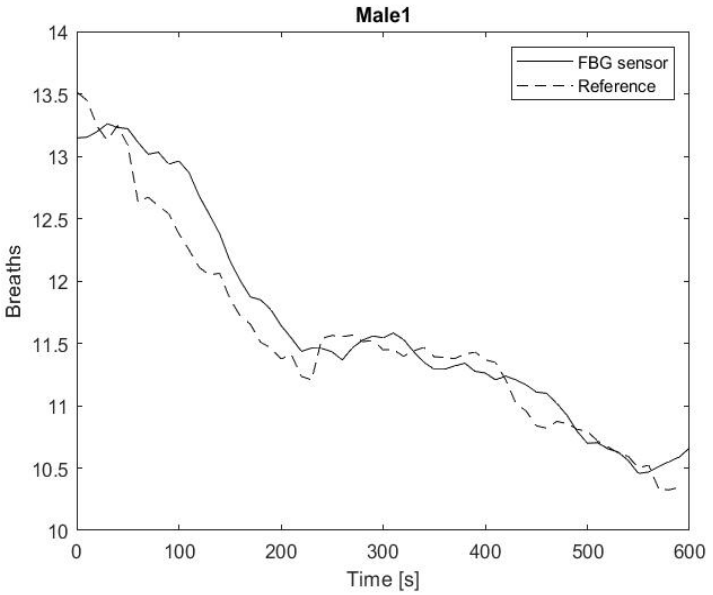

Fig.4. Comparison graph of FBG sensor and reference.

According to the obtained data, it can be said that this method can be used instead of the current conventional respiratory rate sensors of the human body.

In the next step of this research, we will continue to improving the design and construction of the sensor. We will try to do measurement of heart rate monitoring of the human body.

3 Projects

SP2021/45 - Fiber optic sensor systems - faculty FEI
CK01000098 - Unique fiber optic sensor for detecting rail vehicles – faculty FEI
TP01010036 - The complex system of automatic detection and classification of at wheels for rail transportation. PRE SEED fond II - faculty FEI

4 Publications activities

From the date 9/2020 since to the date 7/2021, I have a total of 1 accepted or published papers and 2 utility models.

5 Pedagogic part and other activities at the Department of Telecommunications

In the winter semester, I was part of Fyzika I (FYI I) course as help for academic teachers.

References

1. FAJKUS, Marcel, Jan NEDOMA, Petr ŠIŠKA, Lukáš BEDNÁREK, Stanislav ŽABKA a Vladimír VAŠINEK. Perimeter system based on a combination of a Mach-Zehnder interferometer and the Bragg gratings. *Advances in electrical and electronic engineering* [online]. 2016, 14(3), 318-324 [cit. 2020-07-28]. DOI: 10.15598/aeee.v14i3.1752. ISSN 1804-3119. Dostupné z: http://hdl.handle.net/10084/116602 Author, F., Author, S.: Title of a proceedings paper. In: Editor, F., Editor, S. (eds.) CONFERENCE 2016, LNCS, vol. 9999, pp. 1–13. Springer, Heidelberg (2016).
2. KERSEY, A. D., M. A. DAVIS, H. J. PATRICK, M. LEBLANC, K. P. KOO, C. G. ASKINS, M. A. PUTNAM and E. J. FRIEBELE. Fiber grating sensors. Journal of Lightwave Technology. 1997, vol. 15, no. 8, pp. 1442–1463. ISSN 1558-2213. DOI: 10.1109/50.618377. Author, F.: Contribution title. In: 9th International Proceedings on Proceedings, pp. 1–2. Publisher, Location (2010).
3. Bland, J.M., Altman, D.G. "Measuring agreement in method comparison studies," Stat. Methods Med. Res. (1999), 8, pp. 135–160.

Heart rate FBG sensor tested in a real environment using MRI

Petr Müller

Department of Telecommunications, FEECS,
VSB – Technical University of Ostrava, 17. listopadu 15,
708 00 Ostrava – Poruba, Czech Republic
petr.muller.st@vsb.cz

Abstract. This document deals with the theme of heart rate FBG sensor that was tested in a real environment using magnetic resonance (MRI).
The sensor is applied to the subject and is sensing cardiac activity while magnetic resonance imaging is activated. The sensor is based on the Bragg grating, an optical sensor and a sensor that detects the heartbeat. One of the indisputable advantages of this sensor is its use in magnetic resonance, where otherwise other sensors, due to the properties of magnetic resonance, cannot be used. This document also describes the author's activities in the first year of doctoral studies.

Keywords: FBG sensor, optical fiber, MRI

1 Introduction

In the first section I would like to introduce myself.
My name is Petr Müller and I am a 29-year-old doctoral student at Technical University of Ostrava. I have been studying at the university in Ostrava since I was 20-year-old. I studied and graduated in a programme Computer Science as a bachelor. Then continued and graduated as a master in the same programme focused on telecommunication systems.

After that I decided to take a challenge and started studying Master of Business Administration in Prague institute focused on Cyber Security Management because during my studies I also worked as a Security specialist in a company specialized on provision of information and security services.

After 2 years spent in Prague and finishing MBA studies, I accepted an opportunity to get back to my “Alma mater” studying and basically continue in the area of telecommunication systems and developed my knowledge in the field of optical systems.

During my first year that I have spent as a doctoral student I have participated in few projects and experiments.

The last one where I participated, and I want to write about, was named Measurement of heart rate and breath in MRI which should result in an article which leads to awareness and improvement of pulse and breath sensing in magnetic resonance and also complements my dissertation topic which is Research and development of new methods for monitoring vital functions and heart rate triggering in the environment of MRI.

2 About my project and dissertation thesis

As I mentioned in the previous section, during my first year, I have had few projects. My dissertation thesis is Research and development of new methods for monitoring vital functions and heart rate triggering in the environment of MRI.

In the first year I was participating on designing of a measurement scheme and forms for the creation of the fiber Bragg grating (FBG) sensor which can be used in the harsh magnetic resonance environments (1.5 T and 3 T).

A fiber Bragg grating (FBG) is a very small typically a few millimeters in length that can be photo inscribed in the core of a single mode fiber. This is done by transversely illuminating the fiber with a UV laser beam and using a phase mask to generate an interference pattern in its core. This will induce a permanent change in the physical characteristics of the silica matrix. [1] [4]

This change exists in a periodic modulation of the core index of refraction. It creates a resonant structure. Covered with a primary coating, the diameter of the fiber is 250 micrometers. Without this coating, the fiber has a diameter of 125 micrometers. The light then travels within the core, which has a diameter of approximately 8 micrometers. [1]

Benefits

Operation

The FBG will act as a wavelength selective mirror; it is a narrow band filter. This basically means that if light from a broadband source is injected in the optical fiber, only light within a very narrow spectral width centered at the Bragg wavelength will be back-reflected by the grating. The remaining light will continue through the optical fiber to the next Bragg grating without any loss. [1]

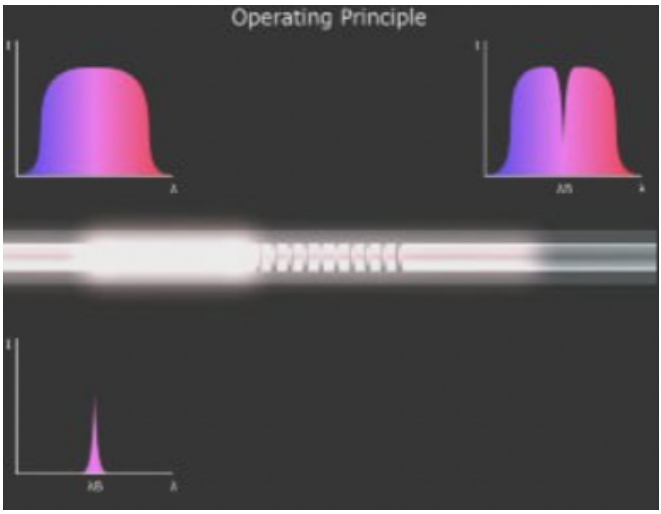

Figure 1 Top left: spectrum of injected light; Top right: spectrum of transmitted light; Center: Optical fiber with an FBG in its core; representation of transmitted and reflected light; Bottom left: spectrum of reflected light

Acting as a strain sensor

The FBG has special characteristics to perform as a sensor, e.g. when the fiber is stretched or compressed, the FBG will measure strain. This happens because the deformation of the optical fiber leads to a change in the period of the microstructure and of the Bragg wavelength. [1]

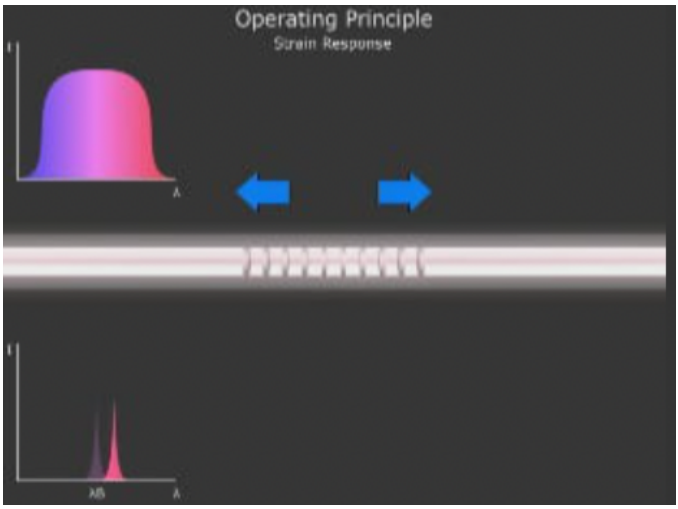

Figure 2 A sensor acting as a strain sensor: Strain response

Acting as a temperature sensor

Sensitivity to temperature is also intrinsic to a fiber Bragg grating. The main contributor to Bragg wavelength change is the variation of the silica refraction index induced by the thermo-optic effect. There is also a contribution from the thermal expansion which alters the period of the microstructure. However, this effect is marginal given the low coefficient of thermal expansion of silica. [1]

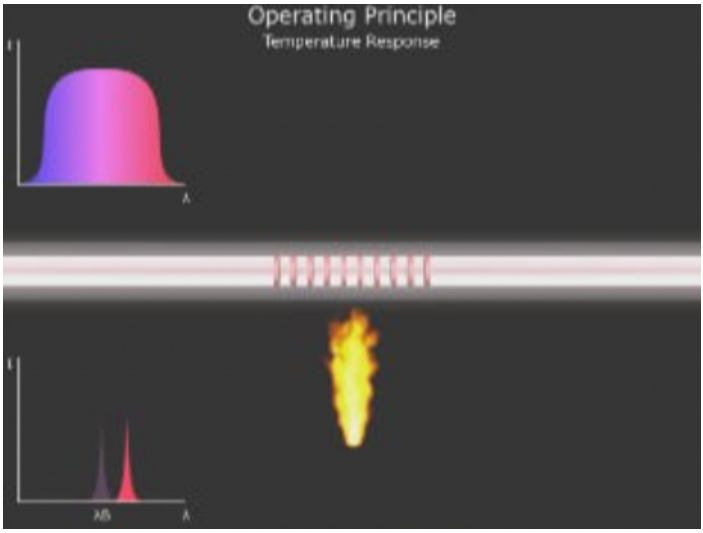

Figure 3 A sensor acting as a temperature sensor: Temperature Response

Vibration and Acoustic Sensing

This sensor works on the principle of the change in the Bragg wavelength induced by the vibration, when the FBG is located intimately in touch with the vibrating object. The stress-induced change in the Bragg wavelength can be extremely small, but there are a few uncomplicated methods for converting the wavelength shift to an amplitude change, e.g. by using one of the two edges of the FBGs spectral shape. [2]

A tighten band FBG is glued to the vibrating object, for example, a wing of an aircraft, or embedded in a turbine blade. Light from a stable single-frequency laser is reflected from one of the cut-on or cut-off filter edges of the FBG. The amplitude of the reflected signal is modulated because the Bragg wavelength shifts approximately linearly as a function of vibration. By amplifying the received signal, small vibrations may be detected. Recently this was demonstrated by gluing an FBG to the vibrating belly of an acoustic guitar to act as a sensitive pickup. [2]

$$\frac{1}{\lambda_B}\frac{\Delta\lambda_B}{\Delta\varepsilon} = 0{,}78.10^{-6} \ \ \mu strain^{-1},$$

$$\frac{1}{\lambda_B}\frac{\Delta\lambda_B}{\Delta T} = 6{,}678.10^{-6} \ \ °C^{-1},$$

where $\Delta\lambda_B$ is the changes in wavelength itself, k is the deformation coefficient, ε is the size of apllied deformation, α_Λ is the coefficient of apllied thermal expansion, $\alpha_n$is the thermo-optic coefficient and ΔT is the changes in temperature.

Our FBG senzor was created in a laboratory using 3D printer. Apodized Bragg grid was used for creating.

A small part of the optical fiber was attached to the 3D model. A pneumatic breath belt was used as a baseline for comparing measurements.

Further research on heart rate triggering in the environment of magnetic resonance using the 3D model will continue in the coming academic year.

2 Publications

As I already mentioned, my first year of doctoral studies has been largely influenced by Coronavirus situation.

Publications could not be realized or successfully completed in this academic year.

3 Pedagogic part

I have been helping to my supervisor Doc. Ing. Jan Nedoma, Ph.D with subjects, exercises and everything else what was needed.

4 Future work

My future publications should cover the FBG heart rate sensor and other projects that I hope will take place in the coming academic year.

Processing of measurement data is still in progress.

Plans for the future with the sensor are such that we will try to reduce the size of the sensor.

References

1. What is a Fiber Bragg Grating? | FBG | Sensors | HBM. Test & Measurement | Load Cell | Transducer | Strain Gage | HBM. https://www.hbm.com/en/4596/what-is-a-fiber-bragg-grating/
2 ScienceDirect. ScienceDirect. https://www.sciencedirect.com/topics/materials-science/fiber-bragg-grating

3. Encapsulation of FBG Sensor into the PDMS and its Effect on Spectral and Temperature Characteristics | Nedoma | Advances in Electrical and Electronic Engineering.http://advances.utc.sk/index.php/AEEE/article/view/1786
4 FBG Principle - FBGS. Tailored fiber optic sensing components & solutions https://fbgs.com/technology/fbg-principle/

Liveness detection using automatic speech recognition system for speaker verification

Martina Slívová[0000−0001−8238−317X]

Department of Telecommunications, FEECS,
VSB – Technical University of Ostrava, 17. listopadu 15,
708 00 Ostrava – Poruba, Czech Republic
martina.slivova@vsb.cz

Abstract. This paper briefly recapitulates the second year of my doctoral study. The beginning contains a short introduction and the second section is a summarization of the publication focused on liveness detection in the speaker verification system. The system is based on isolated word automatic speech recognition which we created last year. In the next section, there are research projects I am included in. The last part is about my educational activity.

Keywords: machine learning · liveness detection · speaker verification.

1 Introduction

At first, I would like to introduce myself. I am Martina Slívová and I am in the second year of my doctoral study at the Faculty of Electrical Engineering and Computer Science at the Technical University of Ostrava. My educational program is Communication Technology and I am included in some research projects and I teach some subjects as well. To this date, I have two published papers.

2 About my publication

In this academic year, I wrote one paper with my colleagues. This publication has the title 'Detection of speaker liveness with CNN isolated word ASR for verification systems' and is published in Multimedia Tools and Application journal [1]. This paper builds upon a previous article which was about automatic speech recognition.

2.1 Biometric authentication

Authentication is the process of the verification of the identity, it can be done in several different ways. There are ways based on identity verification by knowledge (password, PIN code, etc.), another way to prove identity through ownership and the third possibility is using biometric data.

Biometric authentication is based on proving identity using physical or behavioral characteristics (fingerprint, facial geometry, voice, hand geometry, iris,

VSB – Technical University of Ostrava, 2021, ISBN 978-80-248-4523-4 (on-line).

writing dynamics, etc.). Biometric-based systems have several advantages over traditional authentication methods. They are much more reliable than password-based systems and, unlike passwords, cannot be lost or forgotten. Biometric features are very difficult to copy, share or distribute. In addition, they require the presence of an authenticated person at the time of authentication. Attempts to mimic or alter biometric characteristics are possible, but very difficult [5].

Biometric characteristics can be divided into two basic groups [6]:

1. **Physiological biometric characteristics** are unique and time-stable. They are used based on scientific knowledge about the human body (iris, retina, face, shape of the outer ear, fingerprint fingerprints, palms and soles, finger and hand geometry, wrist vein topography, human body odor, salt content in the human body, dimensions, and weights of the human body, DNA, etc.).
2. **Behavioral biometric characteristics** are unique and can be unstable over time. They are associated with some user action and are based on knowledge of the human voice, body movement, knowledge, and writing skills (knowledge of the human voice, locomotion, writing, signature, the dynamics of typing on the keyboard, etc.).

In our research, we focused on biometric authentication using voice.

2.2 Reliability of biometric methods

Measuring the reliability and performance of biometric methods is possible with different characteristics. Biometric verification methods are based on the statistical evaluation of a biometric sample and a biometric template. The most commonly used parameters are FRR (False Rejection Rate) and FAR (False Acceptance Rate), which indicate the probability of false rejection and the probability of false acceptance. Each time a biometric sample is scanned, the values are not precisely the same, so the templates being compared are always different. The degree of similarity between templates is determined, the sensitivity threshold indicates whether the user will be accepted or rejected [6].

- False Rejection Probability (FRR) indicates the probability that the system will evaluate an authorized user as unauthorized.
- Failure probability (FAR), on the other hand, indicates the probability that an unauthorized user will be marked as authorized.

The quality of a biometric system can be determined by the so-called ROC (Receiver Operating Characteristics) curve, which shows the FRR and FAR in one graph. The point at which both errors are equal is called the EER (Equal Error Ratio).

2.3 Liveness detection

As a part of a speaker verification system we needed to prevent presentation attack [2], which consists in the use of the recorded voice of the target speaker.

There are many different ways to perform liveness detection, we chose the text-prompt procedure implemented into the verification process. Our proposed solution is shown in figure 1. The system is made up of three stages. First is the user's access request which may correspond to enclosing the card with identification to the reader. Then follows liveness test with text-prompt, the user has three tries to say correctly numbers which are randomly generated. And at the end, if the liveness test went right speaker verification phase can start.

When designing the liveness detection we used The Speech commands dataset version 2 [3], for automatic speech recognition the Tensorflow framework is used. A classifier incorporates a Convolutional neural network (CNN) and Mel-frequency cepstral coefficients (MFCC) for feature extraction.

The last part is based on Gaussian Mixture Models (GMM) and Universal Background Models (UBM) i-vector speaker verification system [4].

2.4 Proposed solution

The speaker verification system we designed is based on a scenario that will be further described. The prerequisite for our system was the differentiation of the target speaker from an unauthorized person. The result of the verification will affect granting or denying access to a certain secure location.

Usual speaker verification systems contain identification of the user followed by speaker verification. Our solution suggests a liveness test in between those two stages. It can be seen in figure 1:

- **Identification** - access request with given identity (for example using RFID cards or tags).
- **Liveness Test** - test is performed by generating random keywords (three numbers in our case) which must be read correctly. This should prevent the presentation attack.
- **Verification** - if the previous stages passed correctly the speaker's identity is verified with the biometric template from the database

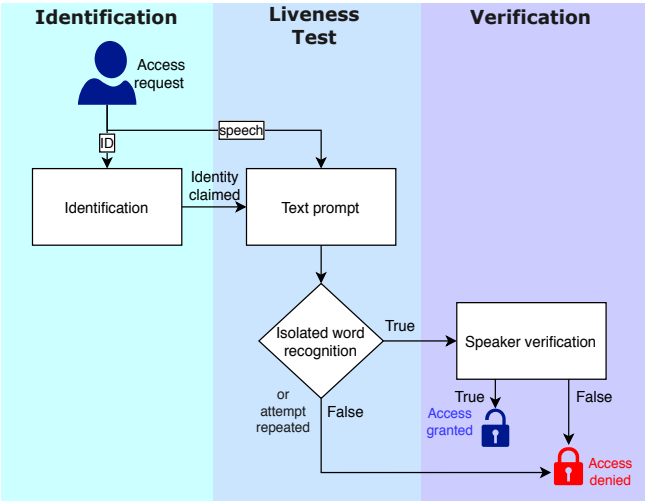

Fig. 1. Design of the system for the speaker verification with liveness detection [1]

3 Projects

As part of my studies, I was actively involved in solving 2 projects, namely:

- CZ.01.1.020.00.019_2620020122 Development of external modules TAMAS II
- S120-440-01 Smlouva o poskytnutí služeb pro společnost T-Mobile Czech Republic, a.s.

3.1 Results

When creating the liveness detection we tested several different sizes of the dataset (from 5 to 35 words) and the resulting system consists of 10 words (0-9 numbers only) with the accuracy of the recognition 96%. With increasing the number of words in the dataset the accuracy was decreasing to the 92% with the biggest dataset (35 words).

Unfortunately, it is not certain that the designed system would be efficient contrary to the highly sophisticated playback attacks. Our future research will therefore focus on this emerging problem in speaker verification [7]

4 Educational activity

During this academic year, I tough the same subjects as last year which are VoIP in the winter semester and Basics of Algorithms and Programming in the summer semester.

References

1. Slivova, M., Voznak, M., Tovarek, J. et al. Detection of speaker liveness with CNN isolated word ASR for verification systems. Multimed Tools Appl (2021). https://doi.org/10.1007/s11042-021-11150-1
2. Fang F, Yamagishi J, Echizen I, Sahidullah MD, Kinnunen T (2018) Transforming acoustic characteristics to deceive playback spoofing countermeasures of speaker verification systems. arXiv:1809.04274
3. Pete Warden. Speech Commands: A Dataset for Limited-Vocabulary Speech Recognition. [online] [cit. 2019-03-09]. Dostupné z http://arxiv.org/abs/1804.03209
4. Reynolds DA, Quatieri TF, Dunn RB (2000) Speaker verification using adapted gaussian mixture models. Digit Signal Process 10(1):19–41
5. JAIN, A.K., A. ROSS a S. PANKANTI. Biometrics: A Tool for Information Security. *IEEE Transactions on Information Forensics and Security* [online]. 2006, 1(2), 125-143 [cit. 2019-03-27]. DOI: 10.1109/TIFS.2006.873653. ISSN 1556-6013. Dostupné z: http://ieeexplore.ieee.org/document/1634356/
6. RAK, Roman, Vašek MATYÁŠ a Zdeněk ŘÍHA. *Biometrie a identita člověka ve forenzních a komerčních aplikacích.* Praha: Grada, 2008. Profesionál. ISBN 978-80-247-2365-5.
7. P. Partila, J. Tovarek, G. H. Ilk, J. Rozhon, and M. Voznak. Deep learning serves voicecloning: How vulnerable are automatic speaker verification systems to spoofing trials? *IEEE Communications Magazine*, 58(2):100–105, 2020.

Optical Probe for Magnetic Field Measurement

Ales Vanderka and Petr Siska

Department of Telecommunications, FEECS,
VSB – Technical University of Ostrava, 17. listopadu 15,
708 00 Ostrava – Poruba, Czech Republic
{ales.vanderka, petr.siska}@vsb.cz

Abstract. This work is a summary of my results achieved during academic year 2020/2021. My research during this academic year was focused on topics related to the use of optical sensors for measuring magnetic fields. The main aim of this research is to develop a magneto-optical probe based on the principle of the Faraday effect in a TGG (Terbium Gallium Garnet) crystal. Optical probes with optical fibers are ideal for use in a space with a large inter-ference from electromagnetic fields. The Faraday effect consists in the rotation of the polarization plane of the beam at the moment when the crystal is exposed to a magnetic field. According to the method of rotation detection, there are two main approaches: polarimetric and interferometric. The polarimetric approach is a direct measurement of polarization changes. The interferometric approach converts the rotation of the polarization plane to a change in amplitude. Optical probes with optical fibers are ideal for use in a space with a large interference from electromagnetic fields. In this case, this interferometric approach was used.

Keywords: electromagnetic field measurements, TGG crystal, Faraday effect.

1 Introduction

Nowadays, measurement of magnetic fields is a current issue. In electromagnetic metal forming or magnetic resonance imaging, is necessary to know the direction and strength of the magnetic field. But in these large magnetic field conditions, conventional electric magnetic field meters cannot be used. Therefore, the use of optical sensors without metallic components is suitable here. Magneto-optical TGG crystals can be used to create the sensor. The sensitivity of the sensor can be changed in several ways, by changing the length of the sensor area, by multi-ple passes of light using reflections, or by changing the wavelength. [1], [2]

VSB – Technical University of Ostrava, 2021, ISBN 978-80-248-4523-4 (on-line).

2 Sensor design

A sensor based on the Faraday effect principle was developed using magneto-optical material TGG for measuring electromagnetic fields. The measuring prin-ciple consists in rotating the polarization plane of the passing electromagnetic wave (light) with a TGG crystal.
Unpolarized light is coupled into the optical fiber from LED, Subsequently, the light enters the optical splitter. From the optical splitter, it enters the optical probe via an optical fiber. Then follows a glass ball which collimates the optical beam.
Linearly polarized light is generated in front of the TGG crystal by a polarizing filter. The action of an electromagnetic field on the TGG crystal rotates the polar-ization plane of light. A reflective layer is vapor deposited on the other end of the TGG crystal. At the other end of the TGG crystal, a reflective layer is vaporized, which reflects light back through the TGG crystal. This light passes through the crystal a second time. Subsequently, the light passes through a polarizing filter a second time, which converts the change in polarization to a change in optical power. The glass ball focuses the light into the optical fiber, where is the optical splitter. The optical splitter separates half of the power to the optical detector. [3]

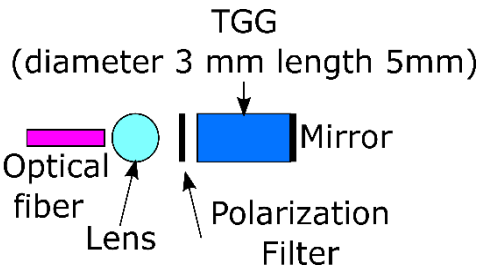

Fig. 1. Sensor system design.

The magnitude of the angular rotation of the polarization plane Δ of light radiation can be expressed by the equation:

$$\Delta = V \cdot l \cdot B \tag{1}$$

where V is the Verdet constant of the transparent material, l is the length of the sensing area (TGG crystal) and B is the intensity of the magnetic field. The direction of passage of light radiation must be parallel to the magnetic field lines.
In our case, the wavelength of 470 nm is used. At this wavelength, the sensor is able to measure a magnetic field up to approximately 1.3 T.

3 Electromagnetic field measurement

The measurement of the assembled sensor was performed using an assembled station, which was controlled by an application created in LabVEW. The measuring station consists of a motorized translation stage MTS50/M-Z8 - 50 mm, which is connected to the driver KDC101. A magnetic probe is placed in the rotary feed, which is composed of a 3D printed part into which the optical components are inserted. An optical fiber with core, sheath and primary protection diameters of 105/128/250 μm and a numerical aperture of 0.22 was used for the measurement. This optical fiber is splits by a splitter into two inputs and one output. On one side of the input there is an LED connected to it and on the second side there is a photodetector, which is directly connected to the PM100D detector from Thorlabs. Both instruments, the motor and the measuring instrument, are connected to a computer and con-trolled by a program in LabVIEW. [3]

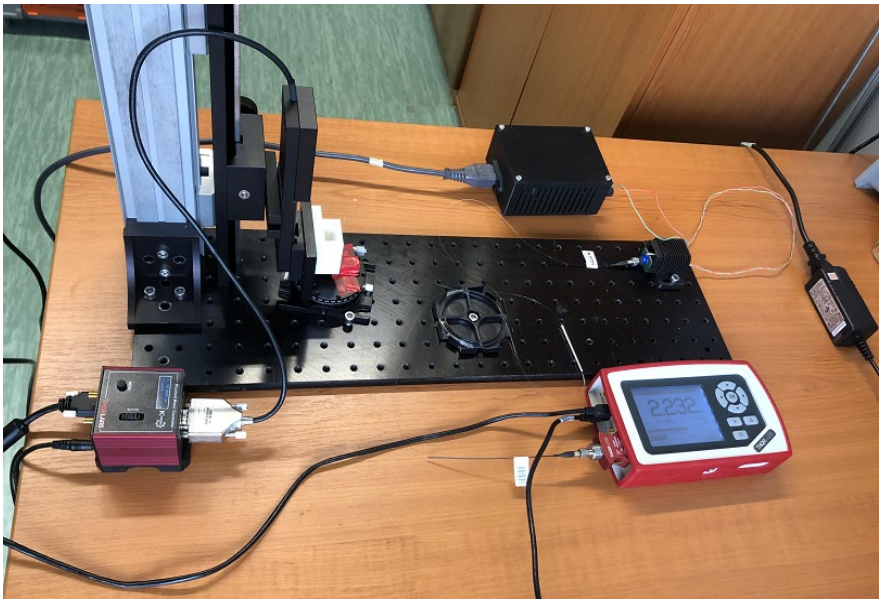

Fig. 2. Measuring set for automatic measuring magnetic field.

Figure 3 shows the effect of the magnitude of the magnetic field on the attenua-tion of the detected signal. At the same time, it shows the effect of rotating the magnetic field lines against the direction of the optical beam in the TGG crystal. With increasing distance of the magnet and with the deflection of the angle of the magnetic field lines from the perpendicular position, the attenuation decreases.

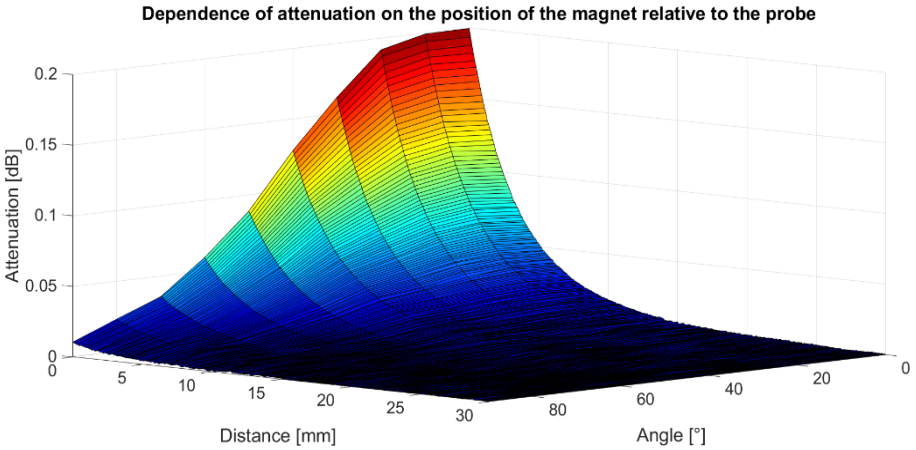

Fig. 3. Dependence of attenuation on the position of the magnet relative to the probe.

4 Conclusion

This experiment verified the possibility of the desire of a magneto-optical sensor for measuring magnetic fields. So far, neodymium magnets with a maximum magnetic field of 150 mT have been used for the experiments. This sensor is built on a magnetic field of 2.2 T (When the polarization is rotated 90 °). But it is possible to measure a much larger magnetic field with it thanks to the possibility of counting the number of polarization revolutions during mag pulses.

5 Projects

The content mentioned above is based on my research at a project supported by the Technology Agency of the Czech Republic (TA CR) named “Development of the method for accelerated aging of passive photonic components with orientation to nuclear plants with a higher degree of ionizing radiation occurrence.”. I participate in other projects such as “Development and testing of hybrid cables, hermetic cable bushings and modulus for nuclear energetics.” and “The unique fiber-optic sensor for detecting rail vehicles”. My interest is focused on applications of fiber optics sensors in the industry.

6 Publication activities

I am author of 31 articles registered on the Scopus database, 4 utility models, and 1 patent.

References

1. Tumanski, S: Handbook of Magnetic Measurements.. 1st edn. CRC Press, Boca Raton (2016).
2. Matias, I. R., Ikezawa, S., Corres, J: Fiber Optic Sensors: Current Status and Future Possibilities. 1st edn. Springer, New York City (2016).
3. Samonilova, B.: Design and Construction of Optical Probe for Magnetic Field Measurement. Bachelor thesis, (2020).

Optical sensors based on guided-mode resonance for relative humidity sensing

Jakub Chylek[1], Petra Urbancová[2], and Petr Hlubina[1]

[1]Department of Physics, FEECS,
VSB – Technical University of Ostrava, 17. listopadu 15,
708 00 Ostrava – Poruba, Czech Republic
[2]Department of Physics, Faculty of Electrical Engineering and Information Technology, University of Žilina, Univerzitná 1, 01026 Žilina, Slovakia
jakub.chylek@vsb.cz, urbancova@fyzika.uniza.sk, petr.hlubina@vsb.cz

Abstract. In this paper, we propose a relative humidity sensor based on guided-mode resonance utilizing an asymmetric planar waveguide structure (PWS). The structure consists of three layers - substrate, gold, photoresist, and the dispersion properties of individual materials were determined by spectral ellipsometry. Three individual modes can be excited in the structure if the resonant condition is met. Fundamental TE mode and first-order TE and TM mode. These leaky modes can be used for relative humidity sensing. The guided-mode phenomenon is analyzed in the spectral domain and achieved sensitivity to the relative humidity is determined. The proposed planar waveguide structure presented is a simple sensing structure with high sensitivity to the refractive index of the analyte with the potential to adjust the sensitivity by choosing a suitable angle of incidence.

Keywords: guided-mode resonance · asymmetric planar waveguide structure · leaky modes · relative humidity · sensitivity.

1 Introduction

The guided-mode resonance phenomenon is based on the excitation of guided modes in a planar waveguide structure. This phenomenon can be achieved by fulfilling the phase-matching condition with the use of a coupling element such as diffraction grating or a prism [1]. Under certain conditions, the guided light can leak from the waveguide and the leaky modes can interfere with the non-coupled reflected or transmitted light waves which result in a narrow resonance dip in the reflectance spectra or a sharp peek in the transmittance spectra. This interaction only happens for a specific wavelength, angle, and polarization [2].

In this paper, an asymmetric planar waveguide structure has been employed in the guided mode resonance sensor for relative humidity sensing. The entire sensing structure consists of a BK7 coupling prism, a substrate made out of fused silica glass, a metal cladding layer made out of gold, AZ1505 photoresist, and the external medium under study which is moist air. Series of measurements

for various angles of incidence utilizing spectral ellipsometry were performed to determine dispersion properties of individual materials.

In the structure, three individual modes can be excited if the resonant condition is met [3–5]. Fundamental TE mode and first-order TE and TM mode. The sensing properties of the employed three-layer planar waveguide structure were estimated based on measured reflectance ratios for different percentages of relative humidity for the external angle of incidence 20.6 degrees. Achieved sensitivity is discussed for all three modes that can be excited in the proposed planar waveguide structure.

2 Theoretical model

The proposed sensing structure consists of three layers. A fused silica glass substrate with the thickness of $t_s = 0.7$ mm and the refractive index n_s, a metal cladding layer formed by the gold layer with the thickness of $t_{Au} = 30$ nm and the complex permittivity ε_{Au}, the waveguide layer formed by AZ1505 photoresist with the thickness of $t_p = 200$ nm and the refractive index n_d. A schematic drawing of the structure is shown in Figure 1. as well as an external medium formed by moist air with the refractive index n_{air} and a coupling prism with the refractive index n_p.

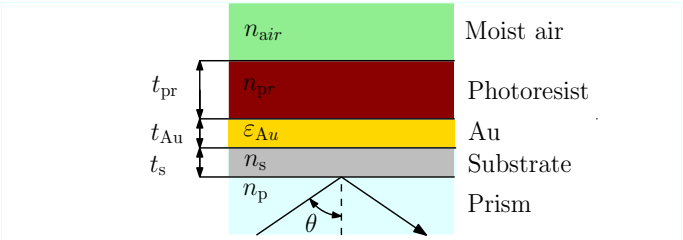

Fig. 1. Schematic drawing of asymmetric planar waveguide structure (PWS).

In order to determine dispersion properties of the employed asymmetric planar waveguide structure, series of measurements for various angles of incidence utilizing spectral ellipsometry were performed. The dispersion properties of individual layers were determined by experimental data fitting to appropriate dispersion models.

In the structure, three individual modes can be excited - fundamental TE mode, first-order TE, and TM mode. In Fig. 2 and Fig. 3, spectral reflectances Rs and Rp are shown which were calculated for refractive index values from 1 to 1.005 with a step of 0.001 and angle of incidence 42.2 degrees. It can be observed that the calculated reflectance spectra in Fig. 2 show well-pronounced dips with a constant width that corresponds to the guided modes - fundamental and first-order TE mode and in Fig. 3 first-order TM mode. It can also be observed that the resonance wavelength shifts towards longer wavelengths with increasing values of the refractive index of the analyte. The largest wavelength shift in terms of a change of refractive index corresponds to fundamental TE mode and the smallest shift to the first order TE mode.

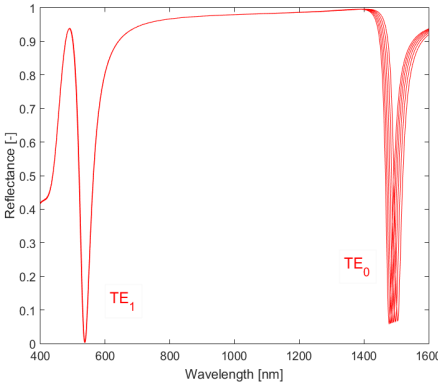

Fig. 2. Theoretical spectral reflectance $R_s(\lambda)$ for the PWS with an analyte of refractive index values in the range $1 - 1.005$ with a step of 0.001 for the angle of incidence $\theta = 42.2°$.

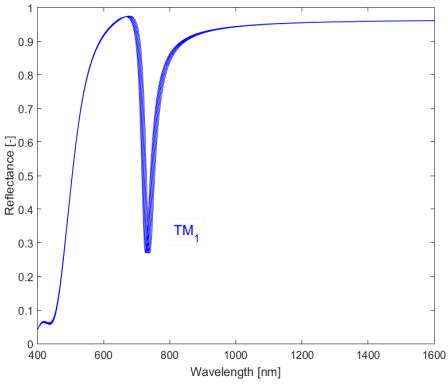

Fig. 3. Theoretical spectral reflectance $R_p(\lambda)$ for the PWS with an analyte of refractive index values in the range $1 - 1.005$ with a step of 0.001 for the angle of incidence $\theta = 42.2°$.

To describe the sensing properties of individual modes, it is important to determine the refractive index sensitivity, which is defined as the change in the resonant wavelength dived by the change of the refractive index.

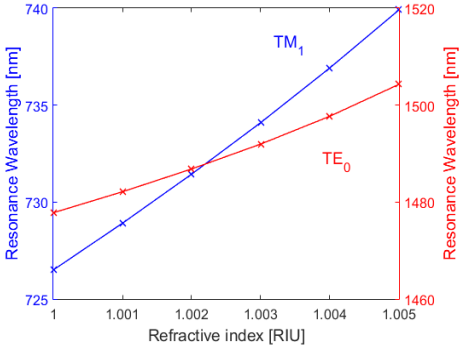

Fig. 4. Resonance wavelength as a function of refractive index of the external medium.

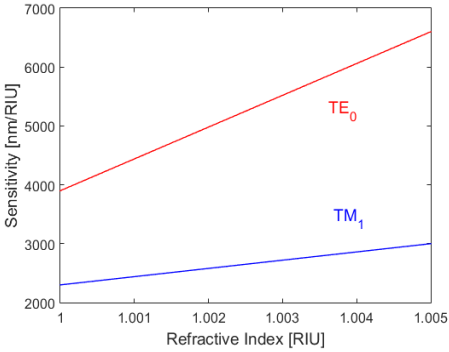

Fig. 5. Sensitivity of the TE_0 and TM_1 modes as a function of refractive index of the external medium.

The resonance wavelength of first-order TM and fundamental TE modes as a function of the refractive index of the analyte is shown in Fig. 4 and the refractive index sensitivity is shown in Fig. 5. Figures show linear dependence with a change in the range of 2300-3000 nm per refractive index unit for the first order TM mode and 3900-6600 nm per refractive index unit for the fundamental TE mode.

3 Experimental Setup

The experimental setup shown in Fig. 8 was used to measure the reflectance response of the planar waveguide structure and the relative humidity sensing ability in the visible and near-infrared spectral ranges.

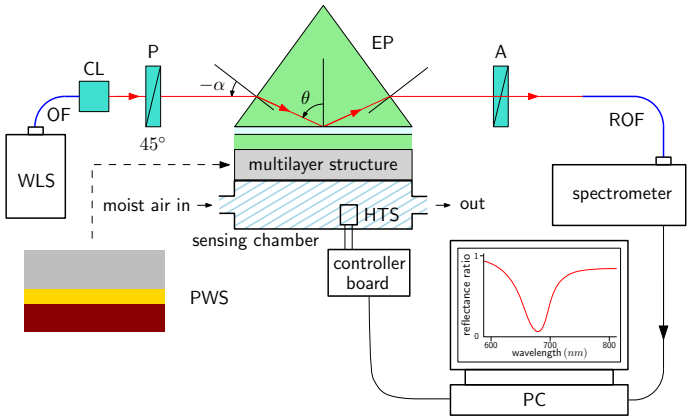

Fig. 6. Schematic drawing of the experimental setup employing the PWS.

4 Experimental Results, Discussion

The measurements of reflectance spectra for different percentages of relative humidity in the range of approximately 35%-85% were performed at a temperature of 22.8-degrees celsius which was kept constant during the experiment.

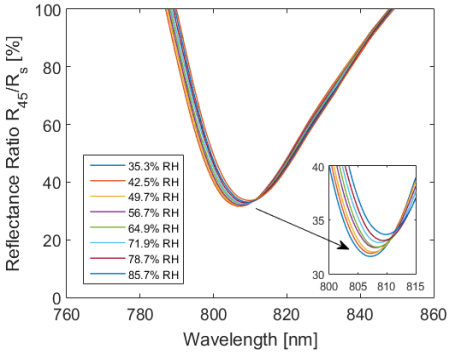

Fig. 7. Measured spectral reflectance ratio $R_{45}(\lambda)/R_s(\lambda)$ for the external angle of incidence $\alpha = 20.6°$.

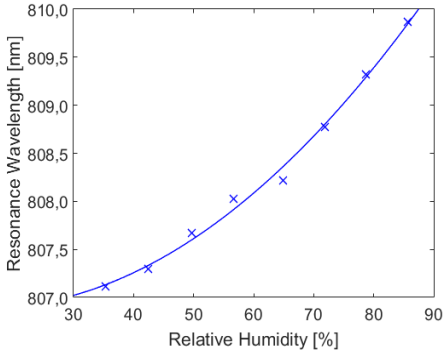

Fig. 8. Resonance wavelength as a function of the relative humidity with a second-order polynomial fit.

Measured reflectance ratios for different percentages of relative humidity for the external angle of incidence 20.6 degrees are shown in Fig. 11. The figure shows the guided-mode resonance for the first-order TM mode. It can be observed that

the resonance wavelength is red-shifted when the relative humidity of moist air increases. The resonance wavelength shift as a function of relative humidity with a second-order polynomial fit is shown in Fig. 12.

Measured reflectance ratios for different percentages of relative humidity for the external angle of incidence 20.6 degrees are shown in Fig. 13. The figure shows the guided-mode resonance for the fundamental TE mode. The resonance wavelength shift as a function of relative humidity with a second-order polynomial fit is shown in Fig. 14.

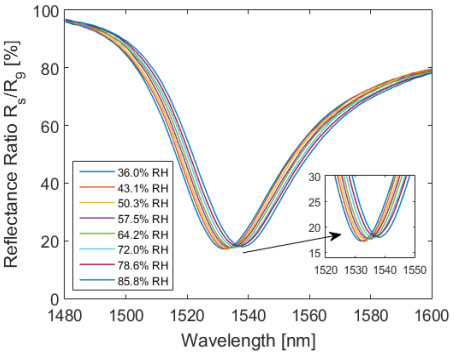

Fig. 9. Measured spectral reflectance ratio $R_s(\lambda)/R_p(\lambda)$ for the external angle of incidence $\alpha = 20.6°$.

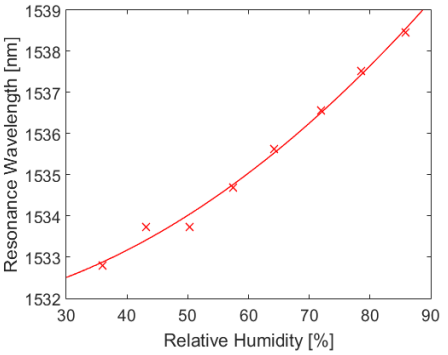

Fig. 10. Resonance wavelength as a function of the relative humidity with a second-order polynomial fit.

To estimate the sensing properties of the planar waveguide structure, it is important to determine the sensitivity to the relative humidity which is defined as the change in the resonant wavelength dived by the change in relative humidity of most air.

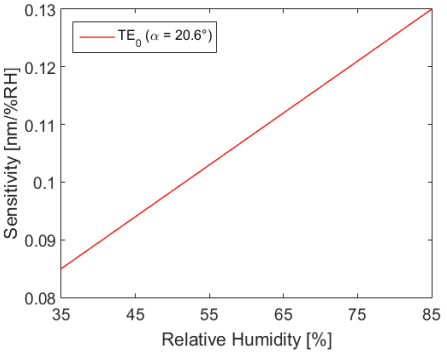

Fig. 11. Sensitivity of TE_0 mode measured at the external angle of incidence $\alpha = 20.6°$.

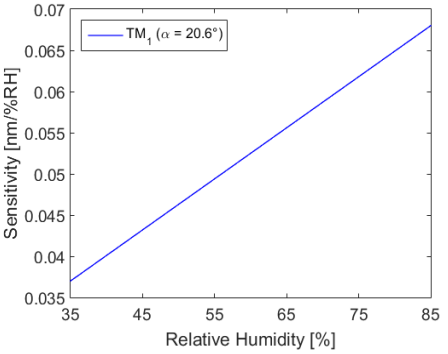

Fig. 12. Sensitivity of TM_1 mode measured at the external angle of incidence $\alpha = 20.6°$.

From the measured shifts of the resonance wavelengths and their dependence on the relative humidity, we can determine the sensitivity of the guided modes

to the relative humidity. Achieved sensitivities to the relative humidity for fundamental TE mode and first-order TM mode are shown in Fig. 15 and 16.

5 Conclusions

In this paper, the sensing properties of the employed three-layer planar waveguide structure were estimated. Achieved sensitivity to the relative humidity of first-order TE mode for the external angle of incidence 20.6 degrees is constant at the value 0.033 $nm/\%RH$, for first-order TM mode the sensitivity varies in the range of 0.037 to 0.068 $nm/\%RH$ and for fundamental TE mode the sensitivity varies in the range of 0.085 to 0.137 $nm/\%RH$. The highest figure of merit which is defined as sensitivity to relative humidity divided by full-width half-maximum $FOM = S_{RH}/FWHM$ corresponds to the fundamental TE mode and attains a value of $3.7 \times 10^{-3}\%RH^{-1}$. The employed planar waveguide structure presented is a simple sensing structure with high sensitivity to the refractive index of the analyte. There is a potential to adjust the sensitivity by choosing a suitable angle of incidence and also that the use of the sensor can be extended to liquid analytes by substituting the polymer with the dielectric layer such as silicon dioxide which can also act as a protective layer for the gold.

Acknowledgments

The work was supported by the student grant system through project SP2021/64 and also by project ERDF/ESF New Composite Materials for Environmental Applications (No. CZ.02.1.01/0.0/0.0/17_048/0007399).

List of publications

P. Urbancova, J. Chylek, P. Hlubina, D. Pudis (2020). "Guided-Mode Resonance-Based Relative Humidity Sensing Employing a Planar Waveguide Structure", In: Sensors, vol. 20 (23),p. 6788.

References

1. Lan,G.; Zhang,S.; Zhang,H.; Zhu,Y.; Qing,L.; Li,D.; Nong,J.; Wang,W.; Chen,L.; Wei,W.: High performance refractive index sensor based on guided-mode resonance in all-dielectric nano-slit array. Phys. Lett., **383**, 1478–1482, (2019).
2. Zhou, Y.; Wang, B.; Guo, Z.; Wu, X.: Guided Mode Resonance Sensors with Optimized Figure of Merit. Nanomaterials, **9**, 837, (2019).
3. Chen, L.: Optical Devices Based on Symmetrical Metal Cladding Waveguides. Optical Devices in Communication and Computation; Xi, P., Ed.; In Tech: Rijeka, Croatia, 127–152, (2012).
4. Nesterenko,D.V.; Hayashi,S.; Sekkat,Z.: Extremely narrow resonances, giant sensitivity and field enhancement in low-loss waveguide sensors. J. Opt., **18**, 065004, (2016).
5. Anous, N.; Ramadan, T.; Abdallah, M.; Qaraqe, K.; Khalil, D.: Planar broad-band and wide-range hybrid plasmonic IMI filters with induced transmission for visible light applications. Appl. Opt., **56**, 8751–8758, (2017).

Relative humidity sensing using a phase shift of the Bloch surface waves

Roman Kaňok, Petr Hlubina, Lucie Gembalová, and Dalibor Ciprian

Department of Physics, FEECS,
VSB – Technical University of Ostrava, 17. listopadu 15,
708 00 Ostrava – Poruba, Czech Republic
{roman.kanok, petr.hlubina, lucie.gembalova, dalibor.ciprian}@vsb.cz

Abstract. A method of relative humidity sensing based on the phase shift of the Bloch surface waves is presented. The waves are excited under resonance condition using a white light source and a one diemnsional photonic crystal. The crystal is deposited on a glass substrate that is attached to a coupling prism in the Kretschmann configuration. A spectral interferometry technique employing a birefringent quartz crystal is used to obtain interference of projections of p and s-polarized light waves reflected from the photonic crystal. The phase shift is then obtained by processing recorded spectral interferograms by the Windowed Fourier transform for various relative humidities. Achieved sensitivity to the humidity is -0.029 rad/%RH. Also an extremal value of a spectral derivative of the phase shift is measured as a function of the relative humidity and achieved sensitivity is 0.094 nm/%. The results show that the proposed method is efficient and has a wide potential, i.g. in relative humidity sensing.

Keywords: Bloch surface waves · Phase detection · Spectral domain interferometry · Photonic crystal · Relative humidity.

1 Introduction

Dielectric structures composed of alternating stratified media called the one dimensional photonic crystals (1DPhC) or the Bragg reflectors are important in various applications. Due to their periodically modified refractive index and layers thicknesses, areas of abandoned wavelengths called the photonic bandgaps exist. Within these bandgaps, light is not allowed to propagate. Thus, the 1DPhCs can be used as optical filters [1]. The 1DPhCs can also act as waveguides [2], and the guided modes can be used in sensing applications [3,4]. Last but not the least, the so called Bloch surface waves (BSWs) propagating along the interface between the 1DPhC and the analyte are widely used in sensing applications [3,5], i.g. in biosensing [6].

In this paper, a method of air humidity sensing based on the BSWs excited on a 1DPhC is introduced. The PhC is on a glass substrate that is attached to a glass prism in the Kretschmann configuration. The BSWs are excited by using a halogen lamp as a white light source. Employing a birefringent quartz crystal, a

compact spectrometer and a combination of polarizers, spectral interference of projections of p and s-polarized light is achieved. Obtained interferograms are processed by the Windowed Fourier transform (WFT) and phase functions are evaluated. The phase shift is then measured as a function of the relative humidity of moist air. Sensor performance is characterized in terms of sensitivity.

2 Materials and methods

A 1DPhC under study is shown in Fig. 1 (left). The 1DPhC is deposited on a glass substrate and consists of six SiO_2/TiO_2 bilayers and of a termination layer of TiO_2. Employing an immersion oil, the substrate is attached to a coupling prism made of BK7 glass in the Kretschmann configuration. In Fig. 1 (right), an image of the structure profile obtained by using scanning electron microscopy is shown. As seen, thicknesses of the layers are different. In characterizing the thin layers, the variable angle spectroscopic ellipsometry (VASE) measurement was employed. Data obtained by the VASE were processed using the CompleteEASE software (J.A. Woollam Co., Inc.) and thicknesses of the layers were determined (summarized in Tab. 1).

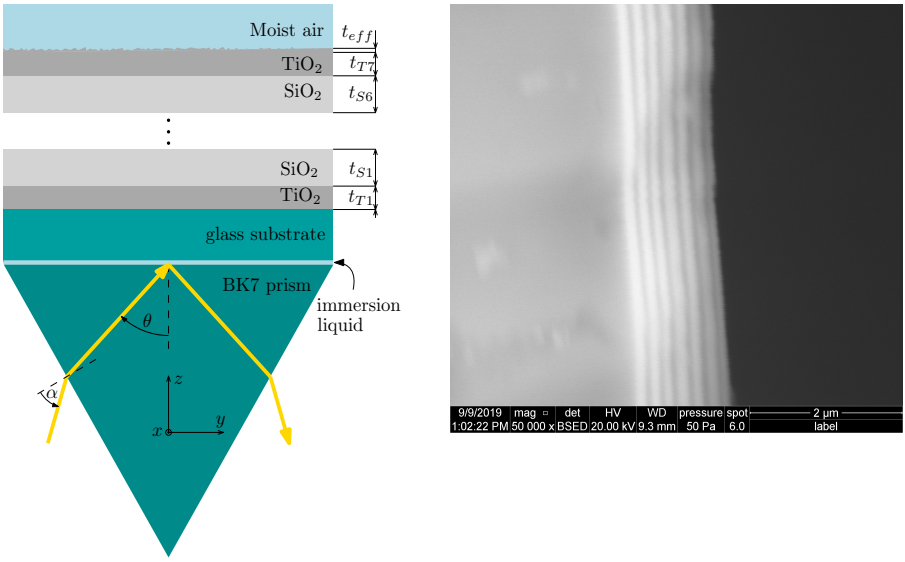

Fig. 1: Left: structure with a photonic crystal under consideration. Right: SEM image of the photonic crystal.

An experimental set-up used for the phase shift measurements is shown in Fig. 2. First, a light beam is generated by a white light source (halogen lamp HL-2000, OceanOptics) and using an optical fibre, the beam is led to collimating

Table 1: Thin layer thicknesses (in nm) obtained by the VASE.

t_{T1}	87.65	t_{T2}	79.09	t_{T3}	77.28	t_{T4}	80.74	t_{T5}	80.89	t_{T6}	76.85	t_{T7}	64.41
t_{S1}	120.21	t_{S2}	101.75	t_{S3}	109.24	t_{S4}	108	t_{S5}	127.3	t_{S6}	125.02	t_{eff}	6.96

lens. The collimated beam then passes through a linear polarizer (LPVIS050, Thorlabs) with optical axis oriented 45° with respect to the plane of incidence, so both polarization components s and p are generated. A birefringence quartz crystal of thickness d=6 mm introduces an optical phase difference $\Delta_{BC}(\lambda)$ between the polarization components. Next, the light beam reflects from the 1DPhC and passes through a linear analyzer (LPVIS050, Thorlabs) with optical axis oriented 45° with respect to the plane of incidence, so the polarization components are projected into one direction of polarization and may interfere. By a microscope objective, the light beam is launched into a read optical fibre (M15L02, Thorlabs) and then led to the spectrometer (USB4000, Oceanoptics). As a result of the described procedure, a spectral interferogram is obtained.

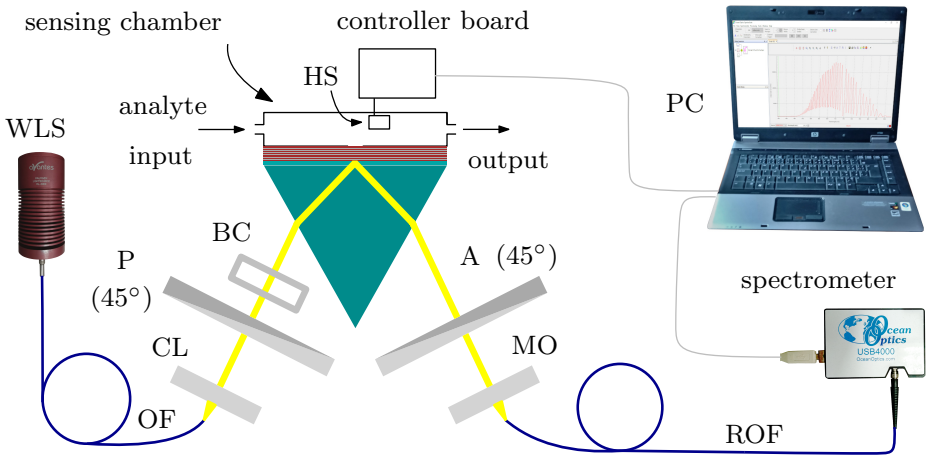

Fig. 2: Experimental set-up consisting of white-light source WLS, optical fibre OF, collimating lens CL, polarizer P, birefringent crystal BC, a coupling prism with a multilayered structure and a sensing chamber, humidity sensor HS, analyzer A, microscope objective MO, read optical fibre ROF, spectrometer S and personal computer PC.

Two such interferograms are needed for determining the phase shift between s and p-polarized waves. The reference one, when BSWs do not occur, and the one for the conditions when the BSWs are generated. By using the WFT [7],

the phase functions $\Phi(\lambda) = \Delta_{BC}(\lambda) + \Delta(\lambda)$ and $\Phi_R(\lambda) = \Delta_{BC}(\lambda) + \Delta_R(\lambda)$ are obtained from the interferograms, where $\Delta(\lambda) = \delta_s(\lambda) - \delta_p(\lambda)$ is phase difference between s and p-polarized waves, when the BSWs are excited, and $\Phi_R(\lambda)$ is the reference phase difference. Finally, the phase shift $\delta_{\mathrm{BSW}}(\lambda) = \Delta(\lambda) - \Delta_R(\lambda)$ can be determined.

The analyte is moist air with different RH (aproximatelly from 38% to 80%). The RI is modified by a system of peristaltic pump, hoses and water tank. The moist air is led to the sensing chamber and for control measurement of the RH, a sensor based on Arduino system is employed in the chamber and connected with the computer.

3 Results and discussion

In Fig. 3 (left), the phase shift as a function of the wavelength for different air humidities is shown. As seen, increasing RI causes a red shift of the phase curves. In Fig. 3 (right), the phase shift at the wavelength of λ=532 nm as a function of the RH is shown. To characterize the sensor performance, the sensitivity parameter is determined, which is defined as a fraction between change of sensed parameter and change in parameter of the analyte. In this case, these are the phase shift δ_{BSW} and the RH, respectively

$$S_\delta = \frac{\Delta\delta_{BSW}}{\Delta \mathrm{RH}}. \tag{1}$$

The sensitivity here is a quadratic function of RH with its maximum value of $S_\delta = -0.0294$ rad/%RH for the RH of aproximatelly 58 %.

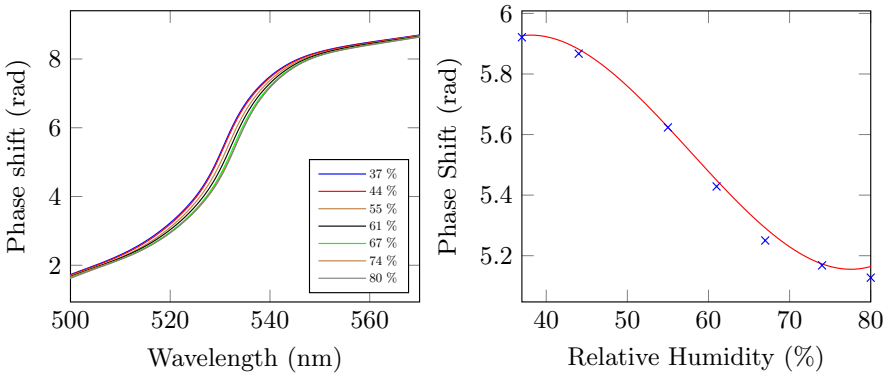

Fig. 3: Left: phase shift as a function of the wavelength. A red shift is occurring with the increasing air humidity. Right: phase shift as a function of the relative humidity. Wavelength $\lambda = 532$ nm, the red curve is a polynomial fit (R^2=0.9965).

In Fig. 4 (left), the derivative of the phase shift as a function of the wavelength for different air humidities is shown. Positions of the derivative maxima

correspond to the wavelengths on which the BSWs are excited. These wavelengths can be detected as a function of the RH (Fig. 4 (right)). In this case, the sensitivity can be expressed as

$$S_\lambda = \frac{\Delta\lambda_R}{\Delta \mathrm{RH}}, \tag{2}$$

where λ_R is wavelength related to the extremal value of the phase shift derivative. Here, the sensitivity is also a quadratic function of RH. Its maximum value is $S_\lambda = 0.0940$ nm/%RH at the RH of approximately 58.40 %. Since the change in the RI of moist air due to RH change is very low ($\Delta\mathrm{RI}(\lambda = 532\ \mathrm{nm}, t = 20\ ^\circ\mathrm{C}, p = 101325\ \mathrm{Pa}) \approx 3.6 \cdot 10^{-7}$, obtained by the Ciddor equation [8]), the mechanism of a high response of the proposed sensor is caused by other phenomena. One of the phenomena is probably a water adsorption on the 1DPhC surface [9]. The next work will be focused on the phenomenon of water adsorption and its influence on the sensor response.

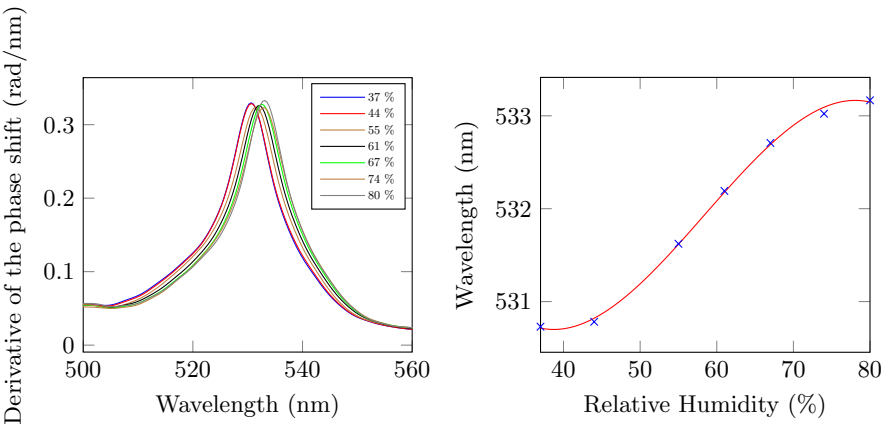

Fig. 4: Left: derivative of the phase shift as a function of the wavelength. Right: wavelength (related to the extreme of the derivative of the phase shift) as a function of the relative humidity. The red curve is a polynomial fit (R^2=0.99765).

4 Conclusions

In this paper, a phase shift detection method based on spectral domain interferometry has been presented. The method has been demonstrated on determining the RH of moist air in a region of 37 % – 80 % by measuring the phase shift induced by the BSWs. In a region of approximately 45 % – 70 %, the phase shift changes linearly with the RH and the highest achieved sensitivity is -0.029 rad/%RH for the RH of approximately 58 %. In the case of measuring the

wavelength corresponding to the extremal value of the spectral derivative, the achieved sensitivity is 0.094 nm/%RH for the RH of approximately 58.40 %. Next work will be focused on the mechanism of water adsorption on the 1DPhC surface. Results are important from point of view of new sensors development and design.

ACKNOWLEDGMENTS

The work was supported by ERDF/ESF project New Composite Materials for Environmental Applications (No. CZ.02.1.01/0.0/0.0/17_048/0007399) and by the student grant system through project SP2021/64.

References

1. Němec, H., Kužel, P., Duvillaret, L., Pashkin, A., Dressel, M., Sebastian, M.T.: Highly tunable photonic crystal filter for the terahertz range. Opt. Lett. **30**(5), 549–551 (2005).
2. Dutta, H.S., Goyal, A.T., Srivastava, V., Pal, S.: Coupling light in photonic crystal waveguides: A review. Photonics and Nanostructures - Fundamentals and Applications **20**, 41–58 (2016).
3. Gryga, M., Ciprian, D., Gembalova, L., Hlubina, P.: Sensing based on Bloch surface wave and self-referenced guided mode resonances employing a one-dimensional photonic crystal. Opt. Express **29**(9), 12996–13010 (2021).
4. Gryga, M., Ciprian, D., Hlubina, P.: Guided-mode resonance based humidity sensing using a multilayer dielectric structure. Opt. Express **28**(20), 28954–28960 (2020).
5. Gryga, M., Ciprian, D., Hlubina, P.: Bloch Surface Wave Resonance Based Sensors as an Alternative to Surface Plasmon Resonance Sensors. Sensors **20**(18), (2020).
6. Sinibaldi, A., Anopchenko, A., Occhicone, A., Michelotti, F., Danz, N., Munzert, P., Schmieder, S., Sonntag, F., Chandrawati, R., Rana, S., Stevens, M.M., Napione, L.: Label-free detection of angiogenesis biomarkers using Bloch surface waves on one dimensional photonic crystals. In: 1st Workshop on Nanotechnology in Instrumentation and Measurement pp. 57–60, IEEE, Italy (2015).
7. Hlubina, P., Luňáček, J., Ciprian, D., Chlebus, R.: Windowed Fourier transform applied in the wavelength domain to process the spectral interference signals. Opt. Commun. **281**(9), 2349–2354 (2008).
8. Ciddor, P.E.: Refractive index of air: new equations for the visible and near infrared. Appl. Opt., **35**(7) 1566–1573 (1996).
9. Du, B., Yang, D., Ruan, Y., Jia, P., Ebendorff-Heidepriem, H.: Compact plasmonic fiber tip for sensitive and fasthumidity and human breath monitoring. Opt. Lett. **45**(4), 985–988 (2020).

List of publications

1. Kanok, R., Hlubina, P., Gembalová, L., Ciprian, D.,: Efficient optical sensing based on the phase shift of waves supported by a 1D photonic crystal. Sensors, (submited).

Investigation of abrasive waterjet tangential turning

Adam Štefek and Libor Hlaváč

Department of Physics, FEECS,
VSB – Technical University of Ostrava, 17. listopadu 15,
708 00 Ostrava – Poruba, Czech Republic
{ste0297, libor.hlavac}@vsb.cz

Abstract. This paper presents investigation of the abrasive waterjet turning (AWJT). Purpose of the article is to investigate significant parameters of the turning process and to evaluate their impact on the turning product. Based on the previous research made in this field, the multi-pass tangential turning method was selected. Rotational speed doesn´t seem to have a significant impact on the AWJ turning process. However, relative position of the jet is a key parameter to improve efficiency of the process. Increasing of the lateral jet shift causes the volume of the material removed increase until the most sufficient impact angle is reached. These findings need to be extended to adjust the AWJT. Without these improvements, the comparison of the jet to the traditional technologies is inappropriate.

Keywords: Abrasive waterjet, Turning, Steel, Unconventional technologies

1 Introduction

One of the special application of AWJ is when the jet is eroding a rotating specimen (AWJT - abrasive waterjet turning). There are new variables associated with the rotational movement of the specimen and with the relative positon of the focusing tube. These are: traverse speed, rotational frequency, direction of rotation, lateral jet shift.
In terms of the relative position of the tube to the surface, we distinguish the radial mode and the tangential mode of the AWJT. If we put focusing tube right above the symmetry axis of a specimen and we move the jet only along this axis, we speak about the radial mode turning (Fig. 1). If the focusing tube is placed arbitrarily above surface and the impact angles are various (in extreme case tangential to the surface), we speak about the tangential (or offset) mode (Fig. 2). In this case, the lateral jet shift is a new variable influencing performance of the jet.

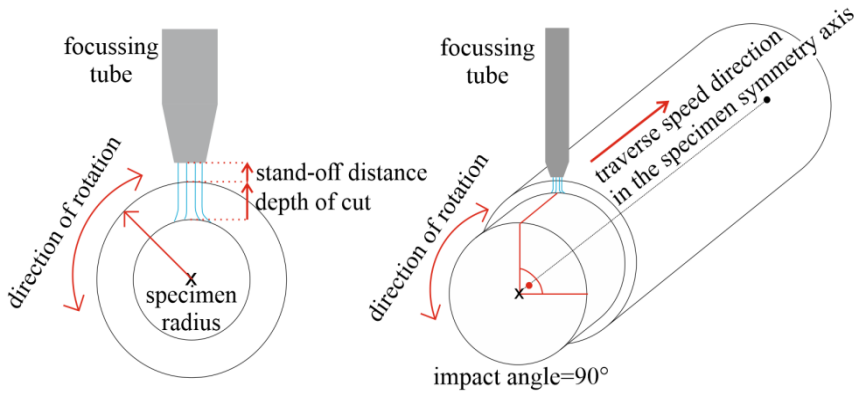

Fig. 1. Scheme of the radial AWJT mode

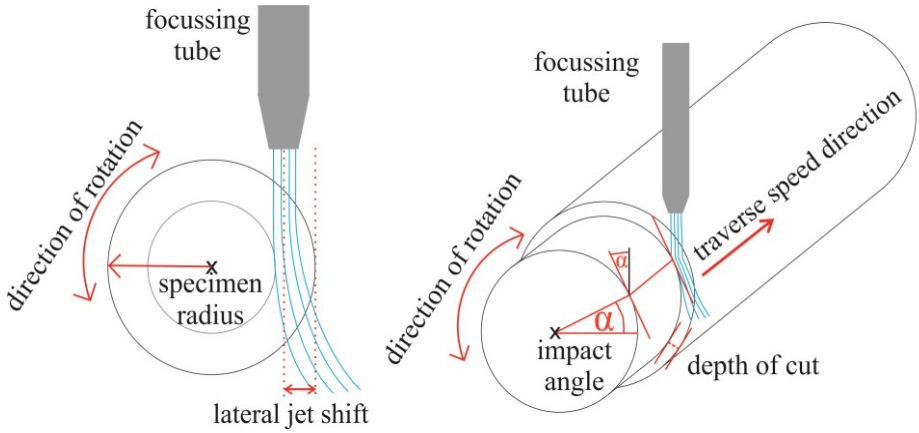

Fig. 2. Scheme of the tangential AWJT mode

Many investigations were already made, some of the most useful information from these articles are listed below:

- Material removal rate of aluminium 6061-T651 increases with growing of the lateral jet shift and the traverse speed until the limit values were reached
- To obtain required diameter of the specimen with high material removal rate, several passes of the jet have to be made with a certain traverse speed
- Most profitable strategy is to use the lateral jet shifts significantly higher than the jet diameter to increase the material removal rate. In order to create the smoother surface, one final improving pass with a lower lateral jet shift should be performed.

This paper is focused on a better understanding of the tangential mode of the AWJT process. Its aim is to find the essential parameters and to evaluate the whole process of the tangential mode of the AWJT.

2 Theoretical background

Compared to the AWJ cutting, several new variables were defined: the direction of rotation, the rotational speed, the lateral jet shift and the radius of specimen.

2.1 Traverse speed and rotational speed

Both traverse speed and rotational speed define jet exposure time. Since the traverse speed determines how many particles will hit the surface of the specimen, it plays the dominant performance role. Influence of the rotational speed was investigated.

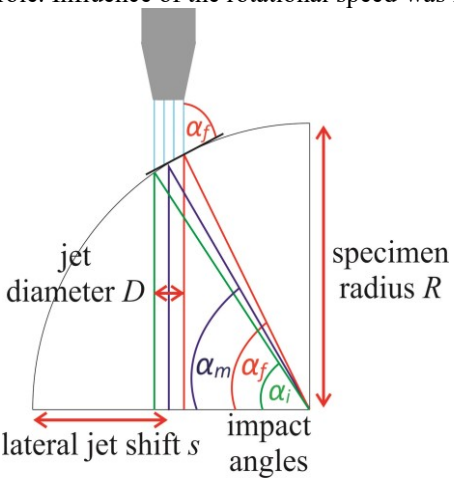

Fig. 3. Relation between lateral jet shift and impact angle

2.2 Lateral jet shift

It is a variable which is relevant only for the tangential AWJ turning. The lateral jet shift (s) is a machine pre-set length of the feed into the material (Fig. 3). In case of using the multi-pass tangential AWJT mode, number of the lateral shifts into material (N_s) is set also. The distance which is counted as a sum of machine made lateral shifts into the material is called the cumulative lateral jet shift (s_c).

The lateral jet position inside the specimen diameter (JP) indicates the radial distance between the edge of the sample and the axis of the center of the focusing tube. It reflects the volume of material removed during every single pass.

Because the jet itself has a diameter, there is not defined a single angle of impact but a set of them. This angle of impact depends also on the diameter of the specimen. The bigger the sample diameter is the lower is the set of impact angles for a selected shift. We can define three impact angles based on a diameter of the specimen and relative position of the focusing tube (Fig. 3). These are α_i - the initial angle of impact, α_m - the medium angle of impact, α_f - the final angle of impact. Based on the literature studied, multi-pass tangential AWJT mode was chosen for experiment.

3 Experimental setup

The first experiment was made to evaluate influence of traverse speed and rotational frequency and the second one to evaluate influence of different lateral jet shifts and angles of impact. The multi-pass tangential mode AWJT was used in all experiments.

The experiments were performed in the Laboratory of Liquid Jet at the VŠB Technical University of Ostrava. The abrasive waterjet cutting table PTV WJ1020-1Z-EKO (PTV s.r.o., Hostivice, Czech Republic) and the pump HSQ 5X (Flow Int., Seattle, USA) were used with the invariables setup summarized in Table 1.

Table 1. Setup of basic experimental variables of the abrasive waterjet (the fixed ones)

Experimental pressure (MPa)	380
Water orifice diameter (mm)	0.25
Focussing tube diameter (mm)	1.02
Abrasive mass flow rate (g/min)	250
Abrasive material average grain size	80 MESH
Type of abrasive	australian garnet

Since these experiments serve as the new investigation of the process, the common 1.0038 steel grade was used (Table 2). The sample original diameter is 20 mm.

Table 2. Mechanical properties of the used steels

steel grade (W.Nr.)	1.0038
Tensile strength σ_m (MPa)	400
Yield strength σ_y (MPa)	260
Young's modulus *E* (GPa)	207
Brinell scale *HB*	130

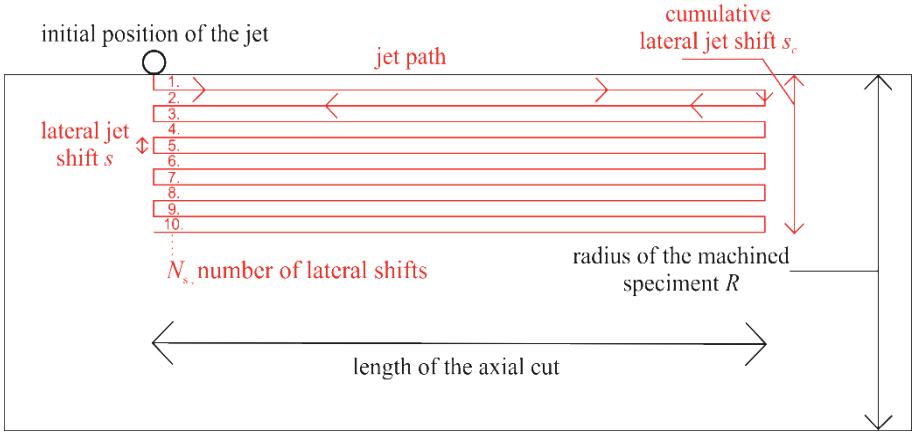

Fig. 4. Top view of the jet trajectory during AWJT of the rounded specimen

4 Results and discussion

Twelve traverse speed and rotational frequency combinations were investigated (rotational frequency 250 RPM, 500 RPM and 1000 RPM). Lateral jet shift was set to 0.5 mm with total of 9 lateral jet shifts into material. In case of ideal volume removal, we should reach 11 mm as final sample diameter. The results are shown in fig. 5.

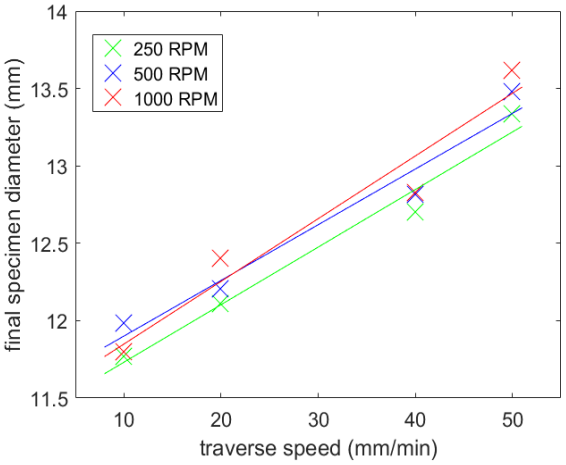

Fig. 5. Diameter of the specimen for certain experimental setup

Influence of different lateral jet shifts on material removed was also tested (0.5 mm 10 shifts, 0.75 mm-6 shifts, 1 mm-5 shifts). The results are shown in fig. 6.

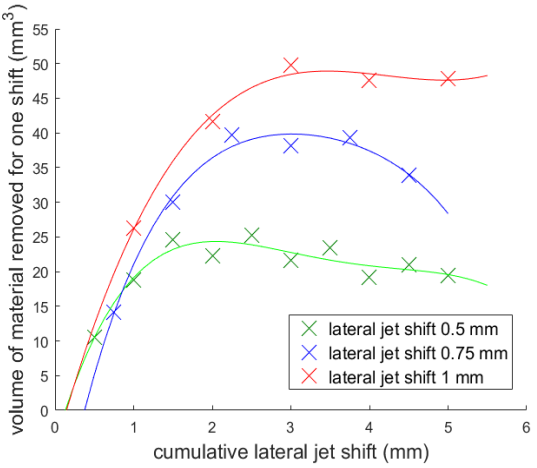

Fig. 6. Dependence of the material removed on the jet cumulative lateral jet shift

The essential information resulting from these figures are given below.

- The traverse speed plays a dominant role for the volume removed compared to the rotational speed. The increasing traverse speed lowers the material removed

volume. The rotational speed doesn´t seem to play a significant role in the AWJT machining.
- Theoretical volume of the specimen to be removed depends on the lateral jet shift for the circular specimens. For a small lateral jet shift (0.5 mm) the jet has enough time to machine a specimen sufficiently. Therefore, the decrease of the volume removed with an increasing total lateral jet shift is apparent.

5 Conclusion

The aim of this research was to evaluate some of the parameters of the AWJT process. Several experiments were performed to test the effect of the traverse speed and the rotational frequency. The effect of the rotational frequency has proven to be low in line with previous findings of other researchers. In addition, the effect of the relative position of the abrasive waterjet and the rotating sample was tested. In almost all experiments the material removal was not ideal and the jet position itself did not guarantee that the desired sample diameter was obtained. However, the experiments enable to determine approximately at what angle of impact/lateral jet shift the highest material removal occurre. The influence of the studied parameters onto the turning process of special materials, such as composites, will be further investigated.

References

1. Ansari, A.I.; Hashish M.; Ohadi, M.M. Flow visualization study of the macromechanics of abrasive-waterjet turning. Experimental Mechanics. 1992, 32, 358–364.
2. Ansari, A.I.; Hashish, H. Effect of Abrasive Waterjet Parameters on Volume Removal Trends in Turning. Journal of Engineering for Industry. 1995, 117, 475–484.
3. Hlaváč, L.M.; Paličkа, P.: Testing of parameters for turning by abrasive water jet. In: Proceedings of the 18th International Conference on Water Jetting, Gdańsk, Poland, 13-15 September 2006; Longman, P, Ed.; BHR Group: Cranfield, UK, 2006; pp. 123-128.
4. Axinte, D.A.; Stepanian, J.P.; Kong, M.C.; McGourlay, J. Abrasive waterjet turning—An efficient method to profile and dress grinding wheels. Int. J. Mach. Tools Manu. 2009, 49, 351–356.

Publications where the results have been published

The results of this research were not published yet, however the article about this topic was written and it is in approval procedure (journal *Materials*).

Awards and grants of the PhD student

This research was funded by the Ministry of Education, Youth and Sports of the Czech Republic, project numbers SP2020/45 and SP2021/64.

AWJ Cutting of Steel – Diagnostics of Vibration Signals

Martin Tyč and Irena Marie Hlaváčová[0000−0002−3621−2449]

Department of Physics, FEECS,
VSB – Technical University of Ostrava, 17. listopadu 15,
708 00 Ostrava – Poruba, Czech Republic
{martin.tyc.st, irena.hlavacova}@vsb.cz

Abstract. In this paper, we measure vibration by 3 accelerometers fastened on the workpiece. We are looking for a suitable tool and procedure for monitoring undercuts or other problems such as cutting without abrasive or inappropriate parameters of the jet during the abrasive water jet (AWJ) cutting of hard-machined materials. Accelerometers are fastened to the workpiece by a special block that we designed for this purpose. After measuring data by the program Signal Express, we process this data in LabVIEW. The LabVIEW Sound and Vibration Toolkit were used for online vibration monitoring. We focus on the analysis of the relationship between the RMS and traverse speed.

Keywords: Abrasive Waterjet, Cutting Monitoring, Accelerometer Signals Processing, RMS, Traverse Speed.

1 Introduction

Abrasive water jet (AWJ) is one of the progressive technologies of machining technologies. This technology has already spread to many industries. The beginning of AWJ dates back to the end of the 70s of the 20th century, when Hashish started adding abrasive to the jet, and thus achieved high efficiency so that in the early 80s it was possible to start cutting steel, concrete, etc. [1]. The main advantages of AWJ are the insignificant thermal influence of materials, practically zero increase in the internal stress of the material, and the versatility of the jet as a tool capable of cutting almost any material. AWJ machining technology is high tech due to developments in many companies. However, due to the expanding market and increasing demand for cutting by AWJ such as 3D machining and machining of hard-machine materials, it is necessary to develop technology for monitoring the cutting process.

Many authors deal with this topic, e.g. Axinte monitors the water jet using acoustic emission (AE) and dynamometer [2], Krenický measures vibrations on various parts of the machine [3], Hreha measures vibrations on the workpiece [4] and Mikler monitors undercut using acoustic emissions [5]. But so far commercially manufactured monitoring equipment has not been launched on the market. For work in the industry as well as in laboratories studying AWJ, it would be a great benefit to have technology capable of online monitor the depth of cut of the workpiece. The abrasive water jet is able to cut thick materials such as steel or rock, but for very thick or hard-machine materials it can

be difficult to correctly determine the parameters of the jet. Then it is important to set the parameters of AWJ for an economically tolerable cut. Separating cut (without the need for cutting quality), is widely used and it is necessary to cut the shortest time as it is possible. Online monitoring of the cut should provide clear answers such as the depth of the jet during a borehole, if during cutting occur undercut, or whether the jet cuts through the material unnecessarily long and uneconomically.

In this paper, we deal with the measurement of vibration using piezoelectric accelerometers fastened to the workpiece. These vibrations should help for monitoring the cut of hard-machine material and thus save on abrasive and time when working in the laboratory. We performed the experiments in the laboratory of AWJ of the Department of Physics VŠB-TUO, where a measuring system from National Instruments and piezoelectric accelerometers from PCB were used to determine the relationship between vibrations and cuts. Our goal was to find the relationship between vibration and the cut. From the results, we design a system for online monitoring of cuts, during cutting thick or hard-machine materials. An important part of optimizing the drilling and cutting of hard-machine materials is to be aware of the relationship between the interaction of the jet with the material and the observed vibroacoustic emissions and to identify their manifestations in the measured signals.

During the cutting of materials with an abrasive water jet, a water jet is used as the medium which carries the abrasive. Abrasive is a component of the jet that erodes the material. The abrasive particles fall on the surface of the material, where the material is removed by erosion. The kinetic energy of these particles is partly used to break the bonds of the material, the part is transferred to the surroundings in the form of acoustic oscillations, part of the energy is converted into heat, etc. When the machine has incorrectly set parameters, the material is not cut, less energy is consumed to breaking bonds and the more energy spreads through the material in the form of acoustic emissions. These emissions can be measured using accelerometers.

Please note that the first paragraph of a section or subsection is not indented. The first paragraphs that follows a table, figure, equation etc. does not have an indent, either.

2 Materials and methods

The technical equipment of the AWJ laboratory of the Department of Physics VŠB Technical University of Ostrava is the abrasive water jet PTV WJ1020-1Z-EKO and the high-pressure pump PTV 19/60; with pressure up to 415 MPa. A measuring system from National Instrument is used to record the signals from the accelerometers. The recording measurement was recorded on an assembly consisting of a five-slot National Instruments PXIe-1073, a NI PXIe-4492 data acquisition module, and an NI PXI-Express Card 8360, which is used to connect a PC to an A/D converter. We use Signal Express software from National Instrument for data recording, and Labview Sound and Vibration Assistant for online signal analysis and recording.

We measured vibrations using three PCB 352C33 accelerometers. To connect the accelerometers to the workpiece, we made a special block where the accelerometers are arranged in three mutually perpendicular axes [X, Y, Z]. This block is fastened to the

workpiece with a single screw (Fig. 1). The advantage of the block lies in the simplicity and speed of mounting the three accelerometers on the workpiece and the possibility to keep the mounting of the accelerometers in the desired position even if the body shape is irregular. In an upgrade version the block was equipped by a special magnet for attaching accelerometers block. The additional upgrade is designed to simplify connection of accelerometers to ferromagnetic materials, making measurement more flexible. Its advantage is non-destructive way of attachment.

Fig. 1. A figure caption is always placed below the illustration. Short captions are centered, while long ones are justified. The macro button chooses the correct format automatically.

We used abrasive Australian garnet mesh 80, water pressure was 380 MPa, nozzle diameter 0.25 mm, focusing tube length 75 mm, and focusing tube diameter 0.76 mm. The standoff distance was 2.5 mm. The signal sampling frequency was 30 kHz.

The measurement was realized in the original version, i.e. using a measuring block fixed with a screw. The cut material had dimensions (109x168) *mm* and the block with accelerometers was attached in the corner of the workpiece. The abrasive water jet cut the material in the X direction, the Y direction was the second lateral accelerometer, Z was the axial (vertical) accelerometer, i.e. parallel with the jet axis. We always measured four sections, 25 mm long, cut with four different traverse speeds. The speeds were increasing, they were designed to produce kerfs with degrading quality of the cut (see Table 1). The measurement cycle was repeated on the same material for all measured thicknesses, the respective limit traverse rates were recalculated for each thickness. The material used for the research was structural steel ČSN EN 10025-2.

Table 1. Traverse rates used for different thicknesses and quality of cutting.

Cutting quality	Thickness in mm	10	15	20	25	30
Excellent	Traverse speed v_p	50	37.5	37.5	25	20
Good		100	75	75	50	40
Separating cut		150	112.5	112.5	75	60
Limit cut		165	123.75	123.75	82.5	66

The vibrations measured by the accelerometers were evaluated in the LabView software, and root mean square (RMS) of the assigned section was calculated. The RMS is defined in equation (1).

$$y_{ef} = \sqrt{\frac{1}{T}\int_0^T y^2 \, \mathrm{d}t} \tag{1}$$

The RMS value is a measure of the energy transmitted by a signal. It can only acquire positive, non-zero and finite values.

The data were statistically processed using the Shapiro - Wilk test, the Bartlett test and the Kruskal – Wallis test. The results will be discussed in the following section.

3 Results and discussion

The results of the above-mentioned statistical tests proved that the RMS changes statistically significantly with the traverse speed, therefore, it can be related with the quality of the cut.

Fig. 2 presents a graph of the RMS dependence on the traverse speed. Each material thickness has its own curve. We can see that the general trend is that RMS increases with the growing traverse speed. In the 20 mm thickness curve we can see that the RMS dropped down for the fastest cut. However, this exception might appear due to inhomogeneities in the material, or other similar unexpected event that caused it. We should note that the separating speed is only by 10% lower than the limit one.

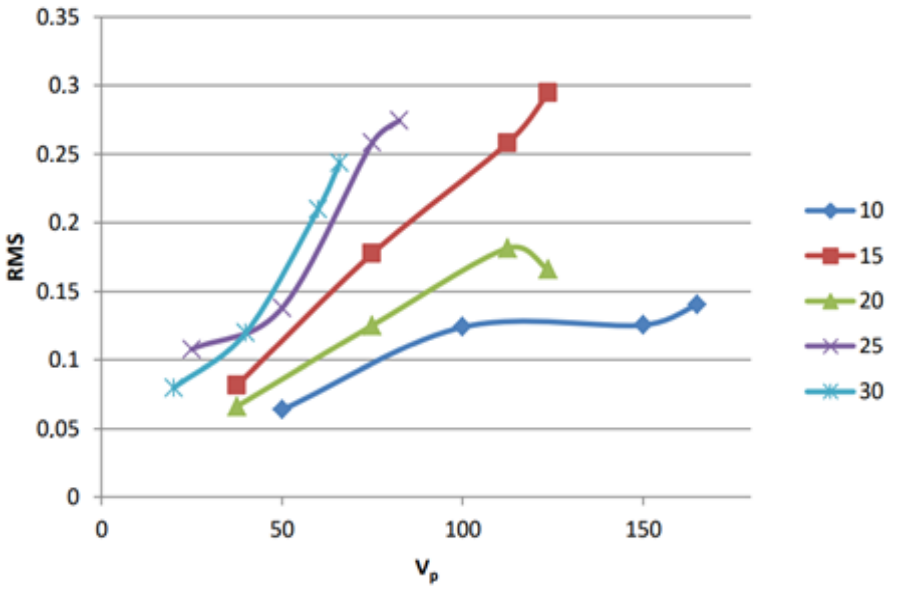

Fig. 2. RMS change with traverse speed for different thicknesses of steel

Furthermore, we wanted to find out, following a thorough statistical analysis, whether the measurement of vibrations on the workpiece is dependent on the axis [X, Y, Z], from which we measure vibrations.

In terms of RMS level, it does not matter in which direction the accelerometers are located. This means that it is statistically best to measure the RMS level with the accelerometer Y (surface parallel to the cutting surface) and the worst with the accelerometer X (cutting direction). For more complex cut shapes, it is definitely more advantageous to measure more accelerometers. For linear cuts, it is sufficient to have one accelerometer mounted on the workpiece surface, i.e. in the jet axis.

4 Conclusions

From the experiments, we described the relationship between RMS and traverse speed. We used statistical analysis to confirm this thesis. It was confirmed that the relationship of the RMS to the traverse speed is statistically significant.

To find out which accelerometers would be the most advantageous to measure vibrations on the machined material, we found that in terms of the RMS level, it does not matter which accelerometer we use to measure vibrations, however, it was statistically significantly proved, that it is best to measure with the accelerometer Y and the worst with the accelerometer X (which is against the direction of the cut) in terms of the RMS level in the laboratory in Ostrava. For more complex cut trajectories or 3D cuts, we recommend measuring with a system of three accelerometers [X, Y, Z], and for simpler linear cuts it is sufficient to measure with one Z accelerometer mounted on the material surface so that the accelerometer detects vibrations parallel to the jet.

5 Acknowledgments

The work was supported by the student grant system through project SP2021/64.

References

1. Kaličinský, J.. Řízení technologických parametrů kapalinového paprsku při porušování materiálů [online]. Ostrava, 2009. Doctoral Thesis. Vysoká škola báňská -Technická univerzita Ostrava. In Czech
2. Axinte, D.A., Kong., M.C.: An integrated monitoring method to supervise waterjet machining. CIRP Annals [online]. 2009, 58(1), 303-306 DOI: 10.1016/j.cirp.2009.03.022. ISSN 00078506.
3. Krenický, T., Rimár, M.: Monitoring of vibrations in the technology of AWJ. Key Engineering Materials [online]. 2011, 2012(496), 229-234. DOI: 10.4028/www.scientific.net/KEM.496.229. ISSN 1662-9795.

4. Hreha, P., Radvanská, A., Knapčiková, L., Królczyk, G., Legutko, S., Królczyk, J., Hloch, S., Monka, P. Roughness parameters calculation by means of on-line vibration monitoring emerging from AWJ interaction with material. Metrology and Measurement Systems [online]. 2015, 22(2), DOI: 10.1515/mms-2015-0024. ISSN 2300-1941.
5. Mikler, J.: On use of acoustic emission in monitoring of under and over abrasion during a water jet milling process. Journal of Machine Engineering [online]. 2014(142), 104-115, last accessed 2021/7/20

Analysis of systemic scleroderma patient dataset*

Tomáš Anlauf[1], Miloš Kudělka[1], Anna Petráčková[2], and Eva Kriegová[2]

[1]Department of Computer Science, FEECS,
VSB – Technical University of Ostrava, 17. listopadu 15,
708 00 Ostrava – Poruba, Czech Republic
[2]Palacky University Olomouc, Hnevotinska 3, 775 15 Olomouc, Czech Republic
tomas.anlauf.st@vsb.cz

Abstract. In this paper, we describe the procedure and present the results of the analysis of a dataset of patients with systemic scleroderma. The aim of the analysis was to classify the data based on three attributes of interest. Before classification, the data needed to be preprocessed into a suitable form. A large number of generally available models were systematically tested, from which the three that showed the best classification quality were selected. In addition to the classification itself, it was also an important task to select those attributes that are relevant for the classification of each attribute of interest.

Keywords: Systemic scleroderma · Classification · Data analysis

1 Introduction

This paper serves as a description of the procedure and presentation of the results in the analysis of a dataset of patients with systemic scleroderma. The data were provided by a collaborating team from the Faculty of Medicine of Palacky University in Olomouc. The aim of the analysis was to classify the data based on three attributes of interest. Before classification, the data needed to be preprocessed into a suitable form. After the classification was performed, the task was further to get an overview of the combination of significant attributes that contribute most to a more accurate classification.

The work is divided into several sections. The first section is devoted to the description and preprocessing of the dataset into a form suitable for obtaining the best results. The second section gives a brief overview of the classification models that, in the experiments, were selected from a number of tested models and showed the best classification quality. This section also includes a listing of the libraries in which the selected models can be found. The last section discusses the actual experiments that were performed with the models.

* The clinical data was provided by Pavel Horak of the Third Department of Internal Medicine – Nephrology, Rheumatology and Endocrinology, University Hospital in Olomouc. The study was supported by the Ministry of Healthy Czech Republic (NU21J-01-00017), MH CZ-DRO (FNOL, 00098892), and IGA_LF _2021 _015.

2 Dataset description

The study cohort consisted of 86 Caucasian patients from a single rheumatology center in Olomouc, Moravia region of the Czech Republic, with autoimmune diseases. All enrolled RA/SLE/SSc patients met the 2010 ACR/EULAR classification criteria for RA, the ACR classification criteria for SLE, and the 2013 ACR/EULAR classification criteria for SSc [8], respectively. To exclude heterogeneity due to the activity and inactivity of the diseases, only cases with active phenotypes of the disease classified according to common activity scores (Disease Activity Score in 28 joints, DAS28; SLE Disease Activity Index, SLEDAI; revised European Scleroderma Trials and Research group (EUSTAR) index) were included: RA (n=36, DAS28 $\geq$ 3.2), SLE (n=28, SLEDAI$>$ 6), and SSc (n=22, revised EUSTAR index $>$ 2.25).

Each patient record contains 104 attributes. Out of this total number of attributes, 35 attributes are numeric, and 67 attributes are categorical. The classification will be done based on 3 attributes, namely *Form of SSc.*, *Death* and *Lung impairment.*

The frequencies of records for the form of Ssc are 36 limited cases and 22 diffuse cases. For the death attribute, 5 patients have passed away, and 53 are still alive. Lastly, the number of patients with lung impairment was 43, and 15 patients have no lung impairment.

The correlation matrix of all numerical attributes is shown in Fig. 1

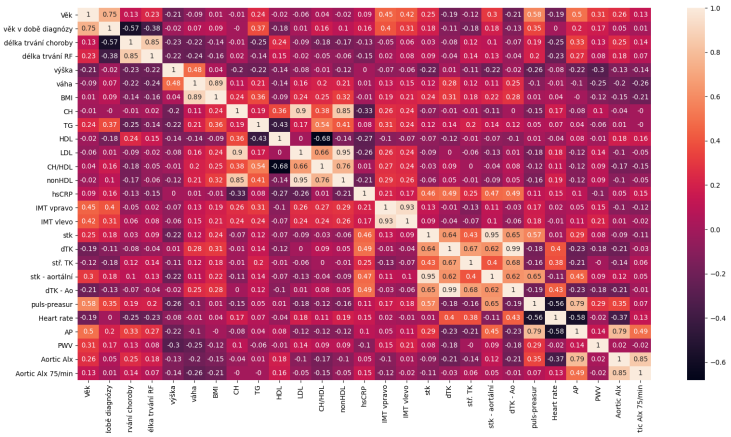

Fig. 1. Correlation matrix of numerical attributes of the patient dataset

Dataset preprocessing The data was processed before the actual learning. Since the dataset is not very large, it was possible to review the dataset and cor-

rect grammatical or value errors manually. The dataset contained duplicate attributes, categorical attributes specified numerically and verbally, and attributes with many missing values. These attributes were removed from the dataset as they did not provide any relevant new information for classification.

Some attributes contained missing values that had to be filled. For such numeric attributes, the missing values were filled by averaging all other values. For categorical attributes, a treatment was chosen that fills in the missing value with the most frequently occurring category and, in addition, creates a new attribute that identifies the rows with the missing value by using a binary value of one.

In the next step, we removed outliers. The z-score was used to determine them. The threshold of this score was set so that only patients whose values differ significantly from the others were removed. Two records were removed in this way.

Since the *sklearn*[5] library models can only operate with numeric attributes, all categorical attributes were converted to numeric attributes. Most categorical attributes contain only two categories. Those attributes that contained more were not ordinal and were therefore binarized, i.e., a new attribute was created for each category that used binary values to determine whether or not a given patient fell into the category. Some attributes had one category expressed by multiple categories. Such categories were merged into one.

3 Classification models for the patient dataset

This section will contain a brief description of used models and libraries. Since the dataset does not contain a test set, it was necessary to create one from the training set. As mentioned in Section 2, the classification will be done according to three attributes. Almost all models, methods for balancing the dataset, and metrics for measuring the quality of the classification were used from the machine learning library *scikit–learn* for Python, except for the XGBoost model, which is available in the XGBoost library[3].

The models used are RandomForest, GradientBoost, and XGBoost. The RandomForest model for classification is made up of a combination of a number of classification trees and has been published by Breiman[1]. Each of these trees makes a prediction and the resulting class is determined based on a vote or as an average of the probabilities.

Gradient Boost is a model that utilizes the boost method to improve its performance. It trains weak models(most often decision trees) sequentially and additively and uses them to minimize a loss function that indicates the magnitude of the error between the actual and predicted values. The model was developed by Friedman [6].

The last model used is XGBoost. This is a variant of Gradient Boosting but optimized for speed and performance. This model was developed by Chen and Guestrin[4] at the University of Washington and is very popular in machine

learning competitions for its prediction quality and speed. It is also considered a state-of-the-art model as far as small to medium datasets are concerned.

The classification was also tested with other algorithms that are not based on decision trees, but their classification quality showed almost the same or worse results. Since the dataset is imbalanced for some classes, the algorithms SMOTE(It generates the virtual training records by linear interpolation for the minority class.)[2], and ADASYN(It uses a weighted distribution for different minority class examples according to their level of difficulty in learning, where more synthetic data is generated for minority class examples that are harder to learn compared to those minority examples that are easier to learn.)[7] were tried to improve the model training quality. Both algorithms are available in Python as a part of the *imblearn* library.

4 Experiments

This section focuses on the actual experiments that were performed on the patient dataset, the quality of the classification, and the subsequent extraction of the list of attributes that contribute most to the correct classification of the records. Accuracy and area under ROC curves (AUROC) metrics were used to measure quality. The classification was tested with all combinations of classification and balance algorithms listed in 3. From these combinations, those that give the best results for the classification of a particular attribute are selected. To increase the confidence of the results, cross-validation was applied by splitting the records into five subsets.

The classification quality results for each attribute of interest are presented successively in Tables 1.

Table 1. Classification quality of each attribute of interest

Attribute \ Model	RandomForest		GradientBoost		XGBoost	
	Accuracy	AUROC	Accuracy	AUROC	Accuracy	AUROC
Form of SSc	0.749	0.843	0.711	0.769	0.752	0.801
Death	0.991	1.000	0.908	0.964	0.991	1.000
Lung impairment	0.965	0.966	0.873	0.888	0.897	0.945

Even though XGBoost is considered a state-of-the-art model for the classification of small to medium datasets, the best results out of all the models used were given by the RandomForest model. Since all the models used a search for attributes that split the dataset in the best way possible with respect to the attributes of interest in their learning process, it was possible to obtain a list of important attributes with their weights directly from the models after the models were trained. The weights from each training of all the algorithms were

averaged, and the top ten most important attributes for each attribute of interest are listed in Table 2. The learning behavior of the models is partially random, so the weights and order may change slightly.

Table 2. The most important attributes for classification of each attribute of interest

Form of SSc		Death		Lung impairment	
Attribute	Weight	Attribute	Weight	Attribute	Weight
anticentromerove	0.070	hsCRP	0.179	GK	0.237
CH	0.063	ENA - positivity	0.083	AP	0.062
GK	0.059	LDL	0.072	DMARDs	0.055
hsCRP	0.052	CH	0.067	vit D	0.039
BMI	0.045	nonHDL	0.058	anticentromerove	0.029
duration of the disease	0.045	HDL	0.030	Aortic Alx	0.026
ANA type - anticentromerove verbally	0.034	dTK	0.030	puls-preasur	0.023
nonHDL	0.032	IMT left	0.028	TG	0.022
LDL	0.028	Scl70	0.028	Aortic Alx 75/min	0.019
HDL	0.026	str. TK	0.025	PH	0.017

5 Conclusion

In this paper, the procedure and presentation of results in the analysis of a dataset of patients with systemic scleroderma were described. The aim of the analysis was to classify the data based on three attributes of interest. A large number of generally available models were systematically tested, from which three were selected that showed the best classification quality.

These selected models included RandomForest, GradientBoost, and XGBoost. Of these three models, RandomForest, together with the combination of the SMOTE balance algorithm, achieved the best classification quality, achieving accuracies ranging from 72 - 77% for Form of SSc, 99% accuracy for Death, and 93 - 97% accuracy for Lung impairment. To examine the attribute weights from the models, the most important attribute for the classification of Form SSc was found to be the *anticentromerove* attribute, for Death the *hsCRP* attribute, and for Lung Impairment the *GK* attribute.

Literature

[1] Leo Breiman. “Random forests”. In: *Machine learning* 45.1 (2001), pp. 5–32.

[2] Nitesh V Chawla et al. “SMOTE: synthetic minority over-sampling technique”. In: *Journal of artificial intelligence research* 16 (2002), pp. 321–357.

[3] Tianqi Chen. *XGBoost*. URL: `https://scikit-learn.org/stable/index.html` (visited on 2021-07-28).

[4] Tianqi Chen and Carlos Guestrin. "Xgboost: A scalable tree boosting system". In: *Proceedings of the 22nd acm sigkdd international conference on knowledge discovery and data mining*. 2016, pp. 785–794.

[5] Alexandre Gramfort Fabian Pedregosa Gael Varoquaux. *scikit-learn*. URL: `https://scikit-learn.org/stable/index.html` (visited on 2021-07-28).

[6] Jerome H Friedman. "Greedy function approximation: a gradient boosting machine". In: *Annals of statistics* (2001), pp. 1189–1232.

[7] Haibo He et al. "ADASYN: Adaptive synthetic sampling approach for imbalanced learning". In: *2008 IEEE international joint conference on neural networks (IEEE world congress on computational intelligence)*. IEEE. 2008, pp. 1322–1328.

[8] Frank Van Den Hoogen et al. "2013 classification criteria for systemic sclerosis: an American College of Rheumatology/European League against Rheumatism collaborative initiative". In: *Arthritis & Rheumatism* 65.11 (2013), pp. 2737–2747.

Utility of patient similarity networks in assessment of disease activity in rheumatoid arthritis

Ondřej Janča[1], Eva Kriegová[2], Anna Petráčková[2], and Miloš Kudělka[1]

[1]Department of Computer Science, FEECS,
VSB – Technical University of Ostrava, 17. listopadu 15,
708 00 Ostrava – Poruba, Czech Republic
[2]Department of Immunology, Faculty of Medicine and Dentistry, Palacký University
in Olomouc, Hněvotínská 976/3 Olomouc, Czech Republic
ondrej.janca@vsb.cz

Abstract. The aim of this paper is to analyze groups of RA patients based on disease activity assessed by DAS28 and determine, whether the parameters of DAS28 scoring system could be improved with new biomarkers, that would better reflect the disease activity. A panel of 74 serum inflammation-related protein parameters and a panel of 123 clinical parameters were analyzed and two subsets of data were used in a construction of patient similarity networks, in which clusters were detected using the Louvain method. Multiple networks for each dataset were found, visualized and explored. Comparison of the resulting networks and DAS28 system groups shows that DAS28 system could be enhanced with new attributes and emphasizes the necessity of a visualization of the network for finding well-interpretable clusters in it.

Keywords: rheumatoid arthritis, DAS28, patient similarity network, LRNet.

1 Introduction

Rheumatoid arthritis (RA) is a chronic autoimmune inflammatory disease in which immune cells attack the synovium, the inner surface of a protective sheath of articulating joints. This leads to an inflammation of the synovial region and destruction of synovial cells, then in later stages to a cartilage and bone erosion. Later stages of RA are accompanied by a reduced mobility and a severe pain, joint deformities and often require a surgical intervention or a total arthroplasty. As per a recent meta-study, the global prevalence of RA between the years 1980 and 2019 was 0.46%, three times more prevalent in women over men, commonly beginning between ages 30 and 60 in women and in men rarely under the age of 45 [1].

The means of disease activity assessment in RA have been thoroughly investigated and multiple scoring systems have been proposed, of which the most popular is DAS28 [2]. DAS28 relies on evaluation of swelling and tenderness of 28 joints, quantification of blood markers of inflammation – erythrocyte sedimentation rate (ESR) or c-reactive protein (CRP) – and subjective well-being of the patient (as a 0–100 scale).

The aim of this work is to analyze currently defined DAS28 groups of RA patients and assess, whether the parameters of DAS28 scoring system could be improved with

new parameters (biomarkers) from a panel of serum proteins, that would better reflect the disease activity.

In this first phase of the study, the data has been cleaned and processed, with logarithmic values being linearized. After obtaining basic statistical parameters of dataset, the workflow then splitting into two parallel paths, investigating two different subsets of parameters. Subset 1 was selected based on initial clinical knowledge of the data background using a statistical test to find significantly different parameter values among 4 clinical groups of patients and was composed of both PEA and clinical data. Subset 2 was selected after constructing a patient similarity network (PSN) of the PEA dataset and based on the contribution of parameters to the separation of the PSN.

This paper is organized as follows: in the first part in the domain and the methods used are presented in the context of related works, then the datasets are characterized, after which the workflow and methodology are described, followed by the results section. At the end of the conclusions of this work are summed up.

2 Related work

Recent progress in genomics, proteomics and other biomolecular methods sparked a tendency to move from the traditional approach of medicine to a personalized treatment of each individual patient in all diseases, including RA [3]. Understanding of the immune system is crucial for understanding RA and this deepened over the last years as well [4]. PSNs are being frequently employed recently in scientific papers, both by our team [5][6] and others [7]. Previous work of our team already successfully employed this method of analysis to reveal gene expression heterogeneity in RA patients [8] and this paper seeks to assess attributes from a serum protein panel and clinical data in the same regard.

3 Dataset characterization

A panel of 74 inflammation-related serum proteins was quantified through a high-sensitivity Proximity Extension Array (Proseek Multiplex, Olink Bioscience, Sweden) in serum of treated RA patients (n=78), labeled PEA dataset. Data, logarithmical in nature, were linearized (2^x). Additional 123 clinical parameters were provided for each patient by the Third Department of Internal Medicine – Nephrology, Rheumatology and Endocrinology, University Hospital in Olomouc, labeled the Clinical dataset. RA patients were subdivided into 4 groups (I–IV) of interest based on the DAS28 score (no – low – medium – high activity). Clinical data were thoroughly cleaned and preprocessed. Characteristics of the patients are summarized in Table 1.

Table 1. Characteristics of the patients.

Characteristic	Count
Males / Females	15 / 63

Characteristic	Median (min–max)
Age in years	55.5 (27–80)
BMI	24.2 (18.4–36.9)
DAS28	3.1 (0.6–6.7)
Disease duration in years	13.5 (1.0–58.0)
Radiological stage	2 (1–4)
CRP in mg/l	3.9 (0.6–65.0)

4 Methodology

Data cleaning and processing, as well as basic statistical descriptions, were done using Excel. Statistical analyses were performed with Kruskal-Wallis statistical test, automated through an R pipeline. Similarity matrixes and similarity networks were constructed using the LRNet method [9], cluster detection was done using the Louvain method [10] and resulting PSNs were visualized using Gephi [11].

Both the PEA and the Clinical dataset were cleaned and processed. A basic statistical description and general evaluation were done using Excel. After that, two approaches were undertaken.

First, the complete PEA dataset was used to construct a PSN. Based on the analysis of the network 15 parameters were selected and labeled Subset 1: CCL3, CCL11, CCL19, CCL23, CCL25, CCL28, CSF1, CXCL6, FGF19, FGF21, IL-6, sIL-10RB, sTNFRSF9, sTWEAK, VEGFA.

Then the PEA dataset together with several clinical parameters were selected and the patients were split according to a clinical parameter “RA groups”, which discerns the patients according to the stage of progression of the disease. An analysis with Kruskal-Wallis statistical test, automated through an R script, was performed and 14 parameters were selected and labeled Subset 2: CCL7, CCL20, CRP, CXCL1, CXCL9, CXCL10, DAS28, Disease duration, FW, GDNF, IL-6, IL-8, IL-12B, sOPG.

These two subsets were then used in construction of PSNs. For each pair of patients, their similarity can be measured based on a selected combination of preoperative parameters: a multivariate comparison of patients with their similarity being the weight of this comparison. These relationships are naturally described and visualized in a weighted undirected network, in this paper a network of patients describing similarities between them with vertices representing patients and edges represent similarities between them.

PSNs were constructed using the LRNet method, in which a similarity matrix is created based on the Gaussian kernel (Equation 1), then the representativeness of all objects is calculated and based on these values a PSN is constructed, after which

the Louvain method for community detection, based on network modularity optimalization (Equation 2), is used to detect clusters within the network.

$$f(x) = \frac{1}{\sigma\sqrt{2\pi}} e^{-\frac{(x-\mu)^2}{2\sigma^2}} \tag{1}$$

$$Q = \frac{1}{2m}\sum_{ij}\left[A_{ij} - \frac{k_i k_j}{2m}\right]\delta(c_i, c_j), \tag{2}$$

Then the PSN was further optimized by sequentially removing the least contributing parameter from the subset and constructing and analyzing a new PSN. This yielded a final parameter set for each subset. Final PSN for Subset 1 was reached with 7 parameters (CCL11, CCL23, CCL25, CSF1, sIL-10RB, sTWEAK, VEGFA), yielding 8 patterns. Final PSN for Subset 2 was reached with 12 parameters for Subset 2 (CCL7, CRP, CXCL1, CXCL10, CXCL9, DAS28, Disease duration (years), FW, GDNF, IL-12B, IL-6, sOPG), yielding 4 patterns. The final PSNs are presented in Figure 1.

Fig. 1. Final similarity network graphs for Subset 1 (left) and Subset 2 (right), colors distinguishing detected patterns.

Then the two final PSNs were recolored according to the four RA groups of patients, as shown in Figure 2.

Fig. 2. Optimal similarity network graphs of Subset 1 (left) and Subset 2 (right), colors distinguishing RA groups.

5 Conclusion

Multivariate analysis is a key technique for working with real-life biological data and it is a strong tool for unraveling their complex nature. Coupled with standard statistical methodology and domain clinical knowledge this technique proves to be the correct approach in the future, more with nowadays trend towards precision medicine and personalized treatment.

Subset 1, composed of parameters selected without prior understanding of the data domain, provided multiple quality clusters, but these failed to bear any prominent link to the RA groups. This result shows that there are clearly distinguished groups among the patients, that are not accounted for by the current scoring system used to assess the stage of the disease.

Subset 2, composed of parameters selected based on domain knowledge, shows substantial similarity with RA groups. There were 4 clusters were detected, corresponding to the 4 RA groups. The overlap is not perfect though and shows, that several patients might be categorized in a different group, should more parameters be used for their classification than there currently are.

Both results show, that PSNs are a very strong method for real-life data and can provide crucial understanding of otherwise hidden relationships within.

Future work will study the newly detected patient groups, discovered in the analysis of Subset 1, and propose new medical markers, which could open a road to designing a system for architecting a precision, individual treatment of individual patients.

6 Acknowledgement

The clinical data was provided by Pavel Horak and Martina Skacelova of the Third Department of Internal Medicine – Nephrology, Rheumatology and Endocrinology, University Hospital in Olomouc. The study was supported by the Ministry of Healthy Czech Republic (NU21J-01-00017), MH CZ-DRO (FNOL, 00098892), and IGA_LF_2021_015.

7 References

1. Almutairi, K. N.: The global prevalence of rheumatoid arthritis: a meta-analysis based on a systematic review. Rheumatol Int (41), 863–877 (2021).
2. van der Heijde, D.M., van 't Hof, M., van Riel, P. L., van de Putte, L. B.: Development of a disease activity score based on judgment in clinical practice by rheumatologists. The Journal of rheumatology 20(3), 579–581 (1993).
3. Song, X, Lin, Q.: Genomics, transcriptomics and proteomics to elucidate the pathogenesis of rheumatoid arthritis. Rheumatol Int 37(8):1257-1265 (2017).
4. Weyand, C. M., Goronzy, J. J. The immunology of rheumatoid arthritis. Nature immunology 22(1), 10–18 (2021).
5. Turcsanyi, P., Kriegova, E., Kudelka, M., Radvansky, M., Kruzova, L., Urbanova, R., Schneiderova, P., Urbankova, H., Papajik, T.: Improving risk-stratification of patients with chronic lymphocytic leukemia using multivariate patient similarity networks. Leukemia research 79, 60–68 (2019).
6. Dyskova, T., Kriegova, E., Slobodova, Z., Zehnalova, S., Kudelka, M., Schneiderova, P., Fillerova, R., Gallo, J.: Inflammation time-axis in aseptic loosening of total knee arthroplasty: A preliminary study. PloS one 14(8), e0221056. (2019)
7. Pai, S., Bader, G. D.: Patient Similarity Networks for Precision Medicine. Journal of molecular biology 430(18 Pt A), 2924–2938 (2018).
8. etrackova, A., Horak, P., Radvansky, M., Fillerova, R., Smotkova Kraiczova, V., Kudelka, M., Mrazek, F., Skacelova, M., Smrzova, A., Kriegova, E.: Revealed heterogeneity in rheumatoid arthritis based on multivariate innate signature analysis. Clinical and experimental rheumatology 38(2), 289–298 (2020).
9. Ochodkova, E., Zehnalova, S., Kudelka, M.: Graph Construction Based on Local Representativeness. In: COCOON 2017: Computing and Combinatorics, pp. 654-665. Springer International Publishing, Hong Kong (2017).
10. Blondel, V. D., Guillaume, J.-L., Lambiotte, R., Lefebvre, E.: Fast unfolding of communities in large networks. Journal of Statistical Mechanics: Theory and Experiment 2008(10), 10008–12 (2008).
11. Bastian, M., Heymann, S., Jacomy, M.: Gephi: an open source software for exploring and manipulating networks. In: International AAAI Conference on Weblogs and Social Media (2009).

Formation and decay of unstable dimer ions in cold rare-gas plasmas

Fresnelle Tenanguena Nongni[1,2] and René Kalus[1]

[1]IT4Innovation, VSB – Technical University of Ostrava,
17. listopadu 15, 708 00 Ostrava – Poruba, Czech Republic
[2]Laboratoire Plasma et Conversion d'Energie, LAPLACE UMR5213 du CNRS,
Université de Toulouse III Paul Sabatier, 118 route de Narbonne,
F-31062 Toulouse Cedex, France
tenanguena.nongni.fresnelle.st@vsb.cz

Abstract. Molecular ions in particular dimeric rare gas ions have a very important influence on the behaviour of rare gas plasmas used in biomedical or space applications. Therefore, the analysis and understanding of their formation is of great importance for the macroscopic modeling of the charge distribution. The main objective of this work is to perform calculations of the formation constants of dimer ions in cold plasmas using rare gases (Ar, Xe, Kr) as carriers over a wide range of reduced fields. One of the major processes leading to the formation of diatomic rare gas ions is the ternary two-step stabilization mechanism. The first step of this mechanism, the formation and decay of unstable diatomic collision complexes, is addressed in the present contribution.

Keywords: Molecular ions · rare gas· cold plasma.

1 Introduction

Plasma is commonly known as the fourth state of matter after the solid, liquid, and gaseous states. It is an ionized gas consisting of electrons, atomics, excited species, and molecular ions. Plasma is used in many fields such as industry for surface treatment (etching, surface deposition), in space we have plasma thrusters that allow us to control the position of satellites on their orbits for telecommunication [1], and in biomedicine for applications of electro-surgery, tissue engineering, surface modification of biocompatible materials, sterilization of materials, treatment of cancer [2–4]. More and more, several researchers are working on this last field, more precisely on the treatment of cancer by plasma-based on rare gases (Ar, Xe, Kr).

When we defined plasma, we saw that it contains molecular ions and it turns out that these ions, more precisely dimer ions, are of primary importance for the elimination of cancer cells [5]. One of the major mechanisms of formation of these dimer ions is the ternary mechanism of stabilization.

$$Rg^+ + 2Rg \rightarrow Rg_2^+ + Rg \tag{1}$$

More specifically, this overall process consists of two elementary steps as follow:

$$Rg^+ + Rg \leftrightarrow [Rg_2^+]^* \tag{2}$$

$$[Rg_2^+]^* + Rg \rightarrow Rg_2^+ + Rg \tag{3}$$

The first step is the formation and decay of the unstable rare gas dimer ion $[Rg_2^+]^*$ which gives rise to the formation rate constants $K_1(\leftarrow)$ and $K_2(\rightarrow)$. The second step is the final stabilization of nascent unstable dimer ions giving rise to the formation rate constant K_3. The main objective of this work is to understand and analyze the formation of rare gas dimer ions in cold plasma. To do so, we started by understanding the formation and decay of the unstable rare gas dimer ion by calculating first the constant K_2 which is the inverse of the collision time.

$$K_2 = \frac{1}{\tau} \tag{4}$$

In this paper, we will present different methods of calculation of the collision time between Rg^+ and Rg (sec.2.1) and some results of calculation of the K_2 constant performed for a specific case of argon. These different calculations done for the ground state of the dimer ion Ar_2^+, $\mathrm{I}(1/2)_u$.

2 Methods and Implementations

2.1 Calculations of collision time τ

Collision time τ can be determined by the one-dimensional integration method or by solving the ordinary differential equations (ODEs) of the motion of two particles.

1D integral

$$\frac{1}{2}\mu\dot{r}^2 + V_{\text{eff}}(r) = E_{\text{coll}}$$

$$\tau = 2\int_{r_0}^{r_{\max}} \sqrt{\frac{\mu}{2[E_{\text{coll}} - V_{\text{eff}}(r)]}}\,dr \tag{5}$$

where E_{coll} is the total collision energy between the two particles (in thier center of mass frame), μ is the reduced mass, and V_{eff} stands for the effective potential energy.

$$V_{\text{eff}} = V(r) + \frac{L^2}{2\mu r^2}$$

Here, $V(r)$ is the potential energy of the interaction between the two colliding particles and L represents the orbital angular momentum of thier motion (again expressed in the center of mass frame).

ODEs of motion: Initial value problem

$$\mu \ddot{\vec{r}} = -\text{grad}V(r) \tag{6}$$

$$\vec{r}_0 = [\sqrt{r_{\max}^2 - b^2}, 0, b] \quad ; \quad \dot{\vec{r}}_0 = [0, 0, -\sqrt{2E_{\text{coll}}\mu}]$$

where b is the collision impact parameter.
However we did not use this method (See fig. 1) to obtain the different results presented in this paper.

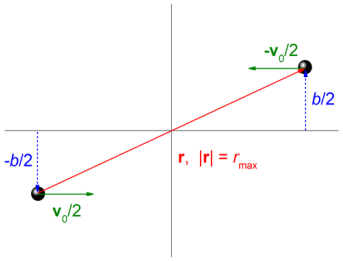

Fig. 1: Initial value problem.

2.2 Implementations

To calculate τ, we used equation by implementing it in a FORTRAN code using trapezoidal rule which is a numerical quadrature method. In mathematics, and more specifically in numerical analysis, the trapezoidal rule is a technique for approximating an definite integral.

$$\int_a^b f(x)dx \approx (b-a)\frac{1}{2}(f(a) - f(b)) \tag{7}$$

$r_{\max} = 10\mathring{A}$, $E_{\text{coll}} = (0.01 - 1eV)$ and $b = (0.1 - 10\mathring{A})$ are the different input data that allowed us to perform the calculation of the collision time integral give in equation. The impact parameter is implemented through the orbital angular momentum of the interaction between the two colliding particles. In fact, the

orbital angular momentum depends in our case on the impact parameter, the collision energy, and the reduced mass μ of the center of mass.

$$L = b\sqrt{\mu E_{\text{coll}}} \tag{8}$$

3 Results

To illustrate our calculations we have taken a rare gas, argon (Rg = Ar). Fig. 2 represents the collision time as a function of the collision energy (E_{coll}) and the impact parameter b for the potential energy surface (PES) of the ground state of the argon dimer ion Ar_2^+. The collision time increases with the impact parameter while τ decreases with increasing collision energy. This behavior can be expected since the increase of the collision energy makes the collisions faster. The observation of the different peaks in space on this figure correspond to long lived, so called *orbiting trajectories* which are known to appear if two particles interact via a potential which goes to zero at infinite distance faster than $1/r^2$. Taking into account that K_2 is the inverse of τ time, K_2 increases with decreasing τ for Ar_2^+, and expectedly also for the other rare gases. Higher values of K_2 correspond to lower values of τ. By taking into account the assumptions given previously with energy, we can say that larger value of K_2 corresponds to the higher collision energy.

Fig. 3 illustrates the various peaks observed in fig. 2 and corresponding to the orbiting trajectories mentioned above. In fact, the peaks may become infinite singularities for a specific dependence of the potential energy on inter-particle distance. It can be seen that the height of these peaks decrease with the collision energy.

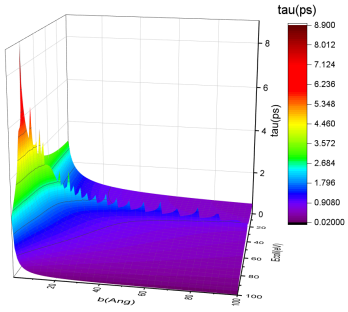

Fig. 2: The collision time τ as a function of the collision energy (E_{coll}) and of the impact parameter b for the potential energy surface (PES) of ground state of Ar_2^+.

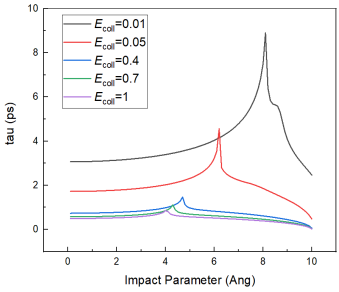

Fig. 3: The time τ as a function of the impact parameter b for different collision energies at the ground state of dimer ion Ar_2^+.

Fig. 4 and 5 allow us to see that the increase in the number of integration does not change much the collision time which may illustrate the superposition of the different tau curves as a function of b for different collision energies. This phenomenon is observed much better above 5000 integration steps, which means that the calculation is well converged in this case. Below this number of integration steps, we notice a slight increase in the collision time. Since the time is practically the same for the different number of integration steps, the rate constant K_2 at will hardly change for these different numbers of integration.

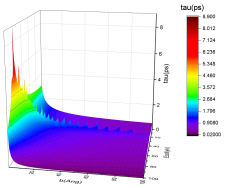

(a) For 1000 integrations

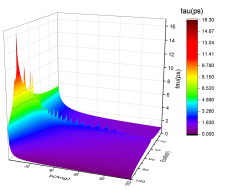

(b) For 5000 integrations

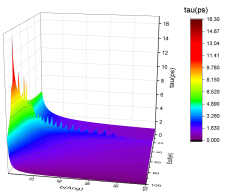

(c) For 10000 integrations

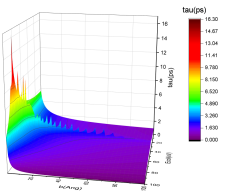

(d) For 50000 integrations

Fig. 4: The collision time τ as a function of the collision energy E_{coll} , the impact parameter b and different numbers of integration steps at as obtained for the ground state of the Ar_2^+ dimer.

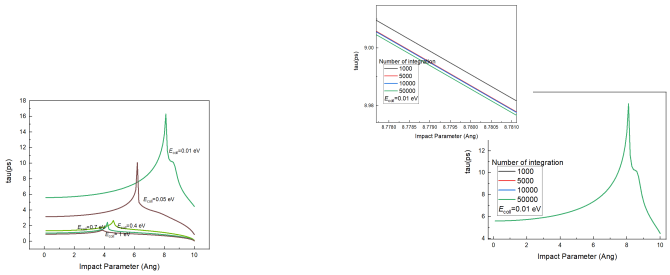

(a) (b)

Fig. 5: The collision time τ as a function of the collision energy E_{coll} , the impact parameter b and different numbers of integration steps at as obtained for the ground state of the Ar_2^+ dimer.

4 Conclusion

Ternary recombination process is one of the major processes of formation of dimer ions in cold rare-gas plasma. This process is follows in two elementary steps with different rate constants, K_1, K_2, and K_3. To calculate a complete kinetic data set for the ternary recombination mechanism, we started with K_2 which correspond to the formation of unstable short lived dimer ions. It follows that, the collision time as calculated for argon, has the higher value for the higher impact parameter and for the lower value of collision energy. Futher more, for high numbers of integration points, the calculated value of collision time is well converged. Results of the performed calculations will be used in the preparation of initial conditions of the second recombination step (unstable dimer stabilization) and also in calculations of the abundance of unstable dimer ions entering this stabilization step if conbined with known formulas for their formation rate.

References

1. AI. Bugrova, AM. Bishaev, AV. Desyatskov, MV. Kozintseva, AS. Lipatov, and M. Dudeck. : Experimental investigations of a krypton stationary plasma thruster. International Journal of Aerospace Engineering, (2013)
2. Ali Ak. Hussain, Hamid H. Murbat, AH. Tawfeeg and Nisreen Kh. Abdalameer. :Influence of Low-Temperature Plasma Argon on Bacteria. IOSR-JDMS **14**(7), 25–31 (2015)
3. F. Sanchez-Estrada, H. Qiu and RB. Timmons. : Molecular tailoring of surfaces via RF pulsed plasma polymerizations: Biochemical and other applications. IEEE International Conference on Plasma Science, 254 (2002)
4. Mounir Laroussi. : Plasma-based sterilization. OLD DOMINION UNIV NORFOLK VA DEPT OF ELECTRICAL AND COMPUTER ENGINEERING, (2003)
5. Michael Keidar. : Plasma for cancer treatment. Plasma Sources Science and Technology **24**(3), (2015)

Control Possibilities of Electric Drive with Frequency converter

Richard Blaho[0000−0002−0285−6633]

Department of Electronics, FEECS,
VSB – Technical University of Ostrava, 17. listopadu 15,
708 00 Ostrava – Poruba, Czech Republic
richard.blaho.st@vsb.cz

Abstract. This paper examines the possibilities of control and operation of an electric drive with a frequency converter using a combination of a PROFINET communication, HMI (Human-Machine Interface) control panel and a PLC (Programmable Logic Controller). In the first part, there are described general possibilities of communication and control of electric drives with a frequency converter in industrial automation. The second part is focused on the analysis and options for control of the frequency converters via the PROFINET communication bus and the standardized PROFIdrive profile. The third part is focused on possibilities of controlling electric drives with the frequency converters using HMI control panel with the SCADA (Supervisory Control And Data Acquisition) visualization and a control PLC. There is described a specific solution using SIEMENS components and devices. The fourth part is focused on the specific design of an instrumentation cabinet for control and operation of selected electric drive. This design can serve as a basic template and universal solution in industrial automation.

Keywords: Electric Drive Control, Frequency Converter, HMI, PROFINET.

1 Introduction

In recent years, electric drives with frequency converters have offered a wide range of options for controlling them. These functions allow optimal interaction between machine and operator contributes significantly to productivity, efficiency, and usability. In operation, these options mean economic and technical savings, which include greater savings in operating costs and in the time of individual production operators. Obsolete push-buttons and light indicators can be replaced by HMI interactive panels. Panels make it easier to work anywhere people must interact with machines and industrial technology. HMI panels provide a solution that is both flexible and can be integrated into communication networks, where it meets the requirements for transparency and data provision. These panels allow the operator to control the software application for controlling the production technology and it is possible to view and save production data. Most applications in the industry often use combi-

nations where the PLC operates as a master control system. The master PLC control slave devices such as an HMI control panel or a frequency converter. Input information to the PLC can be fed via hardware elements or read from the HMI panel communication. Communication between the devices is ensured via a communication bus such as PROFINET.

2 Control of frequency converter via PROFINET

PROFINET is the most widely used industrial Ethernet standard and can be used in industrial applications such as process control in automation. Ethernet uses CSMA/CD technology and therefore cannot guarantee the deterministic real-time (RT) response used in industrial fieldbuses. PROFINET is an open standard and is part of the international electrical standards IEC 61784 and IEC 61158. It allows communication using the classic TCP/IP protocol and can also be used for real-time communication. This function is used for motion control in industrial automation. For this reason, the most used communication model is PROFINET IO (Input/Output), which is adapted specifically for communication in the lowest process layers of the system. It guarantees deterministic real-time response and is specialized for fast data exchange between distributed IO devices. PROFINET IO specifies the communication between controllers (e.g. PLCs) and individual peripheral devices (e.g. frequency converters).

2.1 PROFIdrive

This is a standardized profile according to IEC 61800, which is used for communication with electric drive systems. With PROFIdrive, the behavior and access to internal data of individual electric drive devices can be defined. These are connected to the control device via the PROFINET communication bus.

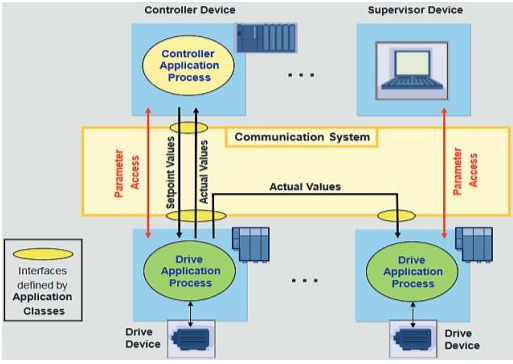

Fig. 1. General application model of the drive using PROFIdrive [3]

Application model. This model defines the possibility of access from control and monitoring devices to individual parameters, write and read data from the frequency converter. At the same time, it is possible to share the current values between

groups of frequency converters, this allows faster response and control of the respective motors. The entire application can be monitored and configured from operator devices. PROFIdrive contains three basic process types: the first control process is located in the frequency converter, this method is most commonly used for current control, speed control or motor position control. The second control process is based on the principle of PLC control, this is most often encountered in applications where the desired value of speed or position is calculated. The third control system consists of communication between the PLC and the frequency converter, the required data is transmitted for both control processes and depends on the selected type of control.

2.2 PROFIdrive application classes

The way in which drives with frequency converters are integrated into automation depends on the application class. Frequency converters contain a wide range of advanced functions that can be performed independently of the master control system. PROFIdrive therefore defines six basic application classes, these are determined by the type of functions on the digital outputs of the converter. The application classes indirectly define the communication between the control system and the frequency converter. A drive can be defined in one or more application classes. This allows manufacturers the flexibility to define and design products to meet specific market requirements.

Table 1. Application classes of frequency converters according to PROFIdrive

Class	Type	Description
1	Standard drive	The control system sets the desired speed value and the speed control is implemented by the drive.
2	Standard drive with additional function	In addition to speed control, the drives provide basic automation functions.
3	Positioning control	The drive also provides position control based on a setpoint from the control system.
4	Central position control	The drive provided speed control and the control system provides position control system. IRT communication required.
5	Central speed control	The drive provided position control and the control system provides speed control system. IRT communication is required.
6	Decentral control	Communication is between the individual drives. It is used, for example, for electronic cams.

3 Control of electric drive with the frequency converter

3.1 HMI – PLC – Frequency converter

Most applications in the industry most often use combinations where the PLC operates as a master control system. The PLC controls slave devices such as an HMI con-

trol panel or a frequency converter to which an electric motor is connected. Input information to the PLC can be fed via hardware elements or read from the HMI panel communication. Communication between the devices is then carried out over a communication bus, in this case a PROFINET network.

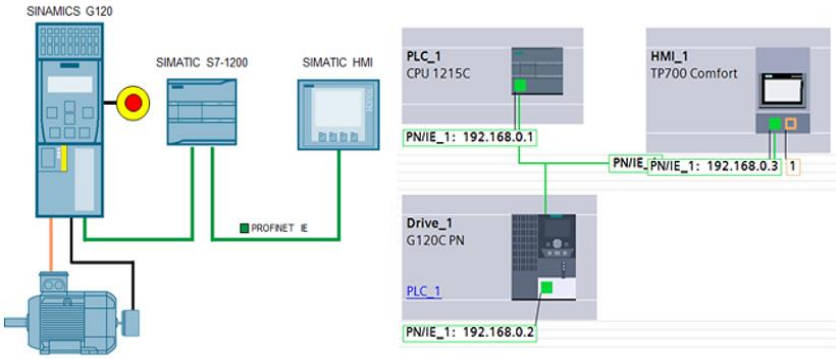

Fig. 2. PROFINET network diagram of electric drive with frequency converter

Each device connected to the PROFINET network has a fixed characteristic IP address set during initial parameterization. A control telegram is transmitted via PROFINET, in which the control words and parameters of the converter are stored. The electric motor parameters together with the ramps are set in the frequency converter, which is only an intermediate link in the application and is controlled from the master PLC. The control ramps can also be set using the PLC, where the frequency converter is used only for electrical motor control. These principles of wiring and control of frequency converters are the most widely used in practice because of the control of most technologies from the main computer application or visualization. In the software application, a procedure is selected where communication with the HMI and frequency converter has been programmed in the PLC control program, the process values of the frequency converter have been set and the feedback from the connected devices is processed. The visualization is located in the HMI control panel. Cyclic communication is used for data transmission, the control system (PLC) operates continuously and data (set-points, action values, measured output variables) are transmitted cyclically regardless of the control method.

3.2 SCADA visualization on HMI panel

For the control of an electric drive with a frequency converter, a visualization is created on the HMI touch panel. The visualization is used for controlling the frequency converter, displaying graphs and includes a service panel of the network connection and a list of users. Using this software visualization, the operator can set the parameters of the frequency converter to define the behavior of the connected motor. The operator can monitor on the HMI panel the current speed, torque, voltage, output frequency, current, power, temperature or frequency of the connected motor.

Assigned variables are expressed in the indicators using real values with the corresponding magnitude. Graphs of the measured and calculated variables of the frequency converter are an integral part of the visualization.

Fig. 3. Preview of the SCADA visualization on HMI panel

4 Design of instrumentation cabinet with frequency converter

Control cabinet is usually designed to control an electric drive with a frequency converter. These instrumentation cabinet contain all the devices necessary for the operation of the drive. There are fuses and surge protectors in the cabinet to protect the converter and the 24 VDC power system, which is designed as a 2PE, 24 VDC, FELV using a stabilized power supply. The frequency converter itself is powered from a three-phase 3NPE, AC 50 Hz, 400/230 V, TN-S supply led to the instrumentation cabinet. The protection of the frequency converter power supply is made according to the manufacturer recommendation in the data sheet, specifically the protection by means of 32 A/gR fuses. The supply is equipped with a type 3 surge protector. This surge protector here represents more sensitive protection, which is installed behind type 1+2 or type 2 arresters. The feeder from which the cabinet is normally supplied is protected by type 1+2 surge protectors and depends on the proper protection of the building from the effects of atmospheric surges as defined in IEC 62305. The HMI control panel is embedded in the cabinet door. This HMI panel is used to control the visualization, through which the motor connected to the converter can be controlled. Frequency converter control units usually contain safety inputs that can be used to provide safety functions. In this design, a safety circuit with STO (Safe Torque Off) function is connected into the safety inputs of the frequency converter control unit and one relay output is also been connected to the white LED indicator. The alarm is located on the door of the control cabinet and when activated, it visually signals the readiness of the frequency converter. The power output from the frequency converter is made by means of a shielded motor power cable for voltage levels 0.6/1 kV, which is directly designed for supplying motors from frequency converters. The cable contains copper shielding, based on which it can be recommended from an EMC point of view.

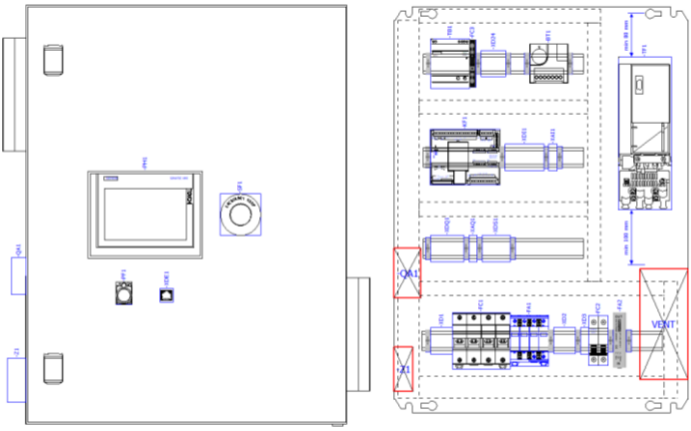

Fig. 4. Preview of the designed instrumentation cabinet and mounting panel

5 Conclusion

Digitalization in industrial electric drive applications with frequency converters has expanded significantly in recent years. Online monitoring devices are increasingly being used in this area to make working with frequency converters more efficient. This results in significant financial and time savings when commissioning new electric drives. The correct design of the control of the electric drive is crucial for the flawless operation of the selected application. HMI control panels can perform both input and display functions. It is a comprehensive solution suitable for selected industrial applications where the status of the technology needs to be monitored. In this paper, a complete universal solution is proposed that can be implemented with minor modifications for industrial applications such as conveyors, fans, pumps and other applications where speed control over time is required.

References

1. BLAHO, R.: Návrh ovládání elektrického pohonu s frekvenčním měničem. Ostrava, 2020. URL: http://hdl.handle.net/10084/140564
2. BRANŠTETTER, Pavel.: Elektrické regulované pohony III, učební texty. Ostrava: VŠB - TU Ostrava, 2012.
3. Profinetuniversity.com. Industrial Automation & Ethernet. URL: <https://profinetuniversity.com/category/industrial-automation-ethernet/>
4. Profinetuniversity.com. PROFIdrive application profile. URL: <https://profinetuniversity.com/application-profiles/profidrive-application-profile/>
5. Siemens. SINAMICS G110M, G120, G120P, G120C, G120D inverters, Fieldbus systems: PROFIBUS, PROFINET, EtherNet/IP, CANopen, USS, Bacnet, Modbus. URL: <https://cache.industry.siemens.com/dl/files/159/99685159/att_83708/v1/G120_Field_busses_FH17_0414_eng_en-US.pdf>
6. Siemens. Machine level visualization with SIMATIC HMI. URL: <https://new.siemens.com/global/en/products/automation/simatic-hmi/panels.html>

Tester of electric motors for vehicle's headlight leveling system

Marek Kubatko[0000−0002−8655−835X]

Department of Electrical Engineering, FEECS,
VSB – Technical University of Ostrava, 17. listopadu 15,
708 00 Ostrava – Poruba, Czech Republic
marek.kubatko@vsb.cz

Abstract. In the first part of the paper are described car lighting systems, how they evolved during past years and what are the main changes between those systems. The meanings of the terms static and dynamic system in the field of roadway illumination by a headlamp are given. Description of the LIN bus together with a brief analysis of the electric motors used for headlamp leveling and bending. The next part is focused on the design, implementation and verification of tester of electric motors for setting the illumination level on road, in the company engaged in the production of automotive lighting. The unique box was designed in cad software and printed on 3D printer, specifically for this purpose. A power supply was designed and made, and the control software was written in the Wiring language, typical for the Arduino development platform. The result of the paper is a portable tester for the analysis of electric motors used for headlamp leveling in cars.

Keywords: LIN bus · Tester · Electric motors

1 Introduction

Nowadays electronics in cars is becoming more and more prevalent, the demand for maintenance is increasing, as well as for the development itself. Incandescent headlights have been replaced by LED headlights, which are much more efficient than their predecessors, but more demanding on the control electronics. All comfort systems, from steering wheel and seat adjustment, window controls, air conditioning and cruise control, to security systems with central locking and immobiliser, to the information and navigation systems.

The previously used symmetrical lighting was replaced by asymmetrical lighting in 1957. The asymmetrical lighting distribution at ground level varies according to the market in which the cars are intended for. In countries with right-hand drive, the range for the dimmed of light has increased significantly without dazzling oncoming vehicles [1].

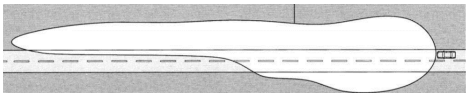

Fig. 1. Asymmetrical dimmed light (taken from [2])

2 Headlamp lighting systems

Headlight systems take care of not only the intensity but also the direction of the beam. They can be divided according to the function of the headlamp range control into manual and automatic. Manual adjustment is done manually by the driver using a switch. This type of lighting height adjustment is subjective, and the driver does not always set the level correctly. Automatic headlight tilt adjustment is provided without the need for driver intervention at all times, which should make it all safer and more secure. Automatic tilt adjustment is further divided into **static** and **dynamic**. The static system only detects the change in vehicle roll due to a change in load condition and adjusts the road illumination level accordingly. Dynamic systems react to both vehicle roll due to changes in load conditions and also to the change in tilt associated with driving by which is meant in particular starting and braking conditions. The most widely used bus for communication with headlights is the LIN bus.

2.1 LIN bus

For headlights, the LIN bus has started to be preferred because it has a lower manufacturing cost compared to the CAN bus and the baud rate for controlling the headlamp electronics is sufficient. The advantage of the LIN bus is the absence of the need to use special controllers. A microcomputer with an internal UART and a simple RC oscillator circuit is sufficient for control. These conditions led to the widespread use of LIN bus [3].

The principle of LIN bus communication It is a single master, multiple slave type of bus. Communicates with other slave nodes, which can be up to 16 in total including the master node 17. The maximum transfer rate of this single-wire bus reaches up to 20 kbit/s. Standardized transfer rates of 2400 bit/s for slow transfer, 9600 bit/s for medium-speed transmission and 19200 bit/s for fast transmission. Synchronization is always performed by the master at the beginning of each transmission [4].

The picture 2 shows an example of communication between a master unit and two slave units. The final LIN bus communication is given by the last line. Each communication is initiated by the master node by sending a header. The source can be the master node itself and this means that after sending the header, it will also initiate the sending of data to the slave unit. In the latter case, the data from the slave unit are requested and therefore after header is received, slave will start sending a response. Message receivers may be all slave units or the message may be intended for only one particular unit[5].

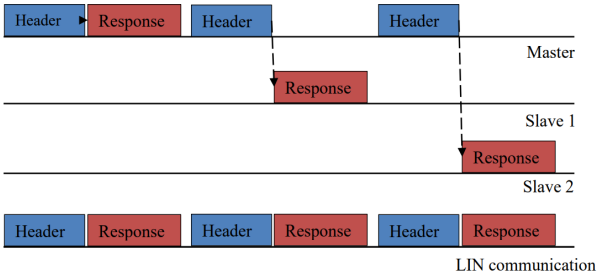

Fig. 2. LIN bus communication, 1 master 2 slave units, Blue rectangle - header, red rectangle - response

Electric motors Stepper motors for leveling headlamps are used in most cars. In this case for controller unit was chosen Arduino platform, so there is used special LIN transceiver TJA1028 to change the control voltage level from $5V$ typical for Arduino to $12V$ typical for the LIN bus. Cheaper variant are DC motors, which are not as accurate as stepper ones and also doesn't need any driver. Many cars also have bending lighting systems which helps light up the road when a car is turning. In the case of electric motor failure, an error message is sent to the control unit and the electric motor is set to an emergency position so that the projector does not dazzle the surroundings.

3 Design of tester for electric motors validation

Blocks like display, current sensor and LIN transceiver shown in picture 3 was expansion modules specially designed for Arduino. Measurement for shaft extension of the motor was realized by digital caliper, there was also need of voltage level shifter because digital caliper works on $1,5V$ Logic unlike Arduino on $5V$ logic. Frames sent by LIN bus will be described in the next chapter.

Comparison of the 3D design and the final tester can be seen in the picture 4. The measurement procedure is as follows, firstly it is chosen which motor will be analyzed, whereby only one type of motor can be tested at a time. User can see on display which option did he chose. There are two more possibilities, manual setting of position which is rather for debugging mode and then there is automatic mode which will execute setup and measurement of the motor, in the end of automatic mode testing station will show on display if the motor works properly or not.

3.1 The communication principle with stepper motor via LIN bus

At the beginning of any communication, it is necessary to ensure initialization of the stepper motor, which in the correct case is done only once and it can be done

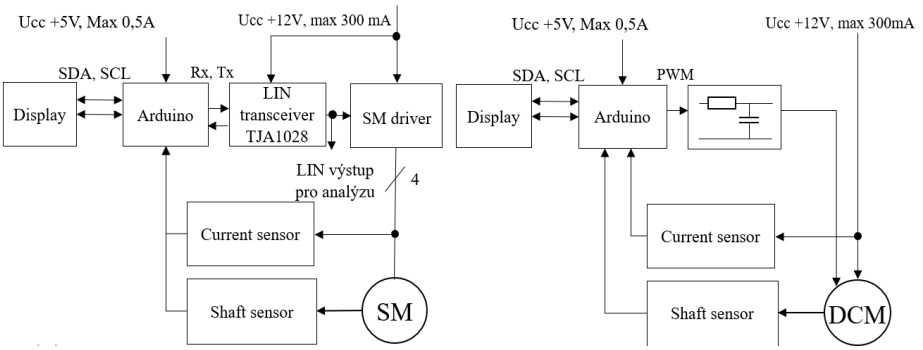

Fig. 3. Block scheme of electric motors tester (stepper motor left, DC motor right)

by static, or dynamic addresses. These determine the action to be performed by the motor, such as movement, setting the nominal position or motor diagnostics. Once the dynamic addresses have been correctly assigned identifiers, motion parameters such as speed and direction must be set using SetMotorParam function [6].

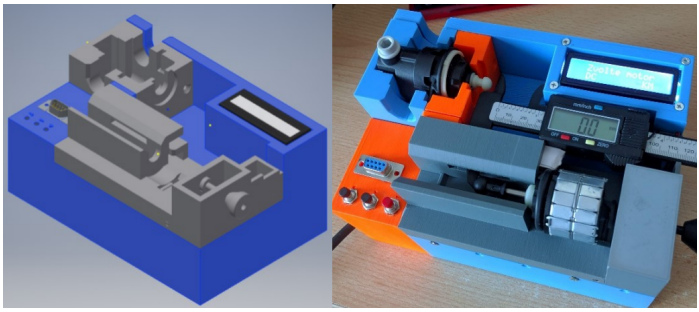

Fig. 4. 3D design versus final form of testing station

The difference between static and dynamic addresses from each other is not only by the initial setting as it is shown in table 1 and table 2. There is also diffrence which is best seen when sending individual commands. By assigning dynamic addresses we can define up to 16 functions that will have a shortened notation. These functions will be defined according to an identifier and when using them it will not be necessary to call the so-called preparing frame first and then the response frame, but it will be sufficient to send only one frame. In a dynamic type of message, a function is wrapped by an identifier along with the address of the slave node, thus facilitating motor control and overall communication on the bus.

Table 1. SetMotorParam function using static addresses

	ID	Data master	Data slave
Set parameter of motor	0x3C	SetMotorParam	
Request for parameter reading from motor	0x3C	GetFullStatus	
Reading parameter from motor	0x3D		SlaveResponse1
Reading parameter from motor	0x3D		SlaveResponse2
Cyclic motor position detection	0x3C	GetActPos	
Cyclic motor position detection	0x3D		ActPosMot

Table 2. SetMotorParam function using dynamic addresses

	ID	Data master	Data slave
Dynamic address assignment	0x3C	DynamicID 1 - 4	
Set parameter of motor	0x3C	SetMotorParam	
Request for parameter reading from motor	0x3C	GetFullStatus	
Reading parameter from motor	0x3D		SlaveResponse1
Reading parameter from motor	0x3D		SlaveResponse2
Cyclic motor position detection	0x24	GetActPos	

4 Verification of tester functionality

A test has been performed to ensure that the tester is working properly, which included verification of error-free communication over the LIN bus. This communication was analyzed using Vector's CANoe software environment using a converter VN8914A and a configuration designed to analyse this bus.

The functionality of the application software was also verified in individual options for both motors. Here the main objective was to debug the program and ensure its functionality in all possible cases that may occur when using it.

Using the CANoe program, the communication between the microcontroller and the stepper motor controller was analyzed. Initialization of the measured motor and subsequent check of the set positions such as maximum, minimum and nominal position. These positions were also verified by the digital caliper. The exact position must match with the address which is got via LIN bus with an accuracy of $+-1mm$.

It was possible to read the measurement displayed on the display of digital caliper and also the data displayed on the serial line using the serial monitor in the programming enviroment arduino.ide. It doesn't matter from which position the sliding scale of caliper starts sending distance values, but it does matter, what is total distance the shaft has traveled.

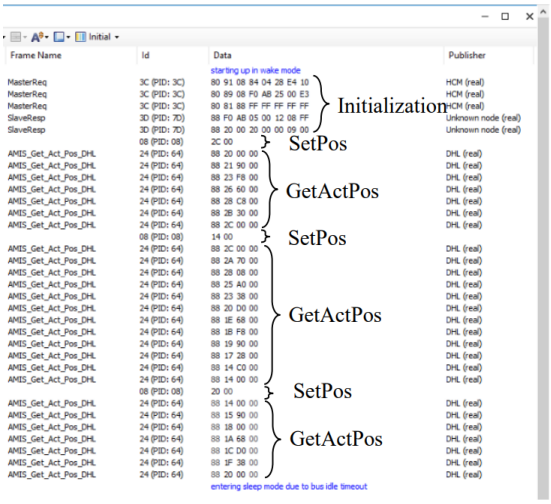

Fig. 5. Record of communication between the controller and stepper motor via LIN bus

5 Conclusion

In the paper, the LIN bus communication and its usage in communication with stepper motors used for headlamp leveling in automotive was described. The testing kit can analyze stepper and DC types of motors used in headlamp systems. The LIN frames for motor initialization were described and difference between static and dynamic addresses were discussed. Verification of tester functionality was performed and a record of the communication between the stepper motor and the controller was displayed in figure 5. The result of the work was the development of a test tool for the analysis of selected types of electric motors.

References

1. VLK, František. *Elektronické systémy motorových vozidel 2*. Brno: TINLIB, 2002. ISBN 80-238-7282-6.
2. OSVĚTLENÍ MOTOROVÝCH VOZIDEL. *Sinz* [online]. Brno, 2006 [cit. 2020-5-12]. http://www.sinz.cz/archiv/docs/si-2006-05-292-300.pdf
3. LIN BUS EXPLAINED. *Csselectronics* [online]. [cit. 2020-2-21]. https://www.csselectronics.com/screen/page/lin-bus-protocol-intro-basics/language/en
4. LIN - Local Interconnect Network. *Automatizace* [online]. 2004 [cit. 2020-2-21]. https://automatizace.hw.cz/clanek/2005101501
5. Sutorý, Tomáš *Local Interconnect Network.* [online]. [cit. 2019-11-8]. http://www.elektrorevue.cz/clanky/04012/index.html
6. AMIS-30621 LIN Microstepping Motordriver. *Alldatasheet* [online]. [cit. 2020-5-1]. https://pdf1.alldatasheet.com/datasheet-pdf/view/192177/AMI/AMIS-30621.html

Peltier Cell Control in Low Temperature Field

Vojtech Sotola[0000−0002−5238−9607]

Department of Electronics, FEECS,
VSB – Technical University of Ostrava, 17. listopadu 15,
708 00 Ostrava – Poruba, Czech Republic
vojtech.sotola@vsb.cz

Abstract. This paper describes various usage of semiconductor thermoelectric elements, usually labelled Peltier cells, which is only trade name. To distinguished two types of Peltier cells, we refer to first type as ThermoElectric Cooler (TEC) and the second type as ThermoElectric Generator (TEG). The paper deals with the controllability of the TEC cell, whether current control (the action is a current signal) or voltage control (the action is a voltage signal) is preferable, because it is not clear whether the TEC behaves as a linear load or a non-linear load. Also decision between continuous signal or pulse-width modulation (PWM) signal for excitation is presented. Measurements were made on several commercially available TEC cells. The work also deals with the control of a multistage TEC module, for which a simulation scheme has been developed and verified by measurements. Pt1000 temperature sensors were used in the verification due to their resolution and good dynamic properties (small time constant τ_{sensor}). Finally, the obtained results were evaluated.

Keywords: Peltier Cell · Thermoelectric Cooler · Multistage · Cooling · Peltier effect · Pulse Width Modulation.

1 Introduction

The use of thermoelectric elements for cooling has been known since the 1960s [3]. These elements work as a heat pump, transferring heat from one side (cold side) to the other (hot side). The advantage over the conventional use of a heat pump with a compressor is that each side can be changed according to the sense of the current flowing into the element. It is also possible to use these elements to generate electricity or the aforementioned cooling. The design varies slightly according to the application. Thermoelectric coolers (TEC) are primarily used for cooling, often used in portable car refrigerators, air dryers etc. But nothing prevents its use as a generator, due to slight design differences compared to a thermoelectric generator (TEG). The efficiency in the region of higher temperature gradients is lower, the maximum possible temperature is different, but in the region of low temperature gradients it can show better characteristics than a TEG, this is discussed in the article by Machacek et al. [5].

This paper focuses on techniques for achieving low temperature on the cold side. It discusses the applicability and controllability of TEC modules. TECs used in commercial electronics commonly reach temperatures near 273.15 K. Theoretically, it is possible to reach very low temperatures, the paper by Gurevich et al. [2] described an achievable temperature around 50 K, but this temperature was achieved by a combination of various cooling means (e.g., the use of liquid gases), which implied special laboratory equipment that prevented deployment in the commercial field. Keeping the warm side close to room temperature (300 K) appeared to be the biggest problem. A suitable temperature sensor must also be selected for appropriate control, hence this issue is also marginally mentioned. Based on the measurements, a simulation scheme for the controller setup was also prepared.

2 Thermoelectric Cooler

The TEC cell was used for cooling. It is a heat pump, which works on the principle of the Peltier effect. The basic arrangement of a single cell is shown in Fig. 1. N and P type semiconductors are placed alternately on a ceramic substrate, which are connected to each other by copper conductors – bridges.

Solid solutions of $A_2^V B_3^{VI}$, mostly tellurides (bismuth and antimony), have proven to be a good semiconductor material. The P-type material is an alloy of 70% Bi_2Te_3 and 30% Sb_2Te_3 with activators. Material type N is composed of 80 % Bi_2Te_3 and 20 % Bi_2Se_3 also with a suitable activator (see [3, 1, 6] for more details). The individual cells can be wired in series or parallel, resulting in a cell (module) that can be purchased commercially. In most cases, individual cells are wired electrically in series and thermally in parallel. The manufacturer usually distinguishes the supply wires by colour; when the power supply is connected correctly, then the cold side, which usually has an indication, starts loosing heat.

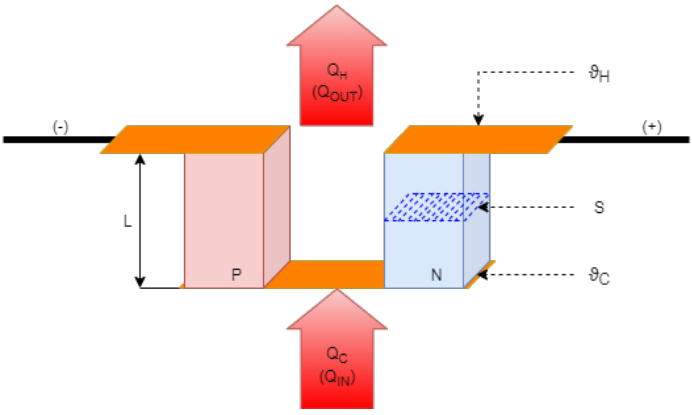

Fig. 1: Peltier cell (taken from [6])

2.1 Mathematical model

The mathematical model is based on Fig. 1. The following assumptions must be made:

- the dimensions of the semiconductor crystals are constant,
- the heat generated by the current flow through the semiconductor is generated throughout the whole volume of the crystal,
- none of the coefficients is temperature dependent.

After introducing these simplifications, the TEC can be described by the following equations:

$$Q_C = 2n \left[S_C I \vartheta_C - \frac{1}{2} R \frac{L}{S} I^2 - K \frac{S}{L} (\vartheta_H - \vartheta_C) \right], \tag{1}$$

$$U = 2n \left[S_C (\vartheta_H - \vartheta_C) + IR \frac{L}{S} \right], \tag{2}$$

Where Q_C the heat is taken on the cold side,
n is the number of active cells,
S_C is the Seebeck coefficient,
R is the electrical resistance,
L is the height of the crystal,
S is the area of the crystal base,
I is an electric current flowing,
K is the thermal conductivity,
ϑ_H is the hot side temperature,
ϑ_C is the cold side temperature,
U is the electrical voltage.

The equation 1 can be decomposed into three components:

$S_C I \vartheta_C$ – Peltier cooling effect,
$\frac{1}{2} R \frac{L}{A} I^2$ – this part represents the losses due to the current flow (Joule heat); the coefficient $\frac{1}{2}$ has this value because it is assumed to be evenly distributed, i.e. one half heats the cold side and the other half the hot side,
$K \frac{S}{L} (\vartheta_H - \vartheta_C)$ – represents the Fourier effect, i.e. the penetration of heat from the hot side to the cold side.

In practice, these relationships provided only a rough estimate, because introduced assumptions simplified problem extensively. For accurate modelling, it is advisable to use the simulation tools of the cell manufacturers, because the they have prepared a model based on accurate measurements on samples. [6]

Several types of TEC cells are available on the market. They differ in cooling power, maximum voltage, current, or maximum operating temperature. They are available in two basic designs: Singlestage, Multistage.

3 Controllability of TEC

For the design of the regulation, it is necessary to know which variable can be controlled. For example, for LED lamps. Current control is found to be preferable to voltage control because the luminous flux is current dependent and LED is not a linear component, hence the unsuitability of voltage control. [4]

Measurements were made at the current and voltage supply of the TEC cells. The steady-state value of the temperature gradient $\Delta\vartheta$ was measured with the excitation signal set. Graphs of 2b to 2d were made from the measured data. The measured TEC cells are listed in table 1.

Table 1: Measured TEC cells

TEC cell	Size	Q_{max}	U_{max}	I_{max}	$\Delta\vartheta_{max}$	ϑ_{max}	R_{module}
	mm	W	V	A	°C	°C	Ω
TEC1-071030	30X30	16	9,2	3	75	90	2,75
TEC1-12710	40X40	90	16,4	10	75	90	1,58
HP-127100	40X44	90	16,4	10	70	200	1,58

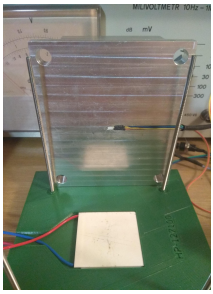

(a) Measuring stand

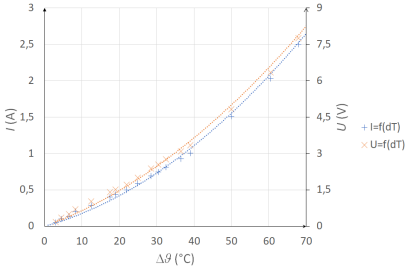

(b) TEC1-071030

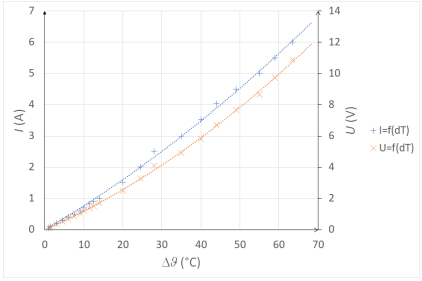

(c) TEC1-12710

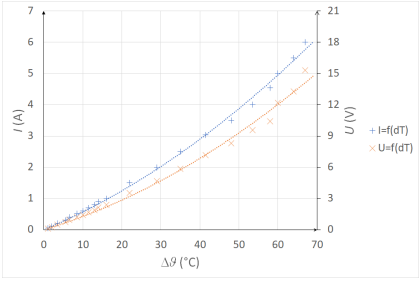

(d) HP-127100

Fig. 2: Measurement of controllability

4 Regulation

It was decided to build a multistage TEC from individual cells because measurement from section 3 pointed out that singlestage TEC had low temperature gradient. The module is connected electrically in parallel, thermally in series, everything is shown in Fig. 3a.

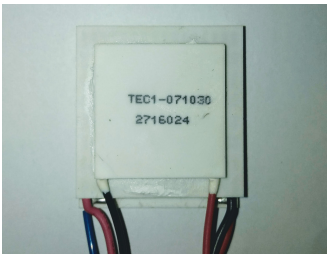

(a) Photo

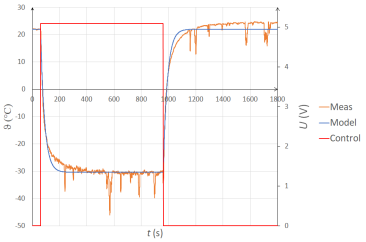

(b) Transient response

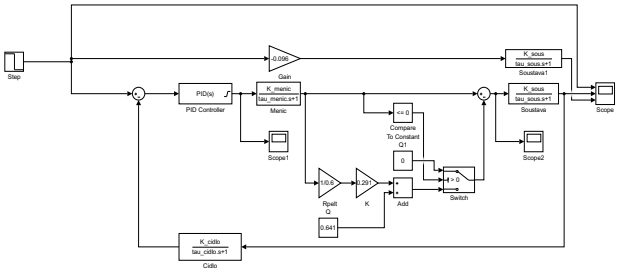

(c) Regulation simulation scheme

Fig. 3: Multistage TEC

The transient characteristic (Fig. 3b) was measured to determine the transfer function (see Eq. 3). The input variable was the value of the 8b register for the PWM module in the MCU, i.e. the maximum value of the input variable was 255, the transfer function (especially the gain) depended on this.

$$P1_{kas} = -\frac{10.429}{1 + 30.025s} \tag{3}$$

This resulted in the simulation circuit shown in Fig. 3c. Simple PI controller was then built on a MCU ATMEGA16. Subsequently, a verification measurement was performed, which is shown in Fig. 4.

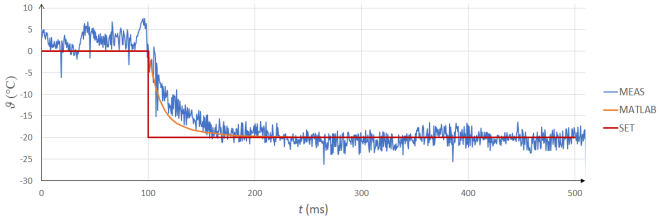

Fig. 4: Transient response of regulation

5 Conclusions

Based on the measurements made in section 3, it can be concluded that there is no deviation of shape of temperature difference whether it was current control or voltage control. The characteristics from Fig. 2b to 2d are nonlinear and can be approximated by a second order polygon, but the difference between current and voltage was only in scale, i.e. the cell itself behaves linearly. The time constants of TECs were large enough to have TEC regulated by PWM signal. From Figure 3c it is clear that the simulation scheme is fully functional when compared with the measured waveform (Figure 4) of the real circuit. The measurement waveform is loaded with noise. Otherwise, the simple transmission model can be used to simulate the behavior and completion of the controller. It must be taken into account that the time constant of the TEC module itself is 30 s, the real measurement is tedious and the simulation is done in few minutes.

The work has met its objectives and found a suitable simplified model of a multistage TEC cell. Future work is needed to verify the effect of the cooled object on the parameters of the whole system.

References

1. Compendium (2012), https://www.meerstetter.ch/customer-center/compendium/
2. Gurevich, Y.G., Logvinov, G.N., Fragoso, O.A., et al.: Lowest temperature at thermoelectric cooling. In: 2007 4th International Conference on Electrical and Electronics Engineering. pp. 369–372 (2007). https://doi.org/10.1109/ICEEE.2007.4345042
3. Hassdenteufel, P.I.J., Květ, I.K., kolektiv: Elektrotechnické materiály. SNTL, Praha, první edn. (1967)
4. Liou, W.R., Lin, C.Y., et al., T.H.C.: Multi-channel constant current led driver with temperature and voltage compensation. In: 2010 International Conference on Communications, Circuits and Systems (ICCCAS). pp. 527–531 (2010). https://doi.org/10.1109/ICCCAS.2010.5581937
5. Machacek, Z., Walendziuk, W., et al., V.S.: An investigation of thermoelectric generators used as energy harvesters in a water consumption meter application. Energies **14**(13), 22 (2021). https://doi.org/10.3390/en14133768, https://www.mdpi.com/1996-1073/14/13/3768
6. Šotola, V.: Optimalizace řízení peltierova článku v oblasti nízkých teplot (2020), http://hdl.handle.net/10084/140503

Author Index

Editors:	Michal Krátký, Jiří Dvorský, Pavel Moravec Dept. of Computer Science VSB – Technical University of Ostrava
Title:	WOFEX 2021
Place, year, edition:	Ostrava, 2021, 1st
Page count:	467
Edit:	VSB – Technical University of Ostrava, 17. listopadu 2172/15, 708 00 Ostrava-Poruba Czech Republic

Not for sale.

ISBN 978-80-248-4523-4 (on-line)
DOI 10.31490/9788024845234